transactions of the ASME

Published Quarterly by
The American Society of
Mechanical Engineers
Volume 95 • Series C • Number 2
MAY 1973

journal of heat transfer

EDITED and PUBLISHED quarterly at the offices of The American Society of Mechanical Engineers, United Engineering Center, 345 E. 47th St., New York, N. Y. 10017. Cable address, "Mechaneer," New York. Second-class postage paid at New York, N. Y., and at additional mailing offices.

CHANGES OF ADDRESS must be received at Society headquarters seven weeks before they are to be effective. Please send old label and new address.

PRICES: To members, $15.00, annually; to nonmembers, $30.00. Single copies, $10.00 each. Add $1.50 for postage to countries outside the United States and Canada.

INDEXED by the Engineering Index, Inc.

(Contents continued on page 262)

CONTENTS

(CONTINUED)

H. W. EMMONS
Gordon McKay Professor of Mechanical Engineering, Division of Engineering and Applied Physics, Harvard University, Cambridge, Mass.
Fellow ASME

Heat Transfer in Fire

The essential role played by heat and mass transfer processes in fire is discussed, and the need for the development of an understanding of fire through the application of analysis and modeling techniques so successful in heat transfer is indicated. Practical design for fire protection today stands where heat transfer design stood 50 years ago. Many of the same techniques that changed heat transfer design from an empirical to a rational process can similarly transform fire safety design and fire control operations.

Introduction

LIKE ALL multifaceted societal problems, the reduction of the U. S. world-beating fire loss record can only be accomplished by attacks on many fronts. The design of safer cities, buildings, and furnishings, the organization of and training for the fire services, the economic tradeoffs implied in the selection of various levels of fire safety, the psychology of carelessness in handling fuels and matches, the national (and international) support of fire research and development, the governmental procedures for code adoption and enforcement are but a few of the necessary considerations.

In this paper I intend to examine only those technical aspects of fire in which physical transfer processes are involved. While we will have to guard against the possibility of developing a "blind man's view of the elephant," fire is such that heat and mass transfer processes are involved in an essential way in nearly every feature.

The simplest but very useful view of a fire is that of the fire triangle, Fig. 1. All three elements are essential to a fire. The lines connecting these three elements are the transfer processes that make it possible for a fire to burn. Extinguishment processes involve the complete removal of one of the three elements or the breaking of the connecting lines.

A fire spreads as fast as the reactants can mix and can be heated to a sufficiently high temperature by feedback heat transfer from the fire.

Fire Phenomena

We are surrounded by fuels. Our clothing, our buildings, our cities are geometric arrays of assorted combustibles. In fact, modern progress in many areas has meant new plastics and new liquid fuels of various kinds. And of course we are intimately surrounded by air containing 21 percent oxygen. Thus the base of the fire triangle is ever present. All we need is heat, from friction, from an electric appliance, from a match, to provide the ignition.

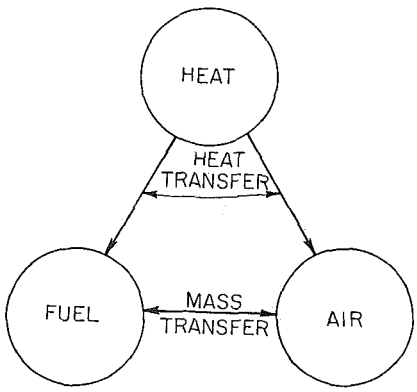

Fig. 1 The fire triangle

Our world is unstable. Once started, the reactions between essential components of our environment produce enough heat to raise the temperature of the as yet uninvolved fuel. Thus the fire spreads.

By the same conductive, convective, and radiative processes that spread the fire, someone (or something) eventually detects the fire and sounds an alarm. The extinguishment process is started. People remove themselves and some of the more valuable fuels. By applying water or other agent, heat is removed, the air is partially excluded, and the normal fire heat transfer mechanisms of the fire triangle are greatly altered. Thus the fire is eventually brought under control.

During the active fire phase, many gaseous products are produced and a great deal of damage is caused by the convective distribution of smoke, soot, and toxic gases. The property value destruction is not only direct by fire or indirect by smoke, but also by the extinguishment process itself. About half of the fire damage claims are paid for water damage.

Over the centuries, man has had to cope with as well as use fire. Present-day procedures of design for fire safety, selection of fire-safe materials, detection methods, and extinguishment actions are based upon a growing knowledge in all relevant scientific and engineering areas as well as upon accumulated experience. This experience, together with the best judgment of many dedicated people, has resulted in our fire codes and standards. Because of the complexity of fire, only the barest begin-

Contributed by the Heat Transfer Division of THE AMERICAN SOCIETY OF MECHANICAL ENGINEERS and presented as an invited lecture at the Winter Annual Meeting, New York, N. Y., November 26-30, 1972. Manuscript received by the Heat Transfer Division September 28, 1972. Paper No. 72-WA/HT-63.

ning has been made on the quantitative prediction of fire behavior. As a consequence, fires frequently present us with surprises, and standard tests have many loopholes.

Our present-day practical fire engineering stands about where heat transfer stood half a century ago. Then, a few pioneers, Saunders, McAdams, etc., saw what the techniques of data correlation could do for heat transfer design—but the practitioners didn't believe it. They preferred specific empirical tests or best judgment. So today with fire, little correlation or analysis has yet been done and there are many who think it unnecessary. But just as heat transfer has been raised to a fair degree of rational engineering during the past 50 years, so I believe fire engineering will be made rational instead of empirical during the next 50 years.

Physical Laws

As useful as the fire triangle has been and still is for qualitative thinking about fire, it must be supplemented with the full force of the known physical laws if rational quantitative results are to be attained.

Perhaps the most powerful physical law is the conservation of mass. In fire this plays an essential role in conserving not only total mass but every individual chemical species that must be quantitatively accounted for except as it may be created or destroyed in the reactions.

All motion is controlled by Newton's laws, and the motions of gases, liquids, and solids in fires are no exceptions. The forces that cause the motions may be a fan, as in a ventilating system, although in fires the overwhelming force available is gravity. Natural convection moves the fire gases, gravity drains the extinguishing water down through a building, hopefully to put the fire out on the way, and gravity causes the building to collapse if the fire (or sometimes only heat) moves too far into the structure.

Finally, the conservation of energy controls the energy distribution throughout the system. The heat transfer mechanisms provide the energy feedback that propagates the fire and determines the amount and distribution of extinguishing agent required to put it out.

These general conservation laws must be supplemented by many other facts and "laws" controlling the whole system. One essential supplement is chemistry [1].[1] Without reactions there is no fire. Both thermodynamic equilibrium chemistry and reaction rate chemistry are essential. We need not only a knowledge of the rapid and obvious reactions with the oxygen of the air but also the many very complex reactions of pyrolysis, some of which occur in the absence of air. Finally, the chemistry of inhibitors plays an important role in preventing or decreasing fire spread. Other important phenomena are the mutual diffusion of gases, the diffusion of liquids and gases through porous solids, the radiation produced by burning materials and the radiation absorbed by other bodies, and the variation of thermodynamic, chemical kinetic, transport, radiative, and mechanical strength properties of materials over the fire temperature range (up to perhaps 1500 deg C).

When we observe that all these phenomena occur intimately intermixed in a complex geometry (my house is not like your house), an expert in any field immediately abandons fire to the hapless and returns to his specialty for a "reasonable" problem. In fact, this is just what should have happened up to the present time, because there was not yet enough known about the individual pieces to attempt to assemble the puzzle. However, now is the time to take a new look, to detect and analyze the simpler parts of a fire, and thus to open up the future to rational approaches.

The remainder of this paper will be devoted to a glance at some of the pieces that have been successfully attacked and some speculation about the future.

The Equations

It is an interesting and not too difficult occupation to develop general equations for the flow of multicomponent gas mixtures with heat conduction, diffusion, viscous friction, and radiation interchange [2, 3]. It is somewhat harder to be sure the equations are correct if we superimpose a rain of water droplets from a sprinkler system. It is still more difficult to write the general equation system for the movement of reacting pyrolysis products through a piece of partially decomposed wood. In fact, some of these equations have not yet been written.

Yet to write them, to solve special cases, and to compare those solutions with experimental results is the only way to learn what is really important. A few illustrative examples will be given in a later section.

We should immediately note, however, that the above scientific approach encounters three major obstacles:

1 turbulence
2 immensely intricate chemistry
3 a general paucity of knowledge of the requisite physical constants as functions of fire temperatures and compositions.

The presently available limited methods for the treatment of turbulent flows can be applied to those encountered in fires. New knowledge of turbulence from any source can of course be used. However, we would expect the greatest success in the fire field to come as it has in every other field, namely, by the *recognition of the key independent dimensionless variables* in the presentation and generalization of experimental data.

In spite of great effort, the full chemistry—equilibrium and kinetic—is known for only about half a dozen combustion reac-

[1] Numbers in brackets designate References at end of paper.

Nomenclature

A = area, window or vertical-shaft cross section
b = thickness of stick in crib
B = heat ratio, heat of combustion plus ambient to surface enthalpy difference/heat required to produce unit mass of fuel vapor
C = wood species burning constant in open region, $\dot{m} = Cb^{-0.5}$
C_p = constant-pressure specific heat
D = diffusion coefficient, diameter
E = chemical kinetic activation energy
f = friction coefficient
g = gravity constant
G = theoretical Froude number = $\frac{w_t}{\sqrt{gh}}\left(\frac{\rho}{\rho - \rho_0}\right)^{1/2}$
h = crib height
H = window height
k = thermal conductivity of combustion gases
L = characteristic length, flame height
$\dot{m}$ = rate of burning
p = pressure
P = perimeter of vertical shaft
Q = heat of combustion
R = gas constant
T = temperature
ΔT = temperature difference, ambient to average gas
U = ambient velocity
w_t = combustion gas velocity in vertical shaft
β = coefficient of thermal expansion of fire gases
ϵ = emissivity, heat required to produce unit mass of fuel vapor
μ = viscosity
ν = kinematic viscosity
λ = ratio of mass flux leaving to mass flux entering a crib shaft
ρ = density
σ = surface tension, Stefan–Boltzmann constant
φ = $\frac{fhP}{2A}$, drag coefficient

Subscripts

0 = ambient
e = srfac su
f = flame
t = shaft

tions, and none of these is of much practical importance. The burning of hydrocarbons, cellulose, and plastics presents enormous difficulties to the attainment of a full knowledge of the chemistry. In fact, it appears that the use of the complete chemistry in fire design calculations would be blocked by its complexity even if it were known. *For each aspect of fire, therefore, we must strive to understand that part of the chemistry that is controlling* and to relegate the remainder to corrections or neglections. Thus, for ignition, the initial low-temperature reactions are important [4, 5]. For flame speed in a premixed mixture, it is necessary to include a considerable number of reactions to get the necessary precision [6, 7]. For a steady burning fire, only a few key reactions or none at all are important. As always, the slowest process in a series system controls the overall speed. At fire temperatures there are many very fast routes from fuels to products, and often the slowest process is the mixing of the fuel and air. This dynamic control may be in a boundary layer or wake near the fuel or it may be the size of the open window that sets the burning rate in a room by limiting the flow of air in and fire gases out.

The limitation set by our lack of knowledge of essential properties of materials must be corrected by measuring them as needed. There will have to be programs in the future to measure and tabulate the thermodynamic, transport, radiative, and chemical kinetic constants needed in the fire field, just as has been done in other fields in the past. Some of the required information is already available in handbooks, but a considerable expansion in the fire range of variables can be anticipated.

Modeling

Most people, seeing this word, conjure up images of a large something or other next to a small laboratory-size geometrically similar device. From years of work in heat transfer, we know that this picture is correct but far too limited. A model need not be smaller, it need not be geometrically similar, and it must have suitable similarity in many more subtle ways than meet the eye.

Modeling is in fact synonymous with dimensional analysis or similarity analysis, namely, the recognition of the really controlling variables in the given system. Any test result obtained in any way other than during actual use requires a knowledge of the independent dimensionless variables if the performance during a subsequent use is to be predicted. This fact has not yet been adequately recognized in fire testing.

Fire is a system more complex than has been encountered in heat transfer. Thus if we make a list of all the physically significant variables we can think of, we get 15 to 25 by the time we have included geometry, dynamics, chemical composition, heats of reactions, chemical kinetic constants, transport coefficients, and radiative properties. A routine dimensional analysis of this list reduces it by 3 to 5 variables, which is not much help. This is not the way to proceed.

To use dimensional analysis on the fire problem taxes one's knowledge of what is really important. The specific fire situation must be understood in a sufficiently intimate way to be able to select the most important variables only, neglecting all others. This accomplishment is made possible but not easy by the fact that high precision is not required. More than the usual degree of judgment is required. Hence care must be taken to experimentally vary all the important physical variables in verifying the completeness of the chosen dimensionless formulation.

The modeling process has only begun to be used in the fire field. Table 1 lists some of the important variables. Many of these are familiar heat transfer numbers. The new ones are various burning rate numbers, Co, Cm, Cn, Ce; various numbers related to heats of evaporation and combustion, Da_2, B; and numbers related to chemical kinetics, E/RT, Da_1.

For fires, B is perhaps the most important new independent variable since it controls the effects of blowing (by fuel pyrolysis) at the fuel surface on the heat and mass transfer and hence the burning rate.

Some Solutions

In this section I will present a brief look at some of the problems that have been attacked by methods familiar to those who work in heat and mass transfer. As I have already said, only a very limited number of fire problems have been attacked in this fashion, and therefore an expert in the fire area has a semiquantitative empirical knowledge of fire over a much greater range of circumstances than is covered in the following discussion.

Flame Speed. If a premixed mixture of reactive gases is ignited, a flame travels through it at a nearly constant rate. I have to say "nearly" because the measured speed varies a little with the geometry and material of the apparatus and with the method of measurement.

The flame is basically a chemical reaction propagated through the mixture by the diffusive mechanism for heat and species. As was first assumed by Mallard and LeChatelier [8], a flame crudely consists of two parts: a preheating zone and a reaction zone. Heat and active molecular species diffuse from the active reaction zone into the unignited mixture and thus control the flame speed. Hirshfelder et al. [6] were the first to write the full equations required for a quantitative calculation of flame speed from given chemical kinetics. For the few reactions for which the full chemical kinetics are known, the predicted speed is within experimental uncertainty. However, recently [7] it has been shown that for

Table 1 Significant dimensionless variables of fire

Some of the new ones have not yet been generally accepted or standardized.

Reynolds number	$\mathrm{Re} = \dfrac{UL}{\nu}$
Grashof number	$\mathrm{Gr} = \dfrac{g\rho^2L^3\beta\Delta T}{\mu^2}$
Prandtl number	$\mathrm{Pr} = \dfrac{C_p\mu}{k}$
Schmidt number	$\mathrm{Sc} = \dfrac{\nu}{D}$
Lewis number	$\mathrm{Le} = \dfrac{k}{C_p\rho D}$
Froude number	$\mathrm{Fr} = \dfrac{U}{\sqrt{gL}}\left(\dfrac{\rho}{\Delta\rho}\right)^{1/2}$
Nusselt number	$\mathrm{Nu} = \dfrac{hL}{k}$
Weber number	$\mathrm{We} = \dfrac{\rho U^2 L}{\sigma}$
Radiation number	$R = \dfrac{\epsilon\sigma T^3}{C_p\rho U}$
Heat ratio	$B = \dfrac{Q + C_p(T - T_s)}{\epsilon}$
2nd Damköhler number	$\mathrm{Da}_2 = \dfrac{Q}{C_pT_0}$
Molecular weights, stoichiometric coefficients, and initial compositions:	
Activation energy numbers	$\dfrac{E}{RT}$
Combustion numbers	$Co = \dfrac{\dot{m}}{\rho U}$
	$Cm = \dfrac{\dot{m}}{\mu L}$
	$Cn = \dfrac{\dot{m}}{\sqrt{\rho(\rho - \rho_0)gL}}$
	$Ce = \dfrac{\dot{m}}{\rho A\sqrt{gH}}$

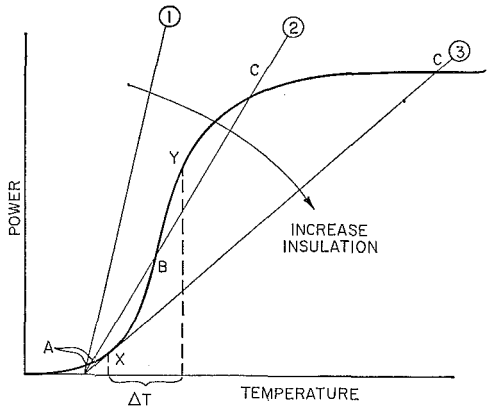

Fig. 2. Ignition process: chemical rate curve AXBYC; ignition temperature range ΔT

the hydrogen–oxygen flame about 15 kinetic equations are required to attain satisfactory accuracy.

For most fuels (e.g., hydrocarbons or wood pyrolysis products in air) the knowledge of the chemistry is far from adequate to compute flame speeds. Thus while the fundamental processes are understood, the complexity is such that flame speeds will be measured, not computed, for many years to come.

Flow fields with flames show many interesting and important instabilities [9–12]. However, these phenomena have not received extensive attention to date.

The movement of a flame across a liquid fuel is now under active study [13, 14]. Interestingly enough, the flame speed in this case is intimately connected with the liquid-fuel motion induced by the variation of surface tension with temperature.

For the flame-speed movement over solid fuels, only the merest beginning has been made [15, 16]. Such studies are seriously hampered by the lack of exact knowledge of the pyrolysis processes, which are often very complex [4, 5].

Ignition. The world we live in, while "unstable" relative to combustion reactions, requires a specific act of ignition to upset its metastability. Something has to be done to raise the temperature before vigorous burning can proceed out of control. The qualitative reason for this is shown in Fig. 2 [17]. The curved line ABC shows how the chemical reaction rate varies with the temperature of the fuel mixture. The "straight" lines (1, 2, 3) show how the heat loss to the surroundings varies with temperature for increasing insulation $1 \rightarrow 2 \rightarrow 3$.

We are normally at A on curve 1 or 2. The reaction rates are very low and are called "deterioration" or "corrosion" (often aided by bacteria). Any temporary small external heat addition (on curves 1 or 2) increases the heat loss above the heat produced, and we promptly return to the metastable point A. If the external heat source raises the temperature above point B, the reactions produce more heat than can be lost, and a fire is started, point C. Point B is the ignition point. Any point between X and Y can be the ignition point, depending upon the insulation. The temperature range corresponding to the X, Y range is the ignition temperature range. The material will possess *an* ignition temperature if the X, Y portion of the reaction rate curve is steep enough to reduce the ignition temperature range to a negligible width. Ignition temperatures do not really exist, but they may serve as adequate approximations for some purposes (and for all purposes in the absence of something better).

This ignition theory could be made quantitatively exact for many simple geometries if enough were known about the quantitative thermal and chemical kinetic aspects of pyrolysis and initial (low-temperature) oxidative reactions. We are a long way from adequate knowledge at present.

Forced-Convective Burning of a Flat Plate. When a flat surface of fuel burns in an air stream, we would expect a boundary layer to develop in the usual way. We further expect to find in that boundary layer several zones, as in Fig. 3. Near the surface it is too cold for significant reactions. However, heat conducts to the fuel, which evaporates and flows and diffuses away from the surface. In the outer part of the boundary layer, the oxygen of the air diffuses inward against a diffusion of products of combustion. Between these two zones, the hot fuel and oxygen react to maintain the high temperature and to produce products of combustion. Since the velocity is high in the combustion zone (of order of half of free stream), the fuel burns downstream of where it evaporates, and thus some of the fuel burns as a flame wake.

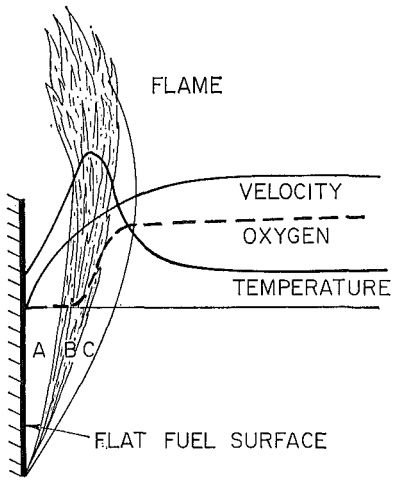

Fig. 3 Forced-convective burning in a boundary layer: A, fuel diffusion zone; B, combustion zone; C, oxygen diffusion zone

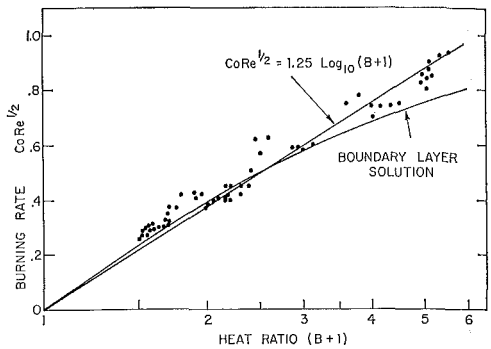

Fig. 4 Forced-convective burning in a boundary layer (data of Spalding on spheres; theory of Spalding [18] and Emmons [19])

The boundary-layer equations have been written and solved [18, 19], with the result shown in Fig. 4. The data shown are for burning fuel spheres [18]. (Since heat transfer data for flat plates, cylinders, and spheres correlate together, we anticipate that burning data will too, and it does.) Note that the fuel characteristic B is the independent parameter and that the empirical formula

$$Co\ \mathrm{Re}^{1/2} = 1.25 \log_{10}(B + 1) \qquad (1)$$

gives a fair fit to the results. The factor $\log (B + 1)$ has been found to be of the right order of magnitude for the effect of fuel vapor production in many fire circumstances.

Not a word has been said about chemical kinetics. In fact, no chemical kinetics were used in developing this solution. For essentially all important steady burning fire problems, the reactions are fast enough to burn up all the oxygen before any reaches the fuel surface. Since the combustion rate is independent of the (fast) chemical kinetics, we might as well assume all chemical rates as infinite.

Solutions giving similar agreement with experiment have been carried out for natural convection [20]. Correlated data are needed for much larger sizes (Reynolds numbers). The stability of the flame on a flat plate is closely bound up with the finite-speed chemical kinetics and the boundary-layer leading edge and has not yet been adequately investigated.

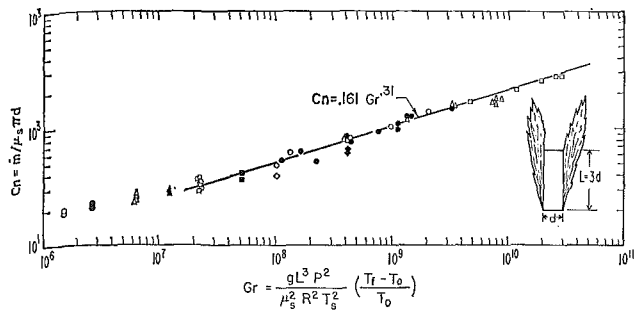

Fig. 5 Pressure modeling of fires: L = 1.875, 2.25, 3.00, 3.75, 4.50, 6.00, 7.50, and 12.00 in.; T_∞ = 300 deg K; T_w = 673 deg K; T_f = 2100 deg K

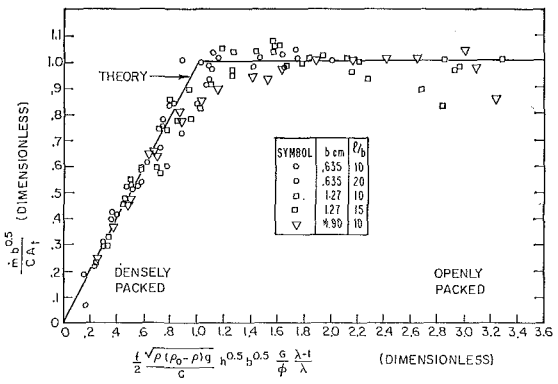

Fig. 6 The burning of a crib

Fire Modeling. As I use the term here, I do mean "modeling" in the restricted sense of testing at small size. If we focus our attention on problems like that above, where chemical kinetics is not important, we would expect the burning rate to depend only on dynamic factors. Under these conditions, we would expect

$$Co = f(\mathrm{Gr}, B) \tag{2}$$

A few years ago DeRis et al. [21] noticed that

$$\mathrm{Gr} = \frac{g\rho^2 D^3 \beta \Delta T}{\mu^2} = \frac{g\beta\Delta T(p^2D^3)}{\mu^2 R^2 T^2} \tag{3}$$

and since temperatures in a fire are nearly independent of ambient pressure, it should be possible to preserve constant Grashof number by testing a reduced size model at increased pressure, the model size being chosen proportional to (pressure)$^{2/3}$. Tests of this idea on some simple models gave the excellent results of Fig. 5.

How general this method will prove to be is now being explored. As more general fire problems are considered, radiation numbers and chemical numbers of various types will become important. It is too much to hope that all of these additional numbers will scale in the same way with pressure. However, it is most important to learn the limitations of pressure modeling since within the range of its validity it could provide a very useful research tool.

Various laboratories have experimented with different size models at atmospheric pressure. While this cannot be done with the precision of pressure modeling, various workers have found them sufficient for their special purposes. Additional careful modeling work is required to establish the potential and limitations of atmospheric modeling.

The Crib. Wood sticks placed at right angles in alternate layers produce an easily reproduced structure and have been favorite experimental arrangements for fire research. A fair correlation of experimental data was obtained by Gross [22], who recognized two burning regimes: one loose packed where the stick burned at a rate independent of the exact distance to its neighbors, the other densely packed where the burning rate was controlled by

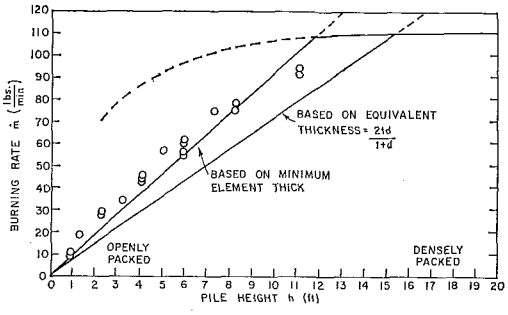

Fig. 7 Variation of pallet burning rate with pile height (courtesy Factory Mutual Research Corp.; theory curves by Block [23])

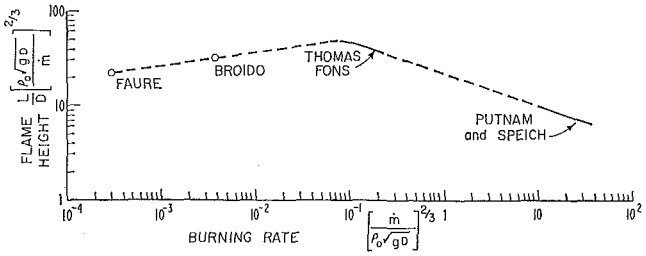

Fig. 8 Dependence of flame height upon burning rate (from Thomas [24])

the air that could get into the interior of the crib through the available holes.

More recently, Block [23] analyzed the flow up through the "chimneys" in a crib and found the approximate relation

$$\frac{\dot{m}b^{1/2}}{CA} = \frac{f}{2}\frac{\sqrt{\rho(\rho-\rho_0)g}}{C} h^{1/2}b^{1/2}\frac{G}{\phi}\left(\frac{\lambda-1}{\lambda}\right) \tag{4}$$

for dense packed cribs.

Since the ratio of hot gas flow to inlet air flow, λ, is related to the heat ratio B by

$$\frac{\lambda-1}{\lambda} = \frac{B - \dfrac{C_p(T-T_s)}{\epsilon}}{B+1} \tag{5}$$

we notice that equation (4) involves the dimensionless variables

$$\frac{\dot{m}b^{1/2}}{CA},\ f,\ G,\ B,\ \frac{\sqrt{\rho(\rho-\rho_0)ghb}}{C},\ \frac{Ph}{A},\ \frac{C_p(T-T_s)}{\epsilon} \tag{6}$$

None of these depends upon chemical kinetics, but several include chemical thermodynamic factors. What happens is that air enters at the bottom of the crib and very rapidly reacts with the wood and wood pyrolysis products. The hot combustion gases flow upward by buoyancy through the vertical shafts and there heat and pyrolyze more wood. The resultant rich mixture then burns as a flame above the crib.

This elementary analysis not only supplied the basis for Block's data correlation, Fig. 6 (essentially that found by Gross), but makes it clear why the burning rate is dependent only upon the vertical shafts and does not depend upon the side openings (which can indeed be closed without significant effect). Finally, the generality of the analysis has made it possible to compute the burning rate of a pile of pallets, Fig. 7, in agreement with the experimental burning measurements made at Factory Mutual Research Corp.

Flame Heights and Fire Plumes. As last examples of what can and should be done to make fire safety more rational, I present Figs. 8 and 9. In Fig. 8 is shown the correlation of a wide range of flame heights by Thomas [24], while Fig. 9 is a presentation of fire plume data taken above a line fire by Lee and Emmons [25]. Both of these curves are only a step toward the needed results, since both depend upon the rate of burning as part of the controlling variable. Ultimately this information must be coupled

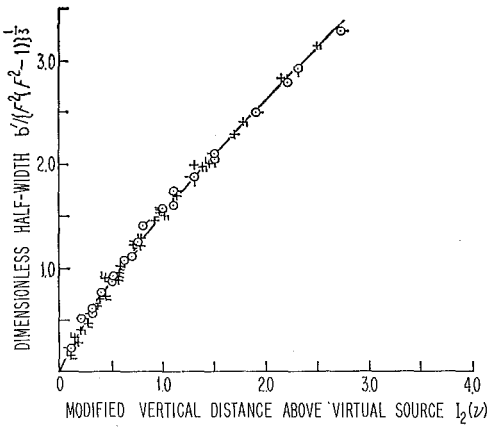

Fig. 9 Half-width of a line fire plume; Froude number of fire momentum = Fr; fire mass flux = *N* (dimensionless);

$$I_2(\nu) = \int_{\nu_0}^{\nu} (\nu^3 + 1)^{-1/3}\nu d\nu \qquad \nu_0 = (\mathrm{Fr}^2 - 1)^{-1/3} \qquad \nu = (\mathrm{Fr}^2 - 1)^{-1/3}N/\mathrm{Fr}$$

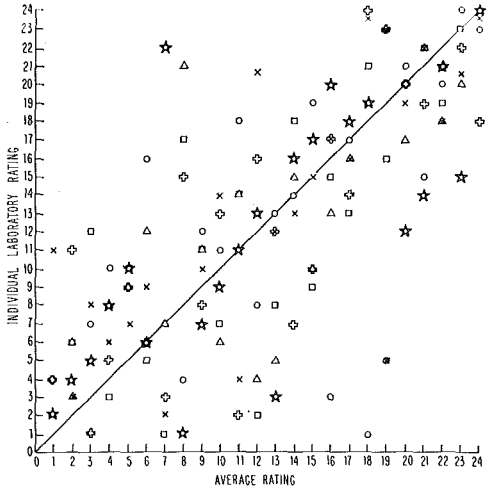

Fig. 10 Flammability ratings of 24 wall materials by six different national standard tests: crosses, Germany; x's, Belgium; circles, Denmark; squares, France; triangles, The Netherlands; stars, England

with a more complete knowledge of what happens in and near the fire so that the burning rate itself can be predicted.

Open Problems. Throughout the above discussion I have mentioned various unsolved problems, mostly in the form of incomplete correlations or needed extensions. In this section I want to mention a number of very practical problems that wait for their complete solution on a better understanding of fire in general and fire heat transfer in particular.

Fire safety in building design is controlled through building code specifications of the flammability of building materials. Just what "flammability" is is not clear. For practical purposes flammability is defined by the specified flammability test. The state of our present understanding is shown by Fig. 10 in which is plotted the order of flammability of 24 wall covering materials as measured by 6 different European countries' standard flammability tests. (The U. S. did not participate in these round-robin tests since we have no flammability standard. The tunnel test developed by the Underwriters' Labs. is the most common test used by cities in the U. S. There is no reason to believe that tunnel-test results would be better than those in Fig. 10.)

The bad scatter from what should have been a 45-deg straight line is graphic evidence of our ignorance. The seriousness of such scatter from the point of view of fire safety control is emphasized by material 18, which is the best of all 24 in Germany and the worst of all 24 in Denmark. Except for the universal elimination of celluloid wallboard and the universal acceptance of cement blocks (neither of which was included in these tests) such test results are little better than random. We must develop an understanding of fire if we are to devise flammability tests that assure fire safety.

So far, no fire in any multistory building has caused the building to collapse with occupants trapped on the upper floors, although rivets have failed and a floor beam has dropped [26]. This may sound like a mechanical strength problem, which it is in part, but it is even more of a heat transfer problem. If steel beams are adequately insulated and the reinforced concrete structures adequately thermally designed, no modern steel or reinforced concrete building will ever collapse. Although the proper procedures for the estimation of heat transfer in fires is a significant research problem, the cure for the fire structural problem is largely one of proper specification of insulation during design and proper installation and inspection during construction.

It is common sense that extinguishment action should begin at the earliest possible moment after a fire is detected. But just how important is it? Should there be a fire house on every corner? Of course not, but how many should there be? Only rule-of-thumb answers are known now. To do better, we need information on the rate of value destruction of property by fire and the effect on this rate of destruction by the extinguishment forces. Fire destroys value by direct consumption, by excessive heating with partial pyrolysis, and by the distribution of smoke and soot. Extinguishment will (hopefully) put out the fire but may do extensive water or other damage in the process. The best system is that which results in the least total cost. Thus the selection of flammability of building materials, the sprinkler or other fire protection of buildings, the best detection device, the control of street lights from the fire apparatus, the number and location of fire houses and the extent of their equipment are all dependent upon the balance between the rate of value destruction, the delay times inherent in fire detection and extinguishment response, and the equipment cost.

The extinguishment process itself has never been scientifically studied. Water will put a fire out, yes, but why and how? Does water merely cool it? If so, how far below the surface? Does the steam produced effectively decrease the availability of oxygen? Water is a very reactive substance. Does it act as an inhibitor by direct chemical intervention in the pyrolysis and combustion reactions or does it sometimes help to spread the fire through the production of hydrogen and carbon monoxide in a water-gas reaction? These questions not only have not been answered, they have not even been seriously asked before. It is time to get some answers.

Although radiation is obviously present in fires and was mentioned while discussing basic phenomena and the basic equations, I have not mentioned it in any of the solutions. This is because the work to date has produced essentially zero useful results. There has been considerable work on spectral output in flames and other special fires. Radiation thus serves as an important research tool. For fire purposes, the energy transfer by radiation is needed, but as yet the information is much too limited to even answer the question of when (if ever) radiation is an essential mechanism. Qualitative observations and common sense give radiation an important place in fire. We need quantitative results to make calculations possible.

The fire problem is in many ways a new and easy problem from an academic point of view. You don't need a billion-dollar accelerator nor spaceship. You don't need a million-dollar wind tunnel or even a thousand-dollar double-pipe heat exchanger. To date, there is no correct basic solution to the problem of the shape of a Bunsen-burner flame, to say nothing of all the intriguing special cases [11]. And even simpler, no one as yet quantitatively understands the burning of a match.

To be sure, some of these simple-to-state problems are extremely difficult, but the field of fire research is so new that many of the easy problems are still waiting around for the ingenious ex-

perimenter and analyst to find them. Also, many of the easy problems will appear academic. However, it is through the complete elucidation of the easy special cases that mankind eventually is able to see through the complexity of our highly interconnected world.

Conclusion

I hope this brief review of the important and challenging field of heat transfer in fire will inspire those of a practical bent and those with scientific inclinations, the experimenters and the analysts, to take another look at the problems posed by the unwanted fire in our environment and decide to spend at least a small portion of their lives making their contribution to this universal problem which costs the U. S. 1 percent of our gross national product and takes a life every 40 minutes.

References

1 Proceedings of a symposium on "The Role of Chemistry in Fire Problems," *Fire Research Abstracts and Reviews*, National Academy of Sciences, Vol. 13, No. 3, 1971.

2 Williams, F. A., *Combustion Theory*, Addison-Wesley, Reading, Mass., 1965.

3 Gouland, R., "Fundamental Equations of Radiation Gas Dynamics—High Temperature Aspects of Hypersonic Flow," AGARDograph No. 68, Pergamon, Elmsford, N. Y., p. 529.

4 Parker, W. J., and Lipska, A. E., "A Proposed Model for the Decomposition of Cellulose and the Effect of Flame Retardants," OCD Work Unit 2531C-NRDL-TR-69, 1969.

5 Einhorn, I. N., "The Chemistry of Fire Resistant Materials and Suppression," *Fire Research Abstracts and Reviews*, National Academy of Sciences, Vol. 13, No. 3, 1971, pp. 236–267.

6 Hirshfelder, J. O., Curtiss, C. F., and Campbell, D. E., "The Theory of Flames and Detonations," *4th Symposium (International) on Combustion*, Williams and Wilkins, 1953, pp. 190–211.

7 Wilde, K. A., "Boundary-Value Solutions of the One-Dimensional Laminar Flame Propagation Equations," *Combustion and Flame*, Vol. 18, No. 1, 1972, pp. 43–52.

8 Mallard, E., and LeChatelier, H., "Combustion of Explosive Gas Mixtures," *Ann. Mines*, Vol. 8, 1883, p. 274.

9 Markstein, G. H., ed., *Non-Steady Flame Propagation*, Pergamon, Elmsford, N. Y., 1964.

10 Peterson, R., and Emmons, H. W., "Stability of Laminar Flames," *Physics of Fluids*, Vol. 4, No. 4, 1961, pp. 456–464.

11 Barr, J., "Diffusion Flames," *4th Symposium (International) on Combustion*, Williams and Wilkins, 1953, pp. 765–771.

12 Orloff, L., and DeRis, J., "Modeling of Ceiling Fires," *13th Symposium (International) on Combustion*, Combustion Institute, 1971, pp. 979–992.

13 Burgoyne, J. H., Roberts, A. F., and Quinton, P. G., "The Spread of Flame across a Liquid Surface," *Proc. Roy. Soc. A*, Vol. 308, 1968, pp. 39–79.

14 Mackinven, R., Hansel, J. G., and Glassman, I., "Influence of Laboratory Parameters on Flame Spread Across Liquid Fuels," *Combustion Science and Technology*, Vol. 1, 1970, pp. 293–306.

15 DeRis, J. N., "Spread of a Laminar Diffusion Flame," *12th Symposium (International) on Combustion*, Combustion Institute, 1969, pp. 241–252.

16 Emmons, H. W., "Fluid Mechanics of Combustion," *13th Symposium (International) on Combustion*, Combustion Institute, 1971, pp. 1–18.

17 Kamenetskii, F., *Diffusion and Heat Transfer in Chemical Kinetics*, Plenum, New York, N. Y., 1969.

18 Spalding, D. B., "A Standard Formulation of the Steady Convective Mass Transfer Problem," *International Journal of Heat and Mass Transfer*, Vol. 1, No. 3, 1960, pp. 192–207.

19 Emmons, H. W., "The Film Combustion of Liquid Fuels," *Zeit. A. Math. Mech.*, Vol. 36, No. 2, 1956, pp. 60–71.

20 Kim, J. S., DeRis, J., and Kroesser, F. W., "Laminar Free-Convective Burning of Fuel Surfaces," *13th Symposium (International) on Combustion*, Combustion Institute, 1971, pp. 949–961.

21 DeRis, J., Kanury, A. M., and Yuen, M. C., "Pressure Modeling of Fires," to appear in: *14th Symposium (International) on Combustion*, Combustion Institute.

22 Gross, D., "Experiments on the Burning of Cross Piles of Wood," *Journal of Research*, National Bureau of Standards, Vol. 66C, No. 2, 1962, p. 99.

23 Block, J. A., "A Theoretical and Experimental Study of Nonpropagating Free-Burning Fires," *13th Symposium (International) on Combustion*, Combustion Institute, 1971, pp. 971–978.

24 Thomas, P. H., "The Size of Flames from Natural Fires," *9th Symposium (International) on Combustion*, Combustion Institute, 1963, pp. 844–859.

25 Lee, S. L., and Emmons, H. W., "A Study of Natural Convection above a Line Fire," *Journal of Fluid Mechanics*, Vol. 11, No. 3, 1961, pp. 353–368.

26 "One New York Plaza Fire," Report of New York Board of Fire Underwriters, Bureau of Fire Prevention and Public Relations, 85 John St., New York, N. Y., 1970, pp. 3–15.

J. H. LIENHARD
Professor.
Mem. ASME

V. K. DHIR
Research Assistant.
Student Mem. ASME

Boiling and Phase Change Laboratory,
Mechanical Engineering Department,
University of Kentucky,
Lexington, Ky.

Hydrodynamic Prediction of Peak Pool-boiling Heat Fluxes from Finite Bodies[1]

Since Zuber made a hydrodynamic prediction of the peak pool-boiling heat flux on an infinite flat plate, his general concept has been used to predict the peak heat flux in two finite heater configurations. These latter predictions have differed from Zuber's in the introduction of a largely empirical variable—the thickness of the vapor escape path around the body. The present study shows how measurements of this thickness can be combined with the hypothesis that the vapor velocity within the vapor blanket must match the vapor velocity in the escaping jet above the heater. The result is a more exact description of the hydrodynamics of vapor removal. This idea is used to suggest the possibility of a universal value for the ratio of the cross-sectional area of escaping jets to the heater area for large finite heaters and for long slender heaters. A set of general ground rules is developed for predicting the peak heat fluxes on both large and small heaters. These rules are used in turn to predict the peak heat flux from horizontal ribbons. They are also used to correct the traditional prediction for infinite-flat-plate heaters. The predictions are supported with new data.

Introduction

THE HYDRODYNAMIC theory of Zuber and Tribus [1, 2][2] showed rationally, in 1958, why the older correlative equation of Kutateladze [3] was the correct expression for the peak pool-boiling heat flux q_{max} on an infinite horizontal flat plate. In the early 1960s Kutateladze and his co-workers began [4] a research effort aimed at correlating q_{max} on horizontal cylinders. In 1964 and 1965 respectively they [5] and Lienhard and Watanabe [6] showed that q_{max} data for cylinders (and other geometries) could be correlated with an expression of the form

$$\frac{q_{max}}{q_{max_F}} = f(L') \tag{1}$$

where q_{max_F} is the "traditional" or accepted form of Zuber's expression for q_{max} on horizontal flat-plate heaters[3]

$$q_{max_F} \equiv \frac{\pi}{24}\rho_g^{1/2}h_{fg}[\sigma g(\rho_f - \rho_g)]^{1/4} \tag{2}$$

and L' is a nondimensionalization of the characteristic length L of the heater

$$L' \equiv L\sqrt{g(\rho_f - \rho_g)/\sigma} \tag{3}$$

The restrictions on equation (1) are discussed fully in [7]. Briefly: the pressure must be enough less than the critical pressure that $\rho_g/\rho_f \ll 1$; the body must be shaped so that fluid motion induced by the rising bubbles draws liquid around (rather than into) the bubble escape path; and the surface must be clean.

During the past four years this laboratory has been involved in formulating hydrodynamic predictions of q_{max} on a variety of finite heaters. In 1970 a hydrodynamic theory for q_{max} on horizontal cylinders was derived by Sun [8]. Ded [9] subsequently provided a prediction of q_{max} on spheres. Both [8] and [9] required the evaluation of a "vapor-blanket thickness" δ. This δ was the thickness of the vapor escape passage around the body, and it generally appeared that experimental data had to be used in its evaluation.

In the present study we shall show how the previous models can be treated using less empirical information than before. We shall infer from these models some general features of any hydrodynamic prediction and so eliminate the need for observed values of δ. Finally we shall use these ideas in the prediction of q_{max} expressions for some new configurations and verify these expressions with new data.

Previous Theoretical Models

Zuber's original formulation began quite simply with the proposition that the maximum or limiting vapor volume flux is

[1] This work was performed with the support of NASA grant NGR-18-001-035 under the cognizance of the Lewis Research Center.

[2] Numbers in brackets designate References at end of paper.

[3] Symbols not explained in the text are ones in common use; they are defined in the Nomenclature.

Contributed by the Heat Transfer Division and presented at the Winter Annual Meeting, New York, N. Y., November 26–30, 1972, of THE AMERICAN SOCIETY OF MECHANICAL ENGINEERS. Manuscript received by the Heat Transfer Division November 12, 1971. Paper No. 72-WA/HT-10.

$$q_{max}/\rho_g h_{fg} = U_H \frac{A_j}{A_h} \tag{4}$$

in which A_j is the combined area of vapor jets leaving a heater surface of area A_h. U_H is the critical vapor velocity within the jets which will cause them to become Helmholtz unstable. Equation (4) is the starting point for everything we shall do here. Each prediction brings with it two component problems which must be solved: A vapor jet configuration must be assumed in order to specify A_j/A_h, and the critical velocity must be obtained. The latter can be shown (see, e.g., [10] page 462 or [11]) to be

$$U_H = \sqrt{2\pi\sigma/\rho_g\lambda_H} \tag{5}$$

where λ_H is the wavelength of the disturbance that gives rise to the instability in the vapor–liquid interface of the jet. Substituting equation (5) in equation (4) and introducing equation (2) we obtain

$$\frac{q_{max}}{q_{max_F}} = \frac{24}{\pi}\sqrt{\frac{2\pi}{\lambda_H\sqrt{g(\rho_f - \rho_g)/\sigma}}}\frac{A_j}{A_h} \tag{6}$$

Infinite Horizontal Flat Plate. Zuber's original derivation of q_{max_F} involved a number of assumptions which we shall want to modify here. Hence we shall speak of $(q_{max})_{flat\ plate}$, which may or may not equal q_{max_F}. Nevertheless there is now considerable historical precedent for using q_{max_F} as defined by equation (2) in the functional equation (1). Accordingly we shall adopt the view that q_{max_F} is a *characteristic heat flux* which approximates $(q_{max})_{flat\ plate}$.

Zuber reasoned that (in the absence of any geometrical features of the heater) the jets of escaping vapor would form on the nodes of the square two-dimensional grid of collapsing Taylor-unstable waves as illustrated at the top of Fig. 1. At the time he could provide no basis for selecting either the minimum unstable Taylor wavelength[4]

$$\lambda_c = 2\pi\sqrt{\sigma/g(\rho_f - \rho_g)} \tag{7}$$

or the most susceptible, or "most dangerous," wavelength[4]

$$\lambda_d = 2\pi\sqrt{3}\sqrt{\sigma/g(\rho_f - \rho_g)} = \sqrt{3}\,\lambda_c \tag{8}$$

Subsequent work with film boiling on cylinders [13, 14] has shown quite conclusively that the rapidly moving waves which occur in boiling and which tend to collapse are of the most susceptible wavelength.

The radius R_j of the escaping jet was assumed to be a given fraction a of the wavelength λ. Thus

$$\frac{A_j}{A_h} = \frac{\pi R_j^2}{\lambda^2} = \pi a^2 \tag{9}$$

Zuber guessed that a should be $1/4$ so his A_j/A_h was $\pi/16$. The wavelength of disturbances in the jet was taken to be equal to the length of the Rayleigh unstable wave. This choice was reasonable since this sort of disturbance will occur naturally in any gas jet moving through a liquid. The wavelength λ_H of Rayleigh waves is equal to the circumference of the jet in which they occur, [10] page 473, $2\pi R_j$ or $2\pi a\lambda$. Using this result and equation (9) in equation (6) gives

$$\left.\frac{q_{max}}{q_{max_F}}\right|_{flat\ plate} = \frac{24a^{3/2}}{\sqrt{2\pi}}\cdot\frac{1}{1\text{ or }\sqrt[4]{3}} \tag{10}$$

Using $a = 1/4$, Zuber obtained for the flat plate

$$q_{max}|_{flat\ plate} = 1.196\ q_{max_F} \quad \text{or} \quad 0.909\ q_{max_F}$$

depending upon whether the correct λ was λ_c or λ_d. He compromised and took equation (2) as a good mean value.

Horizontal Cylinder. The peak heat flux on any finite body will be determined by the configuration of jets above the body since all of the vapor generated below will eventually find its way around the body and up into this jet system. This process is shown schematically for several finite heaters in Fig. 1. The peak heat flux is reached on the body as a whole when these over-

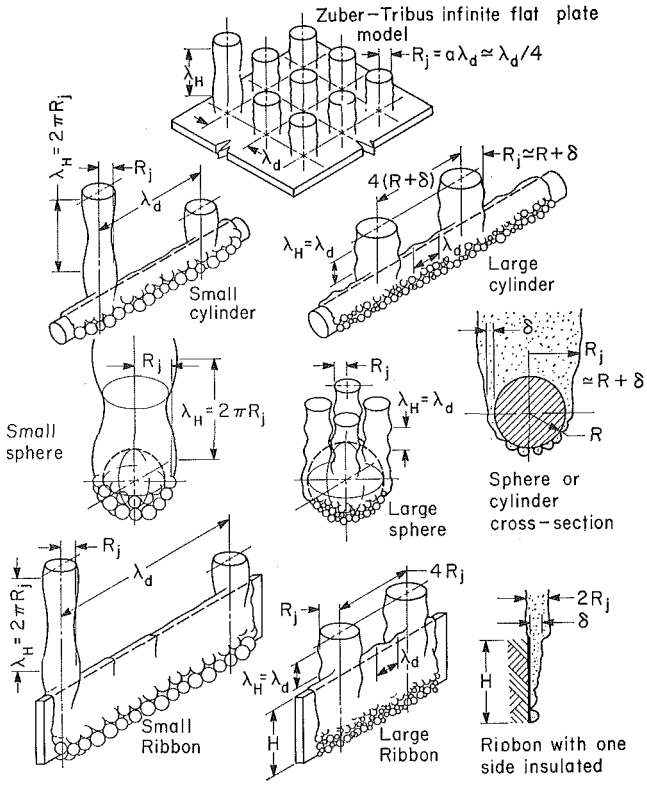

Fig. 1 Vapor-removal configurations near the peak heat flux on a variety of heaters

Nomenclature

A_h = area of heater
A_j = cross-sectional area of vapor jets escaping from A_h
a = R_j/λ_d for flat-plate heater
$f(\ )$ = any function of ( )
g = actual gravity (or body) force acting on heater
g_e = earth-normal gravity
h_{fg} = latent heat of vaporization
H = vertical dimension of horizontal ribbon
L = characteristic dimension (= H or R in certain present applications)
P = length of perimeter of cross section of long slender heater
q_{max} = peak nucleate pool-boiling heat flux
q_{max_F} = characteristic heat flux defined by equation (2), equal to Zuber's prediction for infinite horizontal flat plates
R = radius of cylindrical or spherical heater
R_j = radius of escaping vapor jet
U_H = vapor velocity in jet, for which jet becomes Helmholtz unstable
δ = vapor-blanket thickness
Δ = $\delta\sqrt{g(\rho_f - \rho_g)/\sigma}$
λ = any wavelength in vapor–liquid interface
λ_c = minimum Taylor unstable wavelength, equation (7)
λ_d = most rapidly collapsing Taylor wavelength, $\sqrt{3}\lambda_c$
λ_H = Helmholtz unstable wavelength
ρ_f, ρ_g = saturated liquid and vapor densities
σ = surface tension between liquid and its vapor

Superscript

$'$ denotes a length multiplied by $\sqrt{g(\rho_f - \rho_g)/\sigma}$

[4] These expressions were derived by Bellman and Pennington [12].

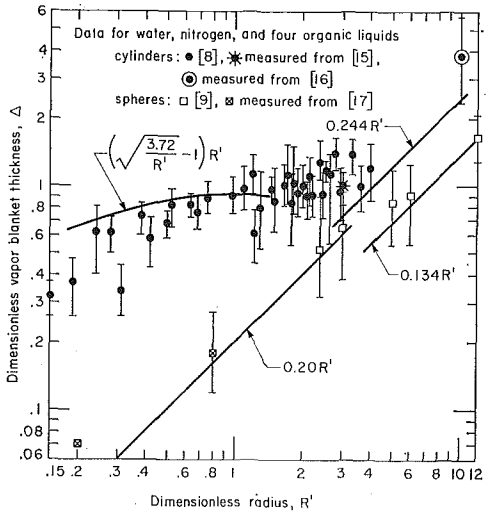

Fig. 2 Vapor-blanket thickness measured on spheres and cylinders

head jets become unstable. Both the configuration and the size of these jets will be determined by the size and shape of the body.

In the specific case of horizontal cylinders—at least on the larger ones—photographic evidence [8] indicates that the jets adjust approximately to the width of the cylinder (plus the thickness of the vapor blankets, 2δ) as shown in Fig. 1. If the wire is small the jets will be small and the spacing can reasonably be assumed equal to λ_d. As the wire increases in size the spacing must eventually spread to beyond λ_d to accommodate jets which now exceed $\lambda_d/2$ in diameter. Sun showed that the spacing was about two jet diameters or about $4(R + \delta)$ in this case. Thus

$$\left.\frac{A_j}{A_h} \simeq \frac{(R+\delta)^2}{2R\lambda_d}\right|_{\substack{\text{small}\\\text{cyls.}}} \qquad \left.\frac{A_j}{A_h} \simeq \frac{R+\delta}{8R}\right|_{\substack{\text{large}\\\text{cyls.}}} \tag{11}$$

Of course equations (11) are true only insofar as $R_j \simeq R + \delta$.

Furthermore, the wavelength λ_d is the dominant disturbance in the interface between the jets on large wires and it is picked up by the jets. The Rayleigh disturbance $2\pi R_j$ is longer than λ_d and would normally become Helmholtz unstable at lower vapor velocities U_H. However, photographic evidence confirmed that vapor jets on large wires were much too short to have collapsed by virtue of the Rayleigh disturbance. This means that the shorter waves of length λ_d are already well developed at the outset, while the Rayleigh waves require some distance to develop. Accordingly, Sun used $\lambda_H = 2\pi R_j \simeq 2\pi(R + \delta)$ for the small cylinders and $\lambda_H = \lambda_d$ for the large ones. Using these λ_H's and equation (11) in equation (6), and using R' to denote L' based on $L = R$, gives

$$\frac{q_{\max}}{q_{\max F}} = \left.\frac{6}{\pi^2\sqrt{3}}\,\frac{(R'+\Delta)^{3/2}}{R'}\right|_{\substack{\text{small}\\\text{cyls.}}} \quad \text{and} \quad \left.\frac{3^{3/4}}{\pi}\,\frac{R'+\Delta}{R'}\right|_{\substack{\text{large}\\\text{cyls.}}} \tag{12}$$

where $\Delta \equiv \delta\sqrt{g(\rho_f - \rho_g)/\sigma}$, a dimensionless blanket thickness. The transition between small and large cylinders occurs somewhere in the neighborhood of $\lambda_d = 4(R + \delta)$ or $R' \simeq 2.5$, depending on the magnitude of δ.

The parameter R', which has been variously named the "Laplace number," the "Rayleigh number," and the square root of the "Bond number," characterizes the ratio of buoyant forces to capillary forces in a system. As R' becomes very large the system should approach a state in which it is no longer subject to capillary forces. In this state we would expect to see no further influence of R' upon $q_{\max}/q_{\max F}$, in much the same way as the Reynolds number ceases to exert an influence on the drag coefficient when it becomes sufficiently large. This is what was found to be the case in [8]. As R' became large, Sun measured $\delta \simeq 0.233\ R$, so equation (11) gave $A_j/A_h \simeq 0.155$, and $q_{\max}/q_{\max F}$ approached a constant value of 0.894.

For small cylinders Sun approximated the measured values of δ with a fairly complicated equation in the form $\Delta = \Delta(R')$. Substitution of this expression in equation (12) gave

$$\left.\frac{q_{\max}}{q_{\max F}}\right|_{\substack{\text{small}\\\text{cyls. [8]}}} = 0.89 + 2.27\exp\left(-3.44\sqrt{R'}\right) \tag{13}$$

which fit approximately 900 data from a large variety of sources.

Sphere. Photographic observation of boiling on spheres [9] shows a difference between large and small R' behavior just as it did for cylinders. For small spheres a single jet of radius $R_j \simeq R + \delta$ rises as shown in Fig. 1. But when the diameter $2R$ reaches roughly λ_d or $R' \simeq 5.5$, the vapor begins to escape alternately around opposing sides of the sphere in a 4-jet pattern as shown in Fig. 1. Once again visual evidence supports the assumption that $\lambda_H = 2\pi R_j$ for small spheres and $\lambda_H = \lambda_d$ for large ones. Thus

$$\left.\frac{q_{\max}}{q_{\max F}}\right|_{\substack{\text{small}\\\text{spheres}}} = \frac{24}{\pi\sqrt{R_j'}}\,\frac{A_j}{A_h} \qquad \left.\frac{q_{\max}}{q_{\max F}}\right|_{\substack{\text{large}\\\text{spheres}}} = \frac{24}{\pi\sqrt[4]{3}}\,\frac{A_j}{A_h} \tag{14}$$

where $R_j' \equiv R_j\sqrt{g(\rho_f - \rho_g)/\sigma}$.

At this point Ded [9] used a notion from this paper to evaluate the unknown area ratio which involves δ. This method is essential to the subsequent developments in this study and we shall take it up next.

Evaluations of A_j/A_h in the $q_{\max}/q_{\max F}$ Formulae

As a first step to determining A_j/A_h we shall offer a hypothesis that the speed of the vapor passing through the blanket equals that in the escaping jet. For the speeds to differ would require the existence of both pressure differences within the vapor escape path and significant dissipative mixing processes in the jet. We do not believe it is reasonable to look for either, and therefore assume that δ simply adjusts to give equal velocities in both passages.

For the large cylinder, this assumption combined with a simple continuity statement (velocity times cross-sectional area is constant) gives

$$2[4(R + \delta)\delta] = \tfrac{1}{2}A_j \tag{15}$$

and for any sphere it gives

$$2\pi(R + \delta/2)\delta = \tfrac{1}{2}A_j \tag{16}$$

For the small cylinder such a balance is not feasible since the vapor must flow horizontally in a long annulus subject to pressure drops. But for the small sphere equation (16) will still be true. From this point two paths can be followed.

The path followed in [8] was to assume a jet configuration in terms of δ and then to complete the derivation using observed values of δ; [8] and [9] give the needed measurements of δ for both cylinders and spheres as scaled from photographs. These data and two additional points scaled from photographs in other papers [15, 16, 17] are combined in Fig. 2. Approximate lines have been fitted through the data in both the large and small R' ranges. The results are

$$\Delta_{\text{small cylinders}} = \left(\sqrt{3.72/R'} - 1\right)R' \tag{17}[5]$$

$$\Delta_{\text{large cylinders}} = 0.244\ R' \tag{18}[6]$$

$$\Delta_{\text{small spheres}} = 0.20\ R' \tag{19}$$

[5] Sun used a more complex fit to the data, one which fit well in the mid-range but was very nearly equal to equation (17) for $R' \leq 1$. We are presently more interested in low-R' behavior than in transitional behavior at higher R'.

[6] This result is a little higher than Sun's and represents a slightly better fit.

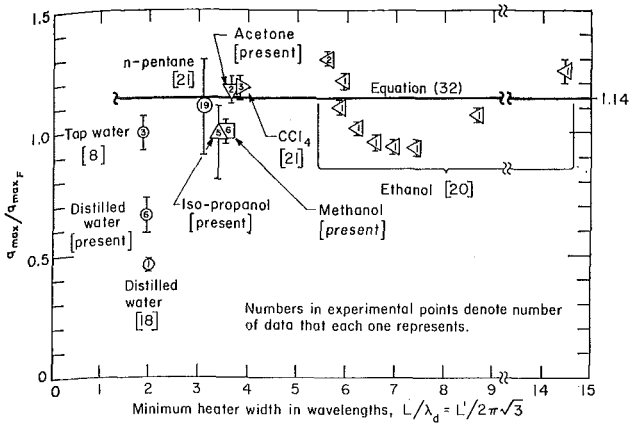

Fig. 3 q_{max} **on broad flat-plate heaters with vertical side walls**

$$\Delta_{\text{large spheres}} = 0.134\,R' \tag{20}$$

Using these equations in equations (15) and (16) leads to

$$\left.\frac{A_j}{A_h}\right|_{\substack{\text{large}\\\text{cyls.}}} = 0.155 \tag{21}$$

$$\left.\frac{A_j}{A_h}\right|_{\substack{\text{large}\\\text{spheres}}} = 0.143 \tag{22}$$

$$\left.\frac{A_j}{A_h}\right|_{\substack{\text{small}\\\text{spheres}}} = 0.220 \tag{23}$$

Ded put equation (22) in equation (14) and obtained

$$\left.\frac{q_{max}}{q_{max_F}}\right|_{\substack{\text{large}\\\text{spheres}}} = 0.84 \tag{24}$$

which differs by 7 percent from the large R' limit of equation (13) for cylinders.

The other approach is to combine the description of the assumed configuration of the jets with equations (15) and (16), solve the result for δ, and then obtain q_{max}/q_{max_F} from equation (12). This is reasonably safe to do in the case of large cylinders since the physical model ($R_j = R + \delta$) is consistent with Sun's photographs. The result is $\delta = 0.244\,R$, which corresponds precisely with the experimental value given in equation (18) and which leads to

$$\left.\frac{q_{max}}{q_{max_F}}\right|_{\substack{\text{large}\\\text{cyls.}}} = 0.904 \tag{25}$$

This is negligibly higher than Sun's result of 0.894, and it is a completely theoretical expression. While this result is accurate, the minor errors in the assumed characteristics of the vapor-escape configuration accumulate more than we would like in other cases. Such errors are particularly troublesome for the small heater configurations.

For small heaters we shall therefore revert to the first approach. In general λ_H should be replaced by $2\pi R_j$ in equation (6), where $R_j = \sqrt{(A_h/\pi)(A_j/A_h)}$. Thus

$$\left.\frac{q_{max}}{q_{max_F}}\right|_{\substack{\text{small}\\\text{heaters}}} = \frac{24}{\pi}\sqrt[4]{\frac{\pi}{A_h}\frac{\sigma}{g(\rho_f - \rho_g)}}\left(\frac{A_j}{A_h}\right)^{3/4} \tag{26}$$

If the heater is long and slender, A_h is equal to the product of the cross-sectional perimeter P times λ_d (cf. Fig. 1) and equation (26) becomes

$$\left.\frac{q_{max}}{q_{max_F}}\right|_{\substack{\text{long slender}\\\text{heaters}}} = \frac{24}{\pi\sqrt[8]{12}\sqrt[4]{P'}}\left(\frac{A_j}{A_h}\right)^{3/4} = \frac{5.62}{\sqrt[4]{P'}}\left(\frac{A_j}{A_h}\right)^{3/4} \tag{27}$$

Thus for spheres ($A_h = 4\pi R^2$) equations (26) and (23) give

$$\left.\frac{q_{max}}{q_{max_F}}\right|_{\substack{\text{small}\\\text{spheres}}} = \frac{1.734}{\sqrt{R'}} \tag{28}$$

For small cylinders A_j/A_h is approximately $(R + \delta)^2/2R\lambda_d$. Thus under the substitution of equation (17) we obtain

$$\left.\frac{A_j}{A_h}\right|_{\substack{\text{small}\\\text{cyls.}}} = 0.171 \tag{29}$$

Substituting equation (29) and $P' = 2\pi R'$ in equation (27) then gives

$$\left.\frac{q_{max}}{q_{max_F}}\right|_{\substack{\text{small}\\\text{cyls.}}} = \frac{0.94}{\sqrt[4]{R'}} \tag{30}$$

q_{max}/q_{max_F} for Flat Plates

A number of suggestions as to how one might improve Zuber's prediction of q_{max} for the flat plate have arisen in the preceding section. For one thing, Sun's large-cylinder model, based on the presumption that the jet spacing cannot be less than $4R_j$, was highly successful. Furthermore his corresponding assumption that $\lambda_H = \lambda_d$ in this case was also justified by the success of the result. We shall adapt these ideas to the flat plate by agreeing with Zuber that R_j equals $1/4$ of the jet spacing without saying precisely what that spacing is.[7] Then we shall use λ_d for λ_H. Then equation (9) gives

$$\left.\frac{A_j}{A_h}\right|_{\substack{\text{flat}\\\text{plate}}} = \frac{\pi}{16} \tag{31}$$

and equation (6) gives

$$\left.\frac{q_{max}}{q_{max_F}}\right|_{\substack{\text{flat}\\\text{plate}}} = \frac{24}{\pi}\sqrt{\frac{2\pi}{2\pi\sqrt{3}}}\,\frac{\pi}{16} = 1.14 \tag{32}$$

Of course an important point relative to Zuber's equation is that it was never systematically tested against data obtained in the configuration for which it was intended. To approximate an infinite flat plate experimentally one must first employ a very clean finite plate, much larger in size than λ_d. Then he must employ vertical side walls to prevent a horizontal inflow of liquid, since this has been shown [18, 19] to seriously influence q_{max}.

The data that we have located which meet these criteria are few. The vast majority of available flat-plate data were obtained with strip or disk heaters in open pools, and are hence unusable. The classical data of Cichelli and Bonilla [20] are for the correct configuration—a $3^3/_4$-in-dia disk heater which formed the bottom of a cylindrical container for the boiled liquid. A great many of their data must be eliminated because they were obtained on "dirty" heaters. Most of the remainder are for nominal fluids of extremely low purity—actually mixtures for which properties are not known and correlations cannot be applied. Only a few of their data for ethanol remain for use. Berenson presented similar data for CCl_4 and n-pentane on 2-in-dia heaters that were subject to very close control of surface condition.

Costello et al. [18] also presented data for a 2-in-wide plate heater in water with side walls, but their data raise more questions than they resolve. Their q_{max} for "tap water" is close to q_{max_F}, but their result for distilled water in a very clean system is lower by a factor of 0.4. No satisfactory explanation is given for this startling result.

Figure 3 gives these data. It also includes additional preliminary flat-plate data which we shall present informally at this

[7] It was shown in [14] that while λ_d is favored, it is favored only very slightly over a broad span of neighboring Taylor wavelengths.

time. They were obtained on a clean smooth copper plate 2.5 in. in diameter as part of another study which has not yet been completed. The existing data are limited in number and scope, and more are needed for other liquids and larger values of L'. However, equation (32) has been included in the figure and it agrees, about as well as any line could, with the existing data.

The fact that our distilled-water data for $L/\lambda_d \simeq 2$ are low (as was Costello's point) suggests that this might represent a peculiarity of the vapor-jet configuration. It is possible that only one jet can be accommodated on the heater when $L/\lambda_d = 2$, while one just slightly larger will accommodate three jets. As L/λ_d increases this kind of fluctuation will decrease rapidly.

Some General Inferences Concerning Hydrodynamic Predictions of q_{max}

At this point it is advantageous to summarize our major findings:

1 $\dfrac{q_{max}}{q_{max_F}} = \dfrac{24}{\pi}\sqrt[4]{\dfrac{\pi}{A_h}\dfrac{\sigma}{g(\rho_f - \rho_g)}}\left(\dfrac{A_j}{A_h}\right)^{3/4}$ for small heaters, equation (26).

2 $$\frac{q_{max}}{q_{max_F}} = \frac{24}{\pi\sqrt[4]{3}}\frac{A_j}{A_h} \quad \text{for large heaters} \tag{33}$$

3 $\lambda_H = 2\pi R_j$ for small heaters.

4 $\lambda_H = \lambda_d$ for large heaters including the flat plate.

5 For small bluff bodies $A_h \sim L^2$ and equation (26) gives

$$\frac{q_{max}}{q_{max_F}} = \frac{\text{constant}}{\sqrt{L'}} \tag{34}$$

where the constant must be determined experimentally because A_j/A_h is only known in one configuration (small spheres).

6 Except for the case of small spheres and infinite flat plates, A_j/A_h seems to be a constant, very nearly independent of configuration. For the known cases (within about 10 percent)

$$\frac{A_j}{A_h} \simeq 0.155 \tag{35}$$

7 Therefore, from equation (14),

$$\left.\frac{q_{max}}{q_{max_F}}\right|_{\substack{\text{large}\\\text{heaters}}} \simeq 0.9 \tag{36}$$

8 For the infinite flat plate

$$\left.\frac{q_{max}}{q_{max_F}}\right|_{\substack{\text{flat}\\\text{plate}}} = 1.14 \tag{37}$$

9 From equations (27) and (35)

$$\left.\frac{q_{max}}{q_{max_F}}\right|_{\substack{\text{long slender}\\\text{heaters}}} \simeq \frac{1.4}{\sqrt[4]{P'}} \tag{38}$$

Equation (30) is very close to being a special case of equation (38), since $0.94/\sqrt[4]{R'} = 1.48/\sqrt[4]{P'}$ when $2\pi R = P$. The 6 percent difference between 1.48 and 1.40 is within the scatter of the experimental data.

10 The transition between large and small heater behavior occurs about where the breadth of the heater is on the order of λ_d, typically where R' is on the order of 5. Past experience [8, 9] indicates that the appropriate forms of equations (26) and (33) can simply be extrapolated to their point of intersection to obtain a continuous prediction.

Of the preceding items, numbers 5, 6, 7, 8, and 10 have been thoroughly validated with data, [8, 9] and the present study, except insofar as item 7 might require further experimental verification and item 5 has only been verified in one configuration. Item 9 is a fairly solid conjecture that should be verified. Items 1-4 and the generalization in 5 have been verified experimentally only in the sense that their overall consistency with data and their self-consistency have been carefully checked.

Illustrative Application: Prediction of q_{max} on Horizontal Vertically Oriented Ribbons and Experimental Verification

Consider next the case of a thin horizontal ribbon heater with the broad side oriented vertically, as shown at the bottom of Fig. 1. We shall also give brief attention to such a ribbon with one side insulated. Items 2, 6, and 7 apply to either of these cases as long as H is large.

When H is small equation (38) should apply to either insulated or uninsulated ribbons as long as the right P' is used.

Table 1 includes original data for vertically oriented ribbon heaters in four liquids: acetone, benzene, methanol, and isopropanol. The ribbons were all of nichrome, 0.009 in. thick and about 4 in. in length, and they varied in height H from 0.041 in. to 0.188 in. They were operated as electrical-resistance heaters and were connected to the heavy power supply electrodes through brass-ribbon attachments which served to prevent vapor hangup by providing a smooth transition section. The range of H' $\left(\equiv H\sqrt{g(\rho_f - \rho_g)/\sigma}\right)$ was greatly increased by observing q_{max} in the University of Kentucky Gravity Boiling Centrifuge Facility, at both elevated gravity and earth-normal gravity g_e.

Complete details of the experimental method and apparatus can be obtained from [8, 22], since exactly the same equipment and procedure were employed. The probable experimental error in q_{max} was about ±4 percent, although intrinsic variability of the data was ≃±15 percent which is typical for such results. All ribbons had a smooth cold-rolled finish (as delivered). Before each test the ribbons were carefully washed in soap and hot water, and then rinsed in the test fluid.

We can be sure that, even on these small ribbons, q_{max} did not occur prematurely by virtue of low-thermal-capacity effects such as Houchin [23] observed, since he was only able to observe the phenomenon in water. Even though he used much thinner ribbons than we, he never witnessed the early burnout in organic liquids.

These data are presented in dimensionless form in Fig. 4.

Table 1 Peak heat flux on vertically oriented horizontal ribbon

fluid	H (in.)	g/g_e	q_{max} $\frac{Btu}{ft^2 hr}$	H'	$\frac{q_{max}}{q_{max_F}}$
Acetone	0.041	1	142,000 ± 5000	0.65	1.34
	0.051	1	156,000 ± 6000	0.80	1.47
	0.080	1	118,000 ± 3000	1.27	1.12
	0.1395	1	107,000 ± 3000	2.207	1.01
	0.188	1	98,000 ± 3000	2.98	0.923
	0.144	4.01	141,000 ± 1000	4.56	0.94
	↓	8.30	165,000 ± 2000	6.56	0.92
		17.84	226,000 ± 1000	9.62	1.03
		32.32	268,000 ± 4000	12.95	1.06
	↓	49.49	305,000 ± 3000	16.03	1.03
Benzene	0.041	1	126,000 ± 2000	0.635	1.31
	0.055	1	118,000 ± 4000	0.85	1.23
	0.0855	1	96,000 ± 3000	1.32	1.00
	0.144	4.01	135,000 ± 2000	2.65	0.99
	↓	7.98	165,500 ± 2500	3.70	1.02
		18.32	203,000 ± 3000	5.60	1.02
		31.68	237,000 ± 2000	7.35	1.03
	↓	49.49	272,000 ± 3000	9.25	1.06
Methanol	0.055	1	201,000 ± 4000	0.88	1.19
	0.099	1	161,000 ± 3000	1.59	0.95
	0.1395	1	140,000 ± 4000	2.25	0.83
	0.188	1	124,000 ± 4000	3.03	0.74
	0.144	4.01	182,000 ± 6000	4.63	0.75
	↓	7.98	221,500 ± 1500	6.54	0.78
		18.32	282,000 ± 8000	9.91	0.80
	↓	32.32	314,000 ± 8000	13.16	0.77
Isopropanol	0.1395	1	101,000 ± 3000	2.34	0.76
	0.188	1	99,000 ± 4000	3.16	0.74
	0.144	4.11	153,000 ± 5000	4.90	0.81
	↓	8.3	180,000 ± 7000	6.96	0.80
		18.56	210,000 ± 2000	10.40	0.76
	↓	32.32	255,000 ± 6000	13.74	0.81

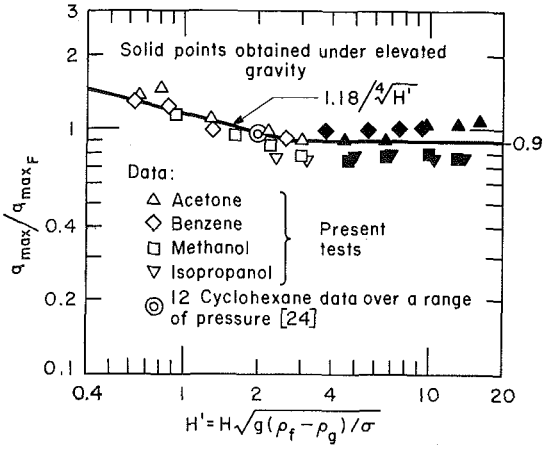

Fig. 4 q_{max} on horizontal ribbon heaters oriented vertically

Following the prescription in the preceding section we represent the data for large L' using equation (36)

$$\left.\frac{q_{max}}{q_{max_F}}\right|_{\substack{\text{large}\\ \text{horiz. ribbons}\\ \text{vert. orient.}}} = 0.9 \qquad (36)$$

And for the range of small H' we use equation (38) with $P' = 2H'$. The result is

$$\left.\frac{q_{max}}{q_{max_F}}\right|_{\substack{\text{small}\\ \text{horiz. ribbons}\\ \text{vert. orient.}}} = \frac{1.18}{\sqrt[4]{H'}} \qquad (39)$$

The correlation is well within the typical scatter for such data. The division between large and small heaters occurs at $H' \simeq 2.7$ in this case.

The peak heat flux was also measured on two 0.009-in-thick horizontal nichrome ribbons, vertically oriented but with one side heavily insulated with Sauereisen cement. A 0.099-in. ribbon was observed in methanol and a 0.188-in. ribbon was observed in acetone. The results were

$$\text{at} \quad H' = 1.59 \qquad 1.19 \leq \frac{q_{max}}{q_{max_F}} \leq 1.30$$

$$\text{at} \quad H' = 2.98 \qquad 1.03 \leq \frac{q_{max}}{q_{max_F}} \leq 1.07$$

respectively. These data are plotted in Fig. 5 along with some high-gravity data given by Adams [25] for higher values of H' in the same geometry.

In this case Adams' data fit the limiting value

$$\left.\frac{q_{max}}{q_{max_F}}\right|_{\substack{\text{large}\\ \text{horiz. ribbon}\\ \text{vert. orient.}\\ \text{1 side insul.}}} = 0.90 \qquad (36)$$

almost perfectly. For small heaters $P' = H'$ and

$$\left.\frac{q_{max}}{q_{max_F}}\right|_{\substack{\text{small}\\ \text{horiz. ribbon}\\ \text{vert. orient.}\\ \text{1 side insul.}}} = \frac{1.4}{\sqrt[4]{H'}} \qquad (40)$$

Both equations (36) and (40) correspond with $A_j/A_h = 0.155$. The transition from large to small H' occurs at 6 when the ribbon is insulated and at 2.6 when it is not.

Conclusions

1 The method of hydrodynamic prediction of the peak heat flux on finite heaters is discussed in detail and certain general guidelines are set up for making such predictions. The assumption that the vapor velocities in the vapor blanket and in the jets must match greatly streamlines prior descriptions and simplifies these guidelines. The guidelines are spelled out in the section "Some General Inferences Concerning Hydrodynamic Predictions of q_{max}."

2 The peak heat flux on an infinite flat plate is 1.14 q_{max_F}, but there is a need for more data in verification of this result.

3 The peak heat fluxes for large and small horizontal ribbons vertically oriented, with and without insulation on one side, are given by equations (36), (39), and (40).

4 The existing hydrodynamic q_{max} predictions for finite bodies are summarized in Fig. 6. The figure includes an indication of the number of data by which each has been verified. This number exceeds the number of points actually shown in Figs. 4 and 5, since more than one observation has been lumped in some of the points. The curves have all been terminated at $L' = 0.1$ on the left side, since hydrodynamic predictions are known to deteriorate for $L' \lesssim 0.1$, see [8, 26].

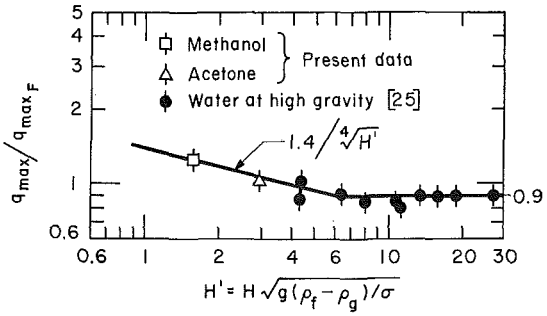

Fig. 5 q_{max} on horizontal ribbon heaters oriented vertically with one side insulated

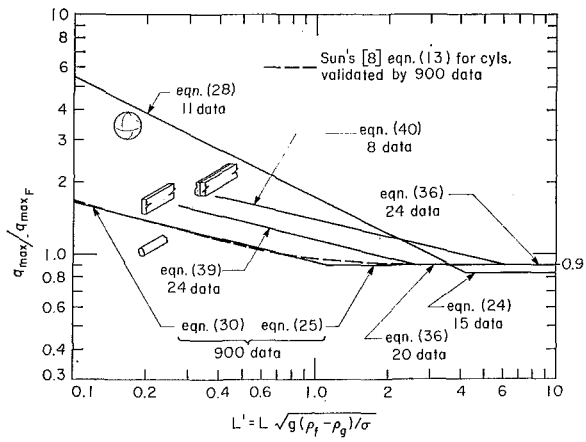

Fig. 6 Collected predictions of q_{max} for four finite heater configurations

References

1 Zuber, N., "Hydrodynamic Aspects of Boiling Heat Transfer," AEC Report No. AECU-4439, Physics and Mathematics, 1959.

2 Zuber, N., Tribus, M., and Westwater, J. W., "The Hydrodynamic Crisis in Pool Boiling of Saturated and Subcooled Liquids," *International Developments in Heat Transfer*, ASME, New York, N. Y., 1963, pp. 230–236.

3 Kutateladze, S. S., "On the Transition to Film Boiling under Natural Convection," *Kotloturbostroenie*, No. 3, 1948, p. 10.

4 Bobrovich, G. I., Gogonin, I. I., Kutateladze, S. S., and Moskvicheva, V. N., "The Critical Heat Flux in Binary Mixtures," *Jour. Appl. Mech. and Tech. Phys.*, No. 4, 1962, pp. 108–111.

5 Bobrovich, G. I., Gogonin, I. I., and Kutateladze, S. S., "Influence of Size of Heater Surface on the Peak Pool Boiling Heat Flux," *Jour. Appl. Mech. and Tech. Phys.*, No. 4, 1964, pp. 137–138.

6 Lienhard, J. H., and Watanabe, K., "On Correlating the Peak and Minimum Boiling Heat Fluxes With Pressure and Heater Configuration," JOURNAL OF HEAT TRANSFER, TRANS. ASME, Series C, Vol. 88, No. 1, Feb. 1966, pp. 94–100.

7 Lienhard, J. H., "Interacting Effects of Gravity and Size upon the Peak and Minimum Pool Boiling Heat Fluxes," NASA CR-1551, May 1970.

8 Sun, K. H., and Lienhard, J. H., "The Peak Pool Boiling Heat Flux on Horizontal Cylinders," *International Journal of Heat and Mass Transfer*, Vol. 13, 1970, pp. 1425–1439.

9 Ded, J. S., and Lienhard, J. H., "The Peak Pool Boiling from a Sphere," *AIChE Journal*, Vol. 18, No. 2, Mar. 1972, pp. 337–342.

10 Lamb, H., *Hydrodynamics*, 6th ed., Dover, New York, N. Y., 1945.

11 Dhir, V., "Some Notes on the Development of the Hydrodynamic Theory of Boiling," University of Kentucky Tech. Report No. 19-70-ME6, Mar. 1970.

12 Bellman, R., and Pennington, R. H., "Effects of Surface Tension and Viscosity on Taylor Instability," *Quart. App. Math.*, Vol. 12, 1954, pp. 151–162.

13 Lienhard, J. H., and Wong, P. T. Y., "The Dominant Unstable Wavelength and Minimum Heat Flux During Film Boiling on a Horizontal Cylinder," JOURNAL OF HEAT TRANSFER, TRANS. ASME, Series C, Vol. 86, No. 2, May 1964, pp. 220–226.

14 Lienhard, J. H., and Sun, K.-H., "Effects of Gravity and Size Upon Film Boiling From Horizontal Cylinders," JOURNAL OF HEAT TRANSFER, TRANS. ASME, Series C, Vol. 92, No. 2, May 1970, pp. 292–298.

15 Westwater, J. W., and Santangelo, J. G., "Photographic Study of Boiling," *Ind. Engr. Chem.*, Vol. 47, 1955, p. 1605.

16 Costello, C. P., and Adams, J. M., "The Interrelation of Geometry, Orientation and Acceleration in the Peak Heat Flux Problem," Mechanical Engineering Department Report, University of Washington, Seattle, Wash., c. 1963.

17 Hendricks, R. C., private communication of unpublished data related to the paper by Hendricks and Baumeister, "Film Boiling from Submerged Spheres," NASA TN D-5124, June 1969.

18 Costello, C. P., Bock, C. O., and Nichols, C. C., "A Study of Induced Convective Effects on Pool Boiling Burnout," *CEP Symposium Series*, Vol. 61, 1965, pp. 271–280.

19 Lienhard, J. H., and Keeling, K. B., Jr., "An Induced-Convection Effect Upon the Peak-Boiling Heat Flux," JOURNAL OF HEAT TRANSFER, TRANS. ASME, Series C, Vol. 92, No. 1, Feb. 1970, pp. 1–5.

20 Cichelli, M. T., and Bonilla, C. F., "Heat Transfer to Liquids Boiling under Pressure," *Trans. AIChE*, Vol. 41, 1945, p. 755.

21 Berenson, P. J., "Transition Boiling Heat Transfer from a Horizontal Surface," M.I.T. Heat Transfer Laboratory Technical Report No. 17, 1960.

22 Sun, K. H., "The Peak Pool Boiling Heat Flux on Horizontal Cylinders," MS thesis, University of Kentucky, 1969 (available as College of Engineering Bulletin No. 88, May 1969).

23 Houchin, W. R., and Lienhard, J. H., "Boiling Burnout in Low Thermal Capacity Heaters," ASME Paper No. 66-WA/HT-40.

24 Lienhard, J. H., and Schrock, V. E., "The Effect of Pressure, Geometry, and the Equation of State Upon the Peak and Minimum Boiling Heat Flux," JOURNAL OF HEAT TRANSFER, TRANS. ASME, Series C, Vol. 85, No. 3, Aug. 1963, pp. 261–272.

25 Adams, J. M., "A Study of the Critical Heat Flux in an Accelerating Pool Boiling System," PhD thesis, University of Washington, Seattle, Wash., Sept. 1962 (also released as University of Washington Mechanical Engineering Department Report to NSF, Sept. 1, 1962).

26 Bakhru, N., and Lienhard, J. H., "Boiling from Small Cylinders," to be published in *International Journal of Heat and Mass Transfer*.

8 Sun, K. H., and Lienhard, J. H., "The Peak Pool Boiling Heat Flux on Horizontal Cylinders," *International Journal of Heat and Mass Transfer*, Vol. 13, 1970, pp. 1425–1439.

9 Ded, J. S., and Lienhard, J. H., "The Peak Pool Boiling from a Sphere," *AIChE Journal*, Vol. 18, No. 2, Mar. 1972, pp. 337–342.

10 Lamb, H., *Hydrodynamics*, 6th ed., Dover, New York, N. Y., 1945.

11 Dhir, V., "Some Notes on the Development of the Hydrodynamic Theory of Boiling," University of Kentucky Tech. Report No. 19-70-ME6, Mar. 1970.

12 Bellman, R., and Pennington, R. H., "Effects of Surface Tension and Viscosity on Taylor Instability," *Quart. App. Math.*, Vol. 12, 1954, pp. 151–162.

13 Lienhard, J. H., and Wong, P. T. Y., "The Dominant Unstable Wavelength and Minimum Heat Flux During Film Boiling on a Horizontal Cylinder," JOURNAL OF HEAT TRANSFER, TRANS. ASME, Series C, Vol. 86, No. 2, May 1964, pp. 220–226.

14 Lienhard, J. H., and Sun, K.-H., "Effects of Gravity and Size Upon Film Boiling From Horizontal Cylinders," JOURNAL OF HEAT TRANSFER, TRANS. ASME, Series C, Vol. 92, No. 2, May 1970, pp. 292–298.

15 Westwater, J. W., and Santangelo, J. G., "Photographic Study of Boiling," *Ind. Engr. Chem.*, Vol. 47, 1955, p. 1605.

16 Costello, C. P., and Adams, J. M., "The Interrelation of Geometry, Orientation and Acceleration in the Peak Heat Flux Problem," Mechanical Engineering Department Report, University of Washington, Seattle, Wash., c. 1963.

17 Hendricks, R. C., private communication of unpublished data related to the paper by Hendricks and Baumeister, "Film Boiling from Submerged Spheres," NASA TN D-5124, June 1969.

18 Costello, C. P., Bock, C. O., and Nichols, C. C., "A Study of Induced Convective Effects on Pool Boiling Burnout," *CEP Symposium Series*, Vol. 61, 1965, pp. 271–280.

19 Lienhard, J. H., and Keeling, K. B., Jr., "An Induced-Convection Effect Upon the Peak-Boiling Heat Flux," JOURNAL OF HEAT TRANSFER, TRANS. ASME, Series C, Vol. 92, No. 1, Feb. 1970, pp. 1–5.

20 Cichelli, M. T., and Bonilla, C. F., "Heat Transfer to Liquids Boiling under Pressure," *Trans. AIChE*, Vol. 41, 1945, p. 755.

21 Berenson, P. J., "Transition Boiling Heat Transfer from a Horizontal Surface," M.I.T. Heat Transfer Laboratory Technical Report No. 17, 1960.

22 Sun, K. H., "The Peak Pool Boiling Heat Flux on Horizontal Cylinders," MS thesis, University of Kentucky, 1969 (available as College of Engineering Bulletin No. 88, May 1969).

23 Houchin, W. R., and Lienhard, J. H., "Boiling Burnout in Low Thermal Capacity Heaters," ASME Paper No. 66-WA/HT-40.

24 Lienhard, J. H., and Schrock, V. E., "The Effect of Pressure, Geometry, and the Equation of State Upon the Peak and Minimum Boiling Heat Flux," JOURNAL OF HEAT TRANSFER, TRANS. ASME, Series C, Vol. 85, No. 3, Aug. 1963, pp. 261–272.

25 Adams, J. M., "A Study of the Critical Heat Flux in an Accelerating Pool Boiling System," PhD thesis, University of Washington, Seattle, Wash., Sept. 1962 (also released as University of Washington Mechanical Engineering Department Report to NSF, Sept. 1, 1962).

26 Bakhru, N., and Lienhard, J. H., "Boiling from Small Cylinders," to be published in *International Journal of Heat and Mass Transfer*.

Discussion

L. M. Trefethen[8]

Professor Lienhard and Dr. Dhir present another step in our understanding of how much heat transfer is possible under boiling conditions. A number of such steps have been made by Professor Lienhard and his associates in the past few years. I should like to ask Professor Lienhard whether, from his present vantage point, he can envision ways to design large surfaces that would have appreciably increased maximum heat fluxes. Since I anticipate that he will probably say "No," or "Not very much," I should also like to ask him whether he would go so far as to predict that we will never be able to raise pool-boiling heat fluxes an order of magnitude above the limits that would now be predicted.

Authors' Closure

True to form, Professor Trefethen raises the \$64 question: How do we apply what we know about pool-boiling mechanisms to get much higher operating heat fluxes during pool boiling on *large* heaters?

There are two ways one can get significant improvements in q_{max}.

1 In a paper presently under review, entitled "Peak Pool Boiling Heat Flux Measurements on Finite Horizontal Flat Plates," we have shown that q_{max} can easily be doubled. The method is to put an egg-crate structure of vertical walls over the heater to break its area into cells of area considerably less than λ_d^2. Burnout then occurs when the single jet squeezed into each cell becomes unstable. This occurs at a greatly elevated heat flux.

2 Dhir's doctoral thesis[9] includes an adaptation of the hydrodynamic theory to the prediction of q_{max} in very viscous liquids. The theory is corroborated by data for saturated cyclohexanol at low temperatures. These data include heat fluxes which are seven to nine times as high as they would have been in the same liquid with zero viscosity.

Thus, we are tempted to answer Professor Trefethen's final question with a very guarded "Yes." We incline to think that there is a possibility of gaining vast improvements of operating pool-boiling heat fluxes.

[8] Professor, Department of Mechanical Engineering, Tufts University, Medford, Mass.

[9] Dhir, V. K., "Viscous Hydrodynamic Instability Theory of the Peak and Minimum Pool Boiling Heat Fluxes," Bulletin No. UKY-100, College of Engineering, University of Kentucky, Lexington, Ky., Nov. 1972.

O. E. DWYER
G. STRICKLAND
S. KALISH[1]
P. J. HLAVAC
G. A. SCHOENER

Brookhaven National Laboratory, Upton, N. Y.

Incipient-boiling Superheats for Sodium in Turbulent Channel Flow: Effect of Rate of Temperature Rise[2]

Using sodium, an experimental study was carried out to determine the effect of rate of temperature rise on the incipient-boiling superheat for fully developed, forced turbulent flow. Three different methods of achieving boiling inception were used. The magnitude of the incipient-boiling superheat was found to be quite reproducible and independent of the experimental method as long as the rate of temperature rise (temperature ramp) was kept constant and kept the same. Moreover, the value of the superheat was found to have a strong dependency on the temperature ramp—the greater the ramp, the larger the superheat. The failure to carefully measure and control temperature ramp is apparently one reason why incipient-boiling-superheat data generally show so much scatter, and those from different laboratories so much disagreement.

Introduction

In the past five years, an increasing number of research papers have appeared in the heat-transfer literature on the subject of incipient-boiling (IB) superheats in liquid alkali metals. This has been mainly a consequence of the development of the sodium-cooled fast-breeder reactor as an energy source for central-station electrical power plants. In such reactor systems it is important from the standpoint of reactor safety considerations to be able to predict the probable magnitude of incipient-boiling superheats in the event of some malfunction of the system that would produce a sudden large increase in core temperature.

In forced-convection boiling, wall superheats up to ≈120 deg F have been reported for potassium [1],[3] and up to ≈160 [2], ≈170 [3], ≈225 [4], and >300 deg F [5] for sodium. The actual magnitude of the superheat depends on a large number of independent variables. One such variable that has not yet been systematically studied, as far as the present authors could determine, is the rate of temperature rise of the heating surface. We shall henceforth also refer to this variable as the temperature ramp. The failure to take it into consideration is apparently one reason why incipient-boiling-superheat (IBS) data generally show so much scatter, and those from different laboratories so much disagreement.

In carrying out forced-convection IB experiments, one of several methods of achieving inception (at a given static pressure) may be employed, such as: (*a*) holding inlet temperature and flow rate constant and gradually increasing the heat flux; (*b*) holding inlet temperature and flow rate constant and increasing the heat flux in steps; (*c*) holding inlet temperature and flow rate constant and imposing a single one-step increase in power to the heater; (*d*) holding heat flux and flow rate constant and gradually increasing the inlet temperature; (*e*) holding heat flux and flow rate constant and increasing the inlet temperature in steps; (*f*) holding heat flux and inlet temperature constant and gradually decreasing flow rate; (*g*) holding heat flux and inlet temperature constant and decreasing the flow rate in steps. From the different methods of effecting an IB event, it is obvious that the temperature ramp can vary over a wide range.

In forced-convection liquid-metal IB studies reported thus far, method (*c*) of conducting the experiments has been the most popular—partly because it is relatively simple to execute and partly because it simulates a sudden burst of reactivity in a nuclear-reactor fuel element. Results of experiments of this type have been published by Pinchera and co-workers [2], Peppler and Schultheiss [5], and Schleisiek [4]. Logan et al. [3] carried out experiments by method (*a*), but the rates of increase of the heat flux were so great that their temperature ramps were, for all practical purposes, very close to what they would have been for method (*c*). Chen [6] employed method (*b*), and Logan et al. [3] employed method (*f*) also, but the rates of decrease of the flow rate were so great that, again, the temperature ramps were very high. Thus with the exception of Chen's experiments, those of the other investigators listed above were carried out in

[1] Currently with Burns and Roe, Inc., Hempstead, N. Y.

[2] This work was performed under the auspices of the U. S. Atomic Energy Commission.

[3] Numbers in brackets designate References at end of paper.

Contributed by the Heat Transfer Division and presented at the Winter Annual Meeting, New York, N. Y., November 26–30, 1972, of The American Society of Mechanical Engineers. Manuscript received by the Heat Transfer Division March 17, 1972. Paper No. 72-WA/HT-11.

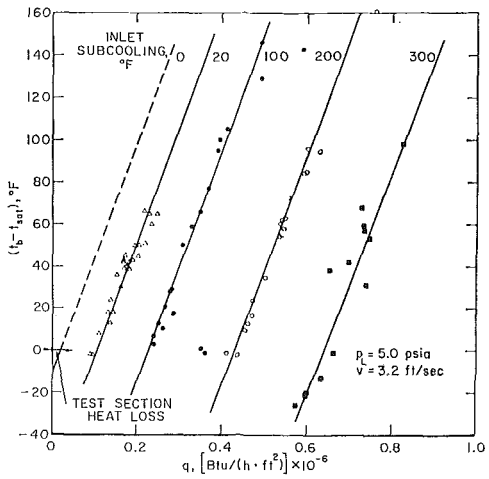

Fig. 1 Incipient-boiling-superheat results for turbulent flow of sodium in an annular channel; the IB experiments were run by fixing the inlet temperature to the test section and rapidly increasing the power on the test heater over a period of considerably less than a minute; the data points fall along the heat-balance lines for the four different inlet temperatures used (from Logan et al. [3])

such a manner that the average temperature ramps were relatively high.

In experiments conducted by method (*c*), even when the average temperature ramp is high, the actual instantaneous ramp at which IB occurs is usually very low, because IB generally occurs at (or near) the end of the temperature transient.

In forced-convection-boiling studies with alkali metals, the effect of heat flux on the IBS is usually represented in the form of plots similar to that shown in Fig. 1. This figure, from the paper by Logan et al. [3], shows bulk superheat data obtained with fully developed sodium flow in an annular channel. The data are given in terms of $t_b - t_{sat}$ rather than $t_w - t_{sat}$ because there were no thermocouples in the smooth stainless-steel heater cladding wall. Further experimental details of that study, along with those of the present study, are summarized in Table 1.

Before examining Fig. 1, let us look at the heat-balance equation

$$t_b - t_{sat} = (t_b - t_{in}) - (t_{sat} - t_{in}) \tag{1}$$

where, for flow in an annulus,

$$t_b - t_{in} = \frac{2qr_1L}{v\rho C_p(r_2^2 - r_1^2)} - \frac{Q}{\pi v\rho C_p(r_2^2 - r_1^2)} \tag{2}$$

Combining equations (1) and (2) gives

$$t_b - t_{sat} = \frac{2qr_1L}{v\rho C_p(r_2^2 - r_1^2)} - \frac{Q}{\pi v\rho C_p(r_2^2 - r_1^2)} - (t_{sat} - t_{in}) \tag{3}$$

which is the equation for the lines in Fig. 1. The four sets of data, represented by the four lines, are for $t_{sat} - t_{in}$ values of 20, 100, 200, and 300 deg F. The fact that the data points fall rather well along the respective all-liquid heat-balance lines shows that, for the most part, IB did not occur until steady-state conditions were attained in the test section, in spite of the fact that IB usually occurred only about 40 sec after the start of power increase on the test heater. The agreement between the heat-balance lines and the data points in Fig. 1 also testifies to the internal consistency of the results.

As Logan et al. point out, a plot such as that shown in Fig. 1 cannot be used to predict IBS. It merely shows the lines along which the data points should fall, and then only when steady-state temperature conditions are approached (i.e., very low ramp) before IB occurs. If steady-state conditions are not reached before IB occurs, then the data points would fall below the related heat-balance line, if $t_b - t_{sat}$ at inception is plotted versus the steady-state value of q. The reason why a plot such as Fig. 1 does not really show the effect of heat flux (on the IB super-

Table 1 Summary of experimental conditions for forced-convection incipient-boiling investigations with sodium

1	Investigators	Logan et al. [3]	present
2	Test section	annular ($^1/_4$-in-dia rod heater in $^3/_4$-in-ID tube)	annular (0.52-in-dia rod heater in 0.93-in-ID tube)
3	Heated length, in.	30	11.5
4	Heating surface	304 s.s.	316 s.s.
5	Surface finish	15–25 μin., and smoother	polished, 14–18 μin. (rms)
6	Method of achieving boiling inception	rapid increase in power on heater (<1 min to reach full power)	a held flux and flow rate constant and gradually increased inlet temp. b held inlet temp. and flow rate constant and gradually increased flux c held inlet temp. and flow rate constant and applied power to heater in one step
7	Location of thermocouples	in flowing stream	embedded underneath 0.013-in-thick s.s. cladding
8	Variables tested	velocity, heat flux, oxygen concentration	temperature ramp
9	Heat flux range, Btu/(hr-ft²)	200,000 to 540,000	50,000 to 200,000
10	p_L range, psia	4.5 to 6.6	3.76 to 3.90
11	Velocity range, ft/sec	3.0 to 8.9	0.80
12	Re range	27,000 to 80,000	11,300
13	Bulk-superheat range	−20 to 130	
14	Wall-superheat range	20 to 170 (calculated)	33 to 240
15	Oxygen, ppm	1 to 5	5 to 8

Nomenclature

C_p = specific heat, Btu(lb_m-deg F)
D_e = $4m$
h = heat-transfer coefficient, Btu/(hr-ft²-deg F)
IB = incipient boiling
IBS = incipient-boiling superheat
m = (cross-sectional flow area)/(wetted perimeter), ft
L = heated length, ft
p_G = partial pressure of inert gas in cavity at time of IB, lb_f/in.²
p_L = static pressure at nucleation site, lb_f/in.²
p_v = vapor pressure of sodium (corresponding to t_L) at time of IB, lb_f/in.²
q = heat flux at heating surface, Btu/(hr-ft²)
Q = heat-loss rate from test section, Btu/hr
r = bubble radius, in.
r_1 = inner radius of annulus, ft
r_2 = outer radius of annulus, ft
Re = $D_e v\rho/\mu$ = Reynolds number, dimensionless
t_b = bulk temperature, deg F
t_{in} = temperature of inlet stream to test section, deg F
t_{sat} = saturation temperature, deg F
t_w = temperature of heating surface, deg F
v = average linear velocity, ft/hr
θ = time, min
μ = viscosity of sodium, lb_m/(ft-hr)
ρ = density of sodium, lb_m/ft^3
σ = surface tension, lb_f/in.

heat) is that another important variable is allowed to change along with it, and that variable is the rate of temperature rise or the temperature ramp—the greater the value of q, the greater will be the average rate of temperature rise, other things being equal. In order to find the true effect of heat flux, therefore, the experimenter must maintain the temperature ramp constant.

Experimental Equipment

Loop. The experiments were conducted with the use of a large figure-8 stainless-steel loop, the cold and hot portions of which were made of type-304 and type-316 (>0.03 percent C) stainless steel, respectively. It was capable of measuring incipient-boiling wall temperatures up to ≈1700 deg F, providing sodium flows up to 40 gpm, and sustaining system pressures up to 100 psig. With the use of cold traps and hot traps, the oxygen concentration in the sodium was controlled to ±1 ppm at concentrations down to ≈5 ppm. The cover gas was ultrahigh-purity argon, whose combined oxygen and water contents were <3 ppm.

The cold portion of the loop, made of schedule-40 nominal $2^1/_2$-in. pipe, contained an air cooler, hot trap, cold trap, plugging indicator, two oxygen meters, a sampling station, an electromagnetic pump, and two electromagnetic flowmeters. The two flowmeters were connected in parallel, one for low flows and one for high. The cold portion of the loop was operated at about 1000 deg F while the hot portion was operated at temperatures up to 1700 deg F. From the intermediate heat exchanger the sodium (in the hot portion) flowed through a preheater, the test section, an air-cooled condenser/surge vessel, and then back to the intermediate heat exchanger. The preheater, used to control the inlet temperature to the test section, was heated by direct passage of alternating electrical current. Sodium flow was generally throttled (by means of a valve) to produce a sufficient flow resistance to stabilize the boiling in the test section following an IB event.

Test Section. The test section was annular, consisting of a $^1/_2$-in-dia rod heater centered in a 0.929-in-ID heavy-wall tube. The sodium entered at the bottom of the test section through four ports (spaced 90 deg apart on the circumference) to achieve a reasonably uniform flow distribution at the inlet end of the test section. The sodium left the test section through two $1^1/_2$-in-dia horizontal outlet pipes spaced 180 deg apart on the circumference.

The length of the annulus was ≈34 in. The rod heater fitted into a socket at the inlet end and was centered at the upper end by a Conoseal joint. Concentricity between the rod and pipe was further maintained by two sets of thin streamlined fin spacers attached to the rod. The lower set was located about 1 in. below the bottom end of the heated zone and the upper set about $6^1/_2$ in. above the top end of the heated zone. The heated zone itself was 11.5 in. long, the bottom end of which was 28 equivalent diameters from the flow inlet point, and the top end of which was 57 equivalent diameters from the flow inlet point and 27.5 from the flow outlet point. Nine thermocouples were embedded below the cladding (on the heater), 40 deg apart on the circumference. Their axial and circumferential locations are given in Table 2. There were five C.E.C. pressure transducers of the strain-gage design, with pressure taps spaced along the test section, as is also indicated in Table 2.

The surface of the stainless-steel cladding in the heated zone of the rod heater was polished (with wet SiC paper No. 240) to a profilometer rms roughness of 14–18 μin. The remainder of the heater, including the fins, was polished (with 3-μ SiC abrasive) to a roughness of 2 to 5 μin. The inner surface of the pipe, the holes in the pipe wall connecting to the pressure transducer lines, and the sheaths on the in-fluid thermocouples were polished (with wet SiC paper No. 600) to a profilometer rms roughness of <2.5 μin. From this it is seen that all parts of the test heater and all inner surfaces of the test section were considerably smoother than the heated zone of the test heater. This, plus the fact that all of the rougher parts of the test section were appreciably colder, suppressed rogue nucleation.

All the thermocouples were the chromel–alumel type, had stainless-steel sheathing, and were calibrated over the temperature range of use. The thermocouples for measuring the temperature in the annular channel were $^1/_{16}$ in. in diameter, while those embedded in the heater under the cladding were 0.020 in. in diameter.

The signal outputs from the thermocouples, flowmeter, and pressure transmitters were recorded on high-speed potentiometric recorders.

The axial location of nucleation was determined by means of a series of voltage taps along the outer wall of the test section. Sufficient voltage was imposed over the length of the test section to produce roughly 100 amp of regulated direct current. The voltage taps were approximately 1 in. apart in the axial region where nucleation occurred. The voltage signals from pairs of taps were amplified and recorded on a FM tape recorder. The location of nucleation and the movement of the liquid–vapor interfaces through the channel were indicated by the recorded voltage signals from the various taps.

Test-Heater Construction. The test heater was specially made for the present study by Watlow Electric Manufacturing Co. It consisted of a coiled Mo resistor that was insulated from a swaged nickel sheath (0.070 in. thick) by compacted BN. Nine thermocouples were embedded in milled round-bottom grooves. Their junctions were ungrounded and located at various axial locations, as shown in Table 2. After the thermocouples were laid in the grooves, the nickel surface was smoothed by burnishing. Then a close-fitting 0.015-in-thick stainless-steel tube was gas-pressure diffusion-bonded onto the nickel.

Operating Procedures

In the present study, boiling-inception runs were made by methods (*a*), (*c*), and (*d*) described in the Introduction, with the vast majority by method (*d*). The rate of rise of the surface temperature of the test heater was controlled by (and essentially equal to) the rate of rise of the bulk temperature of the sodium entering the test section. This rate of temperature rise was

Table 2 Locations of thermocouple junctions and pressure taps in test section

Thermocouples embedded below heater cladding			Pressure-transmitter taps			Thermocouples in annular channel	
No.	Distance above bottom end of heated zone, in.	Circumferential angle from thermocouple No. 8, deg	No.	Distance above bottom end of heated zone, in.	Circumferential angle from thermocouple No. 8	No.	Distance above bottom end of heated zone
1	−8	320	2	6	240	1	−12
2	−4	120	3	8	160	2	−12
3	6	240	4	9	80	3	−12
4	8	40	5	10	0	4	14
5	8	160	6	11	280	5	14
6	8	280				6	14
7	9	80				7	16
8	10	0				8	16
9	10	200				9	16

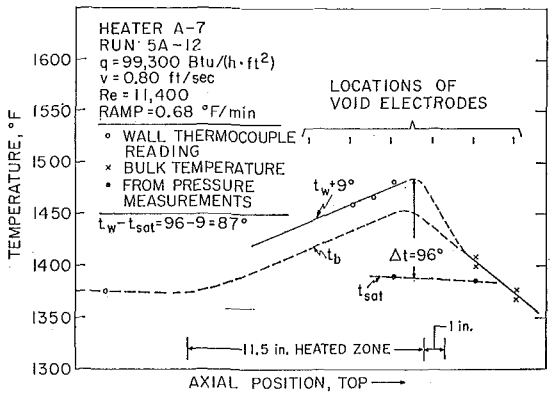

Fig. 2 Typical axial-temperature profiles along the test section at the instant of boiling inception; the radial temperature drop through the stainless-steel cladding was 9 deg F (for $q = 10^5$ Btu/(hr-ft²)

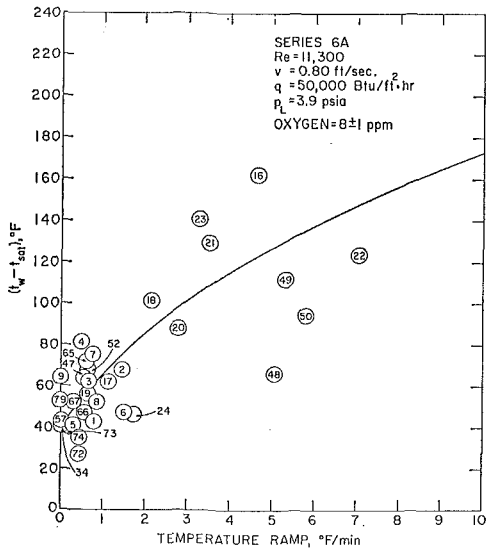

Fig. 3 Effect of rate of rise of heating-wall temperature on IB superheat for turbulent flow of sodium in an annular channel, and for a heat flux (on the inner wall) of 50,000 Btu/(hr-ft²); the IB measurements were made by holding the heat flux constant and gradually increasing the temperature of the heating surface by gradually increasing the power on the preheater

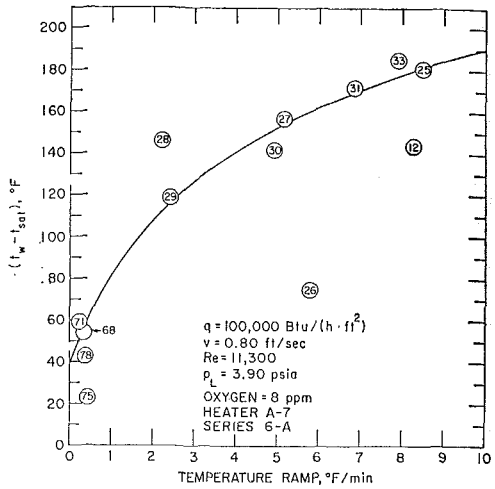

Fig. 4 Effect of rate of rise of heating-surface temperature on IB superheat for turbulent flow of sodium in an annular channel, and for a heat flux (on the inner wall) of 100,000 Btu/(hr-ft²)

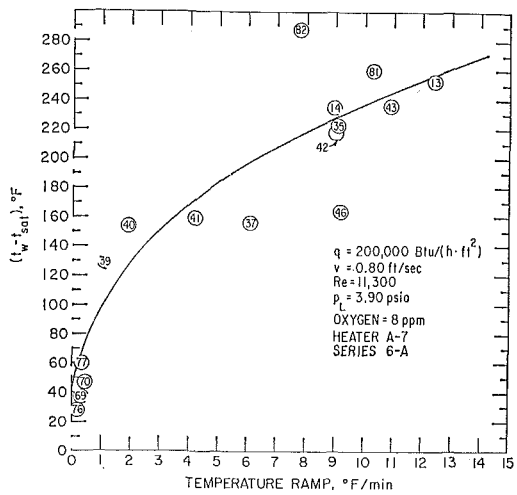

Fig. 5 Effect of rate of rise of heating-surface temperature on IB superheat for turbulent flow of sodium in an annular channel, and for a heat flux (on the inner wall) of 200,000 Btu/(hr-ft²)

maintained by gradual power addition to the preheater. For a given flow rate, the rate of power addition to give a constant temperature ramp was soon known. In the great majority of runs the ramp was maintained constant for at least 3 min before boiling inception occurred. Several wall and fluid temperatures, as well as pressures and flow rate, were recorded on strip charts.

Although the void electrodes were placed 1 in. apart along the test section wall, voltage readings were actually taken on alternate probes and were therefore 2 in. apart. This was done to get good unmistakable signals. As indicated by these signals, nucleation nearly always occurred within an inch of the end of the heated zone of the test heater. When it did not, the run was abandoned. The temperature profiles for a typical run are shown in Fig. 2.

After each IB event, the sodium was allowed to boil in the test section for about 1 to 2 min. Then the test heater power was turned off, the preheater power cut back, and the system subcooled about 40 deg (with reference to the system pressure before boiling inception). Then the pressure on the system was increased by 1 psia and the system kept in the subcooled condition for about 20 min. This was done to condense any vapor pockets left by the previous inception, so that premature nucleation would not occur during the next run.

The instant of boiling inception was clearly shown on the temperature, flowmeter, and pressure charts, and also on the loudspeaker for the audio pickup. The wall and fluid thermocouples showed the usual sudden large temperature drops. Some typical temperature traces are shown in another paper [7].

The experimental equipment was operated 24 hr a day, seven days a week. It generally took about 2½ hr to carry out a single run.

Results

Effect of Temperature Ramp. Figures 3, 4, and 5 show three groups of experimental results, demonstrating the effect of temperature ramp on the IBS as observed in the present study. These three plots are for fixed heat fluxes of 50,000, 100,000, and 200,000 Btu/(hr-ft²), respectively. Each run was made by increasing the wall temperature of the heater at a fixed rate by gradually increasing the power on the preheater.

The effect of temperature ramp on the IBS is seen to be large. As the ramp approaches zero the IBS (according to the drawn curves) approach the same limit, i.e., 40 deg, independently of the heat flux. The large number of points in Fig. 3 at the low end of the abscissa scale is explained by the fact that, throughout the course of the study, runs were frequently made at essentially the same set of conditions to see whether or not there was an effect of running time on the data. As explained later there was a very slight effect.

Referring to the data points in Figs. 3, 4, and 5, the number

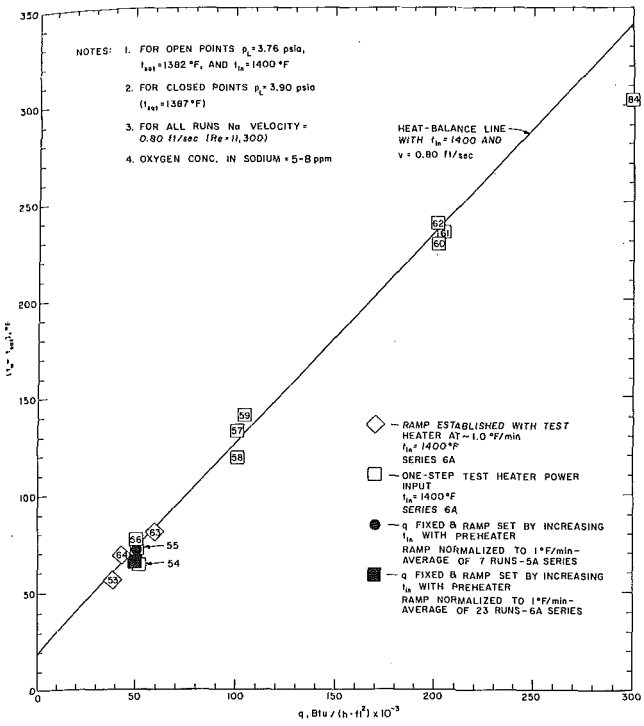

Fig. 6 Comparison of IB superheat measurements obtained by different experimental procedures for turbulent flow of sodium in an annular channel

in each circle represents the run number. The precision of the data is actually quite good, considering the wide scatter generally observed in forced-convection IBS measurements with sodium. No data points were thrown out because they fell far from the average curve drawn through the points. One to three points were discarded from each plot because either the temperature ramp had not been properly established before IB occurred or inception occurred more than $\approx 1^1/_2$ in. beyond the upper end of the heated zone.

Comparison of IB Superheats Obtained by Different Methods. Incipient-boiling superheats obtained by three different methods are compared in Fig. 6. The solid-circle point represents the average of seven IB measurements made in a certain series (5A) of runs, employing method (*d*). The runs were made under conditions where the temperature ramps varied from 0.3 to 1.0 deg F/min, but the majority were obtained at ≈0.7. The IB superheats of the seven runs, before being averaged, were corrected (where necessary) to a common ramp of 1.0 deg F/min, in accordance with the curve in Fig. 3.

The solid-square point in Fig. 6 represents the average of 23 IB measurements made in a different series (6A) of runs. These points are the ones shown in Fig. 3 falling in the ramp range 0 to 1.75 deg F/min, but before the IB values were averaged they were corrected, as before, to a common ramp of 1.0 deg F/min.

The agreement between the two sets of data, taken about a month apart, is very good.

The average value of the inlet temperature at the instant of IB for the 23 runs in series 6A was 1400 deg F, and the straight line in Fig. 6 represents equation (6) with t_{in} = 1400 deg F. The wall temperature t_w was calculated for an axial point $^1/_2$ in. upstream from the downstream end of the heated zone, or, in other words, at the axial location where the surface temperature was a maximum (Fig. 2). This was at, or very close to, the point of boiling inception, as indicated by the void-electrode measurements described earlier.

Data points 53, 63, and 64 in Fig. 6 were obtained by experimental method (*a*), i.e., by fixing the inlet temperature (at 1400 deg F) and gradually increasing t_w (at ≈1.0 deg F/min) by gradually increasing the power on the test heater at a uniform rate. Data points 54 to 56 were obtained by setting the inlet temperature at 1400 deg F and putting the power [equivalent to 50,000 Btu/(hr-ft²)] on the heater in a single step. The excellent agreement between the four sets of data proves without doubt that the IB superheat is a scientific quantity that is independent of experimental procedure, as long as the important independent variables are the same.

Now, the temperature ramp for points 54 to 56 was quite different from that employed in the three previous sets of data. It went through a transient, being very high soon after the power was put on the heater and approaching zero at the time IB occurred. The time between power-on and inception was about 2 min. Throughout most of this period the temperature ramp was relatively high and called for a higher wall superheat than actually existed, but eventually the called-for superheat and the actual superheat coincided and IB occurred. Theoretically, IB should have occurred before the transient ramp approached 0 deg F/min, which would have placed the points slightly below the energy-balance line (which represents a ramp of zero), but the period of time between a low ramp rate (say, ≈1 deg F/min) and ≈0 deg F/min was very short and within the normal nucleation induction period. In other words, inception did not occur in runs 54 to 56 until steady-state conditions had essentially been reached. This is the same result as Logan et al. [3] observed, which has already been discussed and which is illustrated in Fig. 1.

Runs 57 to 59 were carried out in the same manner as that for runs 54 to 56, except the power setting on the heater corresponded to q = 100,000. Likewise the power setting for runs 60 to 62 corresponded to q = 200,000. For these six runs, IB did not occur until steady-state thermal conditions had essentially been established, which took about 3 and 4 min for the 100,000 and 200,000 fluxes, respectively. When the IB runs were carried out by fixing t_{in} at 1400 deg F and imposing a one-step power increase on the test heater, the IB superheat was found to be very much dependent on the steady-state value of q. For example the results in Fig. 6 show that as q was increased from 50,000 to 100,000 to 200,000, the IB wall superheat increased from 72 to 126 to 233 deg F, respectively. This was so because the high-temperature ramps in the early stages of the temperature transients precluded the possibility of lower IB superheats.

Data point 84 in Fig. 6 represents a run that was terminated before IB occurred because the cladding temperature was getting too high. At termination t_w had reached 1684 deg F. All of the results obtained by methods (*a*) and (*c*) are shown in Fig. 6, i.e., no data points were discarded.

Over the period of operation during which the results presented in this paper were obtained, there was no significant change in the magnitude of the measured superheat with time. Many runs were made periodically at the same set of test conditions (Fig. 3). There was, however, a significant drop in superheat observed over several months, but this is discussed in a subsequent paper [7].

Discussion

The results of the present study, the first ever obtained in forced-convection boiling of a liquid metal where temperature ramp was isolated and studied as an independent variable, clearly show that rate of temperature rise has an important bearing on the magnitude of the incipient-boiling superheat. We have shown that if the temperature ramp is held constant, IB superheats are the same, no matter how the test is conducted. But if temperature ramp is not held constant, as in experimental method (*c*), the magnitude of the IB superheat depends on the experimental procedure. Heretofore nearly all experimental IB studies have been carried out by method (*c*). Under those conditions IB does not generally occur until steady-state conditions have been closely approached, and the magnitude of the superheat is given by the ($t_w - t_{sat}$) vs. q energy-balance line, as seen in Figs. 1 and 6.

The present study was very carefully planned and executed, and there is no apparent reason to question the validity of the

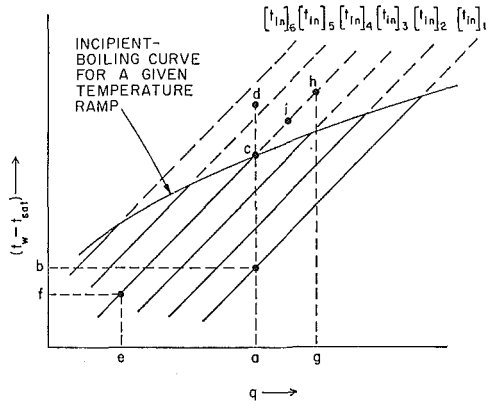

Fig. 7 Effect of heat flux on IB superheat showing the relation between typical IB curve and heat-balance lines

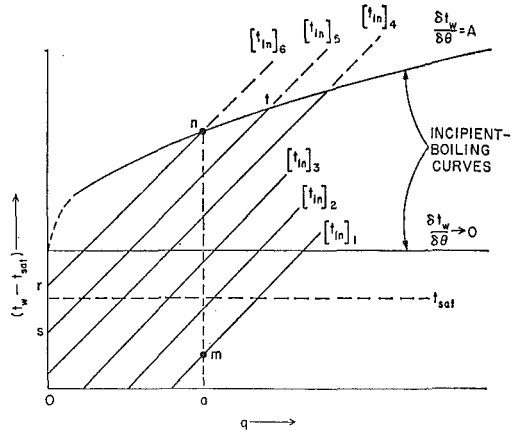

Fig. 8 Effect of heat flux on IB superheat showing the relationship between IB curves and heat-balance lines; the IB curves are a function of the rate of rise of the heating-wall temperature

results. On that basis, we present the following further discussion.

The measurement of IBS, under a given set of experimental conditions, is not a precise measurement, even when all the known operational variables are carefully controlled. And the higher the temperature ramp, the more this is true. The higher the temperature ramp, the more the phenomenon appears to be kinetics-controlled, and the lower the ramp, the more it appears to be equilibrium-controlled. At a zero ramp, and if turbulence is negligible, the phenomenon would appear to be entirely equilibrium-controlled and expressed by the well-known bubble thermal–mechanical equilibrium equation

$$p_v + p_G - p_L = \frac{2\sigma}{r} \tag{4}$$

Thus on this basis one would expect experimental methods (*b*) and (*e*) to give both lower and more precise data than, say, method (*c*), and this seems actually to be the case on the basis of the limited results available. With methods (*b*) and (*e*) the incipient bubble has more time at each temperature step to reach its nucleation threshold. Another way of saying it is that the probability of an IB event occurring is greater the longer the system is kept at a given temperature.

Let us now write the temperature-balance equation

$$t_w - t_{sat} = (t_w - t_b) + (t_b - t_{in}) + (t_{in} - t_{sat}) \tag{5}$$

assuming heat losses to be negligible, and then replace $t_w - t_b$ by q/h and $t_b - t_{in}$ by $2qr_1L/v\rho C_p(r_2^2 - r_1^2)$ for an annular channel. This gives

$$t_w - t_{sat} = q\left[\frac{1}{h} + \frac{2r_1L}{v\rho C_p(r_2^2 - r_1^2)}\right] + (t_{in} - t_{sat}) \tag{6}$$

This equation is represented in Fig. 7 by the six diagonal straight lines representing six different inlet temperatures. Also in Fig. 7 an IB curve is postulated[4] for a given temperature ramp. If we start at the point corresponding to $q = a$ and $t_w - t_{sat} = b$, and gradually increase t_w at the ramp corresponding to that of the particular IB curve shown (by gradually increasing t_{in}), theoretically IB should occur at point *c*. However, if we were to increase t_{in} at a greater rate we would most probably overshoot the IB curve (according to the results of the present study) and IB would occur at some point such as *d*. We can imagine point *d* lying on some other (higher-ramp) IB curve. Now, if we change the procedure and start at the point corresponding to $q = e$ and $t_w - t_{sat} = f$, and increase t_w at the same constant rate we used initially (by gradually increasing q), maintaining the inlet temperature constant at $(t_{in})_4$, theoretically IB should also occur at point *c* (according to the results of the present study). We say *theoretically* because, as explained above, IB measurements are inherently not very precise and therefore not highly reproducible. In any case, if we were to take a large number of IB measurements by each of the two methods described above, the average measurement by each should be the same.

If we now employ a third type of procedure and start at the point corresponding to $q = e$ and $t_w - t_{sat} = f$, again, for inlet temperature $(t_{in})_4$, and suddenly increase the power on the heater to increase q from *e* to *a*, IB should again occur at point *c*, if the temperature rise were fairly rapid (i.e., the heat capacity of the heater is small relative to the rate of heat generation within it) and steady-state conditions were essentially established. In the earlier stages of such a transient the temperature ramp is very high, which puts $t_w - t_{sat}$ at IB above that corresponding to point *c*, but $t_w - t_{sat}$ cannot go higher than that because $q \leq a$.

If, now, we start at the point corresponding to $q = e$ and $t_w - t_{sat} = f$ and suddenly increase q from *e* to *g*, IB should occur at point *h*, again, if the temperature rise were initially rapid and steady-state conditions were essentially established. It is now clear that if one continued to impose (one-step) higher and higher fluxes, a series of IB points would be obtained that fell on the $(t_{in})_4$ line, i.e., if IB did not occur until steady-state conditions had essentially been established (which appears to be generally true). If, in the last case, steady-state conditions had not been reached before IB occurred, then it would occur at some point such as *i* (Fig. 7).

Inlet temperature (or amount of inlet subcooling) is, from a thermodynamics point of view, not an independent variable, but, depending on how a forced-convection IB experiment is carried out, inlet temperature can have an important influence on the result. Let us look at Fig. 8. If we start at point *m*, corresponding to $q = a$ and inlet temperature $(t_{in})_1$, and increase t_{in} at a constant rate such that $\partial t_w/\partial\theta = A$, while maintaining q constant, IB should occur at point *n*. In other words, IB occurs when t_{in} reaches $(t_{in})_6$, and t_{in} at IB is a function of q, $\partial t_w/\partial\theta$, and the heat-transport characteristics of the system. If the heated length were increased, then t_{in} would decrease, all other conditions remaining the same.

Still looking at Fig. 8, if we start at point *r* and steadily increase q so that $\partial t_w/\partial\theta = A$, then IB should also occur at point *n*. However, if we start at point *s* and employ the same temperature ramp, then IB should occur at point *t*. Or, in other words, when t_{in} is held constant and q gradually increased, $t_w - t_{sat}$ at IB depends on t_{in}, the dependency again depending on the heat-transport characteristics of the experimental system.

The study described in this paper was intended to be the first of a series at Brookhaven on the general subject of incipient-boiling superheats for alkali metals in turbulent channel flow. However, because of termination of financial support, the program had to be abandoned. It is hoped that other workers can pick up where we have left off, by first attempting to confirm experimentally the temperature-ramp effect on IBS and then by

[4] The shape of the curve is based on additional experimental results that are to be published in a subsequent paper [7].

developing a satisfactory theory if experimental confirmation is found.

Conclusions

The following conclusions are drawn on the basis of the findings of the present study:

1 Rate of temperature rise (or temperature ramp) is a very important parameter affecting the magnitude of the IB superheat. The higher the temperature ramp, the more the IB phenomenon is kinetics-controlled and the less it is equilibrium-controlled.

2 The higher the temperature ramp, the greater will be the magnitude of the IB superheat, other things being equal.

3 Inlet temperature (or amount of inlet subcooling) is not, thermodynamically speaking, an independent variable affecting the IB superheat. Basically $t_w - t_{sat}$ at IB is a function of q, v, and $dt_w/d\theta$, and t_{in} is a function of t_w, q, v, and the geometry of the test section.

4 For a fixed temperature ramp, the magnitude of the IB superheat is independent of the manner in which the experiment is conducted, e.g., the superheat is the same whether (1) q is held constant and t_w gradually increased by gradually increasing t_{in} or (2) t_{in} is held constant and t_w is gradually increased by gradually increasing q.

5 During a rapid temperature transient produced by a one-step power increase on the heater, IB did not occur until steady-state thermal conditions had essentially been attained.

References

1 Chen, J. C., "Incipient Boiling Superheats in Liquid Metals," JOURNAL OF HEAT TRANSFER, TRANS. ASME, Series C, Vol. 90, No. 3, Aug. 1968, pp. 303–312.

2 Pinchera, G. C., Tomassetti, G., Falzetti, L., and Fornair, G., "Sodium Boiling Researches Related to Fast Reactor Safety," *Transactions of the American Nuclear Society*, Vol. 11, 1968, pp. 691–692.

3 Logan, A. D., Baroczy, C. J., Londoni, J. A., and Morewitz, H. A., "Effects of Velocity, Oxide Level, and Flow Transients on Boiling Initiation in Sodium," in: *Liquid-Metal Heat Transfer and Fluid Dynamics*, ASME, New York, N.Y., 1970, pp. 116–128.

4 Schleisiek, K., "Heat Transfer and Boiling during Forced Convection of Sodium in an Induction-heated Tube," *Nucl. Eng. Design*, Vol. 14, 1970, pp. 60–68.

5 Peppler, W., and Schultheiss, G. F., "Liquid Metal Boiling Research," Report Nos. KFK874 and EUR 4157e, Kernforschungszentrum, Karlsruhe, Germany, Oct. 1968.

6 Chen, J. C., "An Experimental Investigation of Incipient Vaporization of Potassium in Convective Flow," in: *Liquid-Metal Heat Transfer and Fluid Dynamics*, ASME, New York, N.Y., 1970, pp. 129–134.

7 Dwyer, O. E., et al., "Incipient-Boiling Superheats for Sodium in Turbulent, Channel Flow: Effects of Heat Flux and Flow Rate," to be published in *International Journal of Heat and Mass Transfer*.

developing a satisfactory theory if experimental confirmation is found.

Conclusions

The following conclusions are drawn on the basis of the findings of the present study:

1 Rate of temperature rise (or temperature ramp) is a very important parameter affecting the magnitude of the IB superheat. The higher the temperature ramp, the more the IB phenomenon is kinetics-controlled and the less it is equilibrium-controlled.

2 The higher the temperature ramp, the greater will be the magnitude of the IB superheat, other things being equal.

3 Inlet temperature (or amount of inlet subcooling) is not, thermodynamically speaking, an independent variable affecting the IB superheat. Basically $t_w - t_{sat}$ at IB is a function of q, v, and $dt_w/d\theta$, and t_{in} is a function of t_w, q, v, and the geometry of the test section.

4 For a fixed temperature ramp, the magnitude of the IB superheat is independent of the manner in which the experiment is conducted, e.g., the superheat is the same whether (1) q is held constant and t_w gradually increased by gradually increasing t_{in} or (2) t_{in} is held constant and t_w is gradually increased by gradually increasing q.

5 During a rapid temperature transient produced by a one-step power increase on the heater, IB did not occur until steady-state thermal conditions had essentially been attained.

References

1 Chen, J. C., "Incipient Boiling Superheats in Liquid Metals," JOURNAL OF HEAT TRANSFER, TRANS. ASME, Series C, Vol. 90, No. 3, Aug. 1968, pp. 303–312.

2 Pinchera, G. C., Tomassetti, G., Falzetti, L., and Fornair, G., "Sodium Boiling Researches Related to Fast Reactor Safety," *Transactions of the American Nuclear Society*, Vol. 11, 1968, pp. 691–692.

3 Logan, A. D., Baroczy, C. J., Londoni, J. A., and Morewitz, H. A., "Effects of Velocity, Oxide Level, and Flow Transients on Boiling Initiation in Sodium," in: *Liquid-Metal Heat Transfer and Fluid Dynamics*, ASME, New York, N.Y., 1970, pp. 116–128.

4 Schleisiek, K., "Heat Transfer and Boiling during Forced Convection of Sodium in an Induction-heated Tube," *Nucl. Eng. Design*, Vol. 14, 1970, pp. 60–68.

5 Peppler, W., and Schultheiss, G. F., "Liquid Metal Boiling Research," Report Nos. KFK874 and EUR 4157e, Kernforschungszentrum, Karlsruhe, Germany, Oct. 1968.

6 Chen, J. C., "An Experimental Investigation of Incipient Vaporization of Potassium in Convective Flow," in: *Liquid-Metal Heat Transfer and Fluid Dynamics*, ASME, New York, N.Y., 1970, pp. 129–134.

7 Dwyer, O. E., et al., "Incipient-Boiling Superheats for Sodium in Turbulent, Channel Flow: Effects of Heat Flux and Flow Rate," to be published in *International Journal of Heat and Mass Transfer*.

Discussion

Hans K. Fauske[5]

The experiment reported in this paper appears to be carefully executed. The purpose of this discussion is, therefore, not to question the validity of the experimental results but rather to suggest a different interpretation of the experimental results.

The data reported in the paper suggest that the incipient-boiling superheat for sodium in turbulent channel flow exhibits a dependence on the rate of temperature rise, with the inlet temperature increasing in the order of 1 deg F per minute. A brief consideration of the thermal time constants of the experimental system indicates that a quasi-steady state prevails at all times with respect to temperatures of the system, but that the transfer of gas into or out of the surface cavities and/or tiny entrained gas bubbles in the bulk of the liquid is diffusion-controlled and exhibits much longer time constants. Hence, one would suspect some inert-gas effects in the data. It can be shown that the wall superheat at which bubble nucleation can occur is inversely proportional to the mass of noncondensable gas in the bubble. It follows that for a constant velocity, the inert mass of the bubble would tend to decrease with increasing temperature ramp, thereby explaining the noted trend in the data if such bubbles are present in the sodium. Likewise, for an increase in the velocity, the inert-mass concentration present in the bubble at the exit would be increased, since less mass is lost from the bubble as it travels from the inlet to the outlet of the test section, thus suggesting another explanation for the noted velocity effect discussed in reference [7] of the paper. It would therefore appear important that in future forced-convective sodium superheat tests, provisions be made for detecting the presence of any tiny gas bubbles in the coolant in addition to measuring the location of incipient boiling. Any information regarding the magnitude of inert gas present in the experimental system used by the authors would be helpful.

Authors' Closure

In the above comment, Dr. Fauske suggests that the temperature-ramp effect observed in the present study may actually be an inert-gas effect instead, where the gas could be present either in the surface cavities or as tiny entrained bubbles in the flowing sodium. We agree that the thermal time constant for the test system was undoubtedly much less than the diffusion time constant for the transfer of inert gas into the sodium, assuming that inert gas was present in the surface cavities and/or in the form of tiny bubbles entrained in the sodium. If this is so, then we cannot agree with Dr. Fauske's conclusion that "the inert mass of the bubble would tend to decrease with increasing temperature ramp," other things being equal. The opposite would be true, because the greater the temperature ramp, the less time would be available for the inert gas to diffuse out of the bubble into the sodium where it is more soluble. Or, in other words, the greater the ramp, the lower would be the incipient-boiling superheat, because of the greater inert-gas concentration in the bubble. But the opposite effect was observed, showing that inert-gas effects were not involved. Moreover, the sodium residence time in the test section was very short compared with the time constant for inert-gas diffusion in the sodium.

In the course of taking our data, it was observed several times that if the temperature ramp was suddenly lowered, boiling inception would promptly occur, if the wall temperature was high enough for inception to occur at the lower ramp. This again would indicate that the kinetics of inception were not dependent on inert-gas content of bubbles but on the ramp effect alone.

The question of inert-gas entrainment and its apparent negligible effect on the velocity results reported in [7] are discussed in that reference.

We would agree that in future experimental studies of forced-convection superheat with alkali metals it would be highly desirable to determine whether or not entrained gas bubbles are present. When the equipment was built for the present study, there was no workable instrument available for doing this. However, as explained in [7], every conceivable precaution was taken to prevent the incipient-boiling data taken in the present study from being clouded by the possible presence of gas.

We should mention here that during the discussion period that followed the presentation of the subject paper, Prof. J. C. Chen of Lehigh University reported pool-boiling incipient-boiling superheat results that he had obtained on Freon-113, which also showed a similar effect of temperature ramp, and his ramp rates were of the same order as those employed by us. Since the solubility of inert gases in Freon *decreases* with increase in temperature, Professor Chen's results tend to negate the inert-gas effect proposed by Dr. Fauske.

[5] Reactor Analysis and Safety Div., Argonne National Laboratory, Argonne, Ill.

K. J. BAUMEISTER
Mem. ASME

F. F. SIMON

National Aeronautics and Space Administration, Lewis Research Center, Cleveland, Ohio

Leidenfrost Temperature—Its Correlation for Liquid Metals, Cryogens, Hydrocarbons, and Water

A prediction technique for the Leidenfrost and minimum temperatures is presented which considers the effects of the critical temperature of the liquid, thermal properties of the solid, surface energy of the liquid, and surface energy of the solid. The prediction technique is in good agreement with data for liquid metals, cryogens, hydrocarbons, and water.

Introduction

THE PREDICTION of the Leidenfrost temperature T_{Leid} and the minimum temperature T_{min} is currently important in safety considerations in fast breeder liquid-metal-cooled reactors and in the cooldown of cryogenic systems. At the present time, however, there seems to be considerable uncertainty in the literature [1–32][1] as to the numerical value of the Leidenfrost or minimum temperature for a given fluid. The object of the present paper is to delineate the important parameters involved in the measurement of the Leidenfrost and minimum temperatures and to present a means of predicting their values.

The minimum temperature is associated with the minimum point on the conventional pool-boiling curve (heat flux versus temperature). For plate temperatures below the minimum temperature, nucleate or transition boiling will occur, while for plate temperatures greater than the minimum, film boiling will occur.

The Leidenfrost temperature, on the other hand, applies to discrete liquid drops rather than to a liquid pool. Although not as familiar as the conventional pool-boiling curve, the droplet vaporization curve shown in Fig. 1 is used to define the Leidenfrost temperature. In measuring the Leidenfrost temperature, the experimenter sets a plate at an initial temperature T_0, places a liquid drop onto the surface, and measures the time it takes for the liquid drop to evaporate. The experimenter repeats the above measurement for various T_0 and then plots the vaporization time data against T_0 as shown in Fig. 1 and determines the Leidenfrost temperature $T_{Leid,\ meas}$ from this curve. For plate temperatures slightly below the Leidenfrost temperature, nucleate and transition boiling occurs and the droplet vaporization time is very short. For plate temperatures greater than the Leidenfrost temperature, film boiling occurs and the drop vaporization time is very long.

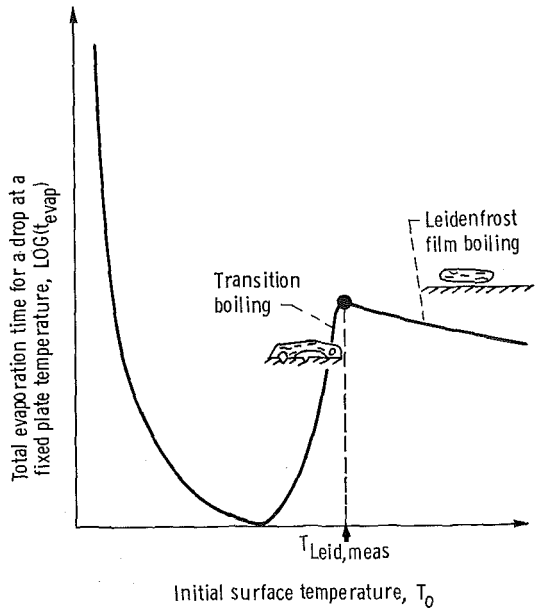

Fig. 1 Evaporation time curve of liquid drops in contact with hot surface for drops of equal volume and equal initial temperature

This paper will develop a model for predicting the Leidenfrost temperature for discrete liquid drops. However, the theory and experimental evidence indicate that under certain conditions the minimum temperature and the Leidenfrost temperature will be equal. Consequently, both Leidenfrost and minimum temperature data will be correlated in the final equation.

In particular, this paper will deal with the following items:

First (Part I), an analytical conduction model will be constructed which will indicate how thermal properties of the supporting surface affect the measured value of the Leidenfrost temperature $T_{Leid,\ meas}$.

[1] Numbers in brackets designate References at end of paper.

Contributed by the Heat Transfer Division for publication (without presentation) in the JOURNAL OF HEAT TRANSFER. Manuscript received by the Heat Transfer Division April 28, 1972. Paper No. 73-HT-F.

Second (Part II), experimental evidence for aluminum, stainless-steel, and glass surfaces will be used to verify the trends predicted in Part I and to ascertain the effects of surface roughness and contamination on both the measured Leidenfrost and minimum temperatures. Also, the experimental evidence indicates under what conditions the measured minimum temperature $T_{min,meas}$ and the measured Leidenfrost temperature $T_{Leid,\ meas}$ will be equal.

Third (Part III), using the results of Parts I and II, a correlation is presented which accounts for the surface conduction effects on the measured value of the Leidenfrost temperature $T_{Leid,\ meas}$.

Present theories for predicting the Leidenfrost or minimum temperature have a common drawback in that they do not account for thermal properties of the solid (conduction and thermal capacity). In Part IV of the report, we will use the theory of Part III to predict what the measured Leidenfrost or minimum temperature would be on an ideal isothermal surface. Next, Spiegler's theory [14] is used to correlate the "isothermal data" for which thermal surface property effects have been removed. However, Spiegler's theory does not account for surface energy effects. Consequently, Spiegler's theory was modified to take into account the surface energy of both the liquid and solid.

Part I—Surface Temperature Criteria

Physical Situation. Consider a surface whose temperature is above the Leidenfrost temperature T_{Leid}. When a drop approaches and touches this surface, the surface temperature begins to decrease because of the heat transferred to the drop. If the surface temperature falls sufficiently, transition or nucleate boiling will occur and the drop will seemingly explode. On the other hand, if the fall in surface temperature is not too severe, the vapor generated beneath the drop will coalesce and form an insulating film. Here the liquid no longer touches (wets) the surface, except possibly for small liquid spikes which can penetrate the vapor layer [3]. The drop will now evaporate slowly in the Leidenfrost boiling state where the vapor film supports the drop.

In gathering vaporization time data for Fig. 1, the experimenter generally does not measure the transient temperature directly beneath the drop at the plate surface; he only measures the initial temperature of the surface. Consequently, the Leidenfrost temperature measured on a surface which does not experience any temperature drop, $T_{Leid,iso}$ (an isothermal surface), will be somewhat less than the Leidenfrost temperature measured on a real surface which experiences a temperature drop, assuming both surfaces have the same finish and wetting characteristics. Thus

$$T_{Leid,iso} < T_{Leid,\ meas} \tag{1}$$

since the surface temperature is measured before the liquid is placed on the surface.

The parameters which affect the decrease in surface temperature beneath the drop can now be found by consideration of the transient conduction equation in the heated plate. The following considerations apply only to the very short time in which the initial transient has occurred, t_b, perhaps 10 msec. For times greater than t_b, the drop enters a steady state of nucleate, transition, or film boiling.

Conduction Model. Consider a hot semi-infinite solid at initial temperature T_0. A drop of liquid of radius R_0 is placed gently on the surface. For simplicity, during the initial but very short transient period, the unknown time-dependent heat transfer coefficient is represented by a time-averaged heat transfer coefficient designated $\bar{h}$. At present, as Harvey [4] points out, we cannot be more specific because we just do not understand what is happening during this extremely short complex transient process. The heat transfer coefficient $\bar{h}$ representation implicitly contains the effect of liquid specific heat and thermal conductivity, as well as the other pertinent thermodynamic properties.

Since the drop is symmetric about the origin, the governing energy equation in the solid material becomes

$$\frac{1}{\alpha}\frac{\partial T}{\partial t} = \frac{\partial^2 T}{\partial r^2} + \frac{1}{r}\frac{\partial T}{\partial r} + \frac{\partial^2 T}{\partial z^2} \tag{2}$$

with the conditions

$$t = 0 \qquad z \geq 0 \qquad T = T_0 \tag{3}$$

$$t > 0 \qquad -k\left.\frac{\partial T}{\partial z}\right|_{\substack{z=0\\ r\leq R_0}} = \bar{h}(T_L - T)\Big|_{\substack{z=0\\ r\leq R_0}} \qquad \left.\frac{\partial T}{\partial z}\right|_{\substack{z=0\\ r>R_0}} = 0 \tag{4}$$

$$t > 0 \qquad \lim_{z\to\infty} T = T_0 \tag{5}$$

Nomenclature

A = atomic number
C = specific heat of heater plate
E = total energy of surface
$\bar{h}$ = time-average heat transfer coefficient
k = thermal conductivity of heater surface
N_τ = dimensionless group, $\bar{h}^2 t_\infty / k\rho C$
P_c = critical pressure
R_0 = radius of drop touching heater surface
r = radius
T = plate temperature (absolute)
T_{crit} = critical temperature (absolute)
T_L = liquid temperature (absolute)
T_{Leid} = Leidenfrost temperature (absolute)
$T_{Leid,\ iso}$ = ideal isothermal value of T_{Leid} (absolute)
$T^*_{Leid,\ iso}$ = $(T_{Leid,\ iso}/T_{crit})$, dimensionless Leidenfrost temperature
$T_{Leid,\ meas}$ = measured value of T_{Leid} (absolute), see Fig. 1
T_{min} = minimum temperature (absolute)
$T_{min,\ iso}$ = ideal isothermal value of T_{min} (absolute)
T_0 = initial plate temperature (absolute)
T_P = surface temperature of plate (absolute)
T_{sat} = saturation temperature (absolute)
t = time
t^* = dimensionless time
t_{evap} = time for a liquid drop to completely evaporate
t_b = characteristic time
z = axial direction perpendicular to plate
z^* = dimensionless z, $\bar{h}z/k$
α = thermal diffusivity, $k/C\rho$
β = $(\rho Ck)^{-1}$
β_c = liquid–solid contact angle
η = dimensionless radius, $\bar{h}r/k$
η_0 = dimensionless surface radius, $\bar{h}R_0/k$
θ = $(T - T_L)/(T_0 - T_L)$
$\theta_{Leid,\ meas}$ = $(T_{Leid,\ iso} - T_L)/(T_{Leid,\ meas} - T_L)$
ρ = heater material density, use g/cm³
σ_{LV} = liquid surface tension (liquid–vapor), use dynes/cm, evaluated at saturation temperature for both saturated and subcooled conditions
σ_s = surface tension of solid (solid–vacuum)
σ_{sv} = surface tension of solid–vapor interface
τ = dimensionless time, $\bar{h}^2 t/k\rho C_p$
Φ = function of molecular properties of solid–liquid combination

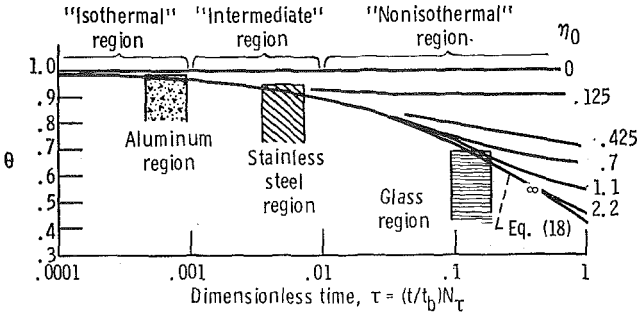

Fig. 2 Effect of N_τ on surface temperature

Introducing the following dimensionless variables

$$\theta = \frac{T - T_L}{T_0 - T_L} \tag{6}$$

$$\eta = \bar{h}r/k \tag{7}$$

$$\eta_0 = \bar{h}R_0/k \tag{8}$$

$$z^* = \bar{h}z/k \tag{9}$$

$$t^* = t/t_b \tag{10}$$

into equation (2) gives

$$\frac{\partial\theta}{\partial t^*} = N_\tau\left(\frac{\partial^2\theta}{\partial\eta^2} + \frac{1}{\eta}\frac{\partial\theta}{\partial\eta} + \frac{\partial^2\theta}{\partial z^{*2}}\right) \tag{11}$$

where

$$N_\tau = \frac{\bar{h}^2 t_b}{k\rho C} = \frac{\bar{h}^2\alpha t_b}{k^2} \tag{12}$$

The initial conditions and boundary conditions become

$$t^* = 0 \qquad z^* \geq 0 \qquad \theta = 1 \tag{13}$$

$$t^* > 0 \left.\begin{aligned} &\left.\frac{\partial\theta}{\partial z^*}\right|_{\substack{z^*=0\\ \eta \leq \eta_0}} = \theta\Big|_{\substack{z^*=0\\ \eta \leq \eta_0}} \\ &\left.\frac{\partial\theta}{\partial z^*}\right|_{\substack{z^*=0\\ \eta > \eta_0}} = 0 \end{aligned}\right\} \tag{14}$$

$$t^* > 0 \lim_{z^* \to \infty} \theta = 1 \tag{15}$$

By inspection of equation (11), if N_τ is large, the time-dependent temperature gradient will be large and the surface is nonisothermal. On the other hand, for small N_τ, the change in surface temperature will be very small and the surface is nearly isothermal. For the case of an infinite drop ($\eta_0 = \infty$), equation (11) becomes

$$\frac{\partial\theta}{\partial\tau} = \frac{\partial^2\theta}{\partial z^{*2}} \qquad \text{for} \quad \eta_0 = \infty \tag{16}$$

where we have chosen the new dimensionless time τ to be of the form

$$\tau = t^* N_\tau = \frac{t}{t_b} N_\tau = \frac{\bar{h}^2 t}{k\rho C} \tag{17}$$

The solution to equation (16) with the conditions (13), (14), and (15) is given in [33, p. 71] and is shown in Fig. 2 as the curve marked η_∞.

$$\theta = \exp(\tau)\,\text{erfc}\,(\sqrt{\tau}) \qquad \text{for} \quad z^* = 0 \tag{18}$$

For finite η_0, the temperature drop is smaller because of radial conduction effects. These curves were determined by a finite-difference solution of equation (11).

Assuming the ratio of t/t_b is of order one, $t/t_b = O(1)$, that is, sufficient time has occurred for the drop to enter the nucleate or film boiling state, then the abscissa in Fig. 2 is equivalent to N_τ.

We label (arbitrarily) the region where $N_\tau < 0.001$ the "isothermal" region. For $N_\tau > 0.01$ the surface will be "nonisothermal." The region between these two regions is labeled the "intermediate" region in Fig. 2.

From estimates of $\bar{h}$ and t_b [4, 5], the relative positions of the various surface material can be established in Fig. 2. From our own high-speed movies, t_b was estimated to be 0.01 sec, which is in agreement with the reported measurements of Wachters [5]. The average heat transfer coefficient $\bar{h}$ was assumed to equal the value associated with the DNB point (departure from nucleate boiling). As seen in Fig. 2, aluminum falls in the isothermal region, stainless steel falls in the intermediate region, and glass in the nonisothermal region. We realize that the measurement of t_b and the calculation of $\bar{h}$ were for one fluid. We assume that other fluids would fall only approximately in the same domain; thus Fig. 2 indicates only in a rough sense the domains of the various materials. When actual data are manipulated in the next three sections of the report, β will be used as the correlating parameter rather than N_τ because β has a unique value independent of the fluid properties and t_b.

Conduction Criteria. In correlating the experimental data to be presented later, it is convenient to write N_τ as the product $\bar{h}^2 t_b$ and β where

$$\beta = \frac{1}{k\rho C} \tag{19}$$

When β approaches zero, for finite $\bar{h}^2 t_b$,

$$\lim_{\beta \to 0} T_p = \lim_{N_\tau \to 0} T_p = T_0 \tag{20}$$

When condition (20) holds, the measured value of the Leidenfrost temperature $T_{\text{Leid, meas}}$ will be equal to the isothermal value

Table 1 Leidenfrost temperatures measured in [7], deg C

	Water				Ethanol		
	0.032-ml drop		6-ml drop		0.0125-ml drop		6-ml drop
Plate material	T_L 100°C	T_L 26°C	T_L 100°C	T_L 26°C	T_L 78.5°C	T_L 26°C	T_L 26°C
Pyrex glass (3–4 rms)	500	>700	...	...	260	360	...
Stainless steel (3–4 rms)	285	285	325	325	~180	190	...
Aluminum (3–4 rms)	...	230	235	235	155	155	157
Aluminum O-gauge (25 rms)	...	...	265	...	...	...	...
Aluminum (fresh polish) (3–4 rms)	...	155	>200	...	...	157	157

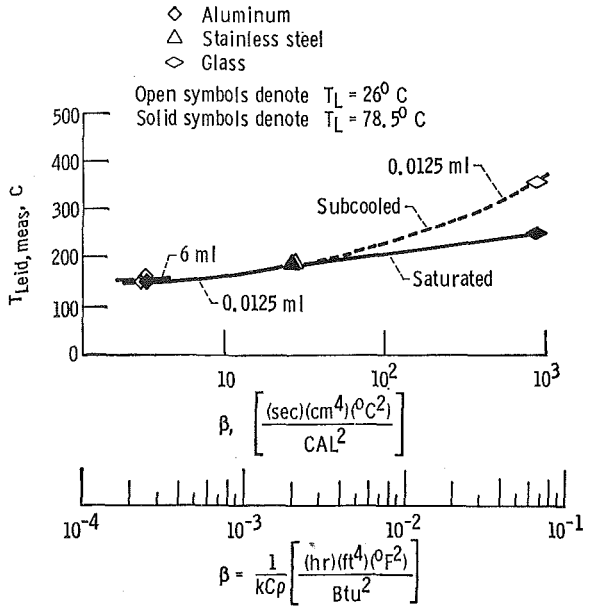

Fig. 3 Effect of surface material on the Leidenfrost temperature of ethanol

of the Leidenfrost temperature $T_{\text{Leid, iso}}$ under the conditions of the particular experiment. That is

$$\lim_{\beta \to 0} T_{\text{Leid, meas}} = T_{\text{Leid, iso}} \tag{21}$$

This key property group $\beta = 1/k\rho C$ has been observed to be an important parameter in drop-impingement studies [5] and for $T_{\min}$ in flow film boiling [6].

Part II—Experimental Surface Conditions

Baumeister, Henry, and Simon [7] fabricated and instrumented stainless-steel, aluminum, gold-plated copper, and Pyrex-glass heating surfaces to measure the Leidenfrost temperature of water and ethanol drops. Their results are tabulated in Table 1. Only some highlights of [7] that are pertinent to correlating procedure will be discussed in this section.

Effects of β, η_0, and Subcooling. According to Part I, for a particular fluid the surface with the smallest β will have the lowest measured Leidenfrost temperature. Plotting the data from Table 1 in Fig. 3, we see the expected decrease in the measured value of the Leidenfrost temperature for decreasing β. Also, the measured values of the Leidenfrost temperature on aluminum were nearly the same for the 0.0125-ml and 6-ml drops, as expected, since the initial liquid radius η_0 has a very small effect on the temperature drop in the isothermal region.

As is seen in Fig. 3, saturated and subcooled drops had the same Leidenfrost temperature for small β. Some early experimental results of Borishansky [8] confirmed that the Leidenfrost temperature is independent of subcooling. For the highly nonisothermal glass surface, however, a large subcooling effect was seen.

Surface Roughness. Hosler and Westwater [9] measured a steady-state *minimum temperature* for water of 258 deg C on an aluminum surface which was polished with "O-gauge" emery paper. This value was slightly higher than the measured Leidenfrost temperature for a 6-ml water drop on aluminum ($T_{\text{Leid, meas}} \approx 235$ deg C) shown in Table 1.

As documented in Table 1, however, the experimental results for the O-gauge roughened surface indicate a measured value of the Leidenfrost temperature of 265 deg C, which is for all practical purposes the same value as measured by Hosler and Westwater.

A recent paper by Cumo, Farello, and Ferrari [10] shows the same trend for increased surface roughness. A coarse sand-blasted surface has a Leidenfrost temperature 70 deg C greater than a smooth lapped surface.

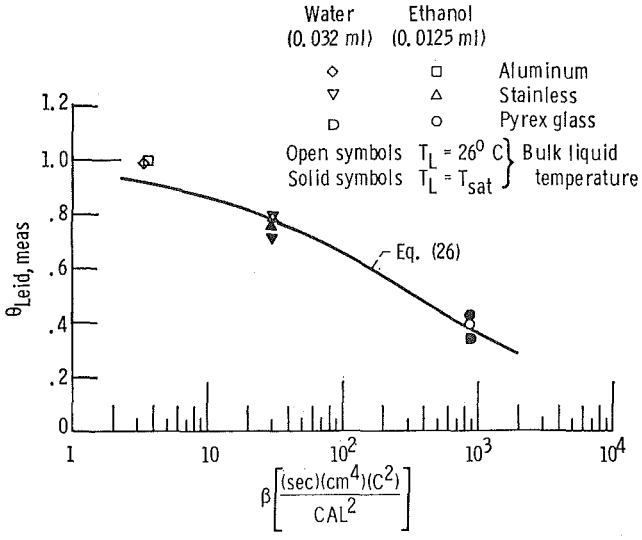

Fig. 4 $\theta_{\text{Leid, meas}}$ as a function of β for $\bar{h}^2 t_\infty$ of 0.00175 [cal^2/cm^4-sec-deg C^2]

Minimum Temperature. Because of the agreement between the measured Leidenfrost and minimum temperatures just discussed, we suspect an equivalence between T_{Leid} and $T_{\min}$ for saturated liquids. This will not be the case for subcooled liquids, for according to Bradfield [11] and Farahat [17], subcooling has a large effect on $T_{\min}$ for a pool. Both report that $T_{\min}$ increases linearly with subcooling. This is contrary to the results for drops as previously discussed in the part of this section on subcooling. The difference between pool and Leidenfrost boiling probably results from the fact that small subcooled liquid drops quickly heat to the saturation temperature, while a subcooled pool continually draws heat away from the boiling interface long after the initial contact between the liquid and the solid. Therefore, we postulate that T_{Leid} equals $T_{\min}$ for saturated liquids on isothermal surfaces, that is,

$$\lim_{\substack{\beta \to 0 \\ T_L \to T_{sat}}} T_{\min} = T_{\min, \text{iso}} = T_{\text{Leid, iso}} \tag{22}$$

Surface Fouling. The Leidenfrost temperature for water strongly depends on surface contamination, while the Leidenfrost temperature of ethanol does not depend on surface contamination. The Leidenfrost temperature of water on a freshly polished surface is approximately 152 deg C (Table 1), which is nearly 75 deg C lower than for the conventional contaminated surface. Peterson and Zaalouk [12] have also confirmed these experimental results using a clean inert platinum wire.

At present, this contamination effect is believed by the authors and others [31] to be brought on by the reaction of water with the fresh aluminum surface or by deposits from dissolved salts which form a residue on the surface after some liquid vaporizes. To the naked eye, however, the contaminated surface still looks clean and highly polished.

Part III—Correlation of Surface Conduction Effects

Based on the concepts developed in Part I of this paper, we can define a dimensionless Leidenfrost temperature as

$$\theta_{\text{Leid, meas}} = \frac{T_{\text{Leid, iso}} - T_L}{T_{\text{Leid, meas}} - T_L} \tag{23}$$

with $\theta_{\text{Leid, meas}}$ represented by the various curves shown in Fig. 2.

Our previous estimates of $\bar{h}$ earlier in this paper lead to the following observation for the drops considered in Part II:

$$\eta_0 \gtrsim 2 \tag{24}$$

Observation of Fig. 2 indicates that for $\eta_0 \gtrsim 2$ the η_∞ line is a good approximation for any value of η_0 from two to infinity. Thus, for practical problems, the η_∞ line is used to represent $\theta_{Leid,\,meas}$

$$\theta_{\text{Leid, meas}} = \frac{T_{\text{Leid, iso}} - T_L}{T_{\text{Leid, meas}} - T_L} = \exp(\bar{h}^2 t_b \beta)\,\text{erfc}\,\sqrt{\bar{h}^2 t_b \beta} \quad (25)$$

Assuming $\bar{h}^2 t_b$ equals 0.00175, equation (25) becomes

$$\theta_{\text{Leid, meas}} = \frac{T_{\text{Leid, iso}} - T_L}{T_{\text{Leid, meas}} - T_L} = \exp(0.00175\beta)\,\text{erfc}\,(0.042\sqrt{\beta}) \quad (26)$$

As is seen in Fig. 4, equation (26) correlates the nonisothermal data of Table 1 for both saturated and subcooled water and ethanol on a stainless-steel and a Pyrex-glass surface. An a posteriori assumption is made here that equation (26) applies to other test fluids. A justification of this assumption will be made following the introduction of equation (27) in Part IV of this paper.

In Fig. 4 we have assumed that the isothermal Leidenfrost temperature equals the value measured on aluminum. This accounts for the aluminum data in Fig. 8 having a $\theta_{Leid,\,meas}$ value of one. For water, the Leidenfrost temperature of a contaminated aluminum surface was used, since the results for the stainless-steel and glass surfaces were also contaminated. At this point we were interested in the relative effects of the various surfaces on the Leidenfrost temperature and not the value that would occur on a clean surface.

Now we shall consider the prediction of the isothermal Leidenfrost temperature.

Part IV—Correlation of the Isothermal Leidenfrost Temperature on Clean Smooth Surfaces

From numerous references, the Leidenfrost and minimum (saturated data) temperatures for many liquid-surface combinations are displayed in Table 2 for smooth clean surfaces. The data in the literature which have a high degree of surface roughness, contamination, or subcooling were excluded. For example, the contaminated water data in Table 1 are not used. The data from contaminated surfaces will require further study as discussed in [7, 31].

In predicting the minimum or Leidenfrost temperature, either Berenson's [13] correlation or Spiegler's theory [14] might be used. Both theories, however, have a common drawback in that they don't account for the thermal properties of the solid. Consequently, in applying either theory, we will correlate isothermal data in which thermal surface properties effects have been removed. Although we cannot measure the isothermal temperature, we can calculate the isothermal value by rearranging equation (26) as follows:

$$T_{\text{Leid, iso}} = T_L + (T_{\text{Leid, meas}} - T_L)\exp(0.00175\beta)\,\text{erfc}\,(0.042\sqrt{\beta}) \quad (27)$$

The estimates of $T_{\text{Leid, iso}}$ are given in Table 2. Further justification of the universality of equations (26) and (27) can be found by comparing the calculated isothermal Leidenfrost temperatures in Table 2. In particular, the correction for the liquid-nitrogen-Teflon combination, although quite large, gives nearly the same isothermal Leidenfrost temperature as the liquid-nitrogen-copper surface.

Berenson's Model. Based on a hydrodynamic model of the film boiling process, Berenson [13] has derived a correlation for the minimum temperature of *n*-pentane and carbon tetrachloride. Unfortunately, subsequent research showed that this correlation does not work for cryogenic fluids [15], liquid metals [16], or water [9]. For example, Berenson's equation [13] predicts a low minimum temperature difference of 51 deg C for saturated liquid sodium, while the experimental value [17] is near 440 deg C. For liquid nitrogen, Berenson's theory predicts a high minimum temperature difference of 48 deg C, while the measured value falls in the range [15, 16] of 14 to 29 deg C. This failure suggests that the hydrodynamic phenomena associated with T_{min} is an effect rather than a cause. In addition, the wave model required for Berenson's equation does not apply to small drops.

Spiegler's Theory. In contrast to the hydrodynamic model, Spiegler's model [14] assumes that T_{Leid} (or T_{min}) is a thermodynamic state property of the fluid in which the minimum temperature corresponds to the maximum superheat temperature of a liquid. Spiegler et al. used a Van der Waals equation of state for a liquid to determine the maximum superheat. Their theory

Table 2 Clean smooth Leidenfrost and minimum data for saturated liquids

Reference	Fluid	Surface	Type experiment	Measured Leidenfrost temperature, K, $T_{Leid,meas}$	Calculated isothermal Leidenfrost temperature, K, equation (27), $T_{Leid,iso}$
20	Hg	Ta	drop	843	811
21	Hg	columbium–1% Zr	drop	856	827
21	Hg	Cu	drop	967	950
22, 23	K	Ta	drop	1588	1505
24	K	stainless	pool/plate	874	825
17	Na	Ta	pool/sphere	1600	1534
Table 2	water	Al	drop	426	423
12	water	Pt	pool/wire	423	423
Table 2	ethanol	Al	drop	428	421
13	pentane	Cu	pool/plate	368	365
25	carbon tet.	Al	pool/plate	432	425
13	carbon tet.	Cu	pool/plate	435	431
25	Freon 113	Al	pool/plate	399	392
26	Freon 11	stainless	pool/rod	375	357
26	Freon 11	Teflon	pool/rod	442	334
15	liquid N_2	Al	drop	91	89
27	liquid N_2	Cu	pool/torus	94	94
28	liquid N_2	Cu	pool/cylinder	104	103
29	liquid N_2	Cu	pool/sphere	96	94
18	liquid N_2	Cu	pool/sphere	106	104
32	liquid N_2	Teflon	pool/sphere	200	105
30	liquid He I	Pt	pool/wire	4.51[a]	4.51

[a] For liquid He I, the value given was estimated from constant heat flux data.

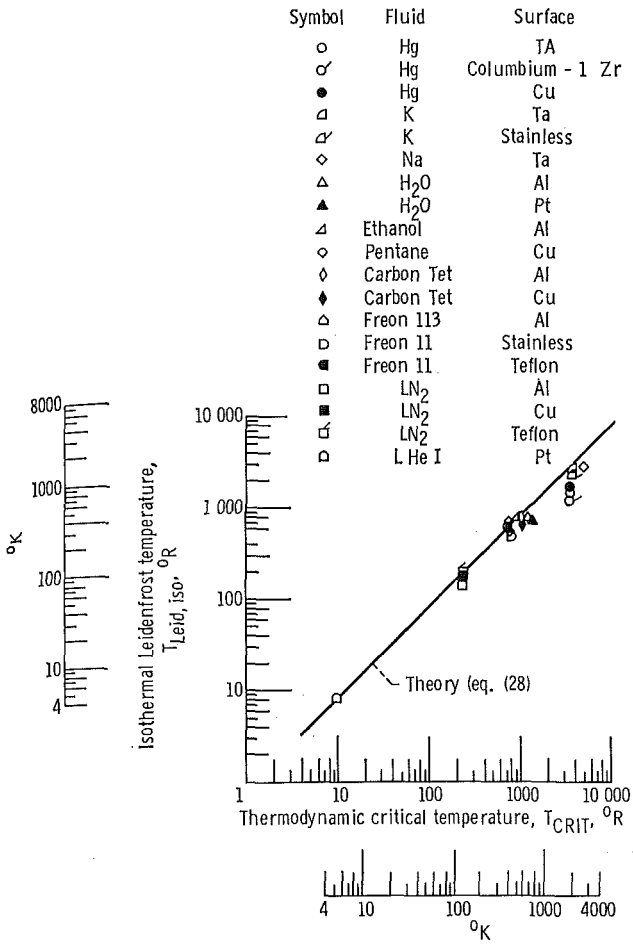

Fig. 5 Isothermal Leidenfrost temperature as a function of the critical temperature for smooth uncontaminated surfaces and saturated liquids

indicates that at pressures well below the critical pressure ($P/P_c \rightarrow 0$)

$$T_{\text{Leid, iso}} = \frac{27}{32} T_{\text{crit}} \tag{28}$$

The isothermal Leidenfrost temperatures listed in Table 2 are plotted against T_{crit}.

As can be seen in Fig. 5, equation (28) correlates the cryogenic fluid with good accuracy; however, a large discrepancy exists between experiment and theory for the liquid-metal data, as well as for carbon tetrachloride and water. This error may arise simply because the simple Van der Waals model of Spiegler's theory does not account for the more complex structure of the liquid metals and the need for considering liquid and solid surface energies.

Liquid Surface Energies. Observation of the data displayed in Fig. 5 indicates that liquid surface energy (surface tension) may account for much of the discrepancy between theory and experiment. Liquid metals, water, and carbon tetrachloride, which show large errors, all have higher values of surface tension than do the fluids like helium, nitrogen, and pentane that are accurately correlated by the theory. In particular, mercury, with the highest value of surface tension, shows the largest difference between experiment and theory. Furthermore, the isothermal Leidenfrost temperature seems also to be a function of the solid's surface tension. For example, we observe in Table 2 that for mercury different surface materials lead to variations in the isothermal Leidenfrost temperature.

As a result of these experimental observations, we now modify equation (28) by assuming

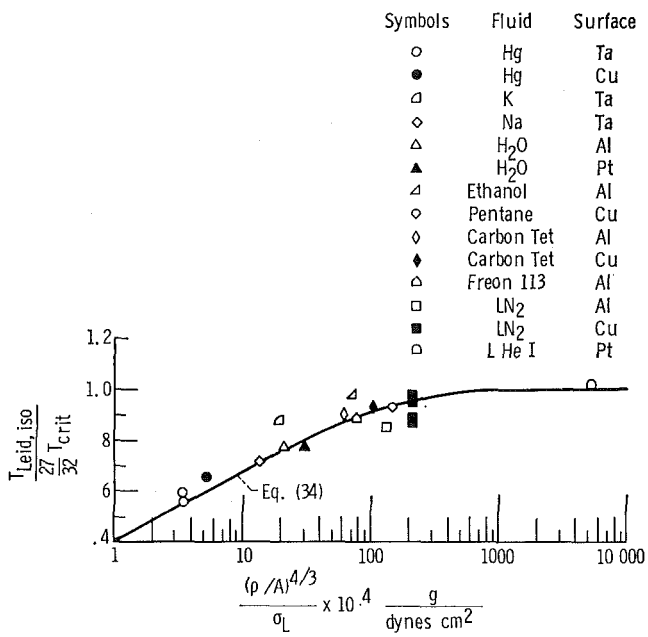

Fig. 6 Correlating effect of solid–liquid surface energy ratio for pure metals and saturated liquids

$$T^*_{\text{Leid, iso}} = \frac{T_{\text{Leid, iso}}}{T_{\text{crit}}} = \frac{27}{32} f(\sigma_s/\sigma_{LV}) \tag{29}$$

Experimental values of the liquid surface tension are well documented; however, because of a lack of experimental evidence we must use theoretical estimates to determine the surface tension of the solid. The surface tension of a solid, σ_s, in a vacuum can be expresed as

$$\sigma_s = E + T \frac{\partial \sigma_s}{\partial T} \tag{30}$$

where E is the total energy of the surface. From estimates, the surface tension gradient term in equation (30) is assumed small; thus

$$\sigma_s \simeq E \tag{31}$$

Semenchenko [19] shows that for a variety of theories

$$E\alpha(\rho/A)^{4/3} \tag{32}$$

where A is the atomic weight. Therefore, equation (29) becomes

$$\frac{T^*_{\text{Leid, iso}}}{27/32} = f\left(\frac{(\rho/A)^{4/3}}{\sigma_{LV}}\right) \tag{33}$$

The experimental data are plotted as a function of the solid to liquid surface energy ratio in Fig. 6. Only the pure metals (elements) are plotted in Fig. 6, since equation (32) does not account for the effects of alloyed elements. An estimate of σ_s will be required for alloy surfaces. As is seen in Fig. 6, the equation for the isothermal Leidenfrost temperature of the form

$$T_{\text{Leid, iso}} = \frac{27}{32} T_{\text{crit}} \left\{1 - \exp\left(-0.52\left[\frac{10^4(\rho/A)^{4/3}}{\sigma_{LV}}\right]^{1/3}\right)\right\} \tag{34}$$

provides a good correlation of the existing data.

The shaded data points in Fig. 6 indicate that experimental data exists for a liquid on two different surfaces. In all cases, the isothermal Leidenfrost temperature increases for increased surface energy. Similarly, the dimensionless isothermal Leidenfrost temperature $T^*_{\text{Leid, iso}}$ decreases for increased liquid surface tension. In the limit of large surface energy and small surface tension, the measured value of the isothermal Leidenfrost tempera-

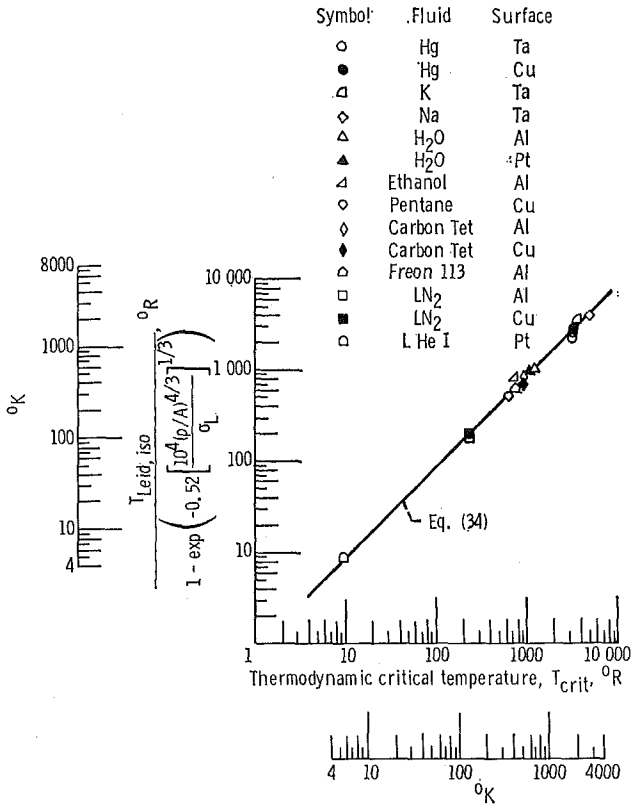

Fig. 7 Energy corrected isothermal Leidenfrost temperature as a function of the critical temperature for smooth uncontaminated pure metallic surfaces and saturated liquids

ture will approach the value predicted by Spiegler et al. [14].

$$\lim_{\frac{(\rho/A)^{4/3}}{\sigma_{LV}} \to \infty} T_{\text{Leid, iso}} = \frac{27}{32} T_{\text{crit}} \tag{35}$$

Figure 7 also shows that introducing the solid–liquid surface energy function as given by equation (34) brings experiment and theory together.

The ratio σ_s/σ_{LV} shown in the previous equations can also be expressed in terms of the liquid contact angle β_c. The relationship between β_c and σ_s/σ_{LV} can be determined by combining the classic Young equation and the recent theory of Good and Girifalco [34], which relates the solid–liquid interface tension to σ_s and σ_{LV}. This combination yields

$$\frac{\sigma_s}{\sigma_{LV}} = \left(\frac{\cos\beta_c + 1 + \psi}{2\Phi}\right)^2 \tag{36}$$

where Φ is a function of the molecular properties of the liquid and solid and where ψ is the ratio of the equilibrium spreading pressure ($\sigma_s - \sigma_{sv}$) to σ_{LV}. In many practical cases, ψ can be neglected.

Final Correlating Equation. We can now combine equations (26) and (34) to give an expression for the measured Leidenfrost (or saturated minimum) temperature as follows:

$$T_{\text{Leid, meas}} = \frac{\frac{27}{32} T_{\text{crit}} \left\{1 - \exp\left(-0.52\left[\frac{10^4(\rho/A)^{4/3}}{\sigma_{LV}}\right]^{1/3}\right)\right\} - T_L}{\exp(0.00175\beta)\,\text{erfc}\,(0.042\sqrt{\beta})} + T_L \tag{37}$$

Conclusions

The thermodynamic critical temperature, solid–liquid surface energy ratio, and thermal properties of the solid are all important parameters in correlating the Leidenfrost and minimum temperatures on smooth clean surfaces.

References

1 Bell, K. J., "The Leidenfrost Phenomenon: A Survey," *Chemical Engineering Progress Symposium Series*, Vol. 63, No. 79, 1967, pp. 73–82.

2 Cumo, M., and Pitimado, D., "On the Determination of the Leidenfrost Temperatures," *Termotecnica*, Vol. 22, No. 8, Aug. 1968, pp. 373–381.

3 Bradfield, W. S., "Liquid-Solid Contact in Stable Film Boiling," *Industrial and Engineering Chemistry Fundamentals*, Vol. 5, No. 2, May 1966, pp. 200–204.

4 Harvey, D. M., "The Impact and Rebound of a Small Water Drop Striking a Hot Surface," PhD thesis, McMaster University, Hamilton, Ont., Canada, 1967.

5 Wachters, L. H. J., Smulders, L., Vermeulen, J. R., and Kleiweg, H. C., "The Heat Transfer from a Hot Wall to Impinging Mist Droplets in the Spheroidal State," *Chemical Engineering Science*, Vol. 21, Dec. 1966, pp. 1231–1238.

6 Kalinin, F. K., Koshkin, V. K., Yarklo, S. A., Berlin, I. J., Kostyuk, V. V., and Kochalaev, Yu. S., "Heat Transfer in Tubes with Rod Regime in the Case of Film Boiling of a Subcooled Liquid," in: *Cocurrent Gas–Liquid Flow*, E. Rhodes and D. S. Scott, edz., Plenum, New York, N. Y., 1969.

7 Baumeister, K. J., Henry, R. E., and Simon, F. F., "Role of the Surface in the Measurement of the Leidenfrost Temperature," in: *Augmentation of Convective Heat and Mass Transfer*, ASME, New York, N. Y., 1970, pp. 91–101.

8 Borishansky, V. M., "Heat Transfer to a Liquid Freely Flowing over a Surface Heater to a Temperature above the Boiling Point," in: *Problems of Heat Transfer during a Change of State: A Collection of Articles*, AEC-tr-3405, 1953, U. S. Atomic Energy Commission, Washington, D. C.

9 Hosler, E. R., and Westwater, J. W., "Film Boiling on a Horizontal Plate," *ARS Journal*, Vol. 32, No. 4, Apr. 1962, pp. 553–558.

10 Cumo, M., Farello, G. E., and Ferrari, G., "Notes on Droplet Heat Transfer," *Chemical Engineering Progress Symposium Series*, Vol. 65, No. 92, 1969, pp. 175–187.

11 Bradfield, W. S., "On the Effect of Subcooling on Wall Superheat in Pool Boiling," JOURNAL OF HEAT TRANSFER, TRANS. ASME, Series C, Vol. 89, No. 3, Aug. 1967, pp. 269–270.

12 Peterson, W. C., and Zaalouk, M. G., "Boiling-Curve Measurements From a Controlled Heat-Transfer Process," JOURNAL OF HEAT TRANSFER, TRANS. ASME, Series C, Vol. 93, No. 4, Nov. 1971, pp. 408–412.

13 Berenson, P. J., "Transition Boiling Heat Transfer from a Horizontal Surface," Tech. Rep. 17, NP-8415, Massachusetts Institute of Technology, Cambridge, Mass., 1960.

14 Spiegler, P., Hopenfeld, J., Silberberg, M., Bumpus, C. F., Jr., and Norman, A., "Onset of Stable Film Boiling and the Foam Limit," *International Journal of Heat and Mass Transfer*, Vol. 6, 1963, pp. 987–994.

15 Kershock, E. G., and Bell, K. J., "Heat Transfer Coefficient Measurements of Liquid Nitrogen Drops Undergoing Film Boiling," in: *Advances in Cryogenic Engineering*, Vol. 15, Plenum, New York, N. Y., 1970, pp. 271–282.

16 Henry, R. E., personal communication.

17 Farahat, M., "Transient Boiling Heat Transfer from Spheres to Sodium," PhD thesis, Northwestern University, Evanston, Ill., 1971.

18 Merte, H., Jr., and Clark, J. A., "Boiling Heat-Transfer Data for Liquid Nitrogen at Standard and Near-Zero Gravity," in: *Advances in Cryogenic Engineering*, Vol. 7, Plenum, New York, N. Y., 1962, pp. 546–550.

19 Semenchenko, V. K., *Surface Phenomena in Metals and Alloys*, Pergamon, Elmsford, N. Y., 1961.

20 Poppendiek, H. F., "SNAP-8 Boiler Performance Degradation and Two-Phase Flow Heat and Momentum Transfer Models," GLR-84, NASA CR-72759, Geoscience, Ltd., Solana Beach, Calif., Aug. 1970.

21 Poppendiek, H. F., et al., "Investigation of Fundamental Mechanisms and Parameters that Influence Steady State and Transient Performance of Rankine Cycle Liquid Metal Systems," GLR-55, SAN-677-15, Geoscience, Ltd., Solana Beach, Calif., June 1967.

22 Poppendiek, H. F., et al., "High Acceleration Field Heat Transfer for Auxiliary Space Nuclear Power Systems," GLR-42, SAN-409-29, Geoscience, Ltd., Solana Beach, Calif., Jan. 1966.

23 Poppendiek, H. F., personal communication.

24 Padilla, A., Jr., "Film Boiling of Potassium on a Horizontal Plate," PhD thesis, University of Michigan, Ann Arbor, Mich., 1966.

25 Kautzky, D. E., and Westwater, J. W., "Film Boiling of a Mixture on a Horizontal Plate," *International Journal of Heat and Mass Transfer*, Vol. 10, 1967, pp. 253–256.

26 Stock, B. J., "Observations on Transition Boiling Heat Transfer Phenomena," ANL-6175, Argonne National Laboratory, Argonne, Ill., June 1960.
27 Bergles, A. E., and Thompson, W. G., Jr., "The Relationship of Quench Data to Steady-State Pool Boiling Data," *International Journal of Heat and Mass Transfer*, Vol. 13, No. 1, Jan. 1970, pp. 55–68.
28 Flynn, T. M., Draper, J. W., and Roos, J., "The Nucleate and Film Boiling Curve of Nitrogen at One Atmosphere," in: *Advances in Cryogenic Engineering*, Vol. 7, Plenum, New York, N. Y., 1962, pp. 539–545.
29 Manson, L., "Cooldown of Shrouded Spherical Vessels in Liquid Nitrogen," in: *Advances in Cryogenic Engineering*, Vol. 12, Plenum, New York, N. Y., 1967, pp. 373–380.
30 Goodling, J. S., and Irey, R. K., "Non-Boiling and Film Boiling Heat Transfer to a Saturated Bath of Liquid Helium," in: *Advances in Cryogenic Engineering*, Vol. 14, Plenum, New York, N. Y., 1969, pp. 159–169.
31 Kovalev, S. A., "An Investigation of Minimum Heat Fluxes in Pool Boiling of Water," *International Journal of Heat and Mass Transfer*, Vol. 9, 1966, pp. 1219–1226.
32 Rhea, L. G., and Nevins, R. G., "Film Boiling Heat Transfer From an Oscillating Sphere," JOURNAL OF HEAT TRANSFER, TRANS. ASME, Series C, Vol. 91, No. 2, May 1969, pp. 267–272.
33 Carslaw, H. S., and Jaeger, J. C., *Conduction of Heat in Solids*, 2nd ed., Clarendon, Oxford, England, 1959.
34 Good, R. J., "The Theory for the Estimation of Surface and Interfacial Energies, Contact Angle Wettability and Adhesion," in: *Advances in Chemistry*, Series 43, American Chemical Society, Washington, D. C., 1964.

J. W. YANG
Associate Professor,
Department of Mechanical Engineering,
State University of New York at Buffalo,
Buffalo, N. Y.

Laminar Film Condensation on a Sphere

A boundary-layer analysis is made for laminar film condensation on a sphere. Similarity transformations are made for two cases. The first case includes both the inertia forces and heat convection; the solutions are valid in the upper stagnation region. The second case excludes the inertia forces; the solutions are valid over the entire surface for high Prandtl numbers. Results of heat-transfer rate, condensation rate, and film thickness are presented. Comparisons with a vertical plate and a horizontal cylinder are discussed.

Introduction

THE PROCESS of heat and mass transfer during filmwise condensation of a vapor has been investigated extensively since the early studies of Nusselt. A number of systems, such as plate, tube, and bank of tubes, have been studied under various conditions. Improvements on Nusselt's simple model have been made by many investigators. For example the boundary-layer analysis was applied to laminar film condensation on a vertical plate and on a horizontal cylinder by Sparrow and Gregg [1, 2].[1] Their analysis has revealed the role of inertia forces and heat convection which were neglected in Nusselt's model. The boundary-layer approach was later extended to include the shear forces at the liquid–vapor interface [3]. The boundary-layer analysis is based on the similarity consideration. Similarity solutions, however, are obtainable only for certain classes of geometries with certain boundary conditions. In particular, the geometry of a sphere does not belong to this category. However, in practice the spherical body is a common engineering element frequently employed in heat-transfer processes.

The present investigation reports a boundary-layer approach for laminar film condensation over spheres. It will be shown that an exact similarity solution exists in the stagnation region only if both the inertia forces and heat convection are included. A similarity solution can also be obtained for the entire spherical surface if the inertia forces are neglected. Utilizing numerical solutions the heat- and mass-transfer results are presented over the Prandtl number range from 100 to 0.03.

Analysis

Governing Equations. The system under consideration is shown in schematic view in Fig. 1. The arc length x is measured along the surface of the sphere and has its initial value of zero at the upper stagnation point, and y is the normal distance from the surface. It is assumed that the sphere is situated in a large body of pure vapor which is at its saturation temperature t_s. The surface of the sphere is maintained at uniform temperature t_w which is less than t_s. A thin layer of condensate in the form of a continuous film runs downward over the sphere. For laminar film condensation the governing equations for steady, nondissipative, axisymmetric, constant-property flow are as follows:

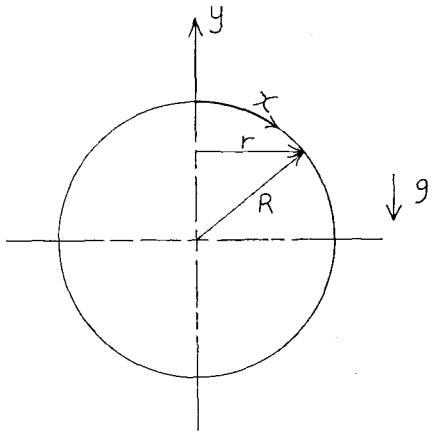

Fig. 1 Coordinate system

$$\frac{\partial}{\partial x}(ur) + \frac{\partial}{\partial y}(vr) = 0 \tag{1}$$

$$u\frac{\partial u}{\partial x} + v\frac{\partial u}{\partial y} = \nu\frac{\partial^2 u}{\partial y^2} + \frac{g(\rho - \rho_v)}{\rho}\sin X \tag{2}$$

$$u\frac{\partial t}{\partial x} + v\frac{\partial t}{\partial y} = \alpha\frac{\partial^2 t}{\partial y^2} \tag{3}$$

The boundary conditions are

$$u = 0 \quad v = 0 \quad t = t_w \quad \text{at} \quad y = 0 \tag{4}$$

$$\frac{\partial u}{\partial y} = 0 \quad t = t_s \quad \text{at} \quad y = \delta \tag{5}$$

[1] Numbers in brackets designate References at end of paper.

Contributed by the Heat Transfer Division for publication (without presentation) in the JOURNAL OF HEAT TRANSFER. Manuscript received by the Heat Transfer Division November 19, 1972. Paper No. 72-HT-R.

where the local film thickness δ is determined by an energy balance at the liquid–vapor interface:

$$k \left.\frac{\partial t}{\partial y}\right|_{\delta} = \frac{\rho h_{fg}}{r} \frac{d}{dx} \int_0^{\delta} urdy \tag{6}$$

Similarity Transformation. The continuity equation (1) is immediately satisfied by the stream function Ψ in the following way:

$$u = \frac{1}{r} \frac{\partial}{\partial y} (\Psi r) \qquad v = -\frac{1}{r} \frac{\partial}{\partial x} (\Psi r) \tag{7}$$

To obtain similar solutions a new independent variable η, a velocity function f, and a dimensionless temperature θ are proposed as:

$$\eta = yC^{1/4}G(X)/R \tag{8}$$

$$\Psi = \nu C^{1/4} H(X) f(\eta) \tag{9}$$

$$\theta = (t - t_s)/(t_w - t_s) \tag{10}$$

and

$$C = g(\rho - \rho_v)R^3/\rho\nu^2 \tag{11}$$

where $G(X)$ and $H(X)$ are undetermined functions of the dimensionless coordinate x/R. From equation (7) the velocities are

$$u = (\nu C^{1/2}/R) H(X) G(X) f' \tag{12}$$

$$v = -\frac{\nu C^{1/4}}{R} \left[\frac{H}{G} \frac{dG}{dX} \eta f' + \left(\frac{dH}{dX} + H \cot X \right) f \right] \tag{13}$$

Substitution of equations (8)–(13) into equations (2) and (3) gives the momentum and energy equations as

$$HG^3 f''' + \left(HG^2 \frac{dH}{dX} + H^2 G^2 \cot X \right) ff'' - HG \frac{d}{dX} (HG) f'^2 + \sin X = 0 \tag{14}$$

$$\theta'' + \Pr \frac{H}{G} \left(\frac{1}{H} \frac{dH}{dX} + \cot X \right) f\theta' = 0 \tag{15}$$

In order that equations (14) and (15) be made ordinary differential equations, it is required that factors which depend on X be eliminated. Specifically it is necessary that

$$HG^3 = a \sin X \tag{16}$$

$$HG^2 \left(\frac{dH}{dX} + H \cot X \right) = b \sin X \tag{17}$$

$$HG \frac{d}{dX} (HG) = c \sin X \tag{18}$$

$$\frac{1}{G} \left(\frac{dH}{dX} + H \cot X \right) = e \sin X \tag{19}$$

where a, b, c, and e are constants. An inspection of the above four equations shows that equation (19) is not independent, i.e., $e = b/a$. Thus three equations remain for determining the two unknowns $G(X)$ and $H(X)$.

Determination of Functions $G(X)$ and $H(X)$. The problem of obtaining unique solutions of the two functions is the same as that encountered in film condensation around a horizontal cylinder [2]. It can be shown that unique solutions exist only in the upper stagnation region. In this region it is assumed that

$$\sin X = X \qquad \text{and} \qquad \cot X = 1/X$$

Equations (16) to (18) thus become

$$HG^3 = aX \tag{20}$$

$$HG^2 \left(\frac{dH}{dX} + \frac{H}{X} \right) = bX \tag{21}$$

$$HG \frac{d(HG)}{dX} = cX \tag{22}$$

The constants b and c are related, i.e., $b = 2c > 0$. The unique solutions are

$$G = a^{1/2}/c^{1/4} = 1 \tag{23}$$

$$H = c^{3/4} X/a^{1/2} = X \tag{24}$$

The constants are selected as $a = 1$, $b = 2$, and $c = 1$. Thus the transformation yields truly ordinary differential equations in the upper stagnation region.

For large X no unique solutions can be obtained. Integrating equation (18) gives

$$HG = [2(1 - \cos X)]^{1/2} \tag{25}$$

Substituting G from equation (25) into equation (16) yields the first set of solutions

$$G_1 = \left(\frac{1 + \cos X}{2} \right)^{1/4} \tag{26}$$

$$H_1 = \left[\frac{8(1 - \cos X)^2}{1 + \cos X} \right]^{1/4} \tag{27}$$

Substituting G from equation (25) into equation (17) yields the second set of solutions

$$G_2 = \left(\frac{1 + \cos X}{2} \right)^{1/2} \tag{28}$$

$$H_2 = \left[\frac{4(1 - \cos X)}{1 + \cos X} \right]^{1/2} \tag{29}$$

Functions G_1, G_2 and functions H_1, H_2 approach equations (23) and (24) respectively as X approaches zero. Comparison of these

Nomenclature

C = dimensionless parameter, equation (11)
c_p = heat capacity at constant pressure
D = diameter of sphere
f = dimensionless velocity function, equation (9)
g = acceleration of gravity
G = function of X appearing in definition of f
h = heat-transfer coefficient
h_{fg} = latent heat of condensation
H = function of X appearing in definition of η
k = thermal conductivity
$\dot{m}$ = condensation rate
Nu = local Nusselt number
$\overline{\text{Nu}}$ = average Nusselt number
Pr = Prandtl number
q = local heat flux
r = radial distance from symmetrical axis, Fig. 1
R = sphere radius
t = temperature
t_s = vapor-saturation temperature
t_w = wall temperature
u = velocity component in x direction
v = velocity component in y direction
x = coordinate measuring distance along circumference from upper stagnation point
X = dimensionless coordinate, x/R
y = coordinate measuring radial distance outward from surface
α = thermal diffusivity of condensate
δ = condensate film thickness
η = similarity variable, equation (8)
θ = dimensionless temperature, equation (10)
μ = dynamic viscosity of condensate
ν = kinematic viscosity of condensate
ρ = density of condensate
ρ_v = density of vapor
Ψ = stream function, equation (9)

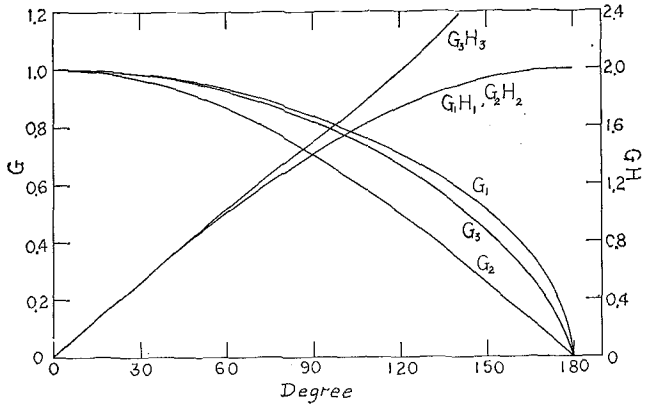

Fig. 2 The functions G(X) and G(X)H(X)

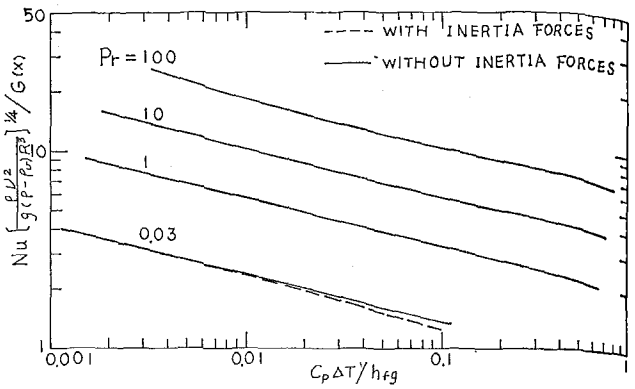

Fig. 3 Heat-transfer results

functions is shown in Fig. 2. The two sets of solutions are approximately, but not rigorously, equal in the upper portion of the sphere.

The difficulty of obtaining unique solutions at larger X can be removed by neglecting the inertia forces in the momentum equation. It has been demonstrated, for the cases of a vertical plate and a horizontal cylinder, that the inertia forces are significant only for fluids of low Prandtl numbers [1, 2]. Therefore it is reasonable to assume that for the case of a spherical body the inertia forces can be neglected at least at high Prandtl numbers. Equation (14) is thus simplified as

$$HGf''' + \sin X = 0 \tag{30}$$

To obtain the similar solutions it is required that

$$HG^3 = A \sin X \tag{31}$$

$$\frac{dH}{dX} + H \cot X = BG \sin X \tag{32}$$

where A and B are constants. The functions $G(X)$ and $H(X)$ are uniquely determined by the above two equations:

$$G_3 = \left(\frac{3A}{4BI}\right)^{1/4} (\sin X)^{2/3} \tag{33}$$

$$H_3 = \left(\frac{4}{3} A^{1/3} BI\right)^{3/4} \Big/ \sin X \tag{34}$$

and

$$I = \int_0^X (\sin X)^{5/3}\, dX \tag{35}$$

The subscript 3 is used to distinguish the solutions from those obtained in equations (26)–(29). The functions G_3 and H_3 are included in Fig. 2 for comparison. Constants A and B have been selected as 1 and 2 respectively to provide an agreement with the exact solutions, equations (26) and (27), at $X = 0$. It is seen that they compare favorably with the other two sets of solutions along the upper portion of the sphere. Near the lower stagnation region, a large difference occurs for the H functions. However, in this region, the boundary-layer analysis may not be valid because of the dropping of the condensate from the sphere surface.

Final Equations. The final form of the momentum equation is

$$f''' + 2ff'' - f'^2 + 1 = 0 \tag{36}$$

when inertia forces are included, and

$$f''' + 1 = 0 \tag{37}$$

when inertia forces are excluded. The energy equation is

$$\theta'' + 2 \Pr f\theta' = 0 \tag{38}$$

The boundary conditions are

$$f = 0 \quad f' = 0 \quad \theta = 1 \quad \text{at} \quad \eta = 0 \tag{39}$$

$$f'' = 0 \quad \theta = 0 \quad \text{at} \quad \eta = \eta_\delta \tag{40}$$

and

$$\frac{c_p(t_s - t_w)}{\Pr h_{fg}} = -\frac{2f(\eta_\delta)}{\theta'(\eta_\delta)} \quad \text{at} \quad \eta = \eta_\delta \tag{41}$$

Knowing the velocity and temperature distributions, the circumferential heat-transfer rate can be determined as

$$\mathrm{Nu}\left[\frac{\rho\nu^2}{g(\rho - \rho_v)R^3}\right]^{1/4} = -2\theta'(0)G(X) \tag{42}$$

where the Nusselt number is based on the diameter of the sphere:

$$\mathrm{Nu} = \frac{h2R}{k} = \frac{2R}{(t_w - t_s)} \left.\frac{\partial t}{\partial y}\right|_0 \tag{43}$$

The average heat-transfer rate is defined as

$$\bar{h} = \frac{1}{x}\int_0^X h\, dx \qquad \overline{\mathrm{Nu}} = \frac{\bar{h}2R}{k} \tag{44}$$

The average Nusselt number is thus expressed as

$$\overline{\mathrm{Nu}}\left[\frac{\rho\nu^2}{g(\rho - \rho_v)R^3}\right]^{1/4} = -2\theta'(0)\frac{1}{X}\int_0^X G\, dX \tag{45}$$

Another quantity of practical interest is the condensation rate. The condensation rate is defined as the total mass rate of condensation up to some angle on the sphere and is computed by the integration of the velocity profile, i.e.,

$$\dot{m} = 2\pi r\rho \int_0^\delta u\, dy \tag{46}$$

In dimensionless form it becomes

$$\dot{m}/2\pi R\mu = H(X)f(\eta_\delta) \tag{47}$$

The local film thickness is determined from equation (8)

$$\frac{\delta}{R}\left[\frac{g(\rho - \rho_v)R^3}{\rho\nu^2}\right]^{1/4} = \frac{\eta_\delta}{G(X)} \tag{48}$$

An inspection of the above equations (42)–(48) shows that all the quantities depend on the functions $G(X)$ and $H(X)$. Hence the analysis provides exact results if the unique solutions of G and H exist. Specifically, exact results are obtained: (a) in the upper stagnation region regardless of Prandtl numbers and (b) over the entire surface for fluids of high Prandtl numbers. Uncertainties arise only at low Prandtl numbers, for which the inertia forces are comparable to the viscous forces.

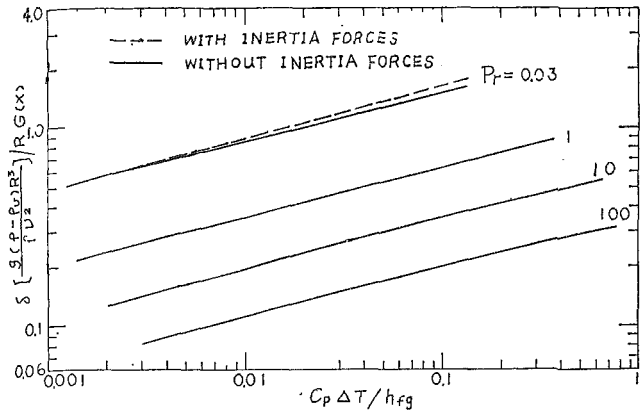

Fig. 4 Film thickness

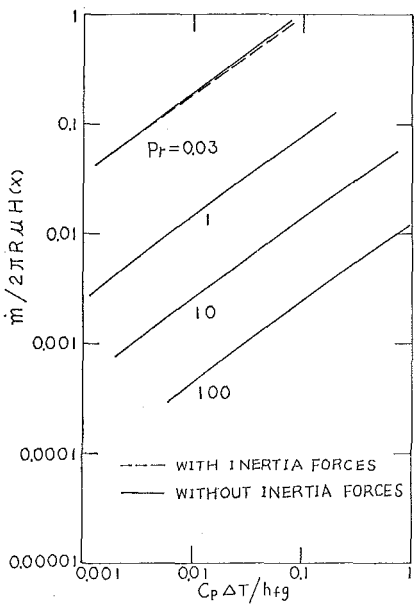

Fig. 5 Condensation rate

Discussion of Results

There are two parameters involved in the condensation process: the Prandtl number and the subcooling term $c_p(t_s - t_w)/h_{fg}$. Numerical solutions were obtained for four Prandtl numbers: 100, 10, 1, and 0.03 in the range of $c_p(t_s - t_w)/h_{fg}$ from 0.001 to 1.

The heat-transfer results are shown in Fig. 3. The Nusselt number increases with Prandtl number and decreases with the increase of subcooling. It is interesting to note that for $Pr > 1$ solutions obtained from equation (36) (with inertia forces) are practically identical to those obtained from equation (37) (without inertia forces). The inertia forces thus have no significant effect for $Pr > 1$. This result agrees with that found for a vertical plate and a horizontal cylinder [1, 2]. At low Prandtl numbers it is known that inertia forces decrease the heat-transfer rate at higher subcooling, as indicated in Fig. 3 for $Pr = 0.03$.

Variations of the dimensionless film thickness and condensation rate are shown in Figs. 4 and 5 respectively. The effects of Prandtl number and subcooling on these two quantities are just opposite to that on heat-transfer rate. This indicates, as in other cases, that the liquid film exhibits the main thermal resistance. The heat-transfer rate is reduced as the film becomes thicker. On the other hand the condensation rate increases with the film thickness. Again, the inertia forces have no significant effect on film thickness and condensation rate for $Pr > 1$. At low Prandtl numbers, $Pr = 0.03$, including the inertia forces yields a thicker film and less condensate. A detailed calculation shows that the amount of condensate is determined by the film thickness and by the liquid-velocity distribution. The inertia forces greatly reduce the liquid velocity and slightly increase the film thickness. The net effect is a smaller condensation rate.

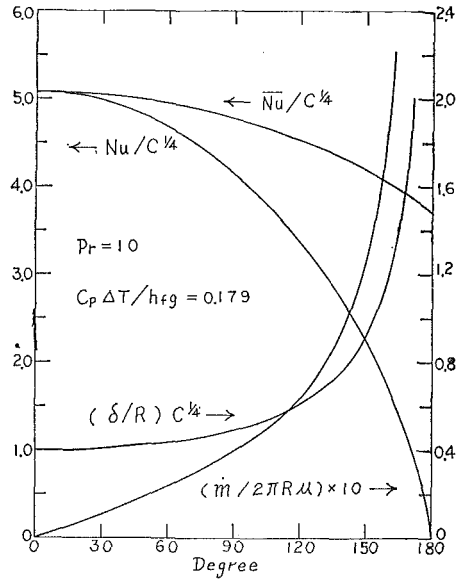

Fig. 6 Circumferential variations, Pr = 10, $c_p(t_s - t_w)/h_{fg} = 0.179$

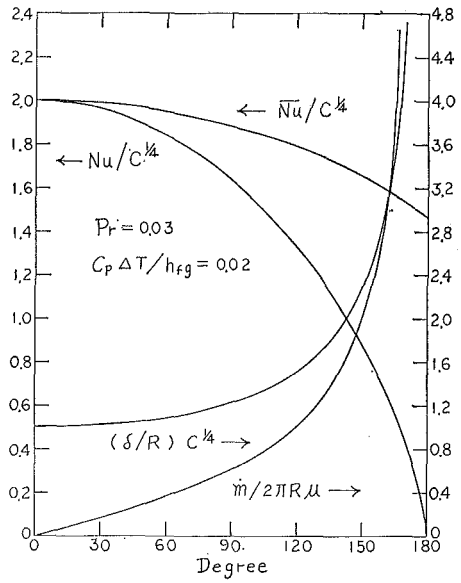

Fig. 7 Circumferential variations, Pr = 0.03, $c_p(t_s - t_w)/h_{fg} = 0.02$

The circumferential variations of the local Nusselt number, the average Nusselt number, the film thickness, and the condensation rate are shown for two representative cases in Figs. 6 and 7. In both cases the inertia forces were neglected, i.e., $G_3(X)$ and $H_3(X)$ were used in computation. The heat-transfer rate is highest at the upper stagnation point. Both the local and average Nusselt numbers decrease monotonically along the circumference of the sphere. The local Nusselt number reaches zero at the lower stagnation point. The film thickness, starting from a finite value at the upper stagnation point, grows rather slowly over the upper portion of the sphere and then increases quite rapidly over the lower portion of the sphere. At the lower stagnation point it becomes infinity, as the analysis indicates. This may be interpreted as the dropping away of the condensate from the surface. The condensation rate exhibits approximately the same behavior as does the film thickness. The condensation rate starts from zero at the upper stagnation point and increases rapidly along the circumference of the sphere. It reaches infinity at the lower stagnation point.

Finally, it is proposed for practical applications that the heat-transfer rate is proportional to $[\mathrm{Pr}\ h_{fg}/c_p(t_s - t_w)]^{1/4}$, i.e.,

$$\mathrm{Nu}/C^{1/4} = K[\mathrm{Pr}\ h_{fg}/c_p(t_s - t_w)]^{1/4} \tag{49}$$

The constant K has been determined empirically from the numerical results for three cases:

$K = 1.8465$, upper stagnation point
$K = 1.7354$, average over the upper hemisphere
$K = 1.3499$, average over the entire sphere

The uncertainty of equation (49) is within 2 percent of the range of $c_p(t_s - t_w)/h_{fg}$ from 0.001 to 1 and $\mathrm{Pr} > 1$.

Equation (49) can be written in an alternate form. For the Nusselt number at the upper stagnation point it is

$$\mathrm{Nu} = 1.098\left[\frac{g(\rho - \rho_v)h_{fg}D^3}{k\nu(t_s - t_w)}\right]^{1/4} \tag{50}$$

The average Nusselt number over the upper hemisphere is

$$\overline{\mathrm{Nu}} = 1.032\left[\frac{g(\rho - \rho_v)h_{fg}D^3}{k\nu(t_s - t_w)}\right]^{1/4} \tag{51}$$

The average Nusselt number over the entire sphere is

$$\overline{\mathrm{Nu}} = 0.803\left[\frac{g(\rho - \rho_v)h_{fg}D^3}{k\nu(t_s - t_w)}\right]^{1/4} \tag{52}$$

It is interesting to compare the overall Nusselt number of a sphere, equation (52), with that of a vertical plate and a horizontal cylinder. From [1, 2] we have

$$\overline{\mathrm{Nu}} = 0.943\left[\frac{g(\rho - \rho_v)h_{fg}L^3}{k\nu(t_s - t_w)}\right]^{1/4} \tag{53}$$

for a vertical plate of height L, and

$$\overline{\mathrm{Nu}} = 0.733\left[\frac{g(\rho - \rho_v)h_{fg}D^3}{k\nu(t_s - t_w)}\right]^{1/4} \tag{54}$$

for a horizontal cylinder of diameter D. Therefore, for a given Prandtl number and subcooling, the average Nusselt number of a sphere of diameter D is 8.8 percent higher than that of a horizontal cylinder of the same diameter D, and is 17.6 percent lower than that of a vertical plate of height D.

It should be pointed out that there are certain conditions for which the analysis does not apply. For example the surface-tension term which is neglected in the momentum equation can be important for small spheres. Bromley [2] has indicated that the surface tension also produces droplets covering appreciable areas on the lower stagnation region.

References

1 Sparrow, E. M., and Gregg, J. L., "A Boundary-Layer Treatment of Laminar-Film Condensation," JOURNAL OF HEAT TRANSFER, TRANS. ASME, Series C, Vol. 81, No. 1, Feb. 1959, pp. 13–18.

2 Sparrow, E. M., and Gregg, J. L., "Laminar Condensation Heat Transfer on a Horizontal Cylinder," JOURNAL OF HEAT TRANSFER, TRANS. ASME, Series C, Vol. 81, No. 4, Nov. 1959, pp. 291–296.

3 Koh, J. C. Y., Sparrow, E. M., and Hartnett, J. P., "The Two Phase Boundary Layer in Laminar Film Condensation," *International Journal of Heat and Mass Transfer*, Vol. 2, 1961, pp. 69–82.

Finally, it is proposed for practical applications that the heat-transfer rate is proportional to $[\mathrm{Pr}\ h_{fg}/c_p(t_s - t_w)]^{1/4}$, i.e.,

$$\mathrm{Nu}/C^{1/4} = K[\mathrm{Pr}\ h_{fg}/c_p(t_s - t_w)]^{1/4} \tag{49}$$

The constant K has been determined empirically from the numerical results for three cases:

$K = 1.8465$, upper stagnation point
$K = 1.7354$, average over the upper hemisphere
$K = 1.3499$, average over the entire sphere

The uncertainty of equation (49) is within 2 percent of the range of $c_p(t_s - t_w)/h_{fg}$ from 0.001 to 1 and $\mathrm{Pr} > 1$.

Equation (49) can be written in an alternate form. For the Nusselt number at the upper stagnation point it is

$$\mathrm{Nu} = 1.098\left[\frac{g(\rho - \rho_v)h_{fg}D^3}{k\nu(t_s - t_w)}\right]^{1/4} \tag{50}$$

The average Nusselt number over the upper hemisphere is

$$\overline{\mathrm{Nu}} = 1.032\left[\frac{g(\rho - \rho_v)h_{fg}D^3}{k\nu(t_s - t_w)}\right]^{1/4} \tag{51}$$

The average Nusselt number over the entire sphere is

$$\overline{\mathrm{Nu}} = 0.803\left[\frac{g(\rho - \rho_v)h_{fg}D^3}{k\nu(t_s - t_w)}\right]^{1/4} \tag{52}$$

It is interesting to compare the overall Nusselt number of a sphere, equation (52), with that of a vertical plate and a horizontal cylinder. From [1, 2] we have

$$\overline{\mathrm{Nu}} = 0.943\left[\frac{g(\rho - \rho_v)h_{fg}L^3}{k\nu(t_s - t_w)}\right]^{1/4} \tag{53}$$

for a vertical plate of height L, and

$$\overline{\mathrm{Nu}} = 0.733\left[\frac{g(\rho - \rho_v)h_{fg}D^3}{k\nu(t_s - t_w)}\right]^{1/4} \tag{54}$$

for a horizontal cylinder of diameter D. Therefore, for a given Prandtl number and subcooling, the average Nusselt number of a sphere of diameter D is 8.8 percent higher than that of a horizontal cylinder of the same diameter D, and is 17.6 percent lower than that of a vertical plate of height D.

It should be pointed out that there are certain conditions for which the analysis does not apply. For example the surface-tension term which is neglected in the momentum equation can be important for small spheres. Bromley [2] has indicated that the surface tension also produces droplets covering appreciable areas on the lower stagnation region.

References

1 Sparrow, E. M., and Gregg, J. L., "A Boundary-Layer Treatment of Laminar-Film Condensation," JOURNAL OF HEAT TRANSFER, TRANS. ASME, Series C, Vol. 81, No. 1, Feb. 1959, pp. 13–18.

2 Sparrow, E. M., and Gregg, J. L., "Laminar Condensation Heat Transfer on a Horizontal Cylinder," JOURNAL OF HEAT TRANSFER, TRANS. ASME, Series C, Vol. 81, No. 4, Nov. 1959, pp. 291–296.

3 Koh, J. C. Y., Sparrow, E. M., and Hartnett, J. P., "The Two Phase Boundary Layer in Laminar Film Condensation," *International Journal of Heat and Mass Transfer*, Vol. 2, 1961, pp. 69–82.

Discussion

J. H. Lienhard[2] and V. K. Dhir[3]

We wish to point out a prior publication on this subject. In 1970 we solved the problem of laminar condensation on a sphere.[4] That paper showed how to replace g with an effective gravity, g_{eff}, in the Nusselt–Rohsenow expression for condensation on a vertical plate. Thus the expression

$$\mathrm{Nu} = 0.707\left[\frac{g_{\mathrm{eff}}(\rho - \rho_v)h_{fg}'x^3}{k\nu(t_s - t_w)}\right]^{1/4} \tag{55}$$

where

$$g_{\mathrm{eff}} \equiv x(gr)^{4/3}\left[\int_0^x g^{1/3}r^{4/3}\,dx\right]^{-1} \tag{56}$$

gave the condensing heat transfer on any axisymmetric (or plane, if $r \to \infty$) body with any variation of gravity, $g(x)$, along the x coordinate. We worked out eight examples, including the sphere, for which the result was

$$\overline{\mathrm{Nu}} = 0.785\left[\frac{g(\rho - \rho_v)h_{fg}'D^3}{k\nu(t_s - t_w)}\right]^{1/4} \tag{57}$$

Three points should be made in comparing this result with Professor Yang's:

1 His equation (52) is 2.3 percent above our result. One might feel that his full boundary-layer treatment has provided a minute improvement over our simple adaptation of the Nusselt–Rohsenow computation.

2 However, in finally obtaining equation (52), he has neglected the sensible heat absorbed by the film. The latent heat for condensation should be corrected to

$$h_{fg}' \equiv h_{fg} + 0.68c_p\Delta T \tag{58}$$

so part of his improvement has already been lost in this omission.

3 The only real ground gained by the present analysis would then appear to be that it can be used when Pr is well below unity—a regime in which the Nusselt–Rohsenow analysis fails. However, even that is misleading. As we pointed out in our paper, this region is one in which neither analysis can be used because of temperature-decrement problems that enter at the outer interface when Pr is small.

Author's Closure

The author would like to thank Drs. Lienhard and Dhir for their comments on the average Nusselt number over a sphere. The agreement or disagreement between the full boundary-layer treatment and the Nusselt–Rohsenow treatment is well established for the cases of a flat plate and a horizontal cylinder. Condensation on spheres is under the same situation. It should be pointed out that the boundary-layer treatment possesses a certain advantage in describing the local variations of heat and mass transfer rate, particularly near the upper stagnation point. For example, the assumption that $\delta = 0$ at $x = 0$ is not required in the boundary-layer treatment but is necessary for the Dhir–Lienhard analysis. This assumption is not realistic and will introduce a certain error on the average Nusselt number.

The correction of the latent heat for condensation is necessary only if the subcooling parameter ($c_p\Delta T$) is comparable with h_{fg}. However, in most cases the sensible heat absorbed is much less than the latent heat transfer. Under these conditions, the correction does not provide significant improvement.

[2] Professor, Boiling and Phase-Change Laboratory, Mechanical Engineering Department, University of Kentucky, Lexington, Ky.

[3] Research Associate, Boiling and Phase-Change Laboratory, Mechanical Engineering Department, University of Kentucky, Lexington, Ky.

[4] Dhir, Vijay, and Lienhard, John, "Laminar Film Condensation on Plane and Axisymmetric Bodies in Nonuniform Gravity," JOURNAL OF HEAT TRANSFER, TRANS. ASME, Series C, Vol. 93, No. 1, Feb. 1971, pp. 97–100.

E. E. ANDERSON[1]
Assistant Professor,
Department of Mechanical Engineering,
Iowa State University,
Ames, Iowa
Assoc. Mem. ASME

R. VISKANTA
Professor.
Mem. ASME

W. H. STEVENSON
Associate Professor.
Assoc. Mem. ASME

School of Mechanical Engineering,
Purdue University,
Lafayette, Ind.

Heat Transfer through Semitransparent Solids[2]

The heat transfer through a plane layer of a semitransparent solid is investigated experimentally for conditions under which the radiative transport must be considered. Temperature profiles measured with a Mach–Zehnder interferometer and the total heat flux are compared to rigorous analysis employing a rectangular multiband model of the spectral-absorption coefficient and simplified approximate techniques. Results for opaque and semitransparent boundary conditions are presented for three sample thicknesses. Fused quartz is employed for the specimen, as its thermophysical properties are similar to those of several materials which are commonly exposed to severe thermal conditions, it has excellent high-temperature and interferometric properties, and its strong infrared absorption peak serves as a critical test of a band model. For the experimental conditions which are considered, it is shown that the coupling of conduction and radiation cannot be neglected for the prediction of the heat transfer, although no appreciable influence on the temperature profile was observed. Approximate analytical techniques are shown to be accurate in this situation.

Introduction

TREATING THE heat transfer in solids as if conduction were the only means of transport is erroneous when the temperatures are such that thermal radiation is significant and the solid is partially or completely transparent to this radiation. These conditions are frequently encountered in practice. For example, radiative transport is known to be significant in the manufacturing and processing of glass, particularly in the glass melting tank where energy transfer by thermal radiation commonly equals or predominates over that of other energy-transfer modes. During the heat-treatment of glass for stress relief or for the creation of residual stresses, radiative transport is an important but often neglected mode. Similar conditions arise in the growth of synthetic crystals from the melt and when semitransparent solids are exposed to high-energy laser radiation or atmospheric reentry conditions.

A number of studies based upon the gray-absorption-coefficient model have been reported in the heat-transfer literature and serve as the current means of evaluating coupled conduction–radiation. The gray approximation has been employed by Kellett [1][3] and Walther et al. [2] for studying heat transfer through glasses. Solids, just as are other media, are not gray but have definite absorption bands for which equivalent gray absorption coefficients cannot be defined. Application of gray results to semitransparent solids is certainly open to question and investigations of the nongray effects are necessary for clarification. Geffcken [3, 4] recognized this problem and introduced an "effective radiative conductivity" based upon Rosseland's diffusion approximation to incorporate the nongray effects of semitransparent solids. The error in the gray model for a specific glass has been demonstrated more rigorously by Gardon et al. [5, 6] using numerical zonal analysis.

Although analytical studies have been extensive, fundamental experimental verification has been retarded by difficulties with instrumentation and creation of controlled experimental conditions. Nishimura et al. [7] have measured local temperatures in a plane layer of molten glass with thermocouples. Significant differences between their analytical predictions and experimental results can be attributed to the gray-spectral-absorption-coefficient model and radiation errors in the temperature measurements. To eliminate the radiation error, Eryou and Glicksman [8] have measured the temperature-dependent attenuation of a He–Ne laser beam traversing a layer of molten glass. Their measurements agree within the experimental error with multiband spectral analysis. Temperatures were not reported, however, in the critical region near the boundaries.

In order to simplify the prediction of coupled heat transfer, several approximate techniques such as the exponential kernel substitution, superposition of the pure radiative and conductive transfer, and others [9] have been suggested and evaluated by comparison to rigorous analysis using idealized absorption spectra. The lack of experimental data has precluded the realistic evaluation of these approaches. This study was undertaken to fill this need for experimental data on heat transfer in semitransparent solids and to evaluate some of the analytical techniques that have been proposed.

Local temperatures and the total heat flux of a one-dimensional

---

[1] Currently with the Department of Mechanical Engineering, University of Southwestern Louisiana, Lafayette, La.

[2] This work was supported by the Advanced Research Projects Agency under institutional grant SD-102.

[3] Numbers in brackets designate References at end of paper.

Contributed by the Heat Transfer Division and presented at the Winter Annual Meeting, New York, N. Y., November 26–30, 1972, of THE AMERICAN SOCIETY OF MECHANICAL ENGINEERS. Manuscript received by the Heat Transfer Division April 10, 1972. Paper No. 72-WA/HT-6.

layer with either opaque or semitransparent boundaries are compared to predictions based on rigorous analysis employing a multiband and a simplified-band model for the semitransparent absorption edge. Results predicted by the superposition of the pure conductive heat transfer and radiative surface exchange through the transparent spectral windows, and an "effective radiative conductivity" [10] approximation, are also compared to experimental and rigorous analytical results in order to ascertain their validity. The influence of the material thickness, temperature level, and surface emittance is demonstrated experimentally for the opaque boundary condition. For the semitransparent boundary condition, experimental results for different material thicknesses and temperature levels are given.

Analysis

The physical system is a plane layer of an absorbing–emitting semitransparent solid of thickness t. It is assumed that the solid is isotropic and does not scatter electromagnetic radiation. Two boundary conditions are considered. In one case the faces of the solid layer are in contact with either an opaque directionally emitting and reflecting isothermal heat sink at temperature T_1 or with a similar heat source at temperature T_2. This will be referred to as the opaque boundary condition. In the case of semitransparent boundaries, the layer is not in contact with isothermal bodies, but rather is irradiated by an energy source or sink which can be quite distant from the solid. Molecular energy transfer between the faces of the layer and heat source or sink may also be taking place. Radiation and optical properties are taken to be frequency-dependent for a general and realistic analysis. Frequency is used for the spectral variable since the wavelength in the surrounding medium is not the same as that within the solid if their refractive indices differ.

Basic Equations. At steady state in the absence of internal heat sources, conservation of energy requires that

$$\frac{d}{dx}\left[-k(T)\frac{dT}{dx}+F\right]=0 \tag{1}$$

be satisfied. This implies that the sum of the conductive and radiative flux must equal the constant total heat flux. The radiative flux is defined by

$$F(x)=2\pi\int_0^\infty\left\{\int_0^1 I_\nu{}^+(x)\mu d\mu-\int_0^{-1} I_\nu{}^-(x)\mu d\mu\right\}d\nu \tag{2}$$

where $I_\nu{}^+(x)$ and $I_\nu{}^-(x)$ are the spectral intensity of radiation in the forward ($\mu > 0$) and backward ($\mu < 0$) directions, respectively. As a result of internal emission of radiation, the intensity is coupled to the temperature distribution in the solid. This coupling is implicitly expressed by the equation of transfer [9]

$$\mu\frac{dI_\nu{}^+}{dx}=\kappa_\nu[T^4 f_\nu(T)-I_\nu{}^+] \qquad 0<\mu\leq 1 \tag{3}$$

where

$$f_\nu(T)=\left(\frac{2k^3n_\nu{}^2}{h^2C_0{}^2T}\right)\frac{(h\nu/kT)^3}{\exp(h\nu/kT)-1} \tag{4}$$

which is the ratio of Planck's function to the fourth power of the temperature. A similar relation can be written for the backward direction ($-1 \leq \mu < 0$). The simultaneous solution of equations (1)–(3) for the local temperature subject to the appropriate boundary condition presents a number of practical limitations even for this simple physical situation.

The spectral integration of equation (2) was accomplished by employing a multiband rectangular model [11] for the spectral-absorption coefficient

$$\kappa_\nu=\kappa_i(T) \qquad \nu_i\leq\nu<\nu_{i+1} \tag{5}$$

In principle this approximation can be made as accurate as desired by adjusting the number of bands. Numerically, the integrals over the domain of μ may be evaluated with an appropriate quadrature such as that of Gauss. Physically, only a fixed number of directions μ_j which are selected in accordance with the quadrature rule are considered. The accuracy of the quadrature is determined by the number of discrete ordinates.

In numerical form, conservation of energy for simultaneous conduction and radiation is then

$$\frac{d}{dx}\left\{-k\frac{dT}{dx}+2\pi\sum_{i=1}^{m}\sum_{j=1}^{n}w_j\mu_j[I_{ij}{}^+(x)-I_{ij}{}^-(x)]\right\}=0 \tag{6}$$

For each band and in each of the discrete directions the forward and backward intensities must satisfy the equation of transfer

$$\frac{dI_{ij}{}^+}{dx}=\frac{\kappa_i}{\mu_j}[T^4 f_i(T)-I_{ij}{}^+] \qquad 0<\mu_j\leq 1 \tag{7a}$$

$$\frac{dI_{ij}{}^-}{dx}=\frac{\kappa_i}{\mu_j}[I_{ij}{}^- - T^4 f_i(T)] \qquad -1\leq\mu_j<0 \tag{7b}$$

where $f_i(T)$ is obtained by integrating equation (4) over the ith band. This system of $2ij + 1$ nonlinear differential equations, with the requisite boundary conditions, was readily solved numerically by the method of successive approximations [12].

Boundary Conditions. In the case of opaque boundaries the presence of conduction insures continuity of temperature. The boundary conditions for equation (6) are then

$$T(0)=T_1 \qquad \text{and} \qquad T(t)=T_2 \tag{8}$$

With semitransparent boundaries an energy balance on the interface gives the required boundary conditions. At the interface $x = 0$ this balance of the emission, absorbed irradiation, molecular energy transfer between the interface and heat source or sink, and conduction gives the boundary condition for the interface temperature

$$-k\left.\frac{dT}{dx}\right|_{x=0}+h_1[T_1-T(0)]+\epsilon_{opq}\{f_{opq}(T_1)T_1{}^4-f_{opq}[T(0)]T^4(0)\}=0 \tag{9}$$

Nomenclature

C_0 = *in-vacuo* speed of light
F = radiant heat flux, w/cm²
FA = frequency-averaged 3-band model
$f_\nu(T)$ = normalized spectral blackbody emissive power, equation (4)
$f_{opq}(T)$ = $f_\nu(T)$ integrated over the opaque spectral region
h = heat-transfer coefficient, w/cm²-deg C; Planck's constant
I = intensity of radiation, w/cm²-steradian
k = thermal conductivity, w/cm-deg C; Boltzmann's constant
MB = multiband model
N = conduction–radiation interaction parameter, $k/4t\sigma T^3$
n = refractive index
q_{co} = pure conductive flux defined as $k\Delta T/t$, w/cm²
q_t = total heat flux, w/cm²
T = temperature, deg K
t = thickness of layer, cm
w = Gaussian-quadrature weights
x = spatial coordinate across layer, cm
ϵ = surface emittance
ϵ_{opq} = surface emittance in opaque spectral region
κ = linear absorption coefficient, 1/cm
μ = direction cosine
ν = frequency, 1/sec
ρ = bidirectional surface reflectance

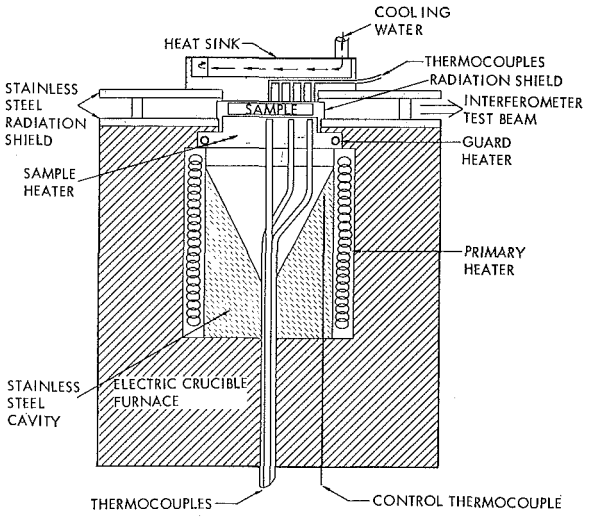

Fig. 1 Cross-sectional view of test assembly

The last term is included to treat the opaque spectral ranges where thermal radiation is a surface phenomenon. According to electromagnetic theory the radiant flux, although directionally redistributed, is conserved across the interface in the transparent and semitransparent spectral regions. They are therefore not included in equation (9).

The intensity leaving an opaque boundary is the sum of that emitted by the source or sink and that reflected by the interface. The intensity in the ith band and jth direction must then satisfy

$$I_{ij}^{+}(0) = \epsilon_{ij} f_i(T_1) T_1^4 + 2 \sum_{l=1}^{n} w_l \mu_l \rho_{il} (\mu_l \rightarrow \mu_j) I_{ij}^{-}(0) \quad (10)$$

where ρ_{il} $(\mu_l \rightarrow \mu_j)$ is the bidirectional reflection function [13]. Semitransparent boundaries are also described by equation (10) if the bidirectional transmission function, obtained for example from Fresnel equations for an optically smooth interface, is substituted for the directional emittance. Expressions similar to equations (9) and (10) can be written for the interface at $x = t$.

Experiment

Of the physical quantities that could have been measured experimentally, the temperature distribution and total energy flux were selected. Local temperature is the more fundamental parameter from which the conductive and radiative heat flux may be calculated. The temperature distribution is typically not predicted accurately by an approximate analysis [10] and thereby serves as a critical evaluation of these approaches. The total energy flux is the primary heat-transfer quantity and was therefore measured independently. It also serves as a check on the temperature measurements. In order to measure the temperature profile without interfering with the temperature and radiation fields or introducing a radiation error in the measurements, a Mach–Zehnder interferometer [14] was used.

Fused quartz[4] was selected for the experimental medium because it has the desired interferometric, thermophysical, and radiation properties. Since it is dimensionally stable, workable to optical tolerances, relatively insensitive to thermal stress and shock, and has a refractive index which depends linearly upon temperature [15], it is an excellent medium for interferometric techniques. The thermal conductivity of fused quartz is similar to that of many amorphous solids while its softening point is significantly greater and it can withstand temperatures up to 900 deg C without damage. Simulation of the conduction–radiation interaction parameter N is then achieved without melting the medium or incurring convective transport. Fused quartz has an absorption peak in the near-infrared which is not present in glasses. This peak provides a critical test of rectangular band models and approximate analysis based upon a rectangular band model.

Test Assembly. Simulating one-dimensional heat transfer in an experimental apparatus of finite size presents a number of difficulties. Errors due to the energy losses from the edges can be minimized by a large length-to-thickness ratio. In the experiments the sample length is limited by the resolvable fringe density, proportional to the length, while a thick specimen is required for the conductive and radiative transfer to be of comparable magnitude. Compromise length-to-thickness ratios from 4 to 16 were used with thicknesses of 0.318 to 1.27 cm. Convective losses were reduced by placing the heater and sample in a vacuum chamber. The chamber could be evacuated to 3 mm Hg, which was limited by outgassing from the heater insulation. At this pressure, the Rayleigh number based on the distance between the heater and sink is 100, thereby virtually eliminating free convection. Radiative edge losses were minimized by radiation shielding and application of a reflective gold film[5] to the edges of the sample while leaving 0.635-cm windows which were polished to interferometric tolerances.

Several designs of the heater assembly were tested for maximum operating temperature as well as uniformity across the radiating surfaces. The design illustrated in Fig. 1 was capable of providing temperatures within 50 deg C of the recommended limits for fused quartz and proved to be the more uniform. Basically the heater consisted of a modified electric-crucible furnace with proportioning temperature controller in which an oxidized stainless-steel conical cavity was placed. The conical cavity irradiated the bottom of a type-303 stainless-steel sample heater. This heater had a 7.62-cm-dia base (about which a nichrome–ceramic guard heater was wrapped in a machined groove) and a 5.72-cm square crown, the face of which irradiated the sample. V-grooves approximately 125 μ deep were stamped into the radiating surface to minimize directional variations in its radiosity. The heater was also oxidized at 650 deg C for several hours to increase its emittance. Transite insulation and a polished stainless-steel radiation shield held the heater in place. The heat sink was fabricated from a 99 percent copper plate. Like the heater, it had a 5.72-cm square crown, the face of which was painted with a high-temperature high-absorption paint.[6] Room-temperature water was circulated through a double-helix heat exchanger which was attached to the cooler by soldering. The cooler was held in position by a polished stainless-steel radiation shield mounted upon guide pins of variable height to accommodate samples of different thicknesses.

The heater assembly was placed in a water-cooled cylindrical vacuum chamber. Optical ports were mounted to flanged stubs on the chamber walls. These stubs were cooled independently to minimize variations in the optical pathlength of the glass viewports. The chamber was set in a Mach–Zehnder interferometer of conventional rectangular design with 7.62-cm-dia optics. A 5-mw He–Ne laser served as the light source. Prior to photographing, the interferogram was magnified with optical elements of long focal length in order that the fringes could be resolved. Interferograms were read with a coordinate-measuring microscope.[7] By repeated reading it was found that the interferograms could be read to within $^1/_{10}$ of a fringe.

Both high- and low-emittance opaque boundary conditions were studied. A high emittance was obtained by applying a coat of Pyromark paint to the interfaces and then setting the sample on the heater, whose V-grooves had been filled with powdered graphite. The low-emittance boundary condition was achieved by applying gold coatings directly to the test sample and then overcoating with Pyromark paint. The sample was mounted on adjustable pins and no coatings were applied for

[4] Corning Glass, code 7940, optical grade.

[5] Englehart Industries, Liquid Bright Gold.

[6] Tempil Corp., Pyromark paint.

[7] Precision Tool and Instrument, Ltd., vernier microscope.

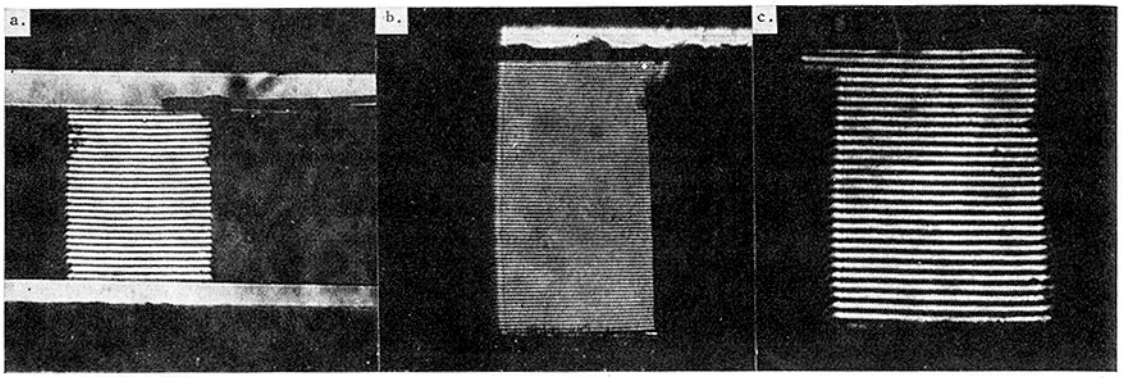

Fig. 2 Typical interferograms for 1.27-cm-thick specimen; (a) semitransparent boundaries, $T_1 = 218$ deg C and $T_2 = 264$ deg C; (b) opaque boundaries, $T_1 = 526$ deg C, $T_2 = 633$ deg C, and $\epsilon = 0.85$; (c) opaque boundaries, $T_1 = 317$ deg C, $T_2 = 355$ deg C, and $\epsilon = 0.05$

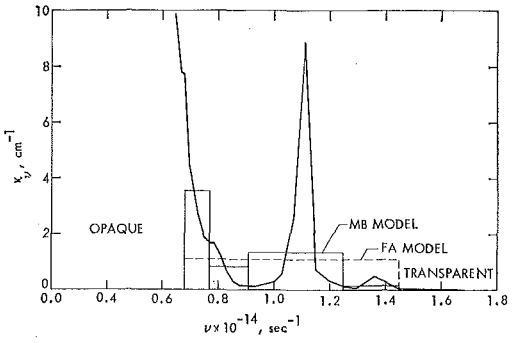

Fig. 3 Spectral-absorption coefficient [17], six-band (MB) and three-band (FA) models of fused quartz

the semitransparent boundary condition. A vacuum gap between the cool-sample and heat-sink interface was maintained as illustrated in the interferograms of Fig. 2 to protect the instrumentation. Necessary emittance and property data for the coatings and fused quartz were obtained from [16, 17].

Instrumentation. Instrumentation for the heater assembly consisted of several chromel–alumel type-K surface thermocouples and a thick-film heat-flux sensor[8] surface-mounted on the heat sink. The output of these transducers was measured with an integrating digital voltmeter with an accuracy of ± 1 μv. Calibration of the thermocouples was performed at the boiling point of water and at the freezing points of NBS cadmium and antimony samples. With proper adjustment of the guard heater and under the critical condition of maximum heating the difference between the center and edge temperatures of the heater and cooler was less than 10 deg C. The heat-flux sensor was calibrated *in situ* by making the gap between the heater and cooler without the test solid as small as possible and measuring the heat transfer between the surfaces. The uncertainty in the emittance of Pyromark paint and oxidized stainless steel limited the accuracy of this calibration to ± 5 percent of the total energy flux. During each data run this calibration was checked in the conduction-dominant limit.

An infinite fringe, which was maintained throughout a test by examining the pattern in the vacuum spaces about the sample, was employed for the reference fringe pattern. The test fringe pattern was then a map of the isotherms. Since the refractive index of fused quartz varies linearly with temperature over a wide range, the change in temperature from one fringe to the next, $\lambda_{He-Ne}/(tdn/dT)$, was constant. The interferograms were then readily interpreted by locating the fringes and independently measuring one temperature of the sample. To obtain the one temperature at the sample interface required for fringe interpretation, a type-K thermocouple was attached with heat-setting silver epoxy for the semitransparent boundaries as shown in the interferogram of Fig. 2(*a*). With opaque boundaries the surface temperature of the heater was used.

Interferometric errors due to the refractive bending of the rays as they traverse the sample were eliminated with corrections obtained from solutions of the eikonal equation. Thermal distortion of the sample was corrected for with thermal strain analysis. Deviations from a one-dimensional profile near the sample edge introduce an error which was estimated from an interferogram taken without the reflective gold coatings or radiation shield surrounding the sample edges. By applying these corrections the total temperature could be measured with an accuracy of 0.3 deg C [18].

Discussion of Results

Interferograms typical of the various boundary conditions are presented in Fig. 2. Within the range of the windows located at the center of the sample, the heat transfer is one-dimensional as evidenced by the degree of parallelism between the fringes and sample interfaces. Interferograms taken without the radiation shields or coatings revealed a region next to the edges of moderate lateral temperature gradient. The extent of this region was about the same as the sample thickness. Under the more severe thermal conditions the edge was 15 to 20 deg C cooler than the center. This is a result of the heat losses from the edges and the temperature variations across the heater surface.

The local temperature gradient is proportional to the fringe spacing. It is apparent from the interferograms that there is only a small variation in the temperature gradient across the sample. In contrast, gray analysis predicts perceptive departure from the pure-conduction temperature profile when the conduction–radiation interaction parameter N is on the order of unity [19]. Experimentally this was the condition, see Table 1, but the influence of the coupling of conduction and radiation on the local temperature was not as pronounced as that of gray theory.

Local Temperatures. The spectral-absorption coefficient of fused quartz and the multiband (MB) approximation employed in the analysis are illustrated in Fig. 3. Within each band the absorption coefficient was determined by a frequency-averaging of the spectral-absorption coefficient computed from the spectral-transmission data of [17]. With the exception of the absorption peak at $\nu = 1.12 \times 10^{14}$ sec^{-1}, the six-band model which includes the transparent and opaque regions is a close approximation to the spectral-absorption coefficient. The range of temperature across the sample was small enough during a given test run that the temperature-dependence of the thermal conductivity and radiation properties could be neglected. Values taken at the mean sample temperature were employed in the analysis.

Experimental temperature profiles are compared to those predicted numerically by the MB model in Figs. 4 and 5, assuming

[8] RDF Corp., microfoil heat-flux sensor.

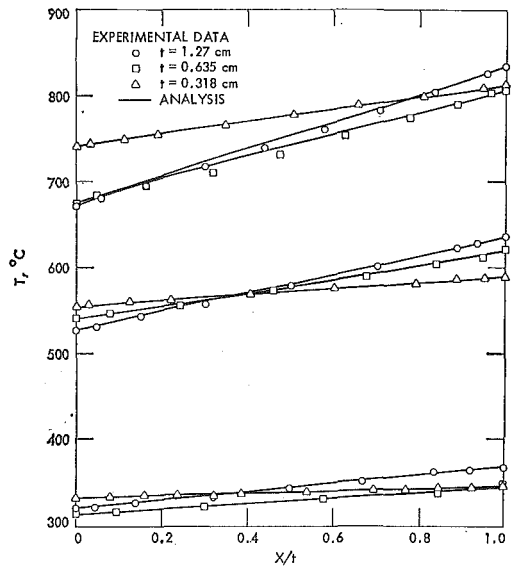

Fig. 4 Comparison of experimentally measured and analytically predicted temperature profiles based on the MB spectral model for fused quartz with opaque high-emittance boundaries, $\epsilon = 0.85$

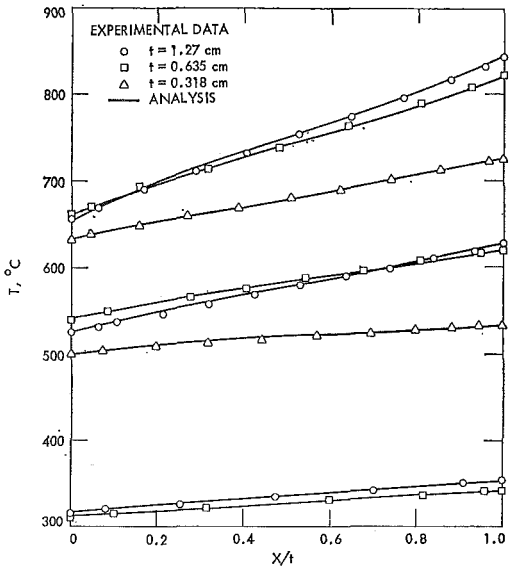

Fig. 5 Comparison of experimentally measured and analytically predicted temperature profiles based on the MB spectral model for fused quartz with opaque low-emittance boundaries, $\epsilon = 0.05$

that the bounding surfaces are diffuse. Analytical and experimental results are in close agreement although the perturbation by radiation of the linear pure-conduction profile is quite small even under the maximum heating conditions where the pure-conductive heat transfer represents only one-half the net heat transfer, see Table 1. For the lower boundary temperatures and thinner layers the energy transfer is dominated by conduction, resulting in a linear variation of temperature with position. As the walls become more reflective the influence of the coupling between conduction and radiation on the temperature in the vicinity of the walls is even more apparent, although conduction is the predominant mode, see Table 1. With reflective walls, elements of the medium are irradiated in part by their own emission due to the reflection. This results in a self-heating effect near the cool wall and a self-cooling effect near the hot wall tending to increase the temperature gradients near the walls while less heat is transported by radiation [20].

In order to more clearly demonstrate the coupling of conduction and radiation, the difference between that predicted or measured and the pure-conduction profile was calculated. In this manner the experimental results can be critically examined and the effect of the band model, reflection–emission characteristics, and ap-

Table 1 Comparison of analytical and experimental total energy flux in percentage deviation

						(Analysis–Experiment)/Experiment			
t (cm)	T_1 (°C)	T_2 (°C)	N	q_t (w/cm²)	q_{co}/q_t	MB (%)	FA (%)	Superposition (%)	[10] (%)
				A Diffuse opaque boundaries, $\epsilon = 0.85$					
	672	830	0.87	6.07	0.51	1.5 (6.3)*	4.9	−39.1	−13.6
1.27	526	633	0.85	2.64	0.78	5.8 (2.6)*	11.1	−11.9	−1.5
	321	367	0.78	0.80	1.02	5.4 (4.8)*	8.7	26.3	10.0
	676	804	1.74	8.02	0.63	−3.5	−0.9	−34.0	−10.5
0.635	537	618	1.69	3.14	0.99	13.4	26.1	3.7	12.9
	313	344	1.55	1.03	1.10	4.4	5.8	2.5	2.5
	741	809	3.47	6.73	0.79	1.5 (7.4)*	2.2	−14.4	0.9
0.318	554	587	3.38	2.60	0.97	6.0 (4.4)*	7.0	−46.2	5.5
	331	345	3.11	0.90	1.10	3.7 (3.3)*	4.6	10.0	10.0
				B Diffuse opaque boundaries, $\epsilon = 0.05$					
	656	843	0.87	5.24	0.70	−11.5 (−13.6)†	−6.7	11.1	−8.8
1.27	525	628	0.85	2.16	0.92	2.6 (1.8)†	5.4	1.1	9.4
	317	355	0.78	0.62	1.08	6.5 (5.8)†	6.7	7.6	14.3
	661	819	1.74	7.34	0.85	−5.6	−5.7	7.2	−2.1
0.635	542	622	1.70	3.19	0.97	1.6	0.2	3.5	5.3
	313	342	1.55	0.98	1.04	2.2	2.6	1.8	8.3
0.318	633	724	3.45	7.23	0.98	0.0 (−2.1)†	−0.8	0.0	−2.1
	500	531	3.33	2.32	1.01	7.3 (7.3)†	6.6	1.8	7.5
				C Semitransparent boundaries					
	479	666	0.85	5.75	0.63	−3.5	14.7	...	...
1.27	354	463	0.80	2.42	0.88	8.9	22.4	...	...
	218	264	0.74	0.79	0.98	4.3	13.3	...	...
	543	645	1.70	6.81	0.58	−4.1	8.0	...	...
0.635	400	454	1.62	2.72	0.73	4.4	17.0	...	...
	256	283	1.50	0.93	0.99	13.8	11.1	...	...
	467	525	3.31	7.09	0.61	−8.1	1.1	...	...
0.318	354	385	3.16	3.09	0.72	−1.9	6.2	...	...
	228	244	2.94	1.16	0.92	0.0	4.8	...	...

* $\epsilon = 0.75$.
† Specular reflection.

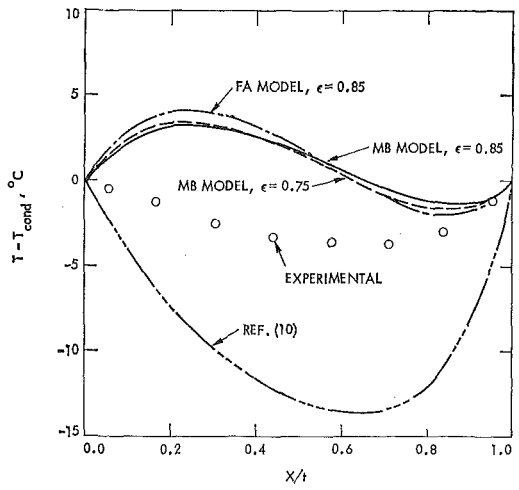

Fig. 6 Deviations from the pure-conduction temperature distribution for *diffuse opaque* walls, t = 1.27 cm, T_1 = 672 deg C, T_2 = 830 deg C, and ϵ = 0.85

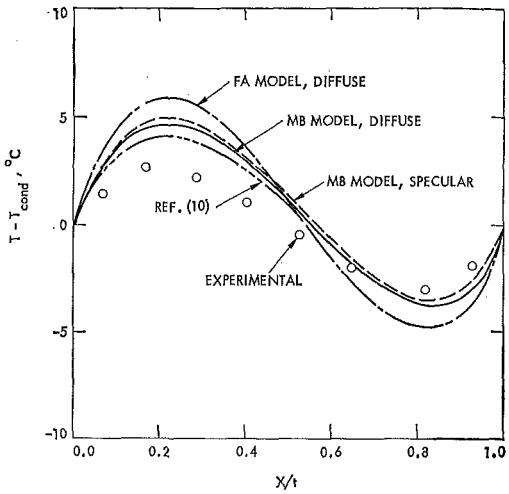

Fig. 7 Deviations from the pure-conduction temperature distribution for opaque walls, t = 1.27 cm, T_1 = 656 deg C, T_2 = 843 deg C, and ϵ = 0.05

proximate analyses ascertained. Local temperature differences for the various boundary conditions are illustrated in Figs. 6, 7, and 8 for the conditions of maximum interaction between the two heat-transfer modes.

The largest difference between multiband analysis and experiment is about 5 deg C or 0.5 percent. The absolute error is about the same as that of Eryou and Glicksman [8]. Contrary to their transmittance technique, the present discrepancies are not due to the measurement technique, as shown by the lack of statistical scatter in the data, but can be attributed to the radiative losses from the edges. This loss acts as a heat sink tending to lower the temperature of the interior, as is clearly evident in the results of Fig. 6.

Data for Pyromark paint [16] show it to be a diffuse emitter with a temperature- and substrate-dependent emittance. Hemispherical emittances ranging from 0.78 to 0.95 have been reported. In another study at lower temperature [21] an emittance as low as 0.72 was recorded. Multiband analyses were conducted for ϵ = 0.75 and 0.85 to bound the variations in the emittance. As shown in the analytical results of Fig. 6 the uncertainty in the emittance of the Pyromark paint has but a small effect on the temperature distribution, which cannot be distinguished from the experimental data. Emittance data for the gold surfaces were obtained from Goldsmith et al. [17]. Diffuse analysis and specular analysis using Fresnel equations were performed for the opaque gold surfaces. From the results of Fig. 7 it is clear that the nature of the reflection is insignificant and well within the experimental error.

With semitransparent boundaries the temperature profiles characteristic of opaque boundaries were neither predicted nor observed [18]. Instead, the temperature was greater than that predicted by pure conduction when the radiative transport to the interface is approximately equal to the molecular transport, as illustrated in Fig. 8. In the only similar study for glass with semitransparent interfaces [6] the predicted temperature was less than that of pure conduction when molecular and radiation heat transfer to the boundary were of the same order of magnitude as in this study. Allowing for the edge losses the present experimental results substantiate the temperature increase with semitransparent boundaries predicted by the present analysis.

Temperature profiles were also calculated using the FA band model for the absorption edge as illustrated in Fig. 3 and the "apparent radiative conductivity" approach of Anderson and Viskanta [10]. Since the coupling of conduction and radiation had a minor effect on the temperature for the experimental conditions studied, the FA model is accurate for the opaque boundaries but is in significant error when the interfaces are semitransparent. In the latter situation the FA model, being more

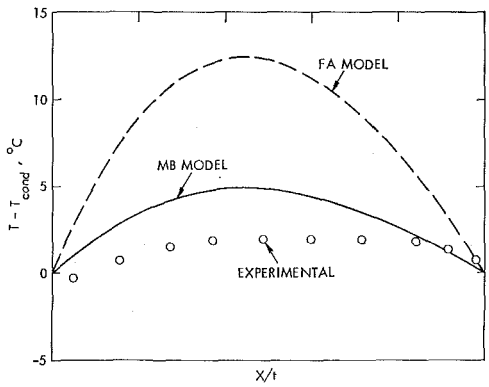

Fig. 8 Deviations from the pure-conduction temperature distribution for semitransparent boundaries, t = 1.27 cm, T_1 = 479 deg C, and T_2 = 666 deg C

"transparent," allows the external radiation to penetrate deeper into the quartz before being absorbed. The heating of the layer by radiation is then greater in the interior, tending to raise the interior temperatures. The "apparent radiative conductivity" only approximates the radiative transfer. It is thus unable to predict the temperature when radiation is significant, as shown in the analytical results of Fig. 6. When radiation is a smaller part of the total heat transfer as in Fig. 7, the "apparent radiative conductivity" is as accurate as the FA model.

Heat Transfer. The experimentally measured net heat flux and the ratio of the pure-conductive to total heat flux q_{co}/q_t are given for the experimental conditions in Table 1. Total heat flux as predicted by the MB model, the FA model, superposition of pure conduction and radiative surface exchange through the transparent spectral regions, and the "apparent radiative conductivity" are also compared to experimental measurements.

The conduction–radiation interaction parameter N is a measure of the ratio of the conductive and radiative transfer. With nongray materials it is advantageous to base N on the sample thickness rather than on a characteristic absorption distance as is commonly done with gray media [19, 20]. The ambiguity of an arbitrarily selected spectral-absorption coefficient is thereby avoided. The values of N tabulated in Table 1 are for a reference temperature of 1000 deg K.

Heat losses through the sample edges were estimated with surface-radiation-exchange theory to be 5 percent of the total heat flux. The net error in total heat-transfer measurements, including that of calibration, is then 10 percent. Analysis based upon the MB model typically predicts the experimental observa-

tions within this limit. This error is also apparent in the comparison with the pure-conductive heat transfer.

Since radiation had but a small influence on the pure-conduction temperature gradient, q_{co} is an accurate measure of the conductive transfer. In the more severe situations the total heat transfer is equally divided between the conduction and radiation modes. The diminishing significance of the radiant transport with increasing N and decreasing temperature and emittance is apparent for the opaque boundary condition. With semitransparent boundaries there is little change in q_{co}/q_t with increasing N.

With high-emittance diffuse boundaries, small variations in the emittance do not appreciably alter the total heat transfer. At the higher temperatures $\epsilon = 0.85$ is the more accurate, while $\epsilon = 0.75$ gives improved results at the lower temperature. This is in agreement with the observation [16] that the emittance of Pyromark paint increases with temperature. For the gold low-emittance surfaces the difference between specular and diffuse reflection is also quite small and of the order predicted for a gray medium [22]. It appears that the specular model is more nearly correct at the lower transfer rates. This suggests a surface-roughness effect. It was found by visual inspection after testing that the gold had a multitude of minute cracks in it. Quantitative measurements of this roughness could not be made.

The FA model typically predicts the experimental results to within the experimental error. This model is also in excellent agreement with multiband results. In contrast, the error in the simplified superposition method which assumes that the conduction and radiation are uncoupled is excessive, except when the conduction dominates as with the low-emittance boundaries. When this is the case the results are independent of the method by which the radiative transfer is predicted. When radiation is appreciable the coupling of the two modes makes this approximation only useful for the roughest of estimates and for bounding the total heat transfer. Unlike the local temperature, the prediction of the total energy transfer with the series-expansion radiative conductivity is accurate. Thus if only the total heat flux is required, this "effective radiative conductivity" approach simplifies the analysis considerably without introducing appreciable error.

When the interfaces are semitransparent, the trends in the experimental data of Table 1 agree with the limited results previously published [6]. Multiband analysis is quite accurate, whereas the error in the FA-model predictions exceeds the experimental error. The FA model overpredicts the total heat flux. In this situation the FA model is too "transparent" and thus unable to predict either the local temperature or energy transport.

Conclusions

The heat transfer through a plane layer of a semitransparent solid has been examined experimentally under conditions where the radiative transport must be considered and data compared with analytical predictions. Under the more critical experimental conditions the error in neglecting the thermal radiation is apparent, particularly as it affects the total heat transfer. Although the radiative and conductive transfer were almost equal in the more critical cases, only small perturbations to the classical conduction temperature profile were observed because of radiation effects.

Agreement between experimental and analytical results using a multiband spectral model was quite good, although a systematic error was apparent. Since an interferometric measurement is not subject to radiative errors and does not disturb the temperature and radiation fields, it is advantageous when radiation occurs simultaneously with other modes of heat transfer. Even under the severe thermal conditions of the present study accurate data were obtained with an interferometer.

Local temperature and the total heat flux were found to be insensitive to small variations in the surface emittance and the nature of the surface reflection for the opaque boundary conditions investigated. This is a result of nongray effects and the experimental levels of interaction which could be simulated. With semitransparent boundaries internal temperatures were observed to be greater than those predicted by considering heat transfer to be by conduction alone. Semitransparent boundaries are frequently encountered in practice and require additional analytical and experimental study.

Several approximate analytical methods were compared to rigorous multiband analysis and experimental data. Treating the entire absorption edge as a single band predicts the temperature distribution and total heat transfer accurately for opaque boundaries under the conditions considered, but is in appreciable error with the more critical semitransparent boundary conditions. Although the total heat flux for opaque boundaries is insensitive to the spectral details when the radiation does not exceed the conduction, the coupling of the two modes cannot be neglected, as demonstrated by the simple superposition results. Analysis based upon an "effective radiative conductivity" which approximates the coupling predicts the heat transfer reliably but does not predict the local temperature except when conduction dominates. It does have the advantage of simplicity, whereas a band analysis is complicated by the "action at a distance" nature of radiative transfer.

References

1 Kellett, B. S., "The Steady Flow of Heat through Hot Glass," *Journal of the Optical Society of America*, Vol. 42, No. 5, May 1952, pp. 339–343.

2 Walther, A., Dörr, J., and Eller, E., "Mathematische Berechnung für Temperatur-verteilung in der Glasschmeltze mit Berücksichtigung von Wärmeleitung und Wärmestrahlung," *Glastechnische Berichte*, Vol. 26, May 1953, pp. 133–140.

3 Geffcken, W., "Zur Fortleitung der Wärme in Glas bei hohen Temperaturen. I. Teil," *Glastechnische Berichte*, Vol. 25, Dec. 1952, pp. 392–396.

4 Geffcken, W., "Zur Fortleitung der Wärme in Glas bei hohen Temperaturen. III. Teil," *Glastechnische Berichte*, Vol. 29, Feb. 1956, pp. 42–49.

5 Gardon, R., "Calculation of Temperature Distributions in Glass Plates undergoing Heat Treatment," *Journal of the American Ceramic Society*, Vol. 41, No. 6, June 1958, pp. 200–208.

6 Chui, G. K., and Gardon, R., "Interaction of Radiation and Conduction in Glass," *Journal of the American Ceramic Society*, Vol. 52, No. 10, Oct. 1969, pp. 548–553.

7 Nishimura, M., Hasatami, M., and Sugiyama, S., "Simultaneous Heat Transfer by Radiation and Conduction. High Temperature One-Dimensional Heat Transfer in Molten Glass," *International Chemical Engineering*, Vol. 8, No. 4, Oct. 1968, pp. 739–745.

8 Eryou, N. D., and Glicksman, L. R., "An Experimental and Analytical Study of Radiative and Conductive Heat Transfer in Molten Glass," JOURNAL OF HEAT TRANSFER, TRANS. ASME, Series C, Vol. 94, No. 2, May 1972, pp. 224–230.

9 Sparrow, E. M., and Cess, R. D., *Radiation Heat Transfer*, Brooks/Cole, Belmont, Calif., 1966.

10 Anderson, E. E., and Viskanta, R., "Effective Conductivity for Conduction–Radiation by Taylor Series Expansion," *International Journal of Heat and Mass Transfer*, Vol. 14, No. 8, Aug. 1971, pp. 1216–1219.

11 Crosbie, A. L., and Viskanta, R., "Interaction of Heat Transfer by Conduction and Radiation in a Nongray Planar Medium," *Warme- und Stoffübertragung*, Vol. 4, No. 4, 1971, pp. 205–212.

12 Ames, W. F., *Nonlinear Ordinary Differential Equations in Transport Processes*, Academic, New York, N. Y., 1968.

13 Dunkle, R. V., "Thermal Radiation Characteristics of Surfaces," in: *Theory and Fundamental Research in Heat Transfer*, J. C. Clark, ed., Pergamon, New York, N. Y., 1963, pp. 1–32.

14 Hauf, W., and Grigull, V., "Optical Methods in Heat Transfer," in: *Advances in Heat Transfer*, Vol. 6, J. P. Hartnett and T. F. Irving, Jr., eds., Academic, New York, N. Y., 1971, pp. 134–366.

15 Wray, J. H., and Neu, J. T., "Refractive Index of Several Glasses as a Function of Wavelength and Temperature," *Journal of the Optical Society of America*, Vol. 59, No. 6, June 1969, pp. 774–776.

16 Wade, W. R., and Slemp, W. S., "Measurements of Total Emittance of Several Refractory Oxides, Cermets, and Ceramics for Temperatures from 600°F to 2000°F," NASA TN D-998, 1961.

17 Goldsmith, A., Waterman, T. E., and Hirschorn, H. J., *Handbook of Thermophysical Properties of Solid Materials*, Macmillan, New York, N. Y., 1961.

18 Anderson, E. E., "Combined Conduction and Radiation in

Semitransparent Soldis: An Experimental and Analytical Study," PhD thesis, Purdue University, Lafayette, Ind., 1972.

19 Viskanta, R., and Grosh, R. J., "Heat Transfer by Simultaneous Conduction and Radiation in an Absorbing Medium," JOURNAL OF HEAT TRANSFER, TRANS. ASME, Series C, Vol. 84, No. 1, Feb. 1962, pp. 63–72.

20 Viskanta, R., and Grosh, R. J., "Effect of Surface Emissivity on Heat Transfer by Simultaneous Conduction and Radiation," *International Journal of Heat and Mass Transfer*, Vol. 5, Aug. 1962, pp. 729–734.

21 Schornhorst, J. R., "An Analytical and Experimental Investigation of Radiant Heat Transfer between Simply Arranged Surfaces," PhD thesis, Purdue University, Lafayette, Ind., 1967.

22 Timmons, D. H., and Mingle, J. O., "Simultaneous Radiation and Conduction with Specular Reflection," AIAA Paper No. 68-28, 1968.

KANEYASU NISHIKAWA
Professor.

TAKEHIRO ITO
Associate Professor.

Department of Mechanical Engineering,
Kyushu University,
Fukuoka, Japan

HIROYUKI YAMASHITA
Instructor,
Department of Mechanical Engineering,
Fukuoka University,
Fukuoka, Japan

Free-Convective Heat Transfer to a Supercritical Fluid

The influence of heater material on free-convective heat transfer from wires to carbon dioxide in the supercritical region was investigated. Three types of flow configuration were observed for nichrome and alumel wires: (a) conventional laminar-flow free convection, (b) an oscillating flow in which (a) and a bubble-like flow alternated, (c) a bubble-like flow in which masses of fluid similar to bubbles appeared successively near the heating surface. Neither (b) nor (c) was observed with a platinum wire. The heat-transfer rate increased suddenly when the flow configuration changed from (a) to (b). The transition in flow structure occurred when the temperature difference between the heater and fluid exceeded about 200 deg C.

Introduction

It has been known that heat transfer to a fluid near the critical point may have unusual characteristics when the pseudocritical temperature of the fluid falls between the temperature of the heating surface and the fluid. To explain this well-known phenomenon, two hypotheses have been advanced: One is that these characteristics may be due to the strong variation with temperature of the fluid properties; the other is that the anomalous characteristics may be attributed to the occurrence of boiling-like phenomena involving fluid masses similar in appearance to boiling heat transfer in the subcritical region.

In regard to the first hypothesis the authors found that in a limited range of small temperature difference between the heating surface and the fluid the experimentally determined coefficients of heat transfer compared favorably with a theoretical analysis by Nishikawa and Ito [1][1] in which the free-convective heat transfer from an isothermal vertical flat plate to supercritical fluids was considered. A solution was determined by assuming similarity and transforming the applicable differential equations. The temperature-dependence of the physical properties involved was accounted for in the numerical integration of these transformed equations. It was noted that the larger the temperature difference, the more the experimentally determined values of the coefficient of heat transfer exceeded the one predicted from the analysis. However, the available experimental data were not considered sufficiently reliable for a definite conclusion to be reached about the effect of the temperature-dependence of the pertinent physical properties.

In regard to the latter hypothesis mentioned above, it was suggested by Nishikawa and Miyabe [2] that the boiling-like phenomena, i.e., similar to nucleate or film boiling, might occur. In addition it was suggested that the normal convection and boiling regime as well as the abnormal regime could be correlated by a unified law, assuming an appropriate two-phase fluid-flow model.

Recently Knapp and Sabersky [3] observed a bubble-like flow near the heating surface in studies on free-convective heat transfer to supercritical carbon dioxide from a horizontal nichrome wire of 0.01-in. diameter. They found that such a flow pattern was accompanied by an increased coefficient of heat transfer α which sometimes was twice as large as that for a platinum wire with the same surface temperature.

More recently, free-convective heat transfer from a platinum wire of 0.015-in. diameter to supercritical carbon dioxide was experimentally investigated by Goldstein and Aung [4]. They also observed bubble-like activity. Although this activity persisted up to the maximum temperature difference achieved, about 830 deg C, the results changed smoothly and no abrupt increase in heat flux was apparent. These results suggest that the heating-surface material may be an important factor in heat transfer to supercritical fluids, and that the mechanism of heat transfer from supercritical fluids may be similar to boiling phenomena.

Recognizing that further study was needed, Sabersky sent a length of the same nichrome wire which he had used to one of the present authors and suggested that additional experiments be carried out. It is the purpose of this paper to describe the investigation conducted.

Apparatus and Procedure

Apparatus. As shown in Fig. 1, the apparatus employed consisted essentially of a cylindrical pressure vessel (100 mm in diameter and 190 mm long) in which a device for supporting the test wire was mounted. The surface temperature of the test element was determined by using it as a resistance thermometer and incorporating it into a Wheatstone-bridge circuit as one of

[1] Numbers in brackets designate References at end of paper.

Contributed by the Heat Transfer Division and presented at the ASME-AIChE Heat Transfer Conference, Tulsa, Okla., August 15–18, 1971. Manuscript received by the Heat Transfer Division April 26, 1971; revised manuscript received October 11, 1971. Paper No. 71-HT-27.

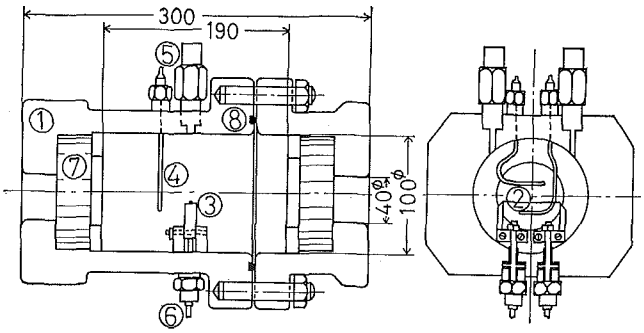

Fig. 1 Test vessel and supporting device for the test wire: (1) pressure vessel, (2) test wire, (3) supporting device, (4) thermocouples, (5) intake and release ports for test fluid, (6) electrical terminal for test wire, (7) glass window, (8) O-ring

the resistance legs. The temperature of the bulk fluid was measured with two chromel–alumel thermocouples. Three kinds of wires, made of nichrome, platinum, and alumel, were used as the heating surface. Carbon dioxide (critical pressure, temperature, and specific volume are 73.8 bar, 31.04 deg C, and 0.00214 m³/kg, respectively) was used as the test fluid because of its relatively low critical pressure and temperature.

Procedure. After a sufficient quantity of carbon dioxide had been introduced into the test vessel from a high-pressure source at approximately 49 bar and 15 deg C, both the intake and relief valves were closed. The following procedure was then followed until the desired initial test condition was obtained. The bulk temperature T_B and system pressure P were controlled by adjusting the electric power supply to the heater in the water bath in which the test vessel was immersed, and by releasing any excess carbon dioxide in the vessel.

The desired measurements were then carried out by supplying current to the heater in stepwise increments. The temperature of the heating surface was determined by measuring the electric resistance of heating wire. The bulk temperature of the test fluid was taken as the average of readings of the temperatures indicated by the two separate thermocouples mounted in the vessel. Fluctuations of the bulk temperature and pressure during a test run were held within 0.1 deg C and 0.1 bar, respectively.

To permit visual observations of the flow pattern near the heating surface, two thick glass windows were installed at each end of the pressure vessel. The heater was illuminated by a light located at the end opposite to the camera. Photographic records were taken with either a still camera or a high-speed moving-picture camera. For these experiments the bulk temperature was fixed at 25 deg C and the pressure at 75.8 bar (1100 psia); the heat flux q was varied from 1 to 10^3 kw/m². Before mounting, the nichrome wire was treated as described in the Appendix.

Flow Patterns

Several photographs of flow patterns representative of the results observed in the present study are shown in Fig. 2 (the locations of the wires are indicated by arrows). Three types of flow pattern, i.e., laminar flow, oscillating flow, and bubble-like flow (all of which were observed and named by Knapp and Sabersky [3]), are clearly recognizable. Photographs of the oscillating flow were taken at 1000 frames/sec. Those shown are for the alumel wire. The same flow patterns were also observed with the nichrome wire.

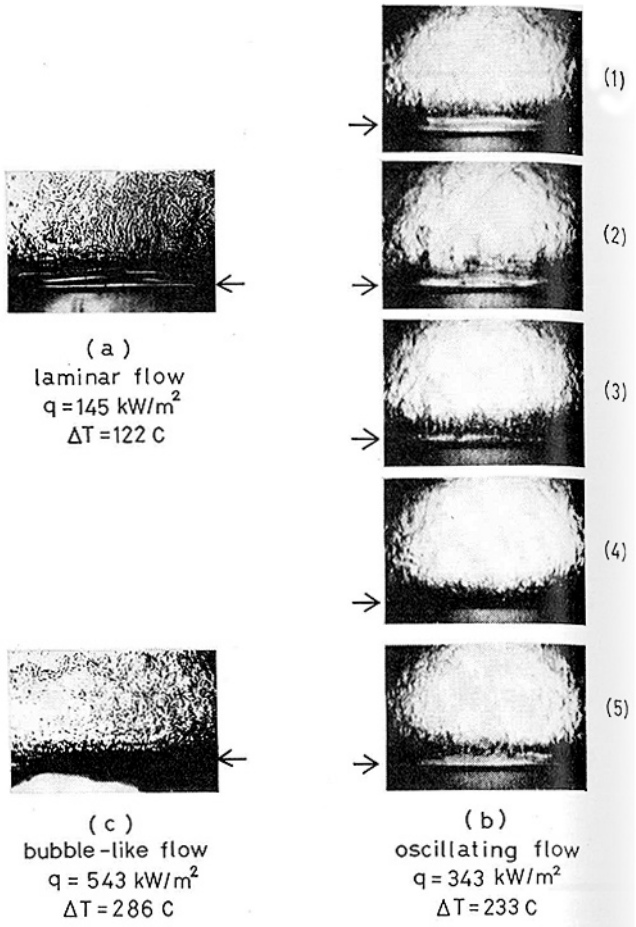

Fig. 2 Flow patterns for P = 75.8 bar (0.3-mm alumel wire)

The laminar flow shown in Fig. 2(a) was observed in the range of temperature difference ΔT less than about 200 deg C. As seen from the figure there exists a domain above the heating surface where no turbulence or disturbance is present. The size of this domain decreased with increase of heat flux. Although the boundary between this domain and the upper disturbed region approached the wire surface with increase of the heat flux, it did not reach the surface while the flow was laminar.

Fig. 2(b) illustrates the oscillating flow pattern. This occurred at temperature differences exceeding approximately 200 deg C. When laminar flow disappeared, the wire was covered with bubble-like fluid elements without, however, the definite phase boundary characteristic of bubbles at subcritical pressures. The successive five frames taken by the high-speed moving-picture camera and reproduced in the figure show a typical cycle of events in the oscillating flow regime in which laminar flow is replaced by bubble-like flow, and then the latter changes into the former. In Fig. 2(b)(1) laminar flow predominates over the wire though there is a disturbed region away from the wire. Then with a nominally fixed heat flux the disturbed region approaches the wire, Fig. 2(b)(2), and finally comes into contact with the wire, Fig. 2(b)(3). In Fig. 2(b)(4) the bubble-like flow pattern has been wholly established. Then the flow pattern is again restored to laminar flow, Fig. 2(b)(5). The frequency of the oscillation varied from 2.5 Hz to 5.5 Hz with increase of the heat flux. In Fig. 2(b) it was about 2.7 Hz.

Nomenclature

D = diameter of wire, mm
L = length of wire, mm
P = system pressure, bar
q = heat flux, kw/m²
T_B = bulk fluid temperature, deg C
T_C = pseudocritical temperature, deg C
T_W = surface temperature of wire, deg C
ΔT = temperature difference, $T_W - T_B$, deg C
α = heat-transfer coefficient, kw/m²-deg C

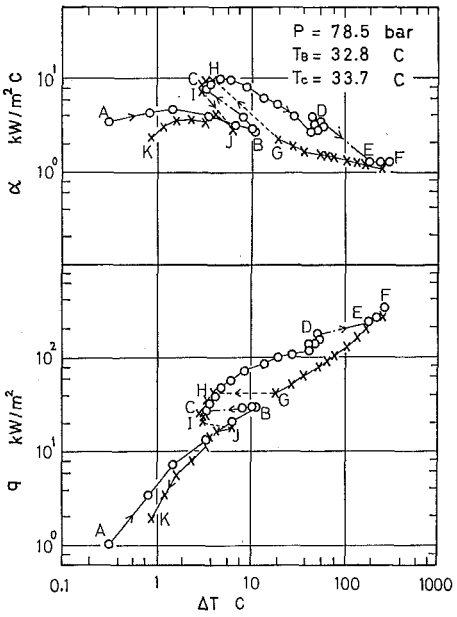

Fig. 3 Heat transfer from a 0.2-mm horizontal platinum wire to supercritical carbon dioxide (Fig. 14 of reference [2])

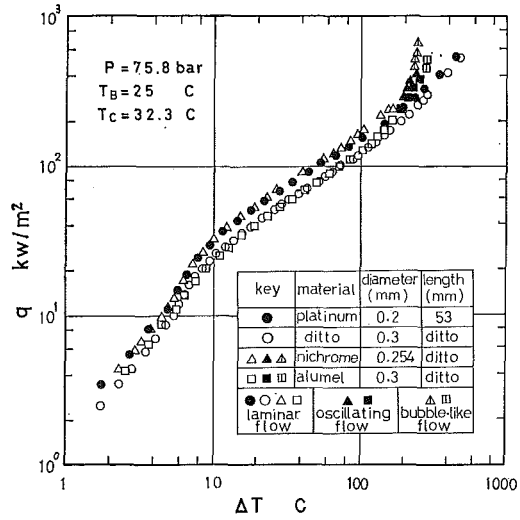

Fig. 4 Relation between heat flux and temperature difference

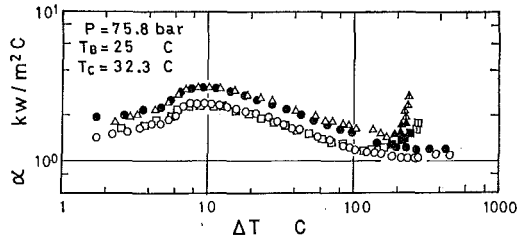

Fig. 5 Relation between heat-transfer coefficient and temperature difference (see Fig. 4 for legend)

The bubble-like flow pattern is shown in Fig. 2(*c*). This occurred at still higher heat fluxes. The laminar-flow part of the oscillating flow was now completely replaced by bubble-like flow. With either the naked eye or photographic observation this bubble-like flow looked like the flow in nucleate boiling, and masses of fluid similar to bubbles seemed to originate directly from the heated surface.

The flow patterns described above occurred with the nichrome and the alumel wires tested. For the platinum wires only laminar flow occurred throughout the experimental range. This was interesting in light of results obtained in a previous study by Nishikawa and Miyabe [2]. This involved free-convective heat transfer from a horizontal platinum wire of 0.2-mm diameter and 30 mm long to carbon dioxide in the supercritical region. This wire was supported horizontally in a small pressure vessel having a cylindrical volume, 44 mm in diameter and 40 mm long, and heated by d-c current. In contrast to the present experiment where only laminar flow was observed, some marked changes occurred in the flow pattern and heat flux at a system pressure of 78.5 bar and a bulk fluid temperature of 32.8 deg C. The pseudocritical temperature for this pressure is 33.7 deg C. These results are reproduced in Fig. 3. The heat-transfer characteristics were described as follows:

"If the heat flux is raised gradually from point A, the wall temperature gradually rises, and heat transfer takes place with normal convection. When the heat flux reaches point B, the behavior changes rapidly with a decrease in wall temperature (from B to C). With further increase in surface heat flux, the temperature increases smoothly along line CD. When the heat flux reaches point D, a second sudden change occurs as the wall temperature jumps from point D to point E. Again with further increase in heat flux, the wall temperature gradually increases along line EF. Now if the heat flux is gradually lowered, no sudden change takes place even when it reaches point E, and it is only after point G has been reached that a sudden change in wall temperature occurs to point H. When the heat flux is lowered further, the wall temperature follows line HI. After passing point C, it makes a sudden change again at point I as the wall temperature jumps from point I to point J. After that, normal convection is maintained along the line JK."

The authors classified the observed behavior into two categories: (1) nucleate-boiling-like and (2) film-boiling-like phenomena, which correspond to the ID and the FG regions in Fig. 3, respectively. In the following the oscillating and the bubble-like flows observed in the present study will be compared to the boiling-like phenomena described in [2].

Heat-flux measurements in the present investigation are presented in Fig. 4; the coefficient of heat transfer is shown in Fig. 5. Though there are some differences in system pressures, bulk fluid temperatures, and diameters of heating wires used for the present measurements (Figs. 4 and 5) and those of the previous experiment (Fig. 3), it is possible to draw some conclusions concerning the differences between the results obtained. In Fig. 3 the boiling-like phenomena were observed for temperature differences less than about 200 deg C and for heat fluxes essentially less than about 200 kw/m². In contrast, the oscillating and the bubble-like flows of the present experiment were obtained under conditions where both the temperature difference and the heat flux were larger than the above-mentioned values. This implies that the unusual flow configurations of the present study (the oscillating and the bubble-like flows) are attributable to temperature differences larger than those in the previous experiment. Although the oscillating and the bubble-like flows were produced with large temperature differences, such as those associated with film boiling at subcritical pressures, their heat-transfer characteristics are similar to those of nucleate boiling in that the slope of the q versus ΔT curve is high. The laminar-flow regime of the present study corresponds to the AJBGEF region of Fig. 3 as far as the temperature difference is concerned.

The oscillating flow in which the laminar and bubble-like flow occur alternately is considered to be in the transitional domain. In nucleate-boiling-like phenomena, columns of fluid lump of low density are observed going up like threads from the heating surface. The bubble-like flow observed in this study is similar to nucleate boiling in appearance except that fluid lumps similar to bubbles seem to originate directly on the heating surface. However, as might be expected in the supercritical region, there is no sharp phase boundary between the fluid lumps and the bulk fluid such as there is with a vapor bubble in a liquid.

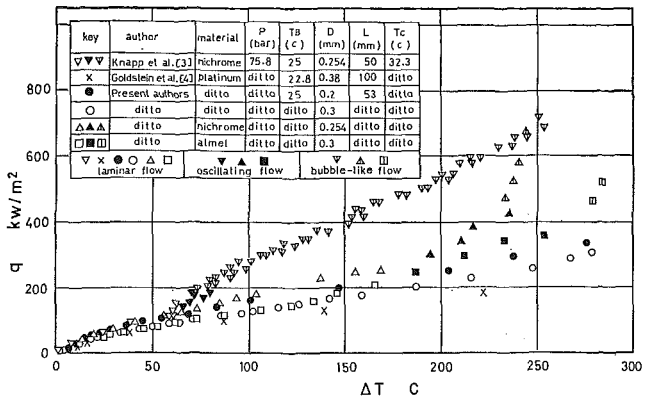

Fig. 6 Comparison of heat-transfer results by various investigators

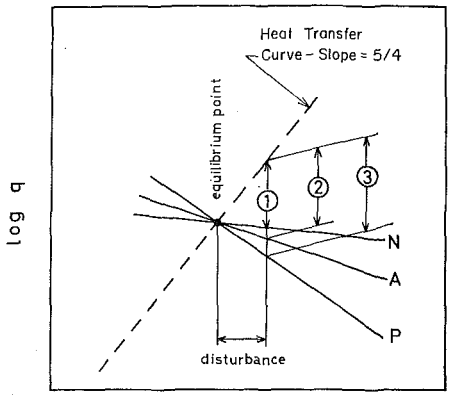

Fig. 7 Restoring force of different wires heated by a constant-voltage power supply for damping out a small temperature disturbance (schematic drawing); N, ① nichrome-test-wire slope: $-0.1 \times 10^{-3} \Delta T$; A, ② alumel-test-wire slope: $-1.2 \times 10^{-3} \Delta T$; P, ③ platinum-test-wire slope: $-3.9 \times 10^{-3} \Delta T$

The above observation suggests that there may be some relation between the heat-transfer mechanisms in nucleate-boiling-like phenomenon and bubble-like flow. However, further work will be necessary to clarify this possibility.

Heat-Transfer Results and Considerations

Measurements were made for a bulk fluid temperature of 25 deg C and a system pressure of 75.8 bar (1100 psia) in order to make comparisons with the studies by Knapp and Sabersky [3] and by Goldstein and Aung [4]. The measured heat flux and coefficient of heat transfer are shown as functions of the temperature difference in Figs. 4 and 5, respectively. Two test runs were done for every bulk fluid condition.

As is evident in Fig. 4, when the oscillating and the bubble-like flows occur, the slope of heat-flux–temperature-difference results at a fixed temperature difference is steeper than when they do not appear. With regard to the nichrome wire, the high heat fluxes reported by Knapp and Sabersky were not obtained in this experiment for temperature differences less than about 200 deg C. However, even in this region slight differences among the platinum, nichrome, and alumel wires were recognized. These differences could not be explained by the variations in the wire diameter or by experimental error. Substantially different heat fluxes for the platinum, nichrome, and alumel wires did result when the temperature difference was raised beyond about 200 deg C, where the oscillating flow or the bubble-like flow appeared.

With a further increase in temperature difference the oscillating flow condition was replaced by the bubble-like flow pattern and the heat flux approached the large magnitudes measured by Knapp and Sabersky.

In Fig. 6 the authors' results are compared with those of Knapp and Sabersky [3] and Goldstein and Aung [4]. Though the three kinds of flow patterns were also recognized in the study by Goldstein and Aung, the temperature difference at which transition occurred was not clearly specified. Therefore identification of flow patterns could not be included in Fig. 6. It is seen from this figure that the heat flux reported by Knapp and Sabersky is approximately two times as large as that of the other two sets of measurements at a temperature difference of 200 deg C. Although there are some differences in the bulk fluid temperature and/or the diameter of test wire among these investigations, these do not appear to provide an explanation for such significantly different results.

The data of Goldstein and Aung show good correspondence with those in the present experiment for platinum wires of 0.2-mm and 0.3-mm diameter, when the difference in wire diameter is accounted for by the conventional correlation of free-convective heat transfer from a horizontal cylinder. When they obtained these data, they recognized the onset of the oscillating flow at the temperature difference of about 220 deg C and observed that what appeared to be bubbles was in contact with the wire (bubble-like activity) at still higher temperature differences.

Knapp and Sabersky reported that the transition of the flow pattern from laminar flow to oscillating flow occurred at a temperature difference of approximately 65 deg C. At a slightly higher heat flux and corresponding temperature difference, the oscillating flow was replaced by the bubble-like flow. Although both the oscillating and the bubble-like flows were observed in this experiment for nichrome and alumel test wires, they occurred at temperature differences greater than about 200 deg C.

Knapp and Sabersky suggest that the occurrence of such flow patterns is dependent not only on the variation of fluid properties with temperature but also on the geometry of the heating surface. This corresponds to the earlier finding of Nishikawa et al. [5] that any unusual flow does not appear in free-convective heat transfer from a vertical flat plate to a fluid in its supercritical state.

Also in this investigation differences exceeding the accuracy of measurement were found in the characteristics of heat transfer depending upon the heating surface material, even at temperature differences less than about 200 deg C, as mentioned above. This is quite obvious when one compares data points for platinum (denoted by ○) with those for alumel (denoted by □), and data points for platinum (denoted by ○ and ●) with those for nichrome (denoted by △). Variations at temperature differences near 200 deg C might possibly be due to faint oscillating flow which is not observable. As mentioned above, in Knapp and Sabersky's experiment oscillating flow appeared at temperature differences as low as 65 deg C. Therefore in the range of temperature difference between about 65 and about 200 deg C the flow pattern was either the oscillating or the bubble-like flow. The reason for this early transition to oscillating flow with an enhanced heat transfer is not known at this time, though some qualitative considerations will be made in the following.

An examination of the experiment suggests the following hypothesis regarding the relative probability of the transition of the flow configuration from the laminar to the oscillating flow. The overall dynamic characteristics of the experimental apparatus, which is composed of a heat-removing fluid body and electrical heat-generating device, must be of an oscillating nature, and these dynamic characteristics may affect the heat transfer. The effect will be amplified in the case of a supercritical fluid. This implies that there were significant differences in the dynamic characteristics between the apparatus described herein and that used by Knapp and Sabersky.

When we discuss the stability of a system of this type, the magnitude of the force that restores the state of the system from a nonequilibrium point to one of equilibrium is an important factor to be considered. Here, nichrome, alumel, and platinum

wires are compared concerning this restoring force when they are connected to an electrical power supply of constant voltage. As is shown in Fig. 7, a curve of heat flux versus temperature difference has a slope of about $^5/_4$ in the laminar-flow regime at any given equilibrium point on a logarithmic plot. On the other hand the characteristics of heat generation in three different kinds of wire will have three different slopes at the same equilibrium point corresponding to the difference in the temperature coefficient of electric resistance. The magnitude of the restoring force which makes the system come back to the original equilibrium point after a disturbance becomes weaker in the order of decreasing temperature coefficient of electric resistance, i.e., platinum, alumel, nichrome.

The interpretation presented above agrees with the trends shown in Fig. 6, where the transition to the oscillating flow appears first for the nichrome wire and then for the alumel wire as the temperature difference increases, but it does not appear for the platinum wire within the range of the temperature difference in this experiment.

Summing up the descriptions of the flow patterns in the preceding section and the discussion of the heat-transfer characteristics in this section, free-convective heat transfer to a supercritical fluid is delicate and is influenced by many factors. The differences in flow configurations and heat-transfer characteristics reported by several authors cannot be clarified definitely at present. Systematic investigations concerning possible factors such as material, surface structure, thermal capacity of heater, and dynamic characteristics of heating circuit are definitely required.

Acknowledgment

The authors would like to thank Dr. Akito Yoshida, Senior Researcher at the Technical Research Institute of the Nippon Steel Corp. for helping them anneal the nichrome wire and to Associate Professor Miyabe of Kyushu Institute of Technology for assisting them in the compilation of physical properties of carbon dioxide.

References

1 Nishikawa, K., and Ito, T., "An Analysis of Free Convective Heat Transfer from an Isothermal Vertical Plate to Supercritical Fluids," *International Journal of Heat and Mass Transfer*, Vol. 12, No. 11, 1969, pp. 1449–1463.

2 Nishikawa, K., Miyabe, K., "On the Boiling-like Phenomena at Supercritical Pressures," *Memoirs of the Faculty of Engineering*, Kyushu University, Vol. 25, No. 1, 1965, pp. 1–25. (Note: $k\varphi$ = 30.1 should be $k\varphi$ = 6.35.)

3 Knapp, K. K., and Sabersky, R. H., "Free Convection Heat Transfer to Carbon Dioxide Near the Critical Point," *International Journal of Heat and Mass Transfer*, Vol. 9, No. 1, 1966, pp. 41–51.

4 Goldstein, R. J., and Aung, W., "Heat Transfer by Free Convection From a Horizontal Wire to Carbon Dioxide in the Critical Region," JOURNAL OF HEAT TRANSFER, TRANS. ASME, Series C, Vol. 90, No. 1, Feb. 1968, pp. 51–55.

5 Nishikawa, K., Ito, T., Kinoshita, M., Hatano, M., and Kanei, H., "Free Convective Heat Transfer from a Vertical Plate to a Supercritical Fluid," *Technical Report of Kyushu University* (in Japanese), Vol. 40, No. 6, 1968, pp. 62–67.

APPENDIX

Prior to the experiment, the nichrome wire was treated by the following procedures. These are essentially the same as those used by Knapp and Sabersky [3].

The first step was to cut the wire to a suitable length. The wire was then degreased in a 3 percent potassium hydroxide solution and rinsed in distilled water. Next the wire was annealed for 4 hr in a vacuum furnace kept below 0.7×10^{-6} mbar at a temperature of 260 deg C and then gradually cooled (for 32 hr) in the furnace to room temperature. The wire was then immersed in a methyl alcohol bath and subjected to ultrasonic cleaning. After these preparations were completed, the wire was examined under a microscope to insure that it was free from serious surface imperfections.

R. M. FAND
Mem. ASME

K. K. KESWANI

Department of Mechanical Engineering,
University of Hawaii,
Honolulu, Hawaii

Mass Rate of Flow in the Natural-Convection Plume above a Heated Horizontal Cylinder Immersed in a Liquid

In this paper, an empirical formula is determined whereby the mass rate of flow in the natural-convection plume above a heated horizontal cylinder immersed in a liquid can be calculated. The formula is based upon experimental data obtained for a heated horizontal cylinder immersed in a tank of water. It is anticipated that the formula will be useful in the design of heaters for liquids stored in tanks.

Introduction

THE HEATING of liquids stored in tanks is a problem of considerable practical importance. Such heating is frequently accomplished by immersion heaters in the form of horizontal cylinders, but relatively little information has been published whereby heaters of this kind can be designed on a rational basis. The total problem is difficult owing to the presence of complex fluid motions that occur in liquids confined in tanks and heated in this way. If a formula were available to calculate the mass rate of flow in natural-convection plumes above heated horizontal cylinders in liquids, the formula would be helpful in designing such heaters. The helpfulness of such a formula would derive from its ability to predict the *total quantity* of liquid whose temperature is eventually raised by the heat transfer process. The objective of the present work was to determine the formula in question by empirical means.

Review of Literature

The problem most closely related to the one at hand, which has been treated extensively in the literature, is the mass rate of flow in the natural-convection plume above a horizontal *line source* of heat. A recent paper by Gebhart, Pera, and Schorr [1][1] contains a thorough literature survey of the work done in the area of natural-convection plumes above horizontal line sources of heat. This paper also contains the clearest analytical formulation of the problem published to date, and it presents theoretically determined expressions for the temperature distribution and mass rate of flow in the plume above a horizontal line source of heat. The expression for the mass rate of flow is reproduced here for reference purposes:

$$\dot{m}_{lx} = 4^{3/5} J \left[\frac{g\beta\rho^2\mu^2 Q}{c_p I}\right]^{1/5} x^{3/5} \tag{1}$$

In equation (1), I and J are functions of the Prandtl number whose values are listed in Table 1 and x denotes the vertical distance upward from the line source to a horizontal plane through which the calculated mass rate of flow passes.

The analysis of Gebhart et al. is based upon the boundary-layer equations of momentum and energy, and since these equations are valid only when the velocity and temperature regions are thin compared with other characteristic dimensions, the authors quite properly discuss in their paper the region of validity of their solutions. To this end they include an interferogram of a plume formed above a heated 0.005-in-dia wire in air; the interferogram shows the extent of the thermal region, which for air is nearly the same as the velocity region. A tracing of the outer contour of half of this thermal region is shown in Fig. 1—the wire is located at the origin of the coordinate system shown. The half-thickness of the thermal region divided by the distance above the centerline of the wire at a point 2 in. above the centerline of the wire (400 diameters) is approximately 0.19. This ratio is not very small in comparison with unity, and hence one cannot expect the boundary-layer equations to predict the mass rate of flow or temperature distribution for this case at distances above the wire less than 2 in. This point is discussed here in detail because, as will be seen subsequently, the present study is based upon experimental data, all of which pertain to distances less than 50 diameters above a heated cylinder, so that boundary-layer theory is clearly not applicable; hence, one cannot expect equation (1) to predict the mass rates of flow for the case studied here. Nevertheless, one might reasonably expect the present experimental data to follow the *general trend*—particularly the dependence on

Table 1 Values of I and J in equation (1), from [1]

P	0.1	0.7	1.0	2.0	6.7	10.0
I	3.090	1.245	1.053	0.756	0.407	0.328
J	4.316	1.896	1.685	1.393	1.094	1.024

[1] Numbers in brackets designate References at end of paper.

Contributed by the Heat Transfer Division for publication (without presentation) in the JOURNAL OF HEAT TRANSFER. Manuscript received by the Heat Transfer Division July 5, 1972. Paper No. 73-HT-B.

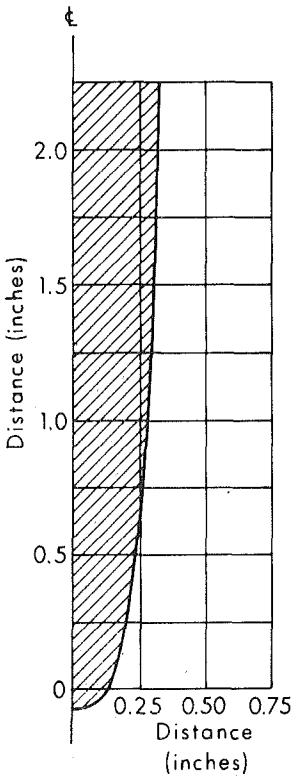

Fig. 1 Thermal region (crosshatched) formed above a heated wire in air: wire diameter = 0.005 in.; heating rate = 54 Btu/hr-ft, from [1]

the distance x—that is exhibited by equation (1). It will be shown that this expectation is, in fact, substantiated.

In a subsequent paper, Schorr and Gebhart [2] performed an experimental investigation of the temperature distribution in natural-convection plumes above horizontal line heat sources. In this study, line sources were approximated by electrically heated fine wires. Schorr and Gebhart found that while the general trend of their experimental results agreed well with the predictions of theory, there were certain discrepancies. Discrepancies of a similar nature had been observed previously by Forstrom and Sparrow [3], who, in an effort to reconcile the results of experiment with theory, employed the concept of a "virtual" line source. They concluded that a horizontal cylinder of finite diameter is equivalent to a virtual line source (zero diameter) that is located two cylinder diameters below the axis of the actual source. When Schorr and Gebhart attempted to use the concept of a virtual source to reconcile their experimental results with theory, they found that in one case the virtual source would have to be located 4 diameters below, in another case 10 diameters above, and in a third case 20 diameters above the actual source. In view of these inconsistent results, Schorr and Gebhart concluded that the virtual-source idea is ambiguous.

Skipper, Holt, and Saunders [4] have performed an experimental study of the heating by natural convection of viscous oils contained in tanks. This study was motivated by the need to obtain criteria for designing immersion heaters in ships' fuel storage tanks and in large cargo tankers. To study these problems, they performed three kinds of experiments: (*a*) measurement of heat transfer coefficients from horizontal cylindrical heaters and from heated wires immersed in fuel oil, including also temperature and velocity traverses in the vicinity of the heaters; (*b*) optical model studies of the convection currents in a viscous fluid (golden syrup); and (*c*) studies of the mixing process between the hot and cold oil in a 200-gal tank, with different kinds and arrangements of heater elements, similar to those used in actual practice. They reached several conclusions on the basis of their experimental work that are particularly relevant to the present investigation, and hence these conclusions will be discussed in detail in what follows.

Skipper et al. found that McAdams' [5] recommended correlation curve for heat transfer by natural convection from horizontal cylinders to gases and nonmetallic liquids agreed with their experimental data for viscous oils. McAdams' correlation curve can be represented with little error by the following algebraic equation:

$$\mathrm{N} = C(\mathrm{GP})^{1/4} \tag{2}$$

where the value of the constant C is 0.52 in the region $10^3 < \mathrm{GP} < 10^9$; here and throughout this paper the fluid properties contained in N, G, and P are evaluated at the mean film temperature defined by $t_f = {}^1/_2(t_s + t_b)$. Skipper et al. also reported "For the simple case of a single horizontal cylindrical heater in the 200 gallon tank it was found that the [flow] pattern consisted of a narrow chimney of hot oil rising almost vertically above the heater and a horizontal layer of hot oil immediately below the free surface separated from the remaining cold oil below by a sharp vertical temperature gradient. The hot oil had a small vertical temperature gradient, with maximum temperature at the top. As the heating process continued the hot oil layer became thicker and thicker, the boundary between it and the cold oil below *remaining horizontal* [emphasis added] regardless of the longitudinal position of the heater within the tank . . . when the whole of the oil above the heater level had become heated, further heating to a depth below the heater took place only very slowly and appeared to depend entirely on conduction."

Skipper et al. found that regardless of the geometry of the heater elements used, the essential characteristics of the heating process were the same as for the simple system comprising a horizontal cylindrical heater. They determined further that the isotherms in the heated layer of fluid that floats beneath the free surface are *nearly flat* and that these isotherms descend at a rate that is governed by the relation $T = cr^n$, where T is the time

Nomenclature

c_p = specific heat at constant pressure
D = depth of submergence
d = cylinder diameter
G = Grashof number, $\mathrm{G} = g\beta\rho^2(\Delta t) \times d^3\mu^{-2}$
g = acceleration of gravity
H = height of tank, see Fig. 2
h = heat transfer coefficient
I, J = functions of Prandtl number listed in Table 1, see equation (1)
K = constant
k = thermal conductivity
m, n = constants
$\dot{m}_{cx}$ = mass rate of flow in the plume above a horizontal heated cylinder per unit length of cylinder
$\dot{m}_{lx}$ = mass rate of flow in the plume above a horizontal line source of heat per unit length of source
L = length of tank, see Fig. 2
N = Nusselt number, $\mathrm{N} = hdk^{-1}$
P = Prandtl number, $\mathrm{P} = c_p\mu k^{-1}$, width of plume
q = rate of heat transfer per unit area
Q = rate of heat dissipation per unit length of a line source of heat
T = time
t = temperature
V = velocity
W = width of tank, see Fig. 2
x = distance vertically above the centerline of a horizontal heat source
β = volumetric coefficient of expansion
Δt = temperature difference, $\Delta t = (t_s - t_b)$
μ = dynamic viscosity
ρ = density

Subscripts

b = bulk fluid conditions
f = fluid conditions at the mean film temperature
s = fluid conditions at a heat transfer surface

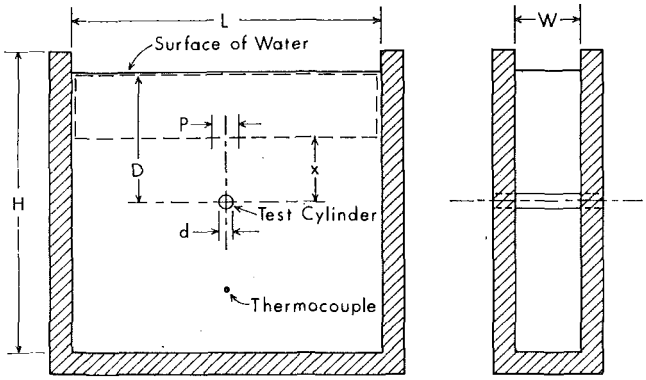

Fig. 2 Sketch of apparatus

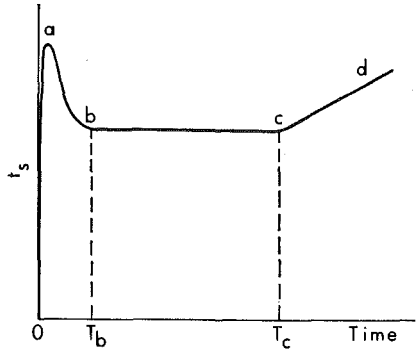

Fig. 3 Typical time history of test-cylinder surface temperature

for a particular isotherm to penetrate to a depth r below the surface and c and n are constants depending upon the isotherm value, heater depth, and arrangement.

Method of Attack

The method used here to determine the mass rate of flow in the natural-convection plume above a heated horizontal cylinder is fundamentally a volumetric "collection" method; that is, the fluid whose mass rate of flow is to be determined is segregated and its volume is measured as a function of time—since the fluid's density is assumed to be known, it follows that its mass rate of flow can be calculated from the volumetric measurements. The collection method employed here is based upon the observation of Skipper et al., which is verified here, that fluid rising in the natural-convection plume above a heated horizontal cylinder immersed in liquid contained in a tank forms a hot layer that floats beneath the free surface. Further, since the fluid in this hot layer does not mix with colder fluid below and heat transfer by conduction is negligible, the excess temperature $t - t_b$, where t is the temperature of a fluid particle and t_b is the bulk temperature of the unheated fluid, serves as a "tag" that identifies that portion of the fluid that has been entrained in the plume. Since the isotherms in the hot layer are for the most part very nearly horizontal, which implies that the lower boundary of the floating layer is also for the most part very nearly horizontal, it follows that the mass rate of flow can be determined by considering a control volume having the relatively simple geometry described below.

Consider a rectangular tank of length L, height H, and width W containing liquid. Assume that a horizontal cylinder of diameter d and length W containing an electrical heating coil and thermocouples to measure its surface temperature is inserted into the tank so that the axis of the cylinder is located in the plane of symmetry of the tank at a depth D below the free surface, as shown in Fig. 2. Assume further that a thermocouple is located beneath the cylinder at a sufficient distance to be outside the thermal boundary layers that develop around the cylinder when electric currents are caused to pass through the cylinder's heating coil—this thermocouple measures the bulk temperature of the unheated liquid. If at a given instant of time, designated T_0, a switch is thrown that causes a steady electric current[2] to pass through the heating coil contained in the cylinder and if all the tank dimensions and the depth D are sufficiently large so that the cylinder "senses" an infinite fluid medium,[3] then a plot of the surface temperature t_s will resemble the time history sketched in Fig. 3. The initial rapid rise of t_s is a result of the self-heating of the cylinder during a short interval of time during which natural convection has not had time to become established and conduction is the dominant mode of heat transfer. The surface temperature then drops along the portion of the curve labeled ab because during this time interval natural convection becomes fully developed. Along bc the surface temperature remains constant *and obeys McAdams' equation.* During the entire interval of time during which the cylinder is heated there is a plume of fluid rising from the cylinder. As explained earlier, when this fluid reaches the free surface it bifurcates and forms a floating heated layer. As the heat transfer process continues, the thickness of this hot layer of fluid continually increases. So long as this hot layer does not reach the cylinder, the cylinder's surface temperature is unaffected thereby and remains in a steady state; however, at some point in time, designated by T_c, corresponding to point c in Fig. 3, the lower boundary of the hot layer reaches the cylinder, and beginning with T_c, the surface temperature rises as indicated by the segment cd. If it is assumed that the mass rate of flow in the plume increases linearly during the transient time, then the experimental determination of T_b and T_c provides sufficient information to calculate the mass rate of flow in the plume during the steady-state portion of the time history, as is demonstrated in what follows.

Consider the control volume indicated by the dashed lines in Fig. 2. The boundaries of this control volume are as follows: (at the top) a plane coincident with the free surface—it is assumed that this surface is adiabatic and that mass transfer effects due to evaporation are negligible; (at the sides) four planes coincident with the containing walls of the tank—it is assumed that this surface is adiabatic; (at the bottom) a plane coincident with the lower boundary of the floating layer of hot fluid—this plane cuts across the plume of fluid that rises from the heated cylinder in the region marked P in Fig. 2.

The principle of continuity leads to the following equation for this control volume:

$$\dot{m}_{cx} = \rho(L - P)V_x \tag{3}$$

where $\dot{m}_{cx}$ is mass rate of flow in the plume per unit length of heated cylinder (a function of x), ρ is fluid density, L is free surface area per unit length of heated cylinder (numerically equal to the length of the tank), P is the width of the plume at a distance x above the central axis of the heated cylinder, and V_x is the magnitude of the velocity of descent of the lower boundary of the control volume (a function of x).

If it is assumed that $P \ll L$, then the preceding equation may be approximated by:

$$\dot{m}_{cx} = \rho L V_x$$

The time dT required for the lower boundary of the control volume to move through a differential distance dx is given by

$$dT = \frac{dx}{V_x} = \frac{\rho L}{\dot{m}_{cx}}\,dx$$

It follows that the time, designated by the symbol T^*, required

[2] The current is assumed to be sufficiently large to induce natural convection but not boiling.

[3] It is assumed in this analysis that the natural-convection field of flow is two-dimensional; this implies that the boundary layers on the lateral faces of the tank are relatively thin.

for the lower boundary of the control volume to travel from the free surface to the surface of the heated cylinder is

$$T^* = L\rho \int_{d/2}^{D} \frac{dx}{\dot{m}_{cx}} \tag{4}$$

The problem now reduces to finding a function $\dot{m}_{cx} = f(x)$, which, when inserted into equation (4) and integrated, will yield values of T^* that agree with experimentally measured values of T^*.

To accomplish this, the next question that needs to be addressed is what *form* shall be adopted for the function $\dot{m}_{cx}$. Three sources of information are available to assist in this determination. These sources will now be listed, together with the insights they furnish:

Dimensional Analysis. If it is assumed that $\dot{m}_{cx}$ depends upon the same parameters as does the heat transfer coefficient plus, in addition, the distance x, then a conventional dimensional analysis leads to the conclusion

$$\frac{\dot{m}_{cx}}{\mu} = f\left(\mathrm{G}, \mathrm{P}, \frac{x}{d}\right) \tag{5}$$

where the viscosity μ is expressed in units of mass per unit time per unit length.

McAdams' Equation. McAdams' equation states that the natural-convection heat transfer coefficient for a horizontal cylinder is proportional to the product $[\mathrm{GP}]^m$, where m is a constant. If it is assumed that $\dot{m}_{cx}$ is a function of this same constellation of parameters, then equation (5) may be written

$$\frac{\dot{m}_{cx}}{\mu} = f\left([\mathrm{GP}]^m, \frac{x}{d}\right) \tag{6}$$

Gebhart, Pera, and Schorr's Equation for $\dot{m}_{lx}$. If it is assumed that the dependence of $\dot{m}_{cx}$ upon the controlling variables—particularly upon x—is similar to the dependence of $\dot{m}_{lx}$ upon the parameters in equation (1), then equation (6) may be particularized to the following form:

$$\frac{\dot{m}_{cx}}{\mu} = K(\mathrm{GP})^m \left(\frac{x}{d}\right)^n \tag{7}$$

where m, n, and K are numerical constants.

If the expression for $\dot{m}_{cx}$ given by equation (7) is inserted into equation (4) and the indicated integration is performed, the result is

$$T^* = \frac{L\rho}{\mu K(\mathrm{GP})^m(1-n)}\left[\left(\frac{D}{d}\right)^{1-n} - \left(\frac{1}{2}\right)^{1-n}\right] \tag{8}$$

Equation (8) may be written in dimensionless form as follows:

$$\frac{T^*\mu(\mathrm{GP})^m}{L\rho} = \frac{1}{K(1-n)}\left[\left(\frac{D}{d}\right)^{1-n} - \left(\frac{1}{2}\right)^{1-n}\right] \tag{9}$$

The problem under investigation has now been reduced to determining numerical values for m, n, and K that will yield values of T^* calculated by equation (8) that agree with experimentally measured values of T^*. If the previously stated assumption that the mass rate of flow in the plume increases linearly during the transient time is accepted, then it follows immediately that $T^*_{\mathrm{exp}} = T_c - {}^1/_2 T_b$. Obviously, if T_b is small in comparison with T_c, the error introduced by this assumption is small.

Apparatus, Procedure, and Experimental Data

The experimental portion of the present study was performed by placing an electrically heated horizontal test cylinder into a well-insulated (wooden) tank containing water as shown schematically in Fig. 2. An insulating board was laid over the open end of the tank (not shown in Fig. 2), which created a dead air space above the upper liquid surface and thereby reduced heat and mass transfer from the surface. The dimensions of the tank were $L = 44.75$ in., $H = 46.00$ in., and $W = 3.5$ in. The diameter of the test cylinder was $d = 0.4555$ in., from which it is apparent that the length and height of the tank were very nearly equal to $100d$. The heated length of the cylinder in contact with water was equal to W. The bulk temperature t_b was measured by means of a thermocouple placed directly below the test cylinder.

The heat transfer cylinder used in the present investigation is described in [6]. The "guarded test section" technique was used in the construction of this test specimen. In this technique the test specimen consists of three cylindrical sections laid end to end—a central "test section" (1 in. long) flanked by two "guard sections"—that are thermally insulated from one another. Each section contains separate electric-resistance heaters and thermocouples to measure its temperature. The guard sections contain one thermocouple each and the test section contains two thermocouples. The function of the guard sections is to prevent the transfer of heat by conduction from the centrally located test section to its supporting structure; this is achieved operationally by adjusting the electrical input to the guard heaters until their temperatures are equal to the temperature of the central test section. Under this condition, the electrical input to the central test section is equal to the heat transferred by convection and radiation from its surface. The heat transferred by radiation from the surface of the central test section was calculated and found to be less than 0.1 percent of the total heat transfer in all tests. Consequently the heat transfer by radiation was neglected in this study. Since the thermocouples contained in the test section were embedded below its surface, the temperature recorded by them was not exactly equal to the local surface temperature of the test section. To determine the cylinder's surface temperature, the radial temperature drop between the geometric centers of the thermocouples and the surface of the test cylinder was calculated by assuming that the simple conduction equation for radial heat transfer through composite cylinders is applicable. The electrical power fed into the test section of the heated cylinder was measured with an error of less than 0.1 percent by means of a carefully calibrated wattmeter; this reading is readily convertible into units of Btu/hr per square foot of cylinder surface area. A precision potentiometer was used to read the output of all thermocouples with an accuracy of better than 0.05 deg F.

The heat transfer coefficient for a cylinder varies along the circumference of the cylinder. Therefore the average surface temperature determined by the two thermocouples embedded in the cylinder is a function of the angular position of the thermocouples relative to the direction of the force of gravity. In the present investigation, the measured difference between the surface and bulk temperatures was found to vary by as much as 4.3 percent depending upon the angular orientation of the test cylinder. In order to cope with this variation, the test specimen was rotated in 30-deg increments of arc, and temperature difference $t_s - t_b$ was measured at each 30-deg interval until the cylinder had been turned through 360 deg. The integrated mean value of temperature difference, designated Δt, was used to calculate the heat transfer coefficient h. The determination of a single value of Δt by the method just described involves 12 measurements. Fortunately it was not necessary to perform the rotation procedure for every data point. It was experimentally verified that the maximum value of the temperature difference, designated $\Delta t_{\max}$, always occurred when the heated test cylinder was located in one and the same angular position. Further, the ratio $\Delta t/\Delta t_{\max}$ was nearly a constant for all test conditions. Therefore, once having experimentally determined the magnitude of the ratio $\Delta t/\Delta t_{\max}$, it was possible to leave the cylinder in the position corresponding to $\Delta t_{\max}$ and to take one temperature reading, i.e., $\Delta t_{\max}$, from which Δt could then readily be calculated. The value of $\Delta t/\Delta t_{\max}$ was found to be 0.977.

The height of the water above the test specimen was regulated by means of a syphon arrangement and measured by means of a hook gauge. An electrically driven stirrer was installed in a bot-

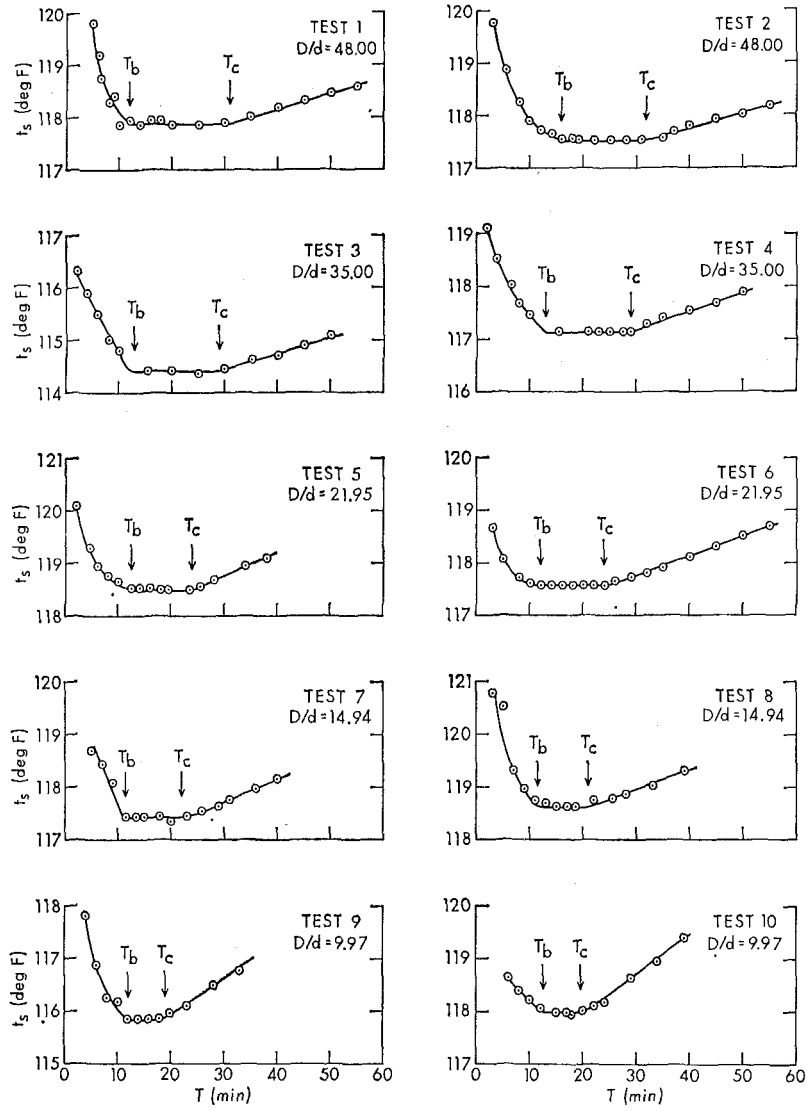

Fig. 4 Experimental results

tom corner of the tank to stir the water before each test in order to obtain uniform water temperature.

Two sets of data were taken: one set with the heat flux held constant at $q = 6675$ Btu/hr-ft^2 and with D/d assuming values equal to approximately 1, 1.5, 3, 5, 7, 10, 15, 22, 35, and 48; the other set with the heat flux held constant at $q = 3364$ Btu/hr-ft^2 and with these same values of D/d. All tests were performed twice to verify repeatability. It was found that for those tests in which $D/d \geq 10$, the steady-state portion of the surface temperature history obeyed equation (2) with $c = 0.50 \pm 0.01$; it was also found that for $D/d < 10$, the value of C in equation (2) diminished progressively with diminishing values of D/d. These observations were interpreted to mean that the cylinder "sensed" an infinite medium if and only if its depth of submergence exceeded 10 cylinder diameters ($D/d \geq 10$).

The time histories of t_s for those tests in which $D/d \geq 10$ and $q = 6675$ Btu/hr-ft^2 are plotted in Fig. 4. The experimental values of T_b and T_c are indicated in each plot and these values are also recorded in Table 2. The time histories of t_s for those tests in which $D/d \geq 10$ and $q = 3364$ Btu/hr-ft^2 were found to be similar to those shown in Fig. 4 and hence are not reproduced here; however, the important experimentally determined quantities for these tests are recorded in Table 2. The time histories of t_s for the tests performed with $D/d < 10$ are not recorded here because they cannot be used to evaluate T^*. This is so because, as explained previously, when D/d was less than 10, the test cylinder no longer "sensed" an infinite medium.

Analysis of Data

The experimental data were analyzed with the aid of an electronic computer. An optimization technique was used to determine the "best" values of m, n, and K in equation (8) based upon two criteria: (*a*) the mean error[4] between the calculated and experimentally determined values of T^* shall be zero; (*b*) the sample standard deviation of the error shall be a minimum. These criteria yielded the following optimum values: $m = 0.53$, $n = 0.70$, and $K = 1.52$; the mean error, standard deviation of the error, and maximum error corresponding to these values of m, n, and K are 0, 4.7, and 12.2 percent, respectively. With these values of m, n, and K, equation (7) becomes

$$\frac{\dot{m}_{cx}}{\mu} = 1.52(\mathrm{GP})^{0.52}\left(\frac{x}{d}\right)^{0.70} \tag{10}$$

For purposes of visual comparison, this result—cast in the form of equation (9)—has been plotted in Fig. 5 together with the comparable experimentally determined quantities.

Discussion

In the preceding material, a formula is derived, which, it is claimed, allows one to calculate the mass rate of flow in the natural-convection plume above a horizontal heated cylinder

[4] The error is defined as $E = (T^*_{\mathrm{calc}} - T^*_{\mathrm{exp}})/T^*_{\mathrm{exp}}$.

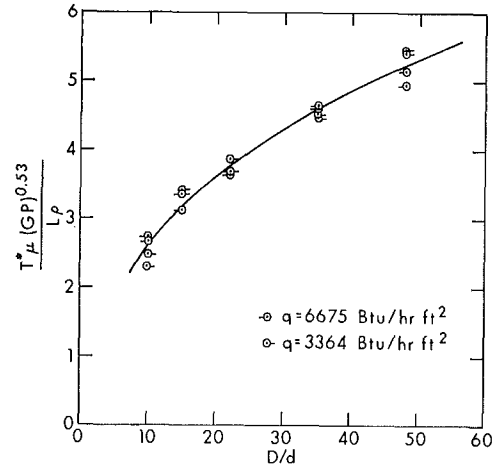

Fig. 5 Graph of equation (9) with $m = 0.53$, $n = 0.70$, and $K = 1.52$, plus comparable experimentally determined data

immersed in a liquid. In the course of deriving this formula, a number of simplifying assumptions were made and stated explicitly, but there is one major assumption that was tacitly accepted. The purpose of this section is to state and discuss this assumption.

The assumption in question is that the mass rate of flow through a horizontal plane located at a distance x above the central axis of a horizontal cylinder submerged to a depth D below the free surface of a finite pool of liquid contained in a tank *is the same as if the cylinder were submerged in an infinite medium.* That this assumption is inexact and constitutes an approximation is obvious, for it is clear that the containing walls of the tank impose boundary conditions that induce circulations throughout the tank that are not induced in an infinite medium; furthermore, the presence of the free surface in the tank causes the vertical plume to bifurcate and then move horizontally; this change in direction does not, of course, occur in an infinite medium.

The circulations induced throughout the tank are thought not to exercise an appreciable effect upon the flow in the plume for the reason that these circulations are much weaker than is the flow in the plume—here the term "weaker" means that the associated velocities, accelerations, and forces have smaller magnitudes. As to the influence of the free surface upon the final result, there are two reasons why this is thought not to be significant: First, for all the experimental results reported here, the free surface was never nearer to the cylinder axis than 10 cylinder diameters, i.e., $D/d \geq 10$. As has been stated earlier, the condition $D/d \geq 10$ insures that McAdams' heat transfer correlation describes the steady-state portion of the cylinder's surface temperature history, and this has been interpreted to mean that the cylinder "sensed" an infinite medium when $D/d \geq 10$. Hence it is concluded that the plume, at least in the vicinity of the cylinder, was uninfluenced by the presence of the free surface in all tests reported here. Second, although the presence of the free surface causes the plume to bifurcate and flow horizontally, representing a major alteration in the *pattern of flow* compared to the case of an infinite medium, this bifurcation can have little influence upon the *total momentum*—and therefore upon the mass rate of flow—in the plume. The reason why the influence of the bifurcation process upon the total momentum is minimal is that the free surface represents a boundary condition of *zero shear force*, and this boundary condition is identically the same as applies to the plane of symmetry of a plume in an infinite medium. In colloquial terms, one might say that the free surface does not cause the plume to "pile up."

For the reasons indicated above it is believed that equation (10), which was derived on the basis of data taken in a finite tank, is applicable to the case of an infinite medium.

Conclusions

1 For the tests conducted here, it was found that equation (2) with $C = 0.50 \pm 0.01$ is applicable when $D/d \geq 10$. The condition $D/d = 10$ is therefore assumed to represent the minimum depth of submergence for which the cylinder used in the present study "sensed" an infinite medium. It is expected that this minimum depth of submergence is, in general, a function of fluid properties and Δt; hence it is not expected that the criterion $D/d = 10$ is universally applicable to all fluids and Δt's. This aspect of the present investigation merits further study.

2 When a heated horizontal cylinder is submerged in a liquid to a depth sufficiently great so that it "senses" an infinite medium, the mass rate of flow in the natural-convection plume above the cylinder is given by the following formula:

$$\frac{\dot{m}_{cx}}{\mu} = 1.52(\mathrm{GP})^{0.52}\left(\frac{x}{d}\right)^{0.70} \tag{10}$$

where x is the distance upward from the cylinder axis to a horizontal plane through which the calculated mass rate of flow passes. This formula has been determined on the basis of experimental data for which $1/2 < x/d < 48$; however, it is estimated that the formula is applicable in the extended range $1/2 < x/d < 100$, which includes most cases of practical interest.

3 Equation (10) predicts mass rates of flow much higher (about 50 times) than are predicted by equation (1). This behavior is consistent with the fact that equation (1) has been derived on the basis of boundary-layer theory, and the basic assumption upon which this theory rests (that the regions of temperature and velocity are relatively thin) was not satisfied in the experiments from which equation (10) was developed. Never-

Table 2 Experimental results

Test No.	q (Btu/hr-ft^{-2})	D/d	t_b (deg F)	t_s, steady state (deg F)	T_b (min)	T_c (min)	$T^* = 1/2(T_c - T_b)$ (min)
1	6675	48.00	74.50	117.89	12.0	31.0	25.0
2	6675	48.00	74.20	117.52	16.0	32.0	24.0
3	6675	35.00	71.04	114.42	13.0	29.0	22.5
4	6675	35.00	73.57	117.14	13.0	29.0	22.5
5	6675	21.95	75.38	118.50	12.5	24.0	17.75
6	6675	21.95	74.50	117.57	12.0	24.0	18.0
7	6675	14.94	73.87	117.43	11.5	22.0	16.25
8	6675	14.94	75.91	118.62	11.5	21.0	15.25
9	6675	9.97	72.14	115.85	12.0	19.0	13.0
10	6675	9.97	74.55	117.98	12.5	19.5	13.25
11	3364	48.00	75.48	101.17	9.0	39.5	35.0
12	3364	48.00	76.70	102.65	11.0	40.5	35.0
13	3364	35.00	76.39	101.75	11.0	35.0	29.5
14	3364	35.00	72.27	98.35	10.0	34.0	29.0
15	3364	21.97	76.70	102.44	12.0	31.0	25.0
16	3364	21.95	75.61	101.21	12.0	30.0	24.0
17	3364	14.94	75.13	100.95	14.0	29.0	22.0
18	3364	14.94	77.14	102.37	12.0	28.0	22.0
19	3364	9.97	76.13	101.75	13.0	21.5	15.0
20	3364	10.01	75.83	101.79	14.0	23.0	16.0

theless, for a given heating rate, the dependence of the mass rate of flow upon x is similar in equations (1) and (10) ($x^{0.6}$ versus $x^{0.7}$), and in view of the many assumptions made in the derivation of both equations, this agreement is considered to be good.

Acknowledgments

M. M. Jotwani assisted in gathering the experimental data. This work was supported by a grant from the National Science Foundation.

References

1 Gebhart, B., Pera, L., and Schorr, A. W., "Steady Laminar Natural Convection Plumes above a Horizontal Line Source," *International Journal of Heat and Mass Transfer*, Vol. 13, 1970, pp. 161–171.

2 Schorr, A. W., and Gebhart, B., "An Experimental Investigation of Natural Convection Wakes above a Line Heat Source," *International Journal of Heat and Mass Transfer*, Vol. 13, 1970, pp. 557–571.

3 Forstrom, R. J., and Sparrow, E. M., "Experiments on the Buoyant Plume above a Heated Horizontal Wire," *International Journal of Heat and Mass Transfer*, Vol. 10, 1967, pp. 321–331.

4 Skipper, R. G. S., Holt, J. S. C., and Saunders, O. A., "Natural Convection in Viscous Oils," *International Developments in Heat Transfer*, Part V, ASME, New York, N. Y., 1961, pp. 1003–1010.

5 McAdams, W. H., *Heat Transmission*, 3rd ed., McGraw-Hill, New York, N. Y., 1954.

6 Fand, R. M., "The Formation of Calcium-Sulfate Scale on a Heated Cylinder in Crossflow and Its Removal by Acoustically Induced Cavitation," JOURNAL OF HEAT TRANSFER, TRANS. ASME, Series C, Vol. 91, No. 1, Feb. 1969, pp. 111–122.

M. F. MODEST
Research Assistant.

C. L. TIEN
Professor.
Mem. ASME

Department of Mechanical Engineering,
University of California,
Berkeley, Calif.

Analysis of Real-Gas and Matrix-Conduction Effects in Cyclic Cryogenic Regenerators

The one-dimensional governing equations for the thermal performance of cryogenic regenerators are developed and simplified by neglecting gas conduction and pressure drop along the matrix. The present formulation includes the effects of matrix conduction and real-gas behavior, which can be quite important in actual situations but were neglected in all previous analyses. The time dependence of the governing equations is eliminated by integration over the compression and expansion periods. Numerical solutions of the resulting time-independent equations are presented for various values of physical parameters and temperature levels. Comparison with the corresponding cases neglecting real-gas and matrix-conduction effects demonstrates the significant nature of these effects for many operating conditions.

Introduction

Compact cryogenic refrigerators based on various operating cycles [1–4][1] have seen extensive applications in superconducting devices, cooled infrared detectors, etc. All these refrigerators use one or more regenerators rather than conventional heat exchangers because of their many advantageous factors, particularly their superior effectiveness and compactness [5]. The regenerators in cryogenic refrigerators are exposed to rapidly cycling flows under steep temperature gradients, and the validity of the early theories [6] on regenerators, dealing with the steady, laminar, incompressible flow of constant-property fluids, is highly questionable. Moreover, the efficiency of refrigeration cycles is very low at cryogenic temperatures, making it essential to design the regenerators for optimal effectiveness and to evaluate the thermal performance accurately. Accordingly, considerable effort has been devoted recently to more sophisticated regenerator analysis [7, 8]. Particularly noteworthy is the analysis made by Rea and Smith [8], which takes proper consideration for variable density, mass flux, and heat transfer coefficient. Major restrictive assumptions in their theory, particularly for applications at very low temperatures, include absence of heat conduction, temperature-independent heat transfer coefficient, and ideal-gas behavior.

It is the purpose of the present investigation to develop a general but simple theory for the thermal performance of cyclic cryogenic regenerators that includes various important real effects discussed above. Numerical results have been obtained and analyzed indicating the significance of these effects in actual situations.

[1] Numbers in brackets designate References at end of paper.

Contributed by the Heat Transfer Division of The American Society of Mechanical Engineers and presented at the AIChE-ASME Heat Transfer Conference, Denver, Colo., August 6–9, 1972. Manuscript received by the Heat Transfer Division April 12, 1972; revised manuscript received May 18, 1972. Paper No. 72-HT-27.

Theoretical Framework

Thermodynamic and Transport Properties. In the following, a brief discussion is presented of the equation of state for a real gas and of transport properties that will be needed for the development of the governing equations.

The real-gas equation of state is expressed in terms of the compressibility factor Z_1:

$$p = \rho R T Z_1 \tag{1}$$

The common form of the virial equation of state has Z_1 expressed in powers of ρ with the virial coefficients as functions of temperature, cf., e.g., [9]. However, if the pressure drop along the regenerator axis is neglected, pressure becomes a known quantity, and an expansion in powers of p will be more convenient:

$$Z_1(p, T) = 1 + \sum_{i=1}^{n_i} \left\{ \sum_{j=0}^{n_j(i)} \frac{m_{ij}}{T^j} \right\} p^i \tag{2}$$

The enthalpy of a real gas is given as [10]

$$h(p, T) = h_0 + \int_0^T c_p{}^0 dT + \int_0^p \left[v - T \left(\frac{\partial v}{\partial T} \right)_p \right]_T dp \tag{3}$$

where $c_p{}^0$ is the limiting value of the specific heat at constant pressure for zero pressure and h_0 is the reference enthalpy. It can be similarly expressed in the form

$$h(p, T) = h_0 + c_p{}^0 T Z_2(p, T) = h_0 + \frac{\gamma}{\gamma - 1} R T Z_2(p, T) \tag{4}$$

where γ is the ratio of specific heats. For the common case in which helium is involved, $c_p{}^0$ is a constant and Z_2 becomes, employing equation (2),

$$Z_2(p, T) = 1 + \frac{\gamma - 1}{\gamma} \sum_{i=1}^{n_i} \left\{ \sum_{j=1}^{n_j(i)} \frac{j}{i} \frac{m_{ij}}{T^j} \right\} p^i \tag{5}$$

It should be noted that for high pressures and very low temperatures, many terms in the expansions for Z_1 and Z_2 are needed. Although the second virial coefficient can be calculated in some gases such as helium from quantum mechanics [11], the third and higher order coefficients become impossible to evaluate theoretically and must be determined by fitting experimental data, for instance the work of Mann [12] for helium.

The heat transfer coefficient h_t is usually given by empirical correlations of the dimensionless form

$$\mathrm{St}\,\mathrm{Pr}^{2/3} = a\,\mathrm{Re}^n \tag{6}$$

where a and n are constants depending on the flow. The Stanton and Reynolds numbers St and Re are based on the hydraulic diameter [13]

$$D_h = 4\frac{\epsilon}{\alpha} \quad \left(= \frac{2}{3}\frac{\epsilon}{1-\epsilon} D_p \text{ for packed spheres}\right) \tag{7}$$

With equation (6), the heat transfer coefficient can be written as

$$h_t = K\left(\frac{\dot{m}}{\bar{\dot{m}}_0}\right)^{n_1}\left(\frac{T}{T_0}\right)^{n_2} \tag{8}$$

where $\bar{\dot{m}}_0$ is the average mass flux at the cold end. The constants K and n_1 are

$$K = a\frac{k_0}{D_h}(\overline{\mathrm{Re}_0})^{n_1}\mathrm{Pr}^{1/3} \qquad n_1 = 1 + n$$

The subscript 0 refers to conditions at the cold end, while the term $(T/T_0)^{n_2}$ accounts for the temperature dependence of the heat transfer coefficient. The most reliable values for a and n for a column of packed spheres are probably given by Rea and Smith [8], as they performed their experiments on a rapidly cycling regenerator. They listed $a = 0.71$ and $n = 0.41$, while others reported slightly different values [14], or $a = 0.237$ and $n = 0.31$ [15].

It will be shown that the effect of gas conduction is negligible, but conduction along the matrix can be significant. However, values for the thermal conductivity of the matrix, k_m, are generally not known because of the associated uncertainties in impurities and contact resistances of the matrix particles, as well as the gas flow situation. Although some information is available, cf., e.g., [16, 17], for an exact calculation of the conductivity effect, k_m will have to be found experimentally for the particular regenerator and flow situation.

Governing Equations in One Dimension. It will be assumed here that the problem is one-dimensional, i.e., the influence of the heat transfer to and from the wall and the inhomogeneity of the matrix are neglected. While the matrix is generally reasonably homogeneous, the wall effects can be justifiably neglected only when the hydraulic diameters of the flow passages are much smaller than the diameter of the regenerator, i.e., if $D_h/D_r \ll 1$.

Consider a control volume dV $(= A\,dx)$, where A is the cross section of the regenerator. Performing energy balances for gas and matrix and a mass balance for the gas yields

gas energy:

$$\frac{\partial}{\partial t}(\rho u) + \frac{\partial}{\partial x}(\rho w h) - \frac{\partial}{\partial x}\left(k\frac{\partial T}{\partial x}\right) + \frac{\alpha}{\epsilon}h_t(T - T_m) = 0 \tag{9}$$

matrix energy:

$$\rho_m\frac{\partial u_m}{\partial t} - \frac{\partial}{\partial x}\left(k_m\frac{\partial T_m}{\partial x}\right) - \frac{\alpha}{1-\epsilon}h_t(T - T_m) = 0 \tag{10}$$

continuity:

$$\frac{\partial}{\partial x}(\rho w) + \frac{\partial \rho}{\partial t} = 0 \tag{11}$$

In equation (9) the additional assumption has been made that the kinetic energy of the gas and viscous dissipation are negligible, while in equation (10) the matrix density is assumed practically constant.

Using equations (1), (4), and (11) as well as the fundamental thermodynamic relation

$$u = h - p/\rho \tag{12}$$

equation (9) can be simplified to

Nomenclature

A = regenerator cross section
c_p = specific heat at constant pressure of the gas
c_m = specific heat of matrix material
C_1 = parameter defined by equation (19)
C_2 = integration constant defined by equation (26)
D_h = hydraulic diameter of flow paths
D_p = diameter of matrix particles
D_r = regenerator diameter
$h(h_0)$ = gas enthalpy (at reference state)
h_t = heat transfer coefficient
k, k_m = thermal conductivity of gas and matrix, respectively
K = proportionality factor for h_t
K_m = conduction–convection parameter, equation (19)
l = regenerator length
m = nondimensional mass flux, $\dot{m}/\bar{\dot{m}}_0$
$\dot{m}$ = mass flux
m_{ij}, M_{ij} = constants for virial coefficients
Nu = Nusselt number, $h_t D_h/k$
p = gas pressure
P = nondimensional gas pressure, $p/2(p_H - p_L)$
Pr = Prandtl number, $\mu c_p/k$
Q_m = matrix heat capacity–convection parameter, equation (19)
R = gas constant
Re = Reynolds number, $\rho w D_h/\mu$
St = Stanton number, $h_t/\rho w c_p$
t = time
T, T_m = gas and matrix temperature
u, u_m = internal energies of gas and matrix
V_r = regenerator void volume, $\epsilon A l$
v = specific volume, $1/\rho$
w = average gas velocity in axial direction
x = axial distance
z = nondimensional axial distance
$Z_1, Z_2, Z_2{}^*$ = compressibility factors
α = heat transfer area per unit volume
β = constant defined by equation (29)
γ = ratio of specific heats at constant pressure and volume
δ = fraction of total cycle time used for compression
ϵ = regenerator porosity = void volume/total volume
η = regenerator effectiveness
θ = nondimensional time
μ = gas viscosity
π = time span of a full cycle
ρ, ρ_m = density of gas and matrix
σ = real-gas factor
τ, τ_m = nondimensional gas and matrix temperature

Subscripts

$0, l$ = denotes location, cold end $(x = 0)$ and hot end $(x = l)$
c, e = values during compression and expansion half-cycles
H, L = values at end of compression and expansion
m = matrix

Superscript

$\bar{}$ = average value over half-cycle

$$\frac{1}{\gamma - 1}\frac{\partial}{\partial t}(\sigma p) + \frac{\gamma}{\gamma - 1} R \frac{\partial}{\partial x}(\rho w T Z_2) - \frac{\partial}{\partial x}\left(k \frac{\partial T}{\partial x}\right) + \frac{\alpha}{\epsilon} h_t (T - T_m) = 0 \quad (13)$$

where

$$\sigma = 1 + \gamma\left(\frac{Z_2}{Z_1} - 1\right) \quad (14)$$

has been introduced. For a perfect gas, σ reduces to unity, as do Z_1 and Z_2.

A simple order-of-magnitude estimate [18] shows that the conduction term in equation (13) is negligible in all practical cases, and equation (13) assumes its final form:

$$\frac{1}{\gamma - 1}\frac{\partial}{\partial t}(\sigma p) + \frac{\gamma}{\gamma - 1} R \frac{\partial}{\partial x}(\rho w T Z_2) + \frac{\alpha}{\epsilon} h_t (T - T_m) = 0 \quad (15)$$

If the pressure drop along the regenerator is neglected, as is done here, the pressure is a known function of time, and equations (15), (10), and (11) form a system of three equations in the three unknowns T, T_m, and (ρw). They are in general subject to the following boundary conditions:

cold end ($x = 0$): $T(0, t) = T_0 = \text{const.}$

$\delta\pi \leq t \leq \pi$ (expansion interval)

hot end ($x = l$): $T(l, t) = T_l = \text{const.}$

$0 \leq t \leq \delta\pi$ (compression interval)

cold end ($x = 0$): $\dot{m}(0, t) = \dot{m}_0(t) \quad 0 \leq t \leq \pi$

The first two conditions state that the temperature of the gas entering the matrix is known and constant (π is the time span of a full cycle and δ is the fraction of π during which compression takes place). From the state of the gas outside the cold end, the mass flow at the regenerator entrance can be calculated to yield the third boundary condition.

Nondimensional Parameters. Before solving the above equations, it is convenient to introduce the following nondimensional independent variables:

$$z = \frac{2(p_H - p_L)V_r}{\bar{\dot{m}}_0 \pi R T_0}\frac{x}{l} \quad \text{and} \quad \theta = \frac{t}{\pi}$$

The new dependent variables will be

$$\tau = T/T_0 \quad \tau_m = T_m/T_0 \quad \text{and} \quad m = \dot{m}/\bar{\dot{m}}_0 = (\rho w)/(\overline{\rho w})_0$$

while a nondimensional pressure will be defined as

$$P = p/2(p_H - p_L)$$

The subscripts H and L stand for values at the end of compression (high pressure) and expansion (low pressure), respectively. Using equation (8), equations (15), (10), and (11) transform to

gas energy:

$$\frac{1}{\gamma}\frac{\partial}{\partial \theta}(\sigma P) + \frac{\partial}{\partial z}(m Z_2 \tau) + C_1 |m|^{n_1} \tau^{n_2} (\tau - \tau_m) = 0 \quad (16)$$

matrix energy:

$$Q_m \frac{\partial \tau_m}{\partial \theta} - \frac{\partial}{\partial z}\left(K_m \frac{\partial \tau_m}{\partial z}\right) - C_1 |m|^{n_1} \tau^{n_2} (\tau - \tau_m) = 0 \quad (17)$$

continuity:

$$\frac{\partial m}{\partial z} + \frac{\partial}{\partial \theta}\left(\frac{P}{Z_1 \tau}\right) = 0 \quad (18)$$

subject to the boundary conditions

cold end ($z = 0$): $m(0, \theta) = m_0(\theta) = \dot{m}_0(\theta)/\bar{\dot{m}}_0$

$\tau(0, \theta) = 1 \quad \delta \leq \theta \leq 1$ (expansion)

hot end ($z = z_l$): $(z_l, \theta) = \tau_l \quad 0 \leq \theta \leq \delta$ (compression)

The parameters C_1, Q_m, and K_m have been defined as

$$C_1 = \frac{\gamma - 1}{\gamma}\frac{\alpha}{\epsilon}\frac{\pi T_0 K}{2(p_H - p_L)}$$

$$Q_m = \frac{\gamma - 1}{\gamma}\frac{1 - \epsilon}{\epsilon}\frac{\rho_m c_m T_0}{2(p_H - p_L)} \quad (19)$$

$$K_m = \frac{\gamma - 1}{\gamma}\frac{1 - \epsilon}{\epsilon}\frac{k_m V_r / l^2}{\bar{\dot{m}}_0 R} z_l$$

with $z_l = z$ ($x = l$). Physically, C_1 is the ratio of convection and work done by compression, while Q_m/C_1 is the ratio of heat storable in the matrix and convected energy. Thus a large Q_m should indicate a small temperature variation of the matrix with time. On the other hand, K_m/C_1 is the ratio of conduction and convection and gives an indication of the importance of the conduction effect.

Regenerator Ineffectiveness. The ineffectiveness of a thermal regenerator can be defined as [5, 8]

$$1 - \eta = \frac{\text{total losses over one cycle}}{\text{ideal heat exchange}}$$

Losses are due to conduction and to the fact that the gas temperature oscillates around the matrix temperature. Thus

$$1 - \eta = \frac{\left|\oint \dot{m} h dt\right| + (1 - \epsilon) A \oint k_m \frac{\partial T_m}{\partial x} dt}{\int_c |\dot{m}_l| h_l dt - \int_e |\dot{m}_0| h_0 dt - \left[\epsilon A \int_0^l \rho u dx\right]_0^{\delta\pi}} \quad (20)$$

The numerator of equation (20) is constant over the entire length of the regenerator, as is easily seen from equations (16) and (17). The integrals in the denominator denote integration over the compression ($\int_c$) and expansion ($\int_e$) half-cycles, respectively, while the last term describes the difference of internal energy of the gas in the regenerator void volume at the end of compression ($t = \delta\pi$) and expansion ($t = 0$ or $t = \pi$). All values of the denominator must be evaluated for the ideal case of $\eta = 1$.

Equation (20) can be simplified to

$$1 - \eta = 2 \times \frac{\left|\oint m Z_2 \tau d\theta\right| + \oint K_m \frac{\partial \tau_m}{\partial z} d\theta}{\oint |m Z_2 \tau|_{lc} d\theta - \oint |m Z_2 \tau|_{0e} d\theta - \frac{2}{\gamma}\int_0^{z_l} [(\sigma P)_H - (\sigma P)_L] dz} \quad (21)$$

Here the subscripts c and e mean that the values during compression and expansion half-cycles, respectively, are to be taken.

Equations for Time-Integrated Properties

For the design of thermal regenerators, it is not crucial to know the time histories of the gas and matrix temperatures and of the mass flux, but it is very important to predict the effectiveness as accurately as possible. Equation (21) reveals that for the performance evaluation only values integrated over a complete cycle are needed. Integration of the governing equations (16)-(18) with respect to time will therefore facilitate a solution without eliminating any valuable information. While an integration over a full cycle does not prove to be practical, an integration over shorter time intervals does [8]. Therefore the regenerator cycle is broken up into the compression period ($0 \leq t \leq \delta\pi$, gas flows from hot to cold end, $\dot{m} < 0$) and the expansion

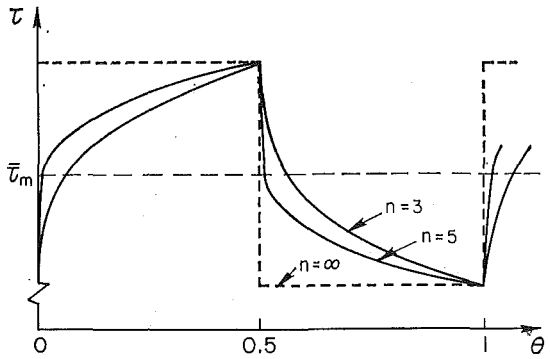

Fig. 1 Typical temperature history during compression and expansion

period ($\delta\pi \leq t \leq \pi$, gas flows from cold to hot end, $\dot{m} > 0$). For mathematical simplicity it is assumed that these periods are of equal length (half-cycles $\delta = 1/2$) and that at all times the mass flux everywhere in the regenerator is in the same direction, i.e., flow reversal occurs everywhere at the same instant.

In order to get simple expressions involving integrated or average values for the unknowns m, τ, and τ_m, it is necessary to make the further assumption that the average of a product equals the product of the averages, i.e.,

$$\overline{(\phi\psi)} \cong \bar{\phi}\cdot\bar{\psi}$$

or (22)

$$\oint \phi\psi d\theta \cong \oint \phi d\theta \cdot \oint \psi d\theta$$

where ϕ and ψ are any functions involving the three unknowns. In general, this can be a rather crude simplification. However, if one of the functions, say ϕ, is only weakly dependent on time θ, one can write

$$\overline{(\phi\psi)} = \oint \phi\psi d\theta \cong \bar{\phi}\cdot\oint \psi d\theta = \bar{\phi}\cdot\bar{\psi} \tag{23}$$

to a very good degree of accuracy even if ψ is a strong function of θ.

All terms in equations (16)–(18) and (21) are readily integrated employing assumption (23), with the exception of $|m|^{n_1}\tau^{n_2}(\tau - \tau_m)$, as m and $(\tau - \tau_m)$ both vary from zero to some maximum value and back to zero. However, this term involves the empirical correlation for the heat transfer coefficient. Redefining h_t as

$$h_t = K\bar{m}^{n_1}\bar{\tau}^{n_2} \tag{24}$$

where $\bar{m} = \oint |m| d\theta$ and $\bar{\tau} = \oint \tau d\theta$, makes the last term also easily integrable.

The results are two coupled ordinary differential equations in $\bar{m}$ and $\bar{\tau}_m$, which must be solved numerically:

$$\frac{d\bar{m}}{dz} = 2\left\{\left(\frac{P}{Z_1\tau}\right)_H - \left(\frac{P}{Z_1\tau}\right)_L\right\} \tag{25}$$

and

$$\frac{2}{\gamma}\{(\sigma P)_H - (\sigma P)_L\} - \frac{d}{dz}(\bar{m}\bar{Z}_{2m}\bar{\tau}_m) + \frac{C_1\bar{m}^{n_1}\tau_m{}^{n_2}}{\bar{m}Z^*_{2m}}\left\{C_2 - \bar{K}_m\frac{d\bar{\tau}_m}{dz}\right\} = 0 \tag{26}$$

where

$$Z^*_{2m} = \frac{d}{d\bar{\tau}_m}(\bar{\tau}_m\bar{Z}_{2m}) = 1 - \frac{\gamma - 1}{\gamma}\sum_{i=1}^{n_i}\sum_{j=1}^{n_j(i)} M_{ij}\frac{j(j-1)}{i}\frac{\bar{P}^i}{\bar{\tau}_m{}^j} \tag{27}$$

and

$$\tau_H = \bar{\tau}_m + \frac{2\beta}{\bar{m}Z^*_{2m}}\left\{C_2 - \bar{K}_m\frac{d\bar{\tau}_m}{dz}\right\}$$
$$\tau_L = \bar{\tau}_m - \frac{2\beta}{\bar{m}Z^*_{2m}}\left\{C_2 - \bar{K}_m\frac{d\bar{\tau}_m}{dz}\right\} \tag{28}$$

Here β is some constant ($1/2 < \beta < 1$) whose value depends on how the gas temperature fluctuates with time. Assuming that this variation can crudely be approximated by a power law, i.e.,

$$\tau - \bar{\tau}_m \sim \theta^{1/n} \qquad n > 3$$

The parameter β turns out to be

$$\beta = \frac{1}{2}\frac{n+1}{n-1} \tag{29}$$

The qualitative nature of such profiles is shown in Fig. 1. It is clear that $n \gg 1$ if $Q_m \to \infty$, i.e., when τ_m does not vary with time, so that $\beta \cong 1/2$. On the other hand, if τ_m varies considerably (e.g., because of a small Q_m at very low temperatures), n will be rather small and β can be expected to be close to one. Whatever the choice of β, its influence should be small.

The integration constant C_2 must be determined through the boundary conditions, to which equations (25) and (26) are subjected:

cold end ($z = 0$): $\bar{m} = 1 \quad \bar{\tau}_m = 1 + \dfrac{1}{Z^*_{2m}}\left\{C_2 - \bar{K}_m\dfrac{d\bar{\tau}_m}{dz}\right\}$

hot end ($z = z_l$): $\bar{\tau}_m = \tau_l - \dfrac{1}{\bar{m}Z^*_{2m}}\left\{C_2 - \bar{K}_m\dfrac{d\bar{\tau}_m}{dz}\right\}$

A detailed discussion of the analysis leading to these results has also been given [16].

Regenerator Ineffectiveness. Once equations (25) and (26) are solved and C_2 is found, the regenerator ineffectiveness can be calculated from

$$1 - \eta = \frac{2C_2}{\bar{m}(z_l)Z_2(\bar{P}, \tau_l)\tau_l - Z_2(\bar{P}, 1) - \dfrac{2}{\gamma}\displaystyle\int_0^{z_l}\{(\sigma P)_H - (\sigma P)_L\}dz} \tag{30}$$

Numerical Results

Equations (25) and (26) can be readily put into finite-difference form. Both equations are of first order and are nonlinear, subject to two boundary conditions at the cold end ($z = 0$). Another condition is available at the warm end ($z = z_l$) for the evaluation of the integration constant C_2, thus making the solution a boundary-value problem. Nevertheless, a treatment based on the initial-value problem is possible by estimating values for C_2. Its exact value can then be found through iteration. An initial value for C_2 must be chosen, and for this purpose a fairly accurate value can be obtained by solving equation (26) for C_2 with an estimated slope $(d\bar{\tau}_m/dz)_{z=0}$. The solution of the governing equations for this value of C_2 yields a value for τ_l. The C_2 must be improved until this τ_l coincides to some required degree of accuracy with the given boundary condition for τ_l. This can be conveniently achieved, for example, by employing the Regula Falsi, which assures fast convergence. The solution for equations (25) and (26) as an initial-value problem can easily be achieved by employing the Runge-Kutta method. It was found that a step size as large as $z_l/20$ already gives accurate results.

Equations (25) and (26) and their boundary conditions are governed by a number of parameters. For the case of a perfect gas without conduction these are n_1, n_2, γ, C_1, z_l, and τ_l, provided that the right-hand side of equation (25) can be approximated

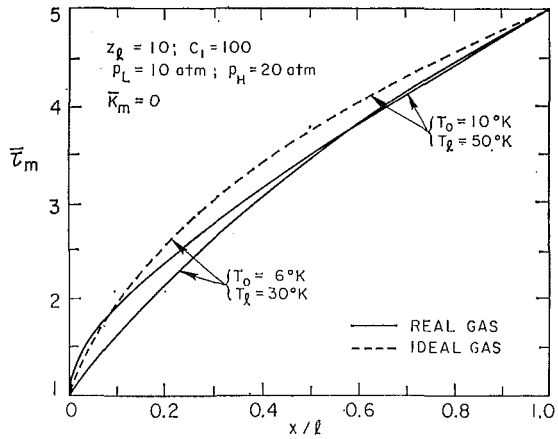

Fig. 2 Real-gas effects on matrix temperature distributions at different temperature levels (z_l = 10, C_1 = 100)

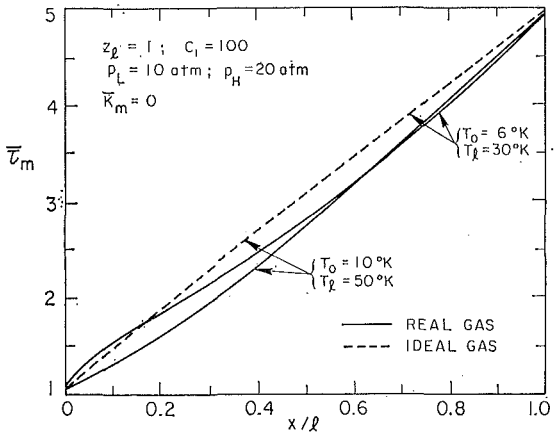

Fig. 3 Real-gas effects on matrix temperature distributions at different temperature levels (z_l = 1, C_1 = 1000)

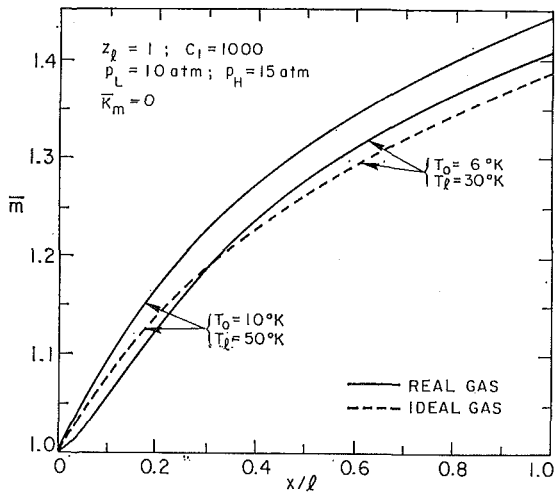

Fig. 4 Real-gas effects on mass-flux distributions at different temperature levels (z_l = 1, C_1 = 1000)

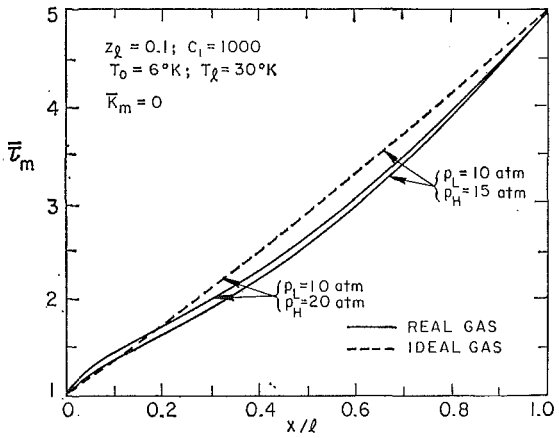

Fig. 5 Real-gas effects on matrix temperature distributions at different pressure levels (z_l = 0.1, C_1 = 1000)

by $1/\bar{\tau}_m$. As n_1, n_2, and γ can only attain a few distinct values for regenerators operating at very low temperatures, a complete set of results could easily be presented in chart form. However, if longitudinal conduction and real-gas effects are taken into account, four other parameters (K_m, T_0, P_H, and P_L) must be added to the system. This makes it rather impractical to obtain extensive numerical results.

Therefore, only a few representative cases for helium were computed here to demonstrate how the solution is influenced by real-gas and matrix-conduction effects. Besides γ = 1.67 and β = 0.80, the correlation

$$h_l = K\bar{m}^{0.59}\bar{\tau}_m{}^{0.20}$$

for the heat transfer coefficient was used throughout the calculations. The choice for n_1 stems from the fact that for very low temperature regenerators a matrix of lead shot generally is used, for which Rea and Smith [8] and Gamson et al. [14] listed n_1 = 0.59. Little is known about the temperature dependence of the heat transfer coefficient, so that the value for n_2 remains rather arbitrary until further research provides a more reliable one.

It is assumed that in regenerators operating at very low temperatures the values of C_1 are between 100 and 1000, while z_l varies between 1 and 10. Figures 2–4 demonstrate the impact of real-gas effects on the temperature and mass-flux profiles at different temperature levels for the special case of $\tau_l = T_l/T_0$ = 5. The compressibility factors for helium are close to unity near 20 deg K. Above this temperature they are slightly greater than one, while they decrease considerably for lower temperatures. Thus above 20 deg K, little influence of real-gas effects is expected. Down to a cold-end temperature of 10 deg K, the curvature of the temperature profile increases (and can even become positive). This indicates that more regenerator length at the cold end is needed for helium below 20 deg K than for an ideal gas to overcome the same temperature difference, thus decreasing the regenerator effectiveness. Below 10 deg K at the cold end, real-gas effects become so strong that temperature and mass-flux profiles develop an inflection point. In general, the effect of different pressure levels is less significant, mainly because the enthalpy is rather insensitive to pressure changes. Figure 5 gives an example of how the temperature profile is affected for the extreme case of T_0 = 6 deg K. It should be noted that the real-gas result for higher P_H comes closer to the ideal-gas solution, although the pressure fluctuation is twice as large as compared with the case of the lower P_H. This is due to the fact that at very low temperatures helium behaves more like an ideal gas around 20 atm. Figure 6, finally, demonstrates how longitudinal conduction tends to straighten the temperature profiles.

The regenerator effectiveness depends primarily on the temperature difference between gas and matrix, as well as on the magnitude of longitudinal conduction. Obviously, a large heat transfer coefficient (large C_1) and a small mass flux (large z_l) reduce the temperature difference. However, a small mass flux also results in a decrease of the heat transfer coefficient, so that an optimum value must be found. Furthermore, the relevant parameter for conduction, $\bar{K}_m$, also increases with C_1 and z_l and therefore must be included in the optimization. Tables 1–3 list the regenerator ineffectiveness for some values of z_l, C_1, and $\bar{K}_m$ for some temperature levels. It appears that in general real-

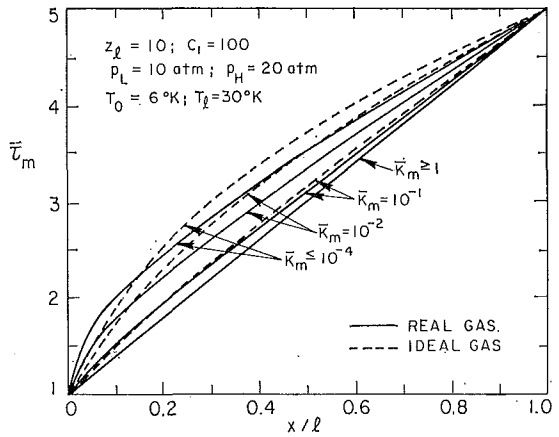

Fig. 6 Conduction effects on matrix temperature distributions ($z_l = 10$, $C_1 = 100$)

Table 1 Regenerator ineffectiveness for ideal-gas and real-gas behavior ($z_l = 0.1$)

C_1	$\bar{K}_m$	$T_0;T_\ell$ [°K]	$p_L;p_H$ [atm]	1 − η [%] ideal	real
1000	$\leq 10^{-6}$	6; 30	10; 20	1.628	1.930
	10^{-4}			1.817	2.093
	10^{-2}			20.814	18.353
	$\leq 10^{-6}$	6; 30	10; 15	1.627	1.956
	10^{-4}			1.816	2.118
	10^{-2}			20.863	18.353
	$\leq 10^{-6}$	10; 50	10; 20	1.628	1.799
	10^{-4}			1.817	1.961
	10^{-2}			20.814	19.080
	$\leq 10^{-6}$	10; 50	10; 15	1.627	1.776
	10^{-4}			1.816	1.952
	10^{-2}			20.863	19.277

gas behavior tends to decrease the regenerator effectiveness, as is anticipated from the figures. In addition, if the overall performance of the regenerator is poor, conduction effects will be unimportant, while for a very high regenerator effectiveness a small value of $\bar{K}_m$ will exhibit a profound influence. It can be stated that conduction is unimportant in most cases as long as

$$\bar{K}_m \frac{\tau_l - 1}{z_l} \ll C_2$$

For larger values its influence can be estimated by, cf. equation (26),

$$\frac{(1-\eta)_{\bar{K}_m}}{(1-\eta)_{\bar{K}_m=0}} \cong 1 + \frac{\bar{K}_m(\tau_l - 1)}{C_2\,(\bar{K}_m = 0)\,z_l}$$

Acknowledgment

The study was conducted under the support of the Lockheed Missiles and Space Co., and many helpful discussions with Dr. A. P. Glassford of Lockheed are particularly appreciated.

References

1 Finkelstein, T., "Generalized Thermodynamic Analysis of Stirling Engines," Paper No. 118B, SAE annual meeting, 1960.

2 Gifford, W. E., and McMahon, H. D., "A New Low-Temperature Gas Expansion Cycle," *Advances in Cryogenic Engineering*, Vol. 5, 1960, p. 354.

3 Gifford, W. E., and Longsworth, R. C., "Pulse-Tube Refrigeration," *Journal of Engineering for Industry*, TRANS. ASME, Series B, Vol. 86, No. 3, Aug. 1964, pp. 264–268.

Table 2 Regenerator ineffectiveness for ideal-gas and real-gas behavior ($z_l = 1.0$)

C_1	$\bar{K}_m$	$T_0;T_\ell$ [°K]	$p_L;p_H$ [atm]	1 − η [%] ideal	real
100	$\leq 10^{-6}$	6; 30	10; 20	1.728	2.023
	10^{-4}			1.743	2.037
	10^{-2}			3.245	3.359
	$\leq 10^{-6}$	6; 30	10; 15	1.718	2.043
	10^{-4}			1.733	2.056
	10^{-2}			3.271	3.387
	$\leq 10^{-6}$	10; 50	10; 20	1.728	1.889
	10^{-4}			1.743	1.903
	10^{-2}			3.245	3.254
	$\leq 10^{-6}$	10; 50	10; 15	1.718	1.869
	10^{-4}			1.733	1.883
	10^{-2}			3.271	3.282
1000	$\leq 10^{-6}$	6; 30	10; 20	0.177	0.206
	10^{-4}			0.192	0.220
	10^{-2}			1.664	1.524
	$\leq 10^{-6}$	6; 30	10; 15	0.177	0.211
	10^{-4}			0.192	0.224
	10^{-2}			1.668	1.487
	$\leq 10^{-6}$	10; 50	10; 20	0.177	0.196
	10^{-4}			0.192	0.208
	10^{-2}			1.664	1.548
	$\leq 10^{-6}$	10; 50	10; 15	0.177	0.195
	10^{-4}			0.192	0.208
	10^{-2}			1.668	1.551

Table 3 Regenerator ineffectiveness for ideal-gas and real-gas behavior ($z_l = 10.0$)

C_1	$\bar{K}_m$	$T_0;T_\ell$ [°K]	$p_L;p_H$ [atm]	1 − η [%] ideal	real
100	$\leq 10^{-6}$	6; 30	10; 20	0.238	0.261
	10^{-4}			0.238	0.261
	10^{-2}			0.299	0.324
	$\leq 10^{-6}$	6; 30	10; 15	0.236	0.271
	10^{-4}			0.237	0.272
	10^{-2}			0.299	0.330
	$\leq 10^{-6}$	10; 50	10; 20	0.238	0.258
	10^{-4}			0.238	0.259
	10^{-2}			0.299	0.309
	$\leq 10^{-6}$	10; 50	10; 15	0.236	0.258
	10^{-4}			0.237	0.259
	10^{-2}			0.299	0.309
1000	$\leq 10^{-6}$	6; 30	10; 20	0.024	0.026
	10^{-4}			0.025	0.027
	10^{-2}			0.073	0.074
	$\leq 10^{-6}$	6; 30	10; 15	0.024	0.027
	10^{-4}			0.025	0.028
	10^{-2}			0.073	0.071
	$\leq 10^{-6}$	10; 50	10; 20	0.024	0.026
	10^{-4}			0.025	0.027
	10^{-2}			0.073	0.071
	$\leq 10^{-6}$	10; 50	10; 15	0.024	0.027
	10^{-4}			0.025	0.027
	10^{-2}			0.073	0.070

4 Sherman, A., "Mathematical Analysis of a Vuilleumier Refrigerator," ASME Paper No. 71-WA/HT-33.

5 Kays, W. M., and London, A. L., *Compact Heat Exchangers*, McGraw-Hill, New York, N. Y., 1964.

6 Jakob, M., *Heat Transfer*, Vol. 2, Chap. 35, John Wiley & Sons, New York, N. Y., 1965.

7 Ackermann, R. A., and Gifford, W. E., "Small Cryogenic Regenerator Performance," *Journal of Engineering for Industry*, TRANS. ASME, Series B, Vol. 91, No. 1, Feb. 1969, pp. 273–281.

8 Rea, S. N., and Smith, J. L., Jr., "The Influence of Pressure Cycling on Thermal Regenerators," *Journal of Engineering for Industry*, TRANS. ASME, Series B, Vol. 89, No. 3, Aug. 1967, pp. 563–569.

9 Van Wylen, G. J., and Sonntag, R. E., *Fundamentals of Classical Thermodynamics*, John Wiley & Sons, New York, N. Y., 1966.

10 Hust, J. G., and Gosman, A. L., "Functions for the Calculation of Entropy, Enthalpy, and Internal Energy for Real Fluids Using Equations of State and Specific Heats," *Advances in Cryogenic Engineering*, Vol. 9, 1963, p. 227.

11 Keller, W. E., *Helium-3 and Helium-4*, Plenum, New York, N. Y., 1969.

12 Mann, D. B., "The Thermodynamic Properties of Helium from 3°K to 300°K between 0.5 and 100 atm.," NBS technical note 154, Jan. 1962.

13 Bird, R. B., Stewart, W. E., and Lightfoot, E. N., *Transport Phenomena*, John Wiley & Sons, New York, N. Y., 1960.

14 Gamson, B. W., Thodos, G., and Hougen, O. A., "Heat, Mass and Momentum Transfer in the Flow of Gases through Granular Solids," *Trans. Am. Inst. Chem. Engrs.*, Vol. 39, 1943, pp. 1–35.

15 Tong, L. S., and London, A. L., "Heat-Transfer and Flow-Friction Characteristics of Woven-Screen and Crossed-Rod Matrices," TRANS. ASME, Vol. 79, Oct. 1957, pp. 1558–1570.

16 Luikov, A. V., Shashkov, A. G., Vasilev, L., and Fraiman, Yu. E., "Thermal Conductivity of Porous Systems," *International Journal of Heat and Mass Transfer*, Vol. 11, 1968, pp. 117–140.

17 Chan, C. K., and Tien, C. L., "Conductance of Packed Spheres in Vacuum," to be published in the JOURNAL OF HEAT TRANSFER.

18 Modest, M. F., "Theoretical Analysis of the Performance of Cryogenic Thermal Regenerators Subjected to Rapidly Cycling Flows," PhD dissertation, Department of Mechanical Engineering, University of California, Berkeley, Calif., 1972.

T. G. SMITH
Assistant Professor.

J. T. BANCHERO
Professor and Chairman.
Assoc. Mem. ASME

Department of Chemical Engineering,
University of Notre Dame,
Notre Dame, Ind.

The Numerical Simulation and Design of a Homogeneous Nonisothermal Multi-pass Shell-and-Tube Reactor

The simulation of a multi-pass shell-and-tube reactor requires the solution of a nonlinear two-point boundary-value problem. Six nonlinear ordinary differential equations describing the production of ethanolamines in 1–2 and 1–4 shell-and-tube reactors are solved numerically using both a quasi-linearization algorithm and a classical shooting method. Despite the presence of five unknown initial values, the shooting-method approach proved superior for this particular problem. The simulation revealed that for exothermic reactions the optimum tube-side temperature profile (and therefore the minimum-size reactor) was most closely approached by designing for the lowest overall heat transfer coefficient and cooling-water flow rate and highest inlet cooling-water temperature, subject to the constraint of a maximum-reaction mixture temperature.

Introduction

A CONSTRAINT encountered in the design of chemical reactors is that of a maximum or minimum permissible reaction mixture temperature. Product decomposition, reaction kinetics, pressure limitations, or any of a number of other design considerations can dictate such a constraint. The imposition of this restraint may require that the reaction be carried out nonadiabatically. If large surface areas are involved, the use of a shell-and-tube reactor would become desirable for the same reasons of economy of construction as those advanced for using a shell-and-tube rather than a double-pipe heat exchanger. However, the simulation and design of a multi-pass or countercurrent single-pass shell-and-tube reactor with nonuniform heat generation requires the solution of a set of nonlinear ordinary differential equations of the two-point boundary-value type involving $r + 1$ unknown initial values, where r is the number of chemical products. The solution of problems of this type, either analytically or numerically, is generally quite difficult.

The first purpose of this work is to simulate numerically the operation of a shell-and-tube reactor and to elucidate those parameters having the dominant influence in the suitable design of such a reactor. The industrially important reaction of ammonia with ethylene oxide to form mono-, di-, and triethanolamines has been chosen for illustration since the kinetics of the system of four exothermic, irreversible, consecutive–competitive chemical reactions approach the complexity normally encountered industrially.

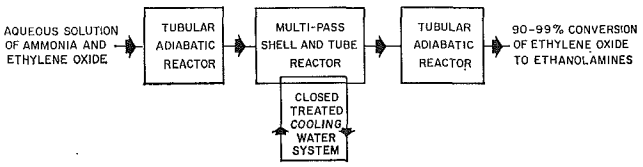

Fig. 1 Overall processing scheme for the production of mono-, di-, and triethanolamines

The second purpose of this work is to compare the efficiency of the method of quasi-linearization as described by Lee [1][1] with that of a modification of the classical numerical technique commonly known as a shooting method. The quasi-linearization method establishes a systematic algorithm for the iterative solution of nonlinear two-point and multi-point boundary-value problems. The classical approach reduces the solution of a boundary-value problem to the iterative solution of an initial-value problem. When nonlinear equations are involved, this approach is sometimes subject to convergence problems.

The shell-and-tube reactor is a component in the general processing scheme shown schematically in Fig. 1. Computer calculations were carried out for the first adiabatic section to determine the temperature and reactant distribution of the feed to the nonadiabatic reactor. A closed treated-cooling-water system is necessary due to cooling-water temperatures in the range of 100 to 200 deg C. The reactant feed rate is based on a

Contributed by the Heat Transfer Division of THE AMERICAN SOCIETY OF MECHANICAL ENGINEERS and presented at the AIChE-ASME Heat Transfer Conference, Denver, Colo., August 6–9, 1972. Manuscript received by the Heat Transfer Division April 12, 1972; revised manuscript received May 16, 1972. Paper No. 72-HT-24.

[1] Numbers in brackets designate References at end of paper.

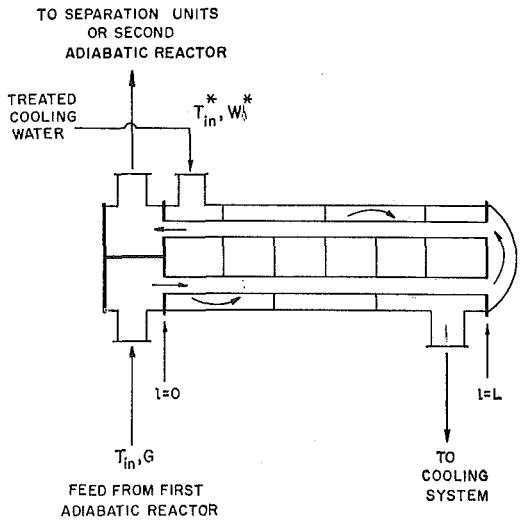

Fig. 2 1-2 shell-and-tube reactor

production rate of 40,000,000 lb per year of ethanolamines, corresponding to a large-sized unit.

Mathematical Model

The system of irreversible consecutive–competitive (or series–parallel) reactions describing the production of ethanolamines may be represented as

$$A + B \xrightarrow{k_1} AB_1$$

$$AB_1 + B \xrightarrow{k_2} AB_2$$

$$AB_2 + B \xrightarrow{k_3} AB_3$$

$$AB_3 + B \xrightarrow{k_4} AB_4$$

where A represents ammonia, B represents ethylene oxide, AB_1 represents monoethanolamine and so on.

From mass balances

$$N_A = N_{A_0} - X_1 = N_{AB_0}$$

$$N_{AB_{i-1}} = X_{i-1} - X_i$$

$$N_B = N_{B_0} - \sum_{i=1}^{4} X_i$$

$$N_{OH} = N_{W_0} + \sum_{i=1}^{3} X_i$$

Using these relations and the rate dependence proposed by Lowe, Butler, and Meade [2], rate equations in terms of the X_i may be written as follows:

$$\frac{dX_i}{dl} = k_i\left(\frac{\rho^4}{G}\right)(X_{i-1} - X_i)\left(N_{B_0} - \sum_{i=1}^{4} X_i\right)\left(N_{W_0} + \sum_{i=1}^{3} X_i\right)^2 \tag{1}$$

for $i = 1, 2, 3, 4$.

Combination of the experimental data of Ferrero, Berbe, and Flamme [3] and that of Lowe, Butler, and Meade yields the following equations for the prediction of the k_i:

$$\ln k_1 = 10.60 - \frac{6983}{T}$$

$$\ln k_2 = 13.96 - \frac{7545}{T}$$

$$\ln k_3 = 12.67 - \frac{7233}{T}$$

$$\ln k_4 = 6.18 - \frac{6048}{T}$$

The units of k_i and T in the above four equations are (liter/gm-mole)^3/min and deg K, respectively. The standard heats of reaction at 25 deg C for the four exothermic reactions are $\Delta H_1 = -53{,}600$, $\Delta H_2 = -48{,}400$, $\Delta H_3 = -50{,}200$, and $\Delta H_4 = -50{,}400$ Btu/lb-mole. These were assumed independent of temperature and composition.

An energy balance is now established for the 1-2 shell-and-tube reactor shown in Fig. 2. For the tube-side reaction mixture, assuming plug flow and neglecting axial conduction and diffusion,

$$\frac{dT}{dl} = \frac{1}{C_p}\sum_{i=1}^{4}(-\Delta H_i)\frac{dX_i}{dl} + \frac{\pi DU'(T^* - T)}{C_p GS} \tag{2}$$

and for the shell-side heat transfer medium, neglecting heat loss to the environment,

$$\frac{dT^*}{dl} = \frac{m\pi DU'(T - T^*)}{W^* C_p^*} \tag{3}$$

For multiple tube-side passes, equations (1) and (2) must be

Nomenclature

A = ammonia, NH_3
AB_1 = monoethanolamine, $NH_2(CH_2)_2OH$
AB_2 = diethanolamine, $NH[(CH_2)_2OH]_2$
AB_3 = triethanolamine, $N[(CH_2)_2OH]_3$
AB_4 = heavier by-products
B = ethylene oxide, $CH_2—CH_2$ (O)
C_p = average heat capacity of reaction mixture, Btu/lb-deg C
C_p^* = average heat capacity of cooling water, Btu/lb-deg C
D = outside tube diameter, ft
G = mass velocity, lb/ft^2-hr
k_i = specific reaction rate constant for reaction i, (ft^3/lb-mole)^3/hr, $i = 1, 2, 3, 4$
l = length, ft
L = length of one tube pass, ft
m = number of tubes per pass
n = number of iterations
N_{A_0}, N_{B_0}, N_{W_0} = pound-moles of ammonia, ethylene oxide, and water, respectively, present in feed to first adiabatic reactor per pound of feed
N_A, N_B, N_{OH} = pound-moles of ammonia, ethylene oxide, and hydroxy groups, respectively, present at length l per pound of feed
N_{AB_i} = pound-moles of AB_i present at length l per pound of feed, $i = 1, 2, 3, 4$
p = total number of tube passes
S = inside cross-sectional area of a single tube, ft^2
T = local temperature of reaction mixture, deg C
T^* = local temperature of cooling water, deg C
U' = overall heat transfer coefficient based on outside tube area, Btu/hr-ft^2-deg C
U = overall heat transfer coefficient based on outside tube area, Btu/hr-ft^2-deg F
W^* = mass flow rate of cooling water, lb/hr
X_i = pound-moles of AB_i formed up to length l per pound of feed, $i = 1, 2, 3, 4$
I, II = first and second pass, respectively
ΔH_i = standard heat of reaction i, Btu/lb-mole, $i = 1, 2, 3, 4$
Δl = step size used with Runge–Kutta algorithm, ft
ρ = local density of reaction mixture, lb/ft^3

applied anew for each tube-side pass. For example, the boundary conditions for a 1-2 reactor are

at $l = 0$

$$T^I = T_{\text{inlet}} \qquad X_i^I = X_{i,\text{inlet}} \qquad T^* = T_{\text{inlet}}^* \qquad i = 1, 2, 3, 4 \tag{4}$$

at $l = L$

$$T^I = T^{II} \qquad X_i^I = X_i^{II} \qquad i = 1, 2, 3, 4 \tag{5}$$

Equations (4) and (5) furnish $2i + 3$ boundary conditions for the $2i + 3$ equations. Analogous boundary conditions hold for a p-pass exchanger by simply applying equation (5) $p - 1$ times.

Numerical Technique

Equations (1), (2), and (3) subject to the boundary values given by equations (4) and (5) were solved first using the quasi-linearization method described by Lee [1]. This is essentially a generalized Newton–Raphson technique for functional equations. The quasi-linearization approach both linearizes the set of ordinary differential equations and provides a sequence of functions which converge (from rough initial approximations of the unknown functions) quadratically and monotonically to the solution of the original nonlinear equations. In addition to its systemization of the solution of nonlinear boundary-value problems and its quadratic convergence, it may have particular usefulness in problems where nonlinearities are of the exponential type as in the Arrhenius reaction rate term of equation (1).

To illustrate the method concisely, equations (1), (2), and (3) are written in vector form as follows:

$$\frac{d\mathbf{X}}{dl} = \mathbf{f}(\mathbf{X}, l) \tag{6}$$

where $\mathbf{X}$ and $\mathbf{f}$ are six-dimensional vectors. $\mathbf{X}$ has components X_1, X_2, X_3, X_4, T, and T^*, while the components of $\mathbf{f}$ are the right-hand sides of equations (1), (2), and (3) respectively. Using the quasi-linearization technique, the following vector recurrence relation can be obtained:

$$\frac{d\mathbf{X}_{n+1}}{dl} = \mathbf{f}(\mathbf{X}_n, l) + J(\mathbf{X}_n)\cdot(\mathbf{X}_{n+1} - \mathbf{X}_n) \tag{7}$$

where $J(\mathbf{X}_n)$ represents the following Jacobi matrix:

$$J(\mathbf{X}_n) = \begin{bmatrix} \dfrac{\partial f_1}{\partial X_{1n}} & \cdots & \dfrac{\partial f_1}{\partial X_{6n}} \\ \cdot & & \cdot \\ \cdot & & \cdot \\ \cdot & & \cdot \\ \dfrac{\partial f_6}{\partial X_{1n}} & \cdots & \dfrac{\partial f_6}{\partial X_{6n}} \end{bmatrix} \tag{8}$$

Note that equation (7) is now linear in $\mathbf{X}_{n+1}$. Due to this linearity, any one of a number of numerical techniques, including initial-value methods, could be used to obtain a solution. However, in view of the exponential dependence of the reaction rate on temperature and the concomitant possibility of numerical instability for an explicit technique, equation (7) was placed in finite-difference form and solved implicitly using a standard Gaussian elimination method (see Carnahan, Luther, and Wilkes [4]). To further guard against numerical instabilities, the reaction mixture temperature during any given iteration was restricted to a certain rather wide range of values, $T_{\min} \leq T \leq T_{\max}$. The initial functional approximations for the components of $\mathbf{X}$ were taken to be simply the initial conditions given by equation (4), i.e., constant functions were used to start the iterative procedure.

Equations (1), (2), and (3) were also solved as an initial-value problem subject to equation (4) and then equation (5). The unknown initial ($l = 0$) conditions on the X_i and T in the second pass were simultaneously satisfied indirectly using a single, more general condition and a trial-and-error approach. The procedure was as follows. Equations (1), (2), and (3) were solved numerically for the first pass, thus establishing a tentative shell-side temperature profile. Using this profile, equations (1) and (2) were solved for the second pass, proceeding, of course, from $l = L$ to $l = 0$. Equations (1), (2), and (3) were then solved again for the first pass but now with the heat transfer that had occurred previously in the second pass added (segmentally) to that occurring in the first pass, thus resulting in an improved shell-side temperature profile. These iterations continued until the shell-side profile converged. A standard fourth-order Runge–Kutta algorithm was used to implement the above calculations. Calculations for a p-pass exchanger follow directly from a straightforward extension of the two-pass trial-and-error procedure.

With either of the two above techniques, an additional trial and error is involved if it is desired to calculate the length (an input parameter) required for a given conversion. In such a case, a half-interval algorithm was used to hunt for the length needed to achieve the desired conversion.

Computations

The computer used was an Univac 1107. For the quasi-linearization method, 100 grid points per pass were needed, yielding a grid spacing of approximately 0.2 ft. Smaller grid spacings were tried without a substantial improvement in results, while larger spacings gave variable results. Convergence was considered complete when no grid point displayed a change in temperature or concentration greater than 0.1 percent from one iteration to the next. Generally, convergence was achieved in 5 to 10 iterations. To reduce the possibility of large temperature oscillations, the allowable maximum and minimum reaction mixture temperatures at any grid point were automatically restricted to 250 and 150 deg C, respectively, during any given iteration.

A variable step size, Δl, was used with the Runge–Kutta algorithm. The computer program determined the local step size in accordance with the local temperature gradient as follows:

$$\frac{\Delta T}{\Delta l} < 1, \Delta l = 1; 1 < \frac{\Delta T}{\Delta l} < 5, \Delta l = 0.2; \frac{\Delta T}{\Delta l} > 5, \Delta l = 0.02$$

When the temperature rise of the cooling water changed by less than 1 deg C relative to the rise on the previous iteration, convergence was complete. Convergence was always reached within 5 iterations.

The various physical properties of the reaction mixture vary longitudinally with both the temperature and the concentration gradient. Due to the scarcity of available data, variations due to concentration are difficult to predict; hence representative average values were used. The variation of viscosity with temperature was represented functionally, and in view of the rather modest temperature ranges involved, heat capacity and thermal conductivity were accounted for adequately by temperature-averaged values. Considering the amount of uncertainty usually present in kinetic data, it was felt that a more accurate description of the physical properties of the system was not warranted. However, since the density of the reaction mixture appears to the fourth power in equation (1), axial density variations were estimated as a function of both temperature and concentration. The overall heat transfer coefficient was determined using standard methods such as described in Kern [5] and assuming thirteen $^3/_4$-in-OD (13 BWG) tubes per pass. The tube-side pressure level was on the order of 2500 psi, rendering pressure-drop considerations of minor importance.

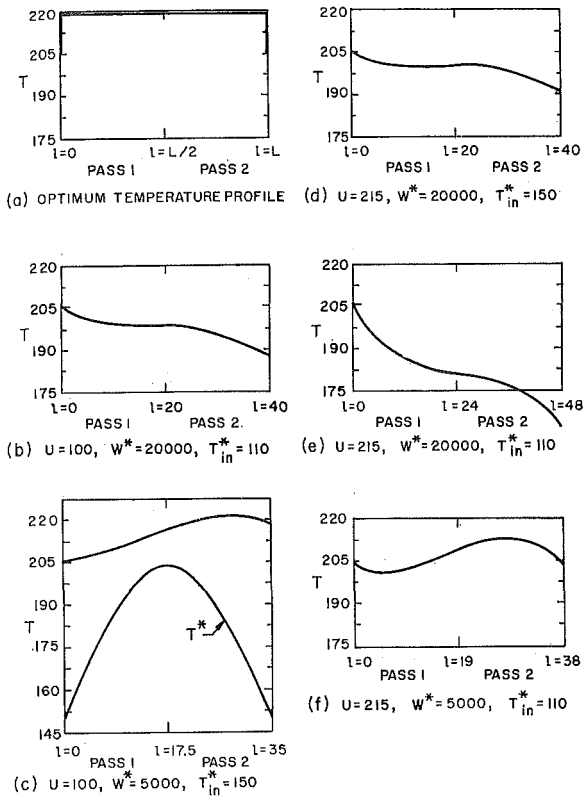

Fig. 3 Tube-side temperature profiles

As mentioned in the Introduction, the shell-and-tube reactor was preceded by a tubular adiabatic reactor. The feed rate to this unit was 14,125 lb/hr consisting of 93.5 moles/hr of ethylene oxide together with 3.7 and 2.45 moles of ammonia and water, respectively, per mole of ethylene oxide. The adiabatic reactor consumed 73.4 percent of the entering ethylene oxide, yielding the following feed composition for the shell-and-tube reactor: $X_{1,\text{in}} = 0.00322$, $X_{2,\text{in}} = 0.00129$, $X_{3,\text{in}} = 0.00035$, $X_{4,\text{in}} = 0.00001$. The feed temperature was 205.4 deg C. In order to maintain the tube-side pressure under a reasonable upper bound and to minimize decomposition of the ethanolamines, the converged reaction mixture temperature was limited to a maximum of 220 deg C.

There were two reasons for using two entirely different numerical algorithms to carry out the computations. The first reason was to provide assurance as to the validity of the calculations by using one program as a check against the other. The second reason was to introduce a comparison, as applied to a realistic and fairly complicated design situation, between a recently proposed algorithm for the systematic solution of nonlinear multi-point boundary-value problems and a standard initial-value trial-and-error approach.

The two methods produced virtually identical results. In addition, the mass and energy balances for both closed to within 1 percent. For an identical set of parameters, the running times for the quasi-linearization technique and the shooting method were approximately the same, namely, 10 sec to reach convergence per case. However, problem development and programming were considerably more difficult using quasi linearization. Incidentally, no stability or convergence problems were encountered with the shooting method. This is no doubt due to the fact that the five unknown initial conditions can be simultaneously satisfied by convergence of the shell-side temperature profile. This in turn is made possible by the floating boundary conditions at $l = L$. In cases where this approach is not possible, a method has recently been advanced by Gray and Smith [6] for determining the unknown initial conditions by means of an optimization procedure. One is then again able to obtain solutions using common marching integration techniques, such as the Runge–Kutta employed herein.

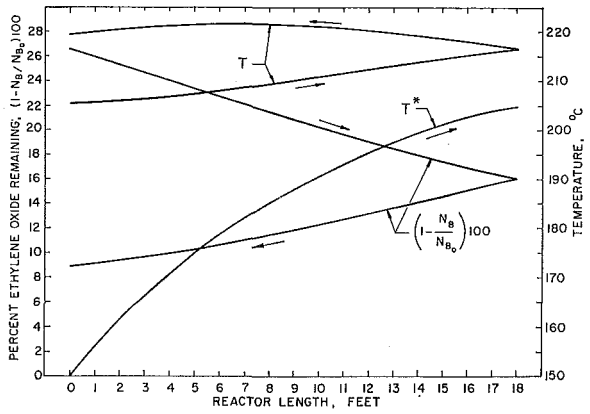

Fig. 4 Concentration and temperature profiles for best case

Various initial functional approximations (all constant functions) in addition to constant functions equal to the initial conditions were tried with the quasi-linearization method. The convergence rate was found to be quite insensitive to the closeness of these initial guesses to the actual profiles. Also, the distribution of the amount of reaction occurring among the various passes has little effect on the convergence of the quasi-linearization technique. However, large amounts of reaction in later passes would make convergence of the shooting method somewhat more difficult.

Results and Discussion

The residence time of the reaction mixture and its temperature profile determine the extent of reaction and therefore the size of nonadiabatic reactor required for the desired conversion. The approximately optimal temperature profile is sketched in Fig. 3(*a*). The true optimal profile would be somewhat different because of the variation of density with temperature and its appearance in the rate equations as ρ^4. Since lower densities oppose the effect of higher temperatures on reaction rate, rather large changes in the shape of the temperature profile are required before reactor size is significantly affected. With a suitable choice of design parameters, the actual temperature profile can be made to approach the optimal, thus reducing residence time and reactor size. The parameters over which one typically has some control in the design phase are the overall heat transfer coefficient and the cooling-water flow rate and inlet temperature.

To test the influence of U, W^*, and T_{in}^* on the size of the reactor, 18 computer runs were carried out involving all possible combinations of $W^* = 5000, 10000, 20000$; $T_{\text{in}}^* = 110, 130, 150$; $U = 100, 215$. In addition, a run with $U = 50$ and another with $T_{\text{in}}^* = 170$ were made for $W^* = 10000$. Five of the resulting temperature profiles are sketched in Fig. 3 (*b–f*). Here L is the length required to reach 91 percent conversion of ethylene oxide. These particular results are for a 1-2 shell-and-tube reactor with cooling water cocurrent with the first pass. Most of the conversion takes place in the first pass, and in order to maintain the reaction mixture temperature under 220 deg C, it is essential to provide a quenching action by having the cooling water cocurrent with the first pass (see also Grens and McKean [7]).

One interesting result concerns the effect of U on the total length required to achieve a given conversion of ethylene oxide. A comparison of Figs. 3(*b*) and 3(*e*) shows a 20 percent reduction in reactor size when U is halved, all other parameters being the same. This effect occurred to some extent for all values of T_{in}^* and W^* but was more pronounced at higher values of W^*. The reason for this trend can be seen graphically by comparing Figs. 3(*b*) and 3(*e*). The lower value of U allows the temperature and therefore the conversion to remain high in both the first and

second pass (i.e., a flatter profile is obtained) without losing the benefit of the first-pass quench provided by cocurrent flow. A decrease in W^* or an increase in T_{in}^* also reduces reactor size for the same reason as given above for the effect of U; compare Figs. 3(*e*) and 3(*f*), 3(*e*) and 3(*d*), respectively. In addition, a low cooling-water flow rate and high inlet temperature minimize operating costs.

Based on these results, the best combination of parameters would be those represented by Fig. 3(*c*). The ethylene oxide concentration profile together with the tube-side and shell-side temperature profiles for this case are shown in Fig. 4. Any further decrease in U or W^*, or increase in T_{in}^*, would cause the 220 deg C temperature constraint to be violated.

Note that U is controlled by shell-side conditions, and its actual value can be varied for design purposes by adjusting the tube layout and baffle spacing. If the tube-side heat transfer coefficient were controlling, a 1-1 cocurrent reactor could become attractive because more than one tube pass would increase U and thus increase reactor size (the optimization of cooling-water flow for a cocurrent 1-1 reactor with exothermic reaction has been studied by Kadlec and Newberger [8]). If the reactions were endothermic, the tube-side coefficient would likely control and a large number of tube-side passes would be desirable since a high value of U would be needed to approach the optimum temperature profile.

Conclusions

The operation of a shell-and-tube reactor for the production of ethanolamines has been simulated using both a quasi linearization and a shooting-method algorithm. For this type of nonlinear two-point boundary problem, the shooting method converges quickly, is as fast as quasi linearization, and is considerably easier to program.

The simulation itself revealed that for exothermic reactions the optimum tube-side temperature profile (and therefore the minimum-size reactor) was most closely approached by designing for the lowest possible U and W^* and highest T_{in}^*, subject to the constraint of a maximum reaction mixture temperature of 220 deg C.

Acknowledgments

We thank M. A. Miller and H. C. Gallagher for programming the shooting method.

References

1 Lee, E. S., *Quasilinearization and Invariant Imbedding*, Academic, New York, N. Y., 1968.

2 Lowe, A. J., Butler, D., and Meade, E. M., "Manufacture of Alkanolamines," U. S. patent 2,823,236, 1958.

3 Ferrero, P., Berbe, F., and Flamme, L. R., "Kinetic Study of Ethanolamines Synthesis," *Bull. Soc. Chim. Belg.*, Vol. 56, 1947, pp. 349–368.

4 Carnahan, B., Luther, H. A., and Wilkes, J. O., *Applied Numerical Methods*, Wiley, New York, N. Y., 1969.

5 Kern, D. Q., *Process Heat Transfer*, McGraw-Hill, New York, N. Y., 1950.

6 Gray, M., and Smith, R. A., "Use of Optimization Methods to Solve Heat Convection Problems with Unknown Wall Boundary Conditions," *International Journal for Numerical Methods in Engineering*, Vol. 2, 1971, pp. 405–413.

7 Grens, E. A., II, and McKean, R. A., "Temperature Maxima in Countercurrent Heat Exchangers with Internal Heat Generation," *Chemical Engineering Science*, Vol. 18, 1963, pp. 291–295.

8 Kadlec, R. H., and Newberger, M. R., "Optimal Operation of a Tubular Chemical Reactor," *AIChE Journal*, Vol. 17, 1971, pp. 1381–1387.

D. S. ROWE
Battelle–Northwest,
Richland, Wash.
Mem. ASME

A Mathematical Model for Transient Subchannel Analysis of Rod-Bundle Nuclear Fuel Elements[1]

This paper presents a mathematical method for analyzing transient flow and enthalpy transport in rod-bundle nuclear fuel elements during both boiling and nonboiling conditions. A mathematical model is formulated by dividing the bundle flow area into flow subchannels that are assumed to contain one-dimensional flow and are coupled to each other by turbulent and diversion crossflow mixing. The mathematical model neglects sonic velocity propagation and neglects temporal and spatial acceleration in the transverse momentum equation. A semiexplicit finite-difference scheme is used to perform a boundary-value solution where the boundary conditions are the inlet enthalpy, inlet flow rate, and exit pressure. Calculations are presented to show the effect of rapid changes in heat flux, inlet enthalpy, and inlet flow rate on the subchannel flow and enthalpy distribution in rod bundles.

Introduction

To ESTABLISH the safe operating limits of nuclear power reactors, the heat transfer and flow behavior in nuclear fuel bundles must be known for all operating conditions, including transients. In many cases this information is obtained from laboratory experiments that use electrically heated models to simulate the fuel design. These experiments give thermal–hydraulic performance parameters such as critical heat flux and fuel temperature for selected conditions. Since the experiments cannot simulate all possible steady-state and transient operating conditions, analytical techniques must be used to extend the experimental results to the reactor. For simple fuel geometries, this may be done by using a one-dimensional analysis; however, this technique is not completely adequate for establishing the economic operating conditions of today's nuclear power reactors that use rod-bundle fuel elements. The enthalpy and mass velocity in some regions of these bundles can be very different from the average conditions during boiling; therefore, more detailed analysis techniques are required.

The purpose of this paper is to present a mathematical method for analyzing the steady-state and transient thermal–hydraulic behavior of rod-bundle nuclear fuel elements for both boiling and nonboiling conditions.

[1] This paper is based on work performed under USAEC contract AT(45-1)-1830. Permission to publish is gratefully acknowledged.

Contributed by the Heat Transfer Division for publication (without presentation) in the JOURNAL OF HEAT TRANSFER. Manuscript received by the Heat Transfer Division November 24, 1971. Paper No. 73-HT-H.

Mathematical Model

The basic approach used in the present mathematical model is to divide the bundle cross section into flow subchannels as shown in Fig. 1. While other subchannel selection schemes are possible, the one shown has gained acceptance [1][2] for steady-state subchannel analysis of single-phase flow in rod-bundle geometries and is assumed to apply for two-phase transient analysis. By making suitable assumptions concerning the crossflow and the flow in these subchannels, a mathematical model can be developed to describe the subchannel flow and enthalpy.

Several steady-state digital computer programs [2–5] have mathematical models based on this approach; however, none of them has been extended to include transients. This paper presents a transient subchannel analysis method that is the basis of the COBRA-III program and that represents an extension of the COBRA-II program [5] to transients analysis.

Basic Assumptions

Several assumptions are required to develop the equations of the mathematical model:

1 One-dimensional two-phase slip flow exists in each selected flow subchannel during boiling.

2 Subchannel density is specified in terms of enthalpy, pressure, flow rate, position, and time.

3 The subchannels are coupled by the two types of crossflow mixing shown in Fig. 1. The first is a turbulent (fluctuating)

[2] Numbers in brackets designate References at end of paper.

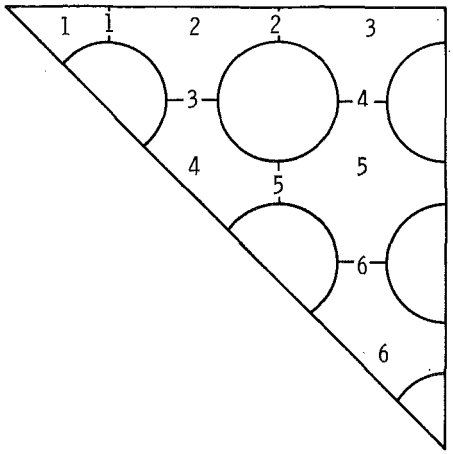

Fig. 1 Method of subchannel selection

crossflow rate per unit length that causes no net flow change ($w_{ij}' = w_{ji}'$). The second is a net diversion crossflow per unit length that results from flow redistribution.

4 Transverse temporal and spatial acceleration is neglected.

5 Sonic velocity propagation is ignored.

The first two assumptions are used for one-dimensional analysis of simple channels. By using the third and fourth assumptions, the model becomes a collection of one-dimensional parallel flow channels that are coupled by the two types of crossflow mixing. The last two assumptions greatly simplify the mathematical model and the numerical solution; however, they limit the model to moderate-speed transients where the time step is greater than the transit time through a node. Neglecting temporal acceleration can be justified for moderate-speed transients since the acceleration of fluid in the gaps between subchannels will be small. The result of this assumption is that the diversion crossflow has instantaneous response to changes in the pressure gradients. Neglecting sonic velocity propagation is also justified for moderate-speed transients. Meyer [6] justifies this assumption for transients with times that are longer than the sonic propagation time through the channel.

Equations of the Mathematical Model. By using the previous assumptions and by applying the general equations of continuity, energy, and momentum to a segment of an arbitrary subchannel, the equations of the mathematical model may be derived in a manner similar to that shown in [5]. For simplicity, the equations are presented for an arbitrary subchannel (i) which is connected to another subchannel (j). The right side of the continuity equation

$$A_i \frac{\partial \rho_i}{\partial t} + \frac{\partial m_i}{\partial x} = -w_{ij} \tag{1}$$

gives the net rate of change of subchannel flow in terms of the diversion crossflow per unit length. By choice, the diversion crossflow is positive when flow is diverted out of subchannel (i). The turbulent crossflow does not appear because it does not cause a net flow change. The time derivative of density gives the component of flow change caused by the fluid expansion or contraction.

The right side of the energy equation

$$\frac{1}{u''}\frac{\partial h_i}{\partial t} + \frac{\partial h_i}{\partial x} = \frac{q_i'}{m_i} - (h_i - h_j)\frac{w_{ij}'}{m_i} + (h_i - h_{ij}^*)\frac{w_{ij}}{m_i} \tag{2}$$

contains three terms for thermal energy transport in a rod-bundle fuel element. The first term is the power-to-flow ratio of a subchannel and gives the rate of enthalpy change if no thermal mixing occurs. The second term accounts for the turbulent enthalpy transport between all interconnected subchannels. The turbulent thermal mixing w' is analogous to eddy diffusion and is defined through empirical correlations [1, 2]. The third term accounts for thermal energy carried by the diversion crossflow. This is a convective term that requires a selection of the enthalpy h^* to be carried by the diversion crossflow. The first term on the left side of equation (2) gives the transient contribution to the spatial rate of enthalpy change. This is a convective term with a transport velocity u''. Since u'' represents the effective velocity for energy transport, the time duration of a transient is related to this velocity. Sonic velocity propagation is ignored by the absence of a $\partial p/\partial t$ term.

The right side of the axial momentum equation

$$\frac{\partial m_i}{\partial t} - 2u_i\frac{\partial \rho_i}{\partial t} + \frac{\partial p_i}{\partial x} = -\left(\frac{m_i}{A_i}\right)^2\left[\frac{v_i f_i \phi_i}{2D_i} + A_i\frac{\partial}{\partial x}\left(\frac{v_i'}{A_i}\right)\right] - \rho_i g\cos\theta - \frac{f_T}{A_i}(u_i - u_j)w_{ij}' + \frac{1}{A_i}(2u_i - u_{ij}^*)w_{ij} \tag{3}$$

Nomenclature

A = cross-sectional area, (L^2)*
C = crossflow resistance, (FT/ML)
D = hydraulic diameter, $4A/P_w$, (L)
f = friction factor based on all-liquid flow, (dimensionless)
f_T = turbulent momentum factor, (dimensionless)
g_c = gravitational constant, (ML-/FT^2)
h = enthalpy, $Xh_g + (1 - X)h_f$, (H/M)
h^* = enthalpy carried by diversion crossflow, (H/M)
$[\Delta h]$ = enthalpy matrix, $\Delta h_k = h_{i(k)} - h_{j(k)}$, (H/M)
m = flow rate, (M/T)
p = pressure, (F/L^2)
P_w = wetted perimeter, (L)
q' = heat addition per unit length, (H/LT)
Q = specific power-to-flow ratio, q'/m, (H/ML)
s = rod spacing, (L)
$[S]$ = matrix transformation, (dimensionless)
u = effective momentum velocity, $u = mv'/A$, (L/T)
u'' = effective energy transport velocity, $u'' = 1/\{A\rho/m[\rho''/\rho + h/\rho\partial(\rho'' - \rho)/\partial h]\}$, (L/T)
u^* = effective velocity carried by diversion crossflow, (L/T)
$[\Delta u]$ = velocity matrix, $\Delta u_k = u_{i(k)} - u_{j(k)}$, (L/T)
v = liquid specific volume, (L^3/M)
v' = effective specific volume for momentum, $(1 - X)^2/\rho_f(1 - \alpha) + X^2/\rho_g\alpha$, ($L^3/M$)
w = diversion crossflow between adjacent subchannels, (M/TL)
w' = turbulent (fluctuating) crossflow between adjacent subchannels, (M/TL)
x = distance, (L)
X = quality, $m_g/(m_g + m_f)$, (dimensionless)
α = void fraction, $A_g/(A_g + A_f)$, (dimensionless)
θ = orientation of channel with respect to vertical, (radians)
ρ = density, $\rho_g\alpha + \rho_f(1 - \alpha)$, ($M/L^3$)
ρ'' = effective density for enthalpy transport, $\rho'' = (\rho_g h_g\alpha - \rho_f h_f(1 - \alpha))/h$, ($M/L^3$)
ϕ = two-phase friction multiplier, (dimensionless)

Subscripts

f, g = saturated conditions for liquid and vapor, respectively
i, j = subchannel identification number
ij, ji = double subscripts imply subchannel connection i to j and j to i, respectively
$i(k), j(k)$ = subchannel pair for connection number (k)
k = subchannel connection number

* Dimensions are denoted by: L = length, T = time, M = mass, θ = temperature, F = ML/T^2 = force, and H = ML^2/T^2 = energy.

contains several terms that govern the axial pressure gradient. Without the crossflow terms, these are the frictional, spatial acceleration, and elevation components of pressure gradient. The turbulent crossflow term tends to equalize the velocities of adjacent subchannels. This is analogous to turbulent stresses in turbulent flow. The factor f_T is included to help account for the imperfect analogy between the turbulent transport of enthalpy and momentum. The diversion crossflow term accounts for changes in subchannel velocity. The first two terms on the left side of equation (3) are the transient components of the axial pressure gradient. The first is caused by the time rate of flow change (temporal acceleration), and the second is caused by the time rate of density change.

With the assumed absence of the transverse acceleration terms, the transverse momentum equation is written as the linearized equation

$$C_{ij}w_{ij} = p_i - p_j \tag{4}$$

where C_{ij} is a crossflow resistance function. Flow-squared pressure losses can be included by letting C depend upon the absolute value of diversion crossflow. The resistance function C must be evaluated empirically at the present time.

An equation of state of the form

$$\rho_i = \rho(h_i, p^*, m_i, x, t) \tag{5}$$

is required to satisfy the second assumption. This equation can be obtained by using the definition for two-phase density together with a correlation for void fraction.

Equations (1)–(4) can be solved for the subchannel flow, enthalpy, pressure, and diversion crossflow. To do this, all other quantities must be specified. Some of these must be specified by assumption because of an incomplete knowledge of steady-state and transient two-phase flow in bundles. For example, h^* and u^* are commonly assumed to be their respective values from the donor subchannels. Other selections of u^* and h^* may be made [7] to account for the nonuniform enthalpy distribution in a subchannel. This usually requires information about the liquid- and vapor-phase distribution. The factor f_T is also unknown, but its effect is usually very weak in the range from one to zero [2]. A value of one implies perfect analogy between eddy diffusivity of heat and momentum. Computations over this range show that f_T can be safely set equal to zero for most problems. Crossflow resistance is also a rather insensitive parameter, but it has an important effect on the numerical solution, as will be discussed later. Changing the crossflow resistance by an order of magnitude in the parameter range of nuclear fuel bundles usually has a negligible effect on the flow solution [2]. The correlations required for calculating the pressure gradient are of major importance. This includes the correlations for friction factor, subcooled void fraction, bulk void fraction, and two-phase friction multiplier. Fortunately, correlations of these effects developed for simple channels may be applied to rod-bundle subchannels for steady state with reasonably good results. Since their accuracy is questionable for high-speed transients, additional experimental work is needed in this area. Turbulent mixing must also be specified from empirical correlations or data. At the present time a definitive correlation for mixing does not exist for all bundle geometries and all flow conditions. Some progress has been made to describe mixing for single [1] and two-phase flow [7–9]; however, very little is known about two-phase mixing processes during transients.

Generalized Form of the Equations. A large number of equations must be considered to perform a solution of the previous set of partial differential equations. Since they become cumbersome for a large bundle, it is convenient to use a vector form where a matrix transformation is used to properly order the crossflows and pressures. This transformation is set up by using the following conventions. Each subchannel is given a number in an arbitrary sequential order as shown in Fig. 1. Next, the gap-connection numbers are assigned in ascending order by considering subchannel (i) and then assigning connection numbers for each successively connected subchannel (j), where j is greater than i. By starting with subchannel (i), each connected subchannel pair is given a unique connection number. The order is recorded by using two column vectors $i(k)$ and $j(k)$. These vectors identify the channels i and j corresponding to each k as shown in the following table for the subchannel layout shown in Fig. 1.

Gap connection number	Subchannel pair corresponding to connection number	
k	$i(k)$	$j(k)$
1	1	2
2	2	3
3	2	4
4	3	5
5	4	5
6	5	6

The above notation allows the crossflows to be designated by w_k, where k implies the subchannel pair $i(k)$, $j(k)$. For $w_k > 0$, the crossflow is chosen to be from subchannel (i) to subchannel (j) where i is less than j.

The basic matrix transformation is set up to satisfy the transverse momentum equation

$$\{Cw\} = [S]\{p\} \tag{6}$$

where $[S]$ is a rectangular matrix transformation and $\{\ \}$ denotes a column vector. For the previous example, the matrix $[S]$ is given by

$$[S] = \begin{bmatrix} 1 & -1 & 0 & 0 & 0 & 0 \\ 0 & 1 & -1 & 0 & 0 & 0 \\ 0 & 1 & 0 & -1 & 0 & 0 \\ 0 & 0 & 1 & 0 & -1 & 0 \\ 0 & 0 & 0 & 1 & -1 & 0 \\ 0 & 0 & 0 & 0 & 1 & -1 \end{bmatrix} \tag{7}$$

Generally, $S_{ki} = 0$, except $S_{ki} = 1$ if $i = i(k)$ and $S_{ki} = -1$ if $i = j(k)$. The transpose of $[S]$ can be shown to properly order the crossflows in the transport equations; therefore equation (1) can be written as

$$\left\{A\frac{\partial \rho}{\partial t}\right\} + \left\{\frac{\partial m}{\partial x}\right\} = -[S]^T\{w\} \tag{8}$$

The energy equation (2) can be written as

$$\left\{\frac{1}{u''}\frac{\partial h}{\partial t}\right\} + \left\{\frac{\partial h}{\partial x}\right\} = \{Q\} - \left[\frac{1}{m}\right][S]^T[\Delta h]\{w'\} + \left[\frac{1}{m}\right]\left[[h][S]^T - [S]^T[h^*]\right]\{w\} \tag{9}$$

In this paper, h^* is assumed to be the enthalpy of the donor subchannel.

The axial momentum equation can be written as

$$\left\{\frac{1}{A}\frac{\partial m}{\partial t}\right\} - \left\{2u\frac{\partial \rho}{\partial t}\right\} + \left\{\frac{\partial p}{\partial x}\right\} = -\{a\} - \left[\frac{1}{A}\right][S]^T[\Delta u]\{f_T w'\} + \left[\frac{1}{A}\right]\left[[2u][S]^T - [S]^T[u^*]\right]\{w\} \tag{10}$$

where

$$\{a\} = \left\{\left(\frac{m}{A}\right)^2\left(\frac{vf\phi}{2D} + A\frac{\partial}{\partial x}\left(\frac{v'}{A}\right)\right) - \rho g\cos\theta\right\} \tag{11}$$

In this paper, u^* is assumed to be the average velocity of the two adjacent subchannels. This choice is as reasonable as and possibly better than selecting u^* to be the velocity of the donor subchannel, since it eliminates a discontinuity when the diversion crossflow changes direction.

Method of Solution

The previous equations are solved as a boundary-value problem by using a semiexplicit finite-difference scheme. The boundary conditions selected for the problem are the inlet enthalpy, inlet flow, and exit pressure. Solving the problem this way is an improvement over the many types of initial-value solutions that are used in present subchannel analysis computer programs. While the use of the initial-value solution can be justified as an approximation to the boundary-value solution [10] if the crossflow resistance is small, it restricts the solutions to a limited class of problems.

The boundary-value problem presented here is limited to the case where the inlet flow can be specified as a function of time. The more difficult alternate boundary condition of allowing the inlet flow to vary as a function of imposed inlet and exit pressure is the objective of continuing work and is not considered here. In either case, a system analysis is required to provide the boundary conditions to the bundle analysis.

Formulating the Problem. It is most convenient to work with equations for enthalpy, flow, and diversion crossflow. Pressure can easily be eliminated explicitly from the problem by differentiating equation (6) and substituting equation (10). The result is

$$\left\{\frac{\partial}{\partial x}(Cw)\right\} = -[S]\{a'\} + [S]\left[\frac{1}{A}\right][[2u][S]^T - [S]^T[u^*]]\{w\} - [S]\left\{\frac{1}{A}\frac{\partial m}{\partial t}\right\} + [S]\left\{2u\frac{\partial \rho}{\partial t}\right\} \quad (12)$$

where

$$\{a'\} = \{a\} + \left[\frac{1}{A}\right][S]^T[\Delta u]\{f_T w'\} \quad (13)$$

Equations (8), (9), and (12) are the equations used to perform the numerical solution. Note that $\partial\rho/\partial t$ is calculated from $\partial h/\partial t$ by using equation (5) at a selected reference pressure p^*. This leaves two time derivatives and three spatial derivatives that require the appropriate initial and boundary conditions. There is no time derivative for the diversion crossflow; therefore it is determined from the boundary conditions. The boundary conditions selected for the spatial derivatives are the inlet flow $\{m(0, t)\}$, inlet enthalpy $\{h(0, t)\}$, and exit diversion crossflow $\{w(L, t)\}$. It is presently assumed that $\{w(L, t)\} = 0$, which implies uniform bundle exit pressure. The steady solution using these boundary conditions at $t = 0$ give the initial conditions of $\{h(x, 0)\}$ and $\{m(x, 0)\}$ that correspond to the two time derivatives of the problem.

Numerical Solution. First-order finite-difference equations are used to approximate equations (8), (9), and (12). These difference equations are presented in the order they are used in the computations to show the numerical procedures.

The combined momentum equation (12) is approximated by the equation

$$\left\{\frac{C(x+\Delta x)w(x+\Delta x) - C(x)w(x)}{\Delta x}\right\} = -[S]\{a'(x)\} + [S]\left[\frac{1}{A(x)}\right][[2u(x)][S]^T - [S]^T[u^*(x)]]\{w(x)\} - [S]\left\{\frac{m(x) - \bar{m}(x)}{A(x)\Delta t}\right\} + [S]\left\{2u(x)\frac{\rho(x) - \bar{\rho}(x)}{\Delta t}\right\} \quad (14)$$

where the overscore bar indicates previous time t and all other quantities are at new time $t + \Delta t$. This can be arranged into a set of simultaneous equations of the form

$$[M]\{w(x)\} = \{b\} \quad (15)$$

where

$$[M] = -[S]\left[\frac{1}{A(x)}\right][[2u(x)][S]^T - [S]^T[u^*(x)]] - \left[\frac{C(x)}{\Delta x}\right] \quad (16)$$

and

$$\{b\} = -[S]\{a'\} - [S]\left\{\frac{m(x) - \bar{m}(x)}{A(x)\Delta t}\right\} + [S]\left\{2u(x)\frac{\rho(x) - \bar{\rho}(x)}{\Delta t}\right\} - \left\{\frac{C(x+\Delta x)\,w(x+\Delta x)}{\Delta x}\right\} \quad (17)$$

Since the values of $\{C(x + \Delta x)\}$ and $\{w(x + \Delta x)\}$ are not known in equation (20), iteration is used to sweep through the channel to solve for $\{w(x)\}$ in terms of the previous iterate values. In most cases only a few (or even one) iteration is required for the solution to converge to within some specified value of crossflow change per iteration. This difference scheme is also used for steady-state calculations where Δt is set equal to a large value. To eliminate the problem of crossflow changing too rapidly, the newly calculated value of crossflow is modified by

$$\{w(x)\} = \delta\{w(x)\}_{\text{new}} + (1 - \delta)\{w(x)\}_{\text{old}} \quad (18)$$

where, for many problems, $\delta = 1$ is sufficient. This is only used for the steady-state calculations.

For both the steady-state and transient analysis, the calculation of diversion crossflow requires solving a set of K simultaneous equations and K unknowns. A solution is possible if $[M]$ is not singular. It should be noted that $[M]$ is the matrix $-[S][1/A][[2u][S]^T - [S]^T[u^*]]$ but with its diagonal elements modified by adding the diagonal matrix $-[C/\Delta x]$. For any rod-bundle problem that has one or more flow paths around a fuel rod (or any transverse flow loop) the matrix $[M]$ is singular without the added diagonal term $-[C/\Delta x]$. Physically, the addition of this term means that the summation of pressure drops around any transverse flow loop must be zero. For many rod bundles these added diagonal elements are small as compared to the other nonzero elements of $[M]$; therefore $[M]$ can be close to singular. Fortunately, there is control over this by selecting a sufficiently small step size for a given crossflow resistance.

The continuity equation (8) is approximated by the difference equation

$$\left\{A(x)\frac{\rho(x) - \bar{\rho}(x)}{\Delta t}\right\} + \left\{\frac{m(x+\Delta x) - m(x)}{\Delta x}\right\} = [S]^T\{w(x)\} \quad (19)$$

All quantities are known in this equation except for $\{m(x + \Delta x)\}$, which can be solved by simply rearranging the difference equation. Since time dependence is lost for large Δt, equation (19) becomes the difference equation used for steady-state calculations.

The energy equation (9) is approximated by the finite-difference equation

$$\left\{\frac{h(x+\Delta x) - \bar{h}(x+\Delta x)}{u''(x)\Delta t}\right\} + \left\{\frac{h(x+\Delta x) - h(x)}{\Delta x}\right\} = \{Q(x)\} - \left[\frac{1}{m(x)}\right][S]^T[\Delta h(x)]\{w'(x)\} - \left[\frac{1}{m(x)}\right][[h(x)][S]^T - [S]^T[h^*(x)]]\{w(x)\} \quad (20)$$

This equation can be solved $\{h(x + \Delta x)\}$ by simply rearranging the equation. When the velocity u'' is positive, this different scheme is stable. If the grid point (x, t) is exchanged with $(x, t + \Delta t)$ or $(x + \Delta x, t)$, then stability limitations [11] are en-

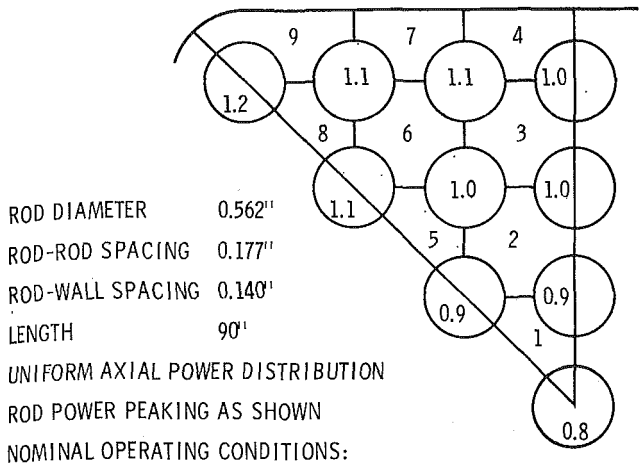

Fig. 2 Subchannel selection for a 7 × 7 rod bundle

countered that are related to the transit time through the distance Δx. For very large Δt, the above finite-difference equation reduces to the equation used for the steady-state solutions.

The above equations do not require detailed pressure information, since pressure is eliminated explicitly in the combined momentum equation. The calculation of pressure is, therefore, only a back calculation. It is calculated from a difference equation which is compatible with the combined momentum equation. The difference approximation to equation (10) is

$$\left\{\frac{m(x)-\bar{m}(x)}{A(x)\Delta t}\right\}-\left\{2u(x)\,\frac{\rho(x)-\bar{\rho}(x)}{\Delta t}\right\}+\left\{\frac{p(x+\Delta x)-p(x)}{\Delta x}\right\}$$

$$=-\{a'\}+\left[\frac{1}{A(x)}\right][[2u(x)][S]^T-[S]^T[u^*(x)]]\{w(x)\} \quad (21)$$

With the exit boundary condition of $p(L)$ given, this equation can be solved directly for $p(L-\Delta x)$ because all data are known for the calculation. The calculation moves backward until the inlet pressure $\{p(0)\}$ is calculated. Since this is just a back calculation which only adds the subchannel pressure drop to the exit pressure, computing time is saved by calculating the pressure drop in the forward direction as the required functions are computed for the flow diversion solution. When the exit is reached, the pressures are corrected to agree with the exit reference pressure.

In summary, the numerical solutions for both steady state and transients are performed in the following way. At the beginning of each node, $\{w(x)\}$ is calculated by using data at the initial

Table 1 Input parameters for sample problems

Water thermodynamic properties	1967 ASME tables
Subchannel friction factor	$f = 0.186R_e^{-0.2}$
Subcooled voids	not included
Void fraction*	$\alpha = Xv_g/[(1-X)v_f + Xv_g]$
Two-phase multiplier*	$\phi = \rho_f/\rho$
Two-phase density*	$\rho = \rho'' = \alpha\rho_g + (1-\alpha)\rho_f$
Two-phase specific volume*	$v' = 1/\rho$
Axial heat flux	uniform
Momentum turbulent factor	$f_T = 0$
Crossflow resistance	$C = 1.0$
Number of axial nodes	30
Time duration of transients	1.0 sec
Number of time steps	20
Turbulent mixing parameter	$\beta = \frac{w'}{sD} = 0.002$

* Homogeneous two-phase flow correlations.

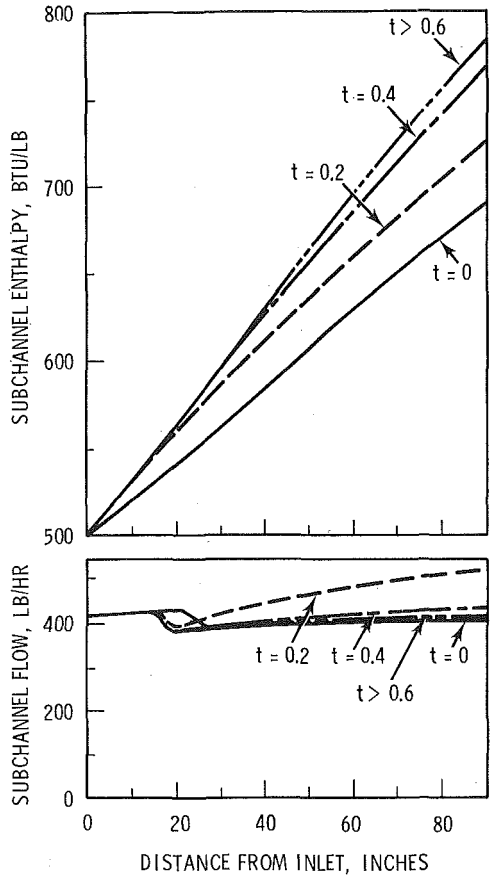

Fig. 3 Subchannel 8 enthalpy and flow following a 50 percent step increase in heat flux

condition, previous time, or previous iteration. The calculation moves forward to $x + \Delta x$ by calculating $\{h(x+\Delta x)\}$, $\{m(x+\Delta x)\}$, and $\{p(x+\Delta x)\}$. This continues until the exit is reached. Then all $\{p(x)\}$ at $t + \Delta t$ are corrected to the exit reference pressure. The calculation sweeps through the channel for another iteration until convergence is achieved as defined by $|w(x) - w_{\text{old}}(x)| < w_{\text{error}}$ for all crossflows $w(x)$. Upon completion of iteration, the converged solution becomes the initial starting point for the next time step. For computations where the crossflow resistance is small, the downstream value of $\{C(x+\Delta x)w(x+\Delta x)\}$ has little influence on the solution, and it is possible to advance to new time without performing successive iterations. Calculational experience has shown that solutions obtained by taking one step to new time and using $\{w(x+\Delta x)\}$ at previous time produce results very close to those obtained by iteration. The second iteration usually achieves convergence in these cases with only minor correction to the first iteration. This procedure should be used with caution, however, because the difference scheme becomes conditionally consistent and might not achieve proper convergence under some circumstances [12].

The previously described method of solution using iteration provides a boundary-value solution that lets downstream flow disturbances be felt upstream. The magnitude of this distance upstream is governed by the crossflow resistance. As previously mentioned, crossflow resistance is a rather weak parameter for most rod bundles; therefore, flow disturbances are only felt a node, or two, upstream in the present model. An additional crossflow momentum term due to "axial inertia," which is not included in this model, would provide higher local resistance, but its effect would decay rapidly with distance from the flow disturbance. This effect can be bounded by choosing a sufficiently large value for C. Although experimental data for an accurate bound is meager, the choice of C is not critical. Additional experimental data would be of value.

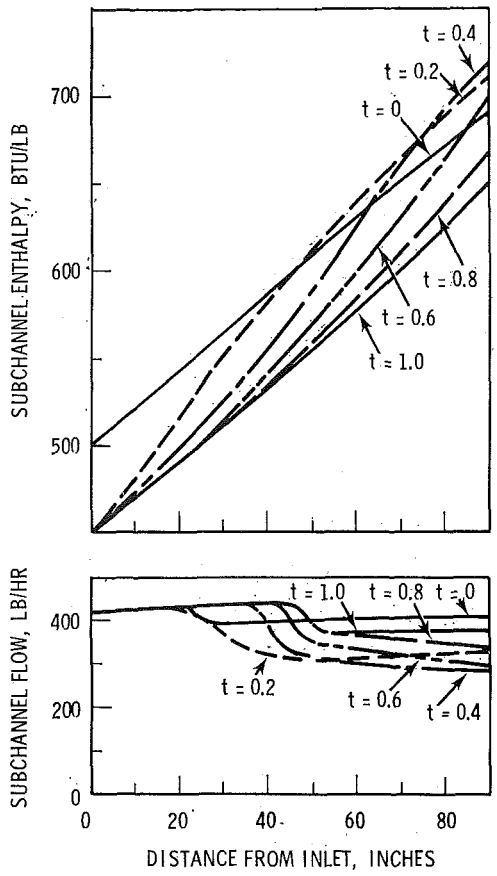

Fig. 4 Subchannel 8 enthalpy and flow following a 50-Btu/lb step decrease in inlet enthalpy

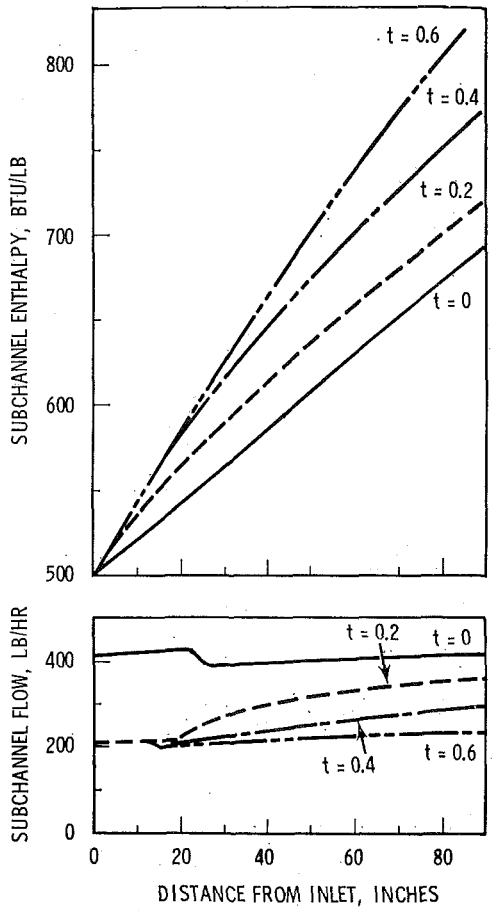

Fig. 5 Subchannel 8 enthalpy and flow following a reduction to one-half flow in 0.1 sec

Sample Problems

To illustrate the features of the transient boundary-value flow solution, the results of several sample calculations are presented for a 49-rod bundle. The input parameters are shown in Table 1.

A $^1/_8$ section of symmetry is used for this bundle. The bundle's size is typical of boiling-water reactor geometry as shown in Fig. 2. The results of three transient calculations are shown in Figs. 3–5. Each of them represents a perturbation on the operating conditions. The data are presented for subchannel 8, which is the hottest.

Figure 3 shows the results of a 50 percent step increase in heat flux. The duration of the flow transient is approximately 0.6 sec, which is the approximate transit time through the bundle. This transit time is directly related to the characteristic velocity in the energy equation (2). During the initial part of the transient, the flow rate increases toward the exit of the bundle. This is caused by expulsion of fluid as the channel average void fraction increases. At the end of the transient, the point of boiling moves to a point farther upstream to correspond to the higher power. The inlet flow does not change because it is a fixed boundary condition.

Figure 4 shows the effect of a step reduction of inlet enthalpy by 50 Btu/lb. The results are rather interesting since they show a significant decrease in exit flow rate that is caused by the collapse of voids in the bundle. Note that the transient is still not complete at 1 sec because the transit time through the bundle is higher due to lower average coolant velocity.

Figure 5 shows a flow reduction to one-half flow in 0.1 sec. The results show that exit flow tends to remain high for a short time following the inlet reduction. This is caused by the void growth, which causes expulsion out the exit of the bundle. This transient is nearly finished in 0.6 sec even though the inlet velocity is reduced to one-half. The transit time through the bundle is not reduced this much because the average void fraction is increasing, which helps maintain the original average velocity.

Conclusions

The previous calculations demonstrate the ability of the mathematical model and its numerical solution to give flow and enthalpy solutions in rod bundles under boiling transient conditions. The numerical solution is a boundary-value solution that allows downstream flow disturbances to be felt upstream. This effect has not been previously considered in other subchannel analyses that use initial-value flow solutions.

Experimental work is needed to verify the mathematical model and to develop empirical input data. Some of the input parameters have a weak effect for many analysis problems; however, transient correlations for two-phase flow and heat transfer are expected to be especially important for meaningful transient analysis.

References

1 Rogers, J. T., and Todreas, N. E., "Coolant Interchannel Mixing in Reactor Fuel Rod Bundles, Single Phase Coolants," *Heat Transfer in Rod Bundles*, ASME, New York, N. Y., 1968, pp. 1–56.

2 Rowe, D. S., "Crossflow Mixing between Parallel Flow Channels during Boiling, Part 1, COBRA—Computer Program for Coolant Boiling in Rod Arrays," BNWL-371, Pt 1, Mar. 1967.

3 Bowring, R. W., "HAMBO, A Computer Programme for the Subchannel Analysis of the Hydraulic and Burnout Characteristics of Rod Clusters, Part 1, General Description," AEEW-R524, 1967.

4 St. Pierre, C. C., "SASS Code 1, Subchannel Analysis for the Steady State," AECL-APPE-41, 1966.

5 Rowe, D. S., "COBRA-II, A Digital Computer Program for Thermal Hydraulic Subchannel Analysis of Rod Bundle Nuclear Fuel Elements," BNWL-1229, Feb. 1970.

6 Meyer, J. E., "Conservation Laws in One-Dimensional Hydro-

dynamics," WAPD-BT-20, Westinghouse Electric Corp., Bettis Atomic Power Laboratory, Pittsburgh, Pa., Sept. 1960, pp. 61–72.

7 Lahey, R. T., Jr., Shiralkar, B. S., and Radcliffe, D. W., "Mass Flux and Enthalpy Distribution in a Rod Bundle for Single- and Two-Phase Flow Conditions," JOURNAL OF HEAT TRANSFER, TRANS. ASME, Series C, Vol. 93, No. 2, May 1971, pp. 197–209.

8 Rowe, D. S., "A Thermal–Hydraulic Subchannel Analysis for Rod Bundle Nuclear Fuel Elements," Paper No. FC-13, 4th International Heat Transfer Conference, Versailles, France, 1970.

9 Casterline, J. E., and Castellana, F. S., "Flow and Enthalpy Redistribution in a Simulated Nuclear Fuel Assembly," CU-187-2, Feb. 1969.

10 Rowe, D. S., "Initial- and Boundary-Value Flow Solutions during Boiling in Two Interconnected Parallel Channels," *American Nuclear Society Transactions*, Vol. 12, No. 2, Nov. 1969, pp. 834–835.

11 Forsythe, F. E., and Wasow, W. R., *Finite-Difference Methods for Partial Differential Equations*, John Wiley & Sons, New York, N. Y. 1960.

12 Isaacson and Keller, *Analysis of Numerical Methods*, Wiley, 1966, p. 516.

E. K. LEVY
Associate Professor.
Assoc. Mem. ASME

S. F. CHOU
Research Assistant.

Department of Mechanical Engineering and Mechanics, Lehigh University, Bethlehem, Pa.

The Sonic Limit in Sodium Heat Pipes

The results of an analytical study of the vapor dissociation–recombination and homogeneous vapor condensation phenomena in sodium heat pipes are described. It is shown that neither the dissociation–recombination reaction nor the vapor condensation process has a large influence on the sonic-limit heat transfer rate. The single most important factor is shown to be the wall shear stress in the heat-pipe vapor passage. The friction effects control the location of the sonic point, determine if the flow in the condenser section will be subsonic or supersonic, and decrease the sonic-limit heat transfer rate to values which can be substantially lower than those which are predicted from inviscid analyses.

Introduction

Gas dynamic choking of the flow in the vapor passage of a heat pipe can place a limitation on the maximum rate of heat transfer. Known as the sonic limit, this phenomenon has been observed experimentally [1–4].[1] In addition, several analytical studies of the sonic limit in which the vapor flow was assumed to be one-dimensional have been published [5–7]. These include analyses of the frictionless flow of a pure monatomic perfect gas in the heat-pipe vapor passage [5, 6] and an analysis in which the fluid in the vapor passage was assumed to be a mixture of liquid and monatomic vapor in phase equilibrium [6]. The possibility that the vapor dissociation–recombination reaction $2Na \rightleftarrows Na_2$ could influence the performance of a sodium heat pipe was raised by [2], after which an analysis treating the vapor as a two-component mixture of Na and Na_2 in chemical equilibrium but frozen with respect to liquid–vapor phase change was reported [7]. Finally, a two-dimensional perfect-gas analysis of the vapor flow patterns in the sonic regime has been published [8].

Some of the factors which remain unaccounted for in the sonic-limit performance of sodium heat pipes are: (1) the vapor dissociation–recombination reaction, (2) the problem of the homogeneous nucleation and growth of liquid droplets in the supersaturated vapor stream, and (3) the influence of the condenser region on the sonic limit. The earlier analyses have treated only the limiting cases of frozen and equilibrium flows of reacting and condensing vapors. However, since the droplet nucleation process is dependent on the degree of vapor supersaturation and this in turn depends on the extent of the dissociation–recombination process, the kinetics of the chemical and droplet nucleation processes must be considered simultaneously.

This paper is the summary of an analytical investigation into the effects of the dissociation–recombination reaction and the droplet nucleation and growth processes on the behavior of the supersaturated vapor flowing in the vapor passage of a sodium heat pipe. In particular, the effects of these phenomena on the sonic-limit heat transfer rate are presented. In addition, the influence which the downstream condenser region can have on the evaporator and condenser flow and on the sonic-limit performance is discussed.

Analysis

The heat pipe considered here is a conventional axisymmetric cylindrical device with a constant-diameter cylindrical vapor passage surrounded by an annular wick. The flow in the vapor portion of the evaporator region can be thought of as a flow in a porous duct with mass injection (evaporation) at the walls. Similarly, the flow in the condenser can be thought of as a porous duct flow with mass suction at the walls. The analogy between the axial flow of vapor in the evaporator, adiabatic, and condenser regions of a heat pipe and the flow of gas through a convergent–divergent nozzle is well documented [5, 7, 9].

Assuming the flow in the vapor passage is steady and one-dimensional and the fluid is a homogeneous mixture of monatomic and diatomic sodium vapor and droplets of liquid sodium, conservation of mass in the vapor passage requires

$$A\frac{d}{dx}(\rho V) = \pm\dot{m}_E \tag{1}$$

$$\frac{d\dot{m}_{V1}}{dx} = \pm\dot{m}_{E1} + A\hat{M}_1\left(\frac{d[\mathrm{Na}]}{dt}\right)_{cr} - \alpha\left(\frac{d\dot{m}_L}{dx}\right)_{\mathrm{cond}} \tag{2}$$

and

$$\frac{d\dot{m}_L}{dx} = \left(\frac{d\dot{m}_L}{dx}\right)_{\mathrm{cond}} \tag{3}$$

where x is the axial distance in the vapor passage measured from the upstream end of the evaporator. Conservation of momentum can be expressed as

[1] Numbers in brackets designate References at end of paper.

Contributed by the Heat Transfer Division and presented at the Winter Annual Meeting, Washington, D. C., November 28–December 2, 1971, of The American Society of Mechanical Engineers. Manuscript received by the Heat Transfer Division July 26, 1971; revised manuscript received March 15, 1972. Paper No. 71-WA/HT-11.

$$\frac{d}{dx}(\rho V^2) = -\frac{dP}{dx} - \frac{4\tau_\omega}{D} \tag{4}$$

and conservation of energy becomes

$$A\frac{d}{dx}\left[\dot{m}\left(h + \frac{V^2}{2}\right)\right] = \pm\dot{m}_E\left(h_E + \frac{V_E{}^2}{2}\right) + Q_{\text{conv}} \tag{5}$$

The plus sign is for injection (evaporator) and the minus sign for suction (condenser). The total heat transfer rate per unit length Q_E to the outside wall of the heat pipe is

$$Q_E = Q_{\text{conv}} \pm \dot{m}_E h_{fg} \tag{6}$$

and is positive in the evaporator, negative in the condenser, and zero in the adiabatic region.

Assuming the monatomic and diatomic species are perfect gases, the density of the mixture of diatomic vapor, monatomic vapor, and liquid can be written

$$\rho = \frac{1}{\dfrac{\mu}{\rho_L} + \dfrac{(1-\mu)R_2T(1+\alpha)}{P}} \tag{7}$$

and the x-derivative of the enthalpy of the mixture becomes

$$\frac{dh}{dx} = (1-\mu)\left[\{\alpha c_{p1} + (1-\alpha)c_{p2}\}\frac{dT}{dx} - l_D\frac{d\alpha}{dx}\right] - h_{fg}\frac{d\mu}{dx} + \mu c_{pL}\frac{dT}{dx} \tag{8}$$

The rate of change in molal concentration of the sodium-vapor atoms due to the dimerization reaction

$$\text{Na} + \text{Na} \underset{k_b}{\overset{k_f}{\rightleftarrows}} \text{Na}_2$$

can be written [9]

$$\left(\frac{d[\text{Na}]}{dt}\right)_{cr} = \frac{2k_f\rho_V{}^3\alpha}{\hat{M}_1{}^3}\left\{-\alpha^2 + \frac{(1-\alpha^2)}{4K_p \cdot P}\right\} \tag{9}$$

where in the temperature range 500 to 1000 deg K the reaction rate is [10]

$$k_f = (9.5 - 0.005T) \times 10^{15} \tag{10}$$

where T has the units deg K and k_f has the units cm^6/sec-moles^2.

The process of liquid formation in the supersaturated vapor stream can be separated into two distinct steps: (1) the formation of the liquid nuclei and (2) the subsequent growth of these nuclei into relatively large liquid drops. The classical theory for the droplet nucleation rate yields [11–13]

$$J = \left(\frac{P}{kT}\right)^2\frac{\hat{M}}{\hat{N}\rho_L}\sqrt{\frac{2\sigma\hat{N}}{\pi\hat{M}}}\exp\left[-\frac{4\pi\sigma r^{*2}}{3kT}\right] \tag{11}$$

where r^*, the critical radius, is given by

$$r^* = \frac{2\sigma\hat{M}}{\rho_L RT \ln P/P_s} \tag{12}$$

and where σ is the flat-film value of surface tension. The rate of growth of a droplet of radius r can be expressed as [11]

$$\frac{dr}{dt} = \frac{1}{\sqrt{2\pi}\,\rho_L}\left[\frac{P}{\sqrt{RT}} - \frac{P_D}{\sqrt{RT_D}}\right] \tag{13}$$

where the drop temperature and pressure are approximated by $T_D = T_{\text{sat}}(P)$ and $P_D = P$. Finally, the rate at which liquid is condensed can be written [11]

$$\left(\frac{d\dot{m}_L}{dx}\right)_{\text{cond}} = \int_0^x 4\pi\rho_L\left[r_1{}^* + \int_{x_1}^x \frac{1}{V}\frac{dr}{dt}\,dx_2\right]^2 \times\left[\frac{d}{dx}\int\frac{1}{V}\frac{dr}{dt}\,dx_2\right]A_1J_1dx_1 + \frac{4}{3}\pi r^{*3}AJ \tag{14}$$

Nomenclature

A = cross-sectional area of vapor passage
c_p = constant-pressure specific heat
c_{p1} = specific heat of monatomic vapor
c_{p2} = specific heat of diatomic vapor
c_{pL} = liquid specific heat
D = diameter of vapor passage
f = friction factor
h = enthalpy
h_{fg} = enthalpy of evaporation
h_1 = enthalpy of monatomic vapor
h_2 = enthalpy of diatomic vapor
$\hat{h}$ = convection heat transfer coefficient
J = critical droplet nucleation rate
k_f = reaction rate
K_p = equilibrium constant
K_T = thermal conductivity
l_D = enthalpy of dimerization, $l_D = h_2 - h_1$
$\dot{m}_E$ = rate of mass injection or suction per unit length
$\dot{m}_{E1}$ = rate of monatomic mass injection or suction per unit length
$\dot{m}_{E2}$ = rate of diatomic mass injection or suction per unit length
$\dot{m}_L$ = liquid flow rate
$\dot{m}_V$ = vapor flow rate, $\dot{m}_V = \dot{m}_{V1} + \dot{m}_{V2}$
$\dot{m}_{V1}$ = monatomic vapor flow rate
$\dot{m}_{V2}$ = diatomic vapor flow rate
$\hat{M}_1$ = molecular weight of monatomic sodium
$\hat{N}$ = Avogadro's number
P = static pressure
P_s, P_{sat} = saturation pressure
Pr = Prandtl number
Q_E = heat transfer to outside wall of heat pipe per unit length
Q_{conv} = heat transfer from liquid–vapor interface to vapor by convection
R = gas constant
R_2 = gas constant of diatomic sodium
Re_D = Reynolds number, $\text{Re}_D = VD/\nu$
T = temperature of vapor
T_E = temperature of liquid–vapor interface
T_{sat} = saturation temperature
V = axial velocity of vapor
V_E = transverse velocity of vapor at liquid–vapor interface
X = axial distance measured from upstream end of evaporator
α = degree of dissociation of vapor, $\alpha \equiv \dot{m}_{V1}/(\dot{m}_{V1} + \dot{m}_{V2})$
α_E = degree of dissociation of injected or rejected vapor, $\alpha_E \equiv \dot{m}_{E1}/(\dot{m}_{E1} + \dot{m}_{E2})$
μ = liquid-mixture mass ratio, $\mu \equiv \dot{m}_L/(\dot{m}_L + \dot{m}_V)$
ν = viscosity
ρ = density
σ = surface tension
τ_ω = wall shear stress
$\left(\frac{d[\text{Na}]}{dt}\right)_{cr}$ = rate of change in molal concentration of monatomic sodium vapor due to chemical reaction
$\left(\frac{d\dot{m}_L}{dx}\right)_{\text{cond}}$ = rate of change in flow rate of liquid sodium due to homogeneous vapor condensation

Subscripts

1 = denotes monatomic sodium
2 = denotes diatomic sodium
L = denotes liquid
V = denotes vapor
E = denotes state of injected or rejected vapor

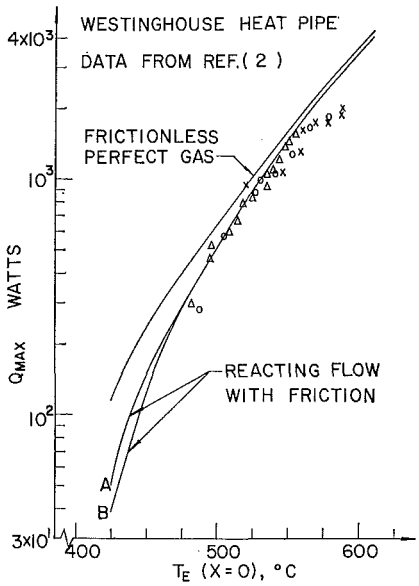

Fig. 1 Sonic-limit heat transfer rate

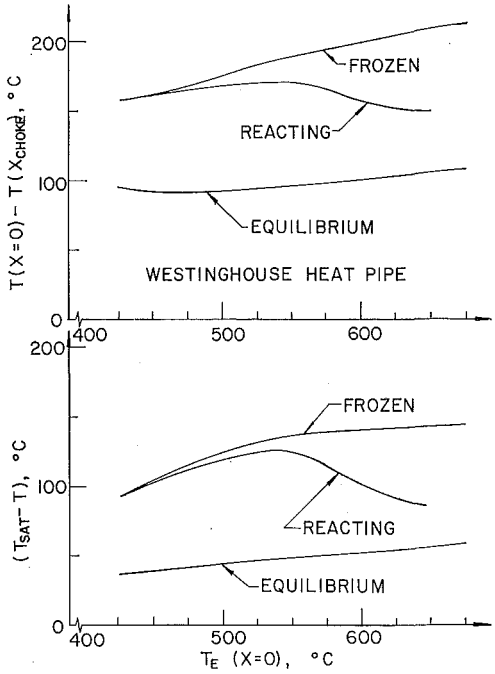

Fig. 2 Variation of axial drop in vapor temperature and vapor supersaturation at choking point

Within the evaporator region, the injected fluid is assumed to be superheated vapor with an equilibrium composition α_E corresponding to the local static pressure P and the local interface temperature T_E (equations to determine the equilibrium composition are found in [9]). The magnitude of the interfacial superheat was taken to be [14]

$$T_E = T_{\text{sat}} \pm \left[\frac{\dot{m}_E}{2\pi D}\right] \frac{(2\pi R)^{1/2} T_{\text{sat}}^{5/2} R}{P h_{fg}} \tag{15}$$

Whereas in the evaporator $T_E > T_{\text{sat}}$, in the adiabatic region the interfacial temperature is equal to the local values of saturation temperature. The temperature of the interface within the condenser region is obtained from equation (15) where the minus sign is now applicable. It is assumed that in the condenser region the rejected fluid $\dot{m}_E$ leaves the vapor passage at the local saturation temperature and pressure and that the vapor composition α_E is the same as that of the bulk vapor α. The fluid removed from the vapor passage by suction is assumed to be pure vapor; no liquid enters or leaves the vapor passage at the liquid–vapor interface. In all cases, both the evaporator mass injection rate and condenser mass suction rate were taken to be uniform over the lengths of the evaporator and condenser regions.

The relation

$$f \equiv \frac{\tau_\omega}{\frac{\rho V^2}{2}} = \frac{2\pi^2}{\text{Re}_D} \tag{16}$$

was used for all laminar shear-stress calculations in the evaporator [15] and

$$f = \frac{16}{\text{Re}_D} \tag{17}$$

for the adiabatic and condenser regions. The equation

$$f = \frac{0.079}{(\text{Re}_D)^{1/4}} \tag{18}$$

was used for all turbulent flow conditions [16] with transition assumed to occur at $\text{Re}_D = 2000$. The equation

$$\hat{h} = 3.66 \frac{K_T}{D} \tag{19}$$

was used for the laminar-flow convective heat transfer coefficient and

$$\hat{h} = 0.023 \frac{K_T}{D} (\text{Re}_D)^{0.8} (\text{Pr})^{0.3} \tag{20}$$

was taken for the turbulent flow case [17].

The thermophysical properties of sodium were obtained from [18–21]. A comprehensive review of those properties pertinent to this study is contained in [9].

Analytical Results

The equations given above can be rearranged to form a system of five simultaneous first-order ordinary differential equations that can be solved numerically for α, μ, P, T, and V as functions of x, provided Q_E is specified. These were solved by digital computer by means of a Runge–Kutta integration scheme. At the upstream end of the evaporator ($x \to 0$), the vapor Mach number is small and the incompressible equations of motion can be used to generate the initial conditions needed for the first step in the integration.

The calculations were made for two different heat pipes. One, with a 1.846-cm-dia vapor passage, a 17.8-cm-long evaporator, a 5.1-cm-long adiabatic region, and a 19.0-cm-long condenser section, corresponds to an experimental sodium heat pipe of Dzakowic et al. [2]. The second heat pipe, tested by Kemme of Los Alamos Scientific Laboratory [1], had a 1.04-cm-dia vapor passage, a 40-cm-long evaporator, a 10-cm-long adiabatic region, and a 75-cm-long condenser.

The calculations were performed in several steps to determine the relative importance of the various phenomena. The first set of results for the Westinghouse heat pipe are summarized in Figs. 1 and 2. The droplet nucleation rate J was artificially set to zero (flow frozen with respect to phase change) and the chemical reaction was alternately taken to be frozen ($k_f = 0$), in equilibrium (see [7] and [9] for a description of the equilibrium calculations) and reacting at a rate given by equation (10). In all these calculations, the evaporator heat transfer rate Q_E was adjusted until sonic flow was attained at the inlet to the condenser.

Table 1 shows the rates of heat transfer required to cause sonic vapor flow at the condenser inlet of the Westinghouse heat pipe. Over the temperature range considered, the differences between the heat transfer rates for the three cases were less than

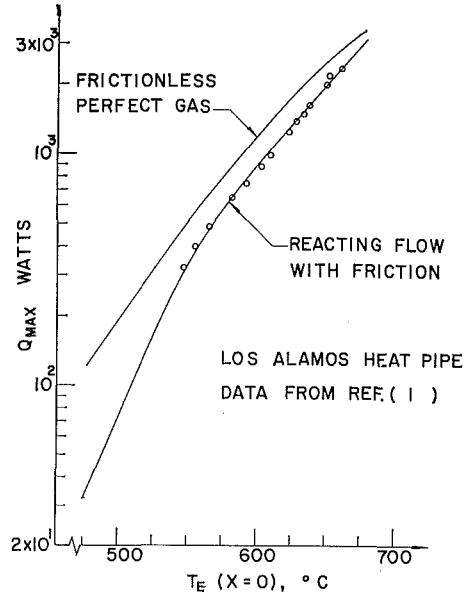

Fig. 3 Sonic-limit heat transfer rate

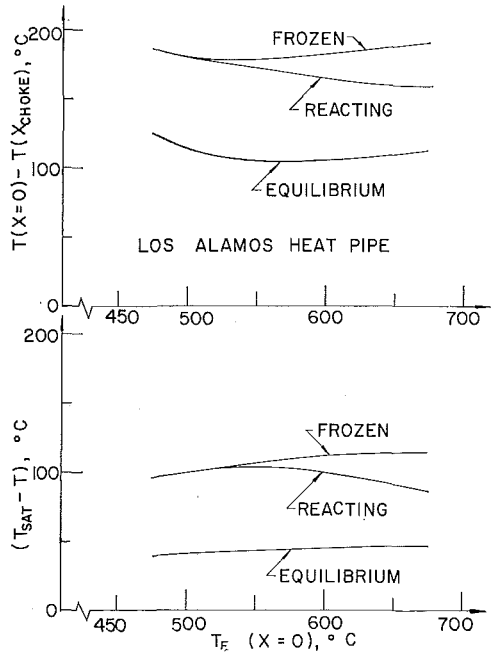

Fig. 4 Variation of axial drop in vapor temperature and vapor supersaturation at choking point

4 percent. A comparison between the experimental sonic-limit data and the reacting flow results is made in Fig. 1, curve A. Shown in Fig. 2 as a function of temperature are the vapor supersaturation at the condenser inlet and the axial drop in vapor temperature from the beginning of the evaporator to the sonic point. Similar results for the LASL heat pipe are given in Figs. 3 and 4 and in Table 1.

Table 1 Comparison of chemical rate models

T(deg C)	Westinghouse heat pipe Q_{max} (watts) frozen	reacting	equilibrium
425	50.9	50.9	50.4
550	1475	1460	1430
600	3490	3420	3360
	LASL heat pipe		
477	32.5	32.4	32
527	173	172	170
577	587	580	575

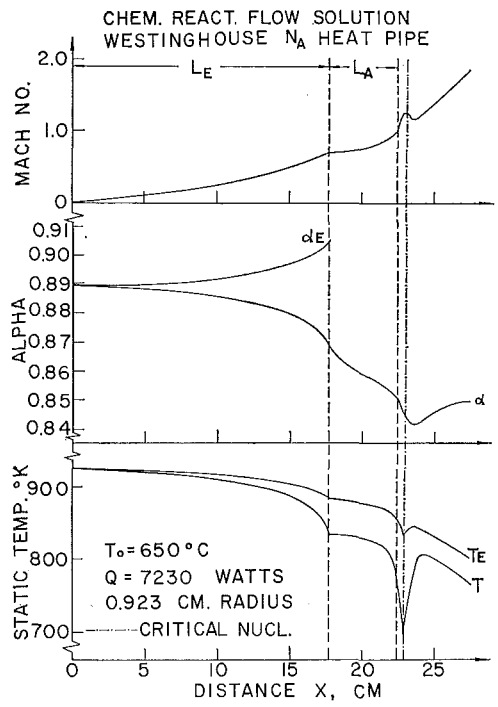

Fig. 5 Axial variation of Mach number, composition, and temperature; T_0 = 650 deg C

Although the differences in the predicted maximum rates of heat transfer are small for the three reaction-rate models, there are significant differences in the amounts of vapor supersaturation. It would appear from the calculations that in the temperature range from 500 to 700 deg C the vapor in a sodium heat pipe is in the transition regime between frozen chemical and chemical equilibrium behavior and that neither limit can be used satisfactorily to predict the vapor supersaturation or vapor temperature variations.

Using equation (11) for the droplet nucleation rate and equation (10) for the chemical reaction rate, the calculations were repeated in the evaporator and adiabatic regions and then extended into the condenser region. This was done to determine if condensation shocks are likely upstream of the choking point, if the droplet nucleation and growth processes affect the sonic-limit heat transfer rate, and if the condenser region can influence the sonic-limit heat transfer rate.

For an upstream evaporator temperature of 650 deg C (Westinghouse heat pipe), Figs. 5 and 6 show the axial variations of vapor Mach number, composition, temperature, liquid mass ratio, and droplet nucleation rate. As before, the heat transfer rate to the evaporator was adjusted to cause choking at the condenser inlet. When the calculations were extended into the condenser region with uniform wall suction, the flow underwent the same type of transition from sonic to supersonic that is encountered in a convergent–divergent nozzle. The analysis predicts the onset of a condensation shock in the condenser region at a Mach number of 1.25. Similar results were obtained in the temperature range from 475 to 650 deg C. In all cases the condensation shock occurred in the condenser region. The sonic-limit heat transfer rate was uninfluenced by the presence of the condensation shock, and the sonic-limit calculations presented in Fig. 1, curve A, are also valid here.

For temperatures below 475 deg C, using a heat addition rate large enough to cause choking at the condenser inlet, the computed vapor velocities could not be made to undergo the transition at the condenser inlet through the sonic point into the supersonic region. At these low temperatures the friction effects are large with respect to suction and prevent the mass suction from accelerating the fluid to supersonic velocities. Therefore, at these temperatures, choking cannot occur at the condenser

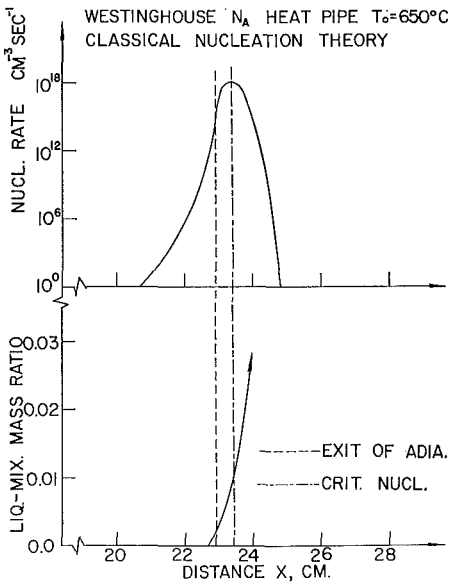

Fig. 6 Axial variation of nucleation rate and moisture content; T_0 = 650 deg C

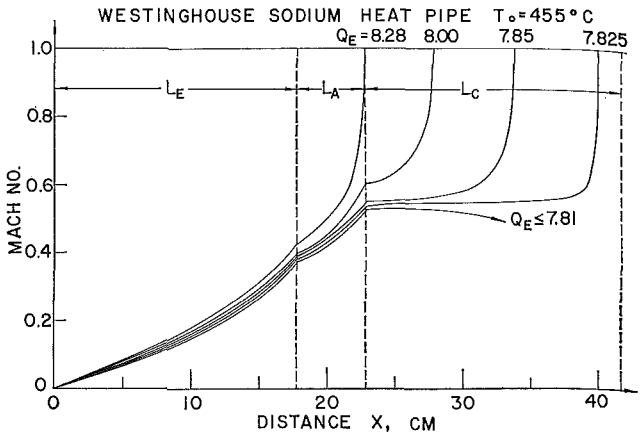

Fig. 7 Axial variation of Mach number; low-temperature operation

inlet and the flow must be subsonic throughout. The calculations were then repeated without the constraint that sonic flow occur at the condenser inlet. For a temperature of 455 deg C, the axial variations of Mach number for several assumed values of uniform evaporator heat addition rate are presented in Fig. 7 for the Westinghouse heat pipe. The maximum possible heat addition rate for this case is Q_E = 7.82 watts/cm, for which choking occurred at the downstream end of the condenser. Similar calculations performed in the range from 425 to 475 deg C are summarized in curve B in Fig. 1.

As was done with the Westinghouse heat pipe, attempts were made to extend the calculations for the LASL device into the condenser region. However, with sonic velocities at the condenser inlet and using uniform rates of suction over the 75-cm-long condenser section, these calculations also could not be made to undergo the transition to supersonic velocities in the condenser. This occurred over the entire range of operating temperatures. Because of the imposed constraint of uniform suction in such a long condenser section, the suction terms in the equations became much smaller in magnitude than the friction terms, and supersonic velocities were not possible. Only by artificially using excessively large suction rates in the vicinity of the condenser inlet could the transition to supersonic velocities be achieved. It is possible that nonuniform suction did occur in the actual experimental device; however, measurements of the axial variation of heat pipe temperature which would indicate if such nonuniformities existed are not available. It is also possible that the shear stresses used in the calculations were unreasonably large; equation (17) does not take into account the reverse-flow phenomena which have been predicted for some condenser vapor flows [15].

Discussion and Concluding Remarks

From the results described above, it appears that it does not really matter what is used for the equation of state for the sodium vapor when calculating the sonic-limit heat transfer rate. The predicted heat transfer rates varied only slightly between the limiting cases of frozen chemical and chemical equilibrium flow. With the classical theory of droplet nucleation, the amount of vapor condensed was found to be negligible upstream of the sonic point and to have a negligible influence on the sonic heat transfer rate.

The wall shear stress in the heat-pipe vapor passage has a much larger effect on the sonic limit than any of the thermophysical phenomena described in this paper. The errors obtained by ignoring friction were found to range from more than 100 percent at 425 deg C to less than 10 percent at 600 deg C in the case of the Westinghouse heat pipe [7]. The performance of the LASL heat pipe with its smaller cross-sectional area and greater length was influenced even more by friction, Figs. 1 and 3. DeMichele obtained similar results from his two-dimensional study [8]. The simplest model which therefore can be expected to yield accurate predictions of the sonic limit is that of the flow of a perfect gas that is both chemically frozen and frozen with respect to phase change in a duct with wall friction. The wall shear-stress effect appears to be the most important and when included in the perfect-gas analysis brings the analytical and experimental results into excellent agreement.

Acknowledgments

This investigation was sponsored by the U. S. Atomic Energy Commission under contract AT(30-1)-4095. The calculations were performed at the Lehigh University Computing Center. The authors are grateful to Professors A. Stenning and J. Sturm for many helpful discussions on various aspects of the study.

References

1 Kemme, J., private communication, Dec. 1969.

2 Dzakowic, G., Tang, Y., and Arcella, F., "Experimental Study of Vapor Velocity Limit in a Sodium Heat Pipe," ASME Paper No. 69-HT-21.

3 Kemme, J., "Ultimate Heat Pipe Performance," *IEEE Transactions on Electron Devices*, Vol. ED-16, No. 8, Aug. 1969, p. 717.

4 Deverall, J., "Mercury as a Heat Pipe Fluid," LASL report LA 4300 MS, Jan. 1970.

5 Deverall, J., Kemme, J., and Florschuetz, L., "Sonic Limitations and Startup Problems of Heat Pipes," LASL report LA 4518, Nov. 1970.

6 Levy, E. K., "Theoretical Investigation of Heat Pipes Operating at Low Vapor Pressures," *Journal of Engineering for Industry*, TRANS. ASME, Series B, Vol. 90, No. 4, Nov. 1968, pp. 547–552.

7 Levy, E., "Effects of Friction on the Sonic Velocity Limit in Sodium Heat Pipes," AIAA 6th Thermophysics Conference, Tullahoma, Tenn., Mar. 1971.

8 DeMichele, D., "A Numerical Solution to Axial Symmetric Compressible Flow with Mass Injection and Its Application to Heat Pipes," PhD thesis, Department of Nuclear Engineering, University of Arizona, Tucson, Ariz., 1970.

9 Levy, E., and Chou, S., "Vapor Compressibility Effects in Heat Pipes," Report NYO-4095-1, Department of Mechanical Engineering, Lehigh University, Bethlehem, Pa., May 1970.

10 Kretschmer, C., and Peterson, H., "Kinetics of Three Body Atom Recombination," *J. Chem. Physics*, Vol. 39, No. 7, 1963, p. 1772.

11 Hill, P., "Condensation of Water Vapour during Supersonic Expansion in Nozzles," *J. Fluid Mech.*, Vol. 25, Part 3, 1966, p. 593.

12 Feder, J., et al., "Homogeneous Nucleation in Condensation," in: *Progress in Astronautics and Aeronautics*, Vol. 15, Academic, New York, N. Y., 1964.

13 Feder, J., et al., "Homogeneous Nucleation and Growth of Droplets in Vapours," *Advances in Physics*, Vol. 15, Jan. 1966, p. 111.

14 Wilcox, S. J., and Rohsenow, W. M., "Film Condensation of

Potassium Using Copper Condensing Block for Precise Wall-Temperature Measurement," JOURNAL OF HEAT TRANSFER, TRANS. ASME, Series C, Vol. 92, No. 3, Aug. 1970, pp. 359–371.

15 Bankston, C. A., and Smith, H. J., "Incompressible Laminar Vapor Flow in Cylindrical Heat Pipes," ASME Paper No. 71-WA/HT-15.

16 Schlichting, H., *Boundary Layer Theory*, 4th ed., McGraw-Hill, New York, N. Y., 1960.

17 Rohsenow, W. M., and Choi, H., *Heat, Mass and Momentum Transfer*, Prentice-Hall, Englewood Cliffs, N. J., 1961.

18 Stone, J., et al., "High Temperature Properties of Sodium," NRL report 6241, Sept. 1965.

19 Benton, A., and Inatomi, T. H., "The Thermodynamic Properties of Sodium Vapor," *J. of Chemical Physics*, Vol. 20, No. 12, Dec. 1952, p. 1946.

20 Makansi, M., et al., "Thermodynamic Properties of Sodium," *Journal of Chemical and Engineering Data*, Vol. 5, No. 4, Oct. 1960, p. 441.

21 Golden, G., and Tokar, J., "Thermophysical Properties of Sodium," ANL 7323, Aug. 1967.

R. M. FAND
Mem. ASME

K. K. KESWANI

Department of Mechanical Engineering,
University of Hawaii,
Honolulu, Hawaii

Recalculation of Hilpert's Constants

In this paper, two new sets of constants are presented for use in conjunction with two empirical correlation equations that represent Hilpert's data for heat transfer from cylinders to air in crossflow.

Introduction

MANY EXPERIMENTAL STUDIES of heat transfer from cylinders to air in crossflow have been performed. However, three publications [1–3][1] contain the data generally accepted as being the most reliable in this area of investigation. The data of Hilpert [1] lie in the range $2 < R_f < 2.3 \times 10^5$; those of King [2] lie in the range $0.1 < R_f < 50$; and those of Collis and Williams [3] lie in the range $0.01 < R_f < 140$. For Reynolds numbers greater than 40, all three sets of data are in close agreement. For Reynolds numbers less than 40, there is some divergence, and in this region the data of Collis and Williams are widely regarded as being the most accurate.

The data referenced above have been correlated by subdividing the overall range of the Reynolds number into five or six subintervals and developing a family of five or six corresponding correlation equations—this approach will be referred to as the "piecewise correlation technique." Hilpert correlated his data by means of a family of equations having the following form:

$$N = BR^m \tag{1}$$

where B and m are constants. He determined the numerical values of B and m corresponding to the following five subintervals of the Reynolds number: 1 to 4; 4 to 40; 40 to 4000; 4000 to 40000; and 40000 to 400000. Collis and Williams employed

$$N_f T' = a + bR_f^c \tag{2}$$

and determined the values of the constants a, b, and c listed in Table 1. The factor $T' = (T_f/T_\infty)^{-0.17}$, called the temperature factor, accounts for variations in the fluid properties of air. It is pertinent to note that $a = 0$ for $R_f > 44$.

Utilization of the piecewise correlation technique sometimes introduces certain difficulties: for example, when repeated calculations by computer need to be made over a broad range of the Reynolds number. To overcome these difficulties, the present authors [4] recently developed a single, continuous correlation equation which accurately represents all the data in [1–3]:

$$N_f T' = 0.184 + 0.324R_f^{0.5} + 0.291R_f^x \tag{3}$$

where $x = 0.247 + 0.0407R_f^{0.168}$.

Table 1 Values of constants in equation (2)

Range of R_f		a	b	c
From	To			
0.02	44	0.24	0.56	0.45
44	140	0	0.48	0.51

Although equation (3) has certain advantages, it is somewhat unwieldy to use when quick slide-rule estimates are needed. Therefore it is deemed desirable to have in hand equation (3) and also a family of correlation equations like equation (2). The main objective of the present work was to determine an appropriate set of constants to use with equation (2) based upon Hilpert's data for Reynolds numbers greater than 40. For Reynolds numbers less than 40, the exclusive use of equation (3) is recommended, because in this region the data cannot be as accurately represented by the piecewise technique.

Discussion of Hilpert's Data and Correlations

In 1933 Hilpert published the results of a carefully conducted and extensive experimental investigation of heat transfer from horizontal circular cylinders to air in crossflow. The cylinders consisted of a series of 12 specimens (wires and pipes) ranging in diameter from 0.0198 mm to 150 mm, the Reynolds number varied from 2 to 2.3×10^5, and the pressure was approximately 1 atm. Most of Hilpert's experiments were performed with temperature differences Δt approximately equal to 80 deg C; only for specimen No. 5 were appreciably greater Δt's employed (up to nearly 1000 deg C). Hilpert's measurements (excluding specimen No. 5) are listed in Table 2, columns I through VI. Although Hilpert's data were obtained nearly 40 years ago, they still represent the most extensive and consistent set of measurements that are available in this area of inquiry.

Hilpert correlated his experimental data (excluding specimen

[1] Numbers in brackets designate References at end of paper.

Contributed by the Heat Transfer Division for publication (without presentation) in the JOURNAL OF HEAT TRANSFER. Manuscript received by the Heat Transfer Division May 30, 1972. Paper No. 73-HT-A.

Table 2 Experimental data of Hilpert and related calculations

	I	II	III	IV	V	VI	VII	VIII	IX	X	XI	XII	XIII
	Pt. No.	Pressure mm Hg	t_s deg C	t_a deg C	V m/sec	h k cal / m²h deg C	$(R_{ih})_{exp}$	$(N_{ih})_{exp}$	$(R_i)_{exp}$	$(N_i)_{exp}$	$(R_f)_{exp}$	$(N_f)_{exp}$	$(N_fT)_{exp}$
Specimen 1 dia = 0.198 mm	1	770	93.5	19.2	1.965	1370	2.11	1.14	2.13	1.11	2.13	1.11	1.08
	2	770	94.2	19.4	2.66	1520	2.85	1.27	2.87	1.23	2.88	1.23	1.20
	3	770	96.1	19.7	3.19	1606	3.41	1.33	3.42	1.29	3.43	1.29	1.26
	4	770	96.1	19.9	4.11	1768	4.39	1.47	4.41	1.42	4.42	1.42	1.39
	5	770	95.4	19.2	4.33	1855	5.25	1.54	V and VII are inconsistent, hence calculations are omitted				
	6	770	95.1	19.0	5.71	1988	6.15	1.65	6.15	1.60	6.17	1.60	1.57
	7	768	96.6	21.4	8.34	2315	8.84	1.92	8.87	1.86	8.89	1.86	1.82
	8	768	98.7	21.1	10.15	2455	10.70	2.03	10.75	1.96	10.77	1.96	1.92
	9	768	97.7	20.7	13.03	2675	13.79	2.21	13.85	2.14	13.88	2.14	2.10
	10	768	96.5	20.4	16.46	2933	17.46	2.44	17.56	2.36	17.61	2.35	2.31
	11	768	99.5	20.0	21.60	3295	22.76	2.72	22.89	2.64	22.94	2.64	2.58
Specimen 2 dia = 0.054 mm	12	746	100.8	20.2	2.88	1322	3.63	1.35	3.65	1.31	3.66	1.31	1.28
	13	746	100.0	20.2	3.34	1397	4.22	1.43	4.25	1.38	4.26	1.38	1.35
	14	746	99.8	20.3	3.83	1467	4.84	1.50	4.87	1.45	4.88	1.45	1.42
	15	746	99.0	20.4	4.52	1558	5.72	1.59	5.76	1.54	5.77	1.54	1.51
	16	746	98.3	20.6	5.34	1652	6.37	1.69	6.81	1.64	6.83	1.64	1.60
	17	746	98.7	20.7	5.89	1728	7.47	1.76	7.50	1.71	7.52	1.71	1.67
Specimen 3 dia = 0.030 mm	18	767	100.1	19.6	2.64	829	7.01	1.73	7.05	1.68	7.07	1.67	1.64
	19	767	101.4	19.9	3.59	939	9.47	1.95	9.55	1.89	9.57	1.89	1.85
	20	767	99.8	20.2	5.08	1070	13.49	2.22	13.56	2.16	13.59	2.16	2.11
	21	767	100.4	20.5	5.66	1102	14.98	2.29	15.07	2.22	15.11	2.22	2.17
	22	772	100.4	20.2	7.01	1215	18.69	2.53	18.80	2.45	18.85	2.45	2.40
	23	772	101.8	20.6	8.24	1288	21.89	2.68	21.99	2.59	22.05	2.59	2.54
	24	772	100.7	21.0	10.78	1426	28.70	2.96	28.82	2.87	28.90	2.87	2.81
	25	772	98.5	21.5	13.28	1572	35.56	3.27	35.68	3.18	35.76	3.17	3.11
	26	761	99.9	22.8	15.82	1675	41.38	3.48	41.60	3.37	41.70	3.37	3.30
	27	761	100.0	22.5	18.45	1797	48.30	3.73	48.54	3.62	48.66	3.62	3.54
	28	761	100.4	22.2	21.70	1924	56.90	4.00	57.07	3.87	57.21	3.87	3.79
	29	761	100.3	22.3	25.50	2092	66.75	4.34	67.07	4.21	67.23	4.21	4.12
Specimen 4 dia = 0.099 mm	30	767	108.1	20.6	3.28	594	16.82	2.42	16.93	2.35	16.99	2.35	2.29
	31	767	108.1	20.8	4.15	650	21.29	2.65	21.42	2.57	21.48	2.57	2.51
	32	767	108.6	20.9	4.82	690	24.70	2.81	24.83	2.73	24.91	2.72	2.66
	33	767	108.5	21.4	5.87	757	30.08	3.08	30.21	2.99	30.30	2.99	2.92
	34	763	99.9	20.5	7.59	835	39.65	3.44	39.85	3.34	39.96	3.34	3.26
	35	763	99.5	20.7	9.42	916	49.25	3.78	49.49	3.66	49.62	3.66	3.58
	36	763	100.1	20.9	11.02	986	57.5	4.07	57.77	3.94	57.92	3.94	3.85
	37	763	99.4	21.0	12.67	1045	66.1	4.34	66.53	4.18	66.70	4.17	4.09
	38	763	100.1	22.4	14.75	1128	76.8	4.64	77.04	4.50	77.22	4.49	4.40
	39	763	98.7	22.3	18.50	1272	96.5	5.24	97.01	5.08	97.24	5.08	4.97
	40	763	100.5	22.2	23.25	1455	120.8	5.98	121.4	5.80	121.7	5.80	5.67
	41	763	106.7	22.6	29.55	1577	150.8	6.37	151.6	6.23	152.0	6.23	6.09
	42	762	99.3	20.4	6.54	776	34.13	3.20	34.36	3.11	34.45	3.10	3.04
	43	762	100.1	20.8	8.27	856	43.05	3.53	43.31	3.42	43.42	3.42	3.34
	44	762	99.5	20.5	9.33	909	48.70	3.75	48.98	3.64	49.10	3.63	3.56
	45	762	101.1	20.6	11.45	997	59.50	4.10	59.84	3.98	59.99	3.98	3.89
	46	762	100.0	20.3	13.28	1075	69.4	4.43	69.66	4.30	69.84	4.30	4.20
Specimen 6 dia = 0.50 mm	47	774	101.8	22.2	2.57	207	68.2	4.29	68.49	4.16	68.67	4.16	4.07
	48	774	101.4	22.0	3.10	228	82.4	4.74	82.75	4.59	82.96	4.58	4.49
	49	785	99.8	19.6	3.88	257	105.8	5.35	106.1	5.20	106.4	5.19	5.08
	50	774	98.8	22.8	4.51	275	120.2	5.71	121.0	5.54	121.3	5.54	5.43
	51	784	100.5	21.0	4.93	289	133.2	6.02	134.0	5.83	134.3	5.82	5.70
	52	774	102.0	23.0	5.14	296	136.0	6.13	136.6	5.94	137.0	5.94	5.81
	53	784	102.6	20.7	5.92	314	159.2	6.51	160.1	6.32	160.5	6.31	6.17
	54	770	98.1	20.6	6.36	327	169.8	6.82	171.0	6.62	171.4	6.61	6.47
	55	770	99.4	20.9	7.85	360	209.3	7.51	210.2	7.27	210.7	7.26	7.11
	56	770	99.0	20.8	11.32	429	301.5	8.94	303.5	8.67	304.2	8.66	8.48
	57	770	99.7	21.6	13.20	459	351.0	9.54	352.5	9.26	353.3	9.25	9.06
	58	781	98.4	22.6	15.63	501	421.5	10.43	423.7	10.11	424.7	10.10	9.90
	59	781	100.3	22.6	19.35	547	519	11.36	521.9	11.01	523.2	11.00	10.77
	60	781	101.3	22.4	23.80	593	636	12.30	640.5	11.92	642.1	11.91	11.66
	61	781	100.5	22.5	29.60	652	739	13.55	798.1	13.12	800.1	13.11	12.84
Specimen 7 dia = 1.00 mm	62	762	100.5	21.5	3.62	170.0	189.9	7.06	191.0	6.85	191.4	6.85	6.70
	63	767	99.0	21.0	4.74	194.0	251.5	8.10	253.0	7.84	253.6	7.83	7.67
	64	762	99.9	21.7	5.15	204.5	270.2	8.50	272.0	8.25	272.6	8.24	8.07
	65	762	99.5	21.6	5.74	212.5	301.2	8.81	303.5	8.57	304.3	8.57	8.39
	66	767	100.1	21.5	7.07	236.0	373.5	9.81	376.8	9.52	376.7	9.51	9.31
	67	766	96.1	20.1	8.38	255.0	449	10.68	451.3	10.35	452.3	10.35	10.13

Table 2 (continued)

	I	II	III	IV	V	VI	VII	VIII	IX	X	XI	XII	XIII
	Pt. No.	Pressure mm Hg	t_s deg C	t_a deg C	V m/sec	h k cal / m²h deg C	$(R_{ih})_{exp}$	$(N_{ih})_{exp}$	$(R_i)_{exp}$	$(N_i)_{exp}$	$(R_f)_{exp}$	$(N_f)_{exp}$	$(N_fT)_{exp}$
Specimen 7 dia = 1.00 mm	68	766	99.5	20.3	9.23	264.0	490	11.02	492.3	10.67	493.5	10.66	10.43
	69	767	100.9	21.5	11.02	284.5	581	11.83	584.5	11.46	586.0	11.45	11.21
	70	766	97.4	20.3	12.07	293.5	644	12.29	647.4	11.89	648.9	11.89	11.64
	71	766	99.9	20.0	13.00	307.2	689	12.81	693.1	12.41	694.9	12.40	12.14
	72	769	100.6	20.9	17.13	343.8	909	14.30	913.1	13.86	915.4	13.85	13.56
	73	769	100.6	21.1	20.27	374.0	1074	15.57	1080	15.08	1083	15.07	14.75
	74	769	98.8	21.6	25.08	415	1331	17.28	1341	16.76	1344	16.75	16.40
	75	767	101.9	22.9	29.60	446	1552	18.48	1560	17.91	1564	17.89	17.52
Specimen 8 dia = 2.59 mm	76	762	100.6	21.6	3.24	92.4	508	11.48	510.8	11.13	512.0	11.12	10.89
	77	762	100.5	21.2	3.93	100.0	616	12.43	620.3	12.05	621.9	12.05	11.79
	78	757	100.9	21.0	4.88	110.3	761	13.70	764.8	13.29	766.8	13.28	13.00
	79	757	101.2	21.2	5.82	119.4	906	14.82	910.9	14.38	913.3	14.37	14.06
	80	760	99.8	21.5	7.99	139.5	1253	16.76	1259	16.82	1262	16.81	16.46
	81	760	100.8	21.2	10.78	159.2	1688	19.79	1697	19.19	1701	19.17	18.76
	82	750	98.7	22.1	11.75	166.5	1822	20.70	1830	20.09	1834	20.08	19.67
	83	757	100.2	21.7	13.45	176.5	2098	21.93	2108	21.27	2113	21.25	20.81
	84	758	99.6	22.4	16.18	193.8	2522	24.10	2539	23.35	2545	23.33	22.85
	85	758	99.4	23.1	20.05	216.5	3125	26.90	3142	26.07	3150	26.05	25.52
	86	758	99.5	20.5	23.98	234.2	3755	29.18	3782	28.29	3792	28.27	27.67
Specimen 9 dia = 25.0 mm	87	754	99.5	21.3	1.89	22.1	2410	22.50	2474	22.30	2480	22.28	21.82
	88	754	99.4	22.7	2.47	25.1	3210	26.06	3223	25.28	3230	25.27	24.75
	89	760	99.8	21.6	3.23	28.5	4230	29.65	4255	28.74	4266	28.71	28.11
	90	760	99.8	21.6	4.01	32.8	5260	34.05	5283	33.07	5296	33.05	32.35
	91	762	99.8	23.1	4.89	37.4	6480	38.75	6435	37.63	6450	37.61	36.84
	92	753	99.6	22.3	6.06	42.8	7800	44.50	7822	43.12	7841	43.09	42.20
	93	751	99.3	22.7	8.40	51.8	10870	53.8	10919	52.19	10945	52.15	51.08
	94	751	99.4	22.7	10.90	61.7	14110	64.1	14165	62.15	14199	62.11	60.83
	95	751	99.4	22.9	13.60	71.3	17580	74.1	17665	71.80	17707	71.75	70.28
	96	756	99.5	21.1	18.64	87.3	24390	90.8	24478	88.11	24539	88.05	86.20
	97	757	99.5	22.1	22.20	99.5	28980	103.4	29118	100.3	29188	100.2	98.15
	98	756	99.6	22.1	28.00	113.5	36510	117.9	36667	114.4	36756	114.3	111.9
Specimen 10 dia = 44.0 mm	99	765	100.3	23.3	2.62	20.7	6040	37.8	6080	36.63	6095	36.60	35.85
	100	759	99.7	21.0	2.99	22.7	6890	41.7	6936	40.32	6954	40.29	39.44
	101	751	99.8	22.7	3.87	26.3	8800	48.0	8842	46.60	8863	46.57	45.61
	102	751	99.7	22.8	5.87	33.7	13350	61.6	13412	59.72	13444	59.67	58.45
	103	754	99.8	22.1	7.74	39.6	17650	72.6	17782	70.23	17825	70.17	68.71
	104	752	99.6	22.6	10.86	48.9	25000	89.5	25095	86.68	25155	86.62	84.84
	105	753	99.8	22.8	14.10	58.4	32300	106.8	32393	103.5	32370	103.4	101.3
	106	754	99.7	21.5	18.28	70.1	41900	128.7	42073	124.4	42177	124.3	121.7
	107	763	100.2	22.2	21.48	79.2	49600	144.7	49872	140.4	49994	140.3	137.3
	108	752	99.8	23.7	24.52	86.8	55750	158.5	55956	153.6	56086	153.5	150.4
Specimen 11 dia = 90.0 mm	109	755	98.6	21.6	3.13	16.98	14790	63.9	14795	61.73	14830	61.68	60.41
	110	752	98.1	22.1	4.43	20.90	20780	78.6	20857	75.98	20906	75.92	74.38
	111	760	98.8	22.4	5.87	25.20	27820	94.8	27858	91.49	27923	91.43	89.56
	112	763	99.4	21.9	8.49	34.83	40320	119.6	40437	115.5	40535	115.5	113.1
	113	763	99.7	22.0	10.86	38.25	51600	143.5	51670	138.8	51796	138.7	135.8
	114	763	99.6	21.8	13.27	45.3	62950	170.5	63186	164.4	63341	164.3	160.9
	115	763	99.6	22.1	15.98	57.3	85400	215.3	85548	207.9	85755	207.7	203.4
	116	760	99.6	21.7	22.22	67.2	105200	252.8	105412	243.9	105671	243.8	238.7
	117	760	99.6	21.7	28.00	82.4	132300	310	132833	299.1	133159	298.9	292.7
Specimen 12 dia = 150 mm	118	764	99.8	22.6	3.93	17.0	30900	106.0	31149	102.7	31234	102.6	100.5
	119	762	99.6	22.4	5.18	21.0	40760	130.7	40992	126.9	41090	126.8	124.2
	120	754	99.4	21.3	5.31	20.9	41600	130.5	41718	126.6	41821	126.5	123.8
	121	762	99.5	23.2	9.63	31.7	75700	197.4	76072	191.4	76249	182.2	178.5
	122	762	99.9	22.8	13.26	42.0	104200	261.3	104741	253.6	104992	253.5	248.2
	123	753	99.4	24.0	15.10	44.9	118000	279.0	117665	270.9	117933	270.7	265.3
	124	764	99.3	22.8	17.00	50.6	133200	316	134852	305.8	135170	305.6	299.1
	125	763	98.8	21.8	18.85	55.7	150300	348	149913	337.3	150273	337.1	330.1
	126	757	98.0	21.1	20.86	59.0	164000	369	165242	358.0	165640	357.7	350.1
	127	758	99.1	21.5	22.18	64.1	174800	391	175093	388.0	175523	387.7	379.6
	128	758	99.2	21.6	25.62	72.1	200080	449	200768	434.8	201214	434.5	425.9
	129	758	99.2	20.9	29.40	82.1	231000	513	232568	497.5	233147	497.1	486.7

No. 5) by the following piecewise continuous algebraic function:

$$N_{ih} = BR_{ih}^{m} \tag{4}$$

where B and m are constants given in Table 3. The entries in Table 3 comprise a modest extrapolation of the original experimental data, inasmuch as the actual experimental range of the Reynolds number was from 2 to 2.3 $\times$ 10^5 while the entries in Table 3 include Reynolds numbers from 1 to 4 $\times$ 10^5.

Hilpert employed integrated mean values of the physical properties of air for correlation purposes, as indicated by the subscripts ih in equation (4); nevertheless, most subsequent investigators and texts assume that the entries in Table 3 refer to properties evaluated at the mean film temperature t_f. In this connection it is also necessary to point out that Hilpert used values for viscosity and thermal conductivity to evaluate the Reynolds and Nusselt numbers that have since been superseded. Therefore, if Reynolds and Nusselt numbers are calculated on the basis of recent information on viscosity and thermal conductivity [5],[2] the calculated values will differ from values obtained by Hilpert for the same temperature limits. These differences are indicated by the following notation: subscript ih refers to integrated mean values published by Hilpert, whereas subscripts i and f refer, respectively, to integrated mean and mean film temperature properties calculated on the basis of information on properties (viscosity and thermal conductivity) contained in [5]. In Table 2, columns VII and VIII contain values of $(R_{ih})_{exp}$ and $(N_{ih})_{exp}$, columns IX and X contain values of $(R_i)_{exp}$ and $(N_i)_{exp}$, columns XI and XII contain values of $(R_f)_{exp}$ and $(N_f)_{exp}$, and

[2] See Appendix.

Nomenclature

A, B, C, D = constants
a, b, c = constants
E = percentage error defined by $E = \left[\frac{(\ )_{calc} - (\ )_{exp}}{(\ )_{exp}}\right] \times 100$
h = heat transfer coefficient
j = constant
m, n = constants
N = Nusselt number based on cylinder diameter
P = Prandtl number
R = Reynolds number based on cylinder diameter
t = temperature
t_f = mean film temperature, $t_f = {}^1/_2(t_s + t_\infty)$
t_s = cylinder surface temperature
t_∞ = ambient fluid temperature (far from cylinder)
T_f = absolute mean film temperature, $T_f = {}^1/_2(T_s + T_\infty)$
T_s = absolute cylinder surface temperature
T_∞ = absolute fluid temperature (far from cylinder)
T = temperature factor defined by $T = (T_f/T_\infty)^{-0.17}$
V = velocity
x = a function of R_f, see equation (3)

Subscripts

calc = refers to calculated values
exp = refers to experimentally determined values
f = refers to properties evaluated at the mean film temperature
i = refers to integrated mean values of properties based upon data in [5]
ih = refers to integrated mean values of properties determined by Hilpert

Table 3 Values of constants in equations (4) and (5)

Range of R_{ih}		B	m	B_5
From	To			
1	4	0.891	0.330	0.872
4	40	0.821	0.385	0.802
40	4,000	0.615	0.466	0.600
4,000	40,000	0.174	0.618	
40,000	400,000	0.0239	0.805	

column XIII contains values of $(N_f T)_{exp}$. From this table the deviations between various quantities can readily be calculated. Thus it may be observed that for the same temperature limits, $(R_{ih})_{exp}$ is less than $(R_i)_{exp}$ by about 0.6 percent, whereas $(N_{ih})_{exp}$ is from 3 to 5 percent higher than $(N_i)_{exp}$.

Hilpert found that equation (4) did not correlate his data for specimen No. 5 (high Δt), and so he developed a second equation for this purpose, namely

$$N_{ih} = B_5 \left[R_{ih} \left(\frac{T_s}{T_\infty} \right)^{1/4} \right]^m \tag{5}$$

with constants B_5 and m as indicated in Table 3. Inclusion of the factor $(T_s/T_\infty)^{1/4}$ in equation (5) represents an effort to account for variations in the fluid properties of air more precisely than they are accounted for by equation (4). Collis and Williams have found that this accounting is better accomplished by means of the temperature factor T, see equation (2).

Recalculation of Hilpert's Constants

If properties are evaluated at t_f and the following form is adopted to correlate Hilpert's data (excluding specimen No. 5)

$$N_f = D R_f^j \tag{6}$$

then the method of least squares leads to the values for D and j listed in Table 4. In order to evaluate the accuracy with which equation (6)[3] represents Hilpert's measurements, the percentage error E was calculated for each data point (for the definition of E see the Nomenclature). It was found that the maximum error is 6.7 percent and the mean value and standard deviation of the errors are −0.06 and 1.9 percent, respectively. If the entries in Table 3 are used instead of those in Table 4 in conjunction with equation (6), then the maximum, mean, and standard deviations of the errors are approximately 12, 4, and 2 percent, respectively.

If the following form is adopted to correlate Hilpert's data (excluding specimen No. 5)

$$N_f T = A R_f^n \tag{7}$$

then the method of least squares leads to the values for A and n listed in Table 5. In this case the maximum, mean, and standard deviations of the errors are 6.7, 0.08, and 2.0 percent, respectively. The values of A and n in Table 5 are nearly the same as the corresponding values of D and j in Table 4 because the temperature factor T is nearly unity for all of Hilpert's data excluding specimen No. 5.

Conclusions

1 Equation (6) together with the constants listed in Table 4 represent Hilpert's data with mean error and standard deviation of error equal to −0.06 and 1.9 percent, respectively.

2 For Reynolds numbers greater than 40, either equation (3) or equation (7) may be used to calculate heat transfer from cylinders to air in crossflow; the choice as to which equation to use in a particular application depends upon which is more convenient. For Reynolds numbers less than 40, the exclusive use of equation (3) is recommended.

[3] As indicated earlier, this is the equation that Hilpert is generally *assumed* to have adopted, whereas, in fact, he used equation (4).

Table 4 Values of constants in equation (6)

Range of R_f		D	j
From	To		
1	4	0.875	0.313
4	40	0.785	0.388
40	4,000	0.590	0.467
4,000	40,000	0.154	0.627
40,000	400,000	0.0247	0.798

Table 5 Values of constants in equation (7)

Range of R_f		A	n
From	To		
40	4,000	0.579	0.467
4,000	40,000	0.151	0.627
40,000	400,000	0.0242	0.798

Acknowledgment

This work was supported by a grant from the National Science Foundation.

References

1 Hilpert, R., "Wärmeabgabe von geheizten Drähten und Rohren im Luftstrom," *Forsch. Gebiete Ingenieurw.*, Vol. 4, 1933, pp. 215–224.

2 King, L. V., "On the Convection of Heat from Small Cylinders in a Stream of Fluid: Determination of the Convection Constants of Small Platinum Wires with Applications to Hot-Wire Anemometry," *Phil. Trans. Roy. Soc., Ser. A*, London, Vol. 214, 1914, pp. 373–432.

3 Collis, D. C., and Williams, M. J., "Two-dimensional Convection from Heated Wires at Low Reynolds Numbers," *Journal of Fluid Mechanics*, Vol. 6, Pt. 3, 1959, pp. 357–384.

4 Fand, R. M., and Keswani, K. K., "A Continuous Correlation Equation for Heat Transfer from Cylinders to Air in Crossflow for Reynolds Numbers from 10^{-2} to 2×10^5," *International Journal of Heat and Mass Transfer*, Vol. 15, 1972, pp. 559–562.

5 *Tables of Thermal Properties of Gases*, National Bureau of Standards Circular 564, U. S. Dept. of Commerce, Nov. 1955.

APPENDIX

Thermal properties of air were calculated from the following equations obtained from [5]:

Dynamic viscosity

$$\mu = \frac{A T^{3/2}}{T + B} \times 10^{-7}$$

where

μ = dynamic viscosity, poise
A = 145.8
B = 110.4
T = temperature, deg K

Thermal conductivity

$$k = \frac{a T^{1/2}}{1 + \frac{b}{T}(10^{-c/T})}$$

where

k = thermal conductivity, cal/cm-sec-deg K
a = 0.6325×10^{-6}
b = 245.4
c = 12
T = temperature, deg K

T. CEBECI
Aerodynamics Research Group,
Douglas Aircraft Co.,
Long Beach, Calif.
Mem. ASME

A Model for Eddy Conductivity and Turbulent Prandtl Number

This paper presents a model for eddy conductivity and turbulent Prandtl number based on the considerations of a Stokes-type flow. The expressions obtained by the model provide continuous velocity and temperature distributions for turbulent flows and are applicable to flows with pressure gradients, mass transfer, and heat transfer. Close to the wall the turbulent Prandtl number appears to be strongly affected by the molecular Prandtl number; away from the wall it is constant, that is, it is independent of the molecular Prandtl number. Calculated results agree well with experiments, including those with fluids having both low and high Prandtl numbers. In addition the results confirm recent experimental findings, in that the mass transfer has no effect on turbulent Prandtl number.

Introduction

At the present time there are no exact methods for calculating turbulent-velocity and temperature boundary layers. The governing equations for such flows contain fluctuation terms that are difficult if not impossible to relate to the dependent variables appearing in the equations. Because of the highly complex nature of the turbulence mechanism it is unlikely that an exact solution of the governing equations will ever be accomplished. In order to proceed at all it is necessary to introduce some empirical assumptions into the governing equations. For this reason, over the years several approaches have been followed and various assumptions for the fluctuation terms have been proposed for calculating the velocity and temperature boundary layers. Prandtl's mixing-length and Boussinesq's eddy-diffusivity coefficients for momentum and for heat are defined by the following expressions:

$$-\rho\overline{u'v'} = \rho\epsilon_m \frac{\partial u}{\partial y} \qquad -\rho\overline{T'v'} = \rho\epsilon_h \frac{\partial T}{\partial y} \tag{1}$$

Sometimes it has been found convenient to introduce a "turbulent Prandtl number" defined by

$$\mathrm{Pr}_t = \epsilon_m/\epsilon_h \tag{2}$$

Of these coefficients, the eddy-viscosity concept has been used quite satisfactorily, together with Prandtl's mixing-length concept, in several prediction methods for turbulent boundary layers.[1] These methods treat the turbulent boundary layer as a composite layer consisting of inner and outer regions. The existence of the two regions is due to the different response to shear and pressure gradient by the fluid near the wall. In general the thickness of the inner region is approximately 10 to 20 percent of the total boundary-layer thickness. The mean velocity distribution may be described by the so-called law of the wall, $u^+ = \phi_1(y^+)$. In addition, if an expression for eddy viscosity is introduced, it can be shown that eddy viscosity in this region varies almost linearly with distance. A popular kinematic eddy-viscosity expression for this region is an expression based on Prandtl's mixing-length theory

$$\epsilon_m = l^2 \frac{\partial u}{\partial y} \tag{3}$$

where l, the mixing length, is given by $l = k_m y$.

In the case of a smooth wall the inner region contains a layer, commonly called the laminar sublayer, adjacent to the wall, where the mean velocity increases linearly with distance from the wall, $u^+ = y^+$. The thickness of this layer is of the order of 0.1 percent to 1 percent of the total boundary-layer thickness.

According to experimental evidence there is also another region between the sublayer and the inner region, which can be called a transitional region. Various assumptions have been made in order to describe the mean velocity distribution there. Hinze [2] gives a good summary of these assumptions. Of the many proposed, one has enjoyed a remarkable success. It is the expression proposed by Van Driest [3], who assumed the following modified expression for Prandtl's mixing-length theory:

Contributed by the Heat Transfer Division and presented at the Winter Annual Meeting, New York, N. Y., November 26–30, 1972, of The American Society of Mechanical Engineers. Manuscript received by the Heat Transfer Division November 3, 1971. Paper No. 72-WA/HT-13.

[1] A summary of the latest prediction methods for incompressible two-dimensional turbulent boundary layers is given by Reynolds [1].[2]

[2] Numbers in brackets designate References at end of paper.

$$l = k_m y[1 - \exp(-y/A)] \quad (4)$$

where A is a damping-length constant defined as $26\nu(\tau_w/\rho)^{-1/2}$. This expression provides a continuous velocity and shear distribution for turbulent flow. Although it was originally developed for flat-plate flows with no mass transfer, it has been generalized and extended to flows with pressure gradient, mass transfer, and heat transfer, e.g., see [4–6].

The outer region contains 80 to 90 percent of the total boundary-layer thickness; the mean velocity distribution is conveniently described by the so-called velocity-defect law, $(u_e - u)/u_\tau = \phi_2(y/\delta)$. The flow in this region is quite similar to wake flow. Near the outer edge it has an intermittent character. In addition, an eddy-viscosity expression, if introduced, has a nearly constant value in this region. For example, as suggested by Clauser [7], the eddy viscosity for the so-called equilibrium boundary layer is

$$\epsilon_m = \alpha \left| \int_0^\infty (u_e - u)dy \right| \quad (5)$$

where α is an empirical constant equal to about 0.0168.

Again, various assumptions have been made about eddy conductivity, and several expressions have been proposed in attempts to predict the mean temperature distribution within the boundary layer. One assumption that has been used extensively is the one due to Reynolds. According to his assumption, heat and momentum are transferred by the same process, which means that the eddy coefficients are the same. This assumption leads to a turbulent Prandtl number of unity. The literature discusses the relationship between these coefficients at great length, without definite conclusions. According to experiments with mercury in pipes, $\mathrm{Pr}_t > 1$, and according to experiments with gases in pipes, $\mathrm{Pr}_t < 1$, see [8]. *It is not clear whether the eddy conductivity and consequently the turbulent Prandtl number are completely independent of the molecular Prandtl number.*

One of the first proposals for a modification of the Reynolds analogy was made by Jenkins [9], who took into consideration the heat conduction to or from an element of an eddy during its movement transverse to the main flow. He assumed that if the temperature of the eddy did not change in flight, the definition of mixing length $l = u_\tau/(\partial u/\partial y)$ and the definition of eddy conductivity $\mathrm{Pr}_t = \epsilon_m/\epsilon_h$ would have $\epsilon_h = lv'$, since $T' = l(\partial T/\partial y)$. However if heat were lost during transit the fluctuation temperature T' would actually be less than that, because of molecular thermal conductivity. Then the eddy conductivity would be

$$\epsilon_h = lv' \frac{T_f - T_i}{l(\partial T/\partial y)} \quad (6)$$

where T_f and T_i are the final and initial eddy mean temperatures respectively. In order to obtain an expression for $(T_f - T_i)/l(\partial T/\partial y)$, Jenkins assumed that the eddies are spheres of radius l, the mixing length, with the surface temperature of the particles varying linearly with time during their movement. The interval of time between an eddy's creation and its destruction is taken as l/v'. Using Carslaw and Jaeger's formula for the average temperature of a sphere under these conditions, Jenkins obtained an expression for (6).

Treating the effect of molecular viscosity on an eddy in movement in the same way as the effect of molecular thermal conductivity, the Jenkins model leads to the following expression for the ratio of eddy conductivity to eddy viscosity:

$$\frac{\epsilon_h}{\epsilon_m} \equiv \frac{1}{\mathrm{Pr}_t} = \frac{1}{\mathrm{Pr}} \times \left\{ \frac{\frac{2}{15} - \frac{12}{\pi^6}\epsilon_m^+ \left\{ \sum_{n=1}^{\infty} \frac{1}{n^6} [1 - \exp(-n^2\pi^2/\epsilon_m^+)] \right\}}{\frac{2}{15} - \frac{12}{\pi^6}\mathrm{Pr}\,\epsilon_m^+ \left\{ \sum_{n=1}^{\infty} \frac{1}{n^6} [1 - \exp(-n^2\pi^2/\mathrm{Pr}\,\epsilon_m^+)] \right\}} \right\} \quad (7)$$

Calculations made at low Prandtl numbers using the above expression are in fair agreement with experiment [10], although the more recent experimental data for liquid metals suggest that the loss of heat by an eddy during flight is not so great as that predicted by Jenkins. Furthermore, according to the experimental data of Page et al. [11] for air at Pr = 0.7, the eddy conductivity is greater than the eddy viscosity. Jenkins' result gives an opposite effect. Some analysts have therefore preferred to use Jenkins' diffusivity ratio multiplied by a constant factor such as 1.10 or 1.20 to bring the results more into line with measurements at Pr = 0.7 [10]. At high Prandtl numbers the Jenkins expression predicts values for ϵ_h/ϵ_m that have no upper bound as the Prandtl number increases, which is not found by experiment.

Studies of the problem have also been made by Deissler [12], and recently by Tyldesley and Silver [13] and by Simpson, Whitten, and Moffat [14]. Deissler's approach is based on a modified mixing-length theory and a method based on correlation coefficients. Neither method leads to an expression for the eddy ratios that can be compared directly with those given by other authors, but the modified mixing-length theory does seem successful in predicting heat transfer in the low-Prandtl-number range. In his other approach he derives from the momentum and the energy equations the correlation between velocities and temperatures at two points in a homogeneous turbulent fluid. His results predict that ϵ_h/ϵ_m depends on the velocity gradient, and that as the gradient increases the value of the ratio approaches unity regardless of the molecular Prandtl number of the fluid.

Nomenclature

A, B = damping-length constants for velocity and temperature fluctuations respectively
A^+, B^+ = damping constants for velocity and temperature fluctuations respectively
c_p = specific heat at constant pressure
$c_f/2$ = local skin-friction coefficient, $2\tau_w/\rho_e u_e^2$
h = specific enthalpy
h^+ = dimensionless enthalpy ratio, $(h_w - h)/h_\tau$
h_τ = $q_w/\rho_w u_\tau$
k = thermal conductivity
k_m, k_h = mixing-length constants for momentum and heat respectively
Nu = Nusselt number
Pe = Peclet number
P^+ = pressure-gradient parameter, $\frac{\nu}{u_e^2}\frac{du_e}{dx}\left(\frac{c_f}{2}\right)^{-3/2}$
Pr, Pr_t = molecular and turbulent Prandtl numbers respectively
R_θ = momentum-thickness Reynolds number, $u_e\theta/\nu$
q = heat flux
t = time
T = temperature
u_τ = friction velocity, $(\tau_w/\rho)^{1/2}$
u^+, v_w^+ = dimensionless velocity ratios u/u_τ and v_w/u_τ respectively
u, v = x and y components of velocity
x, y = rectangular coordinates
y^+ = dimensionless quantity, yu_τ/ν
Z = dimensionless quantity, $R_\theta \times 10^{-3}$
δ = boundary-layer thickness
ϵ_m, ϵ_h = kinematic eddy viscosity and eddy conductivity respectively
$\epsilon_m^+, \epsilon_h^+$ = dimensionless eddy viscosity ϵ_m/ν and eddy conductivity ϵ_h/ν respectively
θ = momentum thickness, $\int_0^\infty \frac{u}{u_e} \times [1 - (u/u_e)]dy$
μ = dynamic viscosity
ν = kinematic viscosity
ρ = density
τ = shear stress
ω = angular velocity

The approach taken by Tyldesley and Silver is quite different from the approaches that have been discussed. These authors abandon the mixing-length concept and investigate the transport properties of a turbulent fluid by using a simple model to represent the detailed fluid behavior, which in the model is attributed to the motions of fluid entities of varying size, shape, and velocity. Their analysis enables them to find expressions for the eddy coefficients for mass, momentum, and energy in terms of properties of the turbulence. For example in the case of momentum and energy their model indicates that the turbulent Prandtl number is a function of the molecular Prandtl number, turbulence intensity, and Reynolds number.

The study of Simpson, Whitten, and Moffat [14] consists of the determination of the turbulent Prandtl number for air from the experimental data of Simpson and Whitten and the comparison of the experimental results with available theories. In addition they investigate the effects of both blowing and suction on the turbulent Prandtl number. These studies are made for low-speed incompressible turbulent flows with relatively low Reynolds number R_x ranging from 1.3×10^5 to 2×10^6. The minimum Reynolds number based on momentum thickness with no mass transfer is approximately 600. The results of their study show that (*a*) their experimental turbulent-Prandtl-number results agree within the experimental uncertainties with Ludweig's pipe results [15], which were obtained for $0.1 < y/\delta < 0.9$, and that (*b*) in the inner region the Jenkins model [8] is found to describe, within experimental uncertainty, the variation of Pr_t with $\epsilon_m{}^+$. In the outer region a new model for Pr_t and ϵ_h is developed. The results from both models fall within the uncertainty envelope of their experimental results and indicate no dependence of Pr_t on blowing or suction.

In this paper we discuss a model for eddy conductivity and turbulent Prandtl number based on the considerations of Stokes flow. We present expressions for eddy viscosity and eddy conductivity for both incompressible and compressible turbulent boundary layers. These expressions, which are obtained by following the modeling of the viscous sublayer to Stokes flow after Van Driest [3], account for flows with pressure gradient, heat transfer, and mass transfer. Furthermore, when these transport coefficients are used to replace the fluctuating quantities in the boundary-layer equations they give good agreement with experiment. The predictions of the model for turbulent Prandtl number also agree well with experiments, *including those with fluids having both low and high Prandtl numbers*. In addition the model confirms recent experimental findings, in that the mass transfer has no effect on turbulent Prandtl number.

In the next sections we describe the development of the turbulent Prandtl number for both incompressible and compressible turbulent boundary layers with pressure gradient, heat transfer, and mass transfer. However, before we do this, it is first appropriate to review Van Driest's modeling of the viscous layer to Stokes flow [3], as well as the extension of his model to flows with heat and mass transfer and pressure gradient [4, 5].

Van Driest's Model of the Viscous Sublayer

We consider Stokes flow, that is, a flow about an infinite flat plate that executes oscillations parallel to itself. The governing momentum equation for the flow is the one-dimensional unsteady-momentum equation. For an incompressible flow it is

$$\frac{\partial u}{\partial t} = \nu \frac{\partial^2 u}{\partial y^2} \tag{8}$$

The solution of (8) subject to the boundary condition $u(0, t) = u_0 \cos \omega t$ is given by the following expression [16]:

$$u = u_0 e^{-\frac{y}{\sqrt{2}\, y_s}} \cos\left(\omega t - \frac{\omega y}{\sqrt{2}\, u_s}\right) \tag{9}$$

where y_s is a length scale associated with the envelope of the oscillatory motion and u_s is the phase velocity of the oscillations. They are given by

$$y_s = \frac{\nu}{(\omega\nu)^{1/2}} \qquad u_s = (\omega\nu)^{1/2} \tag{10}$$

From (9) we see that the amplitude of the motion diminishes with distance from the wall as a consequence of the factor $\exp(-y/\sqrt{2}\, y_s)$. If we now identify u as the fluctuation velocity u', we see that when the plate is fixed and the fluid oscillates relative to the plate the *maximum* fluctuation velocity will be

$$u' = u_0'(1 - e^{-ny})$$

where $n = 1/(\sqrt{2}\, y_s)$ and u_0' is the velocity fluctuation unaffected by the viscosity. The above equation *suggests* that because of the viscous effects it is necessary to correct the velocity fluctuation by $(1 - e^{-ny})$. Furthermore the phase velocity of the oscillations may be thought of as a shear-wave propagation velocity.

If we assume that $u' \sim v'$ and use the definition of Reynolds shear stress we can then write

$$-\rho\overline{u'v'} = -\rho\overline{u_0'v_0'}\,(1 - e^{-ny})^2 \tag{11}$$

Since, according to Prandtl's mixing-length concept,

$$-\overline{u_0'v_0'} = l^2\left(\frac{\partial u}{\partial y}\right)^2 \tag{12}$$

we see that (11) can now be written as

$$-\rho\overline{u'v'} = l^2(1 - e^{-ny})^2\left(\frac{\partial u}{\partial y}\right)^2 \tag{13}$$

If we assume the shear-wave propagation velocity u_s to be the wall friction velocity $(\tau_w/\rho)^{1/2}$ and write $\exp(-ny)$ as $\exp(-y/A)$, then we can write

$$A = A^+\nu\left(\frac{\tau_w}{\rho}\right)^{-1/2} \tag{14}$$

where A^+ is an empirical constant.

For the inner region of the boundary layer, where the law of the wall applies, the mixing length l is proportional to the distance y from the wall, $l = k_m y$. Taking $k_m = 0.4$ and comparing his model with experimental data at high Reynolds number ($R_\theta > 5000$), Van Driest empirically determined the constant in (14) to be 26. However, if this curve-fitting procedure is applied to turbulent boundary layers at low Reynolds number ($R_\theta < 5000$), the parameters k_m and A^+ will vary with Reynolds number. According to the study conducted in [17] for flat-plate flows, this variation is found to be

$$k_m = 0.40 + \frac{0.19}{1 + 0.49Z^2} \qquad A^+ = 26 + \frac{14}{1 + Z^2} \qquad Z \geq 0.3 \tag{15}$$

where $Z = R_\theta \times 10^{-3}$. With these assumptions and constants, (13) becomes

$$-\rho\overline{u'v'} = (k_m y)^2[1 - \exp(-y/A)]^2\left(\frac{\partial u}{\partial y}\right)^2 \tag{16}$$

The eddy-viscosity expression for this region is then

$$(\epsilon_i)_m = (k_m y)^2[1 - \exp(-y/A)]^2\left(\frac{\partial u}{\partial y}\right) \tag{17}$$

The expression (16) or (17) was developed for a flat-plate flow with no mass transfer and should not be used for flows with pressure gradient and mass transfer. For pressure gradient, that is quite obvious, since for flow with an adverse pressure gradient, τ_w may approach zero (flow separation). In such a case the inner

eddy viscosity will be zero.[3] For this reason, in [4, 5] the Van Driest expression was extended to turbulent boundary layers with pressure gradient, mass transfer, and heat transfer. The extension was made by following Van Driest's modeling of the viscous sublayer to Stokes flow, and by taking the shear-wave propagation velocity to be the friction velocity at the edge of the sublayer, $(\tau_s/\rho)^{1/2}$, rather than its wall value $(\tau_w/\rho)^{1/2}$. It is given by

$$\left(\frac{\tau_s}{\rho}\right)^{1/2} = \left(\frac{\tau_w}{\rho_w}\right)^{1/2} \left(\frac{\rho_w}{\rho}\right)^{1/2} N \tag{18}$$

where

$$N = \left\{\frac{\mu}{\mu_e}\left(\frac{\rho_e}{\rho_w}\right)^2 \frac{p^+}{v_w{}^+}\left[1 - \exp\left(11.8\,\frac{\mu_w}{\mu} v_w{}^+\right)\right] + \exp\left(11.8\,\frac{\mu_w}{\mu} v_w{}^+\right)\right\}^{1/4} \tag{19}$$

As a result of this extension for flows with pressure gradient, heat transfer, and mass transfer, the damping-length constant A in (17) becomes

$$A = A^+\nu \left(\frac{\tau_s}{\rho}\right)^{-1/2} \tag{20}$$

Model for Turbulent Prandtl Number

If we neglect the dissipation and pressure-work terms, the steady-state energy equation for a turbulent flow can be written as

$$\rho u \frac{\partial h}{\partial x} + \rho v \frac{\partial h}{\partial y} = \frac{\partial}{\partial y}\left(\frac{k}{c_p}\frac{\partial h}{\partial y} - \rho\overline{h'v'}\right) = -\frac{\partial \dot{q}}{\partial y} \tag{21}$$

where

$$\dot{q} = -\frac{k}{c_p}\frac{\partial h}{\partial y} + \rho\overline{h'v'} = \dot{q}_l + \dot{q}_t \tag{22}$$

With the concept of eddy conductivity ϵ_h, the heat transfer due to the turbulent flow can be expressed in the same mathematical form as that in laminar flow. That is

$$\dot{q}_t = \rho\overline{h'v'} = -\rho\epsilon_h \frac{\partial h}{\partial y} \tag{23}$$

By using (23) we can write (22) as

$$\dot{q} = -\frac{\mu}{\Pr}\frac{\partial h}{\partial y} - \rho\epsilon_h \frac{\partial h}{\partial y} \tag{24}$$

According to Prandtl's mixing-length theory, in the region where the law of the wall applies we assume that

$$h' \sim y\frac{\partial h}{\partial y} = k_h y \frac{\partial h}{\partial y} \qquad v' \sim y\frac{\partial u}{\partial y} = k_m y \frac{\partial u}{\partial y} \tag{25}$$

where the subscripts h and m denote heat and momentum respectively. By means of (25) the definition of ϵ_h becomes

$$\epsilon_h = -\overline{h'v'}\left(\frac{\partial h}{\partial y}\right)^{-1} = k_h k_m y^2 \frac{\partial u}{\partial y} \tag{26}$$

However, mixing-length theory does not apply in the sublayer or in the transition region between the sublayer and the fully turbulent region. For this reason, in order to get a continuous temperature distribution, we use Van Driest's modeling of the viscous sublayer to Stokes flow. Rather than make corrections of the velocity fluctuations alone, we also make corrections of the temperature fluctuations by considering the nonsteady energy equation, which for an incompressible flow is

$$\frac{\partial h}{\partial t} = \frac{\nu}{\Pr}\frac{\partial^2 h}{\partial y^2} \tag{27}$$

The solution of (27) for the boundary condition $h(0, t) = h_0 \cos \omega t$ is given by the following expression:

$$h = h_0 e^{-\frac{y}{\sqrt{2}\,\bar{y}_s}} \cos\left(\omega t - \frac{\omega y}{\sqrt{2}\,\bar{u}_s}\right) \tag{28}$$

where

$$\bar{y}_s = \nu(\omega\nu)^{-1/2}\Pr^{-1/2} \qquad \bar{u}_s = \left(\frac{\omega\nu}{\Pr}\right)^{1/2} \tag{29}$$

If we now identify h as the fluctuation enthalpy h', we see that when the plate is fixed and the fluid enthalpy oscillates relative to the plate the maximum fluctuation enthalpy will be

$$h' = h_0'\left(1 - e^{-\frac{y}{\sqrt{2}\,\bar{y}_s}}\right) \tag{30}$$

From (30) it can be seen that the length scale and phase velocity of the oscillations are functions of molecular Prandtl number Pr. If, as before, we take the shear-wave propagation velocity to be the friction velocity at the edge of the sublayer for a given fluid with a particular Prandtl number, then (30) can be written as

$$h' = h_0'(1 - e^{-y/B}) \tag{31}$$

where

$$B = B^+\nu\left(\frac{\tau_s}{\rho}\right)^{-1/2} \tag{32}$$

In (32) the damping constant for enthalpy fluctuations is a function of Prandtl number

$$B^+ = B^+(\Pr) \tag{33}$$

Since

$$v' = v_0'(1 - e^{-y/A})$$

we have

$$-\rho\overline{h'v'} = -\rho\overline{h_0'v_0'}\,(1 - e^{-y/A})(1 - e^{-y/B}) \tag{34}$$

With the concept of mixing length[4] and eddy conductivity, (34) can also be written as

$$-\rho\overline{h'v'} = \rho\epsilon_h\frac{\partial h}{\partial y} \tag{35}$$

where

$$\epsilon_h = k_m k_h y^2[1 - \exp(-y/A)][1 - \exp(-y/B)]\frac{\partial u}{\partial y} \tag{36}$$

The problem is now to determine the constants k_h and B^+ in (36) and in (32) respectively. Assuming constant heat transfer close to the wall, we can approximate (21) as

$$\dot{q} = \dot{q}_w = \frac{\mu}{\Pr}\frac{dh}{dy} - \rho\epsilon_h\frac{dh}{dy} \tag{37}$$

which, in terms of dimensionless quantities, can also be written for an incompressible flow as

$$h^+ \equiv \frac{h_w - h}{h_\tau} = \int_0^{y^+} \frac{dy^+}{\frac{1}{\Pr} + \epsilon_h{}^+} \tag{38}$$

[3] Writing the ratio y/A in the exponential term as y^+/A^+, we see that if $\tau_w = 0$ then $[1 - \exp(-y/A)]$ will be zero. Thus $(\epsilon_i)_m = 0$.

[4] We note that $v_0' = k_m y\frac{\partial h}{\partial y}$, $h_0' = k_h y\frac{\partial u}{\partial y}$.

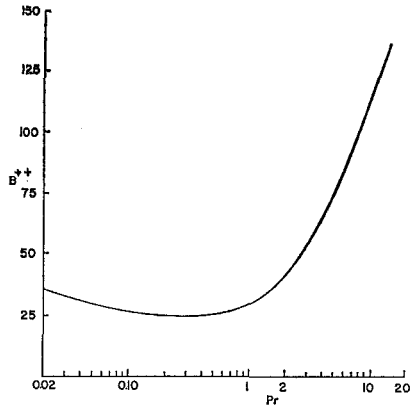

Fig. 1 Variation of turbulent Prandtl number with molecular Prandtl number according to equation (43)

by neglecting the density variation across the boundary layer. Equation (38) shows that for given values of h_w and h_τ we can calculate the dimensionless enthalpy distribution across the boundary layer, provided that the $\epsilon_h{}^+$ variation is known. According to (36) it is necessary to know k_h, B, and $\partial u/\partial y$, since k_m and A are given by (15) and (20) respectively. The term $\partial u/\partial y$, which in terms of dimensionless quantities can also be written as $\partial u^+/\partial y^+$, can be determined by considering the momentum equation close to the wall for a flat-plate flow. It is given by

$$\frac{d\tau}{dy} = 0 \qquad \text{or} \qquad \tau = \tau_w \tag{39}$$

If we denote $\tau = \tau_l + \tau_t = \mu(du/dy) - \rho\overline{u'v'}$ and use (16), we can show that (39) can be written as

$$\frac{du^+}{dy^+} = \frac{2}{1 + \{1 + 4k_m{}^2(y^+)^2[1 - \exp(-y^+/A^+)]^2\}^{1/2}} \tag{40}$$

For a flat-plate flow $B = B^+(\tau_w/\rho)^{-1/2}\nu$; hence the ratio y/B in (36) is y^+/B^+. As a result the problem now reduces to that of finding the empirical constants k_h and B^+ in $\epsilon_h{}^+$.

In the study reported here we have integrated (38) for various values of k_h and B^+ and obtained a "best" fit to the experimental data of Whitten [18], which were obtained for flat-plate incompressible turbulent boundary layers at constant wall temperature for Reynolds numbers R_θ varying from 1000 to 4500. On the basis of this curve-fitting procedure we find that the parameters k_h and B^+ can be approximated by expressions similar to those in (15), as follows:

$$k_h = 0.44 + \frac{0.22}{1 + 0.42Z^2} \qquad B^+ = 35 + \frac{25}{1 + 0.55Z^2} \qquad Z \geq 0.3 \tag{41}$$

The eddy-conductivity expression given by (36) applies only in the inner region of the boundary layer, where the law of the wall holds. If we neglect the exponential term in (36) we see that eddy conductivity varies linearly with y, as does the eddy viscosity given by (17), though with a different slope. Because of the composite nature of a turbulent boundary layer, however, a separate expression for ϵ_h should be used in the outer region, as is usual with ϵ_m-expressions. This can be done either by using, for example, a mixing-length expression $\epsilon_h \sim l^2|\partial u/\partial y|$ and taking l proportional to, say, thermal boundary-layer thickness δ_t, or by using a Clauser expression of the form $\epsilon_h \sim \left|\int_0^\infty (u_e - u)dy\right|$. The proportionality constant in the latter case may be assumed to be approximately 0.0168 as in the ϵ_m-expression.

Once an expression for ϵ_h is known we can write an expression for the turbulent Prandtl number that can be used for the entire boundary layer. Since $\mathrm{Pr}_t = \epsilon_m/\epsilon_h$ we can use (17) and (36) to write

$$\mathrm{Pr}_t = \frac{k_m[1 - \exp(-y/A)]}{k_h[1 - \exp(-y/B)]} \tag{42a}$$

At the wall Pr_t is given by

$$\mathrm{Pr}_t = \frac{k_m}{k_h}\frac{B}{A} = \frac{k_m}{k_h}\frac{B^+}{A^+} \tag{42b}$$

We note that as y becomes larger the exponential terms in (42a) approach zero. The turbulent Prandtl number then becomes

$$\mathrm{Pr}_t = \frac{k_m}{k_h} \tag{42c}$$

We also note from (42) that *the molecular Prandtl number has a strong effect on* Pr_t *close to the wall*, since $B^+ = B^+(\mathrm{Pr})$, and therefore *has no effect on* Pr_t *away from the wall.*

The damping constant in (41) is for air whose Prandtl number is approximately unity. For fluids other than air it varies, since B^+ is a function of molecular Prandtl number, (33). If we assume that k_m, k_h, and A^+ are known and amount to 0.40, 0.44, and 26 respectively, then B^+ can be calculated from (42b) provided that Pr_t is known at the wall. Following this procedure and using the experimental values of Pr_t, Na and Habib [19] expressed the variation of B^+ with molecular Prandtl number by

$$B^+ = \frac{B^{++}}{\sqrt{\mathrm{Pr}}} \tag{43}$$

where B^{++} also varies with Pr as shown in Fig. 1.

The eddy-conductivity expression (36) is developed for an incompressible flow. It can be extended to a compressible flow as follows. We consider the compressible nonsteady energy equation and neglect the dissipation terms, thus limiting the analysis to Mach numbers with negligible dissipation effects.

$$\rho\frac{\partial h}{\partial t} = \frac{\partial}{\partial y}\left(\frac{\mu}{\mathrm{Pr}}\frac{\partial h}{\partial y}\right) \tag{44a}$$

If the variation of Prandtl number with temperature is neglected, then (44a) becomes

$$\rho\frac{\partial h}{\partial t} = \frac{1}{\mathrm{Pr}}\frac{\partial}{\partial y}\left(\mu\frac{\partial h}{\partial y}\right) \tag{44b}$$

Introducing the transformation $dy = \mu dz$ into (44b) and taking $\overline{\rho\mu}$ to be an average over some interval, we get

$$\frac{\partial h}{\partial t} = \frac{\mathrm{Pr}^{-1}}{\overline{\rho\mu}}\frac{\partial^2 h}{\partial z^2} \tag{45}$$

The solution of (45) subject to the boundary condition $h(0, t) = h_0 \cos \omega t$ is

$$h = h_0 e^{-\bar{m}z}\cos(\omega t - \bar{m}z) \tag{46}$$

where

$$\bar{m} = \left(\frac{\omega}{2}\mathrm{Pr}\,\overline{\rho\mu}\right)^{1/2} \tag{47}$$

When the plate is fixed and the fluid oscillates relative to the plate, the maximum fluctuation enthalpy is

$$h' = h_0{}'\left[1 - \exp\left(-\bar{m}\int\frac{1}{\mu}\,dy\right)\right] \tag{48}$$

If we write (47) in the form

$$\bar{m} = \left(\frac{\omega\nu}{2\bar{\nu}}\mathrm{Pr}\,\overline{\rho\mu}\right)^{1/2} = \left(\frac{\tau_s}{\rho}\right)^{1/2}\frac{\bar{\rho}}{\text{const.}} \tag{49}$$

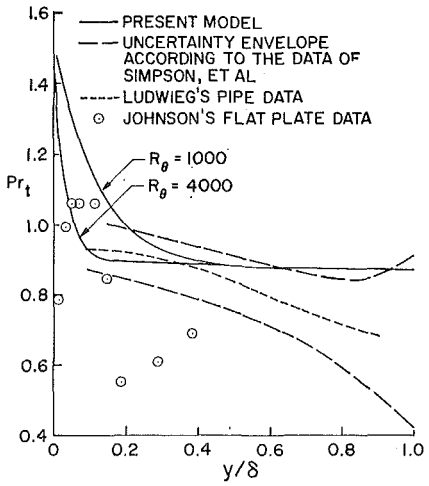

Fig. 2 Comparison of calculated turbulent Prandtl number with experiment

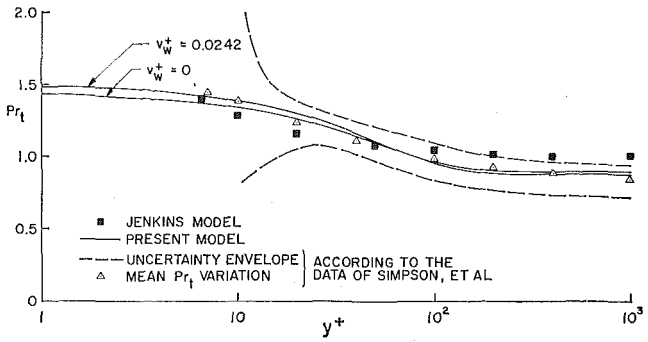

Fig. 3 Effect of mass transfer on turbulent Prandtl number

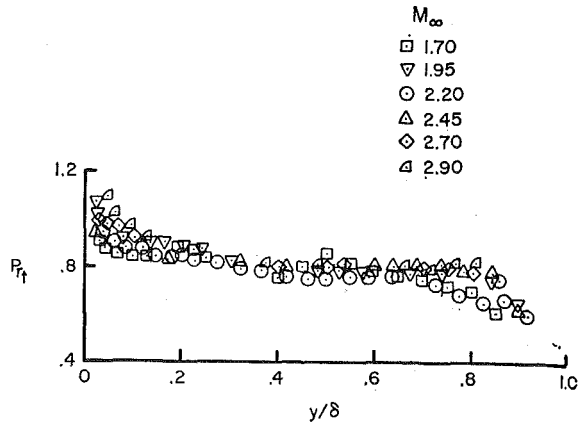

Fig. 4 Turbulent-Prandtl-number variation in the boundary layer according to experiments of Meier and Rotta [21]

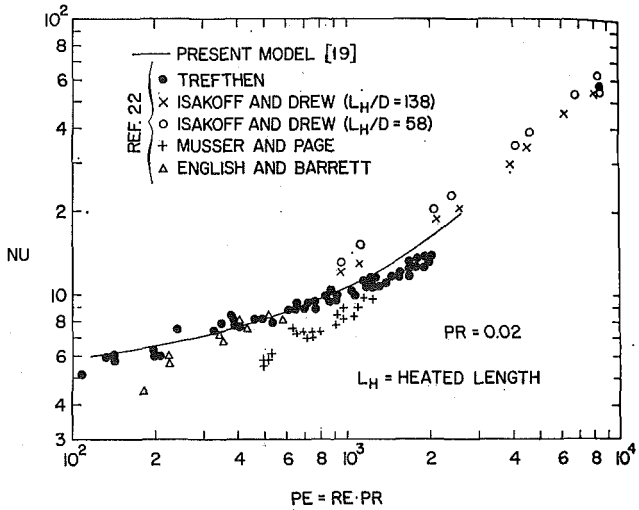

Fig. 5 Comparison of calculated and experimental values of Nusselt number for a turbulent pipe flow at different values of Peclet number

where μ in $\int dy/\mu$ is taken to be $\bar{\mu}$, and if we assume the value of the constant B^+ to be the same as in compressible flows and let $\bar{\nu} = \nu$, then for a compressible flow the damping length for temperature fluctuations can be written as

$$B = B^+\nu\left(\frac{\tau_s}{\rho}\right)^{-1/2} \tag{50}$$

The sublayer friction velocity $(\tau_s/\rho)^{1/2}$, as before, is defined by (18).

The turbulent-Prandtl-number expression given by (42) should now use expressions (20) and (50) for compressible flows.

Comparison with Experiment and with Other Models

The expression for the turbulent Prandtl number given by (42) will now be evaluated for several Reynolds numbers, and its predictions will be compared with the predictions by other expressions, together with the available experimental data on the subject. We shall consider flows with and without mass transfer.

Figure 2 shows the variation of turbulent Prandtl number with y/δ for an incompressible flow with no mass transfer. It also shows the uncertainty envelope and the variation of the mean turbulent Prandtl number determined by Simpson et al. [14] and the experimental data of Johnson [20] and Ludweig [15]. The experimental data of Johnson are for flat-plate flow at high Reynolds numbers. The experimental data of Ludweig on the other hand are based on measurements in a pipe, again at high Reynolds numbers. According to Kestin and Richardson's study, Ludweig's results are the most reliable for air flowing in a pipe [8]. The comparisons in Fig. 2 show that the present results, especially one calculated for $R_\theta = 4000$, agree reasonably well with Ludweig's results for $0.1 \leq y \leq 0.4$ and differ slightly from his results for $y/\delta > 0.4$. However, the predicted results fall within the uncertainty envelope of Simpson et al. It is interesting to note that the predicted results for the region near the wall also agree well with Johnson's data, although the discrepancy is significant away from the wall.

We next study the effect of mass transfer on turbulent Prandtl number. We use the experimental data of Simpson and calculate Pr_t at various values of y^+ and y/δ for given values of R_θ and v_w^+. Figure 3 shows the calculated results for $v_w^+ = 0$ and 0.0247 for $R_\theta = 2000$, together with the uncertainty envelope and the variation of the mean turbulent Prandtl number of Simpson et al. Considering the fact that the calculations were made for a low Reynolds number, it can be said that the results agree reasonably well with the findings of Simpson et al. and show no appreciable effect of mass transfer on the turbulent Prandtl number.

We next compare the present model with the very recent experimental data of Meier and Rotta [21]. These authors present temperature distributions in supersonic flows and turbulent-Prandtl-number distributions obtained from their experimental data. They point out that their turbulent-Prandtl-number distributions for such flows are in excellent agreement with those of Simpson et al. [14], who carried out measurements at low subsonic speeds on a porous plate. They further point out that if they express Prandtl's mixing-length expression in the form written by Van Driest, that is,

$$l_h = k_h y\left[1 - \exp\left(-\frac{y(\tau_w\rho)^{1/2}}{\mu B^+}\right)\right] \tag{51}$$

and use the following restrictions, namely

$$y = 0 \qquad Pr_t = \left(\frac{k_m}{k_h}\frac{B^+}{A^+}\right)^2 \tag{52}$$

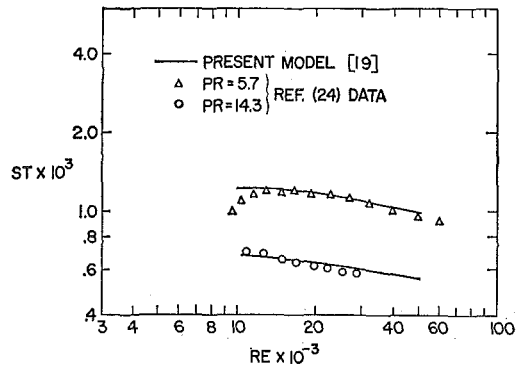

Fig. 6 Comparison of calculated and experimental values of Stanton number for a turbulent pipe flow at different values of Reynolds number

$$y \to \infty \qquad \mathrm{Pr}_t = \left(\frac{k_m}{k_h}\right)^2 \tag{52}$$

then the calculated temperature distributions using these expressions are in excellent agreement with their experimental data, provided that they choose the constants appearing in (51) and (52) as $k_m = 0.40$, $k_h = 0.43$, $A^+ = 26$, and $B^+ = 33.8$, four empirical values that compare well with those used in this paper. Figure 4 shows the experimental Pr_t variation for Meier and Rotta's experiments.

Finally, we show the heat-transfer results obtained for pipe flow by using the present model. The calculations were made by Na and Habib [19]. The authors applied the present model to fluids with low, medium, and high Prandtl numbers. These data represent fluids of practical importance, namely liquid metals (Pr = 0.02) up to water with additives (Pr = 14.3). Figures 5 and 6 show comparisons of calculated and experimental values of Nusselt number for three values of Prandtl number. As can be seen from these comparisons the agreement between theory and experimental data is very good.

Na and Habib also made comparisons between theoretical and experimental temperature distributions. In Fig. 7 we show only the results for Pr = 14.3. For further comparisons, see [19]. Again the agreement is very good.

Concluding Remarks

On the basis of comparisons presented in the previous section it can be said that the present model for eddy conductivity and turbulent Prandtl number seems to agree well with the experimental data. This includes fluids with low, medium, and high molecular Prandtl numbers. The expression for turbulent Prandtl number shows that Pr_t is a strong function of molecular Prandtl number near the wall and that it is a constant away from the wall.

The expression for turbulent Prandtl number also shows that its wall value is greater than unity for the range of molecular Prandtl number considered in this paper. For example, for a liquid-metal fluid (Pr = 0.02) Pr_t is 10.9, and for air (Pr = 0.72) Pr_t is 1.22, $R_\theta > 5000$. In the latter case the predicted value of Pr_t is somewhat higher than the commonly accepted and used value of Pr_t, which is generally taken to be 0.90. However, the effect of higher wall turbulent Prandtl number on the calculated heat-transfer parameters such as Stanton number and temperature profiles is not very pronounced according to the studies conducted using the finite-difference method of Cebeci and Smith [25]. Several incompressible turbulent flows calculated by this method show that with variable turbulent Prandtl number, Stanton numbers are slightly lower than those obtained with a constant turbulent Prandtl number; with the scatter in experimental data it is very difficult to judge which of the calculated values agrees better with experiment. On the other hand the temperature profiles calculated by using a variable turbulent

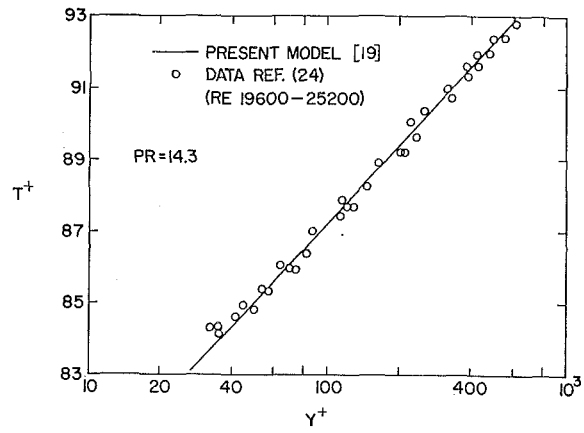

Fig. 7 Comparison of calculated and experimental temperature distribution for a turbulent pipe flow

Prandtl number show better agreement with experiment, although slight, than those obtained by using a constant turbulent Prandtl number.

References

1 Reynolds, W. C., "A Morphology of the Prediction Methods," *Proceedings of the 1968 AFOSR-IFP-Stanford Conference on Computation of Turbulent Boundary Layers*, Vol. 1, Stanford University, Stanford, Calif., pp. 1–15.

2 Hinze, J. O., *Turbulence*, McGraw-Hill, New York, N. Y., 1959.

3 Van Driest, E. R., "On Turbulent Flow near a Wall," *J. Aero. Sci.*, Vol. 23, 1956, pp. 1007.

4 Cebeci, T., "The Behavior of Turbulent Flow near a Porous Wall with Pressure Gradient," *AIAA Journal*, Vol. 8, No. 12, Dec. 1970, pp. 2152–2156.

5 Cebeci, T., "Calculation of Compressible Turbulent Boundary Layers with Heat and Mass Transfer," *AIAA Journal*, Vol. 9, No. 6, June 1971, pp. 1091–1097.

6 Patankar, S. V., and Spalding, D. B., *Heat and Mass Transfer in Boundary Layers*, Intertext Books, London, England, 1967.

7 Clauser, F. H., "The Turbulent Boundary Layer," in: *Advances in Applied Mechanics*, Vol. IV, Academic, New York, N. Y., 1956.

8 Kestin, J., and Richardson, P. D., "Heat Transfer across Turbulent Incompressible Boundary Layers," *International Journal of Heat and Mass Transfer*, Vol. 6, 1963, pp. 147–189.

9 Jenkins, R., "Variation of the Eddy Conductivity with Prandtl Modulus and Its Use in Prediction of Turbulent Heat Transfer Coefficients," *Inst. Heat Transfer Fluid Mech.*, 1951, pp. 147–158.

10 Kays, W. M., *Convective Heat and Mass Transfer*, McGraw-Hill, New York, N. Y., 1966.

11 Page, F., Schlinger, W. G., Breaux, D. K., and Sage, B. H., "Point Values of Eddy Conductivity and Viscosity in Uniform Flow between Parallel Plates," *Ind. Eng. Chem.*, Vol. 44, 1952, p. 424.

12 Deissler, R. G., "Turbulent Heat Transfer and Temperature Fluctuations in a Field with Uniform Velocity and Temperature Gradients," *International Journal of Heat and Mass Transfer*, Vol. 6, 1963, pp. 257–269.

13 Tyldesley, J. R., and Silver, R. S., "The Prediction of the Transport Properties of a Turbulent Fluid," *International Journal of Heat and Mass Transfer*, Vol. 11, 1968, pp. 1325–1340.

14 Simpson, R. L., Whitten, D. G., and Moffat, R. J., "An Experimental Study of the Turbulent Prandtl Number of Air with Injection and Suction," *International Journal of Heat and Mass Transfer*, Vol. 13, 1970, pp. 125–143.

15 Ludweig, H., "Bestimmung des Verhaltnisses der Austauschköffizienten für Warme and Impuls bei turbulenten Grenzschichten," *Z. Flugwiss*, Vol. 4, 1956, pp. 73–81.

16 Schlichting, H., *Boundary-Layer Theory*, McGraw-Hill, New York, N. Y., 1968, p. 85.

17 Cebeci, T., and Mosinskis, G. J., "On the Computation of Turbulent Boundary Layers at Low Reynolds Numbers," *AIAA Journal*, Vol. 9, No. 8, Aug. 1971, pp. 1632–1634.

18 Whitten, D. G., "The Turbulent Boundary Layer on a Porous Plate. Experimental Heat Transfer with Variable Suction, Blowing, and Surface Temperature," PhD thesis, Stanford University, Stanford, Calif., 1967.

19 Na, T. Y., and Habib, I. S., "Heat Transfer in Turbulent Pipe Flow Based on a New Mixing Length Model," to be published.

20 Johnson, D. S., "Velocity and Temperature Fluctuation Mea-

surements in a Turbulent Boundary Layer Downstream of a Stepwise Discontinuity in Wall Temperature," *Journal of Applied Mechanics*, Vol. 26, TRANS. ASME, Series E, Vol. 81, No. 3, Sept. 1959, pp. 325–336.

21 Meier, H. U., and Rotta, J. C., "Experimental and Theoretical Investigations of Temperature Distributions in Supersonic Boundary Layers," AIAA Paper No. 70-744, AIAA Third Fluid and Plasma Dynamics Conference, Los Angeles, Calif., 1970.

22 McAdams, W. H., *Heat Transmission*, 3rd ed., McGraw-Hill, New York, N. Y., 1954, Fig. 9.8.

23 Lawn, C. J., "Turbulent Heat Transfer at Low Reynolds Number," JOURNAL OF HEAT TRANSFER, TRANS. ASME, Series C, Vol. 91, No. 4, Nov. 1969, pp. 532–536 (see Figs. 1 and 2).

24 Gowen, R. A., and Smith, J. W., "The Effect of the Prandtl Number on Temperature Profiles for Heat Transfer in Turbulent Pipe Flow," *Chem. Eng. Sci.*, Vol. 22, 1967, pp. 1701–1711.

25 Cebeci, T., and Smith, A. M. O., "A Finite-Difference Method for Calculating Compressible Laminar and Turbulent Boundary Layers," *Journal of Basic Engineering*, TRANS. ASME, Series B, Vol. 92, No. 3, Sept. 1970, pp. 523–535.

surements in a Turbulent Boundary Layer Downstream of a Stepwise Discontinuity in Wall Temperature," *Journal of Applied Mechanics*, Vol. 26, TRANS. ASME, Series E, Vol. 81, No. 3, Sept. 1959, pp. 325–336.

21 Meier, H. U., and Rotta, J. C., "Experimental and Theoretical Investigations of Temperature Distributions in Supersonic Boundary Layers," AIAA Paper No. 70-744, AIAA Third Fluid and Plasma Dynamics Conference, Los Angeles, Calif., 1970.

22 McAdams, W. H., *Heat Transmission*, 3rd ed., McGraw-Hill, New York, N. Y., 1954, Fig. 9.8.

23 Lawn, C. J., "Turbulent Heat Transfer at Low Reynolds Number," JOURNAL OF HEAT TRANSFER, TRANS. ASME, Series C, Vol. 91, No. 4, Nov. 1969, pp. 532–536 (see Figs. 1 and 2).

24 Gowen, R. A., and Smith, J. W., "The Effect of the Prandtl Number on Temperature Profiles for Heat Transfer in Turbulent Pipe Flow," *Chem. Eng. Sci.*, Vol. 22, 1967, pp. 1701–1711.

25 Cebeci, T., and Smith, A. M. O., "A Finite-Difference Method for Calculating Compressible Laminar and Turbulent Boundary Layers," *Journal of Basic Engineering*, TRANS. ASME, Series B, Vol. 92, No. 3, Sept. 1970, pp. 523–535.

Discussion

T. Y. Na and I. S. Habib[5]

The author is to be congratulated for his contribution to the empirical theory of eddy conductivity. We would like to supplement the paper by pointing out that [19] in this paper refers to our work on turbulent heat transfer in pipes which is soon to appear in the *Journal of Applied Scientific Research*. For the reader's reference, Figs. 5, 6, and 7 in this paper are replots of our Figs. 1, 3, and 6 respectively. As indicated by Dr. Cebeci, we have calculated results for other values of the Prandtl number as well.

Our paper [19] shows that the expression for B^+ is best represented by the equation

$$B^+ = \sum_{i=1}^{5} C_i(\log_{10} \mathrm{Pr})^{i-1}$$

where

$$C_1 = 34.96$$

$$C_2 = 28.79$$

$$C_3 = 33.95$$

$$C_4 = 6.33$$

$$C_5 = -1.186$$

[5] Professors, Division of Engineering, University of Michigan–Dearborn, Dearborn, Mich.

R. V. S. YALAMANCHILI
Research Mechanical Engineer.

S.-C. CHU
Mechanical Engineer.

Research Directorate,
GEN. THOMAS J. RODMAN LABORATORY,
Rock Island Arsenal,
Rock Island, Ill.

Stability and Oscillation Characteristics of Finite-Element, Finite-Difference, and Weighted-Residuals Methods for Transient Two-dimensional Heat Conduction in Solids

The finite-element difference expression was derived by use of the variational principle and finite-element synthesis. Several ordinary finite-difference formulae for the Laplacian term were considered. A particular finite-difference formula for the Laplacian term was chosen to bring the difference expressions of finite-element, finite-difference, and weighted-residuals (Galerkin) methods into the same format. The stability criteria were established for all three techniques by use of the general stability, von Neumann, and Dusinberre concepts. The oscillation characteristics were derived for all three techniques. The finite-element method is more conservative than the finite-difference method, but not so conservative as the Galerkin method in both stability and oscillation characteristics.

Introduction

Carslaw and Jaeger [1][1] summarized numerous analytical solutions for rectangular regions, cylinders, and spheres under a variety of initial and boundary conditions. However, if the body has an irregular shape (such as rifling in the bore of a gun or variable wall thickness), the possibility of obtaining an analytical solution is negligible, and in such situations, numerical methods are used.

Various numerical methods have been used for solutions to the problems of transient heat conduction. The most common ones are the finite-difference method (which represents a direct approximation of the governing partial differential equation) and the finite-element method introduced by Wilson and Nickell [2] based on a variational principle derived by Gurtin [3]. The finite-element method is completely general with respect to geometry and material properties. Complex bodies composed of many different anisotropic materials are easily represented in this method. Temperature or heat-flux boundary conditions may be specified at any point within the finite-element system. Moreover, mathematically, the method can be shown to converge toward the exact solution as the number of elements is increased.

Several references were discussed in previous reports [4–6]. Lemmon and Heaton [7] compared the accuracy, stability, and oscillation characteristics of the finite-element method with the finite-difference method and concluded that the stability and the nonoscillation criteria for one-dimensional problems are more restrictive for the finite-element method, with the truncation error about the same. This type of analysis is not found in the literature for transient two-dimensional heat-conduction problems. Also, no finite-element difference expressions are evident in the literature for two- and three-dimensional cases. The objective of this study was to close these gaps so that the existing resources on both techniques under consideration could be completely utilized.

Finite-Element Difference Expression

Wilson and Nickell [2], following Gurtin's [3] discussion of variational principles for linear initial-value problems, confirmed that the function $T(x, y, t)$, which leads to an extremum of the functional

$$\Omega_t(T) = \frac{1}{2}\int_V \{\rho C_p T^* T + \nabla T^* K^* \nabla T - 2\rho C_p T_0^* T\} dV - \int_S \hat{Q}_i \eta_i^* T dS \quad (1)$$

is the solution of the following transient heat-conduction equation:

[1] Numbers in brackets designate References at end of paper.

Contributed by the Heat Transfer Division for publication (without presentation) in the Journal of Heat Transfer. Manuscript received by the Heat Transfer Division May 21, 1972. Paper No. 73-HT-E.

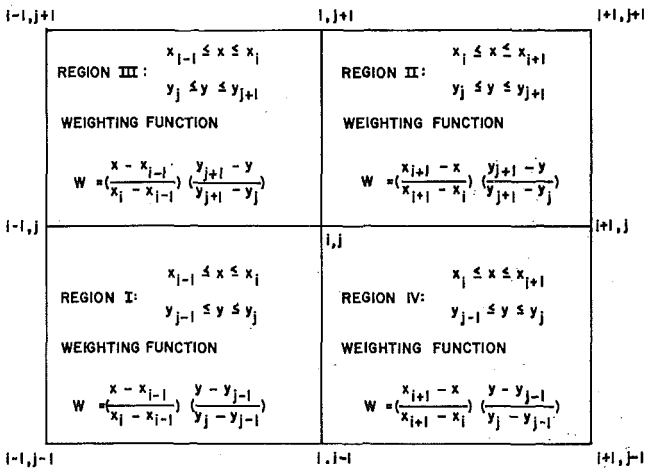

Fig. 1 Two-dimensional elements around (x_i, y_j) and corresponding weighting functions

$$(K^*T_{,i})_{,i} - \rho C_p{}^* \frac{\partial T}{\partial t} = 0 \tag{2}$$

with the boundary condition

$$K^*T_{,i} - \hat{Q}_i = 0 \tag{3}$$

where $T(x, y, t)$ is the temperature at the spatial point (x, y) and at time t, T_0 is initial temperature, ∇T is the gradient of T with respect to spatial coordinates, K is thermal conductivity, ρ is material density, C_p is heat capacity of the material per unit mass, $\hat{Q}_i(x, y, t) = \int_0^t Q_i(x, y, \tau)d\tau$, V is volume, and * is a convolution symbol defined as

$$T^*T = \int_0^t T(x, y, t - \tau)T(x, y, \tau)d\tau$$

$$\nabla T^*\nabla T = \frac{\partial T^*}{\partial x}\frac{\partial T}{\partial x} + \frac{\partial T^*}{\partial y}\frac{\partial T}{\partial y} \tag{4}$$

The two-dimensional solid body is divided into M axial elements (nodes 0 to M) and N transverse elements (nodes 0 to N) so that step sizes are the same in both directions. This restriction (i.e., square element) is introduced to simplify algebraic manipulations involved in the analysis. Instead, a unit step size can be assumed without any loss of generality.

The nodal point i, j $(0 \le i \le M, 0 \le j \le N)$, as shown in Fig. 1, is considered. The temperature of the nodal point will vary as a function of time t. The temperature distribution in a subregion is a function of spatial coordinates (x and y) and surrounding nodal point temperatures. For simplicity, linearity and the same functional distribution are assumed for all elements, i.e.,

$$T(x, y, t) = f_1 + xf_2 + yf_3 + xyf_4 \tag{5}$$

where f_1, f_2, f_3, and f_4 are functions of nodal point temperatures $0 \le x \le 1$ and $0 \le y \le 1$. Functions f_1, f_2, f_3, and f_4 are to be determined by substitution of the coordinates of nodal points into the equation above and by solution of the resulting simultaneous equations. The resulting equation is shown here:

$$T(x, y, t) = (1 - x - y - xy)T_{i,j,k} + x(1 - y)T_{i+1,j,k} + y(1 - x)T_{i,j+1,k} + xyT_{i+1,j+1,k} \tag{6}$$

Integrating over the volume occupied by region I, as shown in Fig. 1, and taking the first variation with respect to $T_{i,j,k+1}$ yields the following result for the first term in equation (1):

$$\frac{2}{9}T_{i,j,k+1} + \frac{1}{9}T_{i,j-1,k+1} + \frac{1}{9}T_{i-1,j,k+1} + \frac{1}{18}T_{i-1,j-1,k+1} \tag{7}$$

Similar results for regions II, III, and IV are given below in that order. The first variation is taken with respect to the same nodal temperature $T_{i,j,k+1}$.

$$\frac{2}{9}T_{i,j,k+1} + \frac{1}{9}T_{i,j+1,k+1} + \frac{1}{9}T_{i+1,j,k+1} + \frac{1}{18}T_{i+1,j+1,k+1}$$

$$\frac{2}{9}T_{i,j,k+1} + \frac{1}{9}T_{i-1,j,k+1} + \frac{1}{9}T_{i,j+1,k+1} + \frac{1}{18}T_{i-1,j+1,k+1}$$

$$\frac{2}{9}T_{i,j,k+1} + \frac{1}{9}T_{i,j-1,k+1} + \frac{1}{9}T_{i+1,j,k+1} + \frac{1}{18}T_{i+1,j-1,k+1} \tag{8}$$

By consideration of the results obtained over all the regions, the entire contribution due to the first term of equation (1) is as follows:

$$\frac{2\rho C_p}{36}\{T_{i-1,j-1,k+1} + 4T_{i-1,j,k+1} + T_{i-1,j+1,k+1} + 4T_{i,j-1,k+1} + 16T_{i,j,k+1} + 4T_{i,j+1,k+1} + T_{i+1,j-1,k+1} + 4T_{i+1,j,k+1} + T_{i+1,j+1,k+1}\} \tag{9}$$

The evaluation of the third term in equation (1) is essentially similar to the evaluation of the first term. The contribution due to the third term of equation (1) is

$$-\frac{2\rho C_p}{36}\{T_{i-1,j-1,k} + 4T_{i-1,j,k} + T_{i-1,j+1,k} + 4T_{i,j-1,k} + 16T_{i,j,k} + 4T_{i,j+1,k} + T_{i+1,j-1,k} + 4T_{i+1,j,k} + T_{i+1,j+1,k}\} \tag{10}$$

The evaluation of the second term in equation (1) involves integration not only over the volume (and the use of variation with respect to the nodal temperature $T_{i,j,k+1}$) but also over the time step due to the additional convolution symbol. Toward this goal, a linear nodal point temperature variation is assumed within each time step. The final expression for the entire second term becomes

$$-\frac{K\Delta t}{3}\{[T_{i-1,j-1,k+1} + T_{i-1,j,k+1} + T_{i-1,j+1,k+1} + T_{i,j-1,k+1} - 8T_{i,j,k+1} + T_{i,j+1,k+1} + T_{i+1,j-1,k+1} + T_{i+1,j,k+1} + T_{i+1,j+1,k+1}] + [T_{i-1,j-1,k} + T_{i-1,j,k} + T_{i-1,j+1,k} + T_{i,j-1,k} - 8T_{i,j,k} + T_{i,j+1,k} + T_{i+1,j-1,k} + T_{i+1,j,k} + T_{i+1,j+1,k}]\} \tag{11}$$

Difference Expression

Summing the previous results of all three terms produces the finite-element difference expression for an internal portion of the solid body. Dividing throughout by ρC_p and generalizing the results for arbitrary spatial step size ΔL instead of unit step size provides the following result:

$$AT_{i-1,j-1,k+1} + BT_{i-1,j,k+1} + AT_{i-1,j+1,k+1} + BT_{i,j-1,k+1} + CT_{i,j,k+1} + BT_{i,j+1,k+1} + AT_{i+1,j-1,k+1} + BT_{i+1,j,k+1} + AT_{i+1,j+1,k+1} = DT_{i-1,j-1,k} + ET_{i-1,j,k} + DT_{i-1,j+1,k} + ET_{i,j-1,k} + FT_{i,j,k} + ET_{i,j+1,k} + DT_{i+1,j-1,k} + ET_{i+1,j,k} + DT_{i+1,j+1,k} \tag{12}$$

where

$$A = \frac{1}{36} - \frac{1}{3}\theta \qquad B = \frac{1}{9} - \frac{1}{3}\theta \qquad C = \frac{4}{9} + \frac{8}{3}\theta$$

$$D = \frac{1}{36} + \frac{1}{3}\theta \qquad E = \frac{1}{9} + \frac{1}{3}\theta \qquad F = \frac{4}{9} - \frac{8}{3}\theta$$

$$\theta = \frac{K\Delta t}{2\rho C_p \Delta L^2} \tag{13}$$

This is the first time such a finite-element difference expression is derived or mentioned in the literature for two-dimensional problems.

Ordinary Finite-Difference Expressions

The governing equation of heat conduction in a two-dimensional body with constant material properties is

$$\frac{2}{3}\frac{\partial T}{\partial t} = \frac{2}{3}\frac{K}{\rho C_p}\left(\frac{\partial^2 T}{\partial x^2} + \frac{\partial^2 T}{\partial y^2}\right) \tag{14}$$

Rewriting the first derivative in a finite-difference form, the governing equation (14) becomes

$$\frac{T_{i,j,k+1} - T_{i,j,k}}{\frac{3}{2}\cdot\frac{K}{\rho C_p}\Delta t} = \phi\left(\frac{\partial^2 T}{\partial x^2} + \frac{\partial^2 T}{\partial y^2}\right)_{i,j,k+1} + \left(\frac{2}{3} - \phi\right)\left(\frac{\partial^2 T}{\partial x^2} + \frac{\partial^2 T}{\partial y^2}\right)_{i,j,k} \tag{15}$$

where $\phi = 0$, explicit scheme, and $0 < \phi \leq 2/3$, implicit scheme.

Numerous difference formulae can be formulated for first- and second-order derivatives, and also for the Laplacian term, depending upon the number of nodes available for taking a derivative and also on the weights of the data at those nodes. Several difference formulae can be constructed for first- and second-order derivatives by expansion of the function in Taylor's series and the use of an elimination process. The Laplacian term is evaluated by use of the central difference formulae for the second-order derivatives. Several difference schemes for the Laplacian term derived by use of well-known techniques are given below:

5-Point Differences

$$\frac{T_{i-1,j} + T_{i,j-1} + T_{i,j+1} + T_{i+1,j} - 4T_{i,j}}{(\Delta L)^2} \tag{16}$$

$$\frac{T_{i-1,j-1} + T_{i-1,j+1} + T_{i+1,j-1} + T_{i+1,j+1} - 4T_{i,j}}{2(\Delta L)^2} \tag{17}$$

9-Point Differences

$$(T_{i-1,j-1} + T_{i-1,j} + T_{i-1,j+1} + T_{i,j-1} - 8T_{i,j} + T_{i,j+1} + T_{i+1,j-1} + T_{i+1,j} + T_{i+1,j+1})/(2\Delta L^2) \tag{18}$$

$$(T_{i-1,j-1} + 4T_{i-1,j} + T_{i-1,j+1} + 4T_{i,j-1} - 20T_{i,j} + 4T_{i,j+1} + T_{i+1,j-1} + 4T_{i+1,j} + T_{i+1,j+1})/(6\Delta L^2) \tag{19}$$

The subscript k is not used in these equations to indicate time. Appropriate additional subscripts should be introduced into these difference formulae before substitution in the appropriate terms of equation (14). The formulae above are constructed with equal spatial step sizes ΔL. Note that the famous Crank–Nicholson scheme can be obtained by setting the parameter ϕ to one-third.

Method of Weighted Residuals (Galerkin)

The method of weighted residuals generalizes many approximate methods of the solution of differential equations that are in use today. In the literature this technique is commonly called the error distribution principle. In the case of one-dimensional problems [7], the method of weighted residuals with a Dirac delta function as the weighting function (collocation method) yields a finite-difference expression; with a distribution function the same as the weighting function (Galerkin method), it yields a finite-element difference expression. By following the same line of attack, one can prove that the collocation method yields a finite-difference expression for two- and three-dimensional problems. In a more formal way [8, 9], variational principles proposed by several authors are all applications of the method of weighted residuals. The Galerkin method is applied to the governing two-dimensional heat conduction equation in the rest of this section.

The parameter ϕ in equation (15) allows a weighted average of two second-order spatial derivatives at the two discrete times. The residual error due to approximations becomes

$$R(x, y) = \phi\left(\frac{\partial^2 T}{\partial x^2} + \frac{\partial^2 T}{\partial y^2}\right)_{i,j,k+1} + \left(\frac{2}{3} - \phi\right)\left(\frac{\partial^2 T}{\partial x^2} + \frac{\partial^2 T}{\partial y^2}\right)_{i,j,k} - \frac{T_{i,j,k+1} - T_{i,j,k}}{\frac{3}{2}\frac{K}{\rho C_p}\Delta t} \tag{20}$$

The objective of applying the method of weighted residuals is to minimize the error and to distribute it, with the help of a weighting function $W(x, y)$, in such a manner that the net result will be zero, i.e.,

$$\iint R(x, y)W(x, y)dxdy = 0 \tag{21}$$

The following temperature distribution function is assumed for region I in Fig. 1:

$$T(x, y, t) = T_{i-1,j-1,k}\left(\frac{x_i - x}{x_i - x_{i-1}}\right)\left(\frac{y_j - y}{y_j - y_{j-1}}\right) + T_{i,j,k}\left(\frac{x - x_{i-1}}{x_i - x_{i-1}}\right)\left(\frac{y - y_{j-1}}{y_j - y_{j-1}}\right) + T_{i,j-1,k}\left(\frac{x - x_{i-1}}{x_i - x_{i-1}}\right)\left(\frac{y_j - y}{y_j - y_{j-1}}\right) + T_{i-1,j,k}\left(\frac{x_i - x}{x_i - x_{i-1}}\right)\left(\frac{y - y_{j-1}}{y_j - y_{j-1}}\right) \tag{22}$$

where $T_{i,j,k}$ is a discrete temperature in both time and space.

Similar temperature distribution functions can be formulated for the remaining regions [4]. The weighting functions (Fig. 1) are chosen to be coefficients of the discrete temperatures mentioned above. Assuming the Laplacian term as constant at that time over all four elements and equal to a particular finite-difference formula, equation (18), and substituting the residual temperature distributions and weighting functions into equation (21) yields

$$A_1T_{i-1,j-1,k+1} + B_1T_{i-1,j,k+1} + A_1T_{i-1,j+1,k+1} + B_1T_{i,j-1,k+1} + C_1T_{i,j,k+1} + B_1T_{i,j+1,k+1} + A_1T_{i+1,j-1,k+1} + B_1T_{i+1,j,k+1} + A_1T_{i+1,j+1,k+1} = D_1T_{i-1,j-1,k} + E_1T_{i-1,j,k} + D_1T_{i-1,j+1,k} + E_1T_{i,j-1,k} + F_1T_{i,j,k} + E_1T_{i,j+1,k} + D_1T_{i+1,j-1,k} + E_1T_{i+1,j,k} + D_1T_{i+1,j+1,k} \tag{23}$$

where

$$A_1 = \frac{1}{36} - \phi\theta_1 \qquad B_1 = \frac{1}{9} - \phi\theta_1 \qquad C_1 = \frac{4}{9} + 8\phi\theta_1$$

$$D_1 = \frac{1}{36} + \left(\frac{2}{3} - \phi\right)\theta_1 \qquad E_1 = \frac{1}{9} + \left(\frac{2}{3} - \phi\right)\theta_1$$

$$F_1 = \frac{4}{9} - 8\left(\frac{2}{3} - \phi\right)\theta_1 \qquad \theta_1 = \frac{3}{2}\cdot\frac{K\Delta t}{2\rho C_p\Delta L^2} = \frac{3}{2}\theta \tag{24}$$

The objective of choosing a particular finite-difference formula for the Laplacian term in the foregoing analysis is to bring the difference expressions of the finite-element method, the finite-difference method, and the method of weighted residuals into the same format. This has been achieved provided ϕ is equal to one-third. However, the only difference that exists between the finite-element difference expression and the Galerkin difference expression is the proportionality constant between θ and θ_1. Otherwise, both are identical.

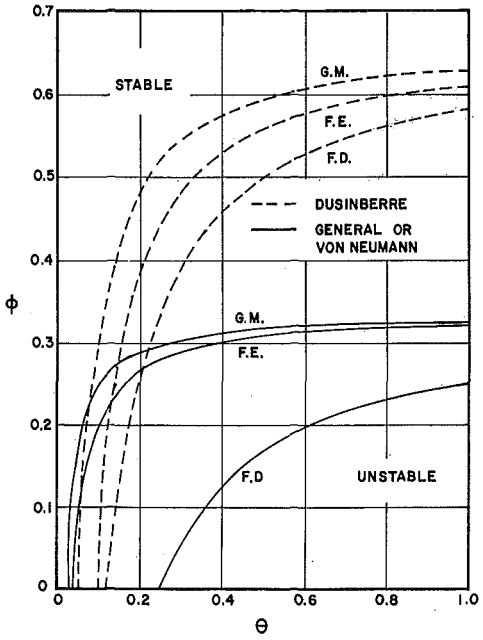

Fig. 2 Various stability criteria

On the basis of the analysis carried out, the parameter ϕ is predicted to equal one-fourth for a three-dimensional problem ($0 \leq \phi \leq 1/2$).

Instead of assuming linear weighting functions in x and y, a power-law assumption (exponent l for x and y functions) yields the same relationship, equation (23), as Galerkin's method, but with different coefficients [4].

Stability Analysis

For any chosen finite-increment (finite-difference or finite-element) formula for a parabolic system with a fixed value of $(K/\rho C_p)\Delta t(1/\Delta x^2 + 1/\Delta y^2)$, the effort required to calculate the solution for a given amount is proportional to the number of spatial nodal points raised to the power of three. The number of spatial points changes drastically for multidimensional problems. Therefore, stability, accuracy, and oscillation characteristics of two- and three-dimensional problems are essential for economical and practical reasons.

The following boundary conditions are assumed to obtain the solution of difference equations derived above:

$$T(0, y, t) = 0 \qquad T(x, 0, t) = 0$$

$$\frac{\partial T}{\partial y}(x, b, t) = 0 \qquad \frac{\partial T}{\partial x}(a, y, t) = 0 \tag{25}$$

where a and b are arbitrary constants denoting the dimensions of the solid body.

Assuming a product solution of the form

$$T_{i,j,k} = X_i Y_j \bar{T}_k \tag{26}$$

in equation (12) and using the method of separation of variables yields the following equations:

$$\bar{T}_{k+1} - \frac{1}{\beta}\bar{T}_k = 0$$

$$Y_{j-1} + \alpha_n Y_j + Y_{j+1} = 0$$

$$X_{i-1} + \lambda_m X_i + X_{i+1} = 0 \tag{27}$$

where

$$\lambda_i = \frac{\alpha_n B - \alpha_n \beta E - C + \beta F}{\alpha_n A - \alpha_n \beta D - B + \beta E}$$

or

$$\frac{1}{\beta} = \frac{F - \alpha_n E + \lambda_m \alpha_n D - \lambda_m E}{C - \alpha_n B + \lambda_m \alpha_n A - \lambda_m B} \tag{28}$$

and α_n and β are separation constants.

Following [4, 7, 10], one may obtain the general solution of difference equation (12) by taking $\alpha_n = -2 \cos \delta_n$ and $\lambda_m = -2 \cos \eta_m$:

$$T_{i,j,k} = \sum_{m=0}^{M}\sum_{n=0}^{N} C_2 \left(\frac{1}{\beta}\right)^k [C_{3n} \cos(j\delta_n) + C_{4n} \sin(j\delta_n)] \times [C_{5m} \cos(i\eta_m) + C_{6m} \sin(i\eta_m)] \tag{29}$$

Substitution of zero-temperature boundary conditions from equation (25) results in $C_{3n} = 0$ and $C_{5m} = 0$. Substitution of adiabatic boundary conditions, i.e., $Y_{N-1} = Y_{N+1}$ and $X_{M-1} = X_{M+1}$ yields the following eigenvalues:

$$\delta_n = \frac{(2n-1)\pi}{2N} \qquad \eta_m = \frac{(2m-1)\pi}{2M} \tag{30}$$

The complete solution of equations (12) and (25) is given by

$$T_{i,j,k} = \sum_{m=1}^{M}\sum_{n=1}^{N} C_{mn} \left(\frac{1}{\beta}\right)^k \sin\left(\frac{2n-1}{N}\frac{j\pi}{2}\right) \times \sin\left(\frac{2m-1}{M}\frac{i\pi}{2}\right) \tag{31}$$

Apparently, $(\lambda_m)_{\max} = 2$ and $(\alpha_n)_{\max} = 2$. Also, $(1/\beta)$ must obviously be less than unity and greater than minus one for the numerical solution to remain stable; therefore

$$\phi > \frac{1}{3} - \frac{1}{72\theta}$$

Similar analysis can be performed on the method of weighted residuals difference expression equation (23). In this method, the stability requirement becomes:

$$\phi > \frac{1}{3} - \frac{1}{72\theta_1} \quad \text{or} \quad \phi > \frac{1}{3} - \frac{1}{108\theta}$$

If the stability analysis given above is carried out on the finite-difference equation, combination of equations (15) and (18), the stability requirement necessitates

$$\phi > \frac{1}{3} - \frac{1}{8\theta_1} \quad \text{or} \quad \phi > \frac{1}{3} - \frac{1}{12\theta}$$

The results of the equations above are shown in Fig. 2. The finite-element method is more conservative than the finite-difference method, but it is not as conservative as the method of weighted residuals (Galerkin). Identical results can be obtained even if the von Neumann stability analysis is applied on appropriate difference equations. Dusinberre [11] in his stability criteria states that negative coefficients in the difference equation should be avoided to enforce stability. The coefficients A, B, and F or A_1, B_1, and F_1 can be negative. The following restrictions, respectively, are needed to keep F and F_1 positive:

$$\phi > \frac{2}{3} - \frac{1}{18\theta}$$

$$\phi > \frac{2}{3} - \frac{1}{18\theta_1} \quad \text{or} \quad \phi > \frac{2}{3} - \frac{1}{27\theta}$$

For a finite-difference method, the Dusinberre stability requirement becomes

$$\phi > \frac{2}{3} - \frac{1}{8\theta_1} \quad \text{or} \quad \phi > \frac{2}{3} - \frac{1}{12\theta}$$

These results are also shown in Fig. 2. In general, the conclusions are the same as those obtained in the general or von Neumann stability analysis. However, in the finite-element and Galerkin techniques, the general stability criteria are conservative compared with Dusinberre's criteria for certain θ ranges, whereas the opposite is true for the remaining θ's.

Oscillation Characteristics

The solution of the difference equations is unnecessary if only a stability analysis is desired. For example, the von Neumann stability analysis provides identical results with the general stability analysis mentioned above. One objective of obtaining the solution of the difference equations is to examine the oscillation characteristics of the various methods that are under investigation.

Recall equation (31) and also the definition of β given in equation (28). The inverse of β should be greater than zero to keep the numerical solution away from oscillation. Therefore, for the finite-element method,

$$\phi > \frac{2}{3} - \frac{1}{72\theta}$$

for the method of weighted residuals,

$$\phi > \frac{2}{3} - \frac{1}{72\theta_1}$$

or

$$\phi > \frac{2}{3} - \frac{1}{108\theta}$$

for the finite-difference method,

$$\phi > \frac{2}{3} - \frac{1}{8\theta_1}$$

or

$$\phi > \frac{2}{3} - \frac{1}{12\theta}$$

These results are shown in Fig. 3. The conclusions for nonoscillation of the numerical results are similar to those conclusions for stability criteria and, therefore, require no further comment.

Conclusions

The literature on the application of the finite-element method to transient heat-conduction problems arouses great interest because of provisions for arbitrary geometry, orthotropic materials, and arbitrary boundary conditions. But disadvantages are apparent because of the requirements for larger computational times and greater core storage. Therefore, of these solution techniques, the one that will eventually be used will be selected after consideration of the advantages and disadvantages of various applications to the problems.

The transient two-dimensional finite-element difference expression is derived and mentioned in the literature for the first time. The finite-difference formulae for the Laplacian term were also derived. A particular 9-point finite-difference formula for the Laplacian term was chosen to bring the difference expressions of the finite-element, the finite-difference, and the weighted-residuals (Galerkin) methods into the same format. The stability criteria were established for all three methods by use of the general stability, the von Neumann, and the Dusinberre methods. The oscillation characteristics were derived for all three techniques. The finite-element method is more conservative than the finite-difference method, but not as conservative as the Galerkin method in both stability and nonoscillation characteristics.

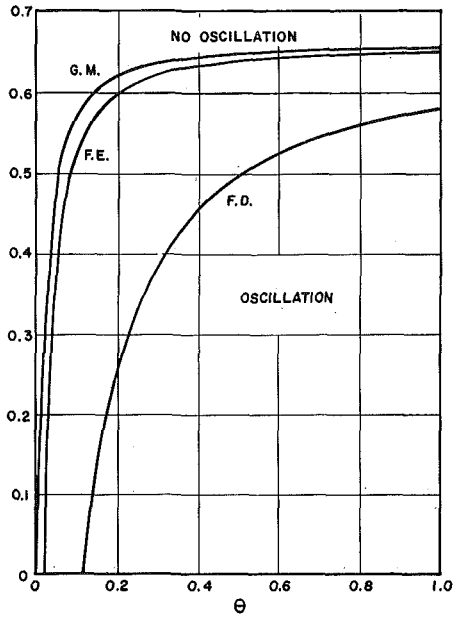

Fig. 3 Various oscillation criteria

The use of the numerical scheme by the finite-element method allows not only for arbitrary geometry, initial conditions, material properties, and linear boundary conditions but also for nonlinear boundary conditions (radiation). Further information about nonlinear boundary conditions and applications to practical examples is available elsewhere [4–6].

References

1 Carslaw, H. S., and Jaeger, J. C., *Conduction of Heat in Solids* Oxford University Press, England, 1959.

2 Wilson, E. L., and Nickell, R. E., "Application of the Finite Element Method to Heat Conduction Analysis," in: *Nuclear Engineering and Design*, Vol. 4, 1966, pp. 276–286.

3 Gurtin, M. E., "Variational Principles for Linear Initial Value Problems," *Quarterly Journal of Applied Mathematics*, Vol. 22, 1964, pp. 252–256.

4 Yalamanchili, R. V. S., and Chu, S.-C., "Application of the Finite-Element Method to Heat-Transfer Problems, Part II. Transient Two-Dimensional Heat Transfer with Convection and Radiation Boundary Conditions," Technical Report RE-TR-71-41, Research Directorate, Weapons Laboratory, U. S. Army Weapons Command, Rock Island, Ill. (AD 726371).

5 Yalamanchili, R. V. S., and Chu, S.-C., "Finite-Element Method to Transient Two-Dimensional Heat Transfer with Convection and Radiation Boundary Conditions," U. S. Army Weapons Command Technical Report RE-70-165 (AD 709604).

6 Chu, S.-C., and Yalamanchili, R. V. S., "Application of the Finite-Element Method to Heat-Transfer Problems, Part I. Finite-Element Method Applied to Heat Conduction in Solids with Nonlinear Boundary Conditions," Technical Report RE-71-37, Research Directorate, Weapons Laboratory, U. S. Army Weapons Command, Rock Island, Ill. (AD 726370).

7 Lemmon, E. C., and Heaton, H. S., "Accuracy, Stability and Oscillation Characteristics of Finite-Element Method for Solving Heat Conduction Equation," ASME Paper No. 69-WA/HT-35.

8 Finlayson, B. A., and Scriven, L. E., "The Method of Weighted Residuals and Its Relation to Certain Variational Principles for the Analysis of Transport Processes," *Chemical Engineering Science*, Vol. 20, 1965, pp. 395–404.

9 Finlayson, B. A., and Scriven, L. E., "The Method of Weighted Residuals—A Review," *Applied Mechanics Reviews*, Vol. 19, No. 9, 1966, pp. 735–748.

10 Crandall, S. H., *Engineering Analysis*, McGraw-Hill, New York, N. Y., 1956.

11 Dusinberre, G. M., *Heat Transfer Calculations by Finite-Differences*, International Publishing, Scranton, Pa., 1961.

G. T. DYOS
Research Officer.

J. LAWTON
Head of Electrophysical Processes.

Electricity Council Research Centre,
Capenhurst, Cheshire, England

The Effects of Vibration and Pulsation on Metal Removal by a Plasma Torch

An experimental study has been carried out on the effects of workpiece vibration and gas pulsations on metal removal rates using plasma jets. In the case of workpiece vibration, increases in removal rates of up to 30 percent were found, which can be accounted for in terms of capillary waves set up in the melt. The influence of pulsation of gas flow velocity and arc current at modulation levels of 10 percent was found to be negligible. A theoretical model has been developed which explains the results in terms of the development of resonance capillary waves in the molten metal and predicts the average depth of the layer of molten metal.

Introduction

In recent years there have been significant developments in the use of plasma torches for the cutting of metals. The principal effort has been directed to producing nozzles with adequate lifetimes and to establishing the optimum cutting conditions for various gauges of material using a transferred torch. The present study, which is part of a larger program to increase plasma cutting speeds, is concerned with the use of vibration of the workpiece and pulsation of the plasma stream as means of increasing rates of melt removal.

Very little work seems to have been carried out on the use of vibration of a surface or pulsation of a heat transfer fluid as means of increasing heat transfer rates in situations like the present one in which melting is occurring. However, there have been various studies on the effect of pulsation of a fluid on heat transfer rates in exterior [1, 2][1] and interior [3, 4] flow geometries and investigations on the enhancement of heat transfer from a gas to a liquid whose surface is rippled [5]. These suggest that there might be some advantage in using vibration and pulsation in the present case.

Apparatus

The experimental system consisted basically of a plasma torch using argon as the working fluid, mounted above a 1-kw vibrator, Fig. 1. Argon entered the arc chamber with a tangential motion and left through the 3-mm-dia copper nozzle as a stream of plasma.

The cathode consisted of a thoriated-tungsten insert brazed into a coaxial water-cooled holder. The arc was struck between this cathode and the sample, which acted as the anode. Samples of 25-mm-dia bright mild steel 25 mm in length were mounted on the vibrator and were oscillated in a direction perpendicular to the impinging plasma jet.

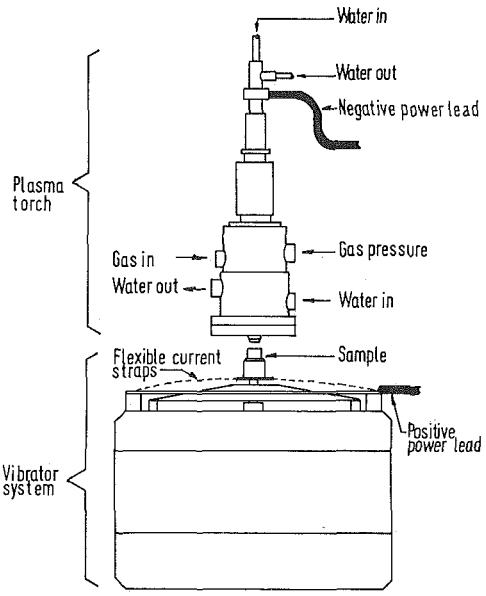

Fig. 1 General arrangement of the plasma torch and vibrator

The equipment used to vibrate the mild-steel samples was capable of operating from 5 Hz to 3 kHz, tests being confined to a range of 10 Hz to 100 Hz. The samples were mounted in a cup attached to the armature of the vibrator. Flexible copper-braid current leads to the cup were attached symmetrically to its base, the armature thereby being allowed to vibrate with a minimum of constraint. The power amplifier driving the vibrator was controlled by means of an audio oscillator which had a variable voltage output, thus enabling the vibrating amplitude of the sample to be varied.

[1] Numbers in brackets designate References at end of paper.

Contributed by the Heat Transfer Division for publication (without presentation) in the Journal of Heat Transfer. Manuscript received by the Heat Transfer Division April 24, 1972. Paper No. 73-HT-C.

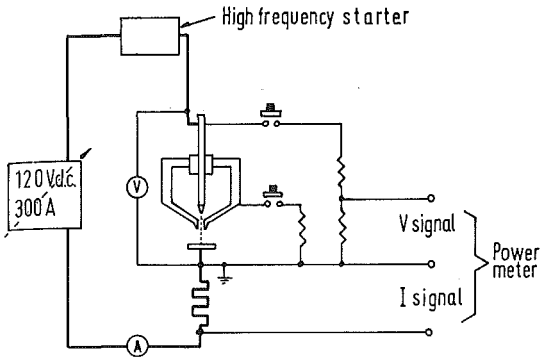

Fig. 2 Schematic of the electrical connections to the plasma torch

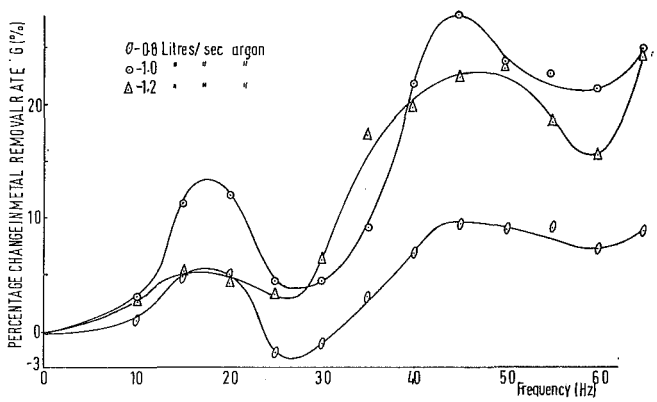

Fig. 3 Percentage change in metal removal rate as a function of vibrator frequency using a transferred arc

Using an accelerometer mounted on the vibrator shaft, acceleration, velocity, and distance of travel of the vibrator armature could be determined.

Power to the plasma torch was obtained from two d-c welding power supplies connected in series output, Fig. 2, each capable of an output of 20 kw. A low-inductance coaxial milliohm resistor was connected in series with the arc power supply on the positive (ground) side. This resistor permitted monitoring the instantaneous current and also supplied a voltage signal proportional to current that was used for monitoring power. Instantaneous and average power were measured using a "quarter-square" multiplying circuit and integrator.

The arc was initiated by a high-voltage radiofrequency discharge within the nozzle of the plasma torch. A resistor was connected from the nozzle to the anode via a contactor, permitting the plasma torch arc to be initiated in the nontransferred mode. A voltage monitoring unit was used to sense the drop in voltage as the arc struck and then removed the resistor from the circuit, thus allowing the arc to transfer through the nozzle and attach to the anode.

A timing circuit was used to initiate the startup sequence, control the duration of the burning of the sample, and switch off the arc after the preset time.

Experimental Procedure and Results

The experiments consisted of vibrating weighed and numbered cylindrical samples of degreased bright mild steel (25 mm in diameter, 25 mm long, and weighing about 100 gm) directly below the nozzle of the plasma torch for predetermined burn times. A conical crater was formed within the sample, surrounded by a collar of dross.

The dross remaining on the surface of the sample was removed before re-weighing. The amount of material removed was determined by difference. The arc power, burn time, voltage, and current were recorded. This procedure was carried out for a series of samples with and without vibration and for a range of frequencies at constant peak-to-peak amplitude (2.5 mm) for a range of argon gas flows to the torch.

All the experimental results have been plotted and are expressed as a function of improvement G versus the frequency f of the shaker, where G is defined as

$$\frac{\text{material removed per kw per sec with vibration}}{\text{material removed per kw per sec without vibration}} \times 100\%$$

The data obtained from the transferred torch are shown in Fig. 3. Each point on the graph is the average of three samples, burnt at constant vibration displacement of 2.5-mm peak-peak amplitude. The argon gas pressure in the torch was held constant at 3 atm absolute. The distance between the nozzle and the sample at the midpoint of the vibration was 7 mm.

Samples corresponding to the above minimum and maximum metal removal rates were potted in epoxy resin for ease of handling, cut along the major axis of the craters, and then ground and polished, Fig. 4. This enabled pertinent data to be obtained such as crater depth and shape.

Nomenclature

$c_{p,l}$ = mean specific heat of liquid, J-kg^{-1}-(deg C)$^{-1}$
$c_{p,s}$ = mean specific heat of solid, J-kg^{-1}-(deg C)$^{-1}$
d = depth of model crater, m
f = frequency of ripples, Hz
g' = component of gravitational acceleration normal to liquid surface, m-sec^{-2}
h = mean depth of molten metal, m
$\bar{k}_l$ = mean thermal conductivity of liquid, w-m^{-1}-(deg C)$^{-1}$
$\bar{k}_s$ = mean thermal conductivity of solid, w-m^{-1}-(deg C)$^{-1}$
l = mean length of molten surface in crater, m
l' = final length of molten surface in crater, m
m_1 = mass of sample, kg
m_2 = mass of sample removed, kg
q = heat flux in x direction, J-m^{-2}-sec^{-1}
r = mean base radius of crater, m
t_1 = initial heating time of sample, sec
t_2 = cutting time of sample, sec
u = wave velocity, m-sec^{-1}
v_s = velocity of propagation of solid–liquid interface into solid, m-sec^{-1}
v_l = velocity of propagation of solid–liquid interface into liquid, m-sec^{-1}
A = surface area of crater, m^2
H = enthalpy per unit mass, J-kg^{-1}
H_s = enthalpy of solid metal unit mass at temperature θ, J-kg^{-1}
$H_{s,m}$ = enthalpy of solid metal per unit mass at temperature θ_m, J-kg^{-1}
$H_{l,m}$ = enthalpy of liquid metal per unit mass at temperature θ_m, J-kg^{-1}
$H_{l,b}$ = enthalpy of liquid metal per unit mass at temperature θ_b, J-kg^{-1}
L = latent heat of fusion of metal, J-kg^{-1}
P = total electrical power, w
Q_m = heat removed by melt, above θ_0 datum, J
Q_s = heat remaining in sample at end of cutting period, J
V_s = crater volume, m^3
α = semi-angle of model crater, rad
γ = surface tension of liquid metal, N-m^{-1}
η = overall efficiency of energy transfer of plasma stream
θ_b = boiling point of molten metal, deg C
θ_f = temperature of molten metal, deg C
θ_m = melting point of metal, deg C
θ_0 = mean metal temperature at commencement of metal removal, deg C
θ_r = room temperature, deg C
ϕ = semi-angle of cone
λ = ripple wavelength, m
ρ_s = density of solid, kg-m^{-3}
ρ_l = density of liquid, kg-m^{-3}

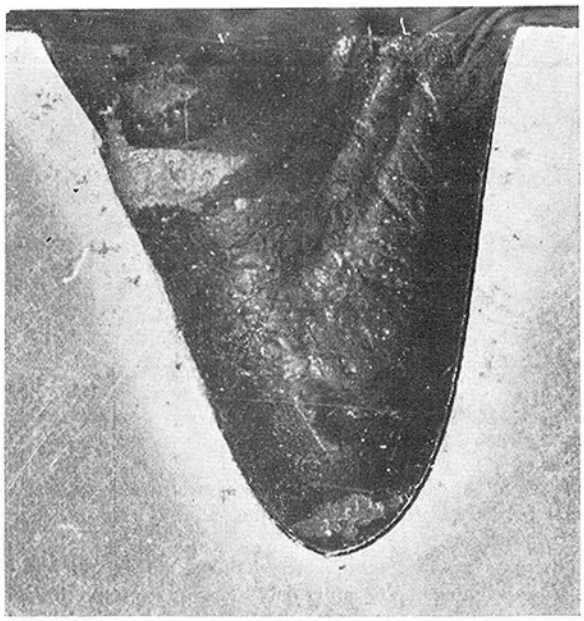

Fig. 4 Photograph of a cross section of a crater after polishing, ×6 magnification

In addition to experiments on vibration, tests were also carried out on the effect of gas pulsation and arc current oscillation. In spite of modulations of the order of 10 percent on both the gas flow and the current, no effects on metal removal or heat transfer rates to a calorimeter were detected, i.e., any effect was less than about 2 percent.

Discussion

Figure 3 shows repeated peaks and troughs that are characteristic of a resonance phenomenon. In view of the lack of any effect of gas pulsation, it seems that any resonances that influence the metal removal rates are more likely to be associated with waves set up in the melt on the surface of the sample than with phenomena in the plasma. Corroboration of this point of view is obtained from high-speed photography, taken for the cases where metal removal rates are at a maximum and a minimum, i.e., corresponding to peaks and troughs in Fig. 3. These show the molten metal on the surface of the sample exhibiting a definite pulsation in which the molten pools grow to a globular form and then neck to form a droplet which is then expelled. This effect was very noticeable at the peaks, shown in Fig. 3, but much less prominent at the corresponding troughs on the curve. Selected frames are shown, Fig. 5, from the high-speed cinematography for the case of no vibration and near the maximum peak for a gas flow of 1.0 l/sec at 50 Hz. At 50 Hz the formation of waves around the crater is clearly shown.

Method of Calculation

The occurrence of peaks and troughs in Fig. 3 can be closely predicted in terms of waves set up in the layer of molten metal within the crater. The generation of ripples on a shallow liquid layer is governed by the Rayleigh wave equation [6]

$$u^2 = \left(\frac{2\pi\gamma}{\rho_l\lambda} + \frac{g'\lambda}{2\pi}\right)\tanh\frac{2\pi h}{\lambda} \tag{1}$$

and

$$u = \lambda f \tag{2}$$

For resonant wave patterns to be set up in the molten metal surface, the length of the molten material measured along the surface must be an integral number of half-wavelengths since the boundary must be a node.

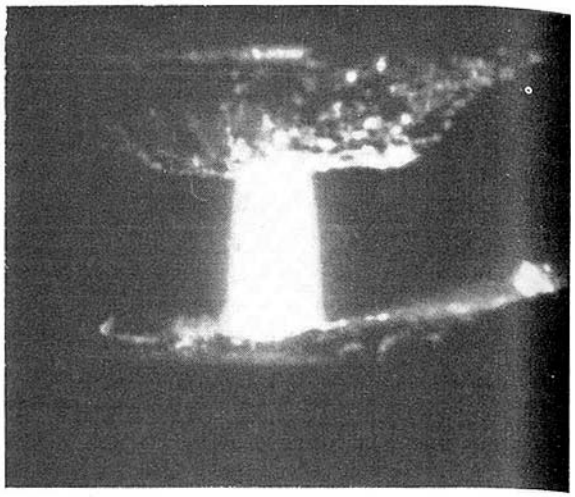

(a) vibration frequency = 0 Hz

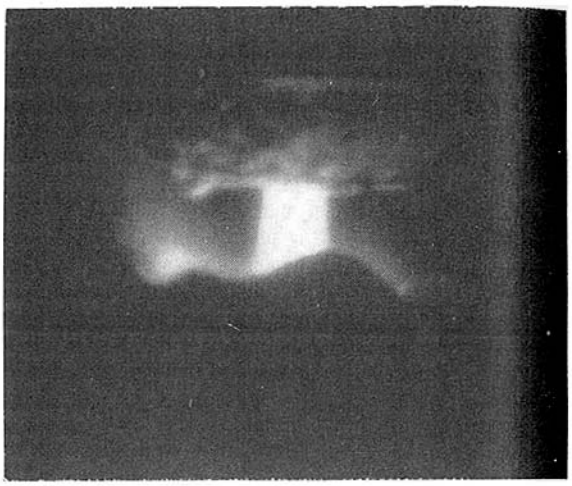

(b) vibration frequency = 50 Hz

Fig. 5 High-speed cinematography of transferred arc with and without vibration of sample

Therefore, if

$$\lambda = l/n \tag{3}$$

then $n = {}^1/_2, 1, 1{}^1/_2, 2, \ldots$, for resonance and $n = {}^3/_4, 1{}^1/_4, 1{}^3/_4, 2{}^1/_4, \ldots$, for the maximum antiresonant mismatch.

Substitution of equations (2) and (3) into equation (1) yields

$$f^2 = \left[\frac{2\pi\lambda}{\rho_l}\left(\frac{n}{l}\right)^3 + \frac{g'}{2\pi}\left(\frac{n}{l}\right)\right]\tanh 2\pi\left(\frac{n}{l}\right)h \tag{4}$$

Using equation (4), the frequencies for resonance and antiresonance can be deduced knowing g', l, and h. The values of g and l can be found directly by measurement of the sample after burning. However, the determination of h, the liquid layer thickness, requires a detailed examination of the heat transfer to the molten surface; this is discussed next.

The general shape of the crater is shown in Fig. 4. For the purpose of this analysis, the details of which are given in the Appendix, the shape is assumed to be conical, as shown in Fig. 6. The volume of the cone is made equal to the volume of melt removed, its base radius set equal to the mean radius of the base of the actual crater, and its depth determined from the expression for the volume of a cone. In practice, the difference between the actual and the ideal geometries was very small.

In order to calculate the thickness of the liquid layer (see Appendix), it was assumed that the interface between solid and melt propagated normally to itself into the solid material at a

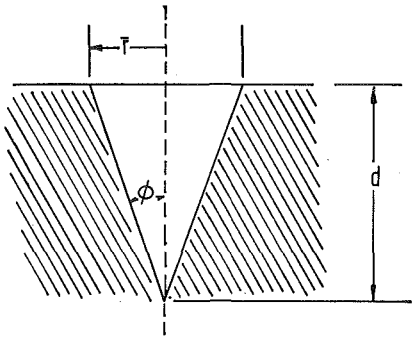

Fig. 6 Crater parameters for theoretical model

constant velocity v_s, the crater maintaining its shape throughout.

$$h = \frac{\bar{k}_l}{\rho_s v_s \bar{c}_{p,l}} \ln\left[1 + \frac{\bar{c}_{p,l}(\theta_f - \theta_m)}{\bar{c}_{p,s}(\theta_m - \theta_0) + L}\right] \quad (5)$$

θ_f is determined from an overall heat balance, taking into account the molten material removed from the sample. In carrying out the calculations it was necessary to assume a torch efficiency of 65 percent [7], the value taken being based upon other experiments using the identical plasma torch under closely similar conditions. In practice the efficiency was found to vary very little over a wide range of operating conditions.

The values of h were deduced for the peaks and troughs on the melt removal curve, Fig. 3, for the highest gas flows, i.e., for the highest rate of melt removal. Full details are given in the Appendix.

In order to evaluate the frequency from equation (1), it is necessary to know the relevant component of gravitational acceleration, g', the wetted length, l, and the depth of liquid, h. The last of these was calculated as previously indicated. The component of gravitational acceleration normal to the surface, g', during cutting was equal to $g \sin \phi$. In the equation (1), the term in g' plays a relatively small role.

In view of the impact of the plasma jet stream at the apex of the cone, it seems likely that only a node could exist there. Therefore, the appropriate wetted length was assumed to be the length of one side of the cone rather than the complete length from base to tip to base.

A mean value of l was taken equal to the length of one side of the idealized conical crater, Fig. 6, at the point where half the melt had been removed.

Thus if l' is the length of the side after the complete burn time,

$$l = \frac{0.5}{\sqrt[3]{2}} l' = 0.4l'$$

Using these data, frequencies corresponding to peaks ($n = \frac{1}{2}$, 1, $1\frac{1}{2}$) and troughs ($n = \frac{3}{4}$, $1\frac{1}{4}$, $1\frac{3}{4}$) were calculated; the values are compared with the experiment in Table 1.

According to the theory, a peak should have occurred at 8 Hz and a trough at 14 Hz. Very few data were taken below 10 Hz; however, there is evidence of a small peak between 5 and 10 Hz. In order to normalize the frequencies to a common basis, the sets of experimental and calculated values of frequency for peaks and troughs were each divided through by the maximum frequency, f max, encountered in each set (this corresponded to a trough). A graph of $(f/f\ \max)_{calc}$ vs. $(f/f\ \max)_{exp}$ should be a straight line at 45 deg passing through the origin. Table 1 and Fig. 7 show an excellent agreement between theory and experiment and leave little doubt that the increases in melt removal observed result from ripples forming on the surface of the melt.

Table 1 Calculated versus experimentally derived values of frequency and frequency ratios at peaks and troughs (vibrated workpiece, transferred arc)

n	f_{exp}, Hz	f_{calc}, Hz	$(f/f\ \max)_{exp}$	$(f/f\ \max)_{calc}$	
0.5	...	8.0	...	0.13	peak
0.75	...	14.0	...	0.23	trough
1.0	18	21.2	0.30	0.34	peak
1.25	27.5	33.2	0.46	0.54	trough
1.50	45.0	46.2	0.75	0.75	peak
1.75	60.0	61.8	1.00	1.00	trough

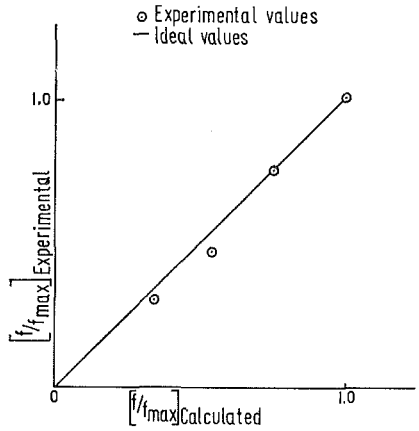

Fig. 7 Graph of experimental and calculated frequency ratios at peaks and troughs

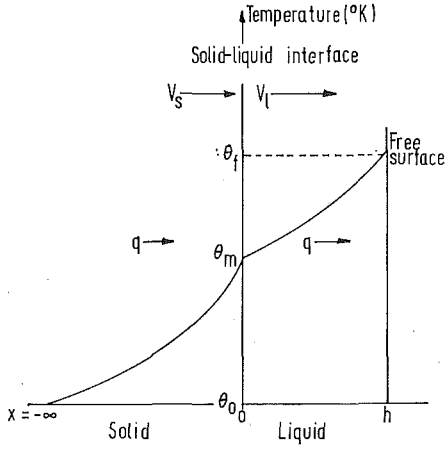

Fig. 8 Temperature versus position in the region of the solid-liquid interface

Conclusions

Experiment has shown conclusively that vibration of a metal surface during cutting with a transferred arc leads to greatly increased metal removal rates (up to 30 percent in the present case), the increase being greatest at higher frequencies. A theory based upon waves set up in the molten region adequately accounts for the frequencies at which peaks and troughs occur in the experimental data.

In practical cutting situations, the shape of the crater and the depth of liquid metal will be different from those of the present study. Obviously, therefore, the resonance curves and increases in mass removal obtained in the present work are only indicators for the practical cutting case and cannot be transferred directly.

The use of pulsations in the gas flow and in the current to the arc, operating in the transferred mode, produced no detectable effects either in rates of heat transfer or of metal removal. This is presumably because it was not possible to couple a significant amount of vibrational energy into the molten layer by this means. The results are not without value, however, since in any practical plasma jet, both the current and gas flow are subjected to quite large and unspecified periodic fluctuations around the mean. The present experiments show that these are very unlikely to affect the cutting performance and need not be considered as important parameters either when building a system or when comparing one system with another.

Acknowledgment

The authors wish to thank the Electricity Council Research Centre for permission to publish this work. Appreciation is expressed to J. D. Williams of E.C.R.C. for his helpful assistance in connection with the building of the test rig and in obtaining the experimental data and to D. Castle for the photography and high-speed cinematography.

References

1 Fand, R. M., "The Influence of Acoustic Vibrations on Heat Transfer by Natural Convection From a Horizontal Cylinder to Water," JOURNAL OF HEAT TRANSFER, TRANS. ASME, Series C, Vol. 87, No. 3, May 1965, pp. 309–310.

2 Lemlich, R., and Rao, M. A., "Effect of Transverse Vibration on Free Convection from a Horizontal Cylinder," *International Journal of Heat and Mass Transfer*, Vol. 8, 1965, pp. 27–33.

3 Lemlich, R., and Armour, J. C., "Forced Convective Heat Transfer to a Pulsed Liquid," *Chemical Engineering Progress*, Vol. 61, 1965, pp. 83–88.

4 Bergles, A. E., "The Influence of Flow Vibrations on Forced-Convection Heat Transfer," JOURNAL OF HEAT TRANSFER, TRANS. ASME, Series C, Vol. 86, No. 4, Nov. 1964, pp. 559–560.

5 Banerjee, S., Rhodes, E., and Scott, D. S., "Mass Transfer to Falling Wavy Liquid Films at Low Reynolds Numbers," *Chemical Engineering Science*, Vol. 22, 1967, pp. 43–48.

6 Newman, F. H., and Searle, V. H. L., *The General Properties of Matter*, 5th ed., Edward Arnold, London, England, 1957, p. 389.

7 Mayo, P. J., and Lawton, J., "The Influence of Secondary Gas Flows on Heat Transfer Distributions from Plasma Torches," Electricity Council Research Centre, Cheshire, England, Report No. M351.

8 Elliot, J. F., *Thermochemistry of Steel Making*, Vol. I, 1962, and Vol. II, 1964, Pergamon, London, England.

9 *Metals Handbook*, Vol. 1, 8th ed., Chapman and Hall, London, England, 1961.

10 *Handbook of Chemistry and Physics*, 4th ed., Chemical Rubber Co., Cleveland, Ohio, 1969.

APPENDIX

Calculation of Depth of Liquid Layer in Crater

In order to carry out the mathematical analysis, certain linearizing simplifications regarding the properties of mild steel are necessary. Thus the following mean values are taken over the whole temperature range:

Property	Mean value	Reference
$\bar{k}_l$	41.8 w-m^{-1}-(deg C)$^{-1}$	[8]
$\bar{c}_{p,l}$	812.1 J-kg^{-1}-(deg C)$^{-1}$	[8]
$\bar{\rho}_s$	7800 kg-m^{-3}	[9]
$\bar{\rho}_l$	7100 kg-m^{-3}	[9]
$\bar{k}_s$	40.19 w-m^{-1}-(deg C)$^{-1}$	[9]
$\bar{\gamma}$	1.8 N-m^{-1}	[10]
$\bar{c}_{p,s}$	669.0 J-kg^{-1}-(deg C)$^{-1}$	[9]
θ_m	1535 deg C	[10]
L	267 kJ-kg^{-1}	[9]

The idealized temperature–enthalpy relationship can be written as, between θ_0 and θ_m

$$H_s = H_{s,0} + \bar{c}_{p,s}(\theta - \theta_0) \tag{A1}$$

and between θ_m and θ_f,

$$H = H_{l,m} + \bar{c}_{p,l}(\theta - \theta_m) \tag{A2}$$

$$= H_{s,m} + L + \bar{c}_{p,l}(\theta - \theta_m) \tag{A3}$$

The analysis is carried out on the assumption that the liquid layer in the crater is of constant depth throughout the cutting operation and that the interface between the solid and liquid propagates normally to itself at a fixed speed. This situation is characteristic of steady-state cutting with a uniform heat flux over the surface of the melt. For the sake of this analysis, the shape of the crater is taken to be that of a straight-sided cone, as shown in Fig. 6, the slanting face of which propagates perpendicularly to itself at v_s with respect to the solid at the solid–liquid interface. The analysis is based on the assumption of one-dimensionality, the mathematical model analyzed being shown in Fig. 8, where for convenience the coordinate system is chosen such that the interface is stationary and solid flows into it at velocity v_s and liquid flows out at velocity v_l.

Since the system is taken to be in the steady state while cutting is in progress, there is no accumulation of energy at any particular point, i.e., for both the solid and liquid phases.

$$\frac{d}{dx}\left(-k\frac{d\theta}{dx} + \rho v H\right) = 0 \tag{A4}$$

or

$$-k\frac{d\theta}{dx} + \rho v H = q \tag{A5}$$

where q represents the heat flux in the x direction.

Consider the liquid first

$$q = \bar{k}_l\frac{d\theta}{dx} + \rho_l v_l[H_{s,m} + L + \bar{c}_{p,l}(\theta - \theta_m)] \tag{A6}$$

After integration between the limits $x = 0$ and $x = h$, equation (A6) becomes

$$h = \frac{\bar{k}_l}{\rho_l v_l \bar{c}_{p,l}} \ln\left[\frac{\rho_l v_l[H_{s,m} + L + \bar{c}_{p,l}(\theta_f - \theta_m)] - q}{\rho_l v_l[H_{s,m} + L] - q}\right] \tag{A7}$$

Now consider the solid. From equation (A5)

$$q = -\bar{k}_s\left(\frac{d\theta}{dx}\right) + \rho_s v_s H_s \tag{A8}$$

at $x = -\infty$, $(d\theta/dx) = 0$, i.e.,

$$H_s = H_{s,0} \tag{A9}$$

and, in addition, mass conservation in the steady state gives

$$\rho_s v_s = \rho_l v_l \tag{A10}$$

Thus, from equations (A8), (A9), and (A10),

$$q = \rho_s v_s H_{s,0} = \rho_l v_l H_{s,0} \tag{A11}$$

Using the value for q from equation (A11), the value for h can be found from equation (A7), making use of the idealized temperature–enthalpy relationship of Fig. 17 and equations (A1), (A2), and (A3):

$$h = \frac{\bar{k}_l}{\rho_l v_l \bar{c}_{p,l}} \ln\left[1 + \frac{\bar{c}_{p,l}(\theta_f - \theta_m)}{\bar{c}_{p,s}(\theta_m - \theta_0) + L}\right] \tag{A12}$$

θ_f and θ_0 must be evaluated by overall heat balances on the sample, the heating of which is divided into two phases. (It is clear that the value of θ_f cannot exceed the boiling point of the molten steel.)

Initially there is no melting, the plasma merely heating up the whole sample for a period of t_1. If the overall efficiency of energy transfer of the plasma stream is η and P is the total electrical power, during the initial period the sample is raised from room temperature θ_r to a mean temperature θ_0 given by

$$\theta_0 = \frac{t_1\eta P}{m_1\bar{c}_{p,s}} + \theta_R \tag{A13}$$

In practice $t_1 \doteqdot 1.6$ sec and $\theta_R \doteqdot 0$ deg C, i.e., for practical purposes

$$\theta_0 = \frac{1.6\eta P}{m_1\bar{c}_{p,s}} \tag{A14}$$

At the end of the initial warming-up period, cutting begins and lasts for t_2 sec. θ_f can be deduced from a heat balance on the re-

mainder of the sample left at the end of the cutting period, t_2, and the melt removed. The heat above the θ_0 datum remaining in the sample at the end of the cutting process is given by

$$Q_s = A\left\{\int_{-\infty}^{0} \rho_s \bar{c}_{p,s}(\theta - \theta_0)dx + \int_0^L \rho_l[\bar{c}_{p,l}(\theta - \theta_m) + L + \bar{c}_{p,s}(\theta_m - \theta_0)dx]\right\} \quad (A15)$$

The temperature distributions in the solid and liquid follow directly from equation (A5).

solid

$$\theta - \theta_0 = (\theta_m - \theta_0)\exp\left[\frac{\rho_l v_l \bar{c}_{p,s} x}{\bar{k}_s}\right] \quad (A16)$$

liquid

$$\theta - \theta_m = \frac{1}{\bar{c}_{p,l}}[\bar{c}_{p,s}(\theta_m - \theta_0) + L]\left[\exp\left(\frac{\rho_l v_l \bar{c}_{p,l} x}{\bar{k}_l}\right) - 1\right] \quad (A17)$$

Substituting for θ from equations (A16) and (A17) into (A15) followed by integration between the limits $x = -\infty$, $\theta = \theta_0$; $x = 0$, $\theta = \theta_m$; $x = L$, $\theta = \theta_f$ yields

$$Q_s = A\left[\left(\frac{\theta_m - \theta_0}{v}\right)\bar{k}_s + \left(\frac{\theta_f - \theta_m}{v}\right)\bar{k}_l\right] \quad (A18)$$

where $v = v_s \doteqdot v_l$, the difference in these velocities being negligible in view of the small difference in liquid and solid densities, see equation (A10).

The energy carried away by the melt above the θ_0 datum is given by

$$Q_m = \rho_s V_s[\bar{c}_{p,s}(\theta_m - \theta_0) + L + \bar{c}_{p,l}(\theta_f - \theta_m)] \quad (A19)$$

Hence the total heat transferred from the plasma to the metal in the period of cutting of duration t_2 is given by

$$Q_s + Q_m = \eta P t_2 \quad (A20)$$

Thus equation (A20) provides an expression for θ_f in terms of known quantities. Substitution in equation (A7) gives the final expression for the depth of the liquid layer

$$h = \frac{\bar{k}_l}{\rho_l v_l \bar{c}_{p,l}} \ln\left\{1 + \frac{\bar{c}_{p,l}\left[\eta P t_2 - (\theta_m - \theta_0)\left(\frac{A\bar{k}_s}{v_l} + \rho_s V_s \bar{c}_{p,s}\right) - \rho_s V_s L\right]}{[\bar{c}_{p,s}(\theta_m - \theta_0) + L]\left[\frac{A\bar{k}_l}{v_l} + \rho_s V_s \bar{c}_{p,l}\right]}\right\} \quad (A21)$$

i.e.,

$$h = \frac{\bar{k}_l}{\rho_l v \bar{c}_{p,l}} \ln\left\{1 + \frac{\bar{c}_{p,l}\left[\eta P t_2 - \left(\theta_m - \frac{1.6\eta P}{m_1 \bar{c}_{p,s}}\right)\left(\frac{A\bar{k}_s}{v} + m_2 \bar{c}_{p,s}\right) - m_2 L\right]}{\left[\bar{c}_{p,s}\left(\theta_m - \frac{1.6\eta P}{m_1 \bar{c}_{p,s}}\right) + L\right]\left[\frac{A\bar{k}_l}{v} + m_2 \bar{c}_{p,l}\right]}\right\} \quad (A22)$$

where θ_0 has been replaced using equation (A14) and $\rho_s V_s$ is set equal to m_2, the weight of material removed. The value of η_0 is determined from equation (A21) by setting $h = 0$ and represents the torch efficiency below which cutting cannot occur in the steady state. Thus

$$\eta_0 = \frac{\theta_m\left(\frac{A\bar{k}_s}{v} + m_2 \bar{c}_{p,s}\right) + m_2 L}{P\left[t_2 + \frac{t_1}{m_1}\left(\frac{A\bar{k}_s}{v\bar{c}_{p,s}} + m_2\right)\right]} \quad (A23)$$

At a particular value η_b, the value of θ_f reaches the boiling point. Clearly, equation (A22) is no longer valid for values of $\eta > \eta_b$, in which case equation (A12) must be used, setting θ_f equal to the boiling point and θ being deduced as before from equations (A13) or (A14).

The expressions developed above were used to evaluate the depth of liquid h for the peaks and troughs corresponding to the experiments carried out using the maximum gas flow in Fig. 3. The torch efficiency was taken as 65 percent, this value being determined by experiment using calorimetry. Its value varied very little over a wide range of operation. The torch power was 12.6 kw and the values of the various transport and thermodynamic properties used are quoted at the beginning of this Appendix.

F. C. WESSLING
Associate Professor,
Department of Mechanical Engineering,
University of New Mexico,
Albuquerque, N. M.
Mem. ASME

P. L. BLACKSHEAR
Professor,
Department of Mechanical Engineering,
University of Minnesota,
Minneapolis, Minn.

The Thermal Properties of Human Blood during the Freezing Process

This paper presents calculations of the density, thermal conductivity, and enthalpy of blood during the freezing process. The calculations are based upon the premise that blood freezes similarly to a mixture of fats, proteins, and sodium chloride in a water solution and freezes so that ice crystals align themselves with the direction of heat flow. The properties were checked by calculating the theoretical temperature–time history of blood freezing in a Teflon-coated stainless-steel tube and comparing the results with experiments. The agreement was within 10 percent over the entire ranges of temperature and time. Hence the derived thermal properties are concluded to be good approximations to the real properties.

Introduction

In order to fully understand the phenomena occurring during the freezing of blood for long-term preservation, a prediction of rates of freezing and of thawing is needed. A survey of the literature uncovered data on the properties of liquid blood but no data on the properties of blood during freezing or thawing. Hence, before heat transfer calculations of the freezing and the thawing of blood are accomplished, the properties must be evaluated. A model used to calculate the density, thermal conductivity, and enthalpy of freezing blood is presented in this paper. The specific heat is obtained from the enthalpy curve. The properties are calculated assuming a freezing process in blood that is similar to the freezing process of a sodium chloride–water solution containing fat and protein solids. The blood components are assumed to align themselves in a direction parallel to the heat flow for the calculation of thermal conductivity, as was suggested by Poppendiek [1].[1] These theoretical values of the properties are used to calculate the temperature distribution occurring during the freezing and thawing of blood inside of a small cylindrical tube. The heat transfer equation is solved utilizing a digital computer. The theoretical predictions of temperature–time histories are then compared with experimental data obtained during laboratory tests of freezing and thawing blood.

Theory

Human blood consists of formed elements and plasma. The formed elements are red blood cells, white blood cells, and platelets. The largest formed element by volume, approximately 43 percent, is the red blood cell. The red blood cell contains hemoglobin, carbonic anhydrase, and salts in a water solution. The plasma is primarily a solution of inorganic salts and proteins. However, when considering the evaluation of properties, the blood can be thought of as consisting of salts, proteins, fats, and water. The blood consists of approximately 80 percent water by weight and 20 percent organic materials by weight. The actual composition used for the calculations of this paper are from [1]. Blood has an osmotic pressure equal to a water solution containing 0.9 gr of sodium chloride per 100 ml (0.9 gr percent) of water. Thus a good model to use for calculating the change in properties during freezing of the liquid portion of the blood is to assume that the liquid portion of the blood freezes as a 0.9 gr percent sodium chloride–water solution and that the organic materials remain unchanged in their thermal properties.

At a temperature −0.5 deg C, the freezing point of the plasma is reached. Then the water begins to freeze out as relatively pure ice, concentrating the salts, plasma proteins, and cells in the remaining liquid water. This process continues until the eutectic temperature of the remaining liquid solution is reached. At the eutectic temperature, the water solidifies and the salts concentrate until a solid solution of hydrated salts and ice forms [2]. Then the solid solution will continue to lower in temperature along with the solid ice and organic materials.

Because the densities of the unfrozen solvent, solid ice, and organic materials are not strongly temperature-dependent during freezing, the volume of the blood changes solely because the amount of ice increases and the amount of unfrozen solvent decreases as the temperature is lowered from −0.5 deg C. The weight of the unfrozen solvent is given by equation (1) and decreases as C increases.

$$W_L = \frac{C_0}{C} W_{L0} \tag{1}$$

[1] Numbers in brackets designate References at end of paper.

Contributed by the Heat Transfer Division and presented at the Winter Annual Meeting, Washington, D. C., November 28–December 2, 1971, of The American Society of Mechanical Engineers. Manuscript received by the Heat Transfer Division August 11, 1971; revised manuscript received May 10, 1972. Paper No. 71-WA/HT-41.

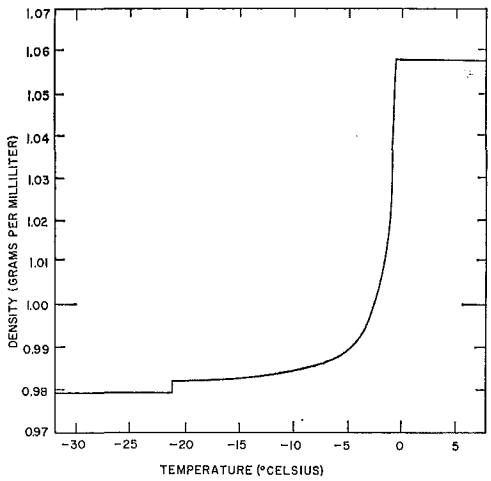

Fig. 1 Density of human blood (hematocrit of 0.43)

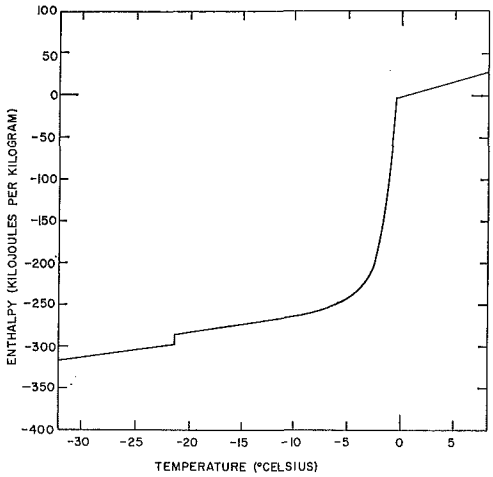

Fig. 2 Enthalpy of human blood (hematocrit of 0.43)

The concentration of salt in the liquid water, C, depends on the temperature and is obtained from an equilibrium diagram. Hence W_L depends on temperature. In a like manner, the amount of ice is given in equation (2)

$$W_I = W_{L0}\left[1 - \frac{C_0}{C}\right] \tag{2}$$

Thus the volume of blood V_B is equal to the sum of the volumes of unfrozen solvent, ice, and organics.

$$V_B = \frac{W_f}{\rho_f} + \frac{W_p}{\rho_p} + \frac{W_{L0}}{\rho_L}\frac{C_0}{C} + \frac{W_{L0}}{\rho_I}\left[1 - \frac{C_0}{C}\right] \tag{3}$$

and the density of the blood, ρ_B, is given by

$$\rho_B = \frac{W_f + W_p + W_{L0}}{V_B} \tag{4}$$

The density is assumed constant above -0.5 deg C. Between -0.5 deg C and -21.2 deg C the density is calculated from equations (1)-(4). The density below -21.2 deg C is assumed equal to the value calculated at -21.2 deg C. The density as a function of temperature is shown in Fig. 1 and equals 1.057 gr/cm³ [3] above -0.5 deg C. The density exhibits its largest change in the temperature region of -0.5 deg C to -3.0 deg C because most of the liquid water changes to ice in that region.

Since the specific heat of blood is 0.86 cal/gr-deg C, this indicates that blood consists of 20 percent by weight of material with a specific heat of 0.3 cal/gr-deg C and 80 percent by weight of water with a specific heat of 1.0 cal/gr-deg C. The specific heat of the organic material does not depend too strongly on temperature and can be considered constant throughout the range of interest. The total energy required to reduce the temperature of the blood below the freezing point of water is equal to the sum of the changes in energy of the various components, including the heat of fusion of the additional ice formed between the temperature steps. Again, assuming that the freezing of the liquid portion of the blood is similar to the freezing of a sodium chloride solution (with 0.9 gr of NaCl per 100 ml of solution of salts), then the enthalpy of the water solution of salts is obtained from an enthalpy salt concentration diagram for a mixture of NaCl and water [4]. One calculates the amount of unfrozen solvent remaining at a given temperature from equation (1) and thus obtains the amount of water frozen at that temperature. With this information, the enthalpy of the freezing blood is calculated as follows:

$$I_B = 0.8\left[(I_I - L_f)\left(1 - \frac{C_0}{C}\right) + I_L\frac{C_0}{C}\right] + (0.2)(0.3)T \tag{5}$$

This equation is valid only for -21.2 deg C $\leq T \leq -0.5$ deg C.

The enthalpies are evaluated at temperature T with 0 deg C reference. Hence all the enthalpies are negative for negative temperature. Using equation (5), an enthalpy temperature curve is calculated as in Fig. 2. The specific heat, the temperature derivative of enthalpy, is constant above the freezing point of water, and hence the enthalpy temperature curve is linear. As the temperature decreases, the enthalpy sharply decreases due to the formation of ice. The figure shows a sharp drop in enthalpy between -0.5 deg C and -3.0 deg C. The slope then moderates, indicating the heat of fusion has less effect on the enthalpy as the temperature gets colder than -3 deg C. At -21.2 deg C the heat of fusion of the eutectic is liberated, causing a jump discontinuity in the enthalpy curve. The enthalpy curve is approximated by a series of straight lines for the computer calculation, yielding step changes in the specific heat.

The thermal conductivity of blood is approximately 86 percent of the thermal conductivity of water and varies similarly with temperature [1]. Hence, for liquid blood, the 0.86 value of water at a given temperature is used. During the frozen state, the thermal conductivity is calculated.

Nomenclature

C = concentration of salt
h = convective heat transfer coefficient, cal/sec-cm²-deg C
I = enthalpy, cal/gr
k = thermal conductivity, cal/cm-sec-deg C
L_f = heat of fusion of ice, cal/gr
Nu = Nusselt number
Pr = Prandtl number
r = radial coordinate, cm
R = radius at a material interface, cm
Re = Reynolds number
T = temperature, deg C
t = time, sec
V = volume, cm³
W = mass, gr
ρ = density, gr/cm³
γ = specific heat, cal/gr-deg C

Subscripts

B = blood
f = fat
I = ice
L = liquid salt water
0 = above the freezing regime
p = proteins
ss = stainless steel
T = Teflon
∞ = isopentane temperature
1 = interface between blood and stainless-steel wall
2 = interface between stainless steel and Teflon
3 = interface between Teflon and isopentane

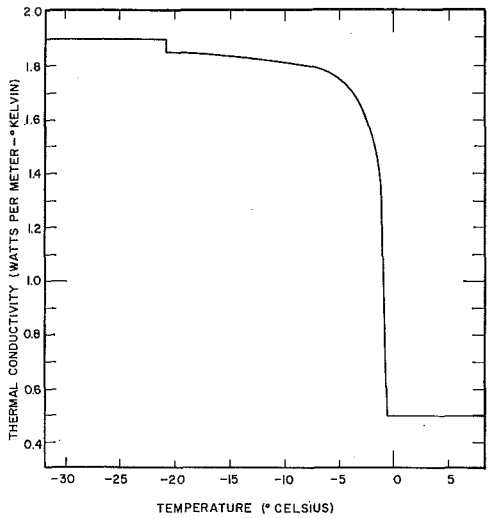

Fig. 3 Thermal conductivity of human blood (hematocrit of 0.43)

If the ice crystals formed during freezing grow in a direction perpendicular to the tube walls so that heat is transferred along the ice crystals in a radial direction, then the constituents can be assumed to be laminae parallel to heat flow according to the method suggested by Poppendiek [1]. Recognizing again that the amount of ice is dependent upon the temperature as in the calculation of enthalpy, the thermal conductivity can be calculated as follows:

$$V_B k_B = \frac{k_f W_f}{\rho_f} + \frac{k_p W_p}{\rho_p} + \frac{k_L W_L}{\rho_L} + \frac{k_I W_I}{\rho_I} \tag{6}$$

$$k_B = \frac{\dfrac{k_f W_f}{\rho_f} + \dfrac{k_p W_p}{\rho_p} + \dfrac{k_L W_{L0}}{\rho_L}\dfrac{C_0}{C} + \dfrac{k_I W_{L0}}{\rho_I}\left(1 - \dfrac{C_0}{C}\right)}{\dfrac{W_f}{\rho_f} + \dfrac{W_p}{\rho_p} + \dfrac{W_{L0}}{\rho_L}\dfrac{C_0}{C} + \dfrac{W_{L0}}{\rho_I}\left(1 - \dfrac{C_0}{C}\right)} \tag{7}$$

The results of equation (7) are presented in Fig. 3.

The sharp change in thermal conductivity at -0.5 deg C is due again to the rapid change from liquid water to ice in the blood. The jump discontinuity at -21.2 deg C is again due to the eutectic of salt water freezing. The value of the thermal conductivity is assumed constant below -21.2 deg C.

Experimental Verification

The properties were evaluated by comparing theoretical temperature–time histories with experimental temperature–time histories. Whole human blood was collected using standard blood-bank procedures in ACD-NIH Formula A anticoagulant. Fresh blood with intact cells was frozen. The human blood that was tested had a hematocrit of 43 percent and a total hemoglobin of 0.138 gr/ml. A small (0.1-mm-dia bead) thermocouple was inserted into a tube and positioned to touch the wall. Because there was essentially only a point contact at the wall and because the thermocouple was immersed in the blood, the temperature indicated was the blood temperature. Because of the thermocouple size, it indicated an average temperature in 12 percent of the tube diameter. The tube was sealed on the bottom with a silicone-rubber cap. The capillary tube filled with the blood and the thermocouple was frozen by manually immersing it into a stirred, temperature-controlled isopentane bath. Details of the technique and apparatus used for freezing are presented elsewhere [5].

The conduction equation [6] was numerically solved for the cylindrical tube utilizing the Crank–Nicholson finite-difference method of the CINDA computer program [7]. The initial temperature was the temperature recorded by the thermocouple. The ends of the tube were considered to be insulated. Movement of the blood during freezing was ignored. The convective heat transfer coefficient h at the exterior cylindrical surface was considered constant and symmetric. Hence the transient conduction equation was one-dimensional and in the radial direction. The value for h was calculated by assuming the tube was submerged in a uniformly flowing isopentane stream and was obtained from equation (8) [8].

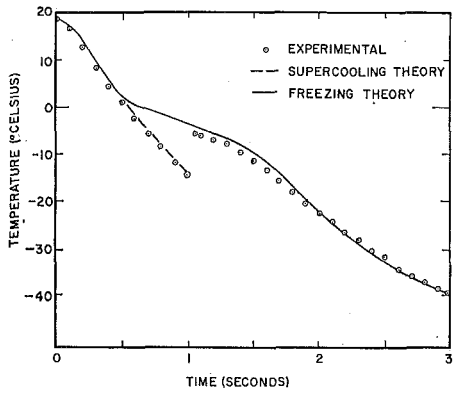

Fig. 4 Temperature–time history of human blood freezing in a Teflon-coated stainless-steel tube

$$\mathrm{Nu} = 0.43 + 0.533\ \mathrm{Re}^{0.5}\ \mathrm{Pr}^{0.31} \tag{8}$$

Thus the system of equations solved was

$$\rho_B \gamma_B \frac{\partial T_B}{\partial t} = \frac{1}{r}\frac{\partial}{\partial r}\left(r k_B \frac{\partial T_B}{\partial r}\right) \tag{9}$$

$$\frac{\partial T_B}{\partial r} = 0 \quad \text{at} \quad r = 0 \tag{10}$$

$$k_B \frac{\partial T_B}{\partial r} = k_{ss} \frac{\partial T_{ss}}{\partial r} \quad \text{at} \quad r = R_1 \tag{11}$$

$$\rho_{ss} \gamma_{ss} \frac{\partial T_{ss}}{\partial t} = \frac{1}{r}\frac{\partial}{\partial r}\left(r k_{ss} \frac{\partial T_{ss}}{\partial r}\right) \tag{12}$$

$$k_{ss} \frac{\partial T_{ss}}{\partial r} = k_t \frac{\partial T_t}{\partial r} \quad \text{at} \quad r = R_2 \tag{13}$$

$$\rho_t \gamma_t \frac{\partial T_t}{\partial t} = \frac{1}{r}\frac{\partial}{\partial r}\left(r k_t \frac{\partial T_t}{\partial r}\right) \tag{14}$$

$$-k_t \frac{\partial T_t}{\partial r} = h[T_t - T_\infty] \quad \text{at} \quad r = R_3 \tag{15}$$

The density ρ_B was calculated from equation (4). The specific heat γ_B was calculated from the derivative of the enthalpy curve. The thermal conductivity k_B was calculated from equation (7). The convection heat transfer coefficient h was calculated from equation (8). The value of h was held constant during the computer run. The properties of the stainless steel and the Teflon were from the open literature.

The heat transfer coefficient was required to yield good agreement between the theoretical analysis and the experimental data in the supercooling region because the properties of liquid blood when no freezing has occurred are well known. The blood was divided into ten nodes of equal radial length for the computer calculation. Thus the nodes were ring-shaped except for the central one which was a solid cylinder. Each node was of uniform temperature. A temperature gradient existed between the center of the tube and the tube's outside wall during cooling. Poppendiek's thermal conductivity model applied to this freezing case can be thought of as resulting in a thin sliver of ice appearing, during freezing, across the entire node in the heat transfer direction. The sliver increased in thickness perpendicular to the

heat transfer direction until all of the water was frozen in the node. Nodes at different radii changed phase at the same time. The values for the ninth node from the center were plotted in Fig. 4 because the thermocouple indicated the temperature of that node. Actually, the temperature of the thermocouple was influenced by nodes eight, nine, and ten, but the average of these three nodes was close to the temperature calculated by the computer for node nine. Additionally, a large portion of the thermocouple was located in the space encompassed by node nine. Theoretical solutions were obtained for the two cases of supercooling with no freezing and freezing with no supercooling.

The results presented in Fig. 4 are for blood freezing inside of an 18-gauge (0.84-mm ID × 1.27-mm OD) stainless-steel tube 25 cm long. These results were for a typical run. They were repeatable for many similar runs. The stainless-steel tube had a Teflon tube of 0.21-mm wall thickness tightly fitted over it. The Teflon was slipped over the stainless steel by lubricating the tubes with a small amount of silicone grease. In Fig. 4, the abscissa is the time in seconds after immersion of the tube into the isopentane bath. The ordinate is the temperature. The temperature is plotted to −40 deg C because the temperature gradually decreases to the bath temperature of −50 deg C. The experimental data (enclosed points) and the theory (solid and dashed lines) agree within 10 percent over the entire range. The supercooling portion of the curve describes the temperature–time history before the onset of freezing. The theoretical calculations of freezing describe the temperature–time history during and after freezing. The largest deviation (10 percent) occurs in the temperature range of −4 deg C to −18 deg C and can be attributed to either the presence of supercooling or to a slight error in the derived thermal properties. The agreement at −40 deg C is within a few percent, indicating that the heat transfer coefficient and the total amount of energy tranferred by the system are relatively accurate. All of the blood reaches a temperature of −40 deg C within 3 sec, plus or minus a few tenths, so position of the thermocouple would not be very critical for evaluating this time. Similar runs using glass, stainless steel, or Teflon tubes gave data that agreed within 20 percent of theoretical. For these tubes, positioning of the thermocouple became critical because large thermal gradients existed in the tubes. The largest deviations occurred also in the temperature range −4 deg C to −18 deg C, as was the case for the Teflon-coated stainless-steel tubes.

Conclusions

This paper presents calculations of the density, thermal conductivity, and enthalpy of blood during the freezing process. The calculations are based upon the premise that blood freezes similarly to a mixture of organic material and salt water, and freezes so that ice crystals align themselves with the direction of heat flow. The properties were checked by calculating the theoretical temperature–time history of blood freezing in a Teflon-coated stainless-steel tube and comparing the results with experiments. The agreement was within 10 percent over the entire ranges of temperature and time. Hence the derived thermal properties are concluded to be good approximations to the real properties.

References

1 Poppendiek, H. F., et al., "Thermal Conductivity Measurements and Predictions for Biological Fluids and Tissues," *Cryobiology*, Vols. 3 and 4, 1966, pp. 318–327.

2 Rey, L. R., "Thermal Analysis of Eutectics in Freezing Solutions," *Annals N. Y. Acad. Sci.*, Vol. 85, Art. 2, 1960, pp. 510–534.

3 Harper, H. A., *Review of Physiological Chemistry*, Lange Medical Publications, El Monte, Calif., 1963.

4 Bosnjakovic, F., *Technical Thermodynamics*, 3rd ed., Holt, Rinehart and Winston, New York, N. Y., 1965.

5 Wessling, F. C., and Blackshear, P. L., "The Effect of Gases on the Recovery of Human Red Blood Cells," *Cryobiology*, Vol. 7, No. 4–6, 1971, pp. 265–273.

6 Carslaw, H., and Jaeger, J., *Conduction of Heat in Solids*, 2nd ed., Oxford at the Clarendon Press, 1959.

7 Lewis, D. R., Gaski, J. D., and Thompson, L. R., "Chrysler Improved Numerical Differencing Analyzer for Third Generation Computers," TN-AP-67-287, Chrysler Corp. Space Div., New Orleans, La., Oct. 1967.

8 Eckert, E. R. G., and Drake, R. M., *Heat and Mass Transfer*, McGraw-Hill, New York, N. Y., 1959.

T. E. COOPER
Assistant Professor.
Assoc. Mem. ASME

J. P. GROFF
LCDR., USN
Assoc. Mem. ASME

Department of Mechanical Engineering,
Naval Postgraduate School,
Monterey, Calif.

Thermal Mapping, via Liquid Crystals, of the Temperature Field near a Heated Surgical Probe

This paper discusses the use of heat for producing clinical lesions in tissue and presents the design and analysis of a resistively heated surgical probe. The probe surface temperature is accurately maintained and controlled by using a Wheatstone bridge. The probe was embedded in a clear agar–water test medium, and the temperature field generated by the probe was measured with liquid crystals, a material that provides a visual display of certain isotherms. Experimental results compare within approximately 10 percent of a two-dimensional numerical solution. A one-dimensional theoretical model is also developed which examines the influence of blood flow on the temperature field.

Introduction

A VARIETY of surgical techniques are presently used to produce clinical lesions. In addition to the familiar mechanical or "scalpel" method, surgical procedures employing chemical, ultrasonic, focused x-ray, radiation, and cooling and heating agencies are used to destroy discrete regions of tissue. Gengler [1][1] presents a summary of the various methods, complete with the advantages and disadvantages of each. The choice of methods depends largely on the nature of the clinical problem. Ideally, the surgeon desires a technique that possesses the following characteristics: (1) safety, (2) reversibility, (3) reproducibility, (4) sharp delimitation, (5) hemostasis, (6) flexibility, (7) simplicity, and (8) speed of application. At times it is not possible to meet all of the above surgical ideals. In such cases the choice of procedures is based largely on an optimization of the ideals, with safety being of paramount importance.

This paper focuses on the use of heat as a lesion-producing agent. In particular, the design and analysis of a resistively heated surgical electrode, henceforth referred to as a probe, is presented. Tissue destruction is accomplished by using the probe as a heating element to raise the temperature of the surgical target above 55 deg C, the lethal thermal threshold for tissue [2]. The unique feature of this probe is that its surface temperature can be accurately measured and controlled by using a Wheatstone bridge. As a result, the temperature field in the medium surrounding the probe can be analytically predicted by solving the heat equation prior to applying the probe. This is quite significant when one considers that the volume of tissue destroyed depends solely on the local tissue temperature.

Temperature fields determined experimentally with the probe embedded in a 0.30 percent agar–99.7 percent water test medium compare within 10 percent of those predicted using the analytical model. A novel, relatively new temperature-sensing device was used in the experimental phase of the study. Liquid crystals, a material that changes color over a known and well-defined temperature range, were employed to obtain a two-dimensional visual display of the transient temperature field that developed around the probe. By using two separate orientations of the liquid crystals, a three-dimensional picture of the temperature field was inferred. In addition to the highly desirable visual aspect of the liquid-crystal material, it also produces a minimum disturbance in the test medium.

The influence of blood flow on lesion size was also investigated using an analytical model. The model indicates that blood flow has a minimum influence on the temperature field surrounding clinical-size probes (1 mm or less in radius).

Summary of Surgical Heating Techniques

Direct Current (dc) Method. Localized lesions have been produced in tissue by applying a direct current between two electrodes. An active electrode is inserted into a predetermined location in the tissue, and an inactive electrode, or ground, is placed on some other part of the body. The resistivity of the tissue causes electrical energy to be converted into heat, thus increasing the local tissue temperature. When the tissue temperature is raised above 55 deg C [2], the tissue is destroyed.

Although small and discrete lesions can be produced by the dc method, it has several disadvantages. Direct current follows

[1] Numbers in brackets designate References at end of paper.

Contributed by the Heat Transfer Division for publication (without presentation) in the JOURNAL OF HEAT TRANSFER. Manuscript received by the Heat Transfer Division February 25, 1972. Paper No. 73-HT-D.

the path of least resistivity and tends to have preferred paths in tissue, thus causing irregular lesions. Gas bubbles, a result of electrolysis, may form around the active electrode and block the flow of current. Herrero [4] states another disadvantage of the dc method: "Animals with dc lesions usually had extensive scar tissue both around and infiltrated with the tissue." In addition, dc devices suffer from polarization, which can produce transients that stimulate muscle and nervous tissue [3]. Nerve stimulation does have one advantage: the probe placement can be checked by observing the patient's reaction to the stimulating effect of the current. It should further be noted that the dc method depends on both the thermal and electrical properties of the tissue. The thermal properties are known within an accuracy of approximately 5 percent [5, 6] and are relatively constant throughout the tissue. However, the electrical properties are not well known, are anisotropic, and tend to vary with location.

One advantage of the dc method is that the electrodes are small, approximately 2 mm or less in diameter. As such, the probe can be relatively painlessly inserted and removed and causes little damage to the surrounding tissue.

In summary, although the dc method can produce localized lesions, the irregularity of the lesions, control difficulties, and possible side effects of the current greatly diminish its usefulness.

Radio-Frequency (rf) Current Method. The radio-frequency technique produces lesions in much the same way as the direct current method. A long, thin, needlelike probe emits low-power, continuous-wave radio-frequency current. An indifferent electrode is placed on some other part of the body and acts as a ground. As current is passed between the electrodes, the resistivity of the tissue causes electrical energy to be converted to tissue internal energy, thereby increasing the local tissue temperature. As in the dc method, lesions are a function of the tissue's thermal and electrical properties.

Unlike direct current, rf current has no preferred path in tissue and no stimulating effect. However, since low-frequency alternating current does have a stimulating effect in tissue, the probe location can first be checked by passing low-frequency current between the electrodes and observing the patient's response.

Brodkey et al. [7] discuss an alternate way of assuring proper probe location. They found that a temperature range of 40 to 49 deg C reversibly blocks nervous function. The probe's position can be checked by observing the patient's response when the local tissue temperature is brought into this reversible range. Like the dc electrode, the radio-frequency probe is small, can be relatively painlessly inserted and removed, and causes little damage to the surrounding tissue.

The rf method does have several disadvantages. The local tissue temperature may exceed 100 deg C, causing boiling, gas formation, carbonization of the tissue, and adherence of coagulum to the probe [2]. Also, defects in the probe insulation have been known to cause irregular lesions along the probe track. However, these difficulties can be avoided by carefully controlling the various physical parameters used in the rf technique.

In summary, the radio-frequency method can be used to produce well-circumscribed lesions, and the probe location can be checked by two methods. However, as in the dc method, lesions are a function of both the thermal and electrical properties of the tissue.

High-Resistance Heating Probe Method. In this method, a high-resistance electrode is inserted into the tissue. Current is passed through the electrode and the resistance of the electrode causes the probe temperature to increase. Heat is conducted away from the probe into the surrounding tissue. A region of destroyed tissue is formed when the local tissue temperature is raised above approximately 55 deg C.

Theoretically, there is less uncertainty in producing lesions purely by heating than there is in the direct current or radio-frequency techniques. The dc method produces both thermal and electrolytic tissue destruction. As the lesion forms, it offers an increased resistance to the passage of current. Thus the parameters are changing as the lesion forms. The rf method minimizes electrolysis but still depends on the electrical and thermal properties of the tissue. The lesions formed with the high-resistance probe depend only on the tissue's thermal properties. As such, the lesions are generally smaller than those produced by either the direct current or radio-frequency current methods.

Since lesions formed using the resistance heating method depend only on the temperature field surrounding the probe, the surface temperature of the probe must be accurately measured and controlled. This has been one of the difficulties of previous resistance probe designs. Watkins [3] used a probe with a thermocouple placed in the tip. He found that the actual temperature of the probe could exceed the recorded temperature by several degrees if the thermocouple was not positioned carefully. Thermocouples placed in the surrounding tissue to record the temperature can distort the temperature field and give erroneous readings.

Carpenter and Whittier [8] attempted to produce lesions in animals by using a heating electrode. Although their results were poor, they concluded that it was due to the crude instruments employed. They stated: "It would seem profitable to explore this technique with a more finely perfected thermocautery." Gildenberg [9] conducted studies with a high-resistance heating electrode and a rf probe and found that the heating probe produced less variable lesions than the rf probe.

In summary, a properly designed high-resistance heating probe can produce small, safe, and predictable lesions. The uncertainty is less than the radio-frequency or direct current methods, since tissue destruction depends only on the thermal properties of the tissue.

Probe Design

Various shaped heating electrodes were considered in the present studies. However, to facilitate the construction of the probe, a cylindrical design was chosen. In order to increase the

Nomenclature

α = thermal diffusivity, cm²/sec
c = specific heat, cal/gm-deg C
c_b = specific heat of blood, cal/gm-deg C
k = thermal conductivity, cal/cm-sec-deg C
$\dot{m}_b$ = blood flow rate, gm/cc-sec
r = radial location, cm
r_c = radial location of T_c isotherm, cm
r_0 = probe radius, cm
t = time, sec
T = temperature, deg C
T_c = critical temperature, deg C
T_0 = initial temperature, deg C
T_p = probe surface temperature, deg C
ρ = density, gm/cm³
u = dummy variable of integration
x = axial location, cm
R = nondimensional radius, r/r_0
R_c = nondimensional critical radius, r_c/r_0
θ = nondimensional temperature, $(T - T_0)/(T_p - T_0)$
θ_c = nondimensional critical temperature, $(T_c - T_0)/(T_p - T_0)$
τ = Fourier number $(\alpha t/r_0^2)$, nondimensional
β = blood flow parameter $(\dot{m}c_b r_0^2/k)$, nondimensional
X = nondimensional axial location, x/r_0
J_0 = zero-order Bessel function of first kind
Y_0 = zero-order Bessel function of second kind
K_0 = zero-order modified Bessel function of first kind
C_0 = defined by equation (4)

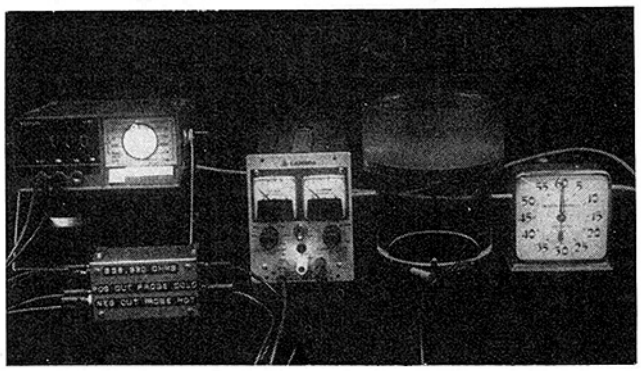

Fig. 1 Overall view of the experimental setup showing the null meter, Wheatstone bridge, power supply, cylindrical test cell partially filled with gel, and timer; the liquid-crystal sheet can be seen on close inspection of the surface of the gel

extent of the temperature field in the experimental test medium, thus increasing the accuracy of the experimental data, the probe was made approximately four times larger than an actual surgical electrode.

The probe was constructed from 4-mm glass tubing wrapped tightly with resistance wire over a length of 40 mm. The resistance wire, a 30 percent Fe–70 percent Ni alloy, was 0.00275 in. in diameter and exhibited an electrical resistivity of 19.9 μohm-cm^{-1} and a temperature coefficient of 0.0045 ohm-ohm^{-1}-deg C^{-1}. A unique feature of the probe is that the resistance wire served not only as a resistance heater but also as a resistance thermometer. By impressing a known resistance across the length of resistance wire, the probe was forced to come to a temperature consistent with the resistance. By placing the resistance wire in one arm of a Wheatstone bridge, accurate surface temperature control was maintained [10].

In an actual surgical application, the probe would be inserted in a diseased region of tissue, activated, and used to raise the local tissue temperature above 55 deg C, the lethal level.

Liquid Crystals

Background. In the studies described here, Rochrome liquid-crystal tapes manufactured by the Hoffman–LaRoche Co. were used as the temperature-sensing agents. The crystals are coated on a mylar substratum with an absorptive black background and an adhesive backing. The overall thickness is approximately 0.005 in. The most striking feature of the material is that it exhibits brilliant changes in color with small changes in temperature. The temperature–color relationship is stable and reappears whenever the material passes through the appropriate temperature range. The property which is the basis of the color change is circular dichroism. An incident beam of unpolarized light, on striking the material, is split into two components having electrical vectors rotated in opposite directions. One component is transmitted and the other is scattered. The scattered light normally has a wavelength peak which occurs in the visible region of the spectrum. Temperature changes in the crystals disturb intermolecular forces and cause a shift in molecular structure resulting in a shift in wavelength of the scattered light and, hence, in a color change. This color change is unique for specific temperatures. A quantitative measurement of temperature is possible within an accuracy of 0.1 deg C or finer if appropriate calibration techniques are employed. Fergason [11–13], in a series of articles, presents excellent discussions on the chemistry, varieties, properties, uses, and limitations of liquid crystals.

Calibration Technique. In the present studies a Rosemount constant-temperature bath, capable of establishing and maintaining temperatures to within ±0.01 deg C accuracy, was used to calibrate the crystals. The human eye was used to determine color. Particular attention was given to the temperature corresponding to the onset of red, since this was the color used as a standard in our experiments.

The liquid-crystal material to be calibrated was sandwiched between two clear microscope slides. The composite was then completely sealed with a clear waterproofing agent. In a typical calibration run, the waterproofed liquid-crystal system was placed in the constant-temperature water bath. The temperature of the bath was then slowly raised until the event temperature of the liquid crystal had been reached. By carefully adjusting the bath temperature, an accurate measure of the event temperature corresponding first to red, then to green, and finally to blue was made. No attempt was made to determine shades of red, green, or blue. It is estimated that temperature was correlated with color to an accuracy of ± 0.1 deg C. It should be noted that the observer who calibrated the crystals also made all determinations of color during the actual experimental runs.

Experimental Procedure

Two clear Plexiglas test cells were used to study the three-dimensional temperature field produced by the probe. A hollow cylindrical container 5 in. in diameter and 4 in. deep was used to observe the radial temperature distribution. A removable ring inserted around the inner perimeter of the cylindrical cell supported the liquid-crystal tape. The tape was attached to a thin (0.003 in.) sheet of clear mylar stretched across the ring. The final arrangement looked much like a tambourine with a small hole (to accommodate the probe) in the center. The probe was inserted through the bottom of the cell and was held in place by a bushing that allowed the height of the probe to be adjusted. See Fig. 1 for a view of the cylindrical test cell and the experimental setup.

The second cell, a rectangular container $4^5/_8 \times 5^1/_2 \times 6$ in., was used to observe the axial temperature field near the probe. The probe was inserted through the side of the container. A removable bracket held the liquid-crystal tape lengthwise along the probe.

To insure that the container walls would not distort the temperature field produced by the probe, both containers were constructed with dimensions large compared to the probe. Further, since the liquid-crystal–mylar composite was only 0.008 in. in thickness, was situated in parallel with the test medium, and had thermal properties similar to water, the arrangement produced no appreciable temperature perturbations.

The test cells were filled with a clear 0.3 percent agar–99.7 percent water gel-like test medium for the experimental runs. In a typical test in the cylindrical cell, the probe was positioned so that there was an equal length of probe above and below the liquid-crystal tape. The probe was covered with the gel-like test medium so that the top of the probe was at least five probe diameters below the gel surface.

Rochrome liquid-crystal tape, lot no. AS-70-36, was used to observe the temperature field produced by the probe. This particular tape had the following temperature-to-color relationship: 29.9 deg C–red, 31.5 deg C–green, 34.2 deg C–blue.

In conducting an experimental run, the probe surface temperature was stepped from an initial temperature of approximately 23.5 deg C to a final value of 48.5 deg C. Probe temperature control was maintained via a Wheatstone bridge, power supply, and null-meter system. Approximately 10 sec were required to bring the probe to its final set point.

Photographs of the isotherms displayed on the liquid-crystal sheet surrounding the probe were taken at various intervals of time using a Graflex 4 × 5 press camera fitted with a Polaroid Land film holder. Polaroid 4 × 5 Land film, type 57, 3000 speed, was used. The lowest temperature isotherm visually displayed by the liquid crystals was red in color and corresponded to a temperature of 29.9 deg C. A nondimensional temperature, referred to as the critical temperature, θ_c, was defined as $\theta_c = (T_c - T_0)/(T_p - T_0)$, where T_c is the temperature corresponding

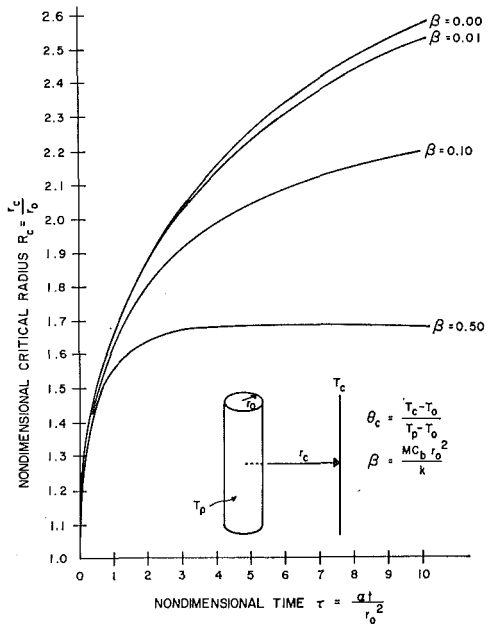

Fig. 2 Influence of blood flow on the radial movement of the $\theta_c = 0.50$ isotherm; results shown were obtained by numerical solution of equation (3)

to the red color band (29.9 deg C), T_0 is the initial medium temperature (23.5 deg C), and T_p is the probe surface temperature (48.5 deg C). Similarly, a nondimensional critical radius R_c corresponding to the radial location of the θ_c isotherm was defined as $R_c = r_c/r_0$, where r_c is the radial location of the 29.9 deg C isotherm and r_0 is the probe radius. Values of R_c versus nondimensional time τ were determined from the photographs of the liquid-crystal sheet. Here, τ is the classical Fourier modulus, $\alpha t/r_0^2$, where α is the test-medium thermal diffusivity and t is time.

In practice, a surgeon would be interested in following the radial movement of the 55 deg C isotherm produced by a probe which might have a surface temperature, say, of 90 deg C. The lesion, or region of destroyed tissue, would encompass all tissue between the 55 deg C isotherm and the probe surface.

Analysis

Two models were considered in analyzing the heat transfer process that takes place between the probe and its surroundings. The first model treats one-dimensional heat flow from a constant-temperature, infinitely long cylinder of radius r_0 into a constant-property infinite medium perfused with isotropic capillary flow. The second model treats two-dimensional heat flow from a cylinder, heated only over a finite length, into a constant-property infinite medium.

One-Dimensional Model. In order to gain a feeling for the influence of blood flow on the temperature field produced by the probe, a one-dimensional radial heat flow model of the probe was developed. This model treated the probe as being an infinite cylinder of radius r_0 maintained at a constant temperature T_p. The medium surrounding the probe was assumed to be homogeneous and infinite in extent, to be initially at a uniform temperature T_0, and to possess constant thermal properties. Further, the medium was assumed to be perfused with capillary flow with a mass flow rate per unit volume of $\dot{m}_b$, a specific heat c_b, and a temperature T_0. In addition to the normal conductive and internal energy terms that appear in the classical one-dimensional, constant-property heat equation, one must also account for convective effects due to the capillary flow. In the absence of information on the directionality of the flow, Pennes [14] suggests that the heat equation takes the form (see Nomenclature for complete definition of terms)

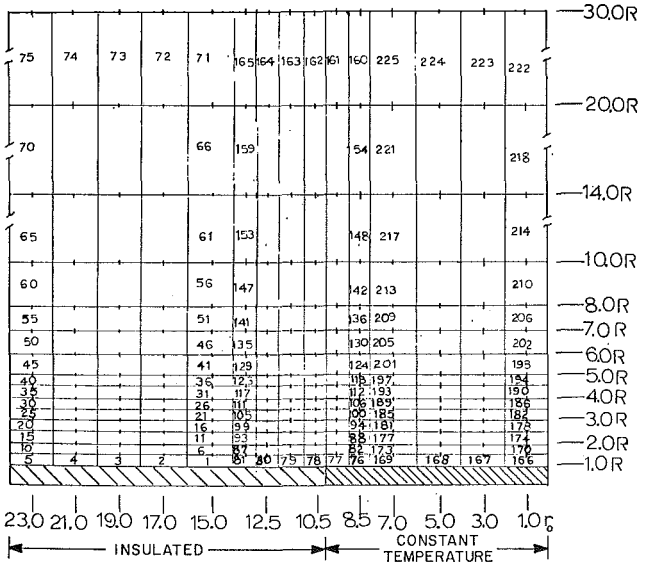

Fig. 3 Nodal network used in solving for the two-dimensional transient temperature field surrounding the heating probe

$$\frac{k}{r}\frac{\partial\left(r\frac{\partial T}{\partial r}\right)}{\partial r} - \dot{m}_b c_b (T - T_0) = \rho c \frac{\partial T}{\partial t} \tag{1}$$

The boundary and initial conditions are

$$T = T_p \quad \text{at} \quad r = r_0$$
$$T \to T_0 \quad \text{as} \quad r \to \infty$$
$$T = T_0 \quad \text{at} \quad t = 0, r > r_0$$

Equation (1) and its boundary and initial conditions may be normalized by introducing the following set of quantities:

$$\theta = \frac{T - T_0}{T_p - T_0} \qquad R = \frac{r}{r_0} \qquad \tau = \frac{\alpha t}{r_0^2} \qquad \beta = \frac{\dot{m}_b c_b r_0^2}{k}$$

When these quantities are substituted into equation (1), it takes the form

$$\frac{1}{R}\frac{\partial\left(R\frac{\partial\theta}{\partial R}\right)}{\partial R} - \beta\theta = \frac{\partial\theta}{\partial\tau} \tag{2}$$

with boundary conditions

$$\theta = 1 \quad \text{at} \quad R = 1$$
$$\theta \to 0 \quad \text{as} \quad R \to \infty$$
$$\theta = 0 \quad \text{at} \quad \tau = 0, R > 1$$

Equation (2) was solved using the Laplace transformation technique [10] and the following solution was obtained:

$$\theta = \frac{K_0(\sqrt{\beta}R)}{K_0(\sqrt{\beta})} - \frac{2}{\pi}\int_0^\infty \frac{e^{-\tau u^2} C_0(u, Ru)du}{(u + \beta/u)[J_0^2(u) + Y_0^2(u)]} \tag{3}$$

where

$$C_0(u, R) = J_0(u)Y_0(uR) - J_0(uR)Y_0(u) \tag{4}$$

J_0, Y_0, and K_0 are Bessel functions, and u is a dummy variable of integration. Values of θ versus R, τ, and β were generated by using Simpson's rule on equation (3). Complete results can be found in [10].

Figure 2 depicts the effect of blood flow on the location of a particular isotherm. In this case, attention is focused on the isotherm corresponding to a nondimensional temperature of $\theta_c = 0.50$. Note that blood flow may have a drastic influence on the

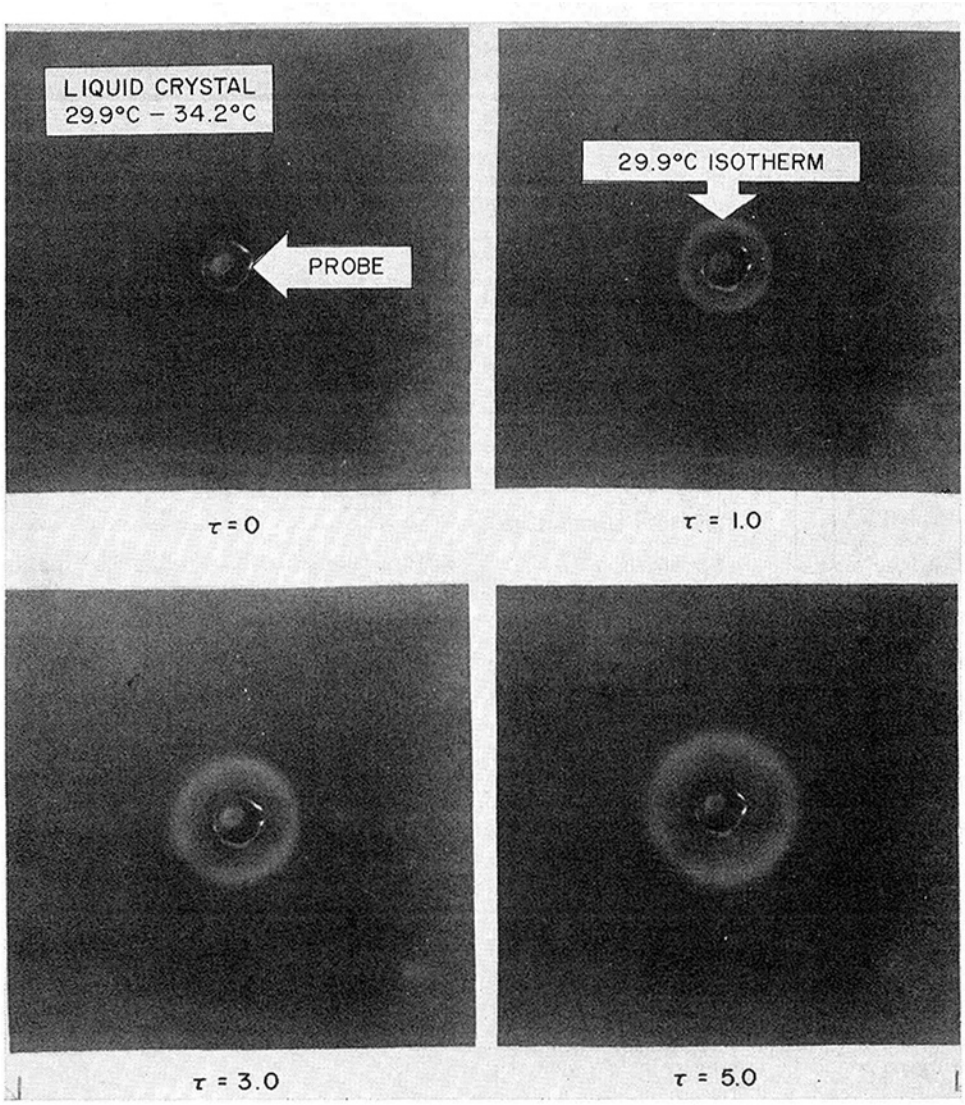

Fig. 4 Liquid-crystal display of the midplane radial temperature field near the surgical probe at various nondimensional times τ

temperature field. Of particular interest is the influence that blood flow would have on the field surrounding a typical surgical probe. Such a probe would in all probability have a diameter of 1 mm or less. As an illustration, assume that a 1-mm probe is to be used in brain tissue. Brain tissue has the following properties: thermal conductivity, 1.26×10^{-3} cal/cm-sec-deg C; density, 1.05 gm/cc; specific rate, 0.88 cal/gm-deg C; thermal diffusivity, 1.36×10^{-3} cm²/sec [5]; and blood flow rate, 8×10^{-3} gm/cc-sec [15]. Using these values, β is calculated to be 0.016. From Fig. 2 it is noted that for this value of β the influence of the blood flow is minimal, at least until large values of time. As can be seen by examining the definition of the blood flow parameter β, large probes will experience much larger blood flow effects than small probes, since β varies as the probe diameter squared.

Two-Dimensional Model. The one-dimensional model assumed that the probe was infinite in extent. An actual surgical probe, however, consists of a constant-temperature section of finite length attached to an unheated cylindrical stem. If the length-to-diameter ratio of the heated section is small, end effects will destroy the one-dimensionality of the heat flow process and the problem will become two-dimensional. The prototype probe under consideration had a heated section with a length-to-diameter ratio of 10. To study the two-dimensional transient temperature field produced by this probe, a digital computer program, with the code name TRUMP [16], was used. The nodal network used in the study is shown in Fig. 3. Due to symmetry it was necessary to generate information for only one-half of the field. Input was supplied to the program in a form which yielded results in nondimensional form. The probe surface was given a constant temperature over the length $0 \leq X \leq 10$ and was treated as thermally insulated over $10 \leq X \leq 24$. The dimensions of the nodal network were chosen large enough so that the boundary conditions at $R = 30$ and $X = 24.0$ did not affect the temperature field during the transient period. The network therefore simulated an "infinite" field. Blood flow effects were not considered in the two-dimensional study.

Results

Figure 4 shows typical experimentally determined radial temperature–time histories at the probe midplane, as displayed by the liquid-crystal material, while Fig. 5 shows typical axial histories. Although color is not shown in these figures, the 29.9 deg C, 31.5 deg C, and 34.2 deg C color bands (red, green, and blue respectively) are clearly evident in color photos. The liquid crystals not only produce a highly desirable visual display of the temperature field surrounding the probe but also yield an accurate means of quantitatively locating various isotherms. Thermocouples and thermistors are extremely difficult to position accurately in applications similar to the one discussed here and, further, give only pointwise information.

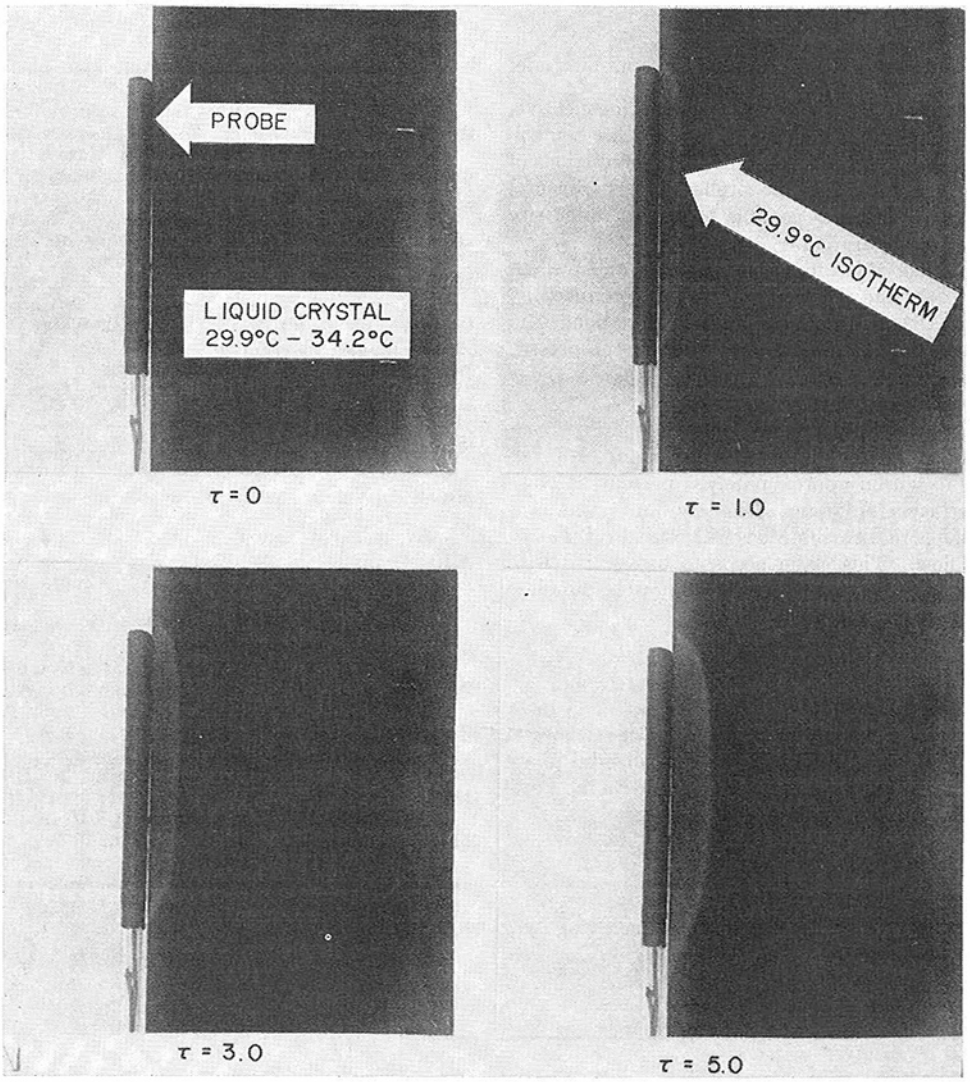

Fig. 5 Liquid-crystal display of the axial temperature field near the surgical probe at various nondimensional times τ

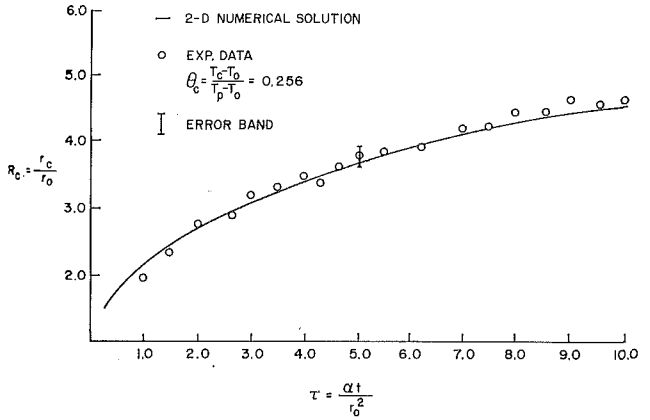

Fig. 6 Comparison of experimentally determined midplane values of the critical radius R_c versus time τ with results obtained from the two-dimensional numerical solution

Experimentally determined values of the radius corresponding to the 29.9 deg C isotherm, R_c, versus nondimensional time τ were compared with the numerical results generated with TRUMP. Figures 6 and 7 show typical comparisons between experiment and theory. In all cases studied, agreement was well within the estimated experimental uncertainty of 10 percent, indicating that theoretical predictions of the temperature field produced by this resistance probe are possible.

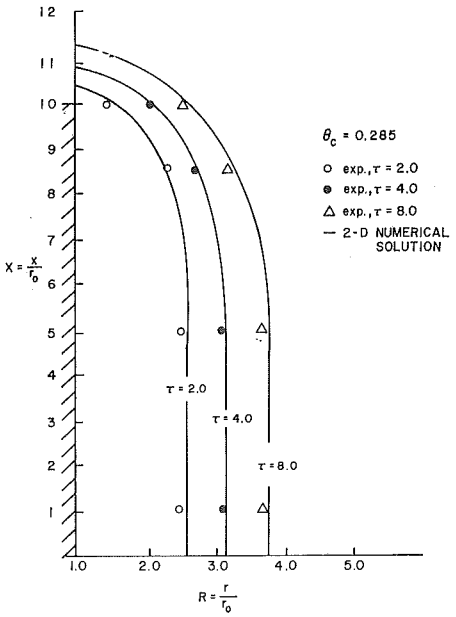

Fig. 7 Comparison of experimentally determined axial values of the critical radius R_c versus time τ with results obtained from the two-dimensional numerical solution

Concluding Remarks

In summarizing our study, several observations can be made:

1 The probe described herein is easy to fabricate, inexpensive, and allows for delicate, predictable surface temperature control.

2 The excellent agreement between theoretical predictions of the temperature field surrounding the probe and experimental measurements indicates that it is possible to predict lesion size as a function of time of application.

3 Liquid crystals embedded in a clear gel offer an excellent means for visually observing the temperature field produced by the heating probe. Although liquid crystals that responded in the range 29.9 deg C to 34.2 deg C were used in the present studies, it is possible to obtain crystals in ranges as low as 0 deg C or as high as 64 deg C.

4 The test medium used in our experiments was 99.7 percent water–0.3 percent agar. Although this mixture simulates tissue thermal properties to within approximately 5 percent, it obviously lacks the perfusion of tissue. The one-dimensional analytical model indicates that small probes will be relatively uninfluenced by blood flow. This claim needs to be verified with either a clever set of experiments which accurately simulate blood flow or with tests on laboratory animals.

Acknowledgment

The authors gratefully acknowledge the excellent technical assistance of Mr. Thomas Christian in the experimental phase of the study. This work was supported by the Naval Postgraduate School Research Foundation.

References

1 Gengler, P. L., *Heat Transfer Analysis of a Radio-Frequency Brain Probe,* MS thesis, Naval Postgraduate School, Monterey, Calif., 1971.

2 Aronow, S., "The Use of Radio-Frequency Power in Making Lesions in the Brain," *J. Neurosurg.*, May 1960, pp. 431–438.

3 Watkins, W. S., "Heat Gains in Brain during Electrocoagulative Lesions," *J. Neurosurg.*, Vol. 23, 1965, pp. 319–328.

4 Herrero, S., "Radio-Frequency Current and Direct Current Lesions in the Ventromedial Hypothalamus," *Am. J. Physio.*, Vol. 217, No. 2, Aug. 1969, pp. 403–410.

5 Cooper, T. E., and Trezek, G. J., "A Probe Technique for Determining the Thermal Conductivity of Tissue," JOURNAL OF HEAT TRANSFER, TRANS. ASME, Series C, Vol. 94, No. 2, May 1972, pp. 133–140.

6 Cooper, T. E., and Trezek, G. J., "Correlation of Thermal Properties of Some Human Tissue with Water Content," *Aerospace Med.*, Vol. 42, Jan. 1971, pp. 24–27.

7 Brodkey, J. S., Miyazaki, Y., Ervin, F. R., and Mark, V. H., "Reversible Heat with Radio Frequency Current," *J. Neurosurg.*, Vol. 22, 1964, pp. 49–53.

8 Carpenter, M., and Whittier, J. R., "Study of Methods for Producing Experimental Lesions of the Central Nervous System with Special Reference to Stereotaxic Technique," *J. of Comp. Neurology*, Vol. 97, 1952, pp. 73–117.

9 Gildenberg, P. L., "Studies in Stereoencephalotomy X," *Confinia Neurologica*, Vol. 20, 1960, pp. 53–65.

10 Groff, J. P., "The Design and Analysis of Resistively Heated Surgical Probe," MS thesis, Naval Postgraduate School, Monterey, Calif., Dec. 1971.

11 Fergason, J. L., "Liquid Crystals," *Scientific American*, Vol. 211, No. 2, Aug. 1964, pp. 76–86.

12 Fergason, J. L., "Liquid Crystals in Non-destructive Testing," *Applied Optics*, Vol. 7, No. 9, Sept. 1968, pp. 1729–1737.

13 Fergason, J. L., "Experiments with Cholesteric Liquid Crystals," *Am. J. of Physics*, Vol. 38, No. 4, Apr. 1970, pp. 425–428.

14 Pennes, H. H., "Analysis of Tissue and Arterial Blood Temperature in the Resting Human Forearm," *J. Appl. Physiol.*, Vol. 1, No. 2, Aug. 1948, pp. 93–122.

15 Ganong, W. F., *In Review of Medical Physiology*, Lange Medical Publications, Los Altos, Calif., 1967, p. 484.

16 Edwards, A. L., "TRUMP: A Computer Program for Transient and Steady State Temperature Distributions in Multi-Dimensional Systems," Lawrence Radiation Laboratory, Rept. UCRL-14754, Rev. 11, 1969.

W. A. BECKMAN
Professor,
Department of Mechanical Engineering.
Mem. ASME

J. W. MITCHELL
Professor,
Department of Mechanical Engineering.
Mem. ASME

W. P. PORTER
Associate Professor,
Department of Zoology.

University of Wisconsin,
Madison, Wisc.

Thermal Model for Prediction of a Desert Iguana's Daily and Seasonal Behavior

A mathematical description of the transient thermal response of the desert iguana, Dipsosaurus dorsalis, *to environmental changes is developed. The thermal model for the lizard was combined with a desert micrometeorological model, and the combination was used to predict diurnal and seasonal thermoregulatory behavior. Comparisons are made between the predictions and observed behavior. The model analysis is sufficiently general so that it can be used to predict the thermoregulatory behavior of other species of lizards.*

Introduction

THE PURPOSE of this paper is to demonstrate how mechanistic principles from engineering and meteorology can be integrated with ecology and physiology to develop models that will predict animal behavior in response to the thermal environment. There is a long history of studies of exchange of energy between animals and their physical environment ranging from work on humans, e.g., [1, 2],[1] to a variety of lower animals, e.g., [3, 4]. Attempts to make predictions of animal behavior for a single day using steady-state models appeared almost simultaneously in papers by Bartlett and Gates [5] and Norris [6]. Subsequently, a more general attempt at steady-state predictions of environmental limits of animals was presented in a paper by Porter and Gates [7]. In this paper, the thermal response of the animal to transient environmental conditions is studied. The Mojave Desert and the desert iguana (*Dipsosaurus d. dorsalis*) have been chosen to illustrate these principles. The activity patterns for this species of desert lizard are predicted for particular days and for an entire year. Figure 1 shows the desert iguana in a schematic representation of the desert microclimate.

Lizard Model

The model for transient thermal processes inside the lizard is based on the core–shell concept of Crosbie et al. [8] and is depicted in Fig. 2. The core, which includes the central portion of the appendages, has a uniform temperature T_c due to blood flow and has a thermal capacitance C_c. Metabolism M supplies

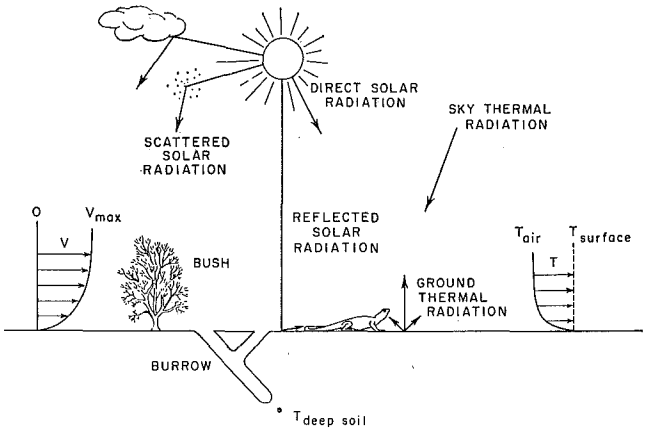

Fig. 1 Schematic of the desert environment showing the energy flows to the desert surface and to a lizard

heat to the core, and energy E leaves due to evaporation of water. Energy is transported to the skin by blood flow in amount $(\dot{m}c)_b(T_c - T_{sk})$, where $\dot{m}$ is blood mass flow rate and c is blood specific heat. Heat is transferred to the center of the skin layer by conduction through the skin resistance R_{sk}. The skin layer is at temperature T_{sk} and has thermal capacitance C_{sk}. Heat is conducted from the center of the skin layer to the surface at T_{surf} through resistance R_{sk}. Solar energy in an amount Q_{abs} is absorbed at the surface. Heat is convected to the air at T_{air} through the convection resistance R_{conv} and radiates to the environment at an effective radiation temperature T_{rad} through the radiation resistance R_{rad}. Heat conducted to the substrate is assumed negligible.

The general thermal model represented by Fig. 2 may be simplified for *Dipsosaurus dorsalis* by considering the relative values of the resistances in the thermal circuit. For a 40-gm

[1] Numbers in brackets designate References at end of paper.

Contributed by the Heat Transfer Division and presented at the Winter Annual Meeting, Washington, D. C., November 28–December 2, 1971, of THE AMERICAN SOCIETY OF MECHANICAL ENGINEERS. Manuscript received by the Heat Transfer Division August 11, 1971; revised manuscript received May 1, 1972. Paper No. 71-WA/HT-35.

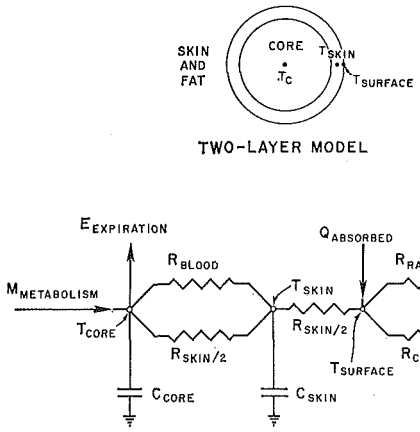

Fig. 2 Core–shell model and the corresponding thermal circuit for a lizard

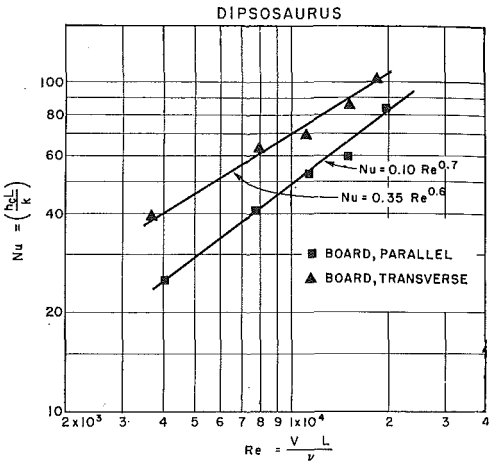

Fig. 3 Nusselt number as a function of Reynolds number for lizard castings (solid symbols) and comparison with results from live lizards (open symbols, Weathers, 1971)

lizard with a surface area of 150 cm², a snout-vent length of 13 cm, and a skin thickness of 0.1 cm, the following are felt to be representative capacitance and resistance values:

core capacitance	C_c	= 23.4 cal/deg C
skin capacitance	C_{sk}	= 12.6 cal/deg C
skin resistance	R_{sk}	= 0.005 min-deg C/cal
blood resistance	R_b	= 0.8 to 8.0 min-deg C/cal
convection resistance	R_{conv}	= 0.2 to 0.6 min-deg C/cal
radiation resistance	R_{rad}	= 0.98 to 1.04 min-deg C/cal

In performing these calculations, the skin mass was taken to be 14 gm and the core 26 gm. The tissue specific heat was taken to be 0.9 cal/gm-deg C and tissue thermal conductivity was taken to be 0.072 cal/cm-min-deg C [9]. Blood flow values were taken to be 0.01 to 0.001 gm/min-cm², which are representative of human values for active and resting tissue [10] and are probably higher than found in the lizard. The convection resistance was calculated from $R_{conv} = 1/h_L A$, where h_L, the lizard's convection heat transfer coefficient, was determined in the wind-tunnel tests described below. The radiation resistance was evaluated as $R_{rad} = (T_{surf} - T_{rad})/[\epsilon\sigma A_{eff}(T_{surf}^4 - T_{rad}^4)]$, where ϵ is the infrared emissivity of the skin and is taken to be unity, σ is the Stefan–Boltzmann constant, and A_{eff} is the effective radiation area and is taken to be 0.8 times the surface area.

The blood and skin resistance act in parallel, facilitating the transfer of heat from the core to the skin. The radiation and convective resistances are two orders of magnitude larger than the equivalent internal resistance, thereby controlling the heat flow from the animal to the environment. Thus all of the internal resistances may be neglected relative to the external resistances. With these simplifications, *Dipsosaurus dorsalis* can be treated as being a single temperature throughout. For larger lizards, this approximation may not be valid, and all of the terms of Fig. 2 may have to be included. The general energy-balance equation for the lizard is then

$$C\frac{dT_c}{dt} = Q_{abs} - \frac{(T_c - T_{air})}{R_{conv}} - \frac{(T_c - T_{rad})}{R_{rad}} + (M - E) \quad (1)$$

where C is $(C_c + C_{sk})$.

Water-loss values, as obtained from [11], were converted to energy flows by multiplying by the latent heat of vaporization, 540 cal/gm. Oxygen-consumption values from [12] were converted to energy flows assuming 5 cal of heat per cc of oxygen consumed. The term $(M - E)/C$ was found to affect core temperature by less than 0.31 deg C over the range of lizard temperatures of 20 to 45 deg C. Under exercise conditions, both M and E will increase, but the resulting term will still be small since the two components tend to cancel each other. Thus the contribution of metabolism and water loss to the energy balance can be regarded as negligible, and the lizard may be represented by the simplified differential equation

$$C\frac{dT_c}{dt} = Q_{abs} - \frac{(T_c - T_{air})}{R_{conv}} - \frac{(T_c - T_{rad})}{R_{rad}} \quad (2)$$

The convection heat transfer coefficient h_L for shapes such as lizards on soil surfaces is unknown and must be determined experimentally. The lost-wax technique was used to obtain aluminum castings of *Dipsosaurus dorsalis*. The procedure required anesthetizing the animal, covering it with dental-investment compound, and later removing the live animal from the flexible mold. A wax casting was then made from the flexible mold, which was then used to obtain an aluminum casting. The aluminum casting was gold-plated to give maximum accuracy in determining the convection coefficient. The lizard casting was placed on a sandy board in a low-speed wind tunnel, 0.51 m² in flow area, heated 10 to 15 deg C above ambient conditions, and then allowed to cool. The convection heat transfer coefficient

Nomenclature

A = total lizard area
C = mass times specific heat
c_p = constant-pressure specific heat
E = evaporation
g = gravitational acceleration
h = convection heat transfer coefficient
K = Karman constant (0.4)
K_H = eddy diffusivity for heat
K_M = eddy diffusivity for momentum
L = Monin–Obukhov length, equation (5)
M = metabolism
$\dot{m}c$ = mass flow rate times specific heat
Q = heat flow
R = thermal resistance
T = temperature
t = time
V = velocity
V^* = shear velocity
α = absorptivity
ϵ = emissivity
ρ = density
σ = Stefan–Boltzmann constant
τ = shear stress

Subscripts

a = air
abs = lizard absorbed solar energy
air = air at lizard height
b = blood
c = core
cond = conduction into soil
conv = convection
eff = effective
inc = incident solar energy
L = lizard
rad = radiation
s = surface of soil
sk = skin
sky = sky
surf = surface of lizard
z = height above the surface

was determined from measurements of the transient temperature response [5, 13].

The heat transfer results (Nusselt number as of function of Reynolds number) are shown in Fig. 3 for parallel and transverse orientation of the casting to the air flow. The characteristic length in both the Nusselt number and the Reynolds number is the snout-vent length. These nondimensional parameters allow extension of the results obtained on one lizard to lizards of different size but of the same geometrical shape (same species).

Heat transfer coefficients deduced from the data of Weathers [14] for heating of live lizards are also presented in Fig. 3. These data are compared with results using the casting placed in the wind tunnel in the same orientation as were Weathers' live lizards. There is excellent agreement between the casting results and the live-animal tests. In addition, the data for 20-, 50-, and 100-gm lizards are correlated by the use of Nu and Re parameters. Thus Fig. 3 establishes the use of castings to determine live-animal heat transfer characteristics.

Micrometeorological Model

The available climatic data are insufficient to completely describe the environment; consequently it was necessary to develop an analytical model to aid in simulation of the desert surface temperature T_s. In this model, the following energy balance was made for the desert surface:

$$\alpha_s Q_{\text{inc}} = \epsilon_s \sigma (T_s^4 - T_{\text{sky}}^4) + h_s (T_s - T_a) + Q_{\text{cond}} \tag{3}$$

where α_s, the soil solar absorptivity, was taken as 0.25 [15] and ϵ_s, the soil long-wavelength emissivity, was taken as unity. The radiation sky temperature T_{sky} was determined from the Swinbank formula [16]. The air temperature T_a was obtained from meteorological measurements of the screen temperature (the temperature measured in a Stevenson screen) at 200 cm above the surface. The maximum and minimum daily air temperatures at this height were taken from the screen temperature records of Palm Springs [17]. The air temperature maxima and minima were assumed to occur at 1300 hr and 1 hr before sunrise, respectively. The shape of the air temperature curve was taken from typical desert air temperature curves in Geiger [18].

The surface heat transfer coefficient h_s is a function of wind speed and surface roughness. When the ground is colder than the air, i.e., neutral (stable) conditions, the flow is completely turbulent and the velocity and temperature profiles are described by [19]

$$V_z/V_a = (T_z - T_a)/(T_s - T_a) = (V^*/V_a \cdot \text{K}) \ln [(z + z_0)/z_0] \tag{4}$$

where V_z and T_z are the velocity and temperature at any specified height above the surface, V_a and T_a are the air velocity and temperature at a reference height, V^* is the shear velocity, K is the Karman constant (0.4), z is the height above the surface, and z_0 is the surface roughness.

Unstable lapse conditions prevail during midday in which the ground surface temperature is higher than air temperature and heat transfer is from the ground to the air. Free-convection currents are set up which alter the temperature and velocity profiles from those in neutral conditions. A measure of the instability of the flow is the Monin–Obukhov length [20].

$$L = -V^{*3} T_z \rho_a c_{p,a} / \text{K} g Q_{s,\text{conv}} \tag{5}$$

The length L is negative under lapse conditions ($T_s > T_a$), approaches infinity under neutral conditions ($T_s \simeq T_a$), and is positive for inversion conditions ($T_s < T_a$). As L becomes smaller in magnitude under lapse conditions, the flow becomes more unstable and free-convection currents affect the profiles more. A relation for the velocity profile under nonneutral conditions is [20]

$$V_z = \frac{V^*}{\text{K}} \ln \frac{e^{(z+z_0)/L} - 1}{e^{(z_0/L)} - 1} \tag{6}$$

As the Monin–Obukhov length L increases, the velocities given by equation (6) approach those given by the relation for neutral conditions, equation (4).

The heat transfer coefficient is determined from a consideration of the transport mechanisms in the turbulent boundary layer. The mechanism equations for the transfers of heat (Q) and momentum (τ) are given in terms of the velocity and temperature gradient [19]

$$Q/\rho_a c_{p,a} = K_H \frac{\partial T_z}{\partial z} \tag{7}$$

$$\tau/\rho_a = K_M \frac{\partial V_z}{\partial z} \tag{8}$$

where the heat flux Q and the shear stress τ are constant throughout the layer near the ground and equal to the values at the surface, $Q_{s,\text{conv}}$ and τ_0. Dividing equation (7) by equation (8) yields the temperature gradient in the air as a function of the velocity gradient

$$\frac{\partial T}{\partial z} = \frac{Q_{s,\text{conv}}}{\tau_s c_{p,a}} \frac{K_M}{K_H} \frac{\partial V_z}{\partial z} \tag{9}$$

Integrating equation (9) from the surface $z = 0$ to a height z yields an expression for the temperature in the air

$$(T_z - T_s) = \frac{Q_{s,\text{conv}}}{\tau_s c_{p,a}} \int_0^z \frac{K_M}{K_H} \frac{\partial V_z}{\partial z} dz \tag{10}$$

With relations for the eddy diffusivities K_H and K_M and with an expression for the velocity profile, equation (10) can be integrated.

Data have been obtained by Swinbank [20] on the ratio of eddy diffusivities K_H/K_M. As discussed by Stewart and Lemon [21], during lapse conditions (negative values of L) the ratio can be represented by

$$K_H/K_M = 3 - 1.4e^{1.5z/L} \tag{11}$$

This equation along with equation (6) can be substituted into equation (10) to yield a relation between the air temperature and height

$$(T_z - T_s) = \frac{Q_{s,\text{conv}}}{\text{K}\rho_a c_{p,a} V^*} \int_0^{z/L} [3 - 1.4e^{1.5z/L}]^{-1} \times \left[\frac{e^{(z+z_0)/L}}{e^{(z+z_0)/L} - 1}\right] d\left(\frac{z}{L}\right) \tag{12}$$

The integral on the right-hand side of equation (12) cannot be evaluated analytically but must be integrated numerically. Defining $F(z/L, z_0/L)$ to be the value of the integral, equation (12) can be rewritten as

$$(T_z - T_s) = \frac{Q_{s,\text{conv}}}{\text{K}\rho_a c_{p,a} V^*} F(z/L, z_0/L) \tag{13}$$

The temperature T_z in the air at any height z can be related to the overall temperature difference

$$\frac{T_z - T_s}{T_a - T_s} = \frac{F(z/L, z_0/L)}{F(z_a/L, z_0/L)} \tag{14}$$

The convection heat transfer $Q_{s,\text{conv}}$ is given by equation (12) in terms of the integral evaluated at some reference height

$$Q_{s,\text{conv}} = \rho_a c_{p,a} \text{K} V^* (T_a - T_s)/F(z_a/L, z_0/L) \tag{15}$$

A computer subroutine has been written to evaluate the length L, the function $F(z/L, z_0/L)$, and the convection heat flow

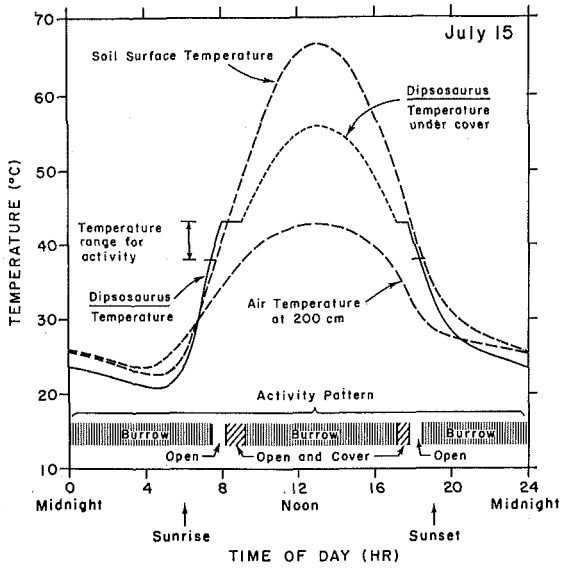

Fig. 4 Lizard, surface, and air temperature as a function of time of day for July 15

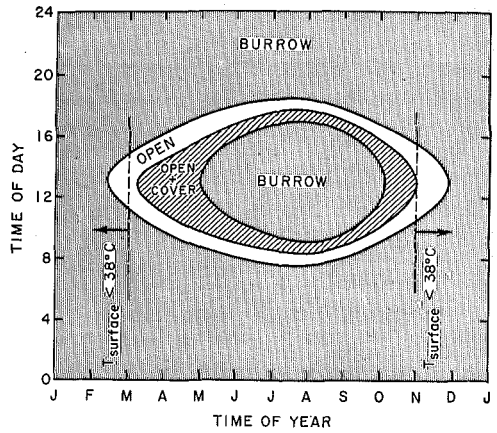

Fig. 5 Behavioral map for *Dipsosaurus dorsalis* as a function of time of day and time during the year

$Q_{s,\,\mathrm{conv}}$ as functions of time of day. The surface roughness z_0 was chosen as 0.05 cm and the wind speed at 200 cm was chosen to be 200 cm/sec. During the midday hours, the length L is on the order of -15 to -25 cm and $F(z/L, z_0/L)$ is approximately 2.5. Under stable (neutral) conditions, $F(z/L, z_0/L)$ is 3.7. Thus the effect of the free-convection currents is to augment the heat transfer from the desert surface during midday.

The heat conducted into the soil, Q_{cond}, was determined using a finite-difference representation for the transient conduction through sand. The sand conductivity was taken to be 0.0084 cal/min-cm-deg C and the thermal diffusivity 0.24 cm²/min [15]. The deep soil temperature at 60 cm was taken to be the average screen temperature for the month.

Daily Behavioral Patterns

The energy balance for the lizard in this desert environment is equation (2) written in terms of radiation and convection properties rather than resistances:

$$C\frac{dT_c}{dt} = Q_{\mathrm{abs}} - \sigma\epsilon A_{\mathrm{eff},\,s}(T_c^4 - T_s^4) - \sigma\epsilon A_{\mathrm{eff},\,\mathrm{sky}}(T_c^4 - T_{\mathrm{sky}}^4) - h_L A(T_c - T_a) \quad (16)$$

where $Q_{\mathrm{abs}} = \alpha_{\mathrm{sk}} Q_{\mathrm{inc}}$ includes direct, scattered, and reflected sunlight. Desert iguanas can change their color and therefore their solar absorptivity α_{sk} between 0.60 and 0.80 [6, 22]. The solar absorptivity was assumed to vary linearly with body temperature between 38.0 and 43.0 deg C from 0.6 to 0.8. Below 38.0 and above 43.0 deg C, the values of 0.6 and 0.8 respectively were used. The effective radiating areas $A_{\mathrm{eff},\,s}$ and $A_{\mathrm{eff},\,\mathrm{sky}}$ are from the lizard to ground and sky, respectively, and each is taken as 0.4 times the surface area. Two lizard sizes, 40 and 100 gm, were considered in the model calculations. The lizard's convection coefficient h_L was obtained from the model results, Fig. 3. The local velocity and temperature that the lizard is exposed to are evaluated from the velocity and temperature profile, equations (6) and (14), using the height of the lizard off the surface.

The results for the average July 15 at Palm Springs, Calif., are presented in Fig. 4. The temperature of the lizard was computed assuming the lizard to be either 1 cm or 5 cm above the surface 24 hr a day. At 1 cm, the lizard is assumed to be on the surface in the sun, and at 5 cm, the lizard is assumed to be in a bush completely shaded from the sun. The desert iguana's temperature, if it stood on the surface all night and into the morning, would not reach 38 deg C, the minimum preferred temperature for activity [23], until about 7:30 A. M. Thus it is expected that the lizard would emerge from his burrow at approximately 7:30 A. M. By 8:15, its temperature would be up to 43 deg C, the panting threshold [11], and to conserve water it could not remain in the full sun on the surface. Between 8:15 and 9:00, the lizard could seek shade either on the ground or in a bush; however, shortly after 9:00 A. M. the deepest shade at 5 cm height is not sufficient to keep the body temperature below 43 deg C, and the lizard must return to its burrow. The body temperature of an animal that remained in the shade at a height of 5 cm and did not pant is shown by the dashed line in the middle of the day. This animal would not survive these severe temperatures. Toward the end of the day, the body temperature drops into the activity temperature range where an animal could be active until about 6:30 P. M. In these and subsequent calculations for the whole year, the assumed wind speed was a constant 200 cm/sec all day. It was found that doubling the wind speed changed emergence times or length of activity time by less than 10 min.

The calculations were also performed for both 40- and 100-gm lizards. Differences of less than 5 min in activity pattern between the two were observed. The times required for each size to come to equilibrium with the environment are so short, relative to the length of the day, that all lizards of the species *Dipsosaurus dorsalis* are essentially at steady-state conditions. Thus from a purely physical standpoint, for desert iguanas of different sizes in the same microclimate, size apparently does not confer a significant thermoregulatory behavioral advantage.

Seasonal Behavioral Patterns

This initial model did not include different heights the animal could climb to, running underground to cool off before returning to the surface, sand-dune geometry, atypical air temperatures, or cloudy days, all of which would modify the predictions. Nevertheless, such a simple model has great utility for seeing broad outlines of behavior patterns which can then be refined. Accordingly, a composite behavioral map for the lizard over the course of an average year at Palm Springs is given in Fig. 5. This figure was constructed using the information from plots like Fig. 4 for the average day for every month.

If the lizard were to wait until the surface temperature reached 38 deg C, it would not be expected to be out before March 1 or after November 1, under typical environmental conditions. *Dipsosaurus dorsalis* could, however, attain 38 deg C body temperature as early as February 15, though only for a few moments. If an animal were out on February 21, it would have about 2 hr for activity since there would be enough solar radiation and warm enough air to allow it to reach at least 38 deg C. The environment is favorable for the lizard during the central portion of the day from March 1 to May 1. From May 1 to October 1, the

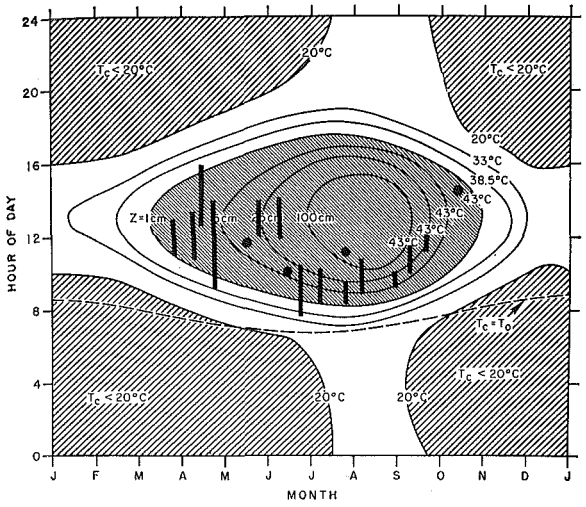

Fig. 6 Behavioral map for *Dipsosaurus dorsalis* including effects of bush height; observations of Mayhew shown as solid bars and circles

temperatures during the middle of the day are too high to permit activity, and the lizard is in general restricted to early morning and late afternoon activity.

Detailed study of the predicted subsurface soil temperatures reveals that during the late afternoon activity period, the soil temperature for the first few centimeters below the surface exceeds the upper limit (43 deg C) for the animal. Thus for the lizard to come from a deep burrow to reach the surface, he must move through a zone of extreme temperatures to reach the favorable environment. The field observations of Norris [24] and Mayhew [25] show that the morning is the major activity period.

These same soil temperature predictions show that during the months of July and August, soil temperatures at depths up to 16 cm are higher than 43 deg C, and at depths up to 25 cm, higher than 38 deg C during the afternoon. To stay below the panting threshold (43 deg C) and thereby minimize water loss, the lizard must have a burrow that extends at least to 15 to 25 cm in depth; this is consistent with the recent findings of DeWitt regarding burrow depth [23].

The natural environment of the desert iguana has different bushes of varying heights, and these allow the desert iguana to extend its activity times. As indicated in Fig. 1, both temperature and wind speed vary depending on the height above the ground. By climbing up into bushes, animals reach not only lower air temperatures but higher wind speeds, which tend to decrease the animal's temperature. Velocity and temperature profiles at any height z in a bush were computed from equations (6) and (14). It was also assumed that the lizard in the bush is shielded from solar radiation and that the infrared radiation exchange is between the lizard and the local surrounding vegetation, which is assumed to be at local air temperature.

The activity pattern for a lizard able to climb to different heights is shown in Fig. 6. The presence of bushes allows a considerable extension of the time available for outside activity. If the animal could climb to 200 cm and still be in deep shade, it could stay out all day even in August.

Because of uncertainty about the lower temperature limit for activity, particularly for emergence at early times of the year, other body temperature contours have also been added to Fig. 6. Another possible emergence criterion could be when the sand surface temperature equals core temperature. This contour is also shown in Fig. 6. The figure also demonstrates that if the animals could be active at a core temperature of 20 deg C they could be nocturnal in the middle of the summer.

The seasonal behavior for *Dipsosaurus dorsalis* is present in Mayhew's accumulation of body temperature and location data collected over more than 10 years at Palm Springs, Calif. [25]. The data come from individuals he found while walking or driving on the desert, as opposed to continuous observation of specific individuals. Figure 6 summarizes all of Mayhew's data for desert iguanas captured at Palm Springs. It is not known how much earlier or later than the time of the observation lizards were present. Thus exact emergence and retreat times are uncertain. The predictions are based on the average thermal environment for the month, while the data of Mayhew are taken on specific days which may differ from the average. For example, the two days with late emergence (May 26 and June 9) were each unusually cool days with the air temperature never exceeding 38 deg C. The agreement between the predictions and data shows that the lizard activity is restricted by the thermal environment.

Mayhew's observations of lack of afternoon activity in the summer and much reduced activity in the fall is intriguing. One possible explanation for this is the high-temperature wave in the sand that might drive the animal deeper into its burrow in the afternoon. Another possible explanation is that there might be a total daily water loss that would be too costly to the animal if it emerged in the afternoon. Thus, while the thermal environment serves as an outer limit on behavior, other constraints exist to further restrict activity.

Conclusions

Despite the simplifications in modeling of *Dipsosaurus dorsalis* and its environment, the analysis of energy exchange mechanisms between the animal and its environment has permitted assessments of the relative importance of various features in the environment and features of the animal's physiology. Knowledge of body temperature preferences and tolerances combined with the knowledge and evaluation of heat transfer mechanisms yield the general features of behavior patterns. This type of analysis offers promise in answering questions concerning the effects of climatic change in the past or in the future.

Acknowledgments

The authors would like to acknowledge the financial support of the University of Wisconsin Departments of Mechanical Engineering and Zoology, the Engineering Experiment Station, the Wisconsin Alumni Research Foundation, and the Madison Academic Computing Center. Portions of this research were also supported by NSF grant GB-31043.

References

1 Winslow, C. E. A., Herrington, L. P., and Gagge, A. P., "Physiological Reactions of the Human Body to Varying Environmental Temperatures," *American Journal of Physiology*, Vol. 120, No. 1, 1937, pp. 1–22.

2 Hardy, J. D., and DuBois, E. F., "The Technique of Measuring Radiation and Convection," *Journal of Nutrition*, Vol. 15, 1938, pp. 461–475.

3 Cowles, R. B., and Bogert, C. M., "A Preliminary Study of the Thermal Requirements of Desert Reptiles," *Bulletin of the American Museum of Natural History*, Vol. 83, 1944, pp. 265–296.

4 Birkebak, R. C., Cremers, C. J., and LeFebvre, E. A., "Thermal Modeling Applied to Animal Systems," JOURNAL OF HEAT TRANSFER, TRANS. ASME, Series C, Vol. 88, No. 1, Feb. 1966, pp. 125–130.

5 Bartlett, P. N., and Gates, D. M., "The Energy Budget of a Lizard on a Tree Trunk," *Ecology*, Vol. 48, 1967, pp. 315–322.

6 Norris, K. S., "Color Adaptation in Desert Reptiles and Its Thermal Relationships," *Symposium on Lizard Ecology*, W. Milstead, ed., University of Missouri Press, Columbia, Mo., 1967, pp. 162–229.

7 Porter, W. P., and Gates, D. M., "Thermodynamic Equilibria of Animals with Environment," *Ecological Monographs*, Vol. 39, 1969, pp. 245–270.

8 Crosbie, R. J., Hardy, J. D., and Fessenden, E., "Electrical Analog Simulation of Temperature Regulation in Man," *IRE Trans.*, Vol. 8, 1961, p. 245.

9 Chato, J. C., "A Survey of Thermal Conductivity and Diffusivity Data on Biological Materials," ASME Paper No. 66-WA/HT-37.

10 Altman, P. L., *Handbook of Circulation*, Vol. 3, Saunders, 1965, p. 132.

11 Templeton, J. R., "Respiration and Water Loss at Higher

Temperatures in the Desert Iguana, *Dipsosaurus dorsalis*," *Physiol. Zool.*, Vol. 33, 1960, p. 136.

12 Dawson, W. R., and Bartholomew, G. A., "Metabolic and Cardiac Response to Temperature in the Lizard *Dipsosaurus dorsalis*," *Physiol. Zool.*, Vol. 30, 1958, p. 100.

13 London, A. L., Nottage, H. B., and Boelter, L. M. K., "Determination of Unit Conductances of Heat and Mass Transfer by the Transient Method," *Industrial and Engineering Chemistry*, Vol. 33, 1941, p. 467.

14 Weathers, W. W., "Physiological Thermoregulation in the Lizard, *Dipsosaurus dorsalis*," *Copeia*, No. 3, 1970, pp. 549–557.

15 Kreith, F., *Principles of Heat Transfer*, 2nd ed., International Textbook Co., Scranton, Pa., 1965, pp. 411.

16 Swinbank, W. C., "Long-wave Radiation from Clear Skies," *Quart. J. Roy. Met. Soc.*, Vol. 89, 1963, p. 339.

17 *ESSA Climatological Data*, California, Vol. 73, 1969.

18 Geiger, R., *The Climate Near the Ground*, Harvard University Press, Cambridge, Mass., 1965.

19 Sellers, W. D., "Physical Climatology," University of Chicago, Chicago, Ill., 1965.

20 Swinbank, W. C., "The Exponential Wind Profile," *Quart. J. Roy. Met. Soc.*, Vol. 90, 1964, p. 119.

21 Stewart, D. W., and Lemon, E. R., "The Energy Budget at the Earth's Surface," Interior Rept. 69-3, U. S. Department of Agriculture and Cornell University, 1969.

22 Porter, W. P., "Solar Radiation Through the Living Body Walls of Vertebrates with Emphasis on Desert Reptiles," *Ecological Monographs*, Vol. 37, 1967, p. 273.

23 DeWitt, C. B., "Precision of Thermoregulation and Its Relation to Environmental Factors in the Desert Iguana, *Diposaurus dorsalis*," *Physiol. Zool.*, Vol. 40, pp. 49–66.

24 Norris, K. S., "The Ecology of the Desert Iguana, *Dipsosaurus dorsalis*," *Ecology*, Vol. 34, 1953, p. 265.

25 Mayhew, W. W., personal communication, 1971.

journal of heat transfer

technical briefs

This section consists of contributions of 1500 words or less (about 5 double-spaced typewritten pages, including figures). Technical briefs will be reviewed and approved by the specific division's reviewing committee prior to publication. After approval such contributions will be published as soon as possible, normally in the next issue of the journal.

Mass Transfer through Binary Gas Mixtures

J. C. HAAS[1] and G. S. SPRINGER[2]

Introduction

In this study mass transfer through a binary monatomic gas mixture contained between two plane parallel surfaces is investigated. Previously such a problem was analyzed by Hamel [1][3] and Perlmutter [2] under the restrictions of (*a*) the mixture is isothermal and (*b*) one of the components is present in a small quantity only. The solution given here is not limited by these assumptions and is valid over the entire density range from free-molecule to continuum conditions. The formulation employs the Boltzmann equation and a moment method of solution with two-sided distribution functions, in a manner similar to that used by Shankar [3] in his study of mass transfer to or from spherical droplets.

Analysis

A binary mixture of monatomic gases is contained between two reservoirs whose surfaces extend to infinity and are plane and parallel to each other, Fig. 1. The surfaces of the reservoirs are impermeable to one of the gases, say gas B, but are permeable by the other component, say gas A, such that a fraction of the A molecules arriving at the surface is absorbed into the reservoir, while a fraction is reemitted into the gas. Thus the reservoirs contain gas A only at the equilibrium temperatures and pressures $T_I{}^A$, $T_{II}{}^A$ and $P_I{}^A$, $P_{II}{}^A$. These "reservoirs" might be, for example, two liquid surfaces (with $P_I{}^A$ and $P_{II}{}^A$ being the saturation pressures corresponding to $T_I{}^A$ and $T_{II}{}^A$) on which gas (vapor) A condenses and from which it evaporates. Using the definition of the mass accommodation, or sticking, coefficient

$$\sigma \equiv (\dot{m}_a - \dot{m}_l)/(\dot{m}_a - \dot{m}_m) \tag{1}$$

the mass fluxes of A and B molecules leaving the surface are (note $\sigma^B = 0$)

$$\dot{m}_l{}^A = (1 - \sigma^A)\dot{m}_a{}^A + \sigma^A \dot{m}_m{}^A \qquad \dot{m}_l{}^B = \dot{m}_a{}^B \tag{2}$$

where $\dot{m}_a$ is the mass flux arriving at the surface and $\dot{m}_m$ is the mass flux which would be emitted from a gas in equilibrium at the temperature and pressure of the reservoir. For gas A, a thermal-accommodation coefficient is defined for the reflected

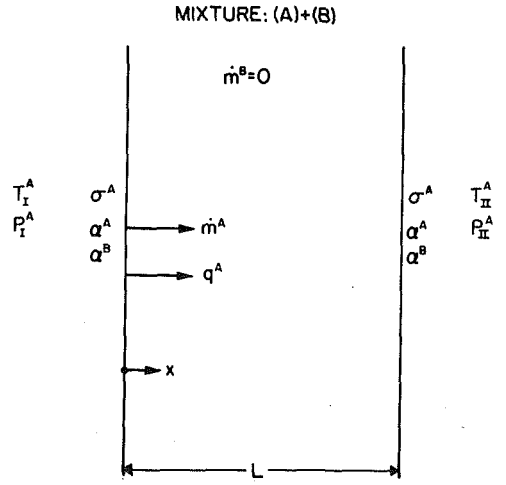

Fig. 1 Description of problem

portion of the molecular stream, while for gas B it is expressed in the usual manner [4], i.e.,

$$\alpha^A \equiv \frac{(1 - \sigma^A)E_a{}^A - E_r{}^A}{(1 - \sigma^A)(E_a{}^A - E_m{}^A)} \qquad \alpha^B \equiv \frac{E_a{}^B - E_r{}^B}{E_a{}^B - E_m{}^B} \tag{3}$$

E_a and E_r are the energy fluxes of the incident and reflected molecules respectively, and E_m is the energy flux of the reflected molecules based on the equilibrium temperature and pressure of the reservoir. Using equation (3) the energy fluxes leaving the surface can be written as

$$E_l{}^A = (E_r{}^A + E_e{}^A) = (1 - \sigma^A)[E_a{}^A - \alpha^A(E_a{}^A - E_m{}^A)] + \sigma^A E_m{}^A \tag{4}$$

$$E_l{}^B = E_r{}^B = E_a{}^B - \alpha^B(E_a{}^B - E_m{}^B) \tag{5}$$

where the energy flux of the evaporating molecules is $E_e{}^A = \sigma^A E_m{}^A$. In order to define the problem completely the amount of gas B in the system must also be specified by specifying either the total number of molecules in the system $n_l{}^B$ or the number density n^B at the surface of one of the reservoirs, i.e.,

$$n_l{}^B = \int_0^L n^B(x)dx \tag{6a}$$

or

$$n^B = n_{II}{}^B \qquad \text{at} \qquad x = L \tag{6b}$$

$n^B(x)$ can be calculated from the equations given in [5]. Equations (2), (4), (5), and (6) constitute the boundary conditions of the problem. The steady one-dimensional mass transfer between the reservoirs is now determined by treating the gases as ideal, composed of monatomic molecules obeying Maxwell's inverse fifth-power law of repulsion. Following Lees [6] the gas

[1] Fluid Dynamics Laboratory, Department of Mechanical Engineering, University of Michigan, Ann Arbor, Mich.

[2] Professor, Fluid Dynamics Laboratory, Department of Mechanical Engineering, University of Michigan, Ann Arbor, Mich. Mem. ASME.

[3] Numbers in brackets designate References at end of technical brief.

Based on a paper contributed by the Heat Transfer Division and presented at the Winter Annual Meeting, Washington, D. C., November 28–December 2, 1971, of The American Society of Mechanical Engineers as Paper No. 71-WA/HT-2. Manuscript received by the Heat Transfer Division June 22, 1971.

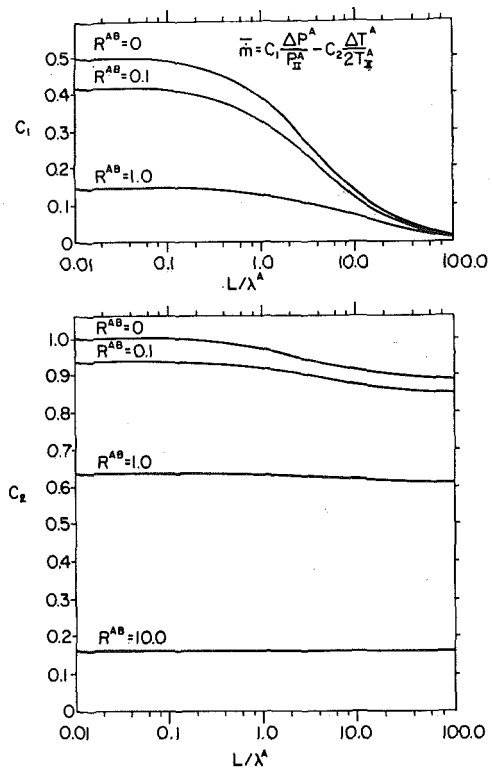

Fig. 2 The variation of the coefficients C_1 and C_2 with inverse Knudsen number and with R^{AB} ($\sigma^A = \alpha^A = \alpha^B = 1$, $m^A/m^B = 1$), $\Delta P^A \equiv P_I{}^A - P_{II}{}^A$, $\Delta T^A = T_I{}^A - T_{II}{}^A$

molecules are divided (in velocity space) into two groups, each of these being characterized by a Maxwellian distribution function of the form

$$f_{1,2} = n_{1,2}{}^i \left(\frac{m^i}{2\pi k T_{1,2}{}^i}\right)^{3/2} \exp\left[\frac{-m^i(\mathbf{v}^i)^2}{2kT_{1,2}{}^i}\right] \tag{7}$$

where the subscripts 1 and 2 are for $v_x > 0$ and $v_x < 0$, respectively. The superscript i denotes the A or B component; k is the Boltzmann constant, m the mass of the molecule, and $\mathbf{v}$ the absolute velocity. The unknown parameters $n_{1,2}{}^A$, $n_{1,2}{}^B$, $T_{1,2}{}^A$, $T_{1,2}{}^B$ are determined by taking moments of the Maxwell integral equation of transfer which, for the present problem, is

$$\frac{d}{dx}\int_{-\infty}^{\infty}\int\int f^i v_x{}^i Q^i dv_x dv_y dv_z = \Delta Q \tag{8}$$

ΔQ represents the collision integral and includes collisions between both like and unlike molecules. By setting $Q^i = m^i$, $Q^i = m^i v_x{}^i$, $Q^i = {}^1/_2 m^i (v^i)^2$, and $Q^i = {}^1/_2 m^i v_x{}^i (v^i)^2$, eight simultaneous first-order nonlinear differential equations are generated [6] which, together with the boundary conditions, could be solved by numerical methods. However, an analytic expression for the mass transfer can be derived by assuming that (*a*) the temperature and pressure differences between the reservoirs are small, $(T_I{}^A - T_{II}{}^A)/T_{II}{}^A \ll 1$ and $(P_I{}^A - P_{II}{}^A)/P_{II}{}^A \ll 1$, and (*b*) the mean temperatures of components A and B are the same at any point in the gas, $T^A(x) = T^B(x)$. The latter assumption is correct in the continuum limit [3], and also in the free-molecule limit provided the thermal-accommodation coefficients are the same for each component, i.e.,

$$\alpha^A(x = 0) = \alpha^A(x = L) \qquad \alpha^B(x = 0) = \alpha^B(x = L) \tag{9}$$

For these accommodation coefficients, $T^A = T^B$ is also expected to be a reasonable assumption at intermediate degrees of rarefaction. Using the above two assumptions, the conditions expressed by equation (9), and $\sigma^A = \sigma^A(x = 0) = \sigma^A(x = L)$, the following expression is obtained for the mass-transfer rate per unit area [6]:

$$\dot{m}^A = n_{II}{}^A \left(\frac{m^A k T_{II}{}^A}{2\pi}\right)^{1/2} \left\{\frac{P_I{}^A - P_{II}{}^A}{P_{II}{}^A}\left[1 + \frac{4}{15}\frac{L}{\lambda^A}\psi + \frac{1}{2}R^{AB}\left(b_2\psi + \frac{\alpha^B}{2-\alpha^B}b_3\right)\right] - \frac{T_I{}^A - T_{II}{}^A}{2T_{II}{}^A}\right\} \times \left\{\frac{2-\sigma^A}{\sigma^A} + \frac{L}{\lambda^A}\left(\frac{4}{15}\psi\frac{2-\sigma^A}{\sigma^A} + \frac{1}{30}\right) + \frac{1}{2}R^{AB}\left[\frac{3}{2} + \frac{4}{15}\frac{L}{\lambda^A}\psi - \frac{b_1}{2} + b_2\left(\psi\frac{2-\sigma^A}{\sigma^A} - \frac{1}{2}\right) + b_3\frac{2-\sigma^A}{\sigma^A}\frac{\alpha^B}{2-\alpha^B} + \frac{1}{2}R^{AB}\left(\psi b_2 + \frac{\alpha^B}{2-\alpha^B}b_3\right)\right]\right\}^{-1} \tag{10}$$

where

$$\psi \equiv [1 - (1 - \sigma^A)(1 - \alpha^A)]/[1 + (1 - \sigma^A)(1 - \alpha^A)] \tag{11a}$$

$$b_1 \equiv -(2/5)\{5M^A - 10[m^A m^B/(m^A + m^B)^2] \times [1 - (A_2/A_1)]\} \tag{11b}$$

$$b_2 \equiv -(2/5)\{-6 + 12M^B - 8(M^B)^2[1 - (A_2/A_1)] - 8M^B(A_2/A_1)\} \tag{11c}$$

$$b_3 \equiv -(16/5)\{m^A[(m^A m^B)^{1/2}/(m^A + m^B)^2][1 - (A_2/A_1)]\} \tag{11d}$$

$$R^{AB} \equiv [n_{II}{}^B/(n_{II}{}^A + n_{II}{}^B)]/[(2\pi k T_{II}{}^A/m^A)^{1/2}L/(\pi D^{AB})] \tag{11e}$$

$$D^{AB} \equiv [kT_{II}{}^A/(m^A m^B A_1)][(m^A + m^B)/K^{AB}]/(n_{II}{}^A + n_{II}{}^B) \tag{11f}$$

λ is the mean free path, $A_1 = 2.6595$, $A_2 = 1.3682$, K is the force constant in the inverse fifth-power law, $M^i = m^i/(m^A + m^B)$, and D^{AB} is the diffusion coefficient.

Discussion

Equation (10) is limited to small temperature and pressure differences. However, it is not restricted to any specific density regime. It is valid for all degrees of rarefaction and yields the correct free-molecule [7, 8] and continuum [9, 10] limits. In order to investigate the behavior of the mass-transfer rate at intermediate Knudsen numbers ($\mathrm{Kn} = \lambda^A/L$), equation (19) is written as

$$\bar{\dot{m}}^A \equiv \frac{\dot{m}^A}{n_{II}{}^A(m^A k T_{II}{}^A/2\pi)^{1/2}} = C_1\frac{P_I{}^A - P_{II}{}^A}{P_{II}{}^A} - C_2\frac{T_I{}^A - T_{II}{}^A}{T_{II}{}^A} \tag{12}$$

The dependence of the coefficients C_1 and C_2 on R^{AB} is shown in Fig. 2. This figure serves to illustrate three points. First, at high Knudsen numbers C_1 and C_2 are of the same order of magnitude and, as expected, both ΔT^A and ΔP^A affect the mass-transfer rate. At low Knudsen numbers, however, $C_1 \gg C_2$ and the influence of the temperature difference becomes negligible. This is consistent with results found for a single-component gas [11, 12]. Second, both C_1 and C_2 approach rapidly their free-molecule and continuum values above $\lambda^A/L \approx 10$ and $\lambda^A/L \approx 0.1$, respectively. Third, the mass transfer is significantly affected by R^{AB}, i.e., by the presence of the "inert" B component. A small increase in the amount of component B reduces the mass transfer considerably. To further demonstrate this effect, mass-transfer rates were calculated through water vapor in the presence of nitrogen and through potassium in the presence of argon. The results given in Fig. 3 show that 0.1 percent and 1.0 percent inert gas ($P_{II}{}^B/[P_{II}{}^A + P_{II}{}^B] = 0.001$ and 0.01) reduce the mass-transfer rate by factors of about two and 20, respectively.

It should be noted that mass-accommodation coefficients σ for vapors are generally determined by measuring the mass-transfer

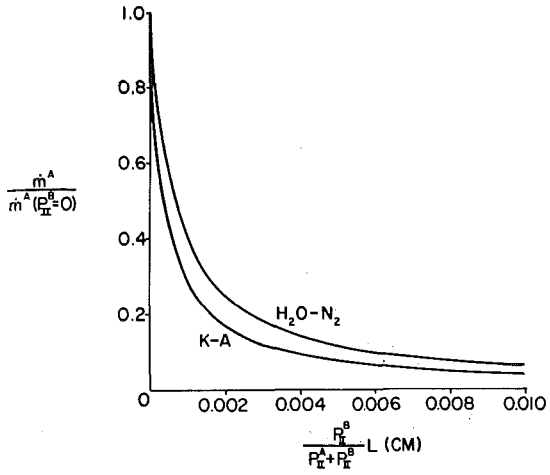

Fig. 3 The effect of nitrogen and argon (*B* gases) on the mass transfer of water vapor and potassium, $\lambda^A/L \to 0$, $\sigma^A = \alpha^A = \alpha^B = 1$; also for H_2O–N_2: $T_{II}^A = 20$ deg C, $P_{II}^A = 0.0229$ atm; for K–A: $T_{II}^A = 565$ deg C, $P_{II}^A = 0.105$ atm

rate and by calculating σ with the assumption that the vapor is pure ($n_{II}^B = 0$). According to the foregoing results, if even a small amount of impurity is present in the system the σ thus calculated is lower than the actual value.

Acknowledgments

The authors wish to thank Prof. V. S. Arpaci for his many helpful comments. This work was supported by the U. S. Atomic Energy Commission.

References

1 Hamel, B. B., "A Study of Some Mass Transfer Problems according to the Kinetic Theory of Gases," PhD thesis, Princeton University, Princeton, N. J., 1963.

2 Perlmutter, M., "Rarefied Diffusion by Model Sampling," NASA TN D-5764, 1970.

3 Shankar, P. N., "A Kinetic Theory of Steady Condensation," *Journal of Fluid Mechanics*, Vol. 40, 1970, pp. 385–400.

4 Kennard, E. H., *Kinetic Theory of Gases*, McGraw-Hill, New York, N. Y., 1938, p. 312.

5 Haas, J. C., and Springer, G. S., "Mass Transfer Through Binary Gas Mixtures," ASME Paper No. 71-WA/HT-2.

6 Lees, L., "A Kinetic Theory Description of Rarefied Gas Flows," Memorandum 51, Guggenheim Aeronautical Laboratory, California Institute of Technology, Pasadena, Calif., 1959.

7 Hertz, H., "Über die Verdunstung der Flüssigkeiten, insbesondere des Quecksilbers, in flutleeren Raume," *Annalen der Physik*, Vol. 17, 1882, pp. 177–200.

8 Knudsen, M., "Die maximale Verdampfungsgeschwindigkeit des Quecksilbers," *Annalen der Physik*, Vol. 47, 1915, pp. 697–708.

9 Maxwell, J. C., *The Scientific Papers of James C. Maxwell*, Vol. II, University Press, Cambridge, England, 1890, pp. 625–646.

10 Stefan, J., "Über die Verdampfung aus einem Kreisformig oder elliptisch begrenzten Becken," *Wien. Ber.*, Vol. 83, 1881, pp. 943–954.

11 Shankar, P. N., "A Kinetic Theory Investigation of Some Condensation–Evaporation Phenomena by a Moment Method," PhD thesis, California Institute of Technology, Pasadena, Calif., 1968.

12 Patton, A. J., and Springer, G. S., "A Kinetic Theory Description of Liquid Vapor Phase Change," in: *Rarefied Gas Dynamics*, Vol. 2, L. Trilling and H. Wachman, eds., Academic Press, New York, N. Y., 1969, pp. 1497–1501.

Film-Cooling Effectiveness in the Near-Slot Region

D. R. BALLAL[1] and A. H. LEFEBVRE[2]

Nomenclature

$C_{f/2}$ = local skin friction coefficient
m = mass velocity ratio ($\rho_c u_c/\rho_m u_m$)
m_{bl} = mass flow in boundary layer
m_c = coolant mass flow
Re_s = Reynolds number based on slot height
Re_θ = Reynolds number based on boundary layer momentum thickness
s = slot height
u = velocity
x = distance downstream of the slot
y = distance normal to wall
δ = boundary layer thickness
μ = viscosity
ρ = fluid density
η = film-cooling effectiveness
ϕ = mass velocity (ρu)

Subscripts

c = pertaining to coolant flow
m = pertaining to mainstream flow
Δ = pertaining to quantities in excess of mainstream values
max = maximum value

Introduction

In recent years many theoretical prediction methods for film-cooling effectiveness have been developed. In the present study, interest is centered on the near-slot region, with particular reference to thin-lipped systems featuring tangential injection of the coolant through two-dimensional unobstructed slots. Expressions for effectiveness are derived which are shown to be in satisfactory agreement with the available experimental data.

Analysis

Turbulent Boundary Layer Model. Stollery and El-Ehwany [1][3] have developed an effectiveness expression for an idealized turbulent boundary layer far downstream of the slot. Their equation, with a modified constant of 4.0 [2] is

$$\eta = 4.0(x/ms)^{-0.8}(\mathrm{Re}_s \cdot \mu_c/\mu_m)^{0.2} \quad (1)$$

It is known that this and similar equations based on the Blasius skin friction relationship cannot satisfactorily predict effectiveness in the near-slot region. This suggests that a better model for this region would be one which employed skin friction coefficients obtained by direct measurement in this zone.

From the study of skin friction data in [3, 4], it is found that for $x/s < 40$

$$C_{f/2} = 0.0615[(\mathrm{Re}_\theta m)^{0.4}(x/ms)]^{-0.625} \quad (2)$$

Substitution of this expression into the analysis of Stollery and El-Ehwany [1] leads to

$$\eta = m_c/m_{bl} = 0.4(x/ms)^{-0.3}(\mathrm{Re}_s m \cdot \mu_c/\mu_m)^{0.2} \quad (3)$$

Equation (3) shows good agreement with the experimental data. Even better prediction can be achieved by reducing the Reynolds-number exponent from 0.2 to 0.15, accompanied by a compensating increase in the value of the constant from 0.4 to 0.6. Thus equation (3) becomes

$$\eta = 0.6(x/ms)^{-0.3}(\mathrm{Re}_s m \cdot \mu_c/\mu_m)^{0.15} \quad (4)$$

As shown in Fig. 1, this simple equation predicts within ±5 percent accuracy all of the available experimental data compiled in [5] within the following range of conditions:

[1] Research Fellow, School of Mechanical Engineering, Cranfield Institute of Technology, Cranfield, Bedford, England.

[2] Professor and Head of the School of Mechanical Engineering, Cranfield Institute of Technology, Cranfield, Bedford, England.

Contributed by the Heat Transfer Division of The American Society of Mechanical Engineers. Manuscript received by the Heat Transfer Division April 24, 1972.

[3] Numbers in brackets designate References at end of technical brief.

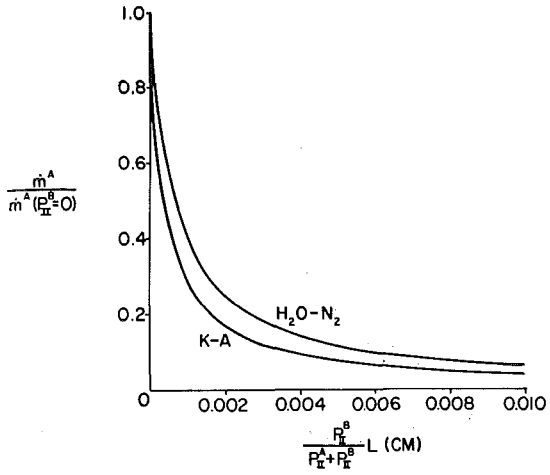

Fig. 3 The effect of nitrogen and argon (*B* gases) on the mass transfer of water vapor and potassium, $\lambda^A/L \to 0$, $\sigma^A = \alpha^A = \alpha^B = 1$; also for H_2O–N_2: $T_{II}^A = 20$ deg C, $P_{II}^A = 0.0229$ atm; for K–A: $T_{II}^A = 565$ deg C, $P_{II}^A = 0.105$ atm

rate and by calculating σ with the assumption that the vapor is pure ($n_{II}^B = 0$). According to the foregoing results, if even a small amount of impurity is present in the system the σ thus calculated is lower than the actual value.

Acknowledgments

The authors wish to thank Prof. V. S. Arpaci for his many helpful comments. This work was supported by the U. S. Atomic Energy Commission.

References

1 Hamel, B. B., "A Study of Some Mass Transfer Problems according to the Kinetic Theory of Gases," PhD thesis, Princeton University, Princeton, N. J., 1963.

2 Perlmutter, M., "Rarefied Diffusion by Model Sampling," NASA TN D-5764, 1970.

3 Shankar, P. N., "A Kinetic Theory of Steady Condensation," *Journal of Fluid Mechanics*, Vol. 40, 1970, pp. 385–400.

4 Kennard, E. H., *Kinetic Theory of Gases*, McGraw-Hill, New York, N. Y., 1938, p. 312.

5 Haas, J. C., and Springer, G. S., "Mass Transfer Through Binary Gas Mixtures," ASME Paper No. 71-WA/HT-2.

6 Lees, L., "A Kinetic Theory Description of Rarefied Gas Flows," Memorandum 51, Guggenheim Aeronautical Laboratory, California Institute of Technology, Pasadena, Calif., 1959.

7 Hertz, H., "Über die Verdunstung der Flüssigkeiten, insbesondere des Quecksilbers, in flutleeren Raume," *Annalen der Physik*, Vol. 17, 1882, pp. 177–200.

8 Knudsen, M., "Die maximale Verdampfungsgeschwindigkeit des Quecksilbers," *Annalen der Physik*, Vol. 47, 1915, pp. 697–708.

9 Maxwell, J. C., *The Scientific Papers of James C. Maxwell*, Vol. II, University Press, Cambridge, England, 1890, pp. 625–646.

10 Stefan, J., "Über die Verdampfung aus einem Kreisformig oder elliptisch begrenzten Becken," *Wien. Ber.*, Vol. 83, 1881, pp. 943–954.

11 Shankar, P. N., "A Kinetic Theory Investigation of Some Condensation–Evaporation Phenomena by a Moment Method," PhD thesis, California Institute of Technology, Pasadena, Calif., 1968.

12 Patton, A. J., and Springer, G. S., "A Kinetic Theory Description of Liquid Vapor Phase Change," in: *Rarefied Gas Dynamics*, Vol. 2, L. Trilling and H. Wachman, eds., Academic Press, New York, N. Y., 1969, pp. 1497–1501.

Film-Cooling Effectiveness in the Near-Slot Region

D. R. BALLAL[1] and A. H. LEFEBVRE[2]

Nomenclature

$C_{f/2}$ = local skin friction coefficient
m = mass velocity ratio ($\rho_c u_c/\rho_m u_m$)
m_{bl} = mass flow in boundary layer
m_c = coolant mass flow
Re_s = Reynolds number based on slot height
Re_θ = Reynolds number based on boundary layer momentum thickness
s = slot height
u = velocity
x = distance downstream of the slot
y = distance normal to wall
δ = boundary layer thickness
μ = viscosity
ρ = fluid density
η = film-cooling effectiveness
ϕ = mass velocity (ρu)

Subscripts

c = pertaining to coolant flow
m = pertaining to mainstream flow
Δ = pertaining to quantities in excess of mainstream values
max = maximum value

Introduction

In recent years many theoretical prediction methods for film-cooling effectiveness have been developed. In the present study, interest is centered on the near-slot region, with particular reference to thin-lipped systems featuring tangential injection of the coolant through two-dimensional unobstructed slots. Expressions for effectiveness are derived which are shown to be in satisfactory agreement with the available experimental data.

Analysis

Turbulent Boundary Layer Model. Stollery and El-Ehwany [1][3] have developed an effectiveness expression for an idealized turbulent boundary layer far downstream of the slot. Their equation, with a modified constant of 4.0 [2] is

$$\eta = 4.0(x/ms)^{-0.8}(\mathrm{Re}_s \cdot \mu_c/\mu_m)^{0.2} \quad (1)$$

It is known that this and similar equations based on the Blasius skin friction relationship cannot satisfactorily predict effectiveness in the near-slot region. This suggests that a better model for this region would be one which employed skin friction coefficients obtained by direct measurement in this zone.

From the study of skin friction data in [3, 4], it is found that for $x/s < 40$

$$C_{f/2} = 0.0615[(\mathrm{Re}_\theta m)^{0.4}(x/ms)]^{-0.625} \quad (2)$$

Substitution of this expression into the analysis of Stollery and El-Ehwany [1] leads to

$$\eta = m_c/m_{bl} = 0.4(x/ms)^{-0.3}(\mathrm{Re}_s m \cdot \mu_c/\mu_m)^{0.2} \quad (3)$$

Equation (3) shows good agreement with the experimental data. Even better prediction can be achieved by reducing the Reynolds-number exponent from 0.2 to 0.15, accompanied by a compensating increase in the value of the constant from 0.4 to 0.6. Thus equation (3) becomes

$$\eta = 0.6(x/ms)^{-0.3}(\mathrm{Re}_s m \cdot \mu_c/\mu_m)^{0.15} \quad (4)$$

As shown in Fig. 1, this simple equation predicts within ±5 percent accuracy all of the available experimental data compiled in [5] within the following range of conditions:

[1] Research Fellow, School of Mechanical Engineering, Cranfield Institute of Technology, Cranfield, Bedford, England.

[2] Professor and Head of the School of Mechanical Engineering, Cranfield Institute of Technology, Cranfield, Bedford, England.

Contributed by the Heat Transfer Division of The American Society of Mechanical Engineers. Manuscript received by the Heat Transfer Division April 24, 1972.

[3] Numbers in brackets designate References at end of technical brief.

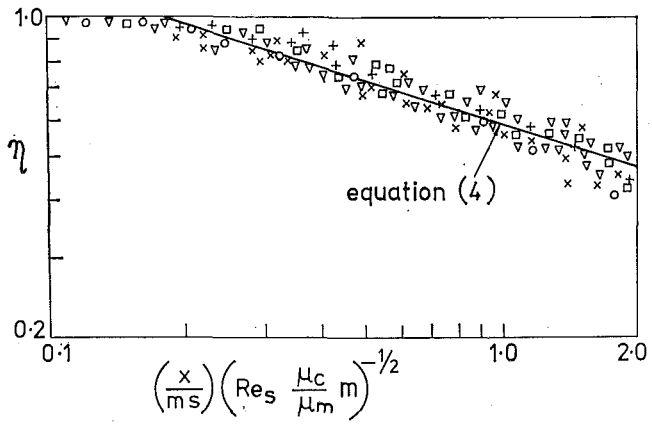

Fig. 1 Illustrations of improvements in effectiveness prediction in near-slot region for $m < 1.3$

m	0.5 to 1.3	ρ_c/ρ_m	0.8 to 2.5
s	0.19 to 0.64 cm	x/s	0 to 150

It can now be shown that if flow transition is assumed to occur at the point of intersection of equations (1) and (4), when $(x/ms)m^{0.15} > 6.6\ (\mathrm{Re}_s \cdot \mu_c/\mu_m)^{0.05}$, (1) is preferable to (4); otherwise equation (4) should be used.

Wall Jet Model. For a wall jet model

$$\eta = m_c/m_{bl} = \phi_c s/(m_{bl1} + m_{bl2}) \tag{5}$$

The mass flow in the inner boundary layer m_{bl1} from [6] is

$$m_{bl1} = 0.009\ \phi_{\max} \cdot x \tag{6}$$

In calculating m_{bl2}, the mass flow in the two-dimensional jet profile, the mass velocity expression is of the type

$$\Delta\phi/\Delta\phi_{\max} = 0.5(1 + \cos \pi \cdot y/\delta_2) \tag{7}$$

Again from [6], $\delta_2 = 0.1x$, and from [7],

$$\phi_{\max}/\phi_c = 2.5\{[(m - 1)/m](s/x)\}^{0.5}$$

Therefore, integrating equation (7) and substituting for various terms, the value of m_{bl2} can be calculated. Substitution of this expression for m_{bl2} together with equation (6) into equation (5) leads to

$$\eta = \{0.15[(x/ms)(m - 1)]^{0.5} + 0.05(x/ms)\}^{-1} \tag{8}$$

The useful range of application of this expression to the experimental data is rather limited, since beyond a certain distance downstream of the slot, the wall jet profile changes into a near-slot boundary layer profile. For $m < 4$, this transition is shown to occur [6] at a mean value of $x/ms = 11$. By restricting its range of application to $x/ms \gtrsim 11$, equation (8) may be simplified to

$$\eta \simeq [0.6 + 0.05(x/ms)]^{-1} \tag{9}$$

The close agreement between the predictions of equation (9) and actual measurements from [5] is illustrated in Fig. 2.

For $x/ms > 11$, the flow situation at the wall approximates more closely to the boundary layer model described above. Equation (4) may thus be employed provided that modifications are made to allow for the fact that the coolant flow can no longer be considered to originate at the slot. A further condition to be satisfied is that when $x/ms = 11$, predicted values of effectiveness must be consistent with equation (9). These considerations combined with the experimental data in this region lead to the following expression for effectiveness:

$$\eta = 0.7(x/s)^{-0.3}(\mathrm{Re}_s \cdot \mu_c/\mu_m)^{0.15} m^{-0.2} \tag{10}$$

Figure 3 shows the experimental and predicted values from [5]. In Figs. 2 and 3, the measurements covered the following range of conditions:

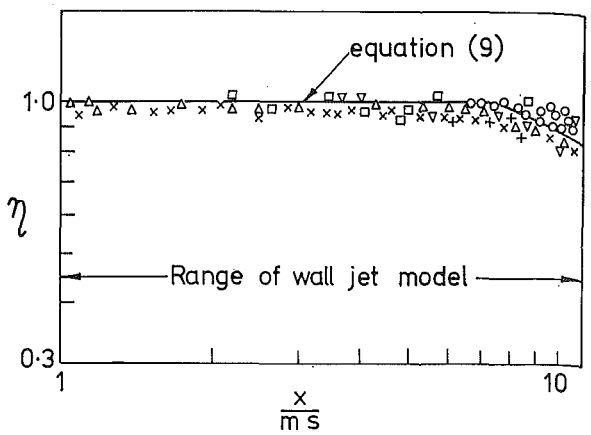

Fig. 2 Comparison between experimental data and prediction formula based on wall jet analysis for $m > 1.3$

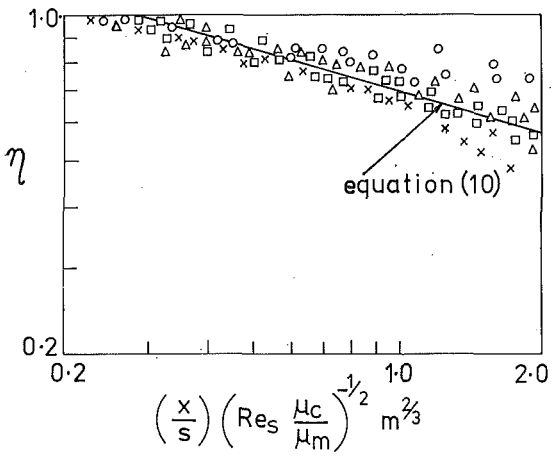

Fig. 3 Comparison between experiment and theory in region downstream of wall jet for $m > 1.3$

m	1.3 to 4.0	x/s	0 to 150
Re_s	3500 to 20,000	ρ_c/ρ_m	0.8 to 2.5

Conclusions

The following expressions for cooling effectiveness in the important near-slot region ($x/s < 150$) are obtained:

(a) boundary layer model (m = 0.5 to 1.3)

$$\eta = 0.6(x/ms)^{-0.3}(\mathrm{Re}_s m \cdot \mu_c/\mu_m)^{0.15}$$

(b) wall jet model (m = 1.3 to 4.0)

for $x/ms < 11$, $\eta = [0.6 + 0.05(x/ms)]^{-1}$

for $x/ms > 11$, $\eta = 0.7(x/s)^{-0.3}(\mathrm{Re}_s \cdot \mu_c/\mu_m)^{0.15} m^{-0.2}$

References

1 Stollery, J. L., and El-Ehwany, A. A., "A Note on the Use of a Boundary Layer Model for Correlating Film Cooling Data," *International Journal of Heat and Mass Transfer*, Vol. 8, 1965, pp. 55–65.

2 Burns, W. K., and Stollery, J. L., "The Influence of Foreign Gas Injection and Slot Geometry on Film-Cooling Effectiveness," *International Journal of Heat and Mass Transfer*, Vol. 12, 1969, pp. 935–951.

3 Leont'ev, A. I., "Heat and Mass Transfer in Turbulent Boundary Layers," in: *Advances in Heat Transfer, Vol. 3*, Academic, New York, N. Y., 1966, pp. 80–100.

4 Whitelaw, J. H., "An Experimental Investigation of Two-Dimensional Wall Jet," *ARC, C. P.*, 1967, p. 942.

5 Goldstein, R. J., "Film Cooling," in: *Advances in Heat Transfer, Vol. 7*, Academic, New York, N. Y., 1971.

6 Abramovich, G. N., *The Theory of Turbulent Jets*, M.I.T. Press, Cambridge, Mass., 1963.

7 Bradbury, L. J. S., "Simple Expressions for the Spread of Turbulent Jets," *Aero. Quarterly*, Vol. 18, May 1967, p. 133.

The Effect of Temperature-dependent Viscosity on Laminar-Condensation Heat Transfer

R. L. LOTT, JR.,[1] and J. D. PARKER[2]

CONSIDERATION of the fluid properties in laminar condensation reveals that the viscosity of the condensate exhibits the greatest variation with temperature. Reid and Sherwood [1][3] recommend the viscosity–temperature relationship $\mu = A \exp(B/T)$ as the best simple expression from the freezing point to the normal boiling point. The constants A and B are positive and T is absolute temperature. The physical model used is the condensation of saturated vapor at temperature T_1 on an infinitely wide vertical isothermal plate at temperature T_0. The condensate flows laminarly under the influence of gravity, g, with a thickness δ which is a function of the vertical distance x down the plate. The x component of the condensate velocity u is a function of the y coordinate normal to the plate. The mass flow rate per unit width at location x is designated as Γ. The average condensing heat-transfer coefficient for a plate of vertical length L is denoted as $\bar{h}$. Using the subscripts 0 and 1 to designate evaluation at $y = 0$ and $y = \delta$ respectively, the following terms are defined:

dimensionless y coordinate: $\bar{y} \equiv y/\delta$
dimensionless viscosity: $\bar{\mu} \equiv \mu_0/\mu(\bar{y})$
dimensionless temperature: $\bar{T} \equiv [T(\bar{y}) - T_1]/\Delta T$
dimensionless velocity: $\bar{u} \equiv 2\mu_0 u(\bar{y})/g(\rho - \rho_v)\delta^2$
dimensionless mass flow rate: $\bar{\Gamma} \equiv 3\mu_0\Gamma/g\rho(\rho - \rho_v)\delta^3$
dimensionless condensate thickness:

$$\bar{\delta} \equiv \delta \Big/ \left[\frac{4\Delta T k \mu_0 x}{g\rho(\rho - \rho_v)h_{fg}}\right]^{1/4}$$

dimensionless heat-transfer coefficient:

$$\bar{H} \equiv \bar{h} \Big/ \left[\frac{64 g\rho(\rho - \rho_v)k^3 h_{fg}}{81 L \mu_0 \Delta T}\right]^{1/4}$$

dimensionless parameter: $\bar{C} = c_p \Delta T/h_{fg}$

The condensate density ρ, specific heat c_p, and thermal conductivity k, as well as the latent heat of vaporization h_{fg}, vapor density ρ_v, and temperature difference $\Delta T = T_1 - T_0$, are considered constant.

The development of equations to describe the inclusion of temperature-dependent viscosity as presented by Lott [2] embodies Nusselt's [3] momentum model, Bromley's [4] consideration of the effect of specific heat, and Rohsenow's [5] evaluation of the cross-flow effect. Equations resulting from these considerations coupled with $\mu = A \exp(B/T)$ are

$$\bar{u} = 2\int_0^{\bar{y}} (1 - \bar{y}) \exp\left[(\bar{T} + 1)\ln\bar{\mu}_1 \Big/ \left(1 + \frac{\Delta T}{T_1}\bar{T}\right)\right] d\bar{y} \quad (1)$$

$$\bar{\Gamma} = \frac{3}{2}\int_0^1 \bar{u}\, d\bar{y} \quad (2)$$

$$\psi \equiv \int_0^{\bar{y}} \bar{T}\bar{u}\, d\bar{y} \quad (3)$$

$$\phi \equiv \int_0^{\bar{y}} \left[\psi - \bar{T}\int_0^{\bar{y}} \bar{u}\, d\bar{y}\right] d\bar{y} \quad (4)$$

$$\bar{T} = \frac{(\bar{\Gamma} - 1.5\bar{C}\psi_1)(\bar{y} - 1) + 1.5\bar{C}(\phi - \phi_1)}{\bar{\Gamma} - 1.5\bar{C}(\psi_1 - \phi_1)} \quad (5)$$

These functions ψ and ϕ evaluated at $\bar{y} = 1$ are involved in describing $\bar{\delta}$ and $\bar{H}$:

$$\left(\frac{d\bar{T}}{d\bar{y}}\right)_0 = (\bar{\Gamma} - 1.5\psi_1\bar{C})/[\bar{\Gamma} - 1.5(\psi_1 - \phi_1)]$$

$$\bar{\delta} = \left[\left(\frac{d\bar{T}}{d\bar{y}}\right)_0 \Big/ (\bar{\Gamma} - 1.5\bar{C}\psi_1)\right]^{1/4} \quad (6)$$

$$\bar{H} = \left(\frac{d\bar{T}}{d\bar{y}}\right)_0 \Big/ \bar{\delta} \quad (7)$$

If a temperature distribution is guessed, then equations (1)–(5) can be evaluated successively yielding a resulting $\bar{T}(\bar{y})$. If the resulting $\bar{T}(\bar{y})$ differs from the guessed $\bar{T}(\bar{y})$, then use of the resulting $\bar{T}(\bar{y})$ as the next guess has been found to "converge" rapidly to an appropriate temperature distribution. Using this technique, as described by Rohsenow [5], the above equations were solved numerically by Lott [2]. The resulting deviation from a linear temperature distribution was small—even with large viscosity variations. Therefore, a linear temperature distribution coupled with $\mu = A \exp(B/T)$ is used to describe $\bar{u}$:

$$\bar{u} = 2\int_0^{\bar{y}} (1 - \bar{y}) \exp\left\{\left[\left(1 + \frac{\Delta T}{T_0}\right)\bar{y}\ln\bar{\mu}_1\right] \Big/ \left[1 + \frac{\Delta T}{T_0}\bar{y}\right]\right\} d\bar{y}$$

This expression for $\bar{u}$ can be closely approximated by

$$\bar{u} \approx 2\int_0^{\bar{y}} (1 - \bar{y}) \exp(\beta\bar{y})\, d\bar{y} \quad (8)$$

where

$$\beta \equiv \left(1 + \frac{\Delta T}{T_0}\right)\left(1 - \frac{\Delta T}{2T_0}\right)\ln\frac{\mu_0}{\mu_1} \quad (9)$$

With these assumptions, equations (1)–(7) can be evaluated to obtain

$$\bar{u} = \frac{2\exp(\beta\bar{y})}{\beta}\left(1 + \frac{1}{\beta} - \bar{y}\right) - \frac{2}{\beta}\left(1 - \frac{1}{\beta}\right) \quad (10)$$

$$\bar{\Gamma} = \frac{6}{\beta^3}\left[\exp(\beta) - \left(1 + \beta + \frac{\beta^2}{2}\right)\right] \quad (11)$$

$$\psi_1 = (1 - \bar{\Gamma})/\beta \quad (12)$$

$$\phi_1 = (1 + 4\bar{\Gamma})/3\beta \quad (13)$$

$$\bar{\delta} = [\bar{\Gamma} - 1.5\bar{C}(\psi_1 - \phi_1)]^{-1/4} \quad (14)$$

$$\bar{H} = (\bar{\Gamma} - 1.5\bar{C}\psi_1)/[\bar{\Gamma} - 1.5\bar{C}(\psi_1 - \phi_1)]^{3/4} \quad (15)$$

The results for $\bar{\delta}$ and $\bar{H}$ are dependent primarily upon $\bar{\Gamma}$. If the viscosity is evaluated at the proper temperature, $T^* = T_0 + C^*\Delta T$, then $\bar{\Gamma}$ can be determined from a constant-viscosity analysis. Use of a linear temperature distribution in equation (8) yields

$$C^* = \frac{\ln(\bar{\Gamma})}{\beta} \quad (16)$$

The expression for $\bar{H}$ can be approximated very closely by

$$\bar{H} = \{\bar{\Gamma}[1 - 1.5\bar{C}(\psi_1 + 3\phi_1)]\}^{1/4} \quad (17)$$

since $\phi_1 < [3/2\bar{\Gamma}(h_{fg}/C\Delta T) - \psi_1]$ for the range of values for β and $\bar{C}$ encountered in condensation. Thus a simple means of accounting for the effect of temperature-dependent viscosity on

[1] Associate Professor, Department of Mechanical Engineering, Vanderbilt University, Nashville, Tenn. Mem. ASME.
[2] Professor, School of Mechanical and Aerospace Engineering, Oklahoma State University, Stillwater, Okla. Mem. ASME.
[3] Numbers in brackets designate References at end of technical brief.

Contributed by the Heat Transfer Division of THE AMERICAN SOCIETY OF MECHANICAL ENGINEERS. Manuscript received by the Heat Transfer Division November 29, 1972.

Table 1 Temperature-dependent Viscosity Correction Terms

β	$\rightarrow 0$	0.5	1.0	1.5	2.0	2.5	3.0	3.5	4.0	4.5	5.0
C^*	$\rightarrow 0.250$	0.260	0.270	0.280	0.292	0.303	0.315	0.328	0.340	0.353	0.366
α	$\rightarrow 0.675$	0.652	0.628	0.603	0.576	0.548	0.519	0.490	0.462	0.433	0.405

condensation heat transfer is to use Nusselt's constant-property results with viscosity evaluated at T^* and with the term $h_{fg}^* = h_{fg}(1 + \alpha\bar{C})$ substituted for h_{fg}, where by definition

$$\alpha = -1.5(\psi_1 + 3\phi_1) = \frac{3(\bar{\Gamma} - 1)(\beta + \psi_1) - 3B}{2\bar{\Gamma}\beta^2} \quad (18)$$

Tabulated results for C^* and α as a function of β are presented in Table 1. For small values of β equation (11) can be expressed in series form:

$$\bar{\Gamma} = 1 + \frac{\beta}{4} + \frac{\beta^2}{20} + \frac{\beta^3}{120} + \frac{\beta^4}{840} + \frac{\beta^5}{6720} + \cdots$$

Constant viscosity corresponds to $\beta = 0$. The case of $\beta \ll 1$ yields $\bar{\Gamma} \rightarrow 1 + \beta/4$, $\psi_1 \rightarrow -1/4 - \beta/20$, $\phi_1 \rightarrow -1/15 - \beta/90$, $C^* \rightarrow 1/4$, and $\alpha \rightarrow 0.675$. The case of $\beta \ll 1$ corresponds to viscosity being inversely proportional to temperature, and yields the recommendation of T. B. Drew and Rohsenow that viscosity be evaluated at $T^* = T_0 + 0.25\Delta T$. The limiting value of α corresponds to Rohsenow's recommendation that h_{fg} be replaced by $h_{fg}' = h_{fg}(1 + 0.68\bar{C})$. Both of these recommendations are valid for small values of β which occur with small ΔT values.

Zozulia [6] considers the viscosity to be inversely proportional to T (deg C) cubed in his analysis of laminar condensation of glycerine. He presents graphical results which demonstrate excellent agreement between his analytical and experimental results for the laminar condensation of glycerine with a vapor saturation temperature of 120 deg C and ΔT ranging from 64 to 101 deg C. A comparison of Zozulia's equivalent $\bar{H}$ with results from equation (16) indicates agreement within 6 percent over the range for which his viscosity–temperature relationship is valid. In this condensing situation β is not small.

The effect of temperature-dependent viscosity on the velocity profile is of interest in the consideration of transition from laminar to turbulent flow, but is not considered in this paper.

This analytical investigation demonstrates that the effect of temperature-dependent viscosity on laminar condensation becomes significant when the value of the parameter β is larger than 1. The recommended method for including the temperature-dependent viscosity effect is to use the simpler Nusselt constant-property analysis with (*a*) viscosity evaluated at $T^* = T_0 + C^*\Delta T$, and (*b*) h_{fg} replaced by $h_{fg}(1 + \alpha\bar{C})$.

References

1 Reid, R. R., and Sherwood, T. K., *The Properties of Gases and Liquids*, 2nd ed., McGraw-Hill, New York, N. Y., 1966.

2 Lott, R. L., Jr., "The Effect of Vapor-borne Sound on Condensation Heat Transfer," PhD thesis, Oklahoma State University, Stillwater, Okla., 1969.

3 Nusselt, W., "Die Oberflachenkondensation des Wasserdampfes," *Zeitschrift des Vereines Deutscher Ingenieure*, Vol. 60, 1916, pp. 541–546.

4 Bromley, L. A., "Effect of Heat Capacity of Condensate in Condensing," *Industrial and Engineering Chemistry*, Vol. 44, No. 12, 1952, pp. 2966–2969.

5 Rohsenow, W. M., "Heat Transfer and Temperature Distribution in Laminar-Film Condensation," TRANS. ASME, Vol. 78, 1956, pp. 1645–1648.

6 Zozulia, M. V., "On the Effect of Condensate Viscosity on Heat Transmission during Condensation of Vapor," *Dokl. Akad. Nauk, Ukrainian SSR*, No. 3, 1958, pp. 272–275.

Similar Solutions for Laminar Film Condensation with Adverse Pressure Gradients

P. M. BECKETT[1]

Steady two-dimensional laminar film condensation is investigated when the saturated vapor has the Falkner–Skan mainstream. Numerical solutions and approximate models are discussed with reference to other published work.

Nomenclature

B = dimensionless parameter = $R/\lambda\chi$
c = length scale
Cf = stress coefficient = $\mu(\partial u/\partial y)/\frac{1}{2}\rho_s U_m^*(x)^2$
c_p = specific heat at constant pressure
E = dimensionless parameter, see [1][2]
h_{fg} = latent heat of condensation
k = thermal conductivity
Nu = Nusselt number = $x(\partial T/\partial y)/\Delta T$
Pr = Prandtl number = $\mu c_p/k$
Re = Reynolds number = $U_m^*(x)(x/\nu)$
R = dimensionless parameter = $(\nu^*/\nu_s)^{1/2}$
T = temperature
u, v = velocity components in (x, y) directions
$U_m^*(x)$ = vapor mainstream velocity = $U_0(x/c)^m$
x = distance measured along wall from leading edge
y = distance measured normal to wall
β = $2m/(m + 1)$
$\delta(x)$ = thickness of condensate layer
$\delta_1(x)$ = vapor displacement thickness = $\int_{\delta(x)}^{\infty} [1 - u^*/U_m^*(x)]dy$
ΔT = $T_s - T_w$
ϵ_p = dimensionless parameter, see [1]
η_δ = dimensionless condensate thickness of Isa and Chen
λ = dimensionless parameter = $(\rho_s\mu_s/\rho^*\mu^*)^{1/2}$
μ = dynamic viscosity
ν = kinematic viscosity = μ/ρ
ρ = density
$\tau_w^*(x)$ = wall shear stress for single-phase flow
ϕ = dimensionless condensate thickness = $(U_m^*(x)/2\nu_s x)^{1/2} \int_0^{\delta(x)} \frac{\rho}{\rho_s} dy$
χ = dimensionless parameter = $c_{p_s}\Delta T/\mathrm{Pr}_s h_{fg}$

Subscripts

s = condition at saturated vapor temperature
w = wall
I = interface

Superscript

$*$ = vapor quantity

Introduction

THE INTEREST in predicting heat transfer characteristics for laminar film condensation has recently been extended to assess the effects of pressure gradients within the vapor phase. Beckett and Poots [1][2] developed so-called thin and thick film models for

[1] Lecturer, Department of Applied Mathematics, University of Hull, Hull, England.

Contributed by the Heat Transfer Division of THE AMERICAN SOCIETY OF MECHANICAL ENGINEERS. Manuscript received by the Heat Transfer Division May 26, 1972.

[2] Numbers in brackets designate References at end of technical brief.

Table 1 Temperature-dependent Viscosity Correction Terms

β	$\rightarrow 0$	0.5	1.0	1.5	2.0	2.5	3.0	3.5	4.0	4.5	5.0
C^*	$\rightarrow 0.250$	0.260	0.270	0.280	0.292	0.303	0.315	0.328	0.340	0.353	0.366
α	$\rightarrow 0.675$	0.652	0.628	0.603	0.576	0.548	0.519	0.490	0.462	0.433	0.405

condensation heat transfer is to use Nusselt's constant-property results with viscosity evaluated at T^* and with the term $h_{fg}^* = h_{fg}(1 + \alpha\bar{C})$ substituted for h_{fg}, where by definition

$$\alpha = -1.5(\psi_1 + 3\phi_1) = \frac{3(\bar{\Gamma} - 1)(\beta + \psi_1) - 3B}{2\bar{\Gamma}\beta^2} \quad (18)$$

Tabulated results for C^* and α as a function of β are presented in Table 1. For small values of β equation (11) can be expressed in series form:

$$\bar{\Gamma} = 1 + \frac{\beta}{4} + \frac{\beta^2}{20} + \frac{\beta^3}{120} + \frac{\beta^4}{840} + \frac{\beta^5}{6720} + \cdots$$

Constant viscosity corresponds to $\beta = 0$. The case of $\beta \ll 1$ yields $\bar{\Gamma} \rightarrow 1 + \beta/4$, $\psi_1 \rightarrow -1/4 - \beta/20$, $\phi_1 \rightarrow -1/15 - \beta/90$, $C^* \rightarrow 1/4$, and $\alpha \rightarrow 0.675$. The case of $\beta \ll 1$ corresponds to viscosity being inversely proportional to temperature, and yields the recommendation of T. B. Drew and Rohsenow that viscosity be evaluated at $T^* = T_0 + 0.25\Delta T$. The limiting value of α corresponds to Rohsenow's recommendation that h_{fg} be replaced by $h_{fg}' = h_{fg}(1 + 0.68\bar{C})$. Both of these recommendations are valid for small values of β which occur with small ΔT values.

Zozulia [6] considers the viscosity to be inversely proportional to T (deg C) cubed in his analysis of laminar condensation of glycerine. He presents graphical results which demonstrate excellent agreement between his analytical and experimental results for the laminar condensation of glycerine with a vapor saturation temperature of 120 deg C and ΔT ranging from 64 to 101 deg C. A comparison of Zozulia's equivalent $\bar{H}$ with results from equation (16) indicates agreement within 6 percent over the range for which his viscosity–temperature relationship is valid. In this condensing situation β is not small.

The effect of temperature-dependent viscosity on the velocity profile is of interest in the consideration of transition from laminar to turbulent flow, but is not considered in this paper.

This analytical investigation demonstrates that the effect of temperature-dependent viscosity on laminar condensation becomes significant when the value of the parameter β is larger than 1. The recommended method for including the temperature-dependent viscosity effect is to use the simpler Nusselt constant-property analysis with (*a*) viscosity evaluated at $T^* = T_0 + C^*\Delta T$, and (*b*) h_{fg} replaced by $h_{fg}(1 + \alpha\bar{C})$.

References

1 Reid, R. R., and Sherwood, T. K., *The Properties of Gases and Liquids*, 2nd ed., McGraw-Hill, New York, N. Y., 1966.

2 Lott, R. L., Jr., "The Effect of Vapor-borne Sound on Condensation Heat Transfer," PhD thesis, Oklahoma State University, Stillwater, Okla., 1969.

3 Nusselt, W., "Die Oberflachenkondensation des Wasserdampfes," *Zeitschrift des Vereines Deutscher Ingenieure*, Vol. 60, 1916, pp. 541–546.

4 Bromley, L. A., "Effect of Heat Capacity of Condensate in Condensing," *Industrial and Engineering Chemistry*, Vol. 44, No. 12, 1952, pp. 2966–2969.

5 Rohsenow, W. M., "Heat Transfer and Temperature Distribution in Laminar-Film Condensation," TRANS. ASME, Vol. 78, 1956, pp. 1645–1648.

6 Zozulia, M. V., "On the Effect of Condensate Viscosity on Heat Transmission during Condensation of Vapor," *Dokl. Akad. Nauk, Ukrainian SSR*, No. 3, 1958, pp. 272–275.

Similar Solutions for Laminar Film Condensation with Adverse Pressure Gradients

P. M. BECKETT[1]

Steady two-dimensional laminar film condensation is investigated when the saturated vapor has the Falkner–Skan mainstream. Numerical solutions and approximate models are discussed with reference to other published work.

Nomenclature

B = dimensionless parameter = $R/\lambda\chi$
c = length scale
Cf = stress coefficient = $\mu(\partial u/\partial y)/\frac{1}{2}\rho_s U_m^*(x)^2$
c_p = specific heat at constant pressure
E = dimensionless parameter, see [1][2]
h_{fg} = latent heat of condensation
k = thermal conductivity
Nu = Nusselt number = $x(\partial T/\partial y)/\Delta T$
Pr = Prandtl number = $\mu c_p/k$
Re = Reynolds number = $U_m^*(x)(x/\nu)$
R = dimensionless parameter = $(\nu^*/\nu_s)^{1/2}$
T = temperature
u, v = velocity components in (x, y) directions
$U_m^*(x)$ = vapor mainstream velocity = $U_0(x/c)^m$
x = distance measured along wall from leading edge
y = distance measured normal to wall
β = $2m/(m + 1)$
$\delta(x)$ = thickness of condensate layer
$\delta_1(x)$ = vapor displacement thickness = $\int_{\delta(x)}^{\infty} [1 - u^*/U_m^*(x)]dy$
ΔT = $T_s - T_w$
ϵ_p = dimensionless parameter, see [1]
η_δ = dimensionless condensate thickness of Isa and Chen
λ = dimensionless parameter = $(\rho_s\mu_s/\rho^*\mu^*)^{1/2}$
μ = dynamic viscosity
ν = kinematic viscosity = μ/ρ
ρ = density
$\tau_w^*(x)$ = wall shear stress for single-phase flow
ϕ = dimensionless condensate thickness = $(U_m^*(x)/2\nu_s x)^{1/2} \int_0^{\delta(x)} \frac{\rho}{\rho_s} dy$
χ = dimensionless parameter = $c_{p_s}\Delta T/\Pr_s h_{fg}$

Subscripts

s = condition at saturated vapor temperature
w = wall
I = interface

Superscript

$*$ = vapor quantity

Introduction

THE INTEREST in predicting heat transfer characteristics for laminar film condensation has recently been extended to assess the effects of pressure gradients within the vapor phase. Beckett and Poots [1][2] developed so-called thin and thick film models for

[1] Lecturer, Department of Applied Mathematics, University of Hull, Hull, England.

Contributed by the Heat Transfer Division of THE AMERICAN SOCIETY OF MECHANICAL ENGINEERS. Manuscript received by the Heat Transfer Division May 26, 1972.

[2] Numbers in brackets designate References at end of technical brief.

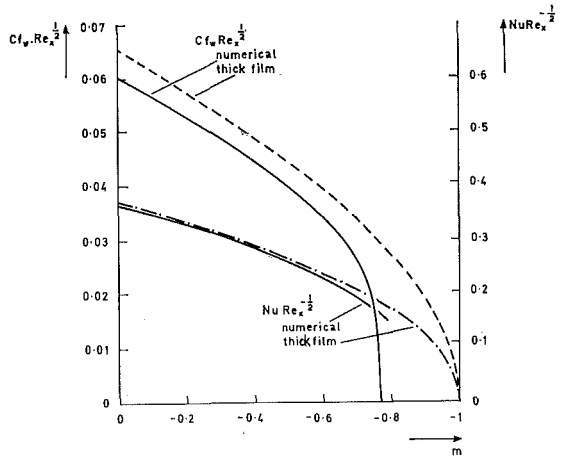

Fig. 1 Dimensionless wall shear and heat transfer as functions of m from the numerical solutions and thick film formulae (6.87), T_w = 0 deg C

the two-dimensional problem of condensation of a saturated vapor with general mainstream velocity $U_m^*(x)$. Isa and Chen [2] imposed the Falkner–Skan mainstream, $U_m^*(x) = U_0(x/c)^m$, but in the interesting range $m < 0$, which corresponds to an adverse pressure gradient, they provide data for only a single value of m and make no reference to flow separation.

In this note, some numerical solutions to the problem considered by Isa and Chen will be presented, and in the light of these, the models proposed in [1] and [2] will be discussed.

The Physical Problem

This is described for the case of a general mainstream in [1] and for the present configuration in [2]. Basically, a saturated vapor flows over a cooler wall, $y = 0$, condenses, and forms a condensate film. It is required to find the velocity distributions in the two phases, the temperature distribution in the condensate, and the location of the liquid–vapor interface, $y = \delta(x)$.

For large Reynolds numbers, the boundary-layer approximation is valid and the resulting equations admit a similar solution. The notation used here is identical to that in [1] except for additional parameters which are introduced in order to facilitate comparison with the work of Isa and Chen; see also the extensive Nomenclature.

Numerical Solutions

Attention will be confined to steam–water condensation when T_s = 100 deg C and T_w = 0 deg C. Physically acceptable solutions exist only for $m > m_0 = -0.7633$. (If $m < m_0$, then $u^* > U_m^*(x)$, somewhere.) The value $m = m_0$ corresponds to a situation where Cf_w is zero, indicating a separation-type velocity profile. The flow and heat transfer characteristics are presented in Table 1, from which it can be confirmed that flow reversal would take place in the condensate because $Cf_w\mathrm{Re}_x^{1/2}$ tends to zero more rapidly than $Cf_I\mathrm{Re}_x^{1/2}$ as $m \to m_0$.

As ΔT is decreased the range of negative m for which solutions exist decreases, and as $\Delta T \to 0$ then $m_0 \to -0.0904$, which is the value found by Hartree [3] for the single-phase problem.

Approximate Solutions

For the case of slight condensation, the *thin film model* yields a solution involving $\tau_w^*(x)$, the wall shear in the corresponding single-phase problem. From [3], for $m > -0.0904$,

$$\tau_w^*(x) = \mu_s(U_0^3(1 + m)/2\nu^*)^{1/2}A_0x^{(3m-1)/2} \tag{1}$$

where A_0 is given for various values of m or β (e.g., $\beta = 1$, $A_0 = 1.2326$; $\beta = 0.5$, $A_0 = 0.9277$; $\beta = -0.1$, $A_0 = 0.3191$). Substitution of (1) into equation (3.18) of [1] yields the following approximate formulae for the flow characteristics:

$$\left.\begin{aligned} \frac{\delta(x)}{x}\,\mathrm{Re}_x^{1/2} &= (m+1)^{-1/2}(4\sqrt{2}\lambda\chi/A_0)^{1/3} \\ Cf_w\mathrm{Re}_x^{1/2} &= \sqrt{2}\lambda^{-1}A_0(1+m)^{1/2} \\ \mathrm{Nu}\,\mathrm{Re}_x^{-1/2} &= (m+1)^{1/2}(4\sqrt{2}\lambda\chi/A_0)^{-1/3} \end{aligned}\right\} \tag{2}$$

Support for the validity of these is given in Table 2. Isa and Chen introduce slightly different parameters, $R = (\nu^*/\nu_s)^{1/2}$, $B = R/\lambda\chi$, and $\eta_\delta = (m+1)^{1/2}\phi/R$, and in terms of these the thin film model yields

$$\eta_\delta = \frac{1}{R}\,(2R/BA_0)^{1/3} \tag{3}$$

From Table 3 it can be seen that there is much better correspondence between (3) and Isa and Chen's approximation for $m > 0$ than for $m < 0$. The validity of (3) has been established for the range $\lambda\chi \ll 1$, which corresponds to $R/B \ll 1$, so we must conclude the error is mainly in Isa and Chen's results. The reason stems from the fact that Isa and Chen apply Pohlhausen's one-parameter method to the vapor flow. In the range $R/B \ll 1$, the condensate rate is slight and the vapor flow approximates to that over a rigid interface. However, it is well known, see Curle and Davies [4], that one-parameter techniques are adequate for

Table 1 Flow characteristics from the numerical solution for T_w = 0 deg C, T_s = 100 deg C

m	$\frac{\delta(x)}{x} \times \mathrm{Re}_x^{1/2}$	$\Gamma\,\mathrm{Re}_x^{1/2}$	$Cf_w\mathrm{Re}_x^{1/2}$	$Cf_I\mathrm{Re}_x^{1/2}$	$\mathrm{Nu} \times \mathrm{Re}_x^{-1/2}$
1	2.27	11.76	0.0878	0.0852	0.531
0	3.22	5.85	0.0601	0.0588	0.373
−0.1	3.41	5.53	0.0566	0.0549	0.353
−0.2	3.62	5.21	0.0530	0.0515	0.332
−0.3	3.88	4.86	0.0491	0.0477	0.310
−0.4	4.20	4.49	0.0448	0.0436	0.286
−0.5	4.62	4.08	0.0400	0.0390	0.260
−0.6	5.22	3.61	0.0343	0.0337	0.230
−0.7	6.20	3.04	0.0265	0.0268	0.194
−0.75	7.14	2.64	0.0199	0.0214	0.168
−0.76	7.54	2.50	0.0171	0.0194	0.159
−0.7625	7.74	2.44	0.0157	0.0185	0.155
−0.7631	7.85	2.40	0.0150	0.0180	0.153
−0.7632	7.92	2.38	0.0144	0.0176	0.152

Table 2 Comparison of numerical results with thin and thick film approximations

	$\frac{\delta(x)}{x}\,\mathrm{Re}_x^{1/2}$	$Cf_w\mathrm{Re}_x^{1/2}$	$\mathrm{Nu}\,\mathrm{Re}_x^{-1/2}$
ΔT = 0.01 deg C, m = 0.5			
Numerical	0.148	0.0132	6.73
Thin film (2)	0.149	0.0129	6.70
ΔT = 0.01 deg C, m = −0.04692			
Numerical	0.335	0.00240	2.99
Thin film (2)	0.335	0.00232	2.65
ΔT = 0.1 deg C, m = −0.04692			
Numerical	0.704	0.00257	1.42
Thin film (2)	0.731	0.00232	1.37
ΔT = 100 deg C, m = 1			
Numerical	2.27	0.0876	0.531
Thick film (4)	2.10	0.0926	0.535
ΔT = 100 deg C, m = −0.4			
Numerical	4.20	0.0448	0.286
Thick film (4)	3.83	0.0507	0.292

Table 3 The characteristic η_δ of Isa and Chen compared with the thin film approximation

β =		−0.1			0.5	
R =	2	10	50	2	10	50
B =	30.79	151.3	753.5	51.64	267.6	134.7
Isa and Chen	0.321	0.0653	0.0131	0.227	0.0439	0.0087
Thin film	0.370	0.0746	0.0149	0.218	0.0432	0.0086

favorable pressure gradients in single-phase flow but become rapidly less accurate when the pressure gradient is large and unfavorable.

When the condensation rate is heavy, $\lambda\chi > 1$, the *thick film approximations* follow from the solution of equation (4.30) in [1]. For this case we then have

$$\left.\begin{aligned} \frac{\delta(x)}{x}\,\mathrm{Re}_x^{1/2} &= 2E\epsilon_p^{-1}(m+1)^{-1/2} \\ Cf_w\mathrm{Re}_x^{1/2} &= Cf_I\mathrm{Re}_x^{1/2} = (m+1)^{1/2}\chi\epsilon_p \\ \mathrm{Nu}\,\mathrm{Re}_x^{-1/2} &= 0.5\epsilon_p(k_s/k_w)(m+1)^{1/2} \end{aligned}\right\} \quad (4)$$

where E and ϵ_p are factors which account for variable condensate properties, see [1]. The comparison between these and the numerical solutions when $\Delta T = 100$ deg C in the case of condensing steam is displayed in Fig. 1.

Assessment of Isa and Chen's results for $\lambda\chi > 1$, that is, $R/B > 1$, is achieved on setting $E = \epsilon_p = 1$ to yield constant condensate properties. Then we have from the thick film approximation that $\eta_\delta = \sqrt{2}/R$, which is readily seen to give their results for heavy condensation, even in the case of an adverse pressure gradient, in Table 1 of [2].

Conclusions

Isa and Chen's constant-property model is applicable to favorable pressure gradients and to adverse pressure gradients provided the condensation rate is heavy.

However, for heavy condensation the variations of thermal conductivity and viscosity are likely to be important factors, and in such cases the thick film formulae (4) should be preferred.

The thin film model is to be recommended for use in the case $\lambda\chi \ll 1$ for negative m, subject to the limitation $m > -0.0904$.

Acknowledgment

The author wishes to express his appreciation to Dr. G. Poots for many helpful discussions and suggestions.

References

1 Beckett, P. M., and Poots, G., "Laminar Film Condensation in Forced Flows," *Quarterly Journal of Mechanics and Applied Mathematics*, Vol. 25, Part 1, 1972, pp. 125–152.

2 Isa, I., and Chen, C. J., "Steady Two-Dimensional Forced Film Condensation with Pressure Gradients for Fluids of Small Prandtl Numbers," JOURNAL OF HEAT TRANSFER, TRANS. ASME, Series C, Vol. 94, No. 1, Feb. 1972, pp. 99–104.

3 Hartree, D. R., "On an Equation Occurring in Falkner and Skan's Approximate Treatment of the Equations of the Boundary Layer," *Proceedings of the Cambridge Philosophical Society*, Vol. 33, 1937, pp. 223–239.

4 Curle, N., and Davies, H. J., *Modern Fluid Dynamics, Vol. 1, Incompressible Flow*, D. Van Nostrand, London, England, 1968, p. 209.

Laminar Film Condensation on the Inside of Slender, Rotating Truncated Cones

P. J. MARTO[1]

Nomenclature

c_p = specific heat of condensate
$\bar{h}$ = average condensation heat transfer coefficient $q/2\pi\left[\left(R_0 + \frac{L}{2}\sin\phi\right)L(T_{sat} - T_w)\right]$
h_{fg} = latent heat of vaporization
k = thermal conductivity of condensate
L = length of condenser surface
$\dot{m}$ = mass flow rate of condensate
$\overline{\mathrm{Nu}}$ = average Nusselt number, $\bar{h}L/k$
Pr = Prandtl number, $\mu c_p/k$
q = heat transfer rate through condenser surface
R_0 = minimum radius of truncated cone
T_{sat} = saturation temperature of vapor
T_w = condenser wall surface temperature
u = velocity of condensate
x = coordinate direction along condenser surface
y = coordinate direction normal to condenser surface
μ = dynamic viscosity of condensate
ν = kinematic viscosity of condensate
ρ = density of condensate
ω = angular velocity of condenser surface
ϕ = half cone angle of condenser
δ = film thickness of condensate
δ_i = initial film thickness of condensate
δ_{min} = minimum film thickness of condensate

Introduction

THE HEAT TRANSFER capability of rotating, non-capillary heat pipes depends primarily upon the condenser performance of these devices [1].[2] This performance is modeled by laminar film condensation on the inside of rotating truncated cones, shown schematically in Fig. 1.

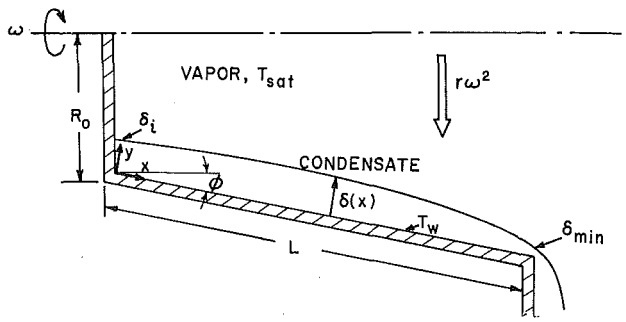

Fig. 1 Coordinate system and geometry for laminar film condensation model showing schematic behavior of condensate film under influence of rotational acceleration

Laminar film condensation has been analyzed for a wide variety of geometrical conditions. Sparrow and Hartnett [2] obtained a numerical solution for condensation on the outside of rotating cones which are not too slender. Their results for the average Nusselt number can be approximated for ordinary fluids by:

$$\overline{\mathrm{Nu}} = 0.904\left(\frac{\omega^2\sin^2\phi L^4}{\nu^2}\,\frac{\mathrm{Pr}}{c_p(T_{sat} - T_w)/h_{fg}}\right)^{1/4} \quad (1)$$

Dhir and Lienhard [3] studied laminar film condensation on axisymmetric bodies in a nonuniform gravity field. Their results, when applied to the case of rotating truncated cones, yield:

$$\overline{\mathrm{Nu}} = 0.904\left(\frac{\omega^2L^2R_0^2}{\nu^2}\,\frac{\mathrm{Pr}}{c_p(T_{sat} - T_w)/h_{fg}}\right)^{1/4} G(\beta) \quad (2)$$

where

$$G(\beta) = \frac{\{(1+\beta)^{8/3} - 1\}^{4/3}}{\sqrt{\beta}\,(2+\beta)} \quad (3)$$

[1] Associate Professor, Department of Mechanical Engineering, Naval Postgraduate School, Monterey, Calif. Assoc. Mem. ASME.

Contributed by the Heat Transfer Division of THE AMERICAN SOCIETY OF MECHANICAL ENGINEERS. Manuscript received by the Heat Transfer Division June 16, 1972.

[2] Numbers in brackets designate References at end of technical brief.

favorable pressure gradients in single-phase flow but become rapidly less accurate when the pressure gradient is large and unfavorable.

When the condensation rate is heavy, $\lambda\chi > 1$, the *thick film approximations* follow from the solution of equation (4.30) in [1]. For this case we then have

$$\left.\begin{aligned} \frac{\delta(x)}{x}\,\mathrm{Re}_x^{1/2} &= 2E\epsilon_p^{-1}(m+1)^{-1/2} \\ Cf_w\mathrm{Re}_x^{1/2} &= Cf_l\mathrm{Re}_x^{1/2} = (m+1)^{1/2}\chi\epsilon_p \\ \mathrm{Nu}\,\mathrm{Re}_x^{-1/2} &= 0.5\epsilon_p(k_s/k_w)(m+1)^{1/2} \end{aligned}\right\} \quad (4)$$

where E and ϵ_p are factors which account for variable condensate properties, see [1]. The comparison between these and the numerical solutions when $\Delta T = 100$ deg C in the case of condensing steam is displayed in Fig. 1.

Assessment of Isa and Chen's results for $\lambda\chi > 1$, that is, $R/B > 1$, is achieved on setting $E = \epsilon_p = 1$ to yield constant condensate properties. Then we have from the thick film approximation that $\eta_\delta = \sqrt{2}/R$, which is readily seen to give their results for heavy condensation, even in the case of an adverse pressure gradient, in Table 1 of [2].

Conclusions

Isa and Chen's constant-property model is applicable to favorable pressure gradients and to adverse pressure gradients provided the condensation rate is heavy.

However, for heavy condensation the variations of thermal conductivity and viscosity are likely to be important factors, and in such cases the thick film formulae (4) should be preferred.

The thin film model is to be recommended for use in the case $\lambda\chi \ll 1$ for negative m, subject to the limitation $m > -0.0904$.

Acknowledgment

The author wishes to express his appreciation to Dr. G. Poots for many helpful discussions and suggestions.

References

1 Beckett, P. M., and Poots, G., "Laminar Film Condensation in Forced Flows," *Quarterly Journal of Mechanics and Applied Mathematics*, Vol. 25, Part 1, 1972, pp. 125–152.

2 Isa, I., and Chen, C. J., "Steady Two-Dimensional Forced Film Condensation with Pressure Gradients for Fluids of Small Prandtl Numbers," JOURNAL OF HEAT TRANSFER, TRANS. ASME, Series C, Vol. 94, No. 1, Feb. 1972, pp. 99–104.

3 Hartree, D. R., "On an Equation Occurring in Falkner and Skan's Approximate Treatment of the Equations of the Boundary Layer," *Proceedings of the Cambridge Philosophical Society*, Vol. 33, 1937, pp. 223–239.

4 Curle, N., and Davies, H. J., *Modern Fluid Dynamics, Vol. 1, Incompressible Flow*, D. Van Nostrand, London, England, 1968, p. 209.

Laminar Film Condensation on the Inside of Slender, Rotating Truncated Cones

P. J. MARTO[1]

Nomenclature

c_p = specific heat of condensate
$\bar{h}$ = average condensation heat transfer coefficient $q/2\pi\left[\left(R_0 + \frac{L}{2}\sin\phi\right)L(T_{sat} - T_w)\right]$
h_{fg} = latent heat of vaporization
k = thermal conductivity of condensate
L = length of condenser surface
$\dot{m}$ = mass flow rate of condensate
$\overline{\mathrm{Nu}}$ = average Nusselt number, $\bar{h}L/k$
Pr = Prandtl number, $\mu c_p/k$
q = heat transfer rate through condenser surface
R_0 = minimum radius of truncated cone
T_{sat} = saturation temperature of vapor
T_w = condenser wall surface temperature
u = velocity of condensate
x = coordinate direction along condenser surface
y = coordinate direction normal to condenser surface
μ = dynamic viscosity of condensate
ν = kinematic viscosity of condensate
ρ = density of condensate
ω = angular velocity of condenser surface
ϕ = half cone angle of condenser
δ = film thickness of condensate
δ_i = initial film thickness of condensate
δ_{min} = minimum film thickness of condensate

Introduction

THE HEAT TRANSFER capability of rotating, non-capillary heat pipes depends primarily upon the condenser performance of these devices [1].[2] This performance is modeled by laminar film condensation on the inside of rotating truncated cones, shown schematically in Fig. 1.

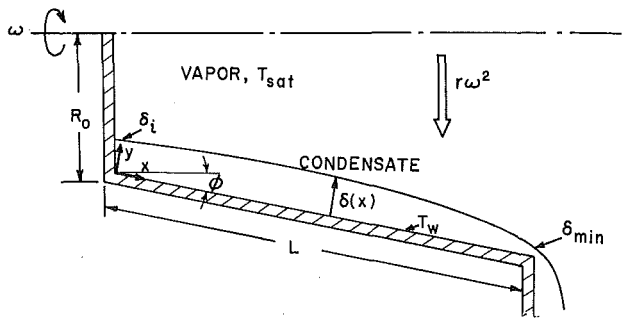

Fig. 1 Coordinate system and geometry for laminar film condensation model showing schematic behavior of condensate film under influence of rotational acceleration

Laminar film condensation has been analyzed for a wide variety of geometrical conditions. Sparrow and Hartnett [2] obtained a numerical solution for condensation on the outside of rotating cones which are not too slender. Their results for the average Nusselt number can be approximated for ordinary fluids by:

$$\overline{\mathrm{Nu}} = 0.904\left(\frac{\omega^2\sin^2\phi L^4}{\nu^2}\,\frac{\mathrm{Pr}}{c_p(T_{sat} - T_w)/h_{fg}}\right)^{1/4} \quad (1)$$

Dhir and Lienhard [3] studied laminar film condensation on axisymmetric bodies in a nonuniform gravity field. Their results, when applied to the case of rotating truncated cones, yield:

$$\overline{\mathrm{Nu}} = 0.904\left(\frac{\omega^2L^2R_0^2}{\nu^2}\,\frac{\mathrm{Pr}}{c_p(T_{sat} - T_w)/h_{fg}}\right)^{1/4} G(\beta) \quad (2)$$

where

$$G(\beta) = \frac{\{(1+\beta)^{8/3} - 1\}^{4/3}}{\sqrt{\beta}\,(2+\beta)} \quad (3)$$

[1] Associate Professor, Department of Mechanical Engineering, Naval Postgraduate School, Monterey, Calif. Assoc. Mem. ASME.

Contributed by the Heat Transfer Division of THE AMERICAN SOCIETY OF MECHANICAL ENGINEERS. Manuscript received by the Heat Transfer Division June 16, 1972.

[2] Numbers in brackets designate References at end of technical brief.

and

$$\beta = \frac{L \sin \phi}{R_0} \tag{4}$$

Equation (2) predicts zero heat transfer as the cone angle ϕ approaches zero (i.e., condensation on the inside of a rotating cylinder). Recently, however, Leppert and Nimmo [4, 5], in studying film condensation on finite horizontal surfaces, have shown that even when the body force is normal to the condensing surface a finite amount of heat transfer can occur if overfall drainage is permitted on the edges. The condensate film thickness and the resulting heat transfer is then governed by hydrostatic pressure changes within the film thickness. Their results can be applied to condensation on the inside of a rotating cylinder ($\phi = 0$) and are approximated by:

$$\overline{\mathrm{Nu}} = 0.82 \left(\frac{\omega^2 L^2 R_0^2}{\nu^2} \frac{\mathrm{Pr}}{c_p (T_{\mathrm{sat}} - T_w)/h_{fg}} \right)^{1/6} \tag{5}$$

The purpose of this work is to establish a solution for film condensation on the inside of slender, rotating truncated cones in the region where the half cone angle ϕ is close to zero and where equation (2) is no longer valid.

Analysis

All the familiar assumptions used in Nusselt's theory of laminar film condensation are assumed valid, including negligible subcooling and momentum changes in the condensate film, no interfacial shear between the condensate and the vapor, and pure conduction within the condensate film. In addition, the centrifugal acceleration is assumed to be much larger than the normal acceleration of earth gravity, the thickness of the film is much less than the radius of the condenser wall, and the vapor space is essentially stagnant. It is further assumed that the truncated end of the condenser is insulated. The above assumptions limit the analysis to ordinary fluids; the results therefore are not valid for liquid metals.

For this case, the condensate film is pictured schematically in Fig. 1. Notice that the condensate has an initial thickness δ_i as well as a minimum thickness $\delta_{\min}$ which occurs at the end of the condenser.

Using a hydrostatic pressure variation within the condensate film (due to centrifugal acceleration), together with the x-direction momentum equation, an expression for the condensate film velocity can be found as:

$$u = \frac{\rho \omega^2}{\mu} \left(\delta y - \frac{y^2}{2} \right) (R_0 + x \sin \phi - \delta \cos \phi) \times \left(\sin \phi - \cos \phi \frac{d\delta}{dx} \right) \tag{6}$$

In the above derivation, surface tension forces due to the curvature of the liquid–vapor interface have been neglected. The analysis is therefore restricted to practical applications where the cone dimensions are not very small.

Continuity requires that

$$\dot{m} = \int_0^\delta \rho u 2\pi (R_0 + x \sin \phi - y \cos \phi) dy$$

or

$$\dot{m} = \frac{2\pi \rho^2 \omega^2}{\mu} \left\{ (R_0 + x \sin \phi - \delta \cos \phi) \left(\sin \phi - \cos \phi \frac{d\delta}{dx} \right) \times \left(\frac{\delta^3}{3} [R_0 + x \sin \phi] - \frac{5}{24} \delta^4 \cos \phi \right) \right\} \tag{7}$$

An energy balance on a differential element of height δ and length dx yields:

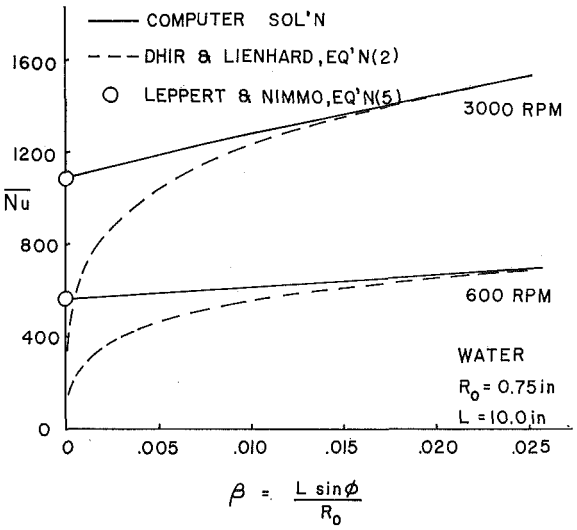

Fig. 2 Results of computer solution for water condensing at 212 deg F

$$\frac{dq}{dx} = 2\pi k (R_0 + x \sin \phi)(T_{\mathrm{sat}} - T_w) = h_{fg} \frac{d\dot{m}}{dx} \tag{8}$$

When equation (7) is substituted into the right side of equation (8), a second-order nonlinear differential equation for the film thickness δ is obtained. The initial conditions are

$$\text{at} \quad x = 0, \qquad \delta = \delta_i \quad \text{and} \quad \frac{d\delta}{dx} = \tan \phi \tag{9}$$

The second condition above is a consequence of the velocity u being zero at $x = 0$, equation (6).

Results and Discussion

A Runge–Kutta numerical integration scheme was used to solve for $\delta(x)$ and q using an IBM 67 digital computer. An initial condensate thickness δ_i was assumed in order to start the integration. The final condensate thickness $\delta_{\min}$ was then compared to a suitably chosen film thickness determined by the overfall condition around the exit corner. As shown by Leppert and Nimmo [6], however, the heat transfer results are insensitive to an exact overfall condition, provided that $\delta_{\min} \leq 0.4\ \delta_i$.

Results for a specific geometry are given in Fig. 2 for water condensing at 212 deg F on a condenser wall maintained at 70 deg F. The computer solution agrees favorably with the Leppert and Nimmo solution, equation (5), when $\beta = 0$ (i.e., $\phi = 0$), and also with the Dhir and Lienhard solution, equation (2), for $\beta > 0.025$. It is interesting to note that equation (2) accurately predicts the average Nusselt number even down to very small half cone angles, which for practical applications are indistinguishable from zero. This is particularly so at higher rpm, when the film thickness profile becomes flatter.

Acknowledgment

This work was supported by NASA Defense Purchase Request W-13,007.

References

1 Marto, P. J., Daley, T. J., and Ballback, L. J., "An Analytical and Experimental Investigation of Rotating, Non-Capillary Heat Pipes," Naval Postgraduate School Report NPS-59Mx70061A, June 1970.

2 Sparrow, E. M., and Hartnett, J. P., "Condensation on a Rotating Cone," JOURNAL OF HEAT TRANSFER, TRANS. ASME, Series C, Vol. 83, No. 1, Feb. 1961, pp. 101–102.

3 Dhir, V., and Lienhard, J., "Laminar Film Condensation on Plane and Axisymmetric Bodies in Nonuniform Gravity," JOURNAL OF HEAT TRANSFER, TRANS. ASME, Series C, Vol. 93, No. 1, Feb. 1971, pp. 97–100.

4 Leppert, G., and Nimmo, B., "Laminar Film Condensation on Surfaces Normal to Body or Inertial Forces," JOURNAL OF HEAT TRANSFER, TRANS. ASME, Series C, Vol. 90, No. 1, Feb. 1968, pp. 178–179.

5 Nimmo, B., and Leppert, G., "Laminar Film Condensation on a Finite Horizontal Surface," *Heat Transfer 1970*, Vol. 6, Elsevier Publishing Co., Amsterdam, 1970.

A Theoretical Analysis of the Recovery Factor for High-Speed Turbulent Flow

L. C. THOMAS[1] **and B. T. F. CHUNG**[2]

Introduction

THE recovery factor R for turbulent high-speed flow is frequently expressed by a relationship of the form [1][3]

$$R \approx \mathrm{Pr}^{1/3} \tag{1}$$

Experimental data for turbulent boundary-layer and tube flow of air generally are in support of this relationship [2–4]. A semi-empirical formulation also has been proposed for the recovery factor by Rotta [5] which is in agreement with equation (1). This formulation is based on the usual eddy-diffusivity approach to turbulence.

In order to provide additional insight into the effects of viscous dissipation, a very simple and straightforward formulation is now presented for the recovery factor on the basis of the surface-renewal-and-penetration model. This model was first set forth by Danckwerts [6] for turbulent mass transfer at a fluid–fluid interface, but has been subsequently adapted to a broad range of turbulent transport processes for fluid–solid interfaces [7–12]. The elementary surface-renewal-and-penetration model is based on the assumption that eddies intermittently move from the turbulent core into the close vicinity of the transport surface. During the residency of elements of fluid at the surface, simple one-dimensional unsteady molecular transfer is assumed to occur.

Analysis

The adaptation of the surface-renewal-and-penetration model to high-speed heat transfer with viscous dissipation involves an energy equation for individual elements of fluid at the surface of the form

$$\rho c_p \left[\frac{\partial T}{\partial \theta} + \frac{1}{2c_p}\frac{\partial u^2}{\partial \theta}\right] = \frac{\partial}{\partial y}\left(k\frac{\partial T}{\partial y}\right) + \frac{\partial}{\partial y}\left(\mu u \frac{\partial u}{\partial y}\right) \tag{2}$$

θ represents the instantaneous contact time. Similarly, the momentum equation can be written as

$$\rho \frac{\partial u}{\partial \theta} = \frac{\partial}{\partial y}\left(\mu \frac{\partial u}{\partial y}\right) \tag{3}$$

The solution of these equations with initial boundary conditions of the form $T\{0, y\} = T_i$, $T\{\theta, \infty\} = T_i$, and $-K\partial T\{\theta, 0\}/\partial y = 0$ provides an expression for the temperature profile T_{aw} for an adiabatic wall condition; the parameter T_i represents the eddy temperature at the instant of renewal.

The solution of these equations for T_{aw} can readily be obtained by the use of the familiar Boltzmann transformation $\eta = y/\sqrt{\nu\theta}$. Accordingly, equations (2) and (3) can be written in terms of η, with the assumption of constant properties, as

$$\psi'' + \frac{\mathrm{Pr}}{2}\eta\psi' + 2\,\mathrm{Pr}\left(\frac{u'}{U_\infty}\right)^2 = 0 \tag{4}$$

with $\psi\{\infty\} = 0$ and $\psi'\{0\} = 0$, where $\psi = 2c_p(T - T_i)/U_\infty^2$ and primes denote derivatives with respect to η. The solution of this system of equations takes the form

$$\psi_{aw} = 2\,\mathrm{Pr}\int_\eta^\infty \left[\exp\left(\frac{-\mathrm{Pr}}{4}\eta^2\right) \times \int_0^\eta \left(\frac{u'}{U_\infty}\right)^2 \exp\left(\frac{\mathrm{Pr}}{4}\eta^2\right) d\eta\right] d\eta \tag{5}$$

Hence the adiabatic wall temperature $T_{aw}(0)$ can be found from equation (5) by setting η in the final integration to zero.

An expression for the instantaneous velocity profile within the wall region can be obtained by the solution of equation (3) with initial and boundary conditions of the form $u\{0, y\} = U_i$, $u\{\theta, \infty\} = U_i$, and $u\{\theta, 0\} = 0$, where U_i represents the eddy velocity at the instant of renewal. The solution takes the form [7, 8]

$$\frac{u}{U_i} = \mathrm{erf}\frac{y}{2\sqrt{\nu\theta}} \tag{6}$$

such that $u'/U_\infty = (U_i/U_\infty)\exp(-\eta^2/4)/\sqrt{\pi}$. The use of this relationship for u' in equation (5) leads to an expression for the adiabatic wall temperature of the form

$$\psi_{aw}(0) = \frac{2\,\mathrm{Pr}}{\pi}\left(\frac{U_i}{U_\infty}\right)^2 \int_0^\infty \left\{\exp\left(-\frac{\mathrm{Pr}\,\eta^2}{4}\right) \times \int_0^\eta \exp\left[-\eta^2\left(\frac{1}{2} - \frac{\mathrm{Pr}}{4}\right)\right] d\eta\right\} d\eta \tag{7}$$

The results of the numerical integration of equation (7) are shown in Fig. 1. These computations are seen to be correlated by an expression of the form

$$\psi_{aw}(0)\left(\frac{U_\infty}{U_i}\right)^2 = \mathrm{Pr}^{0.363} \tag{8}$$

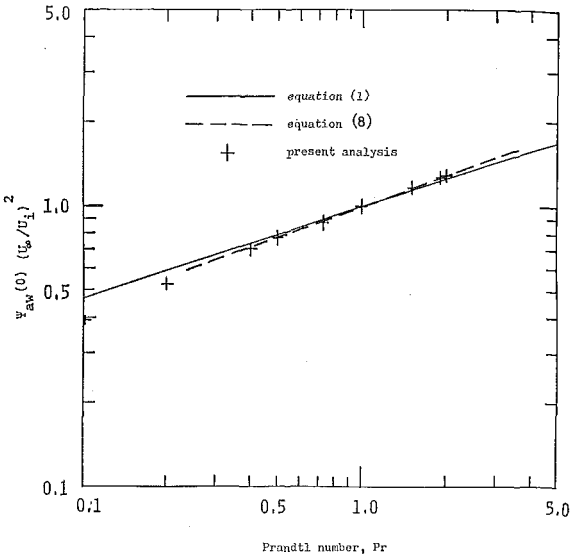

Fig. 1 Computations based on equation (7)

[1] Associate Professor, Mechanical Engineering Department, University of Akron, Akron, Ohio. Mem. ASME.

[2] Assistant Professor, Mechanical Engineering Department, University of Akron, Akron, Ohio. Assoc. Mem. ASME.

[3] Numbers in brackets designate References at end of technical brief.

Contributed by the Heat Transfer Division of THE AMERICAN SOCIETY OF MECHANICAL ENGINEERS. Manuscript received by the Heat Transfer Division May 26, 1972.

4 Leppert, G., and Nimmo, B., "Laminar Film Condensation on Surfaces Normal to Body or Inertial Forces," JOURNAL OF HEAT TRANSFER, TRANS. ASME, Series C, Vol. 90, No. 1, Feb. 1968, pp. 178–179.

5 Nimmo, B., and Leppert, G., "Laminar Film Condensation on a Finite Horizontal Surface," *Heat Transfer 1970*, Vol. 6, Elsevier Publishing Co., Amsterdam, 1970.

A Theoretical Analysis of the Recovery Factor for High-Speed Turbulent Flow

L. C. THOMAS[1] and B. T. F. CHUNG[2]

Introduction

THE recovery factor R for turbulent high-speed flow is frequently expressed by a relationship of the form [1][3]

$$R \approx \mathrm{Pr}^{1/3} \tag{1}$$

Experimental data for turbulent boundary-layer and tube flow of air generally are in support of this relationship [2–4]. A semi-empirical formulation also has been proposed for the recovery factor by Rotta [5] which is in agreement with equation (1). This formulation is based on the usual eddy-diffusivity approach to turbulence.

In order to provide additional insight into the effects of viscous dissipation, a very simple and straightforward formulation is now presented for the recovery factor on the basis of the surface-renewal-and-penetration model. This model was first set forth by Danckwerts [6] for turbulent mass transfer at a fluid–fluid interface, but has been subsequently adapted to a broad range of turbulent transport processes for fluid–solid interfaces [7–12]. The elementary surface-renewal-and-penetration model is based on the assumption that eddies intermittently move from the turbulent core into the close vicinity of the transport surface. During the residency of elements of fluid at the surface, simple one-dimensional unsteady molecular transfer is assumed to occur.

Analysis

The adaptation of the surface-renewal-and-penetration model to high-speed heat transfer with viscous dissipation involves an energy equation for individual elements of fluid at the surface of the form

$$\rho c_p \left[\frac{\partial T}{\partial \theta} + \frac{1}{2c_p}\frac{\partial u^2}{\partial \theta}\right] = \frac{\partial}{\partial y}\left(k\frac{\partial T}{\partial y}\right) + \frac{\partial}{\partial y}\left(\mu u \frac{\partial u}{\partial y}\right) \tag{2}$$

θ represents the instantaneous contact time. Similarly, the momentum equation can be written as

$$\rho \frac{\partial u}{\partial \theta} = \frac{\partial}{\partial y}\left(\mu \frac{\partial u}{\partial y}\right) \tag{3}$$

The solution of these equations with initial boundary conditions of the form $T\{0, y\} = T_i$, $T\{\theta, \infty\} = T_i$, and $-K\partial T\{\theta, 0\}/\partial y = 0$ provides an expression for the temperature profile T_{aw} for an adiabatic wall condition; the parameter T_i represents the eddy temperature at the instant of renewal.

The solution of these equations for T_{aw} can readily be obtained by the use of the familiar Boltzmann transformation $\eta = y/\sqrt{\nu\theta}$. Accordingly, equations (2) and (3) can be written in terms of η, with the assumption of constant properties, as

$$\psi'' + \frac{\mathrm{Pr}}{2}\eta\psi' + 2\,\mathrm{Pr}\left(\frac{u'}{U_\infty}\right)^2 = 0 \tag{4}$$

with $\psi\{\infty\} = 0$ and $\psi'\{0\} = 0$, where $\psi = 2c_p(T - T_i)/U_\infty^2$ and primes denote derivatives with respect to η. The solution of this system of equations takes the form

$$\psi_{aw} = 2\,\mathrm{Pr}\int_\eta^\infty \left[\exp\left(\frac{-\mathrm{Pr}}{4}\eta^2\right) \times \int_0^\eta \left(\frac{u'}{U_\infty}\right)^2 \exp\left(\frac{\mathrm{Pr}}{4}\eta^2\right) d\eta\right] d\eta \tag{5}$$

Hence the adiabatic wall temperature $T_{aw}(0)$ can be found from equation (5) by setting η in the final integration to zero.

An expression for the instantaneous velocity profile within the wall region can be obtained by the solution of equation (3) with initial and boundary conditions of the form $u\{0, y\} = U_i$, $u\{\theta, \infty\} = U_i$, and $u\{\theta, 0\} = 0$, where U_i represents the eddy velocity at the instant of renewal. The solution takes the form [7, 8]

$$\frac{u}{U_i} = \mathrm{erf}\frac{y}{2\sqrt{\nu\theta}} \tag{6}$$

such that $u'/U_\infty = (U_i/U_\infty)\exp(-\eta^2/4)/\sqrt{\pi}$. The use of this relationship for u' in equation (5) leads to an expression for the adiabatic wall temperature of the form

$$\psi_{aw}(0) = \frac{2\,\mathrm{Pr}}{\pi}\left(\frac{U_i}{U_\infty}\right)^2 \int_0^\infty \left\{\exp\left(-\frac{\mathrm{Pr}\,\eta^2}{4}\right) \times \int_0^\eta \exp\left[-\eta^2\left(\frac{1}{2} - \frac{\mathrm{Pr}}{4}\right)\right] d\eta\right\} d\eta \tag{7}$$

The results of the numerical integration of equation (7) are shown in Fig. 1. These computations are seen to be correlated by an expression of the form

$$\psi_{aw}(0)\left(\frac{U_\infty}{U_i}\right)^2 = \mathrm{Pr}^{0.363} \tag{8}$$

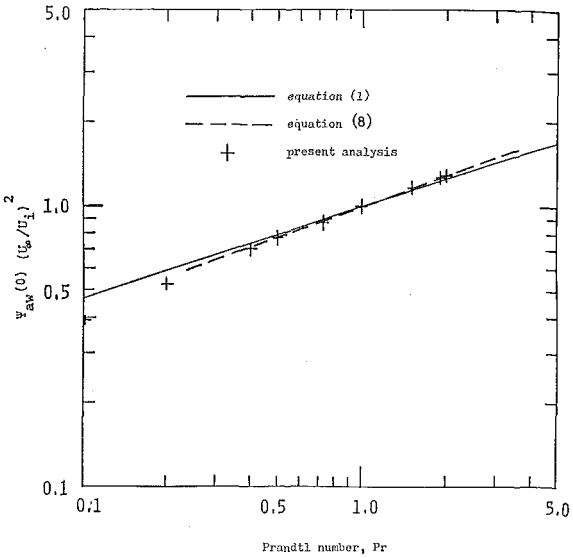

Fig. 1 Computations based on equation (7)

[1] Associate Professor, Mechanical Engineering Department, University of Akron, Akron, Ohio. Mem. ASME.

[2] Assistant Professor, Mechanical Engineering Department, University of Akron, Akron, Ohio. Assoc. Mem. ASME.

[3] Numbers in brackets designate References at end of technical brief.

Contributed by the Heat Transfer Division of THE AMERICAN SOCIETY OF MECHANICAL ENGINEERS. Manuscript received by the Heat Transfer Division May 26, 1972.

Hence, a relationship for the recovery factor can be written on the basis of this analysis as

$$R = \frac{2c_p[T_{aw}(0) - T_\infty]}{U_\infty^2} = \left(\frac{U_i}{U_\infty}\right)^2 \mathrm{Pr}^{0.363} - 2c_p \frac{(T_\infty - T_i)}{U_\infty^2} \quad (9)$$

Discussion

This analysis provides an expression for the recovery factor for turbulent flow in terms of the parameters T_i and U_i. For fluids other than liquid metals, T_i can be approximated well by T_∞; U_i can be reasonably set equal to U_∞ [11]. With these substitutions, equation (9) becomes

$$R = \mathrm{Pr}^{0.363} \quad (10)$$

This expression is seen to be in excellent agreement with equation (1).

It should be noted that the present analysis is restricted to fluids with moderate values of the Prandtl number ($0.5 < \mathrm{Pr} < 5.0$) as well as to the case of uniform properties. For high-Prandtl-number fluids the thermal resistance associated with unreplenished fluid at the surface becomes important [12], whereas the molecular transport to eddies moving toward the wall significantly affects T_i for low-Prandtl-number fluids [10]. In regard to the assumption of uniform properties, Kays [1] has reported that the effect of temperature variation of properties on R for laminar boundary-layer flow is negligible. Further, Deissler [13] found that the effect of radial variation of properties on the turbulent fully developed velocity–temperature profiles and recovery factors for subsonic adiabatic flow is negligible. The agreement of the present predictions with the empirical formulation given by equation (1) indicates that the assumption of uniform properties is reasonable.

Acknowledgment

This investigation was partially supported by the National Science Foundation under grant GK 18815.

References

1 Kays, W. M., *Convection Heat Transfer*, McGraw-Hill, New York, N. Y., 1966.

2 Deissler, R. G., Weiland, W. F., and Lowdermilk, W. H., "Analytical and Experimental Investigation of Temperature Recovery Factors for Fully Developed Flow of Air in a Tube," NACA TN 4376, 1958.

3 Schlichting, H., *Boundary Layer Theory*, McGraw-Hill, New York, N. Y., 1968.

4 Shapiro, A. H., *The Dynamics and Thermodynamics of Compressible Fluid Flow*, Vol. II, Ronald Press, New York, N. Y., 1954.

5 Rotta, J. C., "Temperaturverteilungen in der Turbulenten Grenzschicht an der Ebenen Platte," *International Journal of Heat and Mass Transfer*, Vol. 7, 1964, p. 215.

6 Danckwerts, P. V., "Significance of Liquid Film Coefficient in Gas Absorption," *Industrial and Engineering Chemistry*, Vol. 43, 1951, p. 1460.

7 Einstein, H. A., and Li, H., "The Viscous Sublayer along a Smooth Boundary," *Proceedings ASCE, J. Eng. Mech. Div.*, Vol. 82, No. 1, 1956.

8 Hanratty, T. J., "Turbulent Exchange of Mass and Momentum with a Boundary," *AIChE Journal*, Vol. 2, 1956, p. 359.

9 Thomas, L. C., "Temperature Profiles for Liquid Metals and Moderate-Prandtl-Number Fluids," JOURNAL OF HEAT TRANSFER, TRANS. ASME, Series C, Vol. 92, No. 3, Aug. 1970, pp. 565–567.

10 Thomas, L. C., "A Turbulent Transport Model with Emphasis on Heat Transfer to Liquid Metals," *Canadian Journal of Chemical Engineering*, Vol. 49, 1971, p. 326.

11 Thomas, L. C., "Heat and Momentum Transfer Analogy for Incompressible Turbulent Boundary Layer Flow," *International Journal of Heat and Mass Transfer*, Vol. 14, 1971, p. 715.

12 Thomas, L. C., Chung, B. T. F., and Mahaldar, S. K., "Temperature Profiles for Turbulent Flow of High Prandtl Number Fluids," *International Journal of Heat and Mass Transfer*, Vol. 14, 1971, p. 1465.

13 Deissler, R. G., "Analytical and Experimental Investigation of Adiabatic Turbulent Flow in Smooth Tubes," NACA TN 2138, 1950.

Local Heat Transfer around a Cylinder at Low Reynolds Number

K. M. KRALL[1] and E. R. G. ECKERT[2]

THE present brief reports results of a study to measure local heat transfer around a circular cylinder at low Reynolds numbers in transverse flow of air at a low Mach number (approximately 0.2). The experiments were carried out in a low-density-flow channel specifically designed for this investigation, Fig. 1. The channel is an open system drawing air from the laboratory room. A 20 percent open porous plate and two fine-mesh screens reduced the turbulence and made the flow uniform and equalized the flow in the test chamber. The air was then accelerated in a nozzle with square cross section (3 × 3 cm) especially designed to minimize boundary-layer growth. The resulting velocity distribution in the test section was probed for cylinder Reynolds numbers between 10 and 4610. At the lowest Reynolds number the boundary layers were found to increase the core velocity by 10 percent. With increasing Reynolds number the boundary layer became rapidly thinner. The test cylinder which spanned the test section had a diameter of 4.73 mm ($^3/_{16}$ in). It was manufactured from 302 stainless-steel shimstock 0.0254 mm (0.001 in.) thick. A uniform heat flux from the cylinder wall to the air stream was approximated by Ohmic heating. The shimstock was electrically tested and the local resistivity was

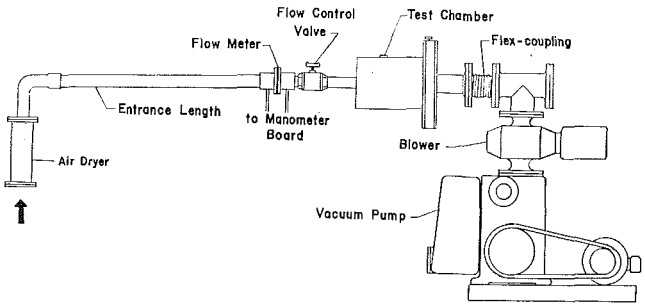

Fig. 1 Sketch of experimental facility

found uniform within 1 percent. Two bus bars were soldered to each end of the cylinder and electrical power leads were attached to them. A single thermocouple of 0.0254-mm iron–constantan wires was attached to the inside wall such that it was electrically insulated from the cylinder wall. The local temperature was measured by rotating the test cylinder around its axis. Thermocouples affixed to the bus bars were used to estimate axial heat-conduction losses. A more extensive discussion of the test setup and the test cylinder is contained in [1].[3]

A local Nusselt number Nu was evaluated from the equation

$$\mathrm{Nu} = \frac{qd}{k_\infty (t_w - t_r)} \quad (1)$$

in which d denotes the cylinder diameter, k_∞ the free-stream conductivity, q the heat flux per unit area, t_w the local wall surface temperature, and t_r the free-stream recovery temperature.

[1] Research Scientist, Advanced Technology Center, Inc., Dallas, Texas. Assoc. Mem. ASME.

[2] Regents Professor, Department of Mechanical Engineering, University of Minnesota, Minneapolis, Minn. Fellow ASME.

Contributed by the Heat Transfer Division of THE AMERICAN SOCIETY OF MECHANICAL ENGINEERS. Manuscript received by the Heat Transfer Division July 3, 1972.

[3] Numbers in brackets designate References at end of technical brief.

Hence, a relationship for the recovery factor can be written on the basis of this analysis as

$$R = \frac{2c_p[T_{aw}(0) - T_\infty]}{U_\infty^2} = \left(\frac{U_i}{U_\infty}\right)^2 \mathrm{Pr}^{0.363} - 2c_p \frac{(T_\infty - T_i)}{U_\infty^2} \quad (9)$$

Discussion

This analysis provides an expression for the recovery factor for turbulent flow in terms of the parameters T_i and U_i. For fluids other than liquid metals, T_i can be approximated well by T_∞; U_i can be reasonably set equal to U_∞ [11]. With these substitutions, equation (9) becomes

$$R = \mathrm{Pr}^{0.363} \quad (10)$$

This expression is seen to be in excellent agreement with equation (1).

It should be noted that the present analysis is restricted to fluids with moderate values of the Prandtl number ($0.5 < \mathrm{Pr} < 5.0$) as well as to the case of uniform properties. For high-Prandtl-number fluids the thermal resistance associated with unreplenished fluid at the surface becomes important [12], whereas the molecular transport to eddies moving toward the wall significantly affects T_i for low-Prandtl-number fluids [10]. In regard to the assumption of uniform properties, Kays [1] has reported that the effect of temperature variation of properties on R for laminar boundary-layer flow is negligible. Further, Deissler [13] found that the effect of radial variation of properties on the turbulent fully developed velocity–temperature profiles and recovery factors for subsonic adiabatic flow is negligible. The agreement of the present predictions with the empirical formulation given by equation (1) indicates that the assumption of uniform properties is reasonable.

Acknowledgment

This investigation was partially supported by the National Science Foundation under grant GK 18815.

References

1 Kays, W. M., *Convection Heat Transfer*, McGraw-Hill, New York, N. Y., 1966.

2 Deissler, R. G., Weiland, W. F., and Lowdermilk, W. H., "Analytical and Experimental Investigation of Temperature Recovery Factors for Fully Developed Flow of Air in a Tube," NACA TN 4376, 1958.

3 Schlichting, H., *Boundary Layer Theory*, McGraw-Hill, New York, N. Y., 1968.

4 Shapiro, A. H., *The Dynamics and Thermodynamics of Compressible Fluid Flow*, Vol. II, Ronald Press, New York, N. Y., 1954.

5 Rotta, J. C., "Temperaturverteilungen in der Turbulenten Grenzschicht an der Ebenen Platte," *International Journal of Heat and Mass Transfer*, Vol. 7, 1964, p. 215.

6 Danckwerts, P. V., "Significance of Liquid Film Coefficient in Gas Absorption," *Industrial and Engineering Chemistry*, Vol. 43, 1951, p. 1460.

7 Einstein, H. A., and Li, H., "The Viscous Sublayer along a Smooth Boundary," *Proceedings ASCE, J. Eng. Mech. Div.*, Vol. 82, No. 1, 1956.

8 Hanratty, T. J., "Turbulent Exchange of Mass and Momentum with a Boundary," *AIChE Journal*, Vol. 2, 1956, p. 359.

9 Thomas, L. C., "Temperature Profiles for Liquid Metals and Moderate-Prandtl-Number Fluids," JOURNAL OF HEAT TRANSFER, TRANS. ASME, Series C, Vol. 92, No. 3, Aug. 1970, pp. 565–567.

10 Thomas, L. C., "A Turbulent Transport Model with Emphasis on Heat Transfer to Liquid Metals," *Canadian Journal of Chemical Engineering*, Vol. 49, 1971, p. 326.

11 Thomas, L. C., "Heat and Momentum Transfer Analogy for Incompressible Turbulent Boundary Layer Flow," *International Journal of Heat and Mass Transfer*, Vol. 14, 1971, p. 715.

12 Thomas, L. C., Chung, B. T. F., and Mahaldar, S. K., "Temperature Profiles for Turbulent Flow of High Prandtl Number Fluids," *International Journal of Heat and Mass Transfer*, Vol. 14, 1971, p. 1465.

13 Deissler, R. G., "Analytical and Experimental Investigation of Adiabatic Turbulent Flow in Smooth Tubes," NACA TN 2138, 1950.

Local Heat Transfer around a Cylinder at Low Reynolds Number

K. M. KRALL[1] **and E. R. G. ECKERT**[2]

THE present brief reports results of a study to measure local heat transfer around a circular cylinder at low Reynolds numbers in transverse flow of air at a low Mach number (approximately 0.2). The experiments were carried out in a low-density-flow channel specifically designed for this investigation, Fig. 1. The channel is an open system drawing air from the laboratory room. A 20 percent open porous plate and two fine-mesh screens reduced the turbulence and made the flow uniform and equalized the flow in the test chamber. The air was then accelerated in a nozzle with square cross section (3 × 3 cm) especially designed to minimize boundary-layer growth. The resulting velocity distribution in the test section was probed for cylinder Reynolds numbers between 10 and 4610. At the lowest Reynolds number the boundary layers were found to increase the core velocity by 10 percent. With increasing Reynolds number the boundary layer became rapidly thinner. The test cylinder which spanned the test section had a diameter of 4.73 mm ($^3/_{16}$ in). It was manufactured from 302 stainless-steel shimstock 0.0254 mm (0.001 in.) thick. A uniform heat flux from the cylinder wall to the air stream was approximated by Ohmic heating. The shimstock was electrically tested and the local resistivity was

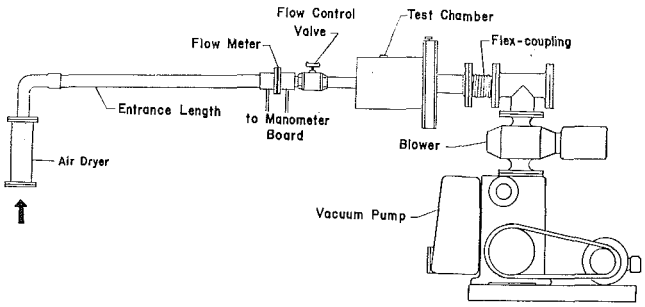

Fig. 1 Sketch of experimental facility

found uniform within 1 percent. Two bus bars were soldered to each end of the cylinder and electrical power leads were attached to them. A single thermocouple of 0.0254-mm iron–constantan wires was attached to the inside wall such that it was electrically insulated from the cylinder wall. The local temperature was measured by rotating the test cylinder around its axis. Thermocouples affixed to the bus bars were used to estimate axial heat-conduction losses. A more extensive discussion of the test setup and the test cylinder is contained in [1].[3]

A local Nusselt number Nu was evaluated from the equation

$$\mathrm{Nu} = \frac{qd}{k_\infty (t_w - t_r)} \quad (1)$$

in which d denotes the cylinder diameter, k_∞ the free-stream conductivity, q the heat flux per unit area, t_w the local wall surface temperature, and t_r the free-stream recovery temperature.

[1] Research Scientist, Advanced Technology Center, Inc., Dallas, Texas. Assoc. Mem. ASME.

[2] Regents Professor, Department of Mechanical Engineering, University of Minnesota, Minneapolis, Minn. Fellow ASME.

Contributed by the Heat Transfer Division of THE AMERICAN SOCIETY OF MECHANICAL ENGINEERS. Manuscript received by the Heat Transfer Division July 3, 1972.

[3] Numbers in brackets designate References at end of technical brief.

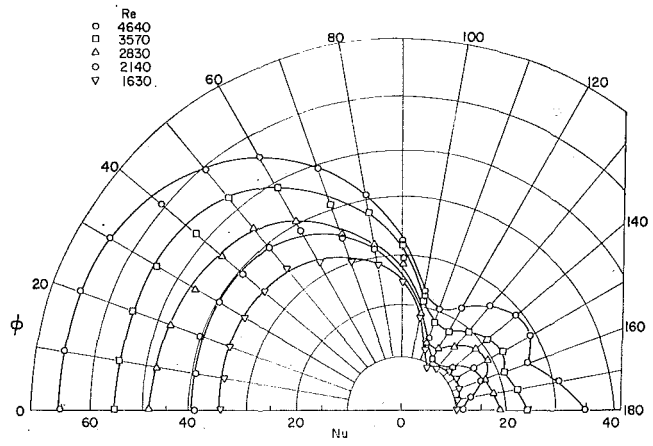

Fig. 2 Local Nusselt numbers around the circumference of a cylinder heated to uniform heat flux in cross flow of air

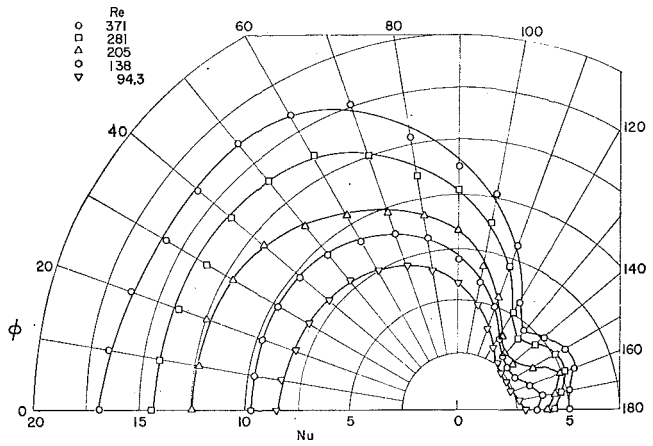

Fig. 3 Local Nusselt numbers around the circumference of a cylinder heated to uniform heat flux in cross flow of air

A Reynolds number Re is defined as

$$\mathrm{Re} = \frac{\rho U d}{\mu_\infty} \tag{2}$$

with μ_∞ denoting the free-stream viscosity. The mass flow rate ρU was obtained from the measurements with the flow meter, and the test-section area and was corrected for the boundary-layer effects. An error analysis of the measured and derived quantities is contained in [1].

Measured local Nusselt numbers defined by equation (1) are plotted in Figs. 2–4 against angular position measured from the forward stagnation line. The distribution of the Nusselt numbers varies with Reynolds number, reflecting the change of the flow around the cylinder from viscous attached flow, to separation with two symmetrical vortices attached to the downstream side of the cylinder, to the development of a vortex street.

The only known data on local heat transfer to an air stream at low Mach number are reported in [2], while [3] is also concerned with local heat transfer but in a supersonic rarefied gas stream. Computed values of local Nusselt number to air at low Reynolds numbers have been reported in [4]. Whereas [2] is concerned with a cylinder of uniform wall temperature, the analysis in [4] considers as boundary conditions uniform heat flux as well as uniform wall temperature. A comparison of these data is presented in [1]. Agreement of corresponding local Nusselt numbers is fair, probably due to the difficulty of performing local measurements at these low Reynolds numbers. It is, however, demonstrated that the Nusselt-number distributions on the upstream half of the cylinder are fuller for uniform heat flux than for uniform wall temperature.

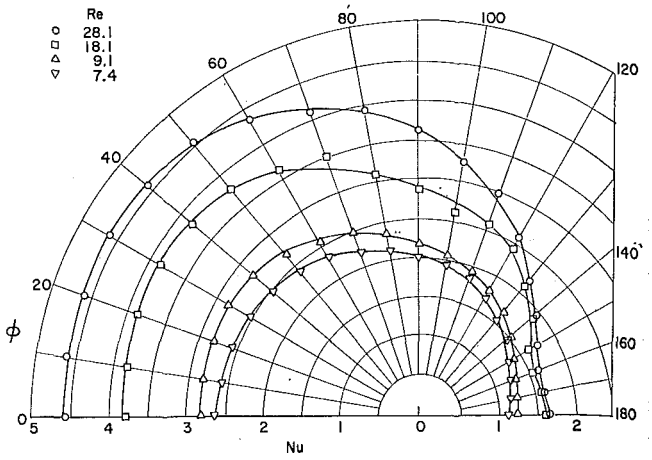

Fig. 4 Local Nusselt numbers around the circumference of a cylinder heated to uniform heat flux in cross flow of air

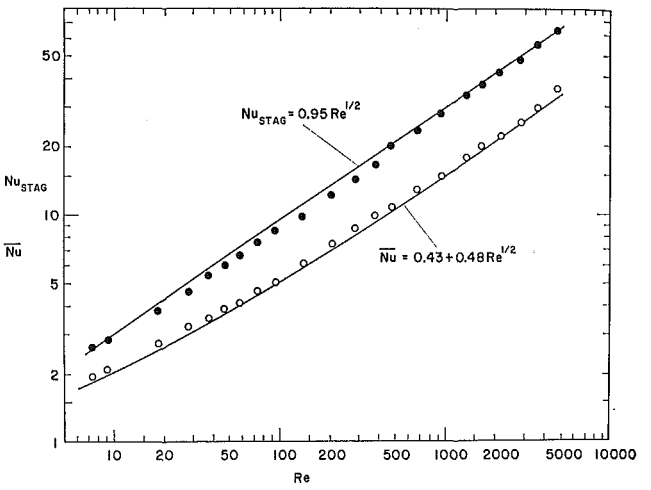

Fig. 5 Stagnation-line Nusselt numbers Nu_{stag} and average Nusselt numbers $\overline{Nu}$ as function of Reynolds number for uniformly heated cylinder in cross flow of air

Nusselt numbers $\overline{Nu}$ averaged over the cylinder surface were also computed from the data with the equation

$$\overline{\mathrm{Nu}} = \frac{qd}{k_\infty (t_w - t_r)} \tag{3}$$

They are plotted in Fig. 5 as open symbols and compared with the equation $\overline{Nu} = 0.43 + 0.48\ \mathrm{Re}^{1/2}$ which holds for isothermal cylinders according to [5]. The measured Nusselt numbers are an average of 7 percent higher, which is probably due to the uniform-heat-flux condition. Local Nusselt numbers measured at the stagnation line of the cylinder are also inserted in Fig. 5 as full symbols and compared with the relation $\mathrm{Nu} = 0.95\ \mathrm{Re}^{1/2}$ [6]. It can be observed that the agreement is very good, especially at the larger Reynolds numbers.

References

1 Krall, J. M., "Local Heat Transfer around a Transverse Circular Cylinder in Slip Flow," PhD thesis, University of Minnesota, Minneapolis, Minn., 1969.

2 Eckert, E. R. G., and Soehngen, E., "Distribution of Heat-Transfer Coefficients Around Circular Cylinders in Crossflow at Reynolds Numbers From 20 to 500," TRANS. ASME, Vol. 74, 1952, pp. 343–347.

3 Tewkif, O. K., and Giedt, W. H., "Heat Transfer, Recovery Factor, and Pressure Distribution around a Circular Cylinder Normal to Supersonic Rarefied Gas Stream," *J. Aerospace Sc.*, Vol. 27, 1960, p. 721.

4 Krall, K. M., and Eckert, E. R. G., "Heat Transfer to a Transverse Circular Cylinder at Low Reynolds Number Including Rarefac-

tion Effects," *Heat Transfer 1970*, U. Grigull and E. Hahne, eds., Vol. III, Elsevier, Amsterdam, The Netherlands, 1970.
5 Eckert, E. R. G., and Drake, R. M., Jr., *Heat and Mass Transfer*, McGraw-Hill, New York, N. Y., 1959, p. 242.
6 Eckert, E. R. G., "Die Berechnung des Wärmeübergangs in der laminaren Grenzschicht umströmter Körper," *VDI*, 1942, p. 416.

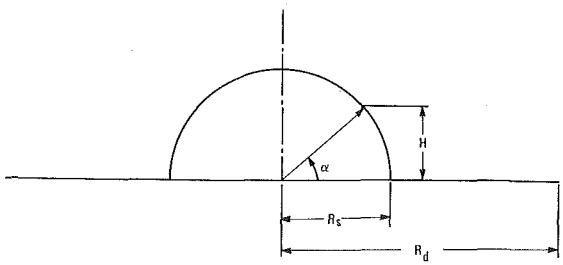

Fig. 1 Generating geometry (side view)

Radiation Configuration Factors for Annular Rings and Hemispherical Sectors

J. O. BALLANCE and J. DONOVAN[1]

Nomenclature

R_s = radius of sphere
R_d = outer radius of annular ring
α = angle determined by section height
H = height of hemispherical section
F_{ng} = radiation configuration factor for surface n with respect to surface g
A_i = area of surface i

Introduction

In the application of Monte Carlo computer techniques to the study of problems in the free molecular flow regime, the analogy between radiation heat transfer with diffuse emissions and the free molecular flow field allows one to use the radiation configuration factors as a test on the operation of the Monte Carlo program. For a recent study we were examining a source plane which was an annular ring of arbitrary radius around a sphere with the center of the disc coincident with the center of the sphere. A search of the literature did not provide the radiation configuration factor for this geometry, which would have helped in determining the correctness of the programming of the problem. Since other indicators seemed to verify the correct operation of the program, the program was used to calculate the radiation configuration factors.

The purpose of this note is to add to the literature the radiation configuration factors for annular rings with respect to a sphere.

Approach

The Monte Carlo techniques used to determine radiation configuration factors are simple and have been described adequately in the literature. For convenience, only one side of the ring was considered to emit and only the hemisphere associated with that side of the ring was tested. The configuration factors for both sides of the ring with respect to the total spherical surface (or sectors) are identical for those given for the one side. Each point presented was obtained by using a sample size of 10,000 paths (except for the case $H/R_s = 1.0$, where the sample size was 60,000). Radius ratios (outer radius of ring/radius of sphere) up to five were considered. (The inner radius of the ring is identical to the radius of the sphere.)

The hemispherical sectors considered are designated by the height H above the ring, Fig. 1. Of course, for each radius R_d there is some height H above which no portion of the ring surface can "see" the sphere. The location of this height H for the ring radius R_d is shown in Fig. 2.

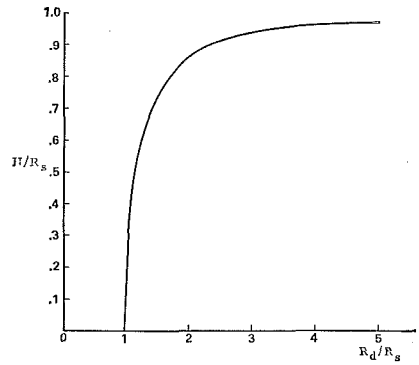

Fig. 2 Maximum sector height for annulus-to-hemisphere interaction

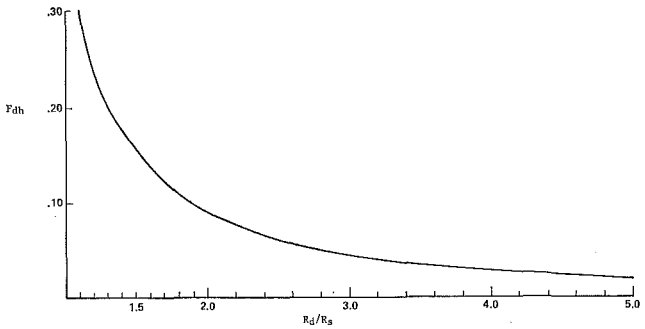

Fig. 3 Configuration factors from annulus to hemisphere for various radius ratios

Results

In Table 1 the radiation configuration factors are given for six different hemispherical sectors where the angle α is measured as indicated in Fig. 1. For the case of $\alpha = 90$ deg, these data are shown graphically in Fig. 3. The value of the configuration factor for $R_d/R_s = 1.0$ is 0.5, which was not determined by the Monte Carlo program but by simple deductive arguments. It is evident from the table that for radius ratios up to 2.0 the major contribution to the value of the configuration factors is the area of the spherical sector with $H = 0.259\ R_s$. Using Table 1 and Fig. 2, one could construct configuration factors for areas of spherical sectors with bases H_i and H_j (i.e., between $H_i = 0.259\ R_s$ and $H_j = 0.500\ R_s$) with respect to the ring. While the general trend of such exercises seems to be correct, the scatter in the data for these small sample sizes does not support that type of analysis. It is believed that with the sample size of 60,000 paths from the ring to the hemisphere the data are accurate to about ± 2 percent. For the sample sizes of 10,000 paths, the data are accurate only to about ± 5 percent. For example, in Table 1, for $R_d/R_s = 1.5$ and $H/R_s = 0.707$ and greater, the configuration factors vary from 0.150 to 0.169, although the geometry of the system would indicate that these four factors should be the same. This much scatter in a Monte Carlo analysis is typical for this application and small sample sizes. Increasing the same size to 100,000 paths should increase the accuracy of the data to near ±

[1] Space Physics Group, Marshall Space Flight Center, Huntsville, Ala.

Contributed by the Heat Transfer Division of The American Society of Mechanical Engineers. Manuscript received by the Heat Transfer Division October 24, 1972.

tion Effects," *Heat Transfer 1970*, U. Grigull and E. Hahne, eds., Vol. III, Elsevier, Amsterdam, The Netherlands, 1970.
5 Eckert, E. R. G., and Drake, R. M., Jr., *Heat and Mass Transfer*, McGraw-Hill, New York, N. Y., 1959, p. 242.
6 Eckert, E. R. G., "Die Berechnung des Wärmeübergangs in der laminaren Grenzschicht umströmter Körper," *VDI*, 1942, p. 416.

Radiation Configuration Factors for Annular Rings and Hemispherical Sectors

J. O. BALLANCE and J. DONOVAN[1]

Nomenclature

R_s = radius of sphere
R_d = outer radius of annular ring
α = angle determined by section height
H = height of hemispherical section
F_{ng} = radiation configuration factor for surface n with respect to surface g
A_i = area of surface i

Introduction

In the application of Monte Carlo computer techniques to the study of problems in the free molecular flow regime, the analogy between radiation heat transfer with diffuse emissions and the free molecular flow field allows one to use the radiation configuration factors as a test on the operation of the Monte Carlo program. For a recent study we were examining a source plane which was an annular ring of arbitrary radius around a sphere with the center of the disc coincident with the center of the sphere. A search of the literature did not provide the radiation configuration factor for this geometry, which would have helped in determining the correctness of the programming of the problem. Since other indicators seemed to verify the correct operation of the program, the program was used to calculate the radiation configuration factors.

The purpose of this note is to add to the literature the radiation configuration factors for annular rings with respect to a sphere.

Approach

The Monte Carlo techniques used to determine radiation configuration factors are simple and have been described adequately in the literature. For convenience, only one side of the ring was considered to emit and only the hemisphere associated with that side of the ring was tested. The configuration factors for both sides of the ring with respect to the total spherical surface (or sectors) are identical for those given for the one side. Each point presented was obtained by using a sample size of 10,000 paths (except for the case $H/R_s = 1.0$, where the sample size was 60,000). Radius ratios (outer radius of ring/radius of sphere) up to five were considered. (The inner radius of the ring is identical to the radius of the sphere.)

The hemispherical sectors considered are designated by the height H above the ring, Fig. 1. Of course, for each radius R_d there is some height H above which no portion of the ring surface can "see" the sphere. The location of this height H for the ring radius R_d is shown in Fig. 2.

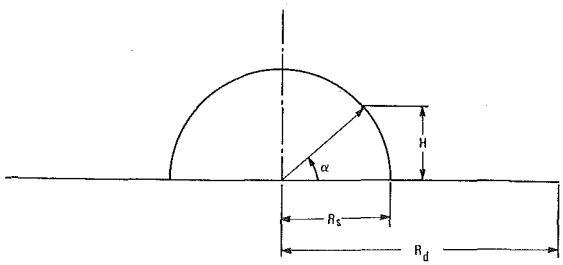

Fig. 1 Generating geometry (side view)

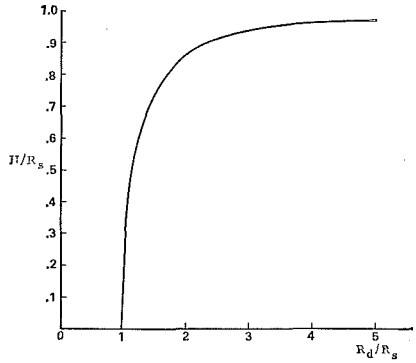

Fig. 2 Maximum sector height for annulus-to-hemisphere interaction

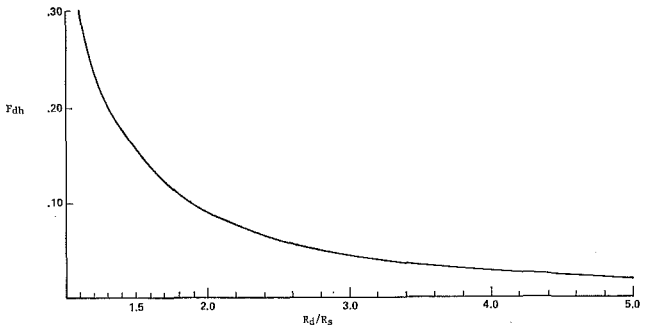

Fig. 3 Configuration factors from annulus to hemisphere for various radius ratios

Results

In Table 1 the radiation configuration factors are given for six different hemispherical sectors where the angle α is measured as indicated in Fig. 1. For the case of $\alpha = 90$ deg, these data are shown graphically in Fig. 3. The value of the configuration factor for $R_d/R_s = 1.0$ is 0.5, which was not determined by the Monte Carlo program but by simple deductive arguments. It is evident from the table that for radius ratios up to 2.0 the major contribution to the value of the configuration factors is the area of the spherical sector with $H = 0.259\ R_s$. Using Table 1 and Fig. 2, one could construct configuration factors for areas of spherical sectors with bases H_i and H_j (i.e., between $H_i = 0.259\ R_s$ and $H_j = 0.500\ R_s$) with respect to the ring. While the general trend of such exercises seems to be correct, the scatter in the data for these small sample sizes does not support that type of analysis. It is believed that with the sample size of 60,000 paths from the ring to the hemisphere the data are accurate to about ± 2 percent. For the sample sizes of 10,000 paths, the data are accurate only to about ± 5 percent. For example, in Table 1, for $R_d/R_s = 1.5$ and $H/R_s = 0.707$ and greater, the configuration factors vary from 0.150 to 0.169, although the geometry of the system would indicate that these four factors should be the same. This much scatter in a Monte Carlo analysis is typical for this application and small sample sizes. Increasing the same size to 100,000 paths should increase the accuracy of the data to near ±

[1] Space Physics Group, Marshall Space Flight Center, Huntsville, Ala.

Contributed by the Heat Transfer Division of The American Society of Mechanical Engineers. Manuscript received by the Heat Transfer Division October 24, 1972.

Table 1 Radiation configuration factors for annular rings to a hemispherical section of height H

	H/R_s					
R_d/R_s	.259 (α = 15°)	.500 (α = 30°)	.707 (α = 45°)	.866 (α = 60°)	.966 (α = 75°)	1.0 (α = 90°)
1.1	.293	.301	.307	.296	.302	.300
1.2	.227	.242	.246	.249	.245	.245
1.3	.184	.206	.208	.203	.207	.209
1.4	.149	.178	.182	.180	.188	.182
1.5	.129	.157	.169	.150	.156	.160
1.6	.109	.144	.141	.143	.142	.143
1.7	.091	.117	.127	.125	.131	.126
1.8	.079	.109	.115	.110	.108	.112
1.9	.071	.096	.103	.106	.102	.103
2.0	.061	.090	.094	.089	.094	.093
2.2	.046	.070	.077	.076	.076	.076
2.4	.040	.061	.065	.068	.065	.066
2.6	.036	.052	.058	.059	.060	.059
2.8	.030	.043	.047	.051	.052	.049
3.0	.027	.040	.041	.046	.045	.045
3.2	.022	.033	.040	.038	.039	.039
3.4	.019	.031	.034	.035	.037	.035
3.6	.018	.030	.025	.033	.032	.032
3.8	.015	.021	.023	.030	.028	.027
4.0	.014	.023	.028	.026	.026	.027
4.2	.011	.020	.022	.024	.023	.024
4.4	.013	.018	.022	.022	.023	.022
4.6	.012	.017	.020	.020	.025	.022
4.8	.009	.015	.020	.020	.018	.019
5.0	.008	.013	.016	.016	.018	.017

1 percent. Computer time availability did not permit the larger sample sizes.

This note adds a new geometry to the general literature on radiation configuration factors. The limitations on the use of the data and the accuracy of the calculations have been explained.

The Radial Radiative Heat Flux in a Cylinder

D. K. EDWARDS[1] and A. T. WASSEL[2]

Nomenclature

B_ν = black-body spectral intensity
c = velocity of light
D_n = cylindrical exponential integral
h = Planck constant
I_ν = spectral intensity
k = Boltzmann constant
k_ν = spectral absorption coefficient
q_ν = spectral radial radiant heat flux
r, r', r'' = local radius
R = tube radius
T = absolute temperature
x = independent variable
α = variable of integration; angle from radial direction to the true line of sight measured in a plane parallel to the tube axis, see [2]
$\gamma, \gamma', \gamma''$ = angle in the cross-sectional plane from the radial direction to the projected line of sight, see Fig. 1
ν = wavenumber, reciprocal wavelength

[1] Professor of Engineering, Department of Energy and Kinetics, School of Engineering, University of California, Los Angeles, Calif. Mem. ASME.

[2] Department of Energy and Kinetics, School of Engineering, University of California, Los Angeles, Calif.

Contributed by the Heat Transfer Division of THE AMERICAN SOCIETY OF MECHANICAL ENGINEERS. Manuscript received by the Heat Transfer Division November 30, 1972.

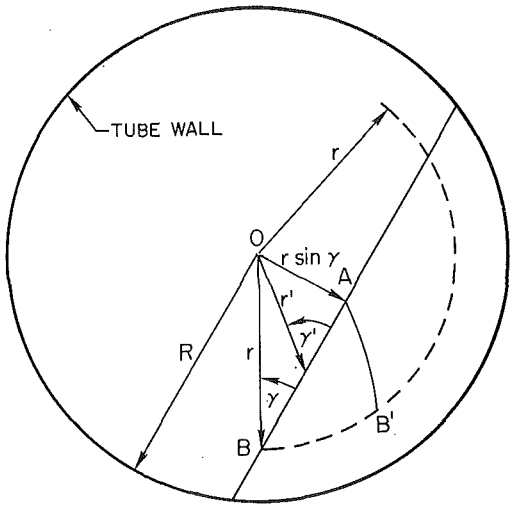

Fig. 1

IN INVESTIGATING radiative transfer in a nongray cylindrical medium, it has been found that some authors [1, 2][3] have approximated the local radial heat flux without discussing the nature of the approximation used. It is the purpose of this note to do so and to show quantitatively the magnitude of error which results for an optically thin isothermal gas.

Consider a cylindrical gas volume of radius R with temperature distribution $T(r')$ in local thermodynamic equilibrium so that the local black-body source intensity is

$$B_\nu(r') = \frac{2hc^2\nu^3}{e^{hc\nu/kT(r')} - 1} \tag{1}$$

The net radial radiative flux at radius r can be written in the following form:

$$\begin{aligned} q_\nu(r) = 4 \int_{\gamma=0}^{\pi/2} \cos\gamma \Bigg\{ I_\nu(R) \Bigg[D_3 \Bigg(\Bigg\{ \int_{r\sin\gamma}^{R} + \int_{r\sin\gamma}^{r} \Bigg\} \left\{ \frac{k_\nu dr'}{\cos\gamma'} \right\} \Bigg) - D_3 \left(\int_r^R \frac{k_\nu dr'}{\cos\gamma'} \right) \Bigg] \\ - \int_r^R D_2 \left(\int_r^{r'} \frac{k_\nu dr''}{\cos\gamma''} \right) \frac{B_\nu k_\nu dr'}{\cos\gamma'} \\ + \int_{r\sin\gamma}^{R} D_2 \left(\Bigg\{ \int_{r\sin\gamma}^{r} + \int_{r\sin\gamma}^{r'} \Bigg\} \left\{ \frac{k_\nu dr''}{\cos\gamma''} \right\} \right) \frac{B_\nu k_\nu dr'}{\cos\gamma'} \\ + \int_{r\sin\gamma}^{r} D_2 \left(\int_{r'}^{r} \frac{k_\nu dr''}{\cos\gamma''} \right) \frac{B_\nu k_\nu dr'}{\cos\gamma'} \Bigg\} d\gamma \end{aligned} \tag{2}$$

where

$$\cos\gamma' = [1 - (r/r')^2 \sin^2\gamma]^{1/2} \tag{3a}$$

$$\cos\gamma'' = [1 - (r/r'')^2 \sin^2\gamma]^{1/2} \tag{3b}$$

$$D_n(x) = \int_0^{\pi/2} \cos^{n-1}\alpha \exp(-x/\cos\alpha) d\alpha \tag{4}$$

Equation (27) of [2] and equation (1) of [1] both omit the primes on γ' and γ'' and show the $\cos\gamma'$ and $\cos\gamma''$ terms as factorable from within the integrals. Thus those equations can be regarded as only approximations.

For an understanding of the nature of the approximations, it need only be noted that the quantity $dr'/\cos\gamma'$ or $dr''/\cos\gamma''$ is an incremental length on a line inclined angle γ in the plane of the cylinder cross section from the original radial direction. Figure 1 indicates this true path AB and the approximate one AB' with constant γ for the integration from $r\sin\gamma$ to r. Note

[3] Numbers in brackets designate References at end of technical brief.

Table 1 Radiation configuration factors for annular rings to a hemispherical section of height H

	H/R_s					
R_d/R_s	.259 (α = 15°)	.500 (α = 30°)	.707 (α = 45°)	.866 (α = 60°)	.966 (α = 75°)	1.0 (α = 90°)
1.1	.293	.301	.307	.296	.302	.300
1.2	.227	.242	.246	.249	.245	.245
1.3	.184	.206	.208	.203	.207	.209
1.4	.149	.178	.182	.180	.188	.182
1.5	.129	.157	.169	.150	.156	.160
1.6	.109	.144	.141	.143	.142	.143
1.7	.091	.117	.127	.125	.131	.126
1.8	.079	.109	.115	.110	.108	.112
1.9	.071	.096	.103	.106	.102	.103
2.0	.061	.090	.094	.089	.094	.093
2.2	.046	.070	.077	.076	.076	.076
2.4	.040	.061	.065	.068	.065	.066
2.6	.036	.052	.058	.059	.060	.059
2.8	.030	.043	.047	.051	.052	.049
3.0	.027	.040	.041	.046	.045	.045
3.2	.022	.033	.040	.038	.039	.039
3.4	.019	.031	.034	.035	.037	.035
3.6	.018	.030	.025	.033	.032	.032
3.8	.015	.021	.023	.030	.028	.027
4.0	.014	.023	.028	.026	.026	.027
4.2	.011	.020	.022	.024	.023	.024
4.4	.013	.018	.022	.022	.023	.022
4.6	.012	.017	.020	.020	.025	.022
4.8	.009	.015	.020	.020	.018	.019
5.0	.008	.013	.016	.016	.018	.017

1 percent. Computer time availability did not permit the larger sample sizes.

This note adds a new geometry to the general literature on radiation configuration factors. The limitations on the use of the data and the accuracy of the calculations have been explained.

The Radial Radiative Heat Flux in a Cylinder

D. K. EDWARDS[1] and A. T. WASSEL[2]

Nomenclature

B_ν = black-body spectral intensity
c = velocity of light
D_n = cylindrical exponential integral
h = Planck constant
I_ν = spectral intensity
k = Boltzmann constant
k_ν = spectral absorption coefficient
q_ν = spectral radial radiant heat flux
r, r', r'' = local radius
R = tube radius
T = absolute temperature
x = independent variable
α = variable of integration; angle from radial direction to the true line of sight measured in a plane parallel to the tube axis, see [2]
$\gamma, \gamma', \gamma''$ = angle in the cross-sectional plane from the radial direction to the projected line of sight, see Fig. 1
ν = wavenumber, reciprocal wavelength

[1] Professor of Engineering, Department of Energy and Kinetics, School of Engineering, University of California, Los Angeles, Calif. Mem. ASME.

[2] Department of Energy and Kinetics, School of Engineering, University of California, Los Angeles, Calif.

Contributed by the Heat Transfer Division of THE AMERICAN SOCIETY OF MECHANICAL ENGINEERS. Manuscript received by the Heat Transfer Division November 30, 1972.

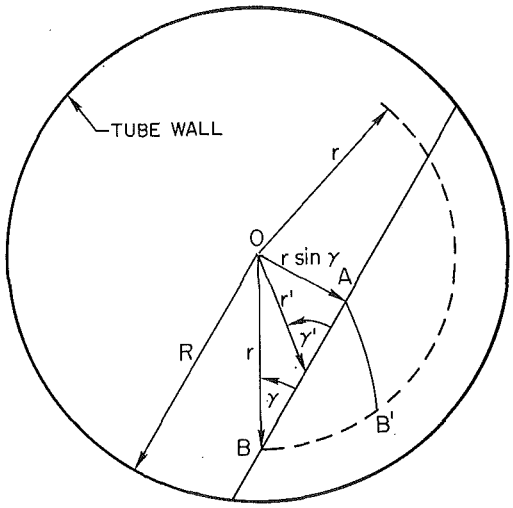

Fig. 1

IN INVESTIGATING radiative transfer in a nongray cylindrical medium, it has been found that some authors [1, 2][3] have approximated the local radial heat flux without discussing the nature of the approximation used. It is the purpose of this note to do so and to show quantitatively the magnitude of error which results for an optically thin isothermal gas.

Consider a cylindrical gas volume of radius R with temperature distribution $T(r')$ in local thermodynamic equilibrium so that the local black-body source intensity is

$$B_\nu(r') = \frac{2hc^2\nu^3}{e^{hc\nu/kT(r')} - 1} \tag{1}$$

The net radial radiative flux at radius r can be written in the following form:

$$\begin{aligned} q_\nu(r) = 4 \int_{\gamma=0}^{\pi/2} \cos\gamma \Bigg\{ I_\nu(R) \Bigg[D_3 \Bigg(\Bigg\{ \int_{r\sin\gamma}^{R} + \int_{r\sin\gamma}^{r} \Bigg\} \left\{ \frac{k_\nu dr'}{\cos\gamma'} \right\} \Bigg) - D_3 \left(\int_r^R \frac{k_\nu dr'}{\cos\gamma'} \right) \Bigg] \\ - \int_r^R D_2 \left(\int_r^{r'} \frac{k_\nu dr''}{\cos\gamma''} \right) \frac{B_\nu k_\nu dr'}{\cos\gamma'} \\ + \int_{r\sin\gamma}^{R} D_2 \left(\Bigg\{ \int_{r\sin\gamma}^{r} + \int_{r\sin\gamma}^{r'} \Bigg\} \left\{ \frac{k_\nu dr''}{\cos\gamma''} \right\} \right) \frac{B_\nu k_\nu dr'}{\cos\gamma'} \\ + \int_{r\sin\gamma}^{r} D_2 \left(\int_{r'}^{r} \frac{k_\nu dr''}{\cos\gamma''} \right) \frac{B_\nu k_\nu dr'}{\cos\gamma'} \Bigg\} d\gamma \end{aligned} \tag{2}$$

where

$$\cos\gamma' = [1 - (r/r')^2 \sin^2\gamma]^{1/2} \tag{3a}$$

$$\cos\gamma'' = [1 - (r/r'')^2 \sin^2\gamma]^{1/2} \tag{3b}$$

$$D_n(x) = \int_0^{\pi/2} \cos^{n-1}\alpha \exp(-x/\cos\alpha) d\alpha \tag{4}$$

Equation (27) of [2] and equation (1) of [1] both omit the primes on γ' and γ'' and show the $\cos\gamma'$ and $\cos\gamma''$ terms as factorable from within the integrals. Thus those equations can be regarded as only approximations.

For an understanding of the nature of the approximations, it need only be noted that the quantity $dr'/\cos\gamma'$ or $dr''/\cos\gamma''$ is an incremental length on a line inclined angle γ in the plane of the cylinder cross section from the original radial direction. Figure 1 indicates this true path AB and the approximate one AB' with constant γ for the integration from $r\sin\gamma$ to r. Note

[3] Numbers in brackets designate References at end of technical brief.

that the approximate path is considerably shorter. Contributions to the outward flux from the vicinity of $r' = r \sin \gamma$ are considerably underestimated, while those from the neighborhood of r itself are correctly evaluated. It is thus strongly suggested that the approximation made in [1, 2] will be inconsequential in the optically thick limit, since only the nearby elements will contribute to the flux. In the optically thin limit, it appears that considerable error will occur in using paths such as AB′ instead of AB in Fig. 1.

As a test of this reasoning, the optically thin limit was investigated. For convenience, a homogeneous isothermal medium bounded by a diffuse wall was assumed. In the homogeneous case the integrals are easily evaluated, particularly in view of Fig. 1. Furthermore, the $D_n(x)$ functions for small argument can be written as

$$D_2(x) = 1 - \frac{\pi}{2} x + O(x^2) \tag{5a}$$

$$D_3(x) = \frac{\pi}{4} - x + O(x^2) \tag{5b}$$

With neglect of terms of order $(k_\nu R)^2$ and smaller, equation (2) reduces to

$$q_\nu(R) = (\pi B_\nu - \pi I_\nu)(2k_\nu R) \tag{6}$$

Similarly, the approximation of setting $\gamma' = \gamma'' = \gamma$ yields

$$q_\nu(R) \doteq (\pi B_\nu - \pi I_\nu)(2k_\nu R)\left(2 - \frac{4}{\pi}\right) \tag{7}$$

Note that equation (6) agrees with the well-known result that the geometric mean beam length for a cylinder is just the diameter $2R$, e.g., [4].

The approximate result is significantly in error, underestimating by $4/\pi - 1 \doteq 27$ percent. Similar analysis can show that the error in the optically thin limit is constant for all radii.

In conclusion, it is pointed out that the approximation made in [1, 2] is significantly in error for optically thin conditions but appears to be valid for optically thick situations. The approximation for $D_2(x)$ introduced in [1] stands apart from the approximation of taking $\gamma' = \gamma'' = \gamma$ discussed here and is indeed a quite useful relationship [5].

References

1 Habib, I. S., and Greif, R., "Nongray Radiative Transport in a Cylindrical Medium," JOURNAL OF HEAT TRANSFER, TRANS. ASME, Series C, Vol. 92, No. 1, Feb. 1970, pp. 28–32.

2 Kestin, A. S., "Radiant Heat Flux Distribution in a Cylindrically Symmetric Nonisothermal Gas with Temperature-Dependent Absorption Coefficient," *J. Quant. Spectrosc. Radiat. Transfer*, Vol. 8, 1968, pp. 419–434.

3 Kuznetsov, Y. S., "Temperature Distribution in an Infinite Cylinder and in a Sphere in a State of Non-Monochromatic Radiation Equilibrium," English translation in the *USSR Computational Mathematics and Mathematical Physics*, Vol. 2, 1963, pp. 230–254.

4 Hottel, H. C., "Radiant Heat Transmission," in: *Heat Transmission*, McAdams, W. H., ed., McGraw-Hill, New York, N. Y., 1964.

5 Chiba, Z., and Greif, R., discussion of "Nongray Radiative Transport in a Cylindrical Medium," JOURNAL OF HEAT TRANSFER TRANS. ASME, Series C, Vol. 95, No. 1, Feb. 1973, p. 142.

Optical Measurements in a Pulsating Flame

D. DURAO,[1] F. DURST,[2] and J. H. WHITELAW[1]

Introduction

THIS paper is concerned with an experiment devised to allow an assessment of the viability of laser anemometry for measurements of instantaneous velocity in combustion systems, and thereby to lay the foundation for its use in the investigation of combustion instabilities such as those considered in [1-3].[3] The experiments described in [1-3] did not make use of laser anemometry and were limited in accuracy because of the high temperatures. To permit the attainment of the present objective, combustion instabilities were introduced by periodically supplying the gas to the burner; the frequency was chosen to accord with those observed in [4] in a premixed flame which did not have imposed fluctuations. Measurements of instantaneous velocity were effected in the resulting oscillating flame with the laser anemometer. Cinematography was employed to assist the physical interpretation of the measurements.

Equipment

The burner tube was 12.5 mm inside diameter by 15 mm outside diameter and 940 mm long. It was connected to a polythene tube through which methane flowed. The polythene tube was squeezed at predetermined and constant frequencies by a motor-driven cam, thereby interrupting the flow and causing the flame to oscillate. The resulting flame was photographed using a Bolex 16-mm camera run at 64 frames/sec with Kodak 4-K film.

Details of the general arrangement of the laser-anemometry system are available in [5-8] and only the essential details need be repeated here. A 5-mw He–Ne laser, an integrated optical unit operating in the fringe mode, a light-collecting system, and a photomultiplier formed the optical arrangement and were secured to an optical bench. The burner tube was fixed to a cathetometer which was located on a milling table and could be traversed in the vertical and horizontal planes. The fringe-mode optics produced approximately 125 fringes and the light-collecting system allowed the photocathode to see only the center 100 fringes. The resulting measuring-control volume was approximately 0.5 mm long by 100 μm in diameter. To increase the number of scattering centers available, atomized silicone-oil particles were added to the gas stream in a concentration sufficient to produce slightly fewer than one particle in the control volume at all times. This concentration of silicone-oil particles had no influence on the observed flame height.

The signal-analysis system made use of a prototype of the DISA frequency-tracking demodulator and permitted measurement of the instantaneous Doppler signal frequency, which is linearly proportional to instantaneous velocity, see [9]. The time-averaged velocity was obtained from an integrator and rms meter; integration times were always long compared with the oscillation period.

Results

Representative samples of the results obtained from the present experimental program are shown in Figs. 1 to 3.

Figure 1 presents three sequences of film obtained for flames with different exit velocities, with the gas stream fluctuating at a frequency of 12.5 Hz and with an rms amplitude corresponding to 12 percent of the center-line exit velocity. Two of the flames are clearly laminar and the third transitional with the turbulent region attained within 10 diameters of the burner exit. The unstable nature of the combustion for each flame is clearly

[1] Department of Mechanical Engineering, Imperial College of Science and Technology, London, England.

[2] Department of Mechanical Engineering, Imperial College of Science and Technology, London, England; presently at University of Karlsruhe, Germany.

[3] Numbers in brackets designate References at end of technical brief.

Based on a paper contributed by the Heat Transfer Division of THE AMERICAN SOCIETY OF MECHANICAL ENGINEERS and presented at the AIChE-ASME Heat Transfer Conference, Denver, Colo, August 6–9, 1972, as Paper No. 72-HT-8. Manuscript received by the Heat Transfer Division August 1, 1972.

that the approximate path is considerably shorter. Contributions to the outward flux from the vicinity of $r' = r \sin \gamma$ are considerably underestimated, while those from the neighborhood of r itself are correctly evaluated. It is thus strongly suggested that the approximation made in [1, 2] will be inconsequential in the optically thick limit, since only the nearby elements will contribute to the flux. In the optically thin limit, it appears that considerable error will occur in using paths such as AB′ instead of AB in Fig. 1.

As a test of this reasoning, the optically thin limit was investigated. For convenience, a homogeneous isothermal medium bounded by a diffuse wall was assumed. In the homogeneous case the integrals are easily evaluated, particularly in view of Fig. 1. Furthermore, the $D_n(x)$ functions for small argument can be written as

$$D_2(x) = 1 - \frac{\pi}{2} x + O(x^2) \tag{5a}$$

$$D_3(x) = \frac{\pi}{4} - x + O(x^2) \tag{5b}$$

With neglect of terms of order $(k_\nu R)^2$ and smaller, equation (2) reduces to

$$q_\nu(R) = (\pi B_\nu - \pi I_\nu)(2k_\nu R) \tag{6}$$

Similarly, the approximation of setting $\gamma' = \gamma'' = \gamma$ yields

$$q_\nu(R) \doteq (\pi B_\nu - \pi I_\nu)(2k_\nu R)\left(2 - \frac{4}{\pi}\right) \tag{7}$$

Note that equation (6) agrees with the well-known result that the geometric mean beam length for a cylinder is just the diameter $2R$, e.g., [4].

The approximate result is significantly in error, underestimating by $4/\pi - 1 \doteq 27$ percent. Similar analysis can show that the error in the optically thin limit is constant for all radii.

In conclusion, it is pointed out that the approximation made in [1, 2] is significantly in error for optically thin conditions but appears to be valid for optically thick situations. The approximation for $D_2(x)$ introduced in [1] stands apart from the approximation of taking $\gamma' = \gamma'' = \gamma$ discussed here and is indeed a quite useful relationship [5].

References

1 Habib, I. S., and Greif, R., "Nongray Radiative Transport in a Cylindrical Medium," JOURNAL OF HEAT TRANSFER, TRANS. ASME, Series C, Vol. 92, No. 1, Feb. 1970, pp. 28–32.

2 Kestin, A. S., "Radiant Heat Flux Distribution in a Cylindrically Symmetric Nonisothermal Gas with Temperature-Dependent Absorption Coefficient," *J. Quant. Spectrosc. Radiat. Transfer*, Vol. 8, 1968, pp. 419–434.

3 Kuznetsov, Y. S., "Temperature Distribution in an Infinite Cylinder and in a Sphere in a State of Non-Monochromatic Radiation Equilibrium," English translation in the *USSR Computational Mathematics and Mathematical Physics*, Vol. 2, 1963, pp. 230–254.

4 Hottel, H. C., "Radiant Heat Transmission," in: *Heat Transmission*, McAdams, W. H., ed., McGraw-Hill, New York, N. Y., 1964.

5 Chiba, Z., and Greif, R., discussion of "Nongray Radiative Transport in a Cylindrical Medium," JOURNAL OF HEAT TRANSFER TRANS. ASME, Series C, Vol. 95, No. 1, Feb. 1973, p. 142.

Optical Measurements in a Pulsating Flame

D. DURAO,[1] F. DURST,[2] and J. H. WHITELAW[1]

Introduction

THIS paper is concerned with an experiment devised to allow an assessment of the viability of laser anemometry for measurements of instantaneous velocity in combustion systems, and thereby to lay the foundation for its use in the investigation of combustion instabilities such as those considered in [1-3].[3] The experiments described in [1-3] did not make use of laser anemometry and were limited in accuracy because of the high temperatures. To permit the attainment of the present objective, combustion instabilities were introduced by periodically supplying the gas to the burner; the frequency was chosen to accord with those observed in [4] in a premixed flame which did not have imposed fluctuations. Measurements of instantaneous velocity were effected in the resulting oscillating flame with the laser anemometer. Cinematography was employed to assist the physical interpretation of the measurements.

Equipment

The burner tube was 12.5 mm inside diameter by 15 mm outside diameter and 940 mm long. It was connected to a polythene tube through which methane flowed. The polythene tube was squeezed at predetermined and constant frequencies by a motor-driven cam, thereby interrupting the flow and causing the flame to oscillate. The resulting flame was photographed using a Bolex 16-mm camera run at 64 frames/sec with Kodak 4-K film.

Details of the general arrangement of the laser-anemometry system are available in [5-8] and only the essential details need be repeated here. A 5-mw He–Ne laser, an integrated optical unit operating in the fringe mode, a light-collecting system, and a photomultiplier formed the optical arrangement and were secured to an optical bench. The burner tube was fixed to a cathetometer which was located on a milling table and could be traversed in the vertical and horizontal planes. The fringe-mode optics produced approximately 125 fringes and the light-collecting system allowed the photocathode to see only the center 100 fringes. The resulting measuring-control volume was approximately 0.5 mm long by 100 μm in diameter. To increase the number of scattering centers available, atomized silicone-oil particles were added to the gas stream in a concentration sufficient to produce slightly fewer than one particle in the control volume at all times. This concentration of silicone-oil particles had no influence on the observed flame height.

The signal-analysis system made use of a prototype of the DISA frequency-tracking demodulator and permitted measurement of the instantaneous Doppler signal frequency, which is linearly proportional to instantaneous velocity, see [9]. The time-averaged velocity was obtained from an integrator and rms meter; integration times were always long compared with the oscillation period.

Results

Representative samples of the results obtained from the present experimental program are shown in Figs. 1 to 3.

Figure 1 presents three sequences of film obtained for flames with different exit velocities, with the gas stream fluctuating at a frequency of 12.5 Hz and with an rms amplitude corresponding to 12 percent of the center-line exit velocity. Two of the flames are clearly laminar and the third transitional with the turbulent region attained within 10 diameters of the burner exit. The unstable nature of the combustion for each flame is clearly

[1] Department of Mechanical Engineering, Imperial College of Science and Technology, London, England.

[2] Department of Mechanical Engineering, Imperial College of Science and Technology, London, England; presently at University of Karlsruhe, Germany.

[3] Numbers in brackets designate References at end of technical brief.

Based on a paper contributed by the Heat Transfer Division of THE AMERICAN SOCIETY OF MECHANICAL ENGINEERS and presented at the AIChE-ASME Heat Transfer Conference, Denver, Colo, August 6–9, 1972, as Paper No. 72-HT-8. Manuscript received by the Heat Transfer Division August 1, 1972.

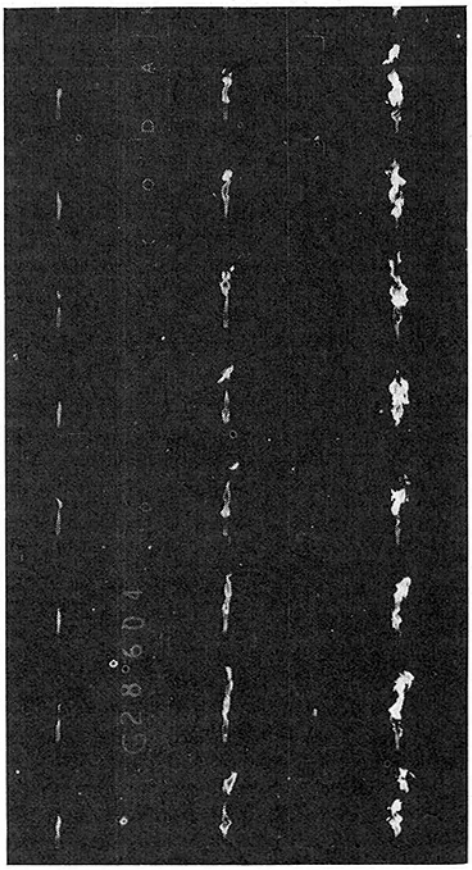

Fig. 1 Photographic record of flame with exit center-line velocity; (a) 0.8 m/sec, (b) 1.6 m/sec, (c) 4.0 m/sec

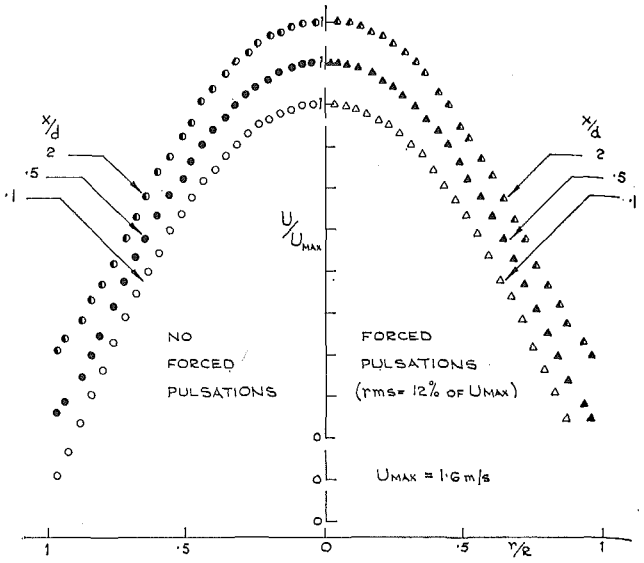

Fig. 2 Mean velocity profiles corresponding to exit center-line velocity of 1.6 m/sec; frequency signal is 12.5 Hz

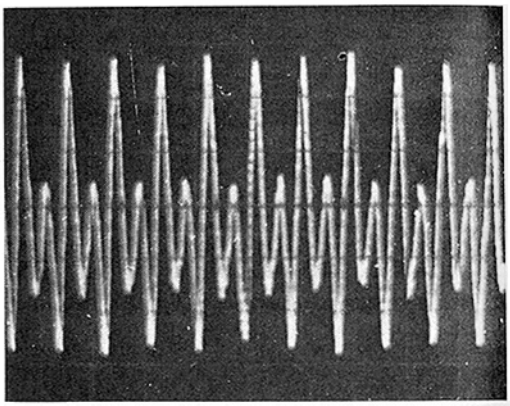

Fig. 3(a) Instantaneous signal corresponding to exit center-line velocity of 1.6 m/sec and x/D of 0.5

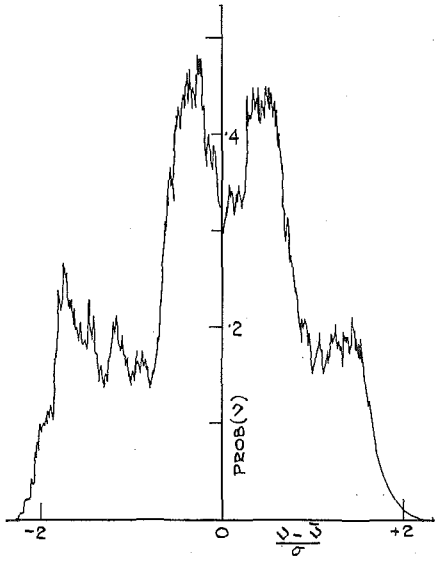

Fig. 3(b) Velocity probability density distribution corresponding to the center line of the 1.6-m/sec flame and x/D of 0.5

demonstrated. In each case the frequency of the imposed fluctuation was the same and may be identified from the increase in the distance between the maxima in flame diameter, corresponding to the increase in exit velocity. The process of the flame breaking up and reforming can also be readily identified.

Measurements of mean velocity obtained with the laser anemometer are shown on the right-hand side of Fig. 2 and correspond to the flame shown in Fig. 1(*b*). The measurements on the left-hand side of Fig. 2 correspond to the flame in the absence of the imposed fluctuation. The measurements on the left-hand side were obtained with an integration time of 2 sec and those on the right-hand side with 10 sec. Clearly the two sets of results are identical and correspond to those of a laminar jet formed from a fully developed laminar pipe flow; a similar conclusion may be shown from measurements obtained in the flame corresponding to Fig. 1(*a*). Detailed measurements were not attempted in the flame corresponding to Fig. 1(*c*), but it is clear that the symmetry of Fig. 2 did not exist in the downstream region due to the earlier transition brought about by the imposed fluctuations.

Traces of the demodulated instantaneous signal frequency, corresponding to the instantaneous longitudinal velocity component, were photographed on a storage oscilloscope, and Fig. 3(*a*) displays one such trace measured in the flame shown in Fig. 1(*b*). This trace shows the imposed fluctuation of 12.5 Hz. The intermediate lower amplitude signal stems from the elastic nature of the tube upon which the cam acted. Figure 3(*b*) displays a probability density distribution corresponding to the measurement of Fig. 3(*a*). The finite width of this distribution is caused by the periodically imposed fluctuation and the four peaks from the large and small amplitude signals of Fig. 3(*a*).

The results displayed in Fig. 2 clearly show that within the range of measurement the imposed fluctuations did not influence the mean flow of this laminar flame; the same situation was observed for the lower velocity flame. Of course, as is shown in Fig. 3(*a*), the instantaneous velocity reveals the presence of the fluctuations. Probability density distributions similar to that displayed in Fig. 3(*b*), but with two single peaks, were previously

observed in [8]. It is probable that this corresponds to sinusoidal velocity fluctuations in the neighborhood of the flame front. Sinusoidal instantaneous velocity fluctuations have subsequently been observed in the neighborhood of flame fronts [4] and the present measurements confirm the reliability of the equipment used to obtain them. The principal alternative means of measuring instantaneous velocity, hot-wire anemometry, does not allow the velocity and temperature response to be adequately separated, as was demonstrated in [10].

The present measurement did not extend to large value of x/D, due partly to the evaporation of the silicone-oil droplets. To achieve measurements at larger values, an alternative source of particles must be devised to generate submicron nonevaporating particles suitable for scattering light. In addition, these particles must not significantly influence the chemical kinetics of the combustion process. The present frequency-tracking demodulator is unable to follow signals with a maximum frequency variation in excess of 70 percent of the center frequency. A similar limitation is likely to apply to all frequency trackers, and frequency shifting must be incorporated to overcome it.

Acknowledgment

The present work was carried out with the financial support of an S.R.C. research grant. One of the authors (D. Durao) is the recipient of a NATO grant obtained from Junta Nacional de Investigacao Cientifica and Tecnologica. Stiftung Volkswagenwerk provided funds for F. Durst in the early stages of the work.

References

1 Markstein, G. H., *Non-steady Flame Propagation*, Pergamon Press, Elmsford, N. Y., 1964.

2 Paul, A., "Das Flackern laminarer Freistrahlflammen," *Chemie-Ing. Techn.*, Vol. 43, 1971, p. 550.

3 Deckker, B. E. L., and Sampath, P., "The Mechanism of Vibration in Enclosed Laminar Diffusion Flames," *Thirteenth Symposium on Combustion*, Combustion Institute, 1971, p. 505.

4 Durst, F., "Development and Application of Optical Anemometers," PhD thesis, University of London, London, England, 1972.

5 Durst, F., and Whitelaw, J. H., "A Guide to Optical Anemometers," *Zeit. Laser*, Vol. 3, 1971, p. 15.

6 Durst, F., and Whitelaw, J. H., "Integrated Optical Units for Laser Anemometry," *J. Phys. E.*, Vol. 4, 1971, p. 804.

7 Durst, F., and Whitelaw, J. H., "Measurements of Mean Velocity, Fluctuating Velocity and Shear Stress in Air, using a Laser Anemometer," *DISA Information*, Vol. 12, 1971, p. 11.

8 Durst, F., Melling, A., and Whitelaw, J. H., "The Application of Optical Anemometry to Measurement in Combustion Systems," *Combustion and Flame*, Vol. 18, 1972, p. 197.

9 Durst, F., and Whitelaw, J. H., "The Optimisation of Optical Anemometers," *Proc. Roy. Soc.*, Vol. A324, 1971, p. 157.

10 Parker, K. H., and Guillan, O., "Local Measurements in a Turbulent Flame by Hot-Wire Anemometry," *Thirteenth Symposium on Combustion*, Combustion Institute, 1971, p. 667.

Refrigerant–Water Scaling of Critical Heat Flux in Round Tubes—Subcooled Forced-Convection Boiling[1]

J. C. PURCUPILE,[2] L. S. TONG,[3] and S. W. GOUSE, Jr.[4]

Subcooled, critical heat-flux test data on refrigerant R-11 flowing vertically in a uniformly heated circular tube is reported. Using the data reported by Coeffield for R-113, a method is presented for obtaining a direct heat-flux scaling factor between refrigerant and water with the same geometry, mass velocity, and local flowing quality when the pressure is adjusted so that the liquid-to-vapor density ratios are equal in both systems.

Nomenclature

D = inside diameter, ft
G = mass velocity, $lb_m/hr\text{-}ft^2$
h_{fg} = latent heat of vaporization, Btu/lb_m
X = flowing equilibrium quality, defined in subcooled region as $H_b - H_s/h_{fg}$
q = critical heat flux, $Btu/hr\text{-}ft^2$
α = void fraction
μ = viscosity, $lb_m/hr\text{-}ft$
ρ = density, lb_m/ft^3

Subscripts

l = liquid
s = saturation condition associated with exit pressure
v = vapor
exit = exit condition

[1] This work was supported by the Office of Naval Research and the Department of Mechanical Engineering, Carnegie–Mellon University, Pittsburgh, Pa.

[2] Associate Professor, Department of Mechanical Engineering, Carnegie–Mellon University, Pittsburgh, Pa. Mem. ASME.

[3] Consultant, Nuclear Energy Systems, Westinghouse Electric Corp., Pittsburgh, Pa. Mem. ASME.

[4] Associate Dean, CIT and School of Urban and Public Affairs, Carnegie–Mellon University, Pittsburgh, Pa. Mem. ASME.

Contributed by the Heat Transfer Division of THE AMERICAN SOCIETY OF MECHANICAL ENGINEERS. Manuscript received by the Heat Transfer Division July 25, 1972.

Introduction

RECENTLY there has been great interest in scaling critical heat flux in water with a fluid that is similar to water. The fluids usually chosen for this scaling are refrigerants, because:

1 The required operating temperature and pressure are low.
2 The low latent heat reduces the power required to 5 to 10 percent of that of an equivalent water test.
3 Refrigerants have already been used extensively in the air-conditioning industry and data are available on their thermodynamic and transport properties.

In the subcooled region, the direct heat-flux scaling method is suggested to replace the Stevens-type [1][5] mass-velocity scaling factor because the critical quality is insensitive to change of the mass velocity at high subcoolings.

New experimental CHF data for refrigerant R-11 in the subcooled boiling region are presented, and the use of the model developed by Purcupile and Gouse [4] is demonstrated to directly scale CHF between water and refrigerant R-113.

Experimental

The test section consisted of a 0.625-in-OD by 0.491-in-ID by 44-in-long tube. CHF was detected with 13 chromel–constantan thermocouples mounted on the outside of the tube. To eliminate flow instabilities, the pressure drop across the throttle valve was always at least five times greater than the pressure drop across the test section. The ambient heat loss was experimentally determined by performing heat balances at various test-section temperatures. The tests were conducted by setting the loop at the required pressure, temperature, and flow. The power to the test section was then increased in small increments until a temperature excursion was noted. The values of the temperature, pressure, flow rate, power, and pressure drop just prior to CHF are recorded as the CHF conditions.

The flowing quality of CHF was calculated by adding the heat input to the inlet enthalpy. The fluid transport properties at the saturation temperature associated with the outlet pressure were used in all calculations.

[5] Numbers in brackets designate References at end of technical brief.

observed in [8]. It is probable that this corresponds to sinusoidal velocity fluctuations in the neighborhood of the flame front. Sinusoidal instantaneous velocity fluctuations have subsequently been observed in the neighborhood of flame fronts [4] and the present measurements confirm the reliability of the equipment used to obtain them. The principal alternative means of measuring instantaneous velocity, hot-wire anemometry, does not allow the velocity and temperature response to be adequately separated, as was demonstrated in [10].

The present measurement did not extend to large value of x/D, due partly to the evaporation of the silicone-oil droplets. To achieve measurements at larger values, an alternative source of particles must be devised to generate submicron nonevaporating particles suitable for scattering light. In addition, these particles must not significantly influence the chemical kinetics of the combustion process. The present frequency-tracking demodulator is unable to follow signals with a maximum frequency variation in excess of 70 percent of the center frequency. A similar limitation is likely to apply to all frequency trackers, and frequency shifting must be incorporated to overcome it.

Acknowledgment

The present work was carried out with the financial support of an S.R.C. research grant. One of the authors (D. Durao) is the recipient of a NATO grant obtained from Junta Nacional de Investigacao Cientifica and Tecnologica. Stiftung Volkswagenwerk provided funds for F. Durst in the early stages of the work.

References

1 Markstein, G. H., *Non-steady Flame Propagation*, Pergamon Press, Elmsford, N. Y., 1964.

2 Paul, A., "Das Flackern laminarer Freistrahlflammen," *Chemie-Ing. Techn.*, Vol. 43, 1971, p. 550.

3 Deckker, B. E. L., and Sampath, P., "The Mechanism of Vibration in Enclosed Laminar Diffusion Flames," *Thirteenth Symposium on Combustion*, Combustion Institute, 1971, p. 505.

4 Durst, F., "Development and Application of Optical Anemometers," PhD thesis, University of London, London, England, 1972.

5 Durst, F., and Whitelaw, J. H., "A Guide to Optical Anemometers," *Zeit. Laser*, Vol. 3, 1971, p. 15.

6 Durst, F., and Whitelaw, J. H., "Integrated Optical Units for Laser Anemometry," *J. Phys. E.*, Vol. 4, 1971, p. 804.

7 Durst, F., and Whitelaw, J. H., "Measurements of Mean Velocity, Fluctuating Velocity and Shear Stress in Air, using a Laser Anemometer," *DISA Information*, Vol. 12, 1971, p. 11.

8 Durst, F., Melling, A., and Whitelaw, J. H., "The Application of Optical Anemometry to Measurement in Combustion Systems," *Combustion and Flame*, Vol. 18, 1972, p. 197.

9 Durst, F., and Whitelaw, J. H., "The Optimisation of Optical Anemometers," *Proc. Roy. Soc.*, Vol. A324, 1971, p. 157.

10 Parker, K. H., and Guillan, O., "Local Measurements in a Turbulent Flame by Hot-Wire Anemometry," *Thirteenth Symposium on Combustion*, Combustion Institute, 1971, p. 667.

Refrigerant–Water Scaling of Critical Heat Flux in Round Tubes—Subcooled Forced-Convection Boiling[1]

J. C. PURCUPILE,[2] L. S. TONG,[3] and S. W. GOUSE, Jr.[4]

Subcooled, critical heat-flux test data on refrigerant R-11 flowing vertically in a uniformly heated circular tube is reported. Using the data reported by Coeffield for R-113, a method is presented for obtaining a direct heat-flux scaling factor between refrigerant and water with the same geometry, mass velocity, and local flowing quality when the pressure is adjusted so that the liquid-to-vapor density ratios are equal in both systems.

Nomenclature

D = inside diameter, ft
G = mass velocity, $lb_m/hr\text{-}ft^2$
h_{fg} = latent heat of vaporization, Btu/lb_m
X = flowing equilibrium quality, defined in subcooled region as $H_b - H_s/h_{fg}$
q = critical heat flux, $Btu/hr\text{-}ft^2$
α = void fraction
μ = viscosity, $lb_m/hr\text{-}ft$
ρ = density, lb_m/ft^3

Subscripts

l = liquid
s = saturation condition associated with exit pressure
v = vapor
exit = exit condition

Introduction

Recently there has been great interest in scaling critical heat flux in water with a fluid that is similar to water. The fluids usually chosen for this scaling are refrigerants, because:

1 The required operating temperature and pressure are low.
2 The low latent heat reduces the power required to 5 to 10 percent of that of an equivalent water test.
3 Refrigerants have already been used extensively in the air-conditioning industry and data are available on their thermodynamic and transport properties.

In the subcooled region, the direct heat-flux scaling method is suggested to replace the Stevens-type [1][5] mass-velocity scaling factor because the critical quality is insensitive to change of the mass velocity at high subcoolings.

New experimental CHF data for refrigerant R-11 in the subcooled boiling region are presented, and the use of the model developed by Purcupile and Gouse [4] is demonstrated to directly scale CHF between water and refrigerant R-113.

Experimental

The test section consisted of a 0.625-in-OD by 0.491-in-ID by 44-in-long tube. CHF was detected with 13 chromel–constantan thermocouples mounted on the outside of the tube. To eliminate flow instabilities, the pressure drop across the throttle valve was always at least five times greater than the pressure drop across the test section. The ambient heat loss was experimentally determined by performing heat balances at various test-section temperatures. The tests were conducted by setting the loop at the required pressure, temperature, and flow. The power to the test section was then increased in small increments until a temperature excursion was noted. The values of the temperature, pressure, flow rate, power, and pressure drop just prior to CHF are recorded as the CHF conditions.

The flowing quality of CHF was calculated by adding the heat input to the inlet enthalpy. The fluid transport properties at the saturation temperature associated with the outlet pressure were used in all calculations.

[1] This work was supported by the Office of Naval Research and the Department of Mechanical Engineering, Carnegie-Mellon University, Pittsburgh, Pa.

[2] Associate Professor, Department of Mechanical Engineering, Carnegie-Mellon University, Pittsburgh, Pa. Mem. ASME.

[3] Consultant, Nuclear Energy Systems, Westinghouse Electric Corp., Pittsburgh, Pa. Mem. ASME.

[4] Associate Dean, CIT and School of Urban and Public Affairs, Carnegie-Mellon University, Pittsburgh, Pa. Mem. ASME.

Contributed by the Heat Transfer Division of The American Society of Mechanical Engineers. Manuscript received by the Heat Transfer Division July 25, 1972.

[5] Numbers in brackets designate References at end of technical brief.

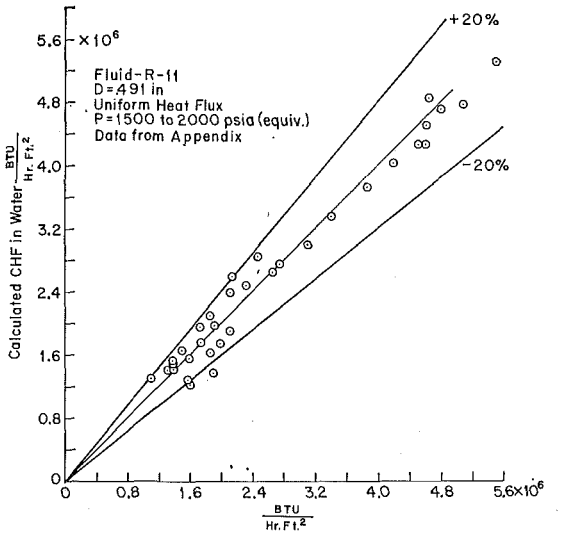

Fig. 1 Scaled CHF in water based on CHF test in R-11 using Stevens' mass-velocity scaling method

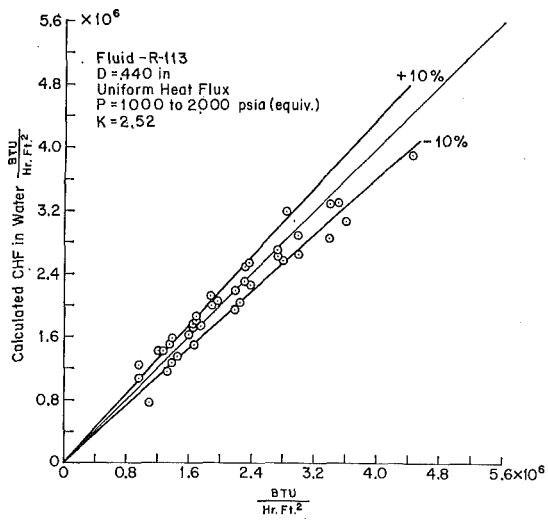

Fig. 2 Scaled CHF in water based on CHF tests in R-113 using direct heat-flux scaling method

Data Reduction Using Stevens' Method

The plotting method proposed by Stevens [1] was used to evaluate the data. A mass-velocity scaling factor was calculated for each point. Based on this calculation, the average mass-velocity scaling factor is 0.65 at 1500 psia and 0.60 at 2000 psia equivalent pressure. Using these values, the R-11 data were used to predict the CHF in water for the same equivalent pressure, local flowing quality, and diameter. This prediction or scaled CHF was then compared with the CHF that would be calculated for a tube with uniform heat flux with the same flow conditions. At 1500 psia, the scaled CHF was compared with the CHF predicted by the Thompson–MacBeth [3] correlation. However, at 2000 psia, the Thompson–MacBeth correlation incorrectly predicted the effect that diameter changes had on the CHF. Therefore, using 67 subcooled data points, reported in [3], a special 2000-psia subcooled CHF correlation was developed, and the scaled CHF was compared with the CHF that was predicted by this code. A plot of the scaled CHF versus the calculated CHF for 1500 and 2000 psia equivalent pressure is presented in Fig. 1.

Data Reduction Using Direct Heat-Flux Scaling Method

The direct heat-flux scaling method is based on the correlation of Purcupile and Gouse for subcooled forced-convection CHF in the subcooled high-velocity region [4]. The nondimensional form of the CHF equation is

$$\frac{q}{h_{fg}G} = c_1\left[0.6 + 0.4\frac{\rho_l}{\rho_v}\right]^{-0.5}\left[\frac{GD}{\mu_l}\right]^{-0.6}\left(\frac{1}{1-\alpha}\right)^{0.4} \times \left[1 + c_2\frac{\rho_l}{\rho_v}X_{\text{exit}}\right] \quad (1)$$

where c_1 depends on the fluid and c_2 is primarily a function of the bubble departure size and the temperature gradient near the wall. In the fluids examined to date (R-113, R-11, water), the relationships among the bubble departure size, value of CHF, and thermal conductivity are all interrelated such that c_2 appears to be constant for various fluids and is only a function of the reduced pressure of the fluid.

Equation (1) can be used to develop the CHF scaling factor between water and refrigerant as follows: At the same liquid-to-vapor density ratio ρ_l/ρ_v, mass velocity G, diameter D, and exit quality X_{exit}, the following relationship is valid:

$$\left[\frac{q}{h_{fg}G}\right]_w = K\left[\frac{1-\alpha_R}{1-\alpha_w}\right]^{0.4}\left[\frac{\mu_w}{\mu_R}\right]^{0.6} \times \frac{\left[1 + c_2\frac{\rho_l}{\rho_v}X_{\text{exit}}\right]_R}{\left[1 + c_2\frac{\rho_l}{\rho_v}X_{\text{exit}}\right]_w}\left[\frac{q}{h_{fg}G}\right]_R \quad (2)$$

where $K = c_{1w}/c_{1R}$, K is the basic heat-flux scaling factor, and subscripts R and w refer to refrigerant and water respectively.

The value of c_2 for the refrigerant and water is approximately the same, since when the pressure is adjusted to make the liquid-to-vapor density ratios ρ_l/ρ_v equal, both liquids are at approximately the same reduced pressure. Therefore, equation (2) can be simplified to

$$\left[\frac{q}{h_{fg}G}\right]_w = K\left[\frac{1-\alpha_R}{1-\alpha_w}\right]^{0.4}\left[\frac{\mu_w}{\mu_R}\right]^{0.6}\left[\frac{q}{h_{fg}G}\right]_R \quad (3)$$

To use this heat-flux scaling method, the void fraction was calculated by Levy's method [5] for both refrigerant and water.

Using equation (3), all the subcooled CHF data reported by Coeffield [2] for R-113 were used to scale the CHF in water at 1000, 1500, and 2000 psia. Using a scaling factor K of 2.52, this scaled CHF was then compared with the Thompson–MacBeth prediction at 1000 and 1500 psia and the special subcooled-boiling correlation prediction at 2000 psia. The results of this comparison are presented in Fig. 2.

References

1 Stevens, G. F., and Kirby, G. J., "A Quantitative Comparison Between Burnout Data for Water at 1000 psia and Freon-12 at 155 psia. Uniformly Heated Round Tubes, Vertical Upflow," AEEW-R327, 1964.

2 Coeffield, R. D., Jr., Rohrer, W. M., Jr., and Tong, L. S., "A Subcooled DNB Investigation of Freon-113 and Its Similarity to Subcooled Water DNB Data," *Nuclear Engineering and Design*, May 19, 1969, pp. C-1–C-11.

3 Thompson, B., and MacBeth, R. V., "Boiling Water Heat Transfer Burnout in Uniformly Heated Round Tubes: A Compilation of World Data with Accurate Correlations," Reactor Development Division, Atomic Energy Establishment, Winfrith, Dorchester, Dorset, Report No. AEW-R-356, 1964.

4 Purcupile, J. C., and Gouse, S. W., "Reynolds Flux Model of Critical Heat Flux in Subcooled Forced Convection Boiling," ASME Paper No. 72-HT-4.

5 Levy, S., "Forced Convection Subcooled Boiling—Prediction of Vapor Volumetric Fraction," *International Journal of Heat and Mass Transfer*, Vol. 10, 1967, pp. 951–965.

APPENDIX

Refrigerant R-11 critical heat-flux data; round-tube vertical flow

(D = 0.491 in., L = 44.0 in.)

Mass velocity $\times 10^6$ $lb_m/hr\text{-}ft^2$	Inlet subcooling Btu/lb	CHF $\times 10^5$ Btu/hr-ft^2	Exit quality	P psia
1.729	−40.89	0.994	−0.400	256.0
2.890	−41.31	2.060	−0.262	256.0
2.792	−37.11	1.846	−0.249	258.0
2.763	−32.86	1.644	−0.178	256.0
4.332	−41.31	2.931	−0.336	257.0
4.297	−36.84	2.670	−0.262	257.0
4.264	−32.61	2.373	−0.244	254.0
5.092	−32.65	2.737	−0.258	257.0
4.671	−36.89	2.812	−0.271	258.0
4.220	−41.10	2.861	−0.310	256.0
1.570	−40.59	1.332	−0.264	253.0
1.912	−41.36	1.522	−0.259	260.0
5.453	−41.10	3.384	−0.345	256.0
5.444	−37.11	3.147	−0.302	258.0
2.764	−37.11	1.897	−0.232	258.0
1.934	−37.11	1.411	−0.205	257.5
1.504	−37.11	1.121	−0.182	257.5
2.667	−33.08	1.691	−0.155	257.5
1.915	−32.86	1.262	−0.364	257.5
1.514	−32.86	1.074	−0.155	257.0
1.092	−51.06	1.093	−0.364	360.0
1.643	−50.85	1.484	−0.412	360.0
2.732	−50.85	2.178	−0.470	362.0
5.468	−50.85	3.628	−0.614	360.0
6.492	−50.85	4.024	−0.619	360.0
6.430	−36.86	3.840	−0.553	360.0
5.387	−46.65	3.361	−0.532	360.0
2.678	−47.07	2.030	−0.428	360.0
1.606	−47.07	1.240	−0.347	360.0
1.118	−47.28	0.986	−0.353	360.0
1.032	−41.98	0.854	−0.281	360.0
1.563	−42.62	1.213	−0.353	360.0
2.651	−42.62	1.868	−0.369	360.0
5.317	−42.40	3.103	−0.454	360.0
6.424	−42.40	3.593	−0.486	360.0
1.556	−41.50	1.351	−0.188	157.0
1.734	−52.98	1.738	−0.347	259.0

Subcooled Boiling of Water in Tape-generated Swirl Flow[1]

R. F. LOPINA[2] and A. E. BERGLES[3]

Introduction

TWISTED-TAPE inserts have been shown by numerous investigators to be an effective and simple means of enhancing heat transfer for both liquids and gases in tube flow. Most of the research effort has been devoted to study of single-phase conditions [1].[4] Data have been reported for subcooled boiling of water [2, 3], low-quality bulk boiling of water and Freon-11 [4, 5], and once-through vaporization of nitrogen [6]. These studies have rather satisfactorily established the effects of twisted tapes on subcooled-boiling burnout, bulk-boiling dryout, and heat transfer coefficients in dispersed-flow film boiling; however, there is considerable confusion regarding the characteristics of subcooled nucleate boiling.

Gambill et al. [2] obtained limited data for subcooled nucleate boiling suggesting that unusually high wall superheats of 200 deg F were possible with water at high heat fluxes. Feinstein and Lundberg [3] appeared to corroborate this behavior with their measurements of superheats approaching 400 deg F at moderate heat fluxes. However, an analysis of the data-reduction procedure of Feinstein and Lundberg suggested that an error was made in evaluating the temperature drop across the electrically heated tube wall [7]. After making the appropriate corrections, it was found that practically all of the subcooled-boiling data were actually non-boiling. The data of Blatt and Adt [4] for nucleate boiling or forced-convection vaporization suggested average superheats for water of as much as 100 deg F at low heat fluxes; however, similar data for Freon-11 were in the expected superheat range of less than 50 deg F. Once again, the discrepancy seems to be due to uncertainty in the heated-surface temperature, in this case through neglect of the steam-side and tube-wall temperature drops. This would cause a negligible error in the reported superheats for Freon-11 but could lead to errors estimated [7] to be as much as 30 deg F for their higher heat-flux water data.

This brief discussion of available data for nucleate boiling with swirl flow indicates that the boiling curve is not well defined. Since this information is essential to the proper design of high-heat-flux cooling systems that might utilize swirl flow, such as electromagnets and microwave power tubes, a study of single-phase swirl flow [8] was extended to boiling conditions.

Experimental Procedure

Data were taken with d-c electrically heated test sections installed in a loop circulating demineralized and degassed water at low pressure. The test sections were made of nickel (Inco alloy 200) tubes of inside diameter 0.198 in. and wall thickness 0.013 in. The full-length tapes were of inconel (Inco alloy 600) with a thickness of 0.014 in. The heated length was defined to be the distance between the inner faces of brass power bushings near each end of a test section. Pressure taps were also installed in these bushings. The tape twists y, expressed as tube diameters per 180 deg twist, ranged from 2.48 to 9.2. Tubes were redrawn over the tapes to a final inside diameter of 0.194 in. to insure about 0.002 in. of penetration of the tape into the tube wall. A Pyrex visual section was installed at the exit of the heated section.

Data recorded included inlet and exit pressures, inlet and exit temperatures, and tube outside temperatures (guarded). The inside tube temperatures were obtained via a computer solution of the conduction equation that accounted for variable thermal and electrical conductivity. The reported q/A values are based on the inside surface area of the tube only, and heat generated in the tape was always a small percentage of the total heat transfer to the fluid (under 3 percent). Further details on the experimental apparatus and procedure can be found in [7, 8].

Results

A typical subcooled-boiling plot of heat flux versus wall superheat is shown in Fig. 1. The degree of subcooling represents an average for the heated length of the test section. The dashed lines represent an extrapolation into the wall superheat regime of the forced-convection heat flux predicted from non-boiling data for the conditions specified. The curves in this figure have the same general appearance as conventional straight-flow boiling curves with three regimes present. At low wall superheats, the heat transfer is by forced convection, and a relatively small increase in q/A occurs for a small increase in wall superheat. At higher superheats, however, a large increase in heat flux occurs

---

[1] This work was performed in the M.I.T. Heat Transfer Laboratory under sponsorship of the National Magnet Laboratory.

[2] Associate Professor, Department of Aeronautics, U. S. Air Force Academy, Colo. Mem. ASME.

[3] Chairman, Department of Mechanical Engineering, Iowa State University, Ames, Iowa. Mem. ASME.

[4] Numbers in brackets designate References at end of technical brief.

Contributed by the Heat Transfer Division of THE AMERICAN SOCIETY OF MECHANICAL ENGINEERS. Manuscript received by the Heat Transfer Division November 28, 1972.

APPENDIX

Refrigerant R-11 critical heat-flux data; round-tube vertical flow

(D = 0.491 in., L = 44.0 in.)

Mass velocity $\times 10^6$ $lb_m/hr\text{-}ft^2$	Inlet subcooling Btu/lb	CHF $\times 10^5$ Btu/hr-ft^2	Exit quality	P psia
1.729	−40.89	0.994	−0.400	256.0
2.890	−41.31	2.060	−0.262	256.0
2.792	−37.11	1.846	−0.249	258.0
2.763	−32.86	1.644	−0.178	256.0
4.332	−41.31	2.931	−0.336	257.0
4.297	−36.84	2.670	−0.262	257.0
4.264	−32.61	2.373	−0.244	254.0
5.092	−32.65	2.737	−0.258	257.0
4.671	−36.89	2.812	−0.271	258.0
4.220	−41.10	2.861	−0.310	256.0
1.570	−40.59	1.332	−0.264	253.0
1.912	−41.36	1.522	−0.259	260.0
5.453	−41.10	3.384	−0.345	256.0
5.444	−37.11	3.147	−0.302	258.0
2.764	−37.11	1.897	−0.232	258.0
1.934	−37.11	1.411	−0.205	257.5
1.504	−37.11	1.121	−0.182	257.5
2.667	−33.08	1.691	−0.155	257.5
1.915	−32.86	1.262	−0.364	257.5
1.514	−32.86	1.074	−0.155	257.0
1.092	−51.06	1.093	−0.364	360.0
1.643	−50.85	1.484	−0.412	360.0
2.732	−50.85	2.178	−0.470	362.0
5.468	−50.85	3.628	−0.614	360.0
6.492	−50.85	4.024	−0.619	360.0
6.430	−36.86	3.840	−0.553	360.0
5.387	−46.65	3.361	−0.532	360.0
2.678	−47.07	2.030	−0.428	360.0
1.606	−47.07	1.240	−0.347	360.0
1.118	−47.28	0.986	−0.353	360.0
1.032	−41.98	0.854	−0.281	360.0
1.563	−42.62	1.213	−0.353	360.0
2.651	−42.62	1.868	−0.369	360.0
5.317	−42.40	3.103	−0.454	360.0
6.424	−42.40	3.593	−0.486	360.0
1.556	−41.50	1.351	−0.188	157.0
1.734	−52.98	1.738	−0.347	259.0

Subcooled Boiling of Water in Tape-generated Swirl Flow[1]

R. F. LOPINA[2] and A. E. BERGLES[3]

Introduction

TWISTED-TAPE inserts have been shown by numerous investigators to be an effective and simple means of enhancing heat transfer for both liquids and gases in tube flow. Most of the research effort has been devoted to study of single-phase conditions [1].[4] Data have been reported for subcooled boiling of water [2, 3], low-quality bulk boiling of water and Freon-11 [4, 5], and once-through vaporization of nitrogen [6]. These studies have rather satisfactorily established the effects of twisted tapes on subcooled-boiling burnout, bulk-boiling dryout, and heat transfer coefficients in dispersed-flow film boiling; however, there is considerable confusion regarding the characteristics of subcooled nucleate boiling.

Gambill et al. [2] obtained limited data for subcooled nucleate boiling suggesting that unusually high wall superheats of 200 deg F were possible with water at high heat fluxes. Feinstein and Lundberg [3] appeared to corroborate this behavior with their measurements of superheats approaching 400 deg F at moderate heat fluxes. However, an analysis of the data-reduction procedure of Feinstein and Lundberg suggested that an error was made in evaluating the temperature drop across the electrically heated tube wall [7]. After making the appropriate corrections, it was found that practically all of the subcooled-boiling data were actually non-boiling. The data of Blatt and Adt [4] for nucleate boiling or forced-convection vaporization suggested average superheats for water of as much as 100 deg F at low heat fluxes; however, similar data for Freon-11 were in the expected superheat range of less than 50 deg F. Once again, the discrepancy seems to be due to uncertainty in the heated-surface temperature, in this case through neglect of the steam-side and tube-wall temperature drops. This would cause a negligible error in the reported superheats for Freon-11 but could lead to errors estimated [7] to be as much as 30 deg F for their higher heat-flux water data.

This brief discussion of available data for nucleate boiling with swirl flow indicates that the boiling curve is not well defined. Since this information is essential to the proper design of high-heat-flux cooling systems that might utilize swirl flow, such as electromagnets and microwave power tubes, a study of single-phase swirl flow [8] was extended to boiling conditions.

Experimental Procedure

Data were taken with d-c electrically heated test sections installed in a loop circulating demineralized and degassed water at low pressure. The test sections were made of nickel (Inco alloy 200) tubes of inside diameter 0.198 in. and wall thickness 0.013 in. The full-length tapes were of inconel (Inco alloy 600) with a thickness of 0.014 in. The heated length was defined to be the distance between the inner faces of brass power bushings near each end of a test section. Pressure taps were also installed in these bushings. The tape twists y, expressed as tube diameters per 180 deg twist, ranged from 2.48 to 9.2. Tubes were redrawn over the tapes to a final inside diameter of 0.194 in. to insure about 0.002 in. of penetration of the tape into the tube wall. A Pyrex visual section was installed at the exit of the heated section.

Data recorded included inlet and exit pressures, inlet and exit temperatures, and tube outside temperatures (guarded). The inside tube temperatures were obtained via a computer solution of the conduction equation that accounted for variable thermal and electrical conductivity. The reported q/A values are based on the inside surface area of the tube only, and heat generated in the tape was always a small percentage of the total heat transfer to the fluid (under 3 percent). Further details on the experimental apparatus and procedure can be found in [7, 8].

Results

A typical subcooled-boiling plot of heat flux versus wall superheat is shown in Fig. 1. The degree of subcooling represents an average for the heated length of the test section. The dashed lines represent an extrapolation into the wall superheat regime of the forced-convection heat flux predicted from non-boiling data for the conditions specified. The curves in this figure have the same general appearance as conventional straight-flow boiling curves with three regimes present. At low wall superheats, the heat transfer is by forced convection, and a relatively small increase in q/A occurs for a small increase in wall superheat. At higher superheats, however, a large increase in heat flux occurs

---

[1] This work was performed in the M.I.T. Heat Transfer Laboratory under sponsorship of the National Magnet Laboratory.

[2] Associate Professor, Department of Aeronautics, U. S. Air Force Academy, Colo. Mem. ASME.

[3] Chairman, Department of Mechanical Engineering, Iowa State University, Ames, Iowa. Mem. ASME.

[4] Numbers in brackets designate References at end of technical brief.

Contributed by the Heat Transfer Division of THE AMERICAN SOCIETY OF MECHANICAL ENGINEERS. Manuscript received by the Heat Transfer Division November 28, 1972.

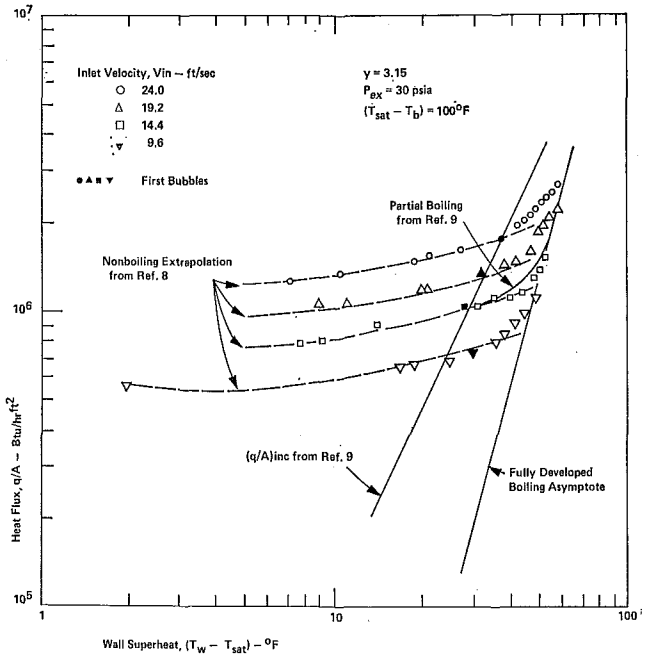

Fig. 1 Subcooled-boiling data for water in swirl flow

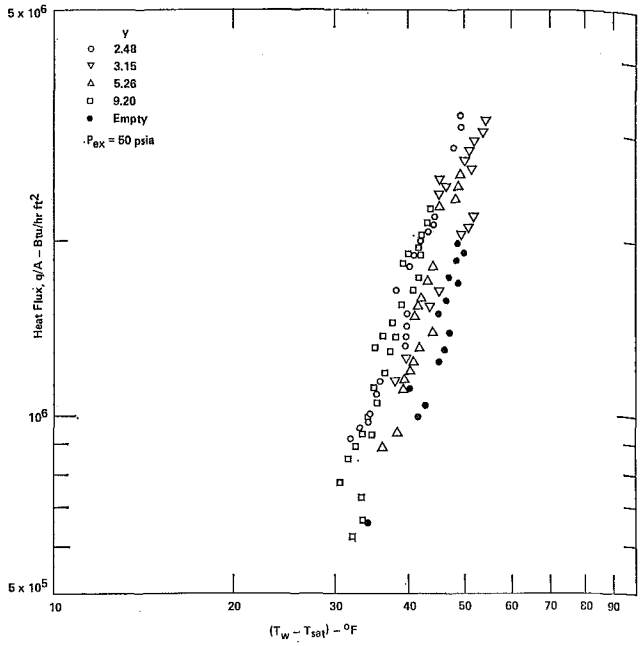

Fig. 2 Composite of fully developed surface-boiling data for straight and swirl flow

for a correspondingly small increase in wall superheat. As is usual with straight-flow boiling, the data for a particular tube at all velocities and subcoolings appear to be asymptotic to a "fully developed" boiling line in the high-superheat region.

The visual exit section was used to observe the inception points noted in Fig. 1. It may be seen that the first visually observed bubbles occurred very close to the predicted boiling inception line of Bergles and Rohsenow [9].

A compilation of data for fully developed boiling is given in Fig. 2. No systematic effect of tape twist can be observed, and the superheats with twisted tapes are essentially the same as for straight flow. The scatter of ±5 deg F in wall superheat is actually quite characteristic of fully developed subcooled boiling. It can thus be concluded that wall superheats for swirl flow are not any higher than those for straight flow. The rather close agreement between the two cases suggests that the mechanism is perhaps similar for the two cases. The water pool-boiling results of Costello and Tuthill [10] and Merte and Clark [11] tend to substantiate this conclusion, since it was reported in both studies that the superheat required for a given heat flux was practically independent of acceleration for heat fluxes above 50,000 Btu/hr-ft².

The final set of results presented in Fig. 3 concerns overall test-section pressure drop for swirl and straight flow. The data follow the usual trend of remaining close to the adiabatic value until appreciable boiling is initiated, whereupon an increase in pressure drop is observed with increasing heat flux. For the range of heat fluxes considered, the pressure drop with swirl flow is considerably higher than that for straight flow. The straight tube burns out before the pressure drop reaches the swirl-flow value; hence it is impossible to speak of swirl-flow enhancement in terms of heat-flux level at equal pressure drop *and* velocity. Of course the swirl tubes would have a substantially higher burnout flux than the empty tube.

Gambill et al. [2] have demonstrated twofold increases in burnout flux with swirl flow over a wide range of flow conditions. In addition, the burnout flux at equal pumping power (velocity variable) was also increased by a factor of two. This latter result is clarified by the present observations. With vigorous subcooled boiling, the swirl data seem to indicate a less pronounced increase in pressure drop than the empty-tube data. This increase is normally due to a rapid buildup of nonequilibrium vapor volume, which increases the momentum component of the pressure drop [12]. The visual observations made in this study

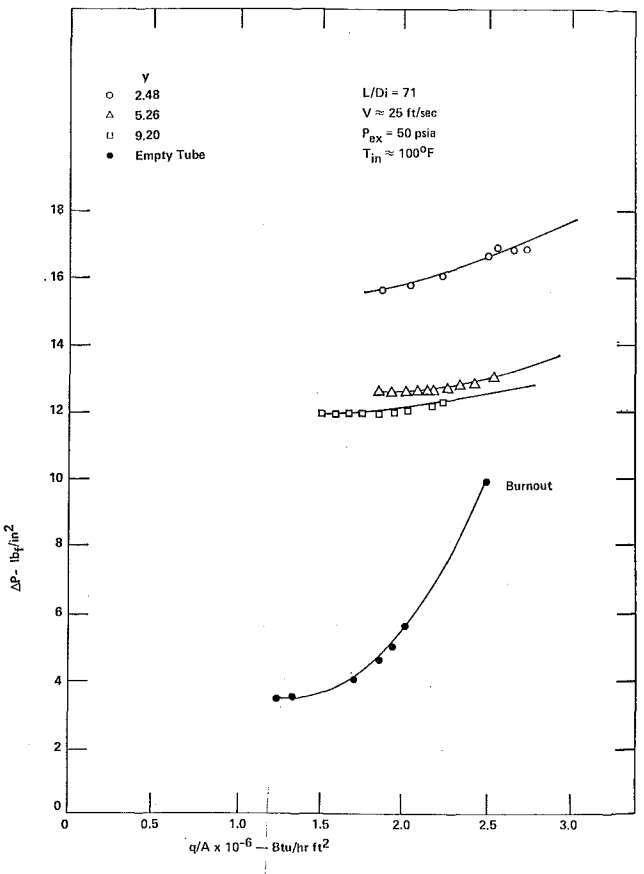

Fig. 3 Overall pressure drop for subcooled boiling of water in swirl flow

confirm that the swirl flow results in displacement of the bubbles from the wall. Upon removal from the superheated wall layer, the bubbles condense and the void fraction is reduced.

References

1 Bergles, A. E., "Survey and Evaluation of Techniques to Augment Convective Heat and Mass Transfer," *International Journal of Heat and Mass Transfer Series, Progress in Heat and Mass Transfer*, Vol. 1, 1969, pp. 331–424.

2 Gambill, W. R., Bundy, R. D., and Wansbrough, R. W., "Heat Transfer, Burnout, and Pressure Drop for Water in Swirl Flow Through Tubes with Internal Twisted Tapes," *Chem. Eng. Prog. Symp. Series*, Vol. 57, No. 32, 1961, pp. 127–137.
3 Feinstein, L., and Lundberg, R. E., "Fluid Friction and Boiling Heat Transfer with Water in Vortex Flow in Tubes Containing an Internal Twisted Tape," RADC-TRR-63-451, AD430889, June 1963.
4 Blatt, T. A., and Adt, R. R., Jr., "The Effects of Twisted Tape Swirl Generation on the Heat Transfer Rate and Pressure Drop of Boiling Freon 11 and Water," ASME Paper No. 63-WA-42.
5 Viskanta, R., "Critical Heat Flux for Water in Swirling Flow," *Nuclear Science and Engineering*, Vol. 10, 1961, pp. 202–203.
6 Bergles, A. E., Fuller, W., and Hynek, S. J., "Dispersed Flow Film Boiling of Nitrogen with Swirl Flow," *International Journal of Heat and Mass Transfer*, Vol. 14, 1971, pp. 1343–1354.
7 Lopina, R. F., and Bergles, A. E., "Heat Transfer and Pressure Drop in Tape Generated Swirl Flow," M.I.T. Engineering Projects Lab Report No. 70281-47, June 1967.
8 Lopina, R. F., and Bergles, A. E., "Heat Transfer and Pressure Drop in Tape-Generated Swirl Flow of Single-Phase Water," JOURNAL OF HEAT TRANSFER, TRANS. ASME, Series C, Vol. 91, No. 3, Aug. 1969, pp. 434–442.
9 Bergles, A. E., and Rohsenow, W. M., "The Determination of Forced-Convection Surface-Boiling Heat Transfer," JOURNAL OF HEAT TRANSFER, TRANS. ASME, Series C, Vol. 86, No. 3, Aug. 1964, pp. 365–372.
10 Costello, C. P., and Tuthill, W. E., "Effects of Acceleration on Nucleate Pool Boiling," *Chem. Eng. Prog. Symp. Series*, Vol. 57, No. 32, 1961, pp. 189–196.
11 Merte, H., and Clark, J. A., "Pool Boiling in an Accelerating System," ASME Paper No. 60-HT-33.
12 Bergles, A. E., and Dormer, T., Jr., "Subcooled Boiling Pressure Drop with Water at Low Pressure," *International Journal of Heat and Mass Transfer*, Vol. 12, 1969, pp. 459–470.

An Analog for Thermal Conduction in Gases

WARREN F. PHILLIPS[1]

Nomenclature

A = surface area
E = molecular energy flux
F = shape factor
k = thermal conductivity
K = Knudsen number
l = a significant length
N = number of surfaces in the enclosure
Q = heat transfer rate
R = thermal resistance
T = absolute temperature
α = thermal accommodation coefficient
λ = molecular mean free path

Introduction

RECOGNIZING the similarity between free molecular conduction and pure radiation, the electrical-network analogy which Oppenheim [1][2] used for radiation analysis may be applied directly to the problem of evaluating the steady diffusion of thermal energy within an enclosure containing a Knudsen gas. Furthermore, with some modification the analogy may be applied in the transition regime. This analog provides a very simple solution technique that can be applied to engineering problems where complex geometries would otherwise force very lengthy numerical solutions. Not only does this approach allow the use of electrical-network computational techniques such as matrix algebra, but a solution may easily be obtained by the use of a passive analog computer. Also, since in rarefied flows radiation is frequently important, the analog solution becomes additionally attractive because of the ease of combining the conductive and radiative analogs.

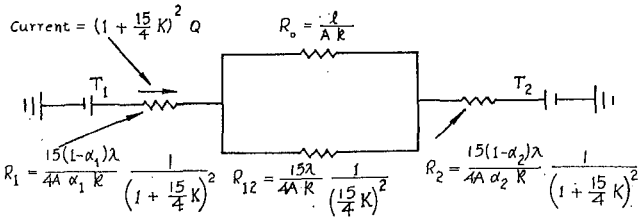

Fig. 1

The Free Molecule Limit

Consider an N-surface enclosure containing a Knudsen gas. A surface is defined as that portion of the enclosure having a uniform temperature, a uniform incident energy flux, and uniform surface properties. It shall be assumed, for the sake of simplicity, that all molecules are diffusely reflected from the surface, but the effects of specular reflection may be accounted for using the same techniques that are normally applied to radiative transfer, see Ziering and Sarofim [2]. In addition, it shall be assumed that all molecular energy modes that enter into an energy exchange with the surface are accommodated to the same degree. Under these assumptions, the thermal boundary condition at the i surface may be written as

$$Q_i = \frac{A_i\alpha_i}{1-\alpha_i}(E_{mi} - E_{ri}) \tag{1}$$

where Q_i is the net heat transfer from the i surface, E_{mi} is the usual Maxwellian energy flux corresponding to the surface temperature T_i, and E_{ri} is the energy flux reflected from surface i.

As was pointed out by Wu [3], the net energy transfer between any two surfaces A_i and A_j may be expressed in terms of the geometric shape factor in the same way that is used for radiative transfer. That is

$$Q_{ij} = A_iF_{ij}(E_{ri} - E_{rj}) \tag{2}$$

where F_{ij} is the diffuse geometric shape factor and Q_{ij} is the net energy transfer, related to Q_i by

$$Q_i = \sum_{j=1}^{N} Q_{ij} \tag{3}$$

Assuming that either the temperature or the heat flux is known at each surface, equations (1)–(3) represent a complete formulation, since the Maxwellian energy flux is related to the surface temperature T_i. For the sake of demonstration, we will consider the case of a monatomic Maxwellian gas, so that equations (1) and (2) become

$$Q_i = \frac{4A_i\alpha_i k}{15(1-\alpha_i)\lambda}(T_i - T_{ri}) \tag{4}$$

$$Q_{ij} = \frac{4A_iF_{ij}k}{15\lambda}(T_{ri} - T_{rj}) \tag{5}$$

where $T_{ri} = 15\lambda E_{ri}/4k$, k is the continuum thermal conductivity, and λ is the mean free path.

Equations (4) and (5) can easily be used to form an analog circuit for any N-surface enclosure. If we let temperature represent potential and heat flux represent current, then the thermal resistance associated with the non-ideal accommodation at any surface is

---

[1] Assistant Professor of Engineering, Oakland University, Rochester, Mich.

[2] Numbers in brackets designate References at end of technical brief.

Contributed by the Heat Transfer Division of THE AMERICAN SOCIETY OF MECHANICAL ENGINEERS. Manuscript received by the Heat Transfer Division April 17, 1972.

2 Gambill, W. R., Bundy, R. D., and Wansbrough, R. W., "Heat Transfer, Burnout, and Pressure Drop for Water in Swirl Flow Through Tubes with Internal Twisted Tapes," *Chem. Eng. Prog. Symp. Series*, Vol. 57, No. 32, 1961, pp. 127–137.
3 Feinstein, L., and Lundberg, R. E., "Fluid Friction and Boiling Heat Transfer with Water in Vortex Flow in Tubes Containing an Internal Twisted Tape," RADC-TRR-63-451, AD430889, June 1963.
4 Blatt, T. A., and Adt, R. R., Jr., "The Effects of Twisted Tape Swirl Generation on the Heat Transfer Rate and Pressure Drop of Boiling Freon 11 and Water," ASME Paper No. 63-WA-42.
5 Viskanta, R., "Critical Heat Flux for Water in Swirling Flow," *Nuclear Science and Engineering*, Vol. 10, 1961, pp. 202–203.
6 Bergles, A. E., Fuller, W., and Hynek, S. J., "Dispersed Flow Film Boiling of Nitrogen with Swirl Flow," *International Journal of Heat and Mass Transfer*, Vol. 14, 1971, pp. 1343–1354.
7 Lopina, R. F., and Bergles, A. E., "Heat Transfer and Pressure Drop in Tape Generated Swirl Flow," M.I.T. Engineering Projects Lab Report No. 70281-47, June 1967.
8 Lopina, R. F., and Bergles, A. E., "Heat Transfer and Pressure Drop in Tape-Generated Swirl Flow of Single-Phase Water," JOURNAL OF HEAT TRANSFER, TRANS. ASME, Series C, Vol. 91, No. 3, Aug. 1969, pp. 434–442.
9 Bergles, A. E., and Rohsenow, W. M., "The Determination of Forced-Convection Surface-Boiling Heat Transfer," JOURNAL OF HEAT TRANSFER, TRANS. ASME, Series C, Vol. 86, No. 3, Aug. 1964, pp. 365–372.
10 Costello, C. P., and Tuthill, W. E., "Effects of Acceleration on Nucleate Pool Boiling," *Chem. Eng. Prog. Symp. Series*, Vol. 57, No. 32, 1961, pp. 189–196.
11 Merte, H., and Clark, J. A., "Pool Boiling in an Accelerating System," ASME Paper No. 60-HT-33.
12 Bergles, A. E., and Dormer, T., Jr., "Subcooled Boiling Pressure Drop with Water at Low Pressure," *International Journal of Heat and Mass Transfer*, Vol. 12, 1969, pp. 459–470.

An Analog for Thermal Conduction in Gases

WARREN F. PHILLIPS[1]

Nomenclature

A = surface area
E = molecular energy flux
F = shape factor
k = thermal conductivity
K = Knudsen number
l = a significant length
N = number of surfaces in the enclosure
Q = heat transfer rate
R = thermal resistance
T = absolute temperature
α = thermal accommodation coefficient
λ = molecular mean free path

Introduction

RECOGNIZING the similarity between free molecular conduction and pure radiation, the electrical-network analogy which Oppenheim [1][2] used for radiation analysis may be applied directly to the problem of evaluating the steady diffusion of thermal energy within an enclosure containing a Knudsen gas. Furthermore, with some modification the analogy may be applied in the transition regime. This analog provides a very simple solution technique that can be applied to engineering problems where complex geometries would otherwise force very lengthy numerical solutions. Not only does this approach allow the use of electrical-network computational techniques such as matrix algebra, but a solution may easily be obtained by the use of a passive analog computer. Also, since in rarefied flows radiation is frequently important, the analog solution becomes additionally attractive because of the ease of combining the conductive and radiative analogs.

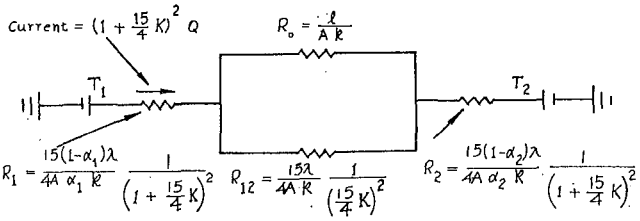

Fig. 1

The Free Molecule Limit

Consider an N-surface enclosure containing a Knudsen gas. A surface is defined as that portion of the enclosure having a uniform temperature, a uniform incident energy flux, and uniform surface properties. It shall be assumed, for the sake of simplicity, that all molecules are diffusely reflected from the surface, but the effects of specular reflection may be accounted for using the same techniques that are normally applied to radiative transfer, see Ziering and Sarofim [2]. In addition, it shall be assumed that all molecular energy modes that enter into an energy exchange with the surface are accommodated to the same degree. Under these assumptions, the thermal boundary condition at the i surface may be written as

$$Q_i = \frac{A_i\alpha_i}{1-\alpha_i}(E_{mi} - E_{ri}) \tag{1}$$

where Q_i is the net heat transfer from the i surface, E_{mi} is the usual Maxwellian energy flux corresponding to the surface temperature T_i, and E_{ri} is the energy flux reflected from surface i.

As was pointed out by Wu [3], the net energy transfer between any two surfaces A_i and A_j may be expressed in terms of the geometric shape factor in the same way that is used for radiative transfer. That is

$$Q_{ij} = A_iF_{ij}(E_{ri} - E_{rj}) \tag{2}$$

where F_{ij} is the diffuse geometric shape factor and Q_{ij} is the net energy transfer, related to Q_i by

$$Q_i = \sum_{j=1}^{N} Q_{ij} \tag{3}$$

Assuming that either the temperature or the heat flux is known at each surface, equations (1)–(3) represent a complete formulation, since the Maxwellian energy flux is related to the surface temperature T_i. For the sake of demonstration, we will consider the case of a monatomic Maxwellian gas, so that equations (1) and (2) become

$$Q_i = \frac{4A_i\alpha_i k}{15(1-\alpha_i)\lambda}(T_i - T_{ri}) \tag{4}$$

$$Q_{ij} = \frac{4A_iF_{ij}k}{15\lambda}(T_{ri} - T_{rj}) \tag{5}$$

where $T_{ri} = 15\lambda E_{ri}/4k$, k is the continuum thermal conductivity, and λ is the mean free path.

Equations (4) and (5) can easily be used to form an analog circuit for any N-surface enclosure. If we let temperature represent potential and heat flux represent current, then the thermal resistance associated with the non-ideal accommodation at any surface is

---

[1] Assistant Professor of Engineering, Oakland University, Rochester, Mich.

[2] Numbers in brackets designate References at end of technical brief.

Contributed by the Heat Transfer Division of THE AMERICAN SOCIETY OF MECHANICAL ENGINEERS. Manuscript received by the Heat Transfer Division April 17, 1972.

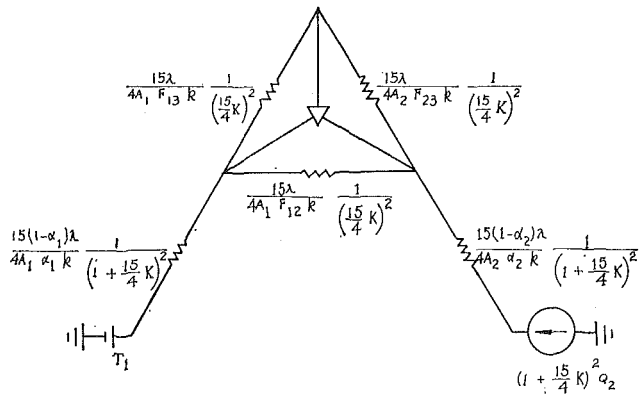

Fig. 2

$$R_i = \frac{15(1 - \alpha_i)\lambda}{4kA_i\alpha_i}$$

and that associated with the geometric relationship between A_i and A_j is

$$R_{ij} = \frac{15\lambda}{4kA_iF_{ij}}$$

The Transition Regime

In the transition regime between free molecule flow and continuum, the boundary conditions are unchanged, so equation (4) still holds. The transport from one surface to another, however, must be modified to include the effect of molecular collisions.

Consider first one-dimensional heat transfer between two parallel plates a distance l part. Lees' [4] moment solution to this problem for a monatomic Maxwellian gas gives the heat transfer from plate 1 to plate 2 as

$$Q_{12} = \frac{1}{1 + \frac{15}{4}\frac{\lambda}{l}}\frac{Ak}{l}(T_{r1} - T_{r2}) \tag{6}$$

For convenience, we multiply both this equation and equation (4) by the factor $\left(1 + \frac{15}{4}\frac{\lambda}{l}\right)^2$ to obtain

$$\left(1 + \frac{15}{4}\mathrm{K}\right)^2 Q_i = \frac{4A_i\alpha_i k}{15(1 - \alpha_i)\lambda}\left(1 + \frac{15}{4}\mathrm{K}\right)^2 (T_i - T_{ri}) \tag{7}$$

$$\left(1 + \frac{15}{4}\mathrm{K}\right)^2 Q_{12} = \left[\frac{Ak}{l} + \frac{4Ak}{15\lambda}\left(\frac{15}{4}\mathrm{K}\right)^2\right](T_{r1} - T_{r2}) \tag{8}$$

where K is the Knudsen number, $\mathrm{K} = \lambda/l$. If we let temperature represent potential and the product of heat flux and the factor $(1 + 15\mathrm{K}/4)^2$ represent current, we may use equations (7) and (8) to form the analog circuit shown in Fig. 1, provided we recognize the fact that the bracketed term in equation (8) may be considered as the equivalent conductance for two resistors in parallel. Notice that R_0 is exactly the continuum resistance for transport between the plates, while R_{12} is the free molecule transport resistance multiplied by the factor $(4/15\ \mathrm{K})^2$ and R_1 and R_2 are the appropriate resistances associated with the non-ideal accommodation at the plate surfaces.

If one is willing to approximate the rarefied effects in a multidimensional problem through a single Knudsen number, then this principle may easily be extended to the multidimensional case. Figure 2 shows the transition analog for a three-surface enclosure where surface 1 has a specified temperature, surface 2 has a specified heat flux, and surface 3 is insulated. Here the central triangle represents the continuum conductive analog for the enclosure, temperature again represents voltage, and $(1 + 15\mathrm{K}/4)^2Q$ is current. Note that this circuit reduces to the exact solution for both $\lambda \to \infty$ and $\lambda \to 0$.

References

1 Oppenheim, A. K., "Radiation Analysis by the Network Method," TRANS. ASME, Vol. 78, 1956, pp. 725–735.

2 Ziering, M. B., and Sarofim, A. F., "The Electrical Network Analog to Radiative Transfer: Allowance for Specular Reflection," JOURNAL OF HEAT TRANSFER, TRANS. ASME, Series C, Vol. 88, No. 3, Aug. 1966, pp. 341–342.

3 Wu, Y., "Kinetic Theory of Thermal Conduction in a Knudsen Gas," ASME Paper No. 69-WA/HT-20.

4 Lees, L., "A Kinetic Theory Description of Rarefied Gas Flows," GALCIT Hypersonic Research Project, Memo No. 51.

Non-Fourier Effects at High Heat Flux

M. J. MAURER[1] and H. A. THOMPSON[2]

This brief investigates analytically non-Fourier effects in high flux conditions using the relaxation model for heat conduction. Unlike the Fourier model, the relaxation model predicts an instantaneous jump in the surface temperature of solids subjected to a step change in the surface heat flux. Under sufficiently high flux, 10^7 w/cm^2, this jump in temperature may be several hundred degrees in magnitude, resulting in severe thermal stresses at the surface.

Introduction

IT IS WELL KNOWN that the Fourier model for heat conduction possesses several pathological anomalies, the most prominent one being an infinite speed of propagation. In order to eliminate these anomalies, Cattaneo [1, 2][3] and Vernotte [3–5] independently postulated a new, time-dependent relaxation model for the heat flux:

$$\mathbf{q} = -K\nabla T - \tau\frac{\partial}{\partial t}(\mathbf{q}) \tag{1}$$

where the dependent variables are the heat-flux vector $\mathbf{q}$ and temperature T and the independent variables are the position vector $\mathbf{x}$ and time t. The transport coefficients for the relaxation model are the thermal conductivity K and the relaxation time τ.

Substitution of the heat-flux relaxation model given by equation (1) into the energy equation for an inexpansible solid yields the relaxation-model form of the heat conduction equation

$$\kappa\nabla^2 T = \frac{\partial T}{\partial t} + \tau\frac{\partial^2 T}{\partial t^2} \tag{2}$$

where κ is the thermal diffusivity. Equation (2) is hyperbolic in form and therefore describes the behavior of a damped temperature wave with a finite speed of propagation v given by $v = \sqrt{\kappa/\tau}$. In the limit as $\tau \to 0$, equation (2) reduces to its usual parabolic form and the relaxation model, equation (1), reduces to the Fourier model for the heat flux. Under steady-state conditions, the relaxation model reduces to the Fourier model even when $\tau \neq 0$. Hence the temperatures predicted by the two models will differ only under non-steady-state conditions.

[1] Assistant Professor, Mechanical Engineering Department, California State University, Los Angeles, Calif.

[2] Professor, Mechanical Engineering Department, Tulane University, New Orleans, La. Mem. ASME.

[3] Numbers in brackets designate References at end of technical brief.

Contributed by the Heat Transfer Division of THE AMERICAN SOCIETY OF MECHANICAL ENGINEERS. Manuscript received by the Heat Transfer Division September 29, 1972.

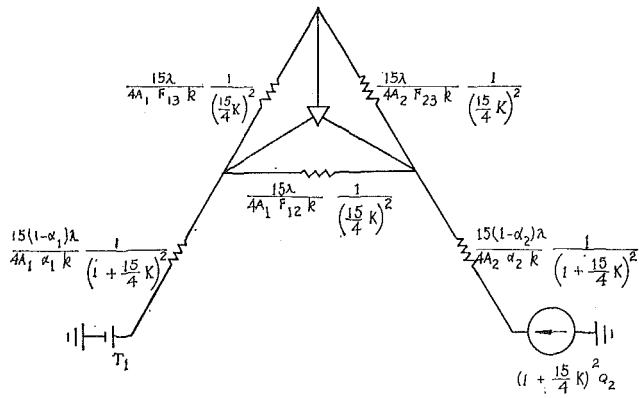

Fig. 2

$$R_i = \frac{15(1 - \alpha_i)\lambda}{4kA_i\alpha_i}$$

and that associated with the geometric relationship between A_i and A_j is

$$R_{ij} = \frac{15\lambda}{4kA_iF_{ij}}$$

The Transition Regime

In the transition regime between free molecule flow and continuum, the boundary conditions are unchanged, so equation (4) still holds. The transport from one surface to another, however, must be modified to include the effect of molecular collisions.

Consider first one-dimensional heat transfer between two parallel plates a distance l part. Lees' [4] moment solution to this problem for a monatomic Maxwellian gas gives the heat transfer from plate 1 to plate 2 as

$$Q_{12} = \frac{1}{1 + \frac{15}{4}\frac{\lambda}{l}}\frac{Ak}{l}(T_{r1} - T_{r2}) \tag{6}$$

For convenience, we multiply both this equation and equation (4) by the factor $\left(1 + \frac{15}{4}\frac{\lambda}{l}\right)^2$ to obtain

$$\left(1 + \frac{15}{4}\mathrm{K}\right)^2 Q_i = \frac{4A_i\alpha_i k}{15(1 - \alpha_i)\lambda}\left(1 + \frac{15}{4}\mathrm{K}\right)^2 (T_i - T_{ri}) \tag{7}$$

$$\left(1 + \frac{15}{4}\mathrm{K}\right)^2 Q_{12} = \left[\frac{Ak}{l} + \frac{4Ak}{15\lambda}\left(\frac{15}{4}\mathrm{K}\right)^2\right](T_{r1} - T_{r2}) \tag{8}$$

where K is the Knudsen number, $\mathrm{K} = \lambda/l$. If we let temperature represent potential and the product of heat flux and the factor $(1 + 15\mathrm{K}/4)^2$ represent current, we may use equations (7) and (8) to form the analog circuit shown in Fig. 1, provided we recognize the fact that the bracketed term in equation (8) may be considered as the equivalent conductance for two resistors in parallel. Notice that R_0 is exactly the continuum resistance for transport between the plates, while R_{12} is the free molecule transport resistance multiplied by the factor $(4/15\ \mathrm{K})^2$ and R_1 and R_2 are the appropriate resistances associated with the non-ideal accommodation at the plate surfaces.

If one is willing to approximate the rarefied effects in a multidimensional problem through a single Knudsen number, then this principle may easily be extended to the multidimensional case. Figure 2 shows the transition analog for a three-surface enclosure where surface 1 has a specified temperature, surface 2 has a specified heat flux, and surface 3 is insulated. Here the central triangle represents the continuum conductive analog for the enclosure, temperature again represents voltage, and $(1 + 15\mathrm{K}/4)^2Q$ is current. Note that this circuit reduces to the exact solution for both $\lambda \to \infty$ and $\lambda \to 0$.

References

1 Oppenheim, A. K., "Radiation Analysis by the Network Method," TRANS. ASME, Vol. 78, 1956, pp. 725–735.

2 Ziering, M. B., and Sarofim, A. F., "The Electrical Network Analog to Radiative Transfer: Allowance for Specular Reflection," JOURNAL OF HEAT TRANSFER, TRANS. ASME, Series C, Vol. 88, No. 3, Aug. 1966, pp. 341–342.

3 Wu, Y., "Kinetic Theory of Thermal Conduction in a Knudsen Gas," ASME Paper No. 69-WA/HT-20.

4 Lees, L., "A Kinetic Theory Description of Rarefied Gas Flows," GALCIT Hypersonic Research Project, Memo No. 51.

Non-Fourier Effects at High Heat Flux

M. J. MAURER[1] and H. A. THOMPSON[2]

This brief investigates analytically non-Fourier effects in high flux conditions using the relaxation model for heat conduction. Unlike the Fourier model, the relaxation model predicts an instantaneous jump in the surface temperature of solids subjected to a step change in the surface heat flux. Under sufficiently high flux, 10^7 w/cm^2, this jump in temperature may be several hundred degrees in magnitude, resulting in severe thermal stresses at the surface.

Introduction

IT IS WELL KNOWN that the Fourier model for heat conduction possesses several pathological anomalies, the most prominent one being an infinite speed of propagation. In order to eliminate these anomalies, Cattaneo [1, 2][3] and Vernotte [3–5] independently postulated a new, time-dependent relaxation model for the heat flux:

$$\mathbf{q} = -K\nabla T - \tau\frac{\partial}{\partial t}(\mathbf{q}) \tag{1}$$

where the dependent variables are the heat-flux vector $\mathbf{q}$ and temperature T and the independent variables are the position vector $\mathbf{x}$ and time t. The transport coefficients for the relaxation model are the thermal conductivity K and the relaxation time τ.

Substitution of the heat-flux relaxation model given by equation (1) into the energy equation for an inexpansible solid yields the relaxation-model form of the heat conduction equation

$$\kappa\nabla^2 T = \frac{\partial T}{\partial t} + \tau\frac{\partial^2 T}{\partial t^2} \tag{2}$$

where κ is the thermal diffusivity. Equation (2) is hyperbolic in form and therefore describes the behavior of a damped temperature wave with a finite speed of propagation v given by $v = \sqrt{\kappa/\tau}$. In the limit as $\tau \to 0$, equation (2) reduces to its usual parabolic form and the relaxation model, equation (1), reduces to the Fourier model for the heat flux. Under steady-state conditions, the relaxation model reduces to the Fourier model even when $\tau \neq 0$. Hence the temperatures predicted by the two models will differ only under non-steady-state conditions.

[1] Assistant Professor, Mechanical Engineering Department, California State University, Los Angeles, Calif.

[2] Professor, Mechanical Engineering Department, Tulane University, New Orleans, La. Mem. ASME.

[3] Numbers in brackets designate References at end of technical brief.

Contributed by the Heat Transfer Division of THE AMERICAN SOCIETY OF MECHANICAL ENGINEERS. Manuscript received by the Heat Transfer Division September 29, 1972.

By introducing a scaling factor δ into equation (2) such that $t = \delta^2 t'$ and $\mathbf{x} = \delta \mathbf{x}'$, it may be shown that relaxation-model solutions asymptotically approach Fourier-model solutions when $\tau/\delta^2 \ll O(1)$, that is, for large t and $\mathbf{x}$. The magnitude of τ plays, therefore, a primary role in distinguishing the domain where the behavior of the temperature is wavelike from the domain of diffusive behavior according to the Fourier model. Various investigators have estimated the magnitude of τ and found it to range from 10^{-10} sec for gases at standard conditions to 10^{-14} sec for metals [6], with the values of τ for liquids [7] and insulators [8] falling within this range.

This work considers a problem posed by Brazel and Nolan [9], who were concerned with the effects of extremely high surface heat fluxes. Examinations of this problem showed that (*a*) Brazel and Nolan improperly applied the relaxation model to the problem they posed, (*b*) an abnormally high temperature was predicted in the vicinity of the surface by a properly formulated relaxation model, and (*c*) the magnitude of the temperature anomaly was significant only at extremely high heat fluxes.

The hyperbolic heat equation has also received some attention in the engineering literature, for instance Baumeister and Hamill [10] and Chan, Low, and Mueller [11].

Heat Pulse Problem

Two major anxieties motivated Brazel and Nolan's [9] investigation of the relaxation model for solids under extremely high surface fluxes. Because of the relaxation term, (*a*) the surface temperatures might be greater than those predicted by the Fourier model and (*b*) the temperature gradient in the vicinity of the surface might also be abnormally high. If these effects occurred, structural failure might result because of excessive thermal stresses near the surface of the solid where the structural strength was already reduced by the abnormally high temperature.

To evaluate the potential for these effects, Brazel and Nolan posed the following boundary-value problem using the relaxation model. They considered the case of a pulse of high-tensity electromagnetic radiation of nuclear origin with a thermal-flux level of the order of 10^7 w/cm^2 having a rise time of the order of 10^{-12} sec with a period of the order of 10^{-9} sec. They supposed that such a heat pulse struck, so that it was uniformly and completely absorbed, a thick slab of refractory, reinforced phenolic char having thermal properties of $K = 0.017$ w/cm^2-deg C, $\kappa = 8.1 \times 10^{-3}$ cm^2/sec, and $\tau = 2.9 \times 10^{-11}$ sec.

Since only the short-time response of the slab was of interest, i.e., $t \sim O(\tau)$, the slab was assumed to be thick relative to vt and was treated as a semi-infinite solid. In addition, since the heat pulse was assumed to be uniformly absorbed, the slab was treated as a one-dimensional semi-infinite solid. The heat pulse, moreover, was simplified and treated as a step change in the surface flux for $t \sim O(\tau)$.

In this problem, assuming the initial temperature distribution of the slab is uniform and the initial heat flux is zero, which is equivalent to requiring the initial time rate of change of the temperature to be zero, yields initial conditions

$$T(x, 0) = 0 \tag{3}$$

and

$$\frac{\partial T}{\partial t}(x, 0) = 0 \quad \text{or} \quad q(x, 0) = 0 \tag{4}$$

where the initial temperature has been used as a reference temperature level. Treating the slab as a semi-infinite solid requires that the solution be bounded at infinity.

The heat-flux boundary condition at $x = 0$ may be formulated as

$$q(0, t) = -K \frac{\partial T}{\partial x}(0, t) - \tau \frac{\partial q}{\partial t}(0, t) = F_0 \tag{5}$$

where F_0 is a constant.

The proper formulation of the condition on the temperature gradient requires that *both* the flux and the time rate of change of the flux at the surface must be specified. Brazel and Nolan in their analysis set the heat flux equal to the temperature gradient, just as would be done in applying the Fourier model, so that they implicitly imposed the hidden boundary condition at the surface that the time rate of change of the heat flux is zero for $t = 0$. This procedure yielded erroneous results concerning the short-time temperature response of the slab, since the effect of the relaxation term at the boundary was neglected.

Taking the Laplace transform of the heat-flux equation (5) yields

$$\hat{q}(0, s) = -K \frac{d\hat{T}}{dx}(0, s) - \tau s \hat{q}(0, s) = F_0/s \tag{6}$$

where s is the Laplace transform variable. Substituting $\hat{q} = F_0/s$ and solving for the temperature gradient yields

$$\frac{d\hat{T}}{dx}(0, s) = -\frac{F_0}{K} \frac{(1 + \tau s)}{s} \tag{7}$$

This result differs from Brazel and Nolan's development by the presence of the τs term.

Taking the Laplace transform of the heat conduction equation (2), using the initial conditions given by equations (3) and (4), and applying the flux boundary condition in the form given by equation (7) yields as the bounded part of the solution as $x \to \infty$

$$\frac{\hat{T}(x, s)}{F_0 \sqrt{\kappa\tau}/K} = \left(1 + \frac{1}{\tau s}\right) \frac{\exp\left\{-\frac{x}{v}\sqrt{s(s + 1/\tau)}\right\}}{\sqrt{s(s + 1/\tau)}} \tag{8}$$

Inversion yields

$$\frac{T(x, t)}{F_0 \sqrt{\kappa\tau}/K} = H(t - x/v)\left\{e^{-t/2\tau} I_0\left(\sqrt{\left(\frac{u}{2\tau}\right)^2 - \frac{x^2}{4\kappa\tau}}\right) + \frac{1}{\tau}\int_0^t e^{-u/2\tau} I_0\left(\sqrt{\left(\frac{u}{2\tau}\right)^2 - \frac{x^2}{4\kappa\tau}}\right) du\right\} \tag{9}$$

where $H(t)$ is the Heaviside unit step function and I_0 is the modified Bessel function of zero order. For $x > 0$ it is necessary to evaluate the integral in equation (9) by some approximate or numerical method. Fortunately, in the special case of $x = 0$, that is, for the surface temperature which is of particular interest, the integral may be evaluated in closed form by inverting equation (8) with $x = 0$.

The solution for the surface temperature is

$$\frac{T(0, t)}{F_0 \sqrt{\kappa\tau}/K} = e^{-t/2\tau}\left[(1 + t/\tau) I_0(t/2\tau) + (t/\tau) I_1(t/2\tau)\right] \tag{10}$$

where I_1 is the modified Bessel function of the first order. Of special interest is the response of the surface temperature as $t \to 0$. As $t \to 0$ the surface temperature given by equation (10) approaches the limit given by

$$\lim_{t \to 0} T(0, t) \to \frac{F_0 \sqrt{\kappa\tau}}{K} \tag{11}$$

indicating that a solid subjected to a step change in the surface flux also experiences a jump in the surface temperature. This response is in sharp contrast to that of the Fourier model in which the surface temperature approaches zero as $t \to 0$. The magnitude of the initial temperature jump for refractory, reinforced phenolic char subjected to a step change in the surface flux of 10^7 w/cm^2 is approximately 300 deg C. It is easily shown, however, that the surface temperature deviation from the Fourier-model value becomes less than 1 percent in about $\tau \sim O(50\tau)$.

Finally, since the complete solution, equation (9), contains a Heaviside unit step function with argument $x = vt$, the thickness of the thermal boundary layer associated with the jump in the surface temperature must be extremely small for $t \sim O(\tau)$. This implies the existence of a large temperature gradient in the vicinity of the surface where the maximum gradient occurs. For $t > 0$ it can be shown to be $-F_0/K$, the same value as the Fourier gradient, but in the limit as $t \to 0$ it can be shown that the temperature gradient at the surface approaches infinity. The magnitude of the temperature gradient at the surface for $t > 0$ is of the order 10^8 deg C/cm for refractory, reinforced char subjected to a flux of 10^7 w/cm^2.

It is clear from the preceding discussion that both the major anxieties which motivated the investigation of Brazel and Nolan were justified, that is, both the temperature and temperature gradient predicted by the relaxation model are greater than the corresponding values for the Fourier model. For heat fluxes of the order of 10^7 w/cm^2 or greater, these deviations from the Fourier model will be significant. The implications of such deviations with regard to structural integrity are also clear; any close design based on the Fourier-model predictions would fail in thermal shock at a sufficiently high flux level.

References

1 Cattaneo, C., "On the Conduction of Heat," Atti Del Seminar, Mat. Fis. Univ., Modena, Vol. 3, 1948, p. 3.

2 Cattaneo, C., "A Form of Heat Conduction Equation which Eliminates the Paradox of Instantaneous Propagation," *Compt. Rend.*, Vol. 247, 1958, p. 431.

3 Vernotte, P., "Paradoxes in the Continuous Theory of the Heat Equation," *Compt. Rend.*, Vol. 246, 1958, p. 3154.

4 Vernotte, P., "The True Heat Equation," *Compt. Rend.*, Vol. 247, 1958, p. 2103.

5 Vernotte, P., "Some Possible Complications in the Phenomena of Thermal Conduction," *Compt. Rend.*, Vol. 252, 1961, p. 2190.

6 Maurer, M. J., "Relaxation Model for Heat Conduction in Metals," *Journal of Applied Physics*, Vol. 40, 1969, p. 5123.

7 Nettleton, R. E., "Relaxation Theory of Thermal Conduction in Liquids," *Physics of Fluids*, Vol. 3, 1960, p. 216.

8 Chester, M., "Second Sound in Solids," *Phys. Rev.*, Vol. 131, 1963, p. 2013.

9 Brazel, J. P., and Nolan, E. J., "Non-Fourier Effects in the Transmission of Heat," *Proceedings 6th Conference on Thermal Conductivity*, Dayton, Ohio, Oct. 19–21, 1966.

10 Baumeister, K. J., and Hamill, T. D., "Hyperbolic Heat-Conduction Equation—A Solution for the Semi-Infinite Body Problem," JOURNAL OF HEAT TRANSFER, TRANS. ASME, Series C, Vol. 93, No. 1, Feb. 1971, pp. 126–127.

11 Chan, S. H., Low, M. J. D., and Mueller, W. K., "Hyperbolic Heat Conduction in Catalytic Supported Crystallites," *AIChE Journal*, Vol. 17, 1971, p. 1499.

Method-of-Characteristics Study of Transient Single-Pass Heat-exchange Processes[1]

W. A. McNEILL[2]

Nomenclature

Starred superscripts denote dimensional quantities.

A^* = heat-exchange area separating streams 1 and 2
A_t^* = maximum value of A^* in counter-flow problem
A = $A^*/(\dot{m}_1^* C_{p1}^*/U^*)$
C_{pi}^*, C_{vi}^* = specific heat at constant pressure and volume, respectively, of ith stream
K_i^* = mass contained in ith stream per unit exchange area ΔA^*
K = $K_2^* C_{v2}^*/(K_1^* C_{v1}^*)$
Δm_i^* = mass contained in ith stream corresponding to increment ΔA^*
$\dot{m}_i^*$ = mass flow rate of ith stream
M = $\dot{m}_2^* C_{p2}^*/(\dot{m}_1^* C_{p1}^*)$
$\mathbf{t}^*$ = time
$\mathbf{t}$ = $\mathbf{t}^*/(K_1^* C_{v1}^*/U^*)$
$\mathbf{t}_s$ = dimensionless time required for steady-state condition to exist
$\mathbf{t}_a$ = dimensionless time required for hot-fluid front to reach A_t
t_i^* = bulk temperature of ith stream
t_h^*, t_c^* = specified inlet temperatures, equations (3), (5)
t_i = $t_i^*/(t_h^* - t_c^*)$
U^* = overall heat-transfer coefficient
α, β = distances measured along characteristic lines

MUCH theoretical work has been devoted to the study of transient effects in recuperative and regenerative heating [1, 2].[3] In one study [2, p. 397] Carslaw and Jaeger demonstrated the application of the Laplace transformation to the transient behavior of an infinite single-pass heat exchanger in counter flow. Lacking is an approach to transient heat exchange which clearly displays its traveling-wave nature, as revealed through the method of characteristics. This method is applied herein to obtain results for parallel flow and counter flow, displayed in concise form suitable for preliminary design work.

The present problem is an extension of the work of Carslaw and Jaeger, and their introductory description will suffice here, noting the following points to be considered in the present problem:

1 The exchanger is finite, and both parallel flow and counter flow are considered.

2 The initial common temperature of the streams is t_c^* (initial temperatures were taken to be zero in [2]).

3 The exchange area A^* is used as an independent variable instead of the distance χ used in [2]. Certain differences in nomenclature from [2] also appear herein.

For parallel flow, an energy balance leads to the following (nondimensional) equations:

$$-\frac{\partial t_1}{\partial A} = t_1 - t_2 + \frac{\partial t_1}{\partial \mathbf{t}} \qquad -M\frac{\partial t_2}{\partial A} = -(t_1 - t_2) + K\frac{\partial t_2}{\partial \mathbf{t}} \quad (1)$$

These equations are hyperbolic provided $K/M \neq 1$. For the hyperbolic case, two distinct sets of characteristic curves exist, having the constant slopes $d\mathbf{t}/dA = K/M$ and $d\mathbf{t}/dA = 1$. The symbols α and β will denote distances along the lines having slopes K/M and 1, respectively. A coordinate transformation is now introduced which permits the governing equations to be written in terms of distances measured along the characteristic lines [3, pp. 38–44]. In matrix notation, the characteristic variables are related to the original variables as follows:

$$\begin{Bmatrix} \mathbf{t} \\ A \end{Bmatrix} = \begin{vmatrix} \dfrac{K/M}{[1 + (K/M)^2]^{0.5}} & \dfrac{1}{(2)^{0.5}} \\ \dfrac{1}{[1 + (K/M)^2]^{0.5}} & \dfrac{1}{(2)^{0.5}} \end{vmatrix} \begin{Bmatrix} \alpha \\ \beta \end{Bmatrix}$$

Equations (1) in terms of the α and β variables become

$$-\frac{\partial t_1}{\partial \beta} + \frac{1}{(2)^{0.5}}(t_2 - t_1) = 0$$

$$\frac{\partial t_2}{\partial \alpha} + \frac{1}{(K^2 + M^2)^{0.5}}(t_2 - t_1) = 0 \quad (2)$$

[1] This research was sponsored by the University of South Alabama Research Committee.

[2] Associate Professor of Mechanical Engineering, University of South Alabama, Mobile, Ala. Assoc. Mem. ASME.

[3] Numbers in brackets designate References at end of technical brief.

Contributed by the Heat Transfer Division of THE AMERICAN SOCIETY OF MECHANICAL ENGINEERS. Manuscript received by the Heat Transfer Division August 17, 1972.

Finally, since the complete solution, equation (9), contains a Heaviside unit step function with argument $x = vt$, the thickness of the thermal boundary layer associated with the jump in the surface temperature must be extremely small for $t \sim O(\tau)$. This implies the existence of a large temperature gradient in the vicinity of the surface where the maximum gradient occurs. For $t > 0$ it can be shown to be $-F_0/K$, the same value as the Fourier gradient, but in the limit as $t \to 0$ it can be shown that the temperature gradient at the surface approaches infinity. The magnitude of the temperature gradient at the surface for $t > 0$ is of the order 10^8 deg C/cm for refractory, reinforced char subjected to a flux of 10^7 w/cm^2.

It is clear from the preceding discussion that both the major anxieties which motivated the investigation of Brazel and Nolan were justified, that is, both the temperature and temperature gradient predicted by the relaxation model are greater than the corresponding values for the Fourier model. For heat fluxes of the order of 10^7 w/cm^2 or greater, these deviations from the Fourier model will be significant. The implications of such deviations with regard to structural integrity are also clear; any close design based on the Fourier-model predictions would fail in thermal shock at a sufficiently high flux level.

References

1 Cattaneo, C., "On the Conduction of Heat," Atti Del Seminar, Mat. Fis. Univ., Modena, Vol. 3, 1948, p. 3.

2 Cattaneo, C., "A Form of Heat Conduction Equation which Eliminates the Paradox of Instantaneous Propagation," *Compt. Rend.*, Vol. 247, 1958, p. 431.

3 Vernotte, P., "Paradoxes in the Continuous Theory of the Heat Equation," *Compt. Rend.*, Vol. 246, 1958, p. 3154.

4 Vernotte, P., "The True Heat Equation," *Compt. Rend.*, Vol. 247, 1958, p. 2103.

5 Vernotte, P., "Some Possible Complications in the Phenomena of Thermal Conduction," *Compt. Rend.*, Vol. 252, 1961, p. 2190.

6 Maurer, M. J., "Relaxation Model for Heat Conduction in Metals," *Journal of Applied Physics*, Vol. 40, 1969, p. 5123.

7 Nettleton, R. E., "Relaxation Theory of Thermal Conduction in Liquids," *Physics of Fluids*, Vol. 3, 1960, p. 216.

8 Chester, M., "Second Sound in Solids," *Phys. Rev.*, Vol. 131, 1963, p. 2013.

9 Brazel, J. P., and Nolan, E. J., "Non-Fourier Effects in the Transmission of Heat," *Proceedings 6th Conference on Thermal Conductivity*, Dayton, Ohio, Oct. 19–21, 1966.

10 Baumeister, K. J., and Hamill, T. D., "Hyperbolic Heat-Conduction Equation—A Solution for the Semi-Infinite Body Problem," JOURNAL OF HEAT TRANSFER, TRANS. ASME, Series C, Vol. 93, No. 1, Feb. 1971, pp. 126–127.

11 Chan, S. H., Low, M. J. D., and Mueller, W. K., "Hyperbolic Heat Conduction in Catalytic Supported Crystallites," *AIChE Journal*, Vol. 17, 1971, p. 1499.

Method-of-Characteristics Study of Transient Single-Pass Heat-exchange Processes[1]

W. A. McNEILL[2]

Nomenclature

Starred superscripts denote dimensional quantities.

A^* = heat-exchange area separating streams 1 and 2
A_l^* = maximum value of A^* in counter-flow problem
A = $A^*/(\dot{m}_1^* C_{p1}^*/U^*)$
C_{pi}^*, C_{vi}^* = specific heat at constant pressure and volume, respectively, of ith stream
K_i^* = mass contained in ith stream per unit exchange area ΔA^*
K = $K_2^* C_{v2}^*/(K_1^* C_{v1}^*)$
Δm_i^* = mass contained in ith stream corresponding to increment ΔA^*
$\dot{m}_i^*$ = mass flow rate of ith stream
M = $\dot{m}_2^* C_{p2}^*/(\dot{m}_1^* C_{p1}^*)$
$\mathbf{t}^*$ = time
$\mathbf{t}$ = $\mathbf{t}^*/(K_1^* C_{v1}^*/U^*)$
$\mathbf{t}_s$ = dimensionless time required for steady-state condition to exist
$\mathbf{t}_a$ = dimensionless time required for hot-fluid front to reach A_l
t_i^* = bulk temperature of ith stream
t_h^*, t_c^* = specified inlet temperatures, equations (3), (5)
t_i = $t_i^*/(t_h^* - t_c^*)$
U^* = overall heat-transfer coefficient
α, β = distances measured along characteristic lines

MUCH theoretical work has been devoted to the study of transient effects in recuperative and regenerative heating [1, 2].[3] In one study [2, p. 397] Carslaw and Jaeger demonstrated the application of the Laplace transformation to the transient behavior of an infinite single-pass heat exchanger in counter flow. Lacking is an approach to transient heat exchange which clearly displays its traveling-wave nature, as revealed through the method of characteristics. This method is applied herein to obtain results for parallel flow and counter flow, displayed in concise form suitable for preliminary design work.

The present problem is an extension of the work of Carslaw and Jaeger, and their introductory description will suffice here, noting the following points to be considered in the present problem:

1 The exchanger is finite, and both parallel flow and counter flow are considered.

2 The initial common temperature of the streams is t_c^* (initial temperatures were taken to be zero in [2]).

3 The exchange area A^* is used as an independent variable instead of the distance χ used in [2]. Certain differences in nomenclature from [2] also appear herein.

For parallel flow, an energy balance leads to the following (nondimensional) equations:

$$-\frac{\partial t_1}{\partial A} = t_1 - t_2 + \frac{\partial t_1}{\partial \mathbf{t}} \qquad -M\frac{\partial t_2}{\partial A} = -(t_1 - t_2) + K\frac{\partial t_2}{\partial \mathbf{t}} \quad (1)$$

These equations are hyperbolic provided $K/M \neq 1$. For the hyperbolic case, two distinct sets of characteristic curves exist, having the constant slopes $d\mathbf{t}/dA = K/M$ and $d\mathbf{t}/dA = 1$. The symbols α and β will denote distances along the lines having slopes K/M and 1, respectively. A coordinate transformation is now introduced which permits the governing equations to be written in terms of distances measured along the characteristic lines [3, pp. 38–44]. In matrix notation, the characteristic variables are related to the original variables as follows:

$$\begin{Bmatrix} \mathbf{t} \\ A \end{Bmatrix} = \begin{vmatrix} \dfrac{K/M}{[1 + (K/M)^2]^{0.5}} & \dfrac{1}{(2)^{0.5}} \\ \dfrac{1}{[1 + (K/M)^2]^{0.5}} & \dfrac{1}{(2)^{0.5}} \end{vmatrix} \begin{Bmatrix} \alpha \\ \beta \end{Bmatrix}$$

Equations (1) in terms of the α and β variables become

$$-\frac{\partial t_1}{\partial \beta} + \frac{1}{(2)^{0.5}}(t_2 - t_1) = 0$$

$$\frac{\partial t_2}{\partial \alpha} + \frac{1}{(K^2 + M^2)^{0.5}}(t_2 - t_1) = 0 \quad (2)$$

---

[1] This research was sponsored by the University of South Alabama Research Committee.

[2] Associate Professor of Mechanical Engineering, University of South Alabama, Mobile, Ala. Assoc. Mem. ASME.

[3] Numbers in brackets designate References at end of technical brief.

Contributed by the Heat Transfer Division of THE AMERICAN SOCIETY OF MECHANICAL ENGINEERS. Manuscript received by the Heat Transfer Division August 17, 1972.

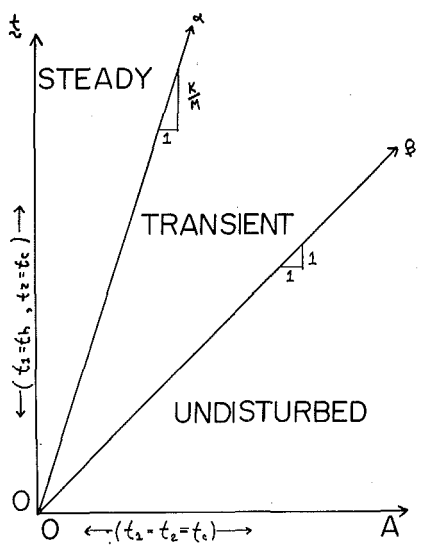

Fig. 1. Characteristic regions for parallel flow with $K/M > 1$

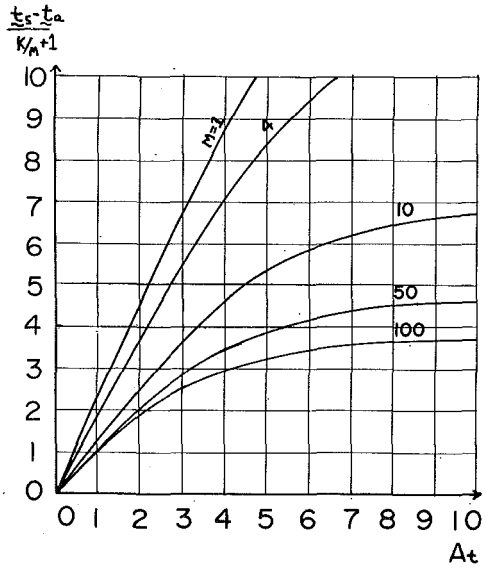

Fig. 2 Dimensionless time for steady state in counter flow

Initial and boundary conditions are

$$t_1^*\Big|_{\substack{t^*=0\\A^*\geq 0}} = t_2^*\Big|_{\substack{t^*=0\\A^*\geq 0}} = t_c^* \qquad t_1^*\Big|_{\substack{t^*>0\\A^*=0}} = t_h^* \qquad t_2^*\Big|_{\substack{t^*>0\\A^*=0}} = t_c^* \tag{3}$$

and are subsequently nondimensionalized for application to equations (2).

The characteristic regions for the problem described by equations (1) and (3) are shown in Fig. 1 for $K/M > 1$. Reference [4] may be consulted for a detailed discussion of characteristic regions of this type. Initial and boundary values of temperatures are listed on the A, $\mathbf{t}$ axes. The β line passing through the origin represents the movement of the "hot-fluid front," that is, the forwardmost point reached by the fluid introduced into stream 1 at $A^* = 0$, $\mathbf{t}^* = 0$. For $K/M > 1$ the temperature at a given point A begins to change when the hot-fluid front passes that position, and reaches the steady state at a time determined by the α line which passes through the origin.

For $K/M < 1$, however, the α line through the origin lies closer to the abscissa than does the corresponding β line. Thus the temperature of the fluid at a given position begins to change before the arrival of the hot-fluid front. In other words, a disturbance precedes the hot-fluid front due to the existence of circumstances under which fluid stream 2 is heated, and, moving more rapidly than stream 1, transfers heat to that part of stream 1 ahead of the hot-fluid front.

If $K/M = 1$, equations (1) are parabolic, having only one set of characteristics. In this special case the transient region disappears, and, ideally, the temperature at any position would go from the undisturbed state directly to the steady state with the passing of the hot-fluid front.

For counter flow, the development of the governing equations proceeds in the same manner as before, and the following dimensionless equations are obtained:

$$-\frac{\partial t_1}{\partial A} = t_1 - t_2 + \frac{\partial t_1}{\partial \mathbf{t}} \qquad M\frac{\partial t_2}{\partial A} = -(t_1 - t_2) + K\frac{\partial t_2}{\partial \mathbf{t}} \tag{4}$$

These equations are always hyperbolic, having two distinct sets of constant-slope characteristics, namely $d\mathbf{t}/dA = -K/M$ (α lines) and $d\mathbf{t}/dA = 1$ (β lines).

As before, a coordinate transformation is introduced so that equations (4) are written in terms of distances measured along the α and β characteristic lines. Interestingly, the transformed equations are precisely equations (2). (It should be emphasized, however, that the α characteristic lines are not the same family for the counter-flow as for the parallel-flow problem.)

For the counter-flow problem, the initial and boundary conditions are

$$t_1^*\Big|_{\substack{t^*=0\\0\leq A^*\leq A_t^*}} = t_2^*\Big|_{\substack{t^*=0\\0\leq A^*\leq A_t^*}} = t_c^* \qquad t_1^*\Big|_{\substack{t^*>0\\A^*=0}} = t_h^* \qquad t_2^*\Big|_{\substack{t^*>0\\A^*=A_t^*}} = t_c^* \tag{5}$$

The β line which passes through the origin represents, as before, the position of the hot-fluid front, and the region below this line is undisturbed for all K, M and $0 \leq A \leq A_t$. It is not possible, however, to identify a distinct steady-state region as was done previously. Instead, the steady condition at any value of A is approached asymptotically with increasing $\mathbf{t}$.

Numerical methods were used to solve the counter-flow problem, replacing the derivative terms in the transformed equations (2) by first-order forward-difference approximations and "marching out" [4] the solutions in increments of $\Delta\mathbf{t}$. The known steady-state solution for $t_1 - t_2$ provided a check on the accuracy of the numerical procedure.

Although the steady state is approached asymptotically, it was observed that it is possible to identify in each numerical solution a point $\mathbf{t} = \mathbf{t}_s$ such that in the neighborhood of this point the solution curve "flattens" considerably, exhibiting a sharply decreased rate of change for $\mathbf{t} > \mathbf{t}_s$. The value $\mathbf{t}_s$ thus represents a logical "steady-state" value for design applications. It was found that a suitable formalization for locating $\mathbf{t}_s$ in the numerical computation was to require that $\mathbf{t}_s$ be the smallest value such that for $\mathbf{t} > \mathbf{t}_s$ and $0 \leq A \leq A_t$ convergence to four decimal places exists over a five-step interval in the integration. A division of the A axis by 45 equally spaced points, with α and β lines originating at each point, was employed to specify the coordinate increments. In all cases considered, a progression of 100 increments in the $\mathbf{t}$ direction was sufficient for convergence. Figure 2 displays the results of these numerical computations over a wide range of the variables involved. The value $\mathbf{t} = \mathbf{t}_a$ in Fig. 2 denotes the arrival of the hot fluid at A_t. (Of course $\mathbf{t}_a$ is numerically equal to A_t, since the slope of the β line is unity.)

In summary, the time required for a steady condition to exist may be obtained as follows:

For parallel flow

$$\mathbf{t}_s = (K/M)A \quad \text{if} \quad K/M > 1$$

$$\mathbf{t}_s = 1 \quad \text{if} \quad K/M \leq 1$$

For counter flow refer to Fig. 2.

References

1 Jakob, M., *Heat Transfer*, Vol. II, John Wiley & Sons, New York, N. Y., 1967, pp. 261–341.

2 Carslaw, H. S., and Jaeger, J. C., *Conduction of Heat in Solids*, 2nd ed., Oxford at the Clarendon Press, 1959, pp. 397–398.

3 Forsythe, G. E., and Wasow, W. R., *Finite-Difference Methods for Partial Differential Equations*, John Wiley & Sons, New York, N. Y., 1967.

4 Crandall, S. H., *Engineering Analysis*, McGraw-Hill, New York, N. Y., 1956, pp. 351–371.

ERRATUM

In the paper "Periodic Heat Transfer in Straight Fins" by Prof. J. W. Yang, which appeared in the JOURNAL OF HEAT TRANSFER, TRANS. ASME, Series C, Vol. 94, No. 3, Aug. 1972, pp. 310–314, the ordinate of Fig. 9 should be $\eta/2$.